INVESTIGATING ENERGY METABOLISM IN MOTOR NEURON DISEASE USING PHOSPHORUS MAGNETIC RESONANCE SPECTROSCOPY

Matilde Sassani

Supervisors:

Thomas M. Jenkins and Iain D. Wilkinson

May 2021

Submitted for the degree of Doctor of Philosophy (PhD)

The University of Sheffield, UK

Department of Neuroscience

Sheffield Institute for Translational Neuroscience (SITraN)

ABSTRACT

Motor neuron disease (MND) is a grievous condition characterised by progressive neurodegeneration and weakness. Death, usually by respiratory failure, ensues after an average of two to three years from diagnosis. No curative treatment is currently available. Development of novel therapies is hampered by incomplete understanding of pathophysiology, as translation of findings from disease models into clinical settings has proven challenging. In addition, the lack of reliable biomarkers contributes to increased duration and costs of clinical trials. Studies in disease models suggest that mitochondrial energy metabolism is dysregulated in MND and development of therapeutics targeting mitochondrial dysfunction may be beneficial. Nonetheless, direct evidence supporting mitochondrial involvement in people living with MND is currently lacking.

The primary aim of this thesis was to use 31-phosphorus magnetic resonance spectroscopy (^{31}P-MRS) to characterise the bioenergetic signature in people living with MND. Experiments in this thesis were designed to characterise cerebral and muscle bioenergetics, to explore central and peripheral components of motor fatigability (a debilitating symptom), and to test the potential of the technique to detect longitudinal changes in skeletal muscle in MND.

Following development and optimisation of acquisition and analysis protocols, ^{31}P-MRS revealed evidence for primary mitochondrial dysfunction in the brainstem of patients, with reduced phosphocreatine and Gibbs free energy of adenosine triphosphate hydrolysis. In resting skeletal muscle, a different bioenergetic signature of elevated inorganic phosphate and phosphomonoesters was identified in MND patients. Dynamic exercise protocols demonstrated differential responses to motor fatigability in muscle between patients and controls. Lastly, a longitudinal decrease in adenosine triphosphate was detected in muscle in patients, suggesting phases of bioenergetic compensation and decompensation.

These findings illustrate that ^{31}P-MRS has potential as a biomarker in MND, contributes to improved understanding of pathophysiology, and represents a new tool for future trials targeting bioenergetic pathways.

DECLARATION

I, the author, confirm that the thesis is my own work. I am aware of the University's Guidance on the Use of Unfair Means (www.sheffield.ac.uk/ssid/unfair-means). This work has not been previously presented for an award at this, or any other, university.

This thesis is my own work. I have participated in the design, conceptualisation, and implementation of all studies. I helped designing and implementing the spectroscopic and imaging protocols. I designed and built the MR-compatible pulley system myself. I designed and implemented the Reproducibility study and, with the supervision of Dr Tom Jenkins, participated in the design and conceptualisation of all the Motor Neuron Disease studies. I recruited and consented all research participants, arranged all research visits, conducted all clinical testing, participated in all research scans, designed the data analysis protocols, wrote and tested the co-registration script, analysed and interpreted all acquired data, and helped securing funding to cover for patients' travel expenses. I wrote the manuscript now published in *Brain*.

I have been supported by my supervisors and colleagues with expertise in the various techniques applied. Dr Tom Jenkins supervised all my work and analyses, helped to conceptualise the studies, secured funding, as well as helping with diagnosis and identification of potential Motor Neuron Disease research participants. Prof Iain D Wilkinson supervised my work and analyses regarding MR physics aspects, developed and implemented the 31-phosphorus spectroscopy acquisition protocols, and secured funding for the Motor Neuron Disease study and Reproducibility study. Prof Mara Cercignani kindly reviewed physics and methodological chapters and appendix. Dr James Alix performed the neurophysiology assessments and helped conceptualising the study described in chapter five. Prof Dame Pam Shaw and Prof Chris McDermott helped with identifying potential patients for the Motor Neuron Disease study and with securing funding. The statistician Kathleen Baster helped significantly with aspects related to statistical analysis in chapter four. Prof Nigel Hoggard reported the scans to assess whether incidental findings were present or not. The radiographer Julia Bigley helped with the radiographic aspects of the MRI scans. Dr Marialena Dounavi advised on computational aspects related to the fuzzy-c segmentation algorithm (which she provided me).

Publications arising from this thesis are listed in the following page. For each publication, all authors reviewed the manuscript and had the chance to comment on it.

Licence to reproduce published work in chapter four has been granted by *Brain* and is attached in the appendix.

Dr. Matilde Sassani

PUBLICATIONS ASSOCIATED WITH THIS THESIS

Orcid ID *https://orcid.org/0000-0002-0384-7296*

Jan 2021 Magnetic resonance spectroscopy reveals mitochondrial dysfunction in amyotrophic lateral sclerosis. ***Brain***

Sassani M, Alix JJ, McDermott CJ, Baster K, Hoggard N, Wild JM, Mortiboys HJ, Shaw PJ, Wilkinson ID, Jenkins TM. Volume 143, Issue 12, December 2020, Pages 3603–3618, https://doi.org/10.1093/brain/awaa340

Aug 2020 Ursodeoxycholic acid as a novel disease-modifying treatment for Parkinson's disease: protocol for a two-centre, randomised, double-blind, placebo-controlled trial, The 'UP' study. ***BMJ Open.***

Payne T, ***Sassani M***, Buckley E, Moll S, Anton A, Appleby M, Maru S, Taylor R, McNeill1 A, Hoggard N, Mazza C, Wilkinson ID, Jenkins T, Foltynie T, Bandmann O. doi: 10.1136/bmjopen-2020-038911

Nov 2019 Metabolic dysfunction in MND: a 31-phosphorus magnetic resonance spectroscopy study. ***Platform Communications****: Abstract Book - 30th International Symposium on ALS/MND, Amyotrophic Lateral Sclerosis and Frontotemporal Degeneration, 20:sup1*

Sassani M, Alix JJ, McDermott CJ, Hoggard N, Shaw PJ, Wilkinson ID, Jenkins TM. doi: 10.1080/21678421.2019.1646546

Apr 2019 Biomarkers in Motor Neuron Disease: A State of the Art Review. ***Front Neurol.***

Verber NS, Shepheard SR, ***Sassani M***, McDonough HE, Moore SA, Alix JJP, Wilkinson ID, Jenkins TM, Shaw PJ. doi: 10.3389/fneur.2019.00291

Mar 2018 Translational approaches to restoring mitochondrial function in Parkinson's disease. ***FEBS Lett.***

Mortiboys H, Macdonald R, Payne T, ***Sassani M***, Jenkins T, Bandmann O. doi: 10.1002/1873-3468.12920

ACKNOWLEDGEMENTS

These years have been incredibly challenging and I owe a debt of gratitude to both my supervisors for leading by example and for their constant encouragement and support. Thank you, Tom, for patiently guiding me through these formative years, for engaging with my ideas and helping me develop them, for reminding me of what really matters at time of great struggle, and for bearing with my (OK, OK, I cannot not acknowledge it) passion for equations and double negatives. Thank you, Iain, for the days spent scanning whilst discussing science, laughing, and drinking coffee. Your pieces of advice have been invaluable and I regret not following some of them sooner. I miss you and I hope this work would make you proud.

I am indebted to Prof Mara who very generously and meticulously reviewed and commented my physics and methodological chapters, her observations have helped me improve my understanding of physics and gave me more confidence.

I am grateful to James for conducting the neurophysiological assessments and for his many (partially fruitful) attempts to educate me on aspects of British culture and sport. I would also like to thank Kathleen Baster for her statistics input into the Brain paper and Julia Bigley for scanning research participants. I am grateful to Prof Dame Pam Shaw who created the foundations to help patients living with MND in Sheffield and to Prof McDermott for his leadership in the department.

To my dear friends Maria, Ilaria, and Harry: un grazie di cuore for always being there in these years, for the long conversations on science, politics, and life and for keeping me sane throughout this last year. Thank you, Sarah, for introducing me to environmental consciousness and for our conversations on “science from the bottom”. Thank you, Haris, for the coffee, help during lockdown, and valuable pieces of advice. A big thank you to Anne and Adrian for their support, patience especially during my attempts in the lab and for the adventurous walks. Thank you, Emma, for bearing with my prosaic expressions, for writing the famous “Smith review”, and for the company during those long weekends at work. Grazie Michela for always having pecorino available at times of crisis. Thank you to my parents, zio Bruno, and Rossana for their inspirational role and encouragement throughout.

Lastly, I wish to thank all patients and volunteers who donated their time to take part in the studies reported in this thesis, without them this work would not have been possible.

This work is dedicated to Iain, Tom, my parents, and all participants who took part in this research

TABLE OF CONTENTS

LIST OF FIGURES

When figures were reproduced from external sources, adequate copyright was sought and citation included. The vast majority of figures were either depiction of own data or drawn by the author of the thesis. This is specified also in relevant captions.

LIST OF TABLES

LIST OF ABBREVIATIONS

ADC: Analogue to digital converter

ADP: Adenosine diphosphate

ALS: Amyotrophic lateral sclerosis

ALSFRS-R: Revised ALS functional rating scale

ALS-FTD: Amyotrophic lateral sclerosis with concomitant frontotemporal dementia

AMARES: Advanced method for accurate, robust, and efficient spectral fitting

ANT: Adenine nucleotide translocator

ATP: Adenosine triphosphate

CHCHD10: Coiled-Coil-Helix-Coiled-Coil-Helix Domain Containing 10

Cho: Choline-containing compounds

CI: Confidence intervals

CMAP: Compound muscle action potential

CNS: Central nervous system

CP: Circularly polarised

Cr: Creatine

CRLB: Cramér-Rao lower bound

CSF: Cerebrospinal fluid

CSI: Chemical shift imaging

CST: Corticospinal tract

CV: Coefficient of variation

C9orf72: chromosome 9 open reading frame 72

DF: Welch corrected degrees of freedom

DN: $NAD(P)^+$ + NAD(P)H

DTI: Diffusion tensor imaging

EMA: European medicines agency

ER: Endoplasmic reticulum

ETC: Electron transport chain

FA: Flip angle

$FADH_2$: Flavin adenine dinucleotide

FDA: U.S. Food and Drug Administration

FID: Free induction decay

fMRI: Functional magnetic resonance imaging

FOV: Field of view

FUS: Fused-in-Sarcoma

GABA: γ-amino-butyrate

Gln: Glutamine

Glu: Glutamate

Glx: Glutamate and glutamine

GPC: Glycerophosphocholine

GPE: Glycerophosphoethanolamine

GSH: Reduced glutathione

^{1}H-MRS: Proton magnetic resonance spectroscopy

ICC: Intra-class correlation coefficient

IR: Inversion recovery

ISIS: Image selected *in vivo* spectroscopy

LLOA: Lower limit of agreement

LMN: Lower motor neuron

LP: Linearly polarised

mI: Myo-inositol

MND: Motor neuron disease

MR: Magnetic resonance

MRI: Magnetic resonance imaging

MRS: Magnetic resonance spectroscopy

MRSI: Magnetic resonance spectroscopic imaging

MUNIX: Motor unit number index

MUSIX: Motor unit size index

MVIC: Maximal voluntary isometric contraction

NAA: N-acetylaspartate

NAAG: N-acetylaspertylglutamate

NAD^+: Oxidised nicotinamide adenine dinucleotide

NADH: Reduced nicotinamide adenine dinucleotide

NICE: The national institute for health and care excellence

NIV: Non-invasive ventilation

NOE: Nuclear Overhauser efect

NS: Non-significant

NSA: Number of signals averages

PA: Pulse acquire

PC: Phosphocholine

PCr: Phosphocreatine

PDE: Phosphodiesters

PE: Phosphoethanolamine

Pi: Inorganic phosphate

PLS: Primary lateral sclerosis

PMA: Progressive muscular atrophy

PME: Phosphomonoesters

^{31}P-MRS: Phosphorus magnetic resonance spectroscopy

Ppm: Parts per million

PRESS: Point resolved spectroscopy

RF: Radio frequency

RNA: Ribonucleic acid

SD: Standard deviation

SEM: Standard error of mean

SNR: Signal to noise ratio

SOD1: Superoxide dismutase 1

STEAM: Stimulated echo acquisition mode

SV: Single voxel

SVC: Slow vital capacity

TARDPB: Transactive response DNA binding protein 43 gene

tCr: Total creatine

TDP-43: Transactive response DNA binding protein 43

TE: Echo time

TI: Inversion time

TMS: Transcranial magnetic stimulation

TR: Repetition time

TSE: Turbo spin echo

ULOA: Upper limit of agreement

UMN: Upper motor neuron

VCP: Valosin-containing protein

VDAC: Voltage-dependent anion channel

VIF: Variance inflation factors

ΔG: Gibbs free energy

ΔG_{ATP}: Gibbs free energy of ATP hydrolysis

CHAPTERS

The aim of this thesis was to develop and utilise 31-phosphorus magnetic resonance spectroscopy to investigate energy metabolism in the brain and muscles of patients living with motor neuron disease. The first chapter describes clinical and biological features of motor neuron disease, highlights areas of need, and reviews how proton magnetic resonance spectroscopy (an analogous technique to 31-phosphorus spectroscopy in more widespread use) has been applied, to date, in motor neuron disease.

Chapter two illustrates experiments conducted to optimise hardware and sequences to produce high quality brain and muscle spectroscopic data.

In chapter three, a detailed analysis of available spectroscopic processing steps is reported, together with experiments aimed at testing agreement and reliability of the technique. These experiments illustrate that choice of software can affect measurement reproducibility. Results informed the development of an optimised spectroscopic processing protocol used for the remainder of the experiments of this thesis.

Experiments in chapter four illustrate that bioenergetic dysfunction is present both in the brain and muscle of patients living with motor neuron disease, as measured by 31-phosphorus magnetic resonance spectroscopy, with a differing signature depending on tissue. Dysfunction appears clinically relevant, as bioenergetic parameters correlate with measures of disability, respiratory dysfunction, denervation, and muscle weakness. This is the first time that direct evidence for cerebral bioenergetic dysfunction has been reported in motor neuron disease in the brain using 31-phosphorus magnetic resonance spectroscopy.

In chapter five, 31-phosphorus magnetic resonance spectroscopy is employed in conjunction with neurophysiology to characterise and model motor fatigability, a disabling symptom in motor neuron disease, in patients and controls. Results demonstrate that motor fatigability is primarily dependent on central factors in patients, whereas peripheral and muscular components appear to predominate in healthy controls.

Chapter six reports longitudinal muscle 31-phosphorus magnetic resonance spectroscopic results in patients and controls. These preliminary data assess the potential of technique as a biomarker of disease progression, and a longitudinal reduction in adenosine triphosphate was demonstrated over time. This is the first time 31-phosphorus magnetic resonance spectroscopy has been applied longitudinally in motor neuron disease.

Chapter seven summarises findings and suggests possible future directions.

CHAPTER 1:
INTRODUCTION TO MOTOR NEURON DISEASE

This chapter introduces motor neuron disease (MND), with a particular focus on imaging applications and bioenergetics.

Section one details epidemiological, aetiological, pathophysiological, and clinical aspects of MND, discussing current challenges and areas of need in the field. Section two briefly reviews applications of magnetic resonance imaging (MRI) in MND and focuses on magnetic resonance spectroscopy (MRS) studies conducted to investigate disease pathophysiology and as a diagnostic, disease progression, and treatment response biomarker. Lastly, section three elaborates on basic bioenergetic concepts to provide a theoretical framework necessary to the understanding and interpretation of experimental results in the following chapters. In section three, the role of mitochondria in pathogenesis is also highlighted (of note, current state of knowledge in the field is reviewed in the introduction of chapter four as well) and arguments for the application of 31-phosphorus magnetic resonance spectroscopy (^{31}P-MRS) in MND are made.

Concepts described in section two were rewritten and published in the imaging section of the review on biomarkers in MND by (Verber, Shepheard et al. 2019), which was written by the author of this thesis with supervision of Dr Thomas M. Jenkins and Prof Iain D. Wilkinson[1].

SECTION 1

Motor neuron disease

1.1.1 Motor neuron disease: epidemiology

With an incidence rate of 2-3 per 100,000 person-years in Europe (Logroscino, Traynor et al. 2010), MND is the third most common adult-onset neurodegenerative disorder after Alzheimer's disease and Parkinson's disease (Talbot 2002). It is slightly more prevalent in men than women (with a ratio of 1.5 to 1) and, even though it can affect all age groups, incidence peaks the late sixties for women and early seventies for men (Logroscino, Traynor et al. 2010). It is a rapidly fatal condition, hence prevalence is relatively low (approximately 5 per 100,000 of total population) (Traynor, Codd et al. 1999) as median survival is about a year and a half from diagnosis and two to three years from symptom onset (del Aguila, Longstreth et al. 2003).

[1] Creative Commons Attribution License (CC BY) copyright.

There is a lack of consensus with regard to which environmental modifiers and risk factors contribute to this disease. Numerous epidemiological studies have investigated whether smokers (Gallo, Bueno-De-Mesquita et al. 2009), military recruits (Weisskopf, Cudkowicz et al. 2015), athletes (Lacorte, Ferrigno et al. 2016), or people exposed to chemico-physical hazards (such as heavy metals, formaldehyde, toxins, pesticides, or electromagnetic fields) (Capozzella, Sacco et al. 2014, Seals, Kioumourtzoglou et al. 2017) are more susceptible to disease development. Caution should be exerted when interpreting the results of these studies: it is likely that specific environmental modifiers increase the risk of disease development only in a genetically predisposed subpopulation, which might not be detectable by standard epidemiological investigations of a disease that has a relatively low incidence (Al-Chalabi and Hardiman 2013). An alternative approach combining Mendelian randomisation, genotyping, and transcriptomics has recently been used to suggest that intense physical exercise may increase the risk of MND (Julian, Glascow et al. 2021).

1.1.2 Motor neuron disease: putative aetiology, pathogenesis, and pathology

Despite a growing body of research, MND remains incompletely understood: its aetiology and pathophysiology have not yet been elucidated satisfactorily and this has hindered development of curative treatments.

At present, most MND cases are sporadic and thought to be caused by a complex interaction between genetic and environmental factors likely to take place in a multi-step process (Shaw 2005, Al-Chalabi and Hardiman 2013, Al-Chalabi, Calvo et al. 2014, Chiò, Mazzini et al. 2018). Various genome-wide association studies have identified several risk-conferring genetic polymorphisms (Renton, Chio et al. 2014), whereas, pathogenic Mendelian-type mutations have been discovered in both familial and sporadic forms of MND[2] and are detected in approximately ten per cent of patients (Mathis, Goizet et al. 2019).

The most prevalent genetic mutation is the intronic hexanucleotide $(G_4C_2)_n$ repeat expansion in the *C9orf72* gene (DeJesus-Hernandez, Mackenzie et al. 2011, Renton, Majounie et al. 2011). Other well-characterised mutations include superoxide dismutase 1 or *SOD1* (Rosen, Siddique et al. 1993), *TARDBP* gene encoding TAR DNA binding protein 43 or TDP-43 (Sreedharan, Blair et al. 2008), and fused-in sarcoma or *FUS* (Kwiatkowski, Bosco et al. 2009, Vance, Rogelj et al. 2009). The relative prevalence of mutations in genetic MND is population specific. *C9orf72* is most commonly found in Europe (34% of genetic MND), followed by *SOD1* (15%), *TARDBP* (less than 5%), and *FUS* (approximately 3%). In Asia, *SOD1* is the most reported muatation (30% of genetic cases), followed by *FUS* (over 6%), *C9orf72* (just over 2%), and *TARDBP* (less than 2%) (Mathis, Goizet et al. 2019).

[2] Classically, the term familial MND has been reserved for the presence of a positive family history.

Mode of inheritance is typically autosomal dominant with variable penetrance, although there are rare mutations (*SOD1* 21q22.1,[3] *alsin* 2q33.1, *spasticin* 15q15-21.1, *optineurin* 10p13, *SIGMAR1* 9p34.11, and *GLE1* 9q34.11) transmitted in autosomal recessive manner (Mathis, Goizet et al. 2019). In addition, mutant *UBQLN2* (Xp11.21) has been shown to be pathogenic and to be transmitted in an X-linked dominant manner with incomplete penetrance (Fahed, McDonough et al. 2014).

The higly conserved *C9orf72* gene comprises eleven exons [4].The $(G_4C_2)_n$ pathogenic repeat expansion is found within intron one. There are three well characterised coding variants and two known isoforms resulting from alternative splicing: one longer isoform (481 amino acids, 54 kDa) and one shorter isoform (222 amino acids, 24 kDa) (DeJesus-Hernandez, Mackenzie et al. 2011). Resulting transcripts and proteins are found primarily in the central nervous system, but are also extensively expressed in cells of myeloid lineage (Rizzu, Blauwendraat et al. 2016). Physiological function of C9orf72 proteins is still to be fully elucidated. To date, evidence suggests that they interact with the "Smith-Magenis syndrome chromosomal region candidate gene 8 protein" (SMCR8) (Amick, Roczniak-Ferguson et al. 2016, Zhang, Burberry et al. 2018) and the "WD repeat domain 41 protein" (WDR41) (Sellier, Campanari et al. 2016) to form a complex that can exchange guanosine diphosphate and guanosine triphosphate, i.e. acting as a Rab guanine nucleotide exchange factor (Sellier, Campanari et al. 2016). This complex is thought to be crucial in the control of vesicular trafficking: specifically, phagocytosis (O'Rourke, Bogdanik et al. 2016), lysosomal homeostasis (Amick, Roczniak-Ferguson et al. 2016), and autophagy (Webster, Smith et al. 2016). These cellular pathways are aberrant in *C9orf72*-associated MND, likely because of loss of function (Waite, Bäumer et al. 2014, van Blitterswijk, Gendron et al. 2015, Tang, Toro et al. 2020). Nonetheless, it is still debated whether haploinsufficiency is sufficient to cause disease or whether pathogenicity is primarily incurred by significant gain of function toxicity. The two hypotheses are not mutually exclusive and it is possible that interactions between gain of function and haploinsufficiency exist (Shi, Lin et al. 2018, Zhu, Jiang et al. 2020). There is increasing evidence that both mRNAs and proteins arising from transcription and translation of expanded[5] *C9orf72* can be toxic. Secondary structures of transcripts comprise repeated guanine which can interact to form G-quadruplexes (Fratta, Mizielinska et al. 2012, Kovanda, Zalar et al. 2015, Conlon, Lu et al. 2016), sequestrating RNA-binding proteins, forming RNA foci, and profoundly disrupting both gene expression and nucleo-cytoplasmic transports (Zhang, Donnelly et al. 2015, McEachin, Parameswaran et al. 2020). In addition to sequestrating proteins, the expanded mRNA can also interact with both double- and single-stranded DNA causing direct damage (Walker, Herranz-Martin et al. 2017). The protein products can also be toxic. Both sense and antisense strands are expressed and no initiation codon is required; hence, five possible products (known as dipeptide repeat proteins) can be

[3] The most prevalent SOD1 mutations have autosomal dominant transmission.
[4] Some databases report 12 as exon one can be divided in 1a and 1b.
[5] In healthy individuals GGGGCC hexanucleotide is repeated no more than ten times. Over 30 repeats are considered pathogenic although some patients may have repeats in the order of thousands.

synthesised: poly-glycine-alanine, poly-glycine-arginine, poly-proline-alanine, poly-proline-arginine, and poly-glycine-proline. The first two dipeptides arise from the sense transcript, the third and fourth from the antisense transcript, and the latter from both the sense and antisense strands (Mann, Rollinson et al. 2013, Mori, Weng et al. 2013). Poly-glycine-arginine and poly-proline-arginine are the most toxic dipeptide repeats. Analogous to toxic mRNAs, these dipeptide repeats have also been shown to disrupt nucleo-cytoplasmic transports (Freibaum, Lu et al. 2015, Shi, Mori et al. 2017) and to cause DNA damage (Nihei, Mori et al. 2020). In addition, they can alter nucleolar and heterochromatin function (Kwon, Xiang et al. 2014, Zhang, Guo et al. 2019), affect axonal transport (Baldwin, Godena et al. 2016), and cause mitochondria toxicity (Lopez-Gonzalez, Lu et al. 2016, Choi, Lopez-Gonzalez et al. 2019). This latter pathophysiological mechanism is relevant to the central thesis of this work and is expanded further in chapter four.

SOD1 was the first pathogenic gene to be discovered and is probably the most studied to date. In fact, a large proportion of the current understanding on MND pathopysiology is derived from research conducted in SOD1 models. This gene is located on the long arm of chromosome 22 and comprises five exons (Bowling, Schulz et al. 1993, Rosen, Siddique et al. 1993). Its protein product is 154 amino acids long and weights 16 kDa. This protein is characterised by β-barrel sheets and, at its catalytic site, contains a binding domain for its cofactors: ionised copper and zinc (Tainer, Getzoff et al. 1983). The quaternary structure is a highly stable homodimer crucial in maintaining appropriate oxidoreductive homeosthasis within cells (Huai and Zhang 2019). Specifically, it is a detoxifying enzyme which catalyses a disproportionation reaction: two superoxide anions (i.e. a type of reactive oxygen species) are dismutated into hydrogen peroxide and dioxygen ($2O_2^{\cdot-} + 2H^+ \leftrightarrow H_2O_2 + O_2$) (Pelmenschikov and Siegbahn 2005). The central role of this enzyme is exemplified by the fact that it is ubiquitously expressed by all tissues (Fagerberg, Hallström et al. 2014) and is highly conserved across species (Wang, Xu et al. 2006). Its subcellular localisation in healthy cells is cytoplasmatic, but it can also be found at lower concentrations in the mitochondrial intermembrane space[6] (Fukai and Ushio-Fukai 2011). Over 160 missense point mutations in the *SOD1* gene have been associated with MND (Huai and Zhang 2019). Most are autosomal dominant, but a few are inherited in a recessive pattern (Mathis, Goizet et al. 2019). Although, for many years (and analogous to the *C9orf72* debate) it was unclear whether pathogenicity was mediated by haploinsufficiency or by gain of function toxicity, a consensus on the latter hypothesis has been reached recently (Sangwan and Eisenberg 2016). It has been argued that loss of function, resulting in pathological accumulation of reactive oxygen species, may not be pathogenic, but could still be relevant to pathophysiology and modulate disease severity. Although many mutant SOD1 proteins can still retain enzymatic activity (Saccon, Bunton-Stasyshyn et al. 2013). Mutant SOD1 during their immature phase (i.e. when the protein has not yet undergone post-

[6] An analogous enzyme, SOD2, having manganese as a cofactor, is found in the mitochondrial matrix, whereas SOD3 (also binding copper and zinc) is extracellular (Fukai and Ushio-Fukai 2011).

translational modifications), they are prone to misfolding and aggregation (Furukawa and O'Halloran 2005). More than 40 possible conformations of mutant SOD1 have been described (Furukawa and O'Halloran 2005): dimers, oligomers, and larger aggregates are all possible (Sangwan and Eisenberg 2016), and can be detected not only in motor neurons, but also in glial cells (Forsberg, Andersen et al. 2011). Hence, aberrant microglial and astrocytic activation have been postulated to contribute to pathopysiology of MND[7] (Ferraiuolo, Higginbottom et al. 2011, Evans, Couch et al. 2013), suggesting that the disease has a non-autonomous cell component with glial and inflammatory cells likely playing a role in modulating disease progression. In addition, SOD1 toxicity is pleiotropic: it affects mitochondrial metabolism (detailed later on in this chapter and in chapter four), aggravates oxidative stress, induces endoplasmic reticulum (ER) stress, altering the unfolded protein response and trafficking with the Golgi, alters retrograde axonal transport, may exacerbate glutamate exitotoxicity, and, again analogous to *C9orf72*, is implicated in aberrant autophagy and gene expression (Van Den Bosch, Van Damme et al. 2006, Bunton-Stasyshyn, Saccon et al. 2015, Moller, Bauer et al. 2017, Huai and Zhang 2019, Mathis, Goizet et al. 2019).

The ubiquitously expressed *FUS* and *TARDBP* genes both encode nuclear RNA-binding proteins. When mutated, they mislocalise to the cytoplasm and induce neurodegeneration via analogous pathophysiology (Lattante, Rouleau et al. 2013). *FUS* is located on chromosome 16. The resulting protein residue is 526 amino acids long, containing an RNA-binding domain as well as nuclear localisation and nuclear export signals (Kwiatkowski, Bosco et al. 2009, Vance, Rogelj et al. 2009). It is pivotal to all phases of gene expression (transcription, splicing, RNA transport to dendrites, and traslation) and homologous and non-homologous DNA repair (Orozco and Edbauer 2013, Yang, Gal et al. 2014, Efimova, Ovchinnikov et al. 2017). Over *FUS* 50 mutations have been associated with MND. The vast majority are autosomal dominant, whilst a notable exception is a single point substitution of glycine into glutamine at position 517, which is inherited recessively (Kwiatkowski, Bosco et al. 2009). Both loss of function (resulting in increased DNA damage and aberrant gene expression) and gain of function (toxic protein in cytoplasm) are thought to be responsible for disease (Efimova, Ovchinnikov et al. 2017, Ishigaki and Sobue 2018).

TARDBP is a highly conserved six exon gene found on the short arm of the first chromosome (Ou, Wu et al. 1995). It encodes a 43 kDa protein primarily localised in the nucleus. Eleven possible isoforms have been characterised (Wang, Wang et al. 2004, Sreedharan, Blair et al. 2008). Analogous to FUS, it contains RNA-recognition sequences, a nuclear localisation domain, and a nuclear export sequence allowing nucleo-cytoplasmic shuttling (Lattante, Rouleau et al. 2013). TARDBP is an RNA-binding protein acting primarily as a transcription factor (Reddi 2017). Other putative functions are: splicing, post-transcriptional regulation, and RNA export into the cytoplasm, including to dendrites and synapses

[7] This has been reported also in sporadic and *C9orf72-associated* MND.

(Ayala, Pantano et al. 2005, Lattante, Rouleau et al. 2013, Briese, Saal-Bauernschubert et al. 2020). Almost 50 *TARDBP* pathogenic missense mutations have been described in MND, penetrance can be incomplete. Mutations tend to cluster around exon six and the C-terminus (Lattante, Rouleau et al. 2013). One nonsense mutation (a tyrosine substitution at position 374) has also been indentified (Daoud, Valdmanis et al. 2009). As in the case of FUS, both gain and loss of function mechanisms are thought to contribute to development of MND (Barmada, Skibinski et al. 2010, Kabashi, Lin et al. 2010).

Mutations in the *TARDBP* gene are found only in a small proportion of patients. However, importantly, sporadic MND is also characterised by cytoplasmic aggregates of ubiquitinated hyper-phosphorylated TDP-43, present in 97% of cases (Prasad, Bharathi et al. 2019). Neurofilament is also seen (intermediate filaments of neuronal cytoskeleton) and accumulates in axonal processes (Neumann, Sampathu et al. 2006). In addition to the abovementioned inclusions, Bunina Bodies (cytoplasmic eosinophilic inclusions approximately 5 micrometres in diameter) are characteristically found in motor neurons of MND patients; their biological relevance is currently unknown. Other histopathological findings include: loss of pyramidal neurons in layer V of primary motor cortex (visualised using a classic hematoxylin and eosin stain) and axonal loss along the corticospinal tract (i.e. lateral and anterior column of spinal cord) which can be visualised on luxol fast blue stain. Other features of neurodegeneration such as vacuolisation, spongiosis, and reactive astrogliosis can also be present (Saberi, Stauffer et al. 2015). *C9orf72* dipeptide repeats have also been shown to co-localise with TDP-43 toxic granules (Chew, Cook et al. 2019). *SOD1* and *FUS* MND are exceptions to the rule of TDP-43 pathology, as misfolded SOD1[8] and FUS are instead the main component of the inclusions (Shang and Huang 2016, Paré, Lehmann et al. 2018), and TDP-43 is not seen. Neuropathological stages of sporadic MND according to histopathological burden of hyper-phosphorylated TDP-43 have been characterised by Braak's and Trojanowski's groups. In this construct, during stage one, TDP-43 proteinopathy is found exclusively in purely motor areas: spinal α motor neurons, somato-motor nuclei of cranial nerves except for those responsible for eye movement, and primary motor cortex. In stage two, proteinopathy extends to red nucleus, pre-cerebellar systems, reticular formation, and middle frontal gyrus. In stage three, prefrontal and postcentral cortex as well as striatum become affected. In the last (fourth) stage, anteriomedial temporal lobe and hippocampus are involved (Brettschneider, Del Tredici et al. 2013). The authors argued for a conserved pattern of disease propagation, likely in a corticofugal manner (i.e. pathology originating in primary motor regions and spreading to other affected regions) suggesting a prion-like spreading via axonal pathways (Braak, Brettschneider et al. 2013, Verde, Del Tredici et al. 2017). This is known as the "dying-forward" hypothesis, but there is still some debate on the direction of disease spreading: a competing hypothesis states that MND begins at neuromuscular synapses and pathology spreads from there to the central nervous system (dying-back), with some even arguing that the locus minoris resistentiae is located at the cortico-α motor neuron

[8] Interestingly, misfolded SOD1 has also been reported in sporadic MND (Forsberg, Andersen et al. 2011).

synapses (dying-outward) (Baker 2014, Tsitkanou, Lindsay et al. 2019). Regardless of site of origin of MND pathology, propagation across contiguous regions is a feature which is consistently observed in clinical practice (Walhout, Verstraete et al. 2018). From a molecular point of view, mutant SOD1 has been shown to have prion-like features *in vitro* and in a few animal studies: it can induce misfolding and aggregation of mutant and non-mutant SOD1 with some evidence suggesting that it can spread to nearby cells and, perhaps, and more controversially, even to other organisms (Bunton-Stasyshyn, Saccon et al. 2015). Evidence for analogous prion-like features for TDP-43, FUS and C9orf72 dipeptides is emerging although further experimental validation is required (Ayers and Cashman 2018).

Although MND pathogenic genes appear to cause disease via diverse downstream mechanisms (as detailed above), accumulation of misfolded protein is a consistent finding. These proteinaceous accumulations are thought to disrupt homeostasis, affect virtually every cellular process, and cause direct mitochondrial toxicity (Gao, Wang et al. 2019). There are also pathophysiological pathways which exacerbate toxic protein accumulations through deleterious positive feedback loops including: aberrant RNA processing (Walsh, Cooper-Knock et al. 2015), ER stress, abnormal endosomal trafficking, and defective proteostasis (Ruegsegger and Saxena 2016). These pathways can all trigger mitochondrial apoptosis by inducing the unfolded protein response, a process activated by cellular, and specifically ER, stress, aimed at counteracting accumulation of misfolded and toxic proteins. Apoptosis is thought to be the main mechanism of cell death in MND, preceded by chromatolysis and somatodendritic attrition. In addition, in MND, expression of pro-apoptotic preteins is increased with cellular morphology recapitulating the characteristic hallmarks of apoptosis (Martin 1999). The possibility of necroptosis taking place has also been suggested and research aimed at targeting this relatively novel pathway is now being undertaken (Chevin and Sébire 2021). In addition to initiating programmed cell death, mitochondria can exacerbate other aspects of MND pathophysiology: for instance, they are the main producers of reactive oxygen species in non-immune cells and contribute to exacerbation of neuronal oxidative stress, another well recognised MND disease mechanism (Barber and Shaw 2010). They are also central to calcium reuptake following action potentials; notably, calcium overload is toxic to the cell and can be caused by glutamate excitotoxicity, another implicated mechanism (Shaw and Ince 1997). Further description of mitochondrial involvment in MND is provided in sections three and subsequent chapters.

Advances in genetic characterisation of MND have led to the development of transgenic, primarily murine, models which have allowed researchers to study the pathophysiology of MND. The most widely used and characterised, to date, is the $SOD1^{G93A}$ transgenic model (Gurney Mark, Pu et al. 1994) although others are also used (De Giorgio, Maduro et al. 2019), including models over-expressing wild type FUS (Mitchell, McGoldrick et al. 2013). Nonetheless, these models would only be representative of a small proportion of genetic MND (i.e. less than a tenth of all MND cases) and do not fully reflect human disease phenotypes (for instance, MND is a disease that occurs typically in the elderly

population, whereas most murine models develop symptoms early in life). Hence, every treatment beneficial in rodents, except for riluzole and, to some degree, edaravone, has failed to demonstrate efficacy in subsequent clinical trials (Petrov, Mansfield et al. 2017). Therefore, the reliability of these rodent models has been questioned and alternative means to investigate MND pathophysiology have been advocated (Perrin 2014). In addition, although promising results are starting to emerge from antisense oligonucleotide trials targeting toxic *SOD1* products (Miller, Cudkowicz et al. 2020) and similar work in *C9orf72* is underway (NCT03626012), therapy for sporadic MND has not yet advanced. A better comprehension of disease pathogenesis is important not only to enable development of more effective treatments, but also to facilitate discovery of reliable diagnostic, progression, and treatment response biomarkers, which is another great area of need in the field (Turner, Kiernan et al. 2009).

1.1.3 Motor neuron disease: clinical aspects

Initial presentation of MND can be insidious and semiology is variable, but progression of motor symptoms is characteristic and unavoidable with death resulting, typically, from respiratory muscle failure leading to type II respiratory failure (Paulukonis, Roberts et al. 2015).

Clinically, MND can be classified into amyotrophic lateral sclerosis (ALS), progressive muscular atrophy (PMA), and primary lateral sclerosis (PLS) according to the regions of the nervous system that are affected. ALS is the most common form of MND. The terms are often used interchangeably in the USA, whereas, in the UK, ALS implies a mixed upper motor neuron (UMN) and lower motor neuron (LMN) phenotype. PLS refers to a pure UMN form, and PMA to a pure LMN phenotype. These subtypes generally progress more slowly than typical ALS. Neurological examination is focused on identifying weakness (which is inevitable in MND) and presence of concomitant UMN and LMN signs that define ALS. UMN signs include hypertonia (spasticity), pathological hyperreflexia, preserved reflexes in a wasted limb, pathological reflexes (e.g. extensor plantar responses), clonus, and pseudobulbar affect. LMN signs include hypotonia, hyporeflexia or areflexia, atrophy, and (often widespread and florid) fasciculations. The relative burden of UMN and LMN involvement is variable: ALS variants with UMN or LMN predominance are also recognised.

1.1.3.1 Amyotrophic lateral sclerosis

The most prevalent site of onset of ALS is in the limbs, which is the case in about two thirds of patients. Bulbar-onset is found in about a third of people and is slightly more common in women, whereas axial and respiratory-onset are the rarest types, each affecting only about two percent of ALS patients (Logroscino, Traynor et al. 2010). Spread of disease often occurs across contiguous anatomical regions

and patterns of regional involvement are sometimes used as an indicator of speed of disease progression (Turner, Brockington et al. 2010).

Limb-onset ALS is more prevalent in males. It presents, typically, with asymmetric distal weakness, more commonly of the dominant limb (Turner, Wicks et al. 2011) although, as disease progresses, the majority of patients (almost 85%) also develop bulbar symptoms. At presentation, patients may complain of problems with walking and/or arm function and fine hand movements. Patients might report gait changes, feeling that one leg is weaker or simply heavier, or present with a foot drop, when they struggle to lift their foot which slaps onto the floor causing them to trip as they walk. Frequent falls are common and, as symptoms progress, mobility aids may be required. Reduced hand dexterity is also characteristic, manifesting as difficulties with writing and other fine hand movements such as fastening and unfastening buttons, playing musical instruments, or handling tennis balls, which were all symptoms reported by patients participating in the research reported in this thesis. Selective atrophy of specific muscle groups in the early stages of disease is characteristic. When upper limbs are involved, thenar atrophy is common and first dorsal interosseous and abductor pollicis brevis tend to be preferentially affected, with finger flexors and hypothenar muscles relatively spared. This pattern is called "the split hand syndrome" and is indicative of ALS (Benny and Shetty 2012, Eisen and Kuwabara 2012). Flail arm and flail leg subtypes are two predominantly LMN variants of limb-onset ALS (Wijesekera, Mathers et al. 2009). The former is also known as brachial amyotrophic diplegia (the "man in the barrel" syndrome) (Hu, Ellis et al. 1998), whereas the latter was referred to, historically, as the pseudopolyneuritic form of ALS (or Patrikios' disease) (Cappellari, Ciammola et al. 2008). Patients affected by brachial amyotrophic diplegia are typically males (the female to male ratio is 1 to 10) (Vucic and Kiernan 2007) and tend to present with progressive upper limb wasting and weakness with subtle lower limb UMN signs. Unlike typical ALS, wasting tends to be proximal and relatively symmetrical, although asymmetry is sometimes detected in the earliest stages (Garg, Park et al. 2017). Flail leg syndrome has a distal and asymmetrical lower limb onset. It can mimic a motor neuropathy as UMN signs may be absent or very subtle at presentation and neurophysiology may initially show only active denervation (Cappellari, Ciammola et al. 2008). Both flail arm and flail leg variants are characterised by slower progression: median survival is over five years (Wijesekera, Mathers et al. 2009), compared to two to three years for typical ALS (del Aguila, Longstreth et al. 2003).

Bulbar-onset ALS (sometimes referred to as progressive bulbar palsy[9]) is more prevalent in women. It affects, initially, the bulbar region and results in dysarthria, dysphagia, and sialorrhea. Emotional lability is also frequent and found in about fifty percent of patients. Progression to limbs is not uncommon and takes place, on average, after 12 months from symptom onset with patients becoming unable to walk after a median interval of two years. Importantly, in this subset of patients, loss of

[9] The term progressive bulbar palsy is used to denote an exclusively, or largely predominant, bulbar presentation.

ambulation is an adverse prognostic factor indicating terminal disease (Turner, Scaber et al. 2010). Initial presentation can be insidious: patients (or carers) may notice that speech is slurred or quieter than normal and may have to repeat or write words to communicate. Complete anarthria often develops, which occurs, in the typical form of bulbar ALS, after a median of a year and a half from disease onset (Turner, Scaber et al. 2010). Swallowing impairment is another debilitating symptom, which can cause post-swallowing residues in the oral cavity and choking on both solids and liquids; these episodes may be accompanied by coughing and/or nasal regurgitation. Both the oral and pharyngeal stages of swallowing can be affected as a result of masticatory and lingual muscle weakness, spasticity, and a reduced swallowing reflex (Jani and Gore 2016). Another consequence of dysfunctional swallowing is excessive saliva in the mouth and drooling. Speech problems almost invariably precede swallowing problems. In clinic, a picture of bilateral tongue atrophy and fasciculations in the presence of a brisk jaw reflex is essentially pathognomonic for ALS. Although bulbar onset is generally considered an adverse prognostic feature and is associated with faster progression (Traxinger, Kelly et al. 2013), there is an UMN predominant form of isolated bulbar palsy, which has a more slowly progressive course, with symptoms and signs remaining confined to the bulbar region for a median of almost two years (Zhang, Chen et al. 2021). This tends to affect older women.

Rarer presentations of ALS include neck drop and stooping due to weakness of extensor axial muscles (Uemura, Kosaka et al. 2013, Pancani, Tindale et al. 2017) and respiratory-onset ALS. The latter is often preceded by weight loss, it can be associated with axial weakness, and is more prevalent in males (Gautier, Verschueren et al. 2010). It can manifest with characteristic symptoms of neuromuscular respiratory dysfunction: initially as disturbed sleep, morning headaches, daytime sleepiness, and fatigue; and then with more overt orthopnoea and dyspnoea inevitably leading to hypercapnic, type II respiratory failure. Crises can be precipitated by lower respiratory tract infections. Prognosis is poor for this subtype of ALS (Gautier, Verschueren et al. 2010).

In addition to motor symptoms; emotional lability, language dysfunction, subtle behavioural changes, and/or executive dysfunction can be detected in approximately fifty percent of people living with ALS. About a tenth of patients develop overt frontotemporal dementia, a condition that shares genetic and pathological features with ALS (i.e. the presence of *C9orf72*, *FUS*, or *TARDBP* mutations and TDP-43 proteinopathy in some patients) (Neumann, Rademakers et al. 2009, Montuschi, Iazzolino et al. 2015, Strong, Abrahams et al. 2017, Balendra and Isaacs 2018, Majumder, Gregory et al. 2018). The clinical characteristics and spectrum of cognitive and behavioural dysfunction are detailed further in following sections.

Lastly, about a third of patients report autonomic symptoms with one in seven having evidence of autonomic failure (Piccione, Sletten et al. 2015). Some sensory abnormalities may be present as well

(Isaacs, Dean et al. 2007) and may be even identifiable by neurophysiological assessments (Pugdahl, Fuglsang-Frederiksen et al. 2007).

Diagnosis of ALS according to the revised El-Escorial criteria requires evidence of both UMN and LMN degeneration, evidence of disease spread to same or contiguous regions, and exclusion of mimic disorders (Brooks, Miller et al. 2000). Diagnostic categories according to degree of certainty are summarised in the table below. In the revised El-Escorial criteria, neurophysiological assessment provides laboratory support for LMN pathology and is especially relevant in the context of clinically probable ALS; specifically, by evidencing acute denervation (fibrillation potentials and positive sharp waves) and chronic partial reinnervation (motor unit potentials that are large and/or unstable with a reduced interference pattern) (Brooks, Miller et al. 2000, de Carvalho, Dengler et al. 2011, Geevasinga, Loy et al. 2016). The more recent Awaji-Shima neurophysiological criteria (de Carvalho, Dengler et al. 2008) recommend a more comprehensive integration of neurophysiological results with clinical data which can be used in conjunction to assess whether a specific anatomic lesion is affected or not; in addition, in the Awaji-Shima criteria fasciculation potentials are also considered evidence of acute denervation. This approach has been shown to increase diagnostic sensitivity (Costa, Swash et al. 2012). Novel and less stringent diagnostic criteria arising from expert consensus have recently been published (Shefner, Al-Chalabi et al. 2020) and await further validation in future studies.

Table 1.1 Diagnostic categories according to the revised El-Escorial criteria (Brooks, Miller et al. 2000).
Upper motor neuron signs are: hypertonia (spasticity), pathological hyperreflexia, preserved reflexes on a wasted limb, clonus, and pseudobulbar affect. Lower motor neuron signs are: weakness[10], hypotonia, hyporeflexia or areflexia, atrophy, and widespread florid fasciculations. Regions assessed are: bulbar, cervical, thoracic, and lumbosacral. Neurophysiological evidence of lower motor neuron dysfunction include: fibrillation potentials, positive sharp waves, motor unit potentials that are large and/or unstable, and reduced interference pattern. The asterisk indicates that upper motor neuron signs need to be rostral to lower motor neuron signs; when this is not the case, clinically possible amyotrophic lateral sclerosis should be considered. The hash symbol indicates that upper and lower motor neuron signs need to be present in the same region.

	Upper motor neuron signs (number of affected regions)	***Lower motor neuron signs (number of affected regions)***	***Neurophysiology (number of affected regions)***
Clinically definite	(3)	(3)	
Clinically probable*	(2)	(2)	
Clinically probable Laboratory supported	(1) or (1)	(1) or (1)	(2) (2)
Clinically possible#	(1) or (≥2)	(1) or (0)	

Common mimics of ALS include other forms of MND and their differential diagnoses (described below): cervical radiculomyelopathy, coexistent cervical myelopathy and peripheral neuropathy, (McDermott and Shaw 2008) and other rare diseases such as: triple A syndrome (Strauss, Koehler et al. 2008), adult hexosaminidase A deficiency (Drory, Birnbaum et al. 2003), adult polyglucosan body disease (Segers, Kadhim et al. 2012), and the controversial entity paraneoplastic ALS (Mélé, Berzero et al. 2018). Imaging of the neural axis, neurophysiology, clinical laboratory tests, and, occasionally, biopsies can aid in excluding the abovementioned conditions (Brooks, Miller et al. 2000, McDermott and Shaw 2008) in the context of an atypical clinical picture, as required on a case-by-case basis.

Recognition of full-blown ALS is generally straightforward in clinic. However, various diagnostic issues remain unresolved. Median diagnostic delay from symptom onset to diagnosis is approximately a year, with about fifty percent of patients being initially misdiagnosed in that timeframe, and many patients visit multiple doctors before receiving the correct diagnosis (Paganoni, Macklin et al. 2014). The insidious symptom onset can partially explain this latency, which could also be ascribed to the fact that a single test able to unequivocally identify ALS has not yet been developed; diagnosis is primarily clinical and relies on the history, neurological examination, and exclusion of mimics. The most important ancillary supportive test is electromyography which enables LMN dysfunction to be

[10] Of note, although weakness appears as a LMN sign in the revised El-Escorial criteria, it is also possible to have weakness with exclusively UMN dysfunction.

corroborated or detected subclinically by demonstrating electrophysiological evidence of active denervation and chronic partial reinnervation (de Carvalho, Dengler et al. 2008). There is no fully approved objective diagnostic test to assess UMN function although transcranial magnetic stimulation (TMS) is under ongoing investigation (Menon, Geevasinga et al. 2015) and numerous advanced imaging modalities are being tested for this purpose. This gap may further contribute to delays in diagnosis, as well as making distinction of the different forms of MND more difficult. There are also implications for clinical trials as potential therapeutics are likely to be mostly beneficial in the early stages of disease, prior to irreversible loss of a substantial proportion of motor neurons. Hence, a sensitive and specific diagnostic biomarker is still required to aid clinicians establish early diagnosis and, ideally, to detect the disease in its prodromal, and potentially reversible, stages.

1.1.3.2 Neuropsychological dysfunction in amyotrophic lateral sclerosis

It is possible to characterise the wide spectrum of neuropsychological dysfunction associated with ALS using the revised Strong diagnostic criteria (Strong, Abrahams et al. 2017) which comprises seven clinical subtypes.

The first subtype is ALS with behavioural impairment. The most common behavioural symptom is apathy, reported in approximately a third of cases (Witgert, Salamone et al. 2010, Santangelo, Siciliano et al. 2017). The Dimensional Apathy Scale can be used to assess and characterise this symptom: initiation apathy is more prominent than executive and emotional apathy and does not correlate with motor disability (Terada, Obi et al. 2011, Radakovic, Stephenson et al. 2016). Other changes indicative of frontotemporal dysfunction, such as lack of inhibition and of sympathy/empathy, as well as stereotypical, compulsive, hyperoral behaviours may also be present, albeit less frequently (Lillo, Mioshi et al. 2011, Strong, Abrahams et al. 2017). The assessment suggested to be most apt to detect behavioural dysfunction in ALS, according to a recent systematic review, is the Beaumont Behavioural Inventory (Gosselt, Nijboer et al. 2020); although there are other tests used to characterise neuropsychological dysfunction (described below) which have behavioural subscales. Presence of apathy or at least two of the symptoms above is sufficient to establish the diagnosis (Strong, Abrahams et al. 2017). In clinic, this subtype may present a diagnostic challenge as reactive mood changes as well as progressive motor and respiratory disability can confound the clinical picture. Hence, a skilful and targeted collateral history is required to assess baseline, timing of onset, and extent of the impairment; this is often carried out in conjunction with screening tests (Strong, Abrahams et al. 2017).

The second subtype is ALS with cognitive impairment, most typically manifested as reduced letter fluency and characteristically presenting with executive and/or language dysfunctions (such as naming tasks, comprehension, repetition, and reading) (Abrahams, Goldstein et al. 2004). Social cognition is often affected (Strong, Abrahams et al. 2017) and selective attention appears reduced in a proportion of

patients (Pinkhardt, Jürgens et al. 2008). Memory and visuoperceptual dysfunction have been reported in ALS, but results of studies are inconsistent (Phukan, Pender et al. 2007). Many centres use letter fluency tasks as a screening tool because deficits are characteristic and tend to occur early in ALS (Abrahams, Leigh et al. 2000). Motor impairment can be a confounder; hence, some have attempted to account for progressive motor disability using the Verbal Fluency Index (Abrahams, Goldstein et al. 1996). Other tests have been applied, for example, the Frontal Assessment Battery at bedside or FAB (Dubois, Slachevsky et al. 2000) can be employed to assess frontal dysfunction whereas the Montreal Cognitive Assessment or MoCA is generally used to characterise cognitive impairment (Nasreddine, Phillips et al. 2005). Both have been used in ALS (Osborne, Sekhon et al. 2014). The Addenbrooke's Cognitive Examination (Mathuranath, Nestor et al. 2000) is another test that is typically used to assess cognitive functions. It may be applied to discriminate between Alzheimer's disease and frontotemporal dementia, but administration in ALS patients poses challenges due to the test not accounting for progressive motor disability (Chenji, Mah et al. 2018). Other commonly used tests which are specific to ALS include the Edinburgh Cognitive and Behavioural ALS Screen (Abrahams, Newton et al. 2014, Niven, Newton et al. 2015) and the Amyotrophic Lateral Sclerosis Cognitive Behavioural Screen (Woolley, York et al. 2010). Both these assessments incorporate behavioural subscales. They are primarily recommended as cognitive screening tools due to their adaptability and validity (Gosselt, Nijboer et al. 2020). The Edinburgh Cognitive and Behavioural ALS Screen is widely used in the UK as it has been shown to improve clinical care and benefit patients, their carers, and healthcare professionals whilst also providing some economic benefit (Hodgins, Mulhern et al. 2020) According to the revised Strong criteria, a diagnosis of ALS with cognitive impairment can be made when ALS is present in conjunction with executive and/or language dysfunction. In this context, executive dysfunction may manifest either as impaired letter fluency or alteration in another executive domain, whereas language impairment needs to be demonstrated on at least two tests which have measures that do not overlap and which demonstrate deficits that are not exclusive to fluency.

The third subtype is ALS with combined cognitive and behavioural impairment. The criteria described above for both cognitive and behavioural subtypes apply. This subtype is found in approximately 25% of ALS patients affected by neuropsychological dysfunction (Phukan, Pender et al. 2007, Strong, Abrahams et al. 2017).

The fourth subtype is ALS with frontotemporal dementia, in which both neurodegenerative diseases are present concurrently. As explained above, genetics and pathology of frontotemporal dementia and MND can overlap with both showing features of TDP-43 proteinopathies (and the other histological characteristics described above) and with a proportion of patients having *C9orf72* expansions, *FUS*, or *TARDBP* mutations (Neumann, Rademakers et al. 2009, Montuschi, Iazzolino et al. 2015, Strong, Abrahams et al. 2017, Balendra and Isaacs 2018, Majumder, Gregory et al. 2018). The main frontotemporal dementia variants are behavioural, semantic, and non-fluent progressive aphasia

(Leyton and Hodges 2010), in which changes in behaviour, language comprehension, or language production predominate, respectively. The behavioural variant is the one most commonly associated with ALS (Bak 2010). Diagnostic criteria for behavioural variant frontotemporal dementia have been published (Rascovsky, Hodges et al. 2011): at least three cognitive-behavioural symptoms must be present, and they must be progressive and persistent. Symptoms include: behavioural disinhibition, apathy, lack of empathy/sympathy, stereotypic or compulsive behaviour, and/or hyperorality. According to the Rascovsky criteria, all diagnostic features must be present within three years of disease onset, with the exception of hyperoral behaviour. On neuropsychological tests, there is, typically, executive dysfunction with sparing of visuospatial skills and episodic memory (Rascovsky, Hodges et al. 2011). Structural imaging, such as CT or anatomical MRI, can illustrate selective atrophy of frontal and anterior temporal lobes, whereas nuclear medicine investigations (single positron emission tomography or positron emission tomography) often demonstrate hypometabolism and hypoperfusion of fronto-temporal regions (Rascovsky, Hodges et al. 2011, Rohrer 2012). Presence of such imaging features strengthens diagnostic certainty (Rascovsky, Hodges et al. 2011). Diagnosis of ALS with frontotemporal dementia can be established when ALS is present in conjunction with three or more progressive[11] cognitive-behavioural symptoms as defined in the Rascovsky criteria (Rascovsky, Hodges et al. 2011, Strong, Abrahams et al. 2017). A diagnosis can also be made when only two of the Rascovsky's criteria are present, provided they are in conjunction with psychotic features or lack of insight (Strong, Abrahams et al. 2017). Less frequently, ALS can also be found in conjunction with semantic or non-fluent variants of frontotemporal dementia (Strong, Abrahams et al. 2017). Although frontotemporal dementia may develop before, concomitantly, or after motor symptoms onset, a characteristic sequence of disease progression has been reported. An insidious onset of psychiatric (delusions and hallucinations) and cognitive-behavioural symptoms is followed by worsening cognitive dysfunction whilst psychotic features tend to self-resolve; lastly, motor symptoms characteristic of ALS manifest, bulbar onset is most common (Bak 2010). When associated with MND, frontotemporal dementia has been reported to progress faster than in its pure "non-motor" form (Bak 2010).

A fifth subtype, ALS with comorbid dementia other than frontotemporal dementia, is also recognised. ALS comorbid with non-frontotemporal dementias (usually Alzheimer's disease and/or vascular dementia) is rare.

The sixth subtype is frontotemporal dementia with MND-like features, in which a diagnosis of frontotemporal dementia can be made and there is evidence of motor degeneration, but this is not sufficient to make a diagnosis of ALS according to the diagnostic criteria outlined above (Brooks, Miller et al. 2000, Strong, Abrahams et al. 2017).

[11] Progression can be demonstrated either by history or with longitudinal follow ups.

Lastly, the seventh subtype is defined as the ALS-Parkinsonism-dementia complex, a clinical subtype almost exclusively found in the island of Guam and Japanese peninsula of Kii (Zoccolella, Palagano et al. 2002, Manno, Lipari et al. 2013). Pathologically, they are characterised by neurofibrillary tangles, hence this may be considered a distinct entity both from a clinical perspective and because of neuropathological differences (Mimuro, Kokubo et al. 2007).

1.1.3.3 Progressive muscular atrophy and primary lateral sclerosis

In addition to ALS, there are two other main subtypes of MND: PMA and PLS.

PMA is the purely lower motor neuron form of MND (Liewluck and Saperstein 2015). It is considered a variant of ALS by some authorities (Yedavalli, Patil et al. 2018) because about half of PMA patients are found to have corticospinal tract degeneration at autopsy (Ince, Evans et al. 2003) and approximately a fifth of those who initially present with purely LMN signs progress clinically to develop central motor neuron dysfunction and, thus, clinically-defined ALS (Kim, Liu et al. 2009). The differential diagnosis for LMN forms of MND includes: benign cramp fasciculation syndrome, inclusion body myositis, myasthenia gravis, monomelic amyotrophy (Hirayama disease), type IV spinomuscular atrophy, spinobulbar muscular atrophy (Kennedy's disease), neuralgic amyotrophy, multifocal motor neuropathy with or without conduction block, motor-predominant chronic inflammatory demyelinating polyneuropathy, radiation-induced neuropathy, and post-polio syndrome (Turner and Talbot 2013, Garg, Park et al. 2017). Hirayama disease sometimes represents a particular challenge as it presents with wasting and weakness of one or both arms, but, in contrast to MND, symptoms plateau and do not progress; hence, it is not a life-limiting condition (Hirayama, Tomonaga et al. 1987).

PLS is characterised by insidiously progressive weakness and spasticity with exclusively UMN signs and has the best prognosis amongst the various forms of MND (Almeida, de Carvalho et al. 2013). Unlike ALS, onset tends to be symmetrical and typically affects the lower limbs, although bulbar onset can also occur (Pringle, Hudson et al. 1992). Bladder dysfunction is not typical, but may develop in the course of the disease (Singer, Statland et al. 2007). Frontal cognitive dysfunction (including rare cases of frontotemporal dementia) has also been reported in PLS (Caselli, Smith et al. 1995, Mackenzie and Feldman 2004, Zago, Poletti et al. 2008). Diagnostic criteria require the patient to be at least 25 years old, for UMN symptoms to be present in a minimum of two regions (bulbar, upper, or lower limbs), evidence of progression over at least two years, and exclusion of mimic disorders. Unlike ALS, PLS diagnostic classification also includes disease duration: probable PLS refers to disease lasting between two and four years from diagnosis, whereas a diagnosis of definite PLS requires at least four years of disease duration (Turner, Barohn et al. 2020). Beside UMN-predominant ALS, hereditary spastic paraparesis is the main differential diagnosis. Additional differential diagnoses include: primary progressive multiple sclerosis, structural or vascular lesions at the level of the foramen magnus or

bilateral parasagittal falcine region, the anti-amphiphysin variant of stiff person syndrome, infectious spastic paraparesis caused by syphilis or human T-cell lymphoma virus I or II, and adult onset adrenoleukodystrophy (adrenomyeloneuropathy) (Turner, Barohn et al. 2020).

1.1.3.4 Motor neuron disease: management

At present, there is no cure for MND. Hence, supportive and symptomatic management aims are to maximise patients' autonomy, dignity, and quality of life (Hobson and McDermott 2016). Multidisciplinary care extends survival and improves quality of life (Traynor, Alexander et al. 2003). Symptoms such as sialorrhoea, bronchial secretions, cramps, spasticity, laryngospasm, mood disturbances, and constipation can be managed with drugs and physiotherapy (McDermott and Shaw 2008). Particular attention should be given to appropriate nutrition and to timely insertion of gastrostomy (ProGas 2015) to ensure that patients do not find themselves in the situation of being hungry, but unable to sustain their nutritional requirements. Additionally, weight loss is an adverse prognostic factor (Moglia, Calvo et al. 2019), so it is possible that appropriate nutritional interventions might improve survival, although this is currently unproven. Appropriate respiratory management is crucial as early use of non-invasive ventilation (NIV) prolongs survival by approximately six months as well as improving quality of life (Bourke, Tomlinson et al. 2006).

Despite a growing body of research, pharmacological treatment aimed at slowing progression is very limited. The EMA and FDA-approved riluzole is the drug of choice for ALS and has been shown to provide a median survival benefit of three months (Bensimon, Lacomblez et al. 1994, Lacomblez, Bensimon et al. 1996, Miller, Mitchell et al. 2012). The benefits of the recently FDA-approved medication, edaravone, (Abe K 2017) are yet to be fully evidenced: inclusion criteria in the recent trial were strict and perhaps not representative of the general MND population (Hardiman and van den Berg 2017). No survival benefit has been demonstrated to date, and concerns have been raised after an analysis based of database data showed that both placebo and control groups in the trial did worse than patients treated with standard of care (Turnbull 2018).

MND is known to be a remarkably heterogeneous condition, not only pathophysiologically, but also from a clinical point of view. Examples of clinical phenotypic heterogeneity include variable presentation, site of disease onset, atypical symptomatology, relative upper and lower motor neuron disease burden, and duration of clinical course. These multiple sources of variability may partially explain why, to date, no validated marker of disease progression exists. This is a problem for clinical trials. Taking the example of variable rates of disease progression, this is not easily predictable at diagnosis and, whilst median survival is two to three years from symptom onset, five to ten per cent of patients survive for over a decade (Turner, Parton et al. 2003). This makes the standard primary endpoints in phase III clinical trials (survival or time to invasive ventilation) problematic, because trials

tend to become biased towards slow progressors, and consequently so prolonged and expensive that many promising agents in the laboratory never reach trial stage. Patient stratification is another problem associated with disease heterogeneity which has not yet been resolved (Swash 2019). Objective biomarkers of disease progression which could potentially act as a surrogate outcomes in clinical trials are the object of intensive research (Verber, Shepheard et al. 2019). At present, disease progression is most frequently evaluated by assessing the rate at which symptoms (such as muscle weakness, swallowing difficulties, and respiratory dysfunction) appear and by scoring disability, typically using the revised ALS functional rating scale (ALSFRS-R) which is reported in the appendix (Cedarbaum, Stambler et al. 1999). Notably, these assessments reflect the symptoms of disease, not primary pathophysiological mechanisms, and some ALSFRS-R questions can be affected by medical interventions. For instance, the saliva score can improve with appropriate management of sialorrhoea, whereas respiratory scores are significantly reduced in people using NIV even if this is indicated exclusively for sleep apnoea (and not MND-related respiratory dysfunction). For these reasons, researchers seek to discover sensitive indicators of underlying molecular processes which change proportionally to disease severity and could potentially provide information about early treatment response and clinical benefit in trials. The discovery of such a biomarker would be invaluable both in clinic, to optimise patient management plans and anticipate complications, and in clinical trials to shorten duration and reduce costs (Verber, Shepheard et al. 2019).

SECTION 2

Magnetic resonance imaging and spectroscopy in motor neuron disease

Conventional anatomical MRI has an important role in the routine clinical workup of MND to exclude mimics. Nonetheless, currently, it is not used as a diagnostic, prognostic, or disease progression marker as sensitivity at individual level is low. Research has focused on employing other advanced MRI modalities to elucidate pathophysiology non-invasively and to explore their potential as imaging biomarkers. Magnetic resonance spectroscopy, in particular, is a promising tool to address the abovementioned issues. This advanced modality is a non-invasive tool to detect and quantify concentrations of molecules *in vivo,* some of which are highly relevant to MND-related disease processes. Furthermore, it can be carried out safely, as it uses non-ionising radiation, and in conjunction with standard clinical MRI, so it has potential to be incorporated into clinical practice.

This section will briefly outline how MRI has been applied in MND research to date and will then focus on proton magnetic resonance spectroscopy (^{1}H-MRS), which is an analogous technique to ^{31}P-MRS, the modality employed in the experiments in this thesis. Currently, only ^{1}H-MRS is employed in clinical neurology (for instance, NICE guidelines recommend it is used in the clinical workup of suspected

gliomas), whereas heteronuclear MRS, such as ^{31}P-MRS, still remains confined to the realm of research. The small number of ^{31}P-MRS studies that have been conducted in muscle in MND to date will be reviewed together with energy metabolism in section three of this chapter, as they provide complementary information on muscle bioenergetic profiling. No previous cranial ^{31}P-MRS studies have been performed in MND to date.

1.2.1 Magnetic resonance imaging

Motor neuron disease-related neuroaxonal degeneration is reflected in focal atrophy of motor regions on conventional MRI evaluated using voxel-based morphometry and surface-based analysis (Ellis, Suckling et al. 2001, Grosskreutz, Kaufmann et al. 2006, Mezzapesa, D'Errico et al. 2013, de Albuquerque, Branco et al. 2017, Grolez, Kyheng et al. 2018). In group-level analyses, atrophy becomes more prominent as disease progresses and correlates with UMN signs (Walhout, Westeneng et al. 2015), disease severity, including cognitive dysfunction (Abrahams, Goldstein et al. 2005, Crespi, Dodich et al. 2018), and speed of disease progression (Charil, Corbo et al. 2009). Nonetheless, this marker is not sensitive enough to be diagnostic at individual patient level.

In addition to atrophy, T_2-, T_2 star-, and susceptibility-weighted hypointensities can occasionally be detected in motor cortex and are likely caused by glial cells containing ferritin (Oba, Araki et al. 1993, Ignjatovic, Stevic et al. 2013, Adachi, Sato et al. 2015). Hyperintensities are sometimes present along the corticospinal tract (Peretti-Viton, Azulay et al. 1999, Hecht, Fellner et al. 2001, Charil, Corbo et al. 2009) on T_2-weighted sequences, although interpretation of these radiological findings is equivocal as they may be indicative of oedema, reactive gliosis, or even myelin damage. Magnetisation transfer imaging, which assesses demyelination and neurodegenerative processes, has also shown alterations along the corticospinal tract (Kato, Matsumura et al. 1997, Tanabe, Vermathen et al. 1998, Cosottini, Pesaresi et al. 2011). From functional MRI (fMRI) investigations, there is evidence of cortical remapping of motor regions (Konrad, Henningsen et al. 2002, Schoenfeld, Tempelmann et al. 2005, Konrad, Jansen et al. 2006, Stanton, Williams et al. 2007) and of loss of inhibitory interneurons leading to increased motor activation in the early stages of disease (Kollewe, Munte et al. 2011). However, as disease progresses, the neurodegenerative process becomes more pervasive and leads to reduced motor activation (Kollewe, Munte et al. 2011).

Quantitative volumetric analyses have shown reduced grey and white matter volumes also in areas which were otherwise thought to be spared by MND-related neurodegeneration, such as corpus callosum, thalamus, cerebellum, temporal, parietal, and occipital lobes (Kassubek, Unrath et al. 2005, Mezzapesa, Ceccarelli et al. 2007, Thivard, Pradat et al. 2007, Zhang, Mao et al. 2014), indicating the multisystem nature of MND. This notion is supported by diffusion tensor imaging (DTI) and fMRI studies. DTI has consistently shown dysruption to callosal tracts (Ellis, Simmons et al. 1999, Graham,

Papadakis et al. 2004, Filippini, Douaud et al. 2010, Tang, Chen et al. 2015) and other extra-motor regions (Agosta, Pagani et al. 2007, Ciccarelli, Behrens et al. 2009, Sage, Van Hecke et al. 2009), whereas fMRI points towards changes in executive, limbic, and even sensory regions (Lule, Diekmann et al. 2007, Lule, Diekmann et al. 2010, Palmieri, Naccarato et al. 2010, Goldstein, Newsom-Davis et al. 2011).

1.2.2 Proton magnetic resonance spectroscopy

Magnetic resonance spectroscopy is a complementary technique to structural MRI, that aims to quantify the relative concentrations of biochemical metabolites. The basic principle underpinning MRS is that the resonant frequency of a given molecule is affected by the molecular environment, resulting in different chemical groups that contain the same atom (e.g. ^{1}H) to be separated in frequency. The physics underlying this phenomenon is detailed in the appendix.

Proton magnetic resonance spectroscopy allows detection of N-acetylaspartate (NAA), N-acetylaspertylglutamate (NAAG), total creatine (tCr, i.e. phosphocreatine and creatine), and choline-containing compounds (Cho). Additionally, other metabolites can be resolved by altering acquisition parameters (e.g. by employing a short echo time or TE) or by using specific spectral editing techniques which naturally denoise the signal to allow discrimination of metabolites otherwise concealed by the main ^{1}H-MRS peaks. Examples of additional resonances that can then be resolved include the product of anaerobic glycolysis, lactate; sugars, such as myoinositol (mI); and amino acids, such as glutamate (Glu), glutamine (Gln), alanine, reduced glutathione (GSH), and γ-amino-butyrate (GABA) (Govindaraju, Young et al. 2000, Weiduschat, Mao et al. 2014). An example of a ^{1}H-MRS spectrum is shown in Figure 1.1 (data courtesy of Prof Nigel Hoggard, University of Sheffield).

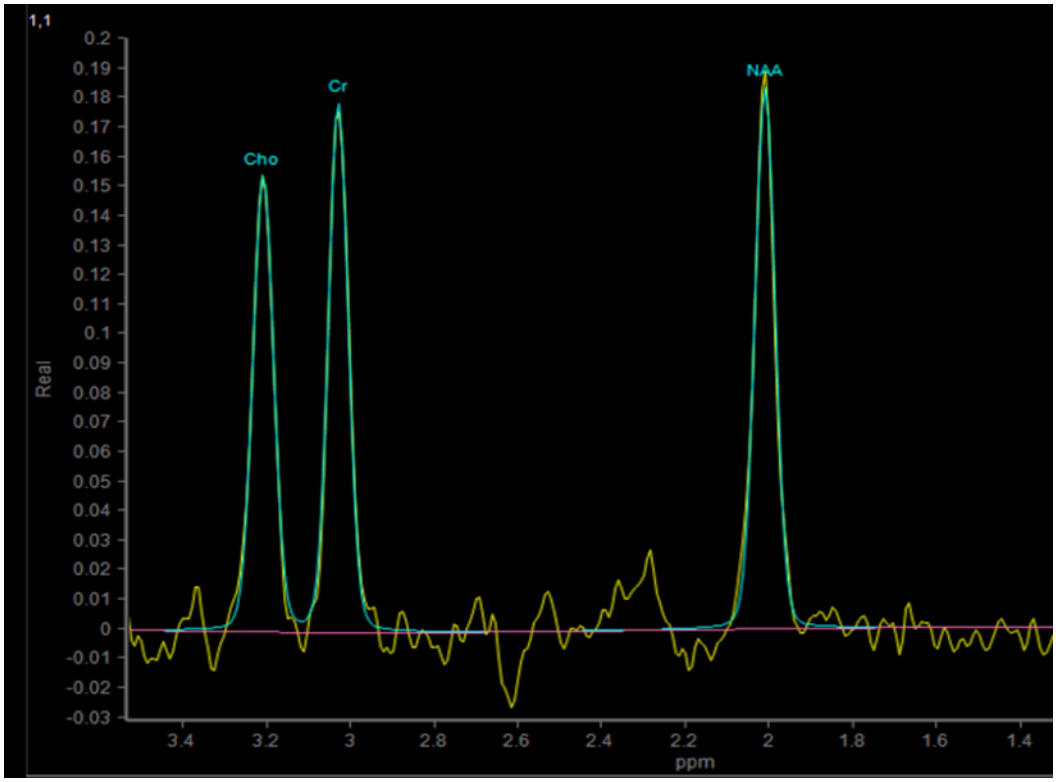

Figure 1.1 A proton spectrum acquired from the cerebellum of a healthy control at 3 tesla with a long echo time.
The spectrum is characterised by the following main peaks: a resonance at 2.01 parts per million (ppm), primarily comprising N-acetylaspartate (NAA) and containing a minor contribution of N-acetylaspertylglutamate (NAAG), a peak at 3.03 ppm often denoted tCr or simply Cr containing resonances from both creatine and phosphocreatine, and a 3.18 ppm resonance representative of various choline-containing compounds (Cho). Additionally, other metabolites that can be resolved by altering the MRI sequences or using specific J-editing techniques include: lactate at 1.31 ppm, alanine at 1.46 ppm, glutamate and glutamine resolved as an individual peak denoted Glx at 2.04 to 2.45 ppm, reduced glutathione at 2.98 ppm, γ-amino-butyrate at 3.03, scylloinositol at 3.34, and myoinositol at 3.52 (Govindaraju, Young et al. 2000, Weiduschat, Mao et al. 2014). The units on the x-axis are parts per million (ppm), indicating resonance frequency, whereas on the y-axis the real amplitude values are expressed in arbitrary units. Spectrum courtesy of Prof Nigel Hoggard, University of Sheffield.

The area underneath each peak is proportional to the density of protons contributing to the signal, thus providing a proxy of metabolite levels. Most spectroscopic studies in MND have employed ^{1}H-MRS and focused on identifying characteristic variations of brain metabolites to probe pathophysiology and test ^{1}H-MRS as a potential biomarker. A qualitative description of these research articles is provided. Quantitative comparison between spectroscopic studies in the absence of the raw data is not feasible because of variation in types of hardware used, acquisition parameters, localisation methods, analysis techniques and software, and reported results in the literature. As further detailed in the description of MRS physics provided in the 8.6, all these factors can ultimately affect the resulting values and perhaps represent a reason that, despite a large body of literature on the subject, no consensus has yet been reached in regard to many MRS-related research questions in MND.

1.2.2.1 Explorative proton magnetic resonance spectroscopy studies and insights into pathophysiology

Considering that MND inevitably affects the pyramidal tracts, most explorative studies, summarised in Table 1.2, have acquired spectra from primary motor cortex and regions spanned by the corticospinal-corticobulbar tracts. The precentral gyrus was the region of interest in most cases (Jones, Gunawardena et al. 1995, Gredal, Rosenbaum et al. 1997, Ellis, Simmons et al. 1998, Schuff, Rooney et al. 2001, Han and Ma 2010, Sivak, Bittsansky et al. 2010, Foerster, Callaghan et al. 2012, Foerster, Pomper et al. 2013, Weiduschat, Mao et al. 2014, Sako, Abe et al. 2016, Atassi, Xu et al. 2017, Cheong, Marjanska et al. 2017, Wang, Li et al. 2017), while a smaller number of studies imaged the brainstem (Pioro 1997, Cwik, Hanstock et al. 1998, Pioro, Majors et al. 1999, Sivak, Bittsansky et al. 2010, Foerster, Pomper et al. 2013, Cheong, Marjanska et al. 2017), and even fewer reported results from cervical spinal cord (Carew, Nair et al. 2011, Ikeda, Murata et al. 2013). The relative dearth of studies assessing the spinal cord is likely due to technical limitations: the diameter of the cord is only slightly larger than the minimum volume that can currently be resolved by ^{1}H-MRS, causing acquisitions to have inherently low signal-to-noise ratios. In addition, even the slightest movement in that region (e.g. due to respiration or the cardiac cycle) results in significant motion artefact which, when combined with partial volume effects (i.e. some signal is acquired from surrounding cerebrospinal fluid – CSF), can confound results (Ikeda, Murata et al. 2013). This is because, in ^{1}H-MRS, water is often used as a reference to quantify other molecules; water is present in both CSF and brain tissue, whereas other metabolites are found exclusively in cerebral matter. This discrepancy can be accounted for during the absolute quantification process if the relative proportion of CSF in the region of interest is known; nonetheless, if motion occurs during spectroscopic acquisition, the correction for partial volume effect may also be confounded and results may be biased (Kreis 2004). Another factor to consider is that the spinal cord is a particularly magnetically inhomogeneous area, a feature that renders it prone to magnetic susceptibility artefacts caused at interfaces between differing tissues. This issue, in conjunction with motion, may render interpretations of results still more challenging (Ikeda, Murata et al. 2013).

To date, every spectroscopic study in MND of the primary motor cortex, brainstem, and spinal cord has shown a significant average reduction of NAA, with the exception of a single study (Ellis, Simmons et al. 1998) which described a non-significant reduction of the NAA/tCr ratio in sixteen patients compared to eight healthy controls. Interpretation of this finding is controversial. Traditionally, NAA has been employed as a marker of neuronal viability since early immunohistochemical (Simmons, Frondoza et al. 1991) and chromatographic (Urenjak, Williams et al. 1992) studies showed it to be exclusively localised in neurons. According to this interpretation, an NAA decrease directly reflects neuronal loss which is characteristic of MND. However, it is possible to argue against this simplistic view which does not account for the complex biochemistry of the amino acid. Considering that NAA is synthesised in both mitochondria (Patel and Clark 1979) and the endoplasmic reticulum (Lu, Chakraborty et al. 2004),

MND-related bioenergetic deficits and endoplasmic reticular stress (Ruegsegger and Saxena 2016, Smith, Shaw et al. 2017) could each potentially decrease its concentration in the absence of neuronal cell death (Ciccarelli, Toosy et al. 2010). Novel discoveries might offer a third alternative explanation. Recently it has been demonstrated that, although the NAA synthetic enzyme, acetyl-CoA/l-aspartate N-acetyltransferase, is expressed by neuronal cells (Wiame, Tyteca et al. 2009), its catabolic enzyme, aspartoacylase, is found in oligodendrocytes (Madhavarao, Moffett et al. 2004). In line with these findings, other groups (Bhakoo and Pearce 2000, Nordengen, Heuser et al. 2015) showed that NAA could also be detected in mature oligodendrocytes, casting doubt on the hypothesis that NAA is exclusively a neuronal marker. It has been hypothesised that the role of NAA is to store acyl groups and transfer them from neurons to oligodendrocytes (Ariyannur, Moffett et al. 2010) for myelin synthesis and maintenance (Chakraborty, Mekala et al. 2001). This could signify that NAA is analogous to molecules such as lactate and glutamate which are shuttled between neurons and glial cells. In MND, dysregulation of this cross-talk for lactate (Ferraiuolo, Higginbottom et al. 2011) and glutamate (Shaw and Ince 1997) is a well characterised pathophysiological mechanism. Accordingly, alterations in NAA concentration could be another indicator of dysfunctional neuronal-oligodendrocyte interactions in this disease. Further research is needed to clarify the precise pathophysiology that a reduction in NAA represents.

With the exception of tCr, which appears unchanged by the disease process, as studies consistently show no significant difference between patients and healthy controls (Schuff, Rooney et al. 2001, Govind, Sharma et al. 2012, Atassi, Xu et al. 2017), it is unclear whether the concentration of the other metabolites measured by ^{1}H-MRS is systematically altered by MND. Previously, consensus had been reached regarding a putative increase of Glx (quantified as (Glu+Gln)/tCr) (Pioro 1997, Pioro, Majors et al. 1999, Han and Ma 2010) until (Atassi, Xu et al. 2017) recently reported that absolute Glu was decreased and Gln was unchanged in their high-field 7T study. The group employed a very short TE (5 ms) which minimises potential alterations caused by T_2 variations induced by the disease process, and adjusting for this confound argues for the validity of their results. Consequently, the previously observed apparent (Glu+Gln)/tCr) increases could be alternatively interpreted as a consequence of T_2 disparities between patients and controls, although it is important to notice that alterations in Glu metabolism are thought to be highly relevant to MND excitotoxicity (Van Den Bosch, Van Damme et al. 2006). In the section 8.4, putative effects of TE and T_2 relaxation on measured signal intensity are discussed.

In a similar manner, (Foerster, Pomper et al. 2013, Ikeda, Murata et al. 2013) both showed an elevation of the glial marker mI in patients, a finding that was not replicated by (Atassi, Xu et al. 2017). With regard to Cho concentration, one study reported a decrease (Carew, Nair et al. 2011), two an increase (Schuff, Rooney et al. 2001, Govind, Sharma et al. 2012), and three studies a non-significant change (Cwik, Hanstock et al. 1998, Pioro, Majors et al. 1999, Atassi, Xu et al. 2017).

Spectral editing has allowed quantification of two molecules thought to be particularly relevant to the pathogenesis of MND: GABA, an inhibitory neurotransmitter, possibly reduced as a consequence of glutamate excitotoxicity (King, Woodhouse et al. 2016), and GSH, one of the molecules involved in maintenance of cellular oxidoreductive homeostasis, likely altered by MND-associated oxidative stress (Barber and Shaw 2010). Both metabolites were shown to be decreased by (Foerster, Callaghan et al. 2012, Foerster, Pomper et al. 2013, Weiduschat, Mao et al. 2014), but were reported unchanged by (Atassi, Xu et al. 2017, Cheong, Marjanska et al. 2017). Considering the significance of these molecules to the pathophysiology of this neurodegenerative disease and the fact that they may be reflective of alterations in pathways that can be mitigated by pharmacological interventions (e.g. riluzole for glutamate excitotoxicity), additional research is warranted, possibly involving a translational approach linking spectroscopic data to measurements of metabolites in CSF.

Table 1.2 Explorative ^{1}H-MRS studies of motor regions: primary motor cortex, brainstem, and spinal cord.
Cho: Choline, Cr: Creatine, GABA: γ-amino-butyrate, Glu: Glutamate, Glx: Glutamate, glutamine, and γ-amino-butyrate resonance peak, GSH: Glutathione, mI: Myo-inositol, NAA: N-acetylaspartate, NS: Non-significant, PMA: Progressive muscular atrophy, PMC: Primary motor cortex, tCr: Creatine and phosphocreatine

Study	*Anatomical area of interest*	*Number patients/ controls*	*Significant results*
(Jones, Gunawardena et al. 1995)	PMC	7/7	NAA/tCr ↓, NAA/Cho ↓
(Gredal, Rosenbaum et al. 1997)	PMC	10/8	NAA ↓, NAA unchanged in PMA
(Pioro 1997)	Medulla	6/6	NAA/tCr ↓, NAA ↓, Glx/tCr ↑, Glu ↑
(Cwik, Hanstock et al. 1998)	Pons and Medulla	12/17	NAA/tCr ↓
(Ellis, Simmons et al. 1998)	PMC	16/8	NS
(Pioro, Majors et al. 1999)	Medulla	10/7	NAA/tCr ↓, NAA ↓, Glx/tCr ↑
(Schuff, Rooney et al. 2001)	PMC, Anterior and posterior limb of internal capsule	10/9	NAA ↓ PMC, Cho ↑ Posterior limb of internal capsule
(Han and Ma 2010)	PMC, Posterior limb of internal capsule	15/15	NAA/Cr ↓ PMC and posterior limb of internal capsule, Glu/Cr ↑ PMC and posterior limb of internal capsule, Glx/Cr ↑ PMC and posterior limb of internal capsule
(Sivak, Bittsansky et al. 2010)	PMC, Pons and Medulla, Occipital lobe	11/11	NAA/tCr ↓ PMC
(Carew, Nair et al. 2011)	Cervical spinal cord (C2)	14/16	NAA/tCr ↓, NAA/mI ↓, Cho/tCr ↓
(Foerster, Callaghan et al. 2012)	PMC, Subcortical white matter	10/9	GABA ↓ PMC
(Govind, Sharma et al. 2012)	PMC, Centrum semiovale Corona radiata Posterior limb of internal capsule Cerebral peduncle	38/70	NAA ↓, Cho ↑ Cho/NAA ↑
(Ikeda, Murata et al. 2013)	Cervical spinal cord (C1-C3)	19/20	NAA/tCr ↓ NAA/mI ↓ mI/tCr ↑
(Foerster, Pomper et al. 2013)	PMC, Sub-cortical white matter, Pons	29/30	GABA ↓ PMC NAA ↓ PMC, subcortical white matter, and pons, mI ↑ PMC, subcortical white matter
(Weiduschat, Mao et al. 2014)	PMC	11/11	GSH/totH_2O ↓, GSH/tCr ↓, NAA/tCr ↓
(Cheong, Marjanska et al. 2017)	PMC, Pons	19/17	NAA/mI ↓
(Atassi, Xu et al. 2017)	PMC	13/12	NAA ↓, Glu ↓, mI/NAA ↑, GSH and GABA NS
(Wang, Li et al. 2017)	Hand motor cortex, Postcentral gyrus	14/14	NAA/tCr ↓

Spectroscopic evidence of involvement of non-motor areas in MND is yet to be conclusively provided and ^{1}H-MRS studies are summarised in Table 1.3.

Given the prevalence of cognitive and behavioural dysfunction in MND, three studies measured NAA concentration in brain areas involved in cognition. An early study was perhaps underpowered, but showed relatively lower NAA in the anterior cingulate gyrus in a subgroup of patients (Strong, Grace et al. 1999); whereas (Usman, Choi et al. 2011) did not detect any significant differences in metabolites in the mesial prefrontal cortex. Lastly, (Quinn, Elman et al. 2012) compared patients with and without compromised verbal fluency while attempting to correlate the outcome of the test with NAA/tCr in the dorsolateral prefrontal cortex; no significant differences emerged from this study, which only assessed letter fluency and had no healthy control group. Thalamic involvement was assessed by two groups (Sharma, Saigal et al. 2011, Sudharshan, Hanstock et al. 2011). The first group reported no metabolite alterations, while the second showed a decrease of NAA and an increase in Cho.

Considering the small number of studies and heterogeneity of areas investigated, it remains problematic to conclude whether non-motor area abnormalities are consistently detectable using ^{1}H-MRS in MND. Advances in MRS imaging techniques which allow spectroscopic acquisitions from the entire brain could provide more certainty and remove a potential anatomical selection bias. Two of the three studies that employed this procedure detected anatomically feasible metabolic alterations of NAA along the corticospinal tracts (Govind, Sharma et al. 2012, Stagg, Knight et al. 2013). Interestingly, (Verma, Woo et al. 2013), also reported NAA/Cho changes in numerous cortical and subcortical areas including the striatum, the lingual gyrus, and the occipital lobe; the latter region is generally considered to be spared by the disease process and people with MND do not develop visual clinical features.

Table 1.3 Additional ^{1}H-MRS explorative studies conducted in non-primary motor regions.
ALS: Amyotrophic lateral sclerosis, ALS-FTD: Amyotrophic lateral sclerosis with concomitant frontotemporal dementia, Cho: choline, mI: Myo-inositol, NAA: N-acetylaspartate, NS: Non-significant, tCr: creatine and phosphocreatine.

Study	***Anatomical area of interest***	***Number of patients/health controls***	***Significant results***
(Strong, Grace et al. 1999)	Anterior cingulate gyrus	13/5	NAA/tCr ↓ in bulbar onset ALS
(Sudharshan, Hanstock et al. 2011)	Mid-cingulate gyrus Thalamus	14/14	NAA/Cho ↓ Mid Cingulate gyrus NAA/Cho NS Thalamus
(Usman, Choi et al. 2011)	Mesial prefrontal cortex	24/15 (of which 2 ALS-FTD)	NAA/mI ↓ NAA NS mI NS
(Sharma, Saigal et al. 2011)	Basal ganglia Thalamus	14/17	NAA ↓ basal ganglia and thalamus Cho ↑ basal ganglia and thalamus (not in caudate) NAA/Cho ↓ basal ganglia and thalamus (not in caudate)
(Quinn, Elman et al. 2012)	Dorsolateral Prefrontal Cortex Occipital region	25/no healthy controls	NS

1.2.2.2 Proton magnetic resonance spectroscopy as a putative diagnostic marker

Proton magnetic resonance spectroscopy has been proposed as a possible diagnostic biomarker of MND based on potential as an objective indicator of UMN dysfunction. Some spectroscopic studies have shown an inverse correlation between UMN signs and NAA concentration in the precentral gyrus (Ellis, Simmons et al. 1998, Schuff, Rooney et al. 2001, Mitsumoto, Ulug et al. 2007); moreover, no changes in NAA were present in patients affected by PMA (Gredal, Rosenbaum et al. 1997). Consequently, five studies (Chan, Shungu et al. 1999, Pohl, Block et al. 2001, Kaufmann, Pullman et al. 2004, Pyra, Hui et al. 2010, Cervo, Cocozza et al. 2015) calculated the sensitivity and specificity of ^{1}H-MRS as compared to other candidate diagnostic tests, namely, standard structural MRI, DTI, and TMS. Studies are summarised in Table 1.4. Overall, ^{1}H-MRS appeared more sensitive and specific than conventional MRI, DTI, and TMS. Additionally, (Foerster, Carlos et al. 2014) used Bayesian analysis and demonstrated that the combination of ^{1}H-MRS and DTI yielded a very good positive likelihood ratio (6.20) and an excellent negative likelihood ratio (0.08), effectively advocating use of multimodal MRI in the diagnosis of MND.

However, to be validated as a diagnostic marker to detect subclinical central motor dysfunction and to demonstrate superiority to the current standard of clinical assessment, ^{1}H-MRS should be compared to neurological examination and ideally validated by neuropathology. Definitive demonstration of corticospinal degeneration can only be provided by a pathologist with tissue obtained either through biopsy or at *post-mortem*. This approach, albeit scientifically sound, is generally impractical: brain biopsies are invasive procedures not warranted in this group of patients, while the period between testing and autopsies (rarely performed clinically in the UK) is inevitably uncertain. Despite these barriers, this study design was adopted by (Kaufmann, Pullman et al. 2004) and their data suggested that MRS is able to detect subclinical UMN pathology. A limitation of the study is that relatively few autopsies were performed, decreasing statistical power. Additional evidence supporting ^{1}H-MRS as a sensitive modality to detect pre- and subclinical dysfunction was provided by a study that investigated 24 asymptomatic *SOD1* mutation carriers. Interestingly, the spectroscopic metabolic phenotype observed in the spinal cord was analogous to patients clinically affected by MND (Carew, Nair et al. 2011).

Table 1.4 Diagnostic sensitivity and specificity of ^{1}H-MRS compared to other modalities.
ALS: Amyotrophic lateral sclerosis, Cho: choline, CST: Corticospinal tract, DTI: Diffusion tensor imaging, FA: Fractional anisotropy, NA: Not applicable, NAA: N-acetylaspartate, tCr: creatine and phosphocreatine, TMS: Transcranial magnetic stimulation.

Study	***Modalities***	***^{1}H-MRS: sensitivity***	***^{1}H-MRS: specificity***	***Alternative modality: sensitivity***	***Alternative modality: specificity***
(Chan, Shungu et al. 1999)	^{1}H-MRS (NAA/tCr cut-off: 2.5) MRI (CST hyperintensity)	73%	90%	43%	7%
(Pohl, Block et al. 2001)	^{1}H-MRS (NAA/Cho cut-off: NA) TMS	53%	NA: no healthy controls were included in the study	63%	NA: no healthy controls were included in the study
(Kaufmann, Pullman et al. 2004)	^{1}H-MRS (NAA/tCr cut-off: 2.5) TMS	86%	37%	77%	38%
(Pyra, Hui et al. 2010)	^{1}H-MRS (NAA/Cho cut-off: 5.640, NAA/tCr cut-off: 1.8) DTI (FA cut-off 0.422)	100%(NAA/Cho) 54%(NAA/tCr)	85% (NAA/Cho) 100% (NAA/tCr)	79%	79%
(Cervo, Cocozza et al. 2015)	^{1}H-MRS (NAA/tCr cut-off: NA) MRI (CST hypointensity)	71%	75%	63%	71%

1.2.2.3 Proton magnetic resonance spectroscopy as a putative marker of disease progression

Longitudinal studies investigating whether ^{1}H-MRS can be employed as a marker of MND progression are few and limited by small cohort sizes. Perhaps, this is because in a terminal disease, such as MND, longitudinal studies are subjected to substantial attrition and an inherent selection bias since only those patients with well-preserved respiratory function (required to be able to lie flat in the scanner for the duration of the MRS session) can be recruited.

(Unrath, Ludolph et al. 2007) showed a significant decrease over time in NAA/tCr+Cho in the precentral gyrus of six patients assessed over a six-month period. (Bowen, Pattany et al. 2000) did not show any change in NAA in five patients scanned after a two-week interval, whereas they demonstrated a reduction in three patients scanned after three months. A NAA trend reported by (Rule, Suhy et al. 2004) is inconsistent with other studies, but derived from the largest longitudinal cohort to date: average NAA decreased in the first three months of the study, but then rose above baseline levels in 13 patients.

It remains unclear whether there is an association between proton spectroscopic data and other parameters employed to assess disease progression and disability, namely the ALSFRS-R, and forced vital capacity. Correlation was shown by some groups in cross-sectional studies (Ellis, Simmons et al. 1998, Pioro, Majors et al. 1999, Sivak, Bittsansky et al. 2010, Govind, Sharma et al. 2012, Foerster, Pomper et al. 2013, Ikeda, Murata et al. 2013, Stagg, Knight et al. 2013, Foerster, Carlos et al. 2014, Atassi, Xu et al. 2017), but not by others (Sarchielli, Pelliccioli et al. 2001, Carew, Nair et al. 2011, Weiduschat, Mao et al. 2014, Liu, Jiang et al. 2015, Sako, Abe et al. 2016, Wang, Li et al. 2017).

1.2.2.4 Proton magnetic resonance spectroscopy as a putative marker of treatment response

Following two publications (Kalra, Cashman et al. 1998, Kalra, Tai et al. 2006) in which an amelioration of the NAA/tCr ratio early after initiation of treatment with riluzole was shown (measured after three weeks in the first study and after one day in the second), various other groups have employed ^{1}H-MRS as a therapeutic response biomarker.

(Kalra, Cashman et al. 2003, Khiat, D'Amour et al. 2010, Sacca, Quarantelli et al. 2012) carried out trials of gabapentin, minocycline, and growth hormone, respectively, and assessed whether ^{1}H-MRS could detect any NAA change. These trials were negative and no alteration in ^{1}H-MRS spectra following therapy was detected.

In a recent longitudinal study, autologous bone marrow cells were infused intrathecally in 11 MND patients. One year post-infusion, an increase in NAA/tCr ratio was shown in the precentral gyrus compared to 11 untreated MND controls. Additionally, there appeared to be a correlation between baseline NAA and survival (Garcia Santos, Inuggi et al. 2016).

(Atassi, Ratai et al. 2010) employed ^{1}H-MRS in a phase I study to establish the pharmacokinetics of creatine monohydrate. Interestingly, acquired spectra demonstrated a dose-dependent tCr increase as well as a Glu decrease, arguing that oral creatine monohydrate crosses the blood-brain barrier and suggesting that it might contribute to improvements in glutamate excitotoxicity.

1.2.2.5 Proton magnetic resonance spectroscopy in motor neuron disease: conclusions

Overall, spectroscopic studies have provided strong evidence of NAA reduction in motor regions in people living with MND. Further research is needed to determine the significance of this finding, to show whether other metabolites are consistently altered during the disease process, and to assess whether spectral variations can be systematically detected in non-motor areas of the brain.

There is a need for further research to determine whether ^{1}H-MRS is effective at discriminating MND from its common mimics in order to clarify a potential role in routine clinical practice. Moreover, it is important to assess whether the introduction of ^{1}H-MRS would effectively benefit patients in regard to earlier diagnosis and improvement of care. This could be achieved in large randomised trials in which suspected patients would be randomly allocated work-up with and without ^{1}H-MRS, as well as long-term surveillance studies (Gluud and Gluud 2005).

Given the variability of evidence to date, as well as the very small sample size of longitudinal studies, it is impossible yet to draw conclusions on whether ^{1}H-MRS is useful in the assessment of MND progression. Further studies would benefit from evaluation of larger cohorts of patients.

Some proof of concept studies suggest that ^{1}H-MRS could act as a biomarker to assess treatment response. However, further research is needed to determine whether spectroscopy can be employed as a valid surrogate endpoint in clinical trials; response biomarkers reflect changes in a biological parameter following treatment, whereas surrogate biomarkers should also provide an indication of clinical benefit. This correlation between spectroscopy and clinical outcome is yet to be provided.

Lastly, the field would significantly benefit from standardisation of study protocols and analysis techniques which would enable a more consistent comparison of study results.

^{1}H-MRS studies have demonstrated the potential of MRS to assess molecules *in vivo* in MND and as a biomarker. This has paved the way for exploring alternative spectroscopic modalities, especially ^{31}P-MRS, which is the spectroscopic modality of choice to assess bioenergetic dysfunction, a putative pathogenic mechanism in MND, and the main subject of this thesis.

SECTION 3

Principles of bioenergetics

This section introduces parameters that can be measured with ^{31}P-MRS, elaborates on established rudiments of mitochondrial bioenergetics for which the following source was used (Nicholls 2013), and reviews current evidence for mitochondrial alterations in MND.

1.3.1 Phosphorus magnetic resonance spectroscopy: metabolites

31-phosphorus magnetic resonance spectroscopy, analogously to ^{1}H-MRS, allows detection of metabolites. These are chemical moieties containing phosphorus: i.e. chemicals central to energy processes such as adenosine triphosphate (ATP), phosphocreatine (PCr), inorganic phosphate (Pi), and nicotinamide adenine dinucleotide (NAD(P)H and $NAD(P)^{+}$). Their biological role is detailed in the remainder of this chapter. In addition, phosphorus is present in detectable concentrations in biological membranes, specifically in phospholipid anabolites (phosphomonoesters – PME) and catabolic products (phosphodiesters – PDE). Measurement of pH, free intracellular magnesium concentration (Mg^{++}), adenosine diphosphate (ADP), and Gibbs free energy of ATP hydrolysis (ΔG_{ATP}) is also possible by mechanisms detailed in later chapters. A typical phosphorus spectrum is reproduced in the next chapter.

1.3.2 Oxidative phosphorylation and creatine kinase system: mechanistic description

In animal biology, bioenergetic processes are, strictly speaking, those energy transducing reactions that occur across the inner mitochondrial membrane and are referred to as oxidative phosphorylation. During oxidative phosphorylation, oxidation of reducing equivalents (nicotinamide adenine dinucleotide – NADH, and flavin adenine dinucleotide – $FADH_2$) is coupled to phosphorylation of ADP to synthesise ATP, which is the main energy currency of the cell and required in all endergonic cellular reactions. Endergonic reactions are not spontaneous and necessitate energy to be carried out; in living organisms, this energy is transduced directly or indirectly via ATP hydrolysis. This is the reason that appropriate oxidative phosphorylation function is crucial to cellular processes and survival.

Oxidative phosphorylation, depicted in Figure 1.2, is carried out by five complexes located across the inner mitochondrial membrane, which has a very low permeability to protons. Electrons derived from the substrates NADH and $FADH_2$ (synthesised primarily in the tricarboxylic acid cycle, in the pyruvate dehydrogenase reaction, and during glycolysis) are tunnelled across electron transport chain (ETC) complexes until they are transferred onto oxygen which is reduced to water by complex IV (cytochrome

c oxidase). These exergonic reactions are coupled to the endergonic translocation of protons from the mitochondrial matrix to the intermembrane space by ETC complexes I (NADH dehydrogenase or, also known as ubiquinone oxidoreductase), III (cytochrome c reductase), and IV. It is of note that complex II (succinate dehydrogenase) only introduces electrons into the system without concomitant pumping of protons. The combined end result of these processes is to establish an electrochemical gradient across the inner mitochondrial membrane which, in turn, drives ATP synthesis by ATP synthase or complex V.

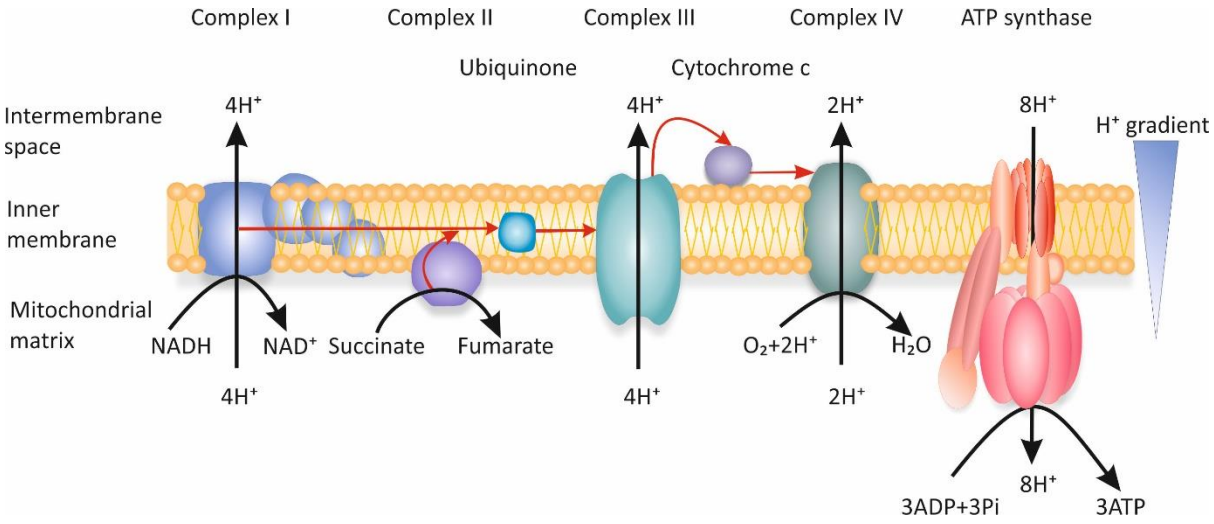

Figure 1.2 Mitochondrial oxidative phosphorylation.
The figure illustrates electron transport chain complexes, located across the inner mitochondrial membrane (yellow), which is characterised by very limited permeability to most ionic particles. Red arrows represent electrons tunnelling from reducing equivalents (NADH and $FADH_2$) to complex IV where water is generated. Tunnelling is coupled to active transport of hydrogen nuclei in complex I, III, and IV generating the electrochemical gradient which drives synthesis of ATP by complex V (also known as ATP synthase). The figure was drawn by the author.

In cells in which energy requirements change rapidly over short timescales, such as neurons and myocytes, oxidative phosphorylation is tightly coupled to the creatine kinase system (Figure 1.3). Upon a neuronal action potential or muscular contraction, cellular energy needs increase rapidly, and the creatine kinase reactions ensure that ATP concentration is maintained stable over time. Specifically, PCr acts as a buffer trans-phosphorylating ADP into ATP. Consequently, PCr concentration decreases at times of elevated energy requirements, whilst ATP concentration remains constant. When resting conditions are re-established, the PCr pool is replenished by oxidative phosphorylation and by mitochondrial creatine kinase; hence the rate at which PCr returns to its resting state values (measured by the PCr recovery constant) is considered an indirect measure of ETC activity. In this regard, it is important to notice that ATP is also synthesised by glycolysis (although at substantially lower stoichiometry compared to oxidative phosphorylation) and that alterations in pH affect PCr recovery, which is, hence, not an absolute measure of mitochondrial capacity. It is likely that this system is active also at times of chronic bioenergetic stress and dysfunction and, hence, PCr concentration reduction may be an early sign of dysfunctional energy metabolism.

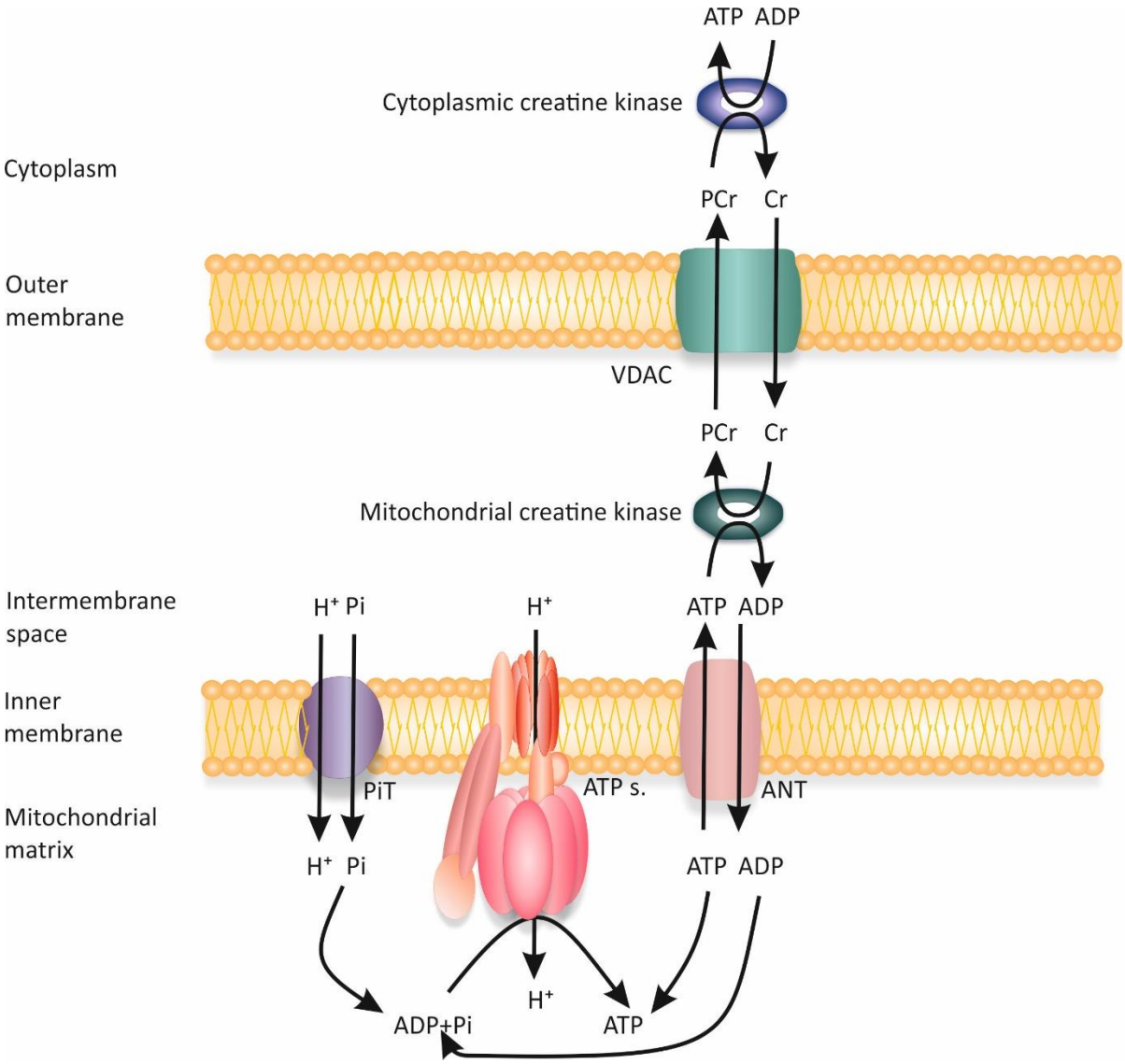

Figure 1.3 The creatine kinase system.
The figure illustrates the mechanism by which adenosine triphosphate (ATP), following synthesis by the ATP synthase, is transported in the mitochondrial intermembrane space by the adenine nucleotide translocator (ANT) in exchange for adenosine diphosphate (ADP). In the intermembrane space, ATP trans-phosphorylates creatine (Cr) to synthesise phosphocreatine (PCr) by the mitochondrial creatine kinase. PCr can exit the mitochondrion through voltage dependent anion channels (VDAC) and, in the cytoplasm, it can be substrate of the cytoplasmic creatine kinase which produces ATP. The figure was drawn by the author.

It is also possible to approach cellular bioenergetics from a thermodynamic perspective. Generally, when assessing the thermodynamic status of a system, a main parameters of interest is Gibbs free energy (ΔG). ΔG provides a useful indicator of the potential for maximal useful energy release (i.e. work) of a closed system. The formal mathematical formulation of ΔG is as per equation 1.1:

Equation 1.1

$$\Delta G = \Delta H - T\Delta S$$

Where H is enthalpy and S is entropy and T is temperature.

Although living organisms are, by definition, open systems (i.e. systems in which both energy and matter are exchanged with their surroundings), it is still possible to use equilibrium thermodynamics (which is typically reserved to systems in which no matter is exchanged, i.e. isolated and closed systems) to characterise the thermodynamic status of specific sets of biological reactions. Specifically, this framework can be used when it can be reasonably assumed that the concentrations of products and reactants are in dynamic equilibrium (i.e. there is no net change in reactants or products being added/removed) and that pressure is constant. Under such circumstances, the system can be considered closed. Equilibrium thermodynamics is particularly useful when assessing processes leading to ATP synthesis which, as shown below, are inherently linked to the maximal amount of useful energy that can be released from ATP hydrolysis.

Every reversible reaction [A] ↔[B] is characterised by its own equilibrium constant, K, defined as the ratio of concentration of products at equilibrium [B_{eq}] over the concentration of reactants at equilibrium [A_{eq}], i.e. K=([B_{eq}])/([A_{eq}]). The ratio of measured products [B_{meas}] to measured reactants [A_{meas}] is defined as the observed mass action ratio ($\mathbb{\Gamma}$), i.e. $\mathbb{\Gamma}$=([B_{meas}])/([A_{meas}]). There is a relationship between ΔG and the degree of displacement of $\mathbb{\Gamma}$ from the reaction's equilibrium, K. Specifically, ΔG as a function of log($\mathbb{\Gamma}$/K) results in an ascending parabola centred around one. This signifies that, when $\mathbb{\Gamma}$=K, and hence log($\mathbb{\Gamma}$/K)=1, ΔG is at its minimum (ΔG slope, i.e. ΔG "content"=0). As a consequence, when the reaction is at equilibrium, no useful energy can be released and no work can be done. As $\mathbb{\Gamma}$ is displaced from equilibrium (a process that requires energy), the magnitude value of ΔG (i.e. ΔG's slope) increases. This is effectively what happens to the mass action of the ATP reactions in living cells; ATP is substantially displaced from its natural equilibrium state, and it is this displacement that renders ATP the main source of "useful energy" (not the presence of the so-called "high energy phosphates") (Nicholls 2013). On this basis, it is possible to derive the equation for ΔG_{ATP}:

Equation 1.2

$$\Delta G_{ATP} = \Delta G' + RT \ln \frac{[ADP] + [Pi]}{[ATP]}$$

Where R is the gas constant and T is temperature. ΔG' depends on cellular conditions, primarily on intracellular ionic milieu determined by pH, Mg^{++}, sodium, and potassium; notably calcium is considered negligible as largely bound to anionic proteins. ΔG' can be calculated empirically using ^{31}P-MRS, and in this thesis the method by (Iotti, Frassineti et al. 2005) was used.

^{31}P-MRS can be employed to measure ΔG_{ATP} which can, hence, be utilised as a measure of how much "useful energy" is potentially available from ATP hydrolysis. ΔG_{ATP} is also a measure of cellular ability to ensure the ATP reactions remain displaced from their natural equilibrium, as ATP concentration is maintained in large excess compared to ADP concentration by the ETC. Bioenergetic dysfunction, can, hence, be represented in a reduction of the ΔG_{ATP} magnitude value, reflected in a drop in ATP to ADP ratio.

Mechanistically, ETC dysfunction can manifest in two ways, either as inhibition of ETC complexes or as mitochondrial uncoupling, and notably the two processes are not mutually exclusive. Complex inhibition leads to a decrease in the electrochemical gradient across the inner mitochondrial membrane and consequent reduction in ATP production. In mitochondrial uncoupling, electron transport across the ETC (oxidation) is no longer associated with ATP synthesis (phosphorylation). This condition is caused by a low-resistance pathway that allows protons to enter the mitochondrial matrix bypassing the ATP synthase; the uncoupled mitochondria oxidise substrate, but produce relatively less ATP, hence efficiency is reduced. Although mild uncoupling is an effective antioxidant defence and is considered to be beneficial, in severe uncoupling, the ATP synthase reverses and hydrolyses ATP triggering a severe energetic deficit.

1.3.3 Bioenergetic dysfunction in motor neuron disease

In ALS mouse and *in vitro* models, it has been consistently shown that the basal rate of mitochondrial ATP synthesis is decreased and that this is associated with mitochondrial depolarisation (Smith, Shaw et al. 2017). As described in above sections, mitochondrial depolarisation with concomitant reduction of ADP phosphorylation can result either from inhibition of the complexes of the ETC (which causes NADH to increase and oxygen consumption to drop), or from mitochondrial uncoupling (typically characterised by a reduction in NADH and increased oxygen utilisation) (Nicholls 2013). In MND, evidence for both hypotheses has been published (Smith, Shaw et al. 2017). Additionally, mitochondrial uncoupling has been suggested to underpin the paradoxical hypermetabolic state characteristically found in about fifty percent of patients (Dupuis, di Scala et al. 2003, Bouteloup, Desport et al. 2009, Dupuis, Gonzalez de Aguilar et al. 2009). Notably, in MND, hypermetabolism is considered to contribute to weight loss, which is an adverse prognostic factor (Marin, Desport et al. 2011). Various hypotheses have been proposed to identify pathogenic mechanisms that could cause these bioenergetic changes. For instance, a role for TDP-43 direct mitochondrial toxicity has been postulated (Gao, Wang et al. 2019), with recent studies suggesting that other proteinaceous aggregates characteristic of MND (the dipeptide repeat proteins $(GR)_{80}$ found in *C9orf72*-related MND, mutant FUS, and SOD1) may also disrupt mitochondrial function (Mattiazzi, D'Aurelio et al. 2002, Onesto, Colombrita et al. 2016, Deng, Wang et al. 2018, Choi, Lopez-Gonzalez et al. 2019). Interestingly, mutations in some genes

encoding mitochondrial proteins (vesicle-associated membrane protein-associated protein B – *VAPB*, coiled-coil-helix-coiled-coil-helix-domain containing protein 10 *CHCHD10*, and valosin-containing protein *VCP*), can be pathogenic for MND (De Vos, Morotz et al. 2012, Bartolome, Wu et al. 2013, Genin, Plutino et al. 2016). It has been difficult to demonstrate that the mitochondrial ETC is impaired in patients' motor neurons, primarily because investigations require a tissue sample which can generally only be acquired by biopsy, which is impractical, or autopsy, which would cause the sample to be affected by the dying process. Additionally, complex activities (particularly complex IV) can be compromised if a sample is inappropriately stored (Pache and Reichmann 1990). Studies appear to have focused on measurement of complex I to IV enzymatic activity and not on ATP synthesis. (Wiedemann, Manfredi et al. 2002) and have shown that complex I, II, III, and IV activity was reduced in the spinal cord of patients. Reduction of complex IV activity in spinal cord was also reported by (Fujita, Yamauchi et al. 1996) and (Borthwick, Johnson et al. 1999). These findings are in contrast to results from (Browne, Bowling et al. 1998) who showed that, in the brain, activity of complex I, II, and III of familial MND patients was elevated compared to patients with sporadic disease (who did not show any variation in ETC function) and to disease controls. In line with these findings, (Bowling, Schulz et al. 1993) showed elevated complex I activity in the motor cortex of a SOD1 patient.

Other research has focussed on assessing metabolism in peripheral tissues, following the argument that MND is a multisystem disease. Skeletal muscles have received particular attention as they represent the effector tissue in MND. Despite numerous published studies, evidence for ETC dysfunction from biopsies is inconclusive (Wiedemann, Winkler et al. 1998, Vielhaber, Winkler et al. 1999, Krasnianski, Deschauer et al. 2005, Echaniz-Laguna, Zoll et al. 2006, Soraru, Vergani et al. 2007, Crugnola, Lamperti et al. 2010). 31-phosphorus magnetic resonance spectroscopy has also been applied in muscle (Table 1.5), but, analogous to histopathological studies, no consensus has yet been reached on whether bioenergetic dysfunction is present in MND muscle.

Table 1.5 ^{31}P-MRS studies conducted in motor neuron disease patients.
ATP: Adenosine triphosphate, NS: Non-significant change. PCr: Phosphocreatine, Pi: Inorganic phosphate.

Study	***Anatomical area of interest***	***Number of patients/ healthy controls***	***Results***
(Zochodne, Thompson et al. 1988)	Forearm flexors	11/30	PCr/Pi ↓ rest pH ↑ rest ATP/ (PCr + Pi) NS
(Sharma, Kent-Braun et al. 1995)	Tibialis anterior	5/5	PCr, Pi, PCr/Pi, and pH NS rest PCr consumption NS exercise
(Kent-Braun and Miller 2000)	Tibialis anterior	6/6	Pi/PCr NS rest
(Grehl, Fischer et al. 2007)	Triceps surae	8/38	PCr/ATP ↑ rest PCr consumption ↓ exercise PCr recovery constant NS
(Ryan, Erickson et al. 2014)	Triceps surae	6/11	PCr, pH rest NS PCr recovery constant ↑

In muscle, PCr recovery in patients was found to be prolonged by (Ryan, Erickson et al. 2014), but unchanged by (Grehl, Fischer et al. 2007). Additionally, there appears to be a decreased drop in PCr upon muscular contraction in MND patients. These phenomena were ascribed to denervation changes and lack of recruitment of motor units (Zochodne, Thompson et al. 1988), but other hypotheses, such as impaired central activation or even existence of MND related primary muscular changes, were also proposed (Sharma, Kent-Braun et al. 1995, Kent-Braun and Miller 2000). These studies concluded that no striking alterations of the bioenergetic status of myocytes can be detected in MND patients, but were perhaps limited by small sample sizes and heterogeneous reporting of resting parameters.

Therefore, whilst ^{31}P-MRS appears an ideally suited technique to investigate hypotheses of bioenergetic dysfunction in MND and may have practical potential as a biomarker of energy metabolism, this field remains in its infancy. The initial research question is whether ^{31}P-MRS is feasible in brain motor regions. To determine utility as a future biomarker, characterisation of the reliability and reproducibility of the technique is necessary. The next step is to apply ^{31}P-MRS to people with MND to determine whether patients can be differentiated from controls, whether there are disease-specific changes in metabolites in brain and in muscle. It is important to assess clinical relevance and sensitivity to longitudinal change. Lastly, this thesis aims to determine whether 31-phosphorus magnetic resonance spectroscopy can be applied in conjunction with other techniques to interrogate specific hypotheses of pathophysiological mechanisms underpinning individual aspects of MND, such as motor fatigability.

CHAPTER 2:
METHODOLOGICAL CONSIDERATIONS IN ESTABLISHING AN IN VIVO 31-PHOSPHORUS MAGNETIC RESONANCE SPECTROSCOPY PROTOCOL IN BRAIN AND MUSCLE

This chapter presents a description of the work that went into establishing the ^{31}P-MRS acquisition protocol employed in the rest of the experiments of this thesis. The main aims were to acquire spectra with optimal signal to noise ratio (SNR) and localised to areas primarily affected by MND. Although some improvements to SNR and spatial resolution may be performed at the post-processing level, this cannot replace optimal acquisition methodology, which depends upon employing optimised hardware and sequences. The initial section of this chapter provides a brief introduction to MRS, using the following sources (de Graaf 2007, Keeler 2010). The methodology, results, and discussion sections report the experiments that were undertaken to solve practical issues that arose during protocol set-up. Specifically, following RF calibration, the aim of initial experiments was to ensure that the phosphorus coils worked appropriately and to optimise a localisation sequence. The selected sequence was then tested to assess signal response to phantoms of incrementing phosphorus concentration (to assess methodological accuracy), and these experiments also guided the choice of an external reference phantom for quantification. Different T_1-weighted volumetric sequences were tested to select optimal parameters for co-registration and segmentation algorithms. Lastly, a protocol for rest and dynamic acquisition of muscle spectra was developed using an MR compatible pulley system built in-house.

2.1 INTRODUCTION

MRS signal is generated as follows: in an MR scanner, a proportion of nuclear spins is aligned parallel with the scanner's magnetic field. When subjected to a radio frequency (RF) pulse which encompasses the Larmor frequency, nuclear resonance is generated. As the pulse subsides, spins return to their original arrangement in a process denoted relaxation and characterised by the T_1 and T_2 relaxation constants. The receiver coil detects the voltage induced by the current generated by the time-varying magnetisation in the transverse plane. The specific chemical environment in which some nuclei are embedded alters their characteristic resonance frequency and thus the energy these nuclei absorb and release. These changes, although minute, can be detected by spectrometers and result in multiple spectral peaks each representing a group of nuclei in their distinctive chemical milieu i.e. a specific molecule. Hydrogen and phosphorus nuclei are characterised by inherently different Larmor

frequencies. Consequently, whilst proton spectra can be acquired using standard clinical MRI hardware, which transmits and receives at hydrogen resonance frequency (127.9 MHz at 3 tesla), ^{31}P-MRS requires a special coil that transmits and detects frequencies encompassing phosphorus Larmor frequency (51.6 MHz at 3 tesla). This is not routinely available on most clinical scanners.

The detected signal is an electrical current proportional to the magnitude of the transverse component of the net transverse magnetisation vector which, in turn, is proportional to the concentration of resonating nuclei. However, numerous other factors affect signal intensity, including longitudinal relaxation constants (T_1) and repetition time (TR), transverse relaxation constants (T_2) and echo time (TE), the magnetic field strength of the scanner, localisation techniques, coil loading, coil sensitivity, and receiver gain. The contribution of some, but not all, of these factors can be eliminated by employing metabolite ratios. In ^{1}H-MRS, tCr or total water is often assumed to be constant and used at the denominator as an internal reference to calculate ratios. However, there is no evidence that the concentration of any metabolite resolved by ^{31}P-MRS is maintained constant across brain regions and in disease, so no absolute internal standard in ^{31}P-MRS has yet been agreed. A potential alternative solution to this problem is to employ an external reference, although this also poses significant challenges, explored in chapter two and three.

T_1 and T_2 relaxation constants vary among different nuclei, molecules, biological tissues, and pathologies. It is possible to exploit such differences to discriminate between tissues and identify disease processes by providing contrast in anatomical MRI, for instance between white matter, grey matter, and CSF. Specifically, this can be done by choosing optimal TE and TR values: T_1 contrast (i.e. based on differences in T_1 relaxation) is maximised using sequences with a relatively short TR (i.e. T_1-weighted images in which both TR and TE are short), whereas T_2 contrast is enhanced by long TE (and long TR) sequences which produce T_2-weighted images. Sequences in which a long TR and short TE are employed minimise both T_1 and T_2 relaxation components and yield images primarily representative of proton concentration, i.e. proton density-weighted images in standard MRI. The same principles apply to spectroscopy, where T_1 and T_2 relaxation effects are often considered confounders requiring correction, as the technique is mainly used as a (semi)quantitative measure of metabolite concentration *in vivo*. The relaxation properties of phosphorus and protons differ: the T_1 of neuro-metabolites resolved by ^{31}P-MRS is a few seconds in duration, whereas it is shorter for ^{1}H-MRS. To minimise effects of T_1 relaxation on signal intensity, long TR acquisitions are needed. A practical consequence is that, in ^{31}P-MRS, a typical long TR value is 4 to 5 seconds (as compared to ^{1}H-MRS where a long TR is usually 2 seconds); this translates into significantly longer scan times in ^{31}P-MRS compared to ^{1}H-MRS.

Owing to the greater natural abundance *in vivo* and relatively larger gyromagnetic ratio of hydrogen, ^{1}H-MRS generates spectra characterised by higher signal and is inherently more sensitive compared to ^{31}P-MRS. Although both ^{1}H-MRS and ^{31}P-MRS can detect compounds of concentration as low as a few

millimolar, the lower sensitivity of ^{31}P-MRS implies that spatial resolution of phosphorus spectroscopy is limited compared to ^{1}H-MRS; in ^{31}P-MRS, minimal size acquisition voxels are typically approximately 30 mm^3 compared to a few cubic mm for proton spectroscopy.

2.2 AIMS AND OBJECTIVES

The aim was to establish a working brain and muscle ^{31}P-MRS protocol to be used for investigation of energy metabolism in MND.

The specific objectives of experiments here described were:

1) ensuring the appropriate functioning of available radiofrequency coils
2) selection and optimisation of a localisation sequence to obtain well resolved, high SNR ^{31}P-MRS brain spectra from regions primarily affected by MND
3) assessment of selected sequence accuracy, experimentally determined by assessment of linear variation of signal intensity as a function of phantom metabolite concentration
4) establishment of a phantom to be scanned concomitantly with research participants as an external reference with a view to quantification applications
5) determination of optimal T_1-weighted volumetric images for segmentation to correct for partial volume effects in later analyses
6) establishment of rest and dynamic muscle protocols for characterisation of metabolic changes at rest, during, and after muscle contraction. This required a system to measure MVIC prior to ^{31}P-MRS experiments and an in-house made pulley system to gauge force of contraction within the MRI scanner.

2.3 MATERIALS AND METHODS

2.3.1 Participants

Four healthy volunteers took part in the experiments to establish the ^{31}P-MRS brain protocol and six healthy volunteers were scanned to optimise muscle ^{31}P-MRS sequences. Written informed consent was obtained from all participants following approval by the local ethical committee (STH 15418 Yorkshire and Humber REC 09/H1310/79) and according to the Declaration of Helsinki. Exclusion criteria were: pregnancy, previous history of neurological disease, pacemaker or any other non-MR compatible magnetic/electronic implant, and cognitive problems sufficient to impair informed consent.

2.3.2 Hardware

All scans were conducted on a 3 Tesla Philips Ingenia wide bore MR system (Philips Healthcare, Best, The Netherlands) with heteronuclear capability. Two dual-tuned ($^{31}P/^{1}H$) transmit-receive quadrature birdcage head coils (Rapid Biomed GmbH, Würzburg-Rimpar, Germany), here denoted Rapid coil one and Rapid coil two, were used for brain MR. This is because, as illustrated in further sections, technical issues emerged with the first Rapid coil which had to be replaced. Rapid coil one was employed exclusively for the experiments described in section 2.4.1.1 and 2.4.1.2. The remainder of brain imaging and spectroscopic acquisitions were carried out using Rapid coil two. A phosphorus receiver Philips surface coil (Philips Healthcare, Best, The Netherlands) was adopted for muscle scans, and transmission was carried out using the scanner body coil.

2.3.3 MR phantoms

The following phantoms were used to assess SNR of the Rapid coils, to determine maximal accuracy of spectroscopic measurements, and in experiments to establish an external reference.

1) Philips' Sphere B (Philips Healthcare, Best, The Netherlands): containing 524 cc of 30 g/l methylphosphonic acid ($CH_3P(OH)_2$) which produces a quadruplet (J coupling constant = 17.2 Hz) at 32.5 ppm. Sphere B was adopted as a phantom in RF pulse calibration and in spectral SNR measurements of both Rapid coils (section 2.4.1.1 and 2.4.1.3).
2) A 150-mL polystyrene cylinder made in-house: containing 85% phosphoric acid (H_3PO_4). This phantom was used to measure image SNR from Rapid coil one (section 2.4.1.2).
3) Six 500-mL plastic containers made in-house: one filled with water and the remainder filled with incrementing concentrations (five mM, ten mM, 50 mM, 100 mM, and 200 mM) of disodium phosphate (Na_2HPO_4,) all resonating at approximately 4.8 ppm and employed to assess the dependence of signal intensity on Na_2HPO_4 concentration, i.e. the technique's accuracy. Initially, all five plastic bottles containing disodium phosphate were scanned simultaneously to assess strength of linear relationship between concentration and signal intensity. Subsequently, each 500-mL containers was scanned individually, starting with the lowest concentration (five mM), proceeding through increasing concentrations, and scanning the water phantom last. For each acquisition, every care was taken to ensure that each phantom was placed in exactly the same position within the coil and accuracy of placement was confirmed by two observers using an anatomical image prior to running the spectroscopic sequences. To prevent recalibration, the scanner was not moved between the various acquisitions. Results of accuracy measurements and rationale for the need to scan phantoms separately are reported in section 2.4.1.6.

4) Two 450-mL glass containers made in-house: filled with ten and 50 mM Na_2HPO_4 (Pi) and autoclaved for sterility used as external reference for *in vivo* brain acquisitions (section 2.4.1.7).
5) Several 100-mL sodium chloride (NaCl) 0.9% w/v and two two-litre plastic bottles containing five g/l NaCl each (made in-house) were used for coil loading in all isolated phantom experiments.

2.3.4 Sequences

The sequence parameters employed for RF pulse calibration of the Rapid coils and ^{31}P-MRS spectra in brain are detailed in Table 2.1 and Table 2.2. Table 2.3 includes the sequences used for structural brain MRI images. The sequences used in muscle ^{31}P-MRS acquisitions are listed in Table 2.4. Table 2.2, Table 2.3, and Table 2.4 list test sequences that were used in developing the protocol, the final protocol included sequence 15, 18, 24, and 26. Phosphorus spectra were acquired at 51.7 Hz centre-frequency[12], spectral bandwidth 3000 Hz, and 2048 sample points. Second order pencil beam shimming was employed. Manual tuning and matching was conducted by the author prior to all muscle ^{31}P-MRS acquisitions. For all cranial acquisitions in humans, the glabella was used to localise each subject's head to the centre of the coil. A coronal localisation scheme was used. In muscle, the coil was placed two and a half centimetres below the tibial tuberosity onto the anterior compartment of the leg. Positioning was performed every time by the same radiographer and visually checked for reproducibility by the author.

[12] RF pulses and detection cannot occur only at one frequency, but always need to encompass a range. In this case, the central frequency of that range was the ^{31}P nuclei resonance frequency.

Table 2.1 Sequences employed for radiofrequency pulses calibration of Rapid coils.
CSI: Chemical shift imaging, FA: Flip angle, ISIS: Image selected in vivo spectroscopy, N: number, NOE: Nuclear overhauser effect, TE: echo time, TR: repetition time.

Sequence number	***Description***	***Localisation (decupling /NOE)***	***TR (s)***	***TE (ms)***	***Initial FA (deg)***	***FA spacing (deg)***	***N of FA***	***Scan length (min)***
Sequence 1	^{31}P FA calibration Rapid coil one and two	^{31}P 1D CSI, ISIS (off/off)	10	0.428	10	10 evenly spaced	21	7:00
Sequence 2	^{31}P FA calibration Rapid coil two	^{31}P 1D CSI, ISIS (off/off)	5	0.428	10	10 evenly spaced	21	3:30
Sequence 3	^{31}P FA calibration Rapid coil two	^{31}P 1D CSI, ISIS (off/off)	1	0.428	10	10 evenly spaced	21	1:45
Sequence 4	^{31}P FA calibration Rapid coil two	^{31}P 1D CSI, ISIS (off/off)	20	0.428	10	10 evenly spaced	21	14:00

Table 2.2 Sequences employed to acquire brain phosphorus spectra
CSI: Chemical shift imaging, ISIS: Image selected in vivo spectroscopy, NOE: Nuclear overhauser effect, NSA: Number of signal averages, PA: Pulse acquire, SNR: Signal to noise ratio, SV: Single voxel, TE: echo time, TR: repetition time.

Sequence	***Description***	***Localisation***	***Decoupling /NOE***	***TR (s)***	***TE (ms)***	***NSA***	***Voxel size (mm/mm/mm)***	***Scan length (min)***
Sequence 5	^{31}P spectral SNR	^{31}P PA	off/off	4.50	0.0956	4	-	2:15
Sequence 6	^{31}P PA brain	^{31}P PA	off/off	4.50	0.0956	4	-	2:15
Sequence 7	^{31}P SV brain 64 NSA	^{31}P SV, ISIS	off/off	4.50	0.0956	64	30/30/30	4:57
Sequence 8	^{31}P SV brain 128 NSA	^{31}P SV, ISIS	off/off	4.50	0.0956	128	30/30/30	9:45
Sequence 9	^{31}P SV brain larger voxel	^{31}P SV, ISIS	off/off	4.50	0.0956	64	62/60/60	4:57
Sequence 10	^{31}P SV brain long TR	^{31}P SV, ISIS	off/off	4.00	0.0956	128	60/60/40	8:40
Sequence 11	^{31}P SV brain short TR	^{31}P SV, ISIS	off/off	0.72	0.0956	128	60/60/40	1:34
Sequence 12	^{31}P 1D CSI brain	^{31}P 1D CSI, ISIS	off/off	3.91	0.2465	20	40/300/300	9:15
Sequence 13	^{31}P 2D CSI brain short TE	^{31}P 2D CSI, ISIS	On (WALTZ-4)/on	4.00	0.2353	2	300/300/30	11.36
Sequence 14	^{31}P 2D CSI brain long TE	^{31}P 2D CSI, ISIS	On (WALTZ-4)/on	4.00	0.8958	2	175/126/83	5:52
Sequence 15	^{31}P 2D CSI brain optimised	^{31}P 2D CSI, ISIS	On (WALTZ-4)/on	4.00	0.2599	2	25/25/40	16:24
Sequence 16	^{31}P 2D CSI brain 4 NSA	^{31}P 2D CSI, ISIS	On (WALTZ-4)/on	4.00	0.2599	4	25/25/40	32:40

Table 2.3 Sequences used in structural brain MRI acquisitions.
FA: Flip angle, FOV: Field of view, IR: Inversion recovery, SNR: Signal to noise ratio, SV: Single voxel, TE: echo time, TI: Inversion time, TR: repetition time, TSE: Turbo spin echo.

Sequence	***Description***	***TR (ms)***	***TE (ms)***	***TI (ms)***	***FA (deg)***	***Oversampling***	***Number of images***	***Number of slices***	***Acquisition Voxel (mm /mm /mm) -- gap (mm)***	***FOV (mm)***	***Reconstructed matrix and reconstructed voxel size (mm /mm /mm)***	***Scan length (min)***
Sequence 17	Image SNR	50	10	-	25	-	-	1	1.41/1.41/10 -- 0	180	-	0:52
Sequence 18	T1w IR	8.4	3.9	1000	8	2	60	60	1.00/1.08/1.00 -- 0	240	256 (0.94/0.94/1)	6:02
Sequence 19	T1w IR	8.4	3.9	1000	8	-	60	60	1.00/1.08/1.00 -- 0	240	256 (0.94/0.94/1)	3:53
Sequence 20	T1w IR	7.8	3.6	1000	8	2	55	55	1.09/1.16/1.10 -- 0	257	320 (0.80/0.80/1.10)	5:32
Sequence 21	T1w IR	7.2	3.6	1000	8	2	55	55	1.09/1.16/2.20 -- 11	257	256 (1.00/1.01/1.10)	2:47
Sequence 22	T1w IR	8.4	3.9	1400	8	2	60	60	1.00/1.08/1.00 -- 0	240	256 (0.94/0.94/1.00)	6:02
Sequence 23	T2w TSE	3000	80	-	90	-	-	33	0.55/0.67/4.00 -- 0	230	432 (0.53/0.53/4.00)	3:48

Table 2.4 Sequences employed in muscle phosphorus acquisitions.
NOE: Nuclear overhauser effect, NSA: Number of signal averages, PA: Pulse acquire, TE: echo time, TR: repetition time.

Sequence	*Description*	*Localisation*	*Decoupling/NOE*	*TR (s)*	*TE (ms)*	*NSA*	*Dynamics*	*Scan length (min)*
Sequence 24	^{31}P muscle PA	^{31}P PA	on/on	4.5	0.10	32	NA	2.29
Sequence 25	^{31}P muscle dynamic acquisition, 6 NSA	^{31}P PA	on/on	5	0.10	6	16	8:00
Sequence 26	^{31}P muscle dynamic Acquisition, 3 NSA	^{31}P PA	on/on	5	0.10	3	32	8:00

2.3.5 Fitting software and calculated parameters

2.3.5.1 Software employed for data analysis

Spectroscopic data were analysed using SpectroView (Philips Healthcare, Best, The Netherlands). Image signal intensities and standard deviations (SD) were obtained using the Philips' vendor image analysis software.

2.3.5.2 Pre-processing

Prior to Fourier transformation, the free induction decay (FID) signal was multiplied by a decaying exponential: multiplication factor -1.5 for pulse acquire (PA) and single voxel (SV) -3 for chemical shift imaging (CSI). A Gaussian function (multiplication factor 12) was uused to enhance both spectral linewidth and SNR. The real part of the spectrum was manually phased to a purely absorptive line shape using both zeroth and first-order terms and peak frequency was manually shifted to assign a value of 0 ppm to PCr. Further description of effects of these weighting functions and of phasing and frequency shift is provided in the next chapter which is dedicated to pre- and post-processing of MRS spectra.

2.3.5.3 Post-processing

Real parts of metabolite peaks were fitted with a Voigt curve (Gaussian character 90%) using an iterative non-linear least-square algorithm[13]. Linewidths of the resonances of each ATP phosphate were assumed to be equal. The baseline was estimated using a polynomial curve (using 11 terms for brain and four for muscle).

2.3.5.4 Resulting parameters

Parameters relating to peak SNR, peak linewidth (i.e. the distance on the x-axis in ppm of a peak calculated at its half-maximum height), fitted metabolite areas, and metabolite area ratios resulted from the abovementioned analysis. In the experiments in 2.4.1.6, four voxels were contained within the volume of each phantom, and data reported as their amplitude mean.

Image SNR of Rapid coil one was calculated as mean signal intensity divided by SD of signal intensity (Dietrich, Raya et al. 2007). It was not necessary to calculate image SNR for Rapid coil two as spectral SNR was deemed to be appropriate.

Contrast to noise ratio of T_1-weighted volumetric images was calculated as: (mean white matter signal intensity - mean grey matter signal intensity) / noise SD. Sampling of relevant grey and white matter was carried out as depicted below for all T_1-weighted volumetric images. All images were sampled in the same location using same sampling volume with two regions of interests placed bilaterally outside the brain and four regions over paracentral lobules: two in grey matter and two in white matter as illustrated in figure below

[13] To improve robustness of the fit, the software assumes that peaks have a pre-determined shape. In this specific case, a Voigt curve was chosen (i.e. a curve that has both Gaussian and broader Lorentzian curve components).

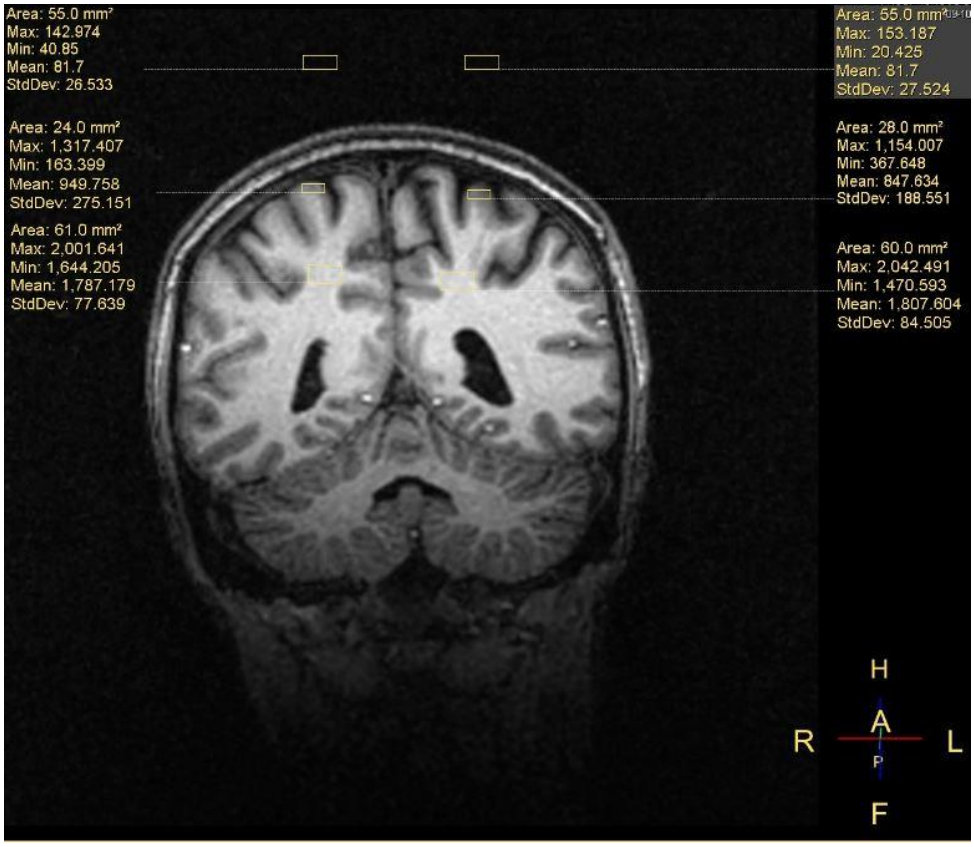

Figure 2.1 An illustration of sampling of signal intensities and standard deviations from T_1-weighted anatomical images. *All T_1-weighted volumetrics were assessed as above maintaining the locations sampled constant. Coronal orientation at the level of the cerebellar vermis/fourth ventricle was used and paracentral lobule sampled bilaterally for white and grey matter.*

Coefficients of variability (CV) were calculated as SD/mean and reported as percentages.

Data in this chapter were reported to the first decimal point, except for linewidths to two decimal points, as this was the precision of the measurements returned by the Philips software.

2.3.6 Measurements and gauging of force of contraction

To conduct dynamic ^{31}P-MRS measurements, it was necessary to gauge force of contraction in the MRI scanner. In addition, an objective clinical measurement or muscle power was required in MND patients, as one of the main features of disease is muscle weakness. Hence the following protocol was developed.

Prior to every experiment, volunteers were carefully trained and all performed at least one practice test. They were instructed to do their best but, should they feel that the effort or weight applied was too much for them, they could stop the contraction at any time. This did not occur in any of the experiments conducted.

Firstly, objective measurements of muscle force were conducted in a dedicated room outside the scanner. Maximal voluntary isometric contraction (MVIC) of tibialis anterior was assessed by asking

participants to dorsiflex their ankle using their maximal strength against resistance. Measurements were conducted using both a hand-held dynamometer (MicroFET 2, Hoggan Scientific LLC, Salt Lake City, UT, USA) and a fixed myometry system (Quantitative Muscle Strength Assessment – QMA, Aeverl Medical, Gainesville, GA). The latter apparatus was attached to a fixed frame using a dedicated foot pedal and straps. With each device, three measurements, each lasting five seconds, were conducted and the best of three was taken as MVIC. Importantly, the QMA apparatus returns a force-time curve measurement which clearly showed a "ramp time" i.e. the time taken for the muscle to initiate contraction from zero to maximal force. Ramp time was approximately one second, hence, for consistency MVIC was calculated from the average of the last four seconds.

Secondly, once MVIC measurements were established, the same measurement set-up was replicated in the MRI scanner: the participant in the bore used the same MR-compatible foot pedal and straps and maximal care was taken to ensure body position from the preceding QMA experiments was the same, including using an MR-compatible spirit level to ensure that angle of straps were the same (i.e. parallel to the floor). A load equivalent to participants' MVIC was applied as well as loads which were a proportion to a fourth and half of measured MVIC.

For the dynamic ^{31}P-MRS experiments, following a two-minute baseline acquisition, volunteers were cued in to dorsiflex their ankle and hold the applied weight. This isometric muscle contraction lasted for one minute in one experiment and two minutes in another two experiments, then participants were instructed to relax and acquisition continued until the end of the sequence (for four and five extra minutes, respectively) to measure recovery parameters. Different contraction times (one or two minutes) were tested to characterise the kinetics of any metabolite changes. The author was present in the MR room during all dynamic muscle acquisitions to release and take the weight at the beginning and end of muscle contraction and to ensure optimal performance of the protocol, which was appropriately performed by all participants.

2.4 RESULTS

In order to provide a logical explanation of the sequence of experiments performed. it has been necessary to introduce elements of discussion and reiterate some methodological points throughout this results section. The discussion will focus on the overall conclusions of the experiments.

2.4.1 Experiments conducted to optimise cranial protocol

2.4.1.1 Radio frequency pulse calibration of Rapid coil one

Figure 2.2 shows spectra acquired to calibrate RF of Rapid coil one (Sphere B, sequence 1). No signal was recorded in spectrum 1.16 (red box) which, therefore, corresponds to a 180˚ flip angle (FA). The maximum of the curve was at spectrum 1.7 which, provided that the experiment was conducted in conditions of full longitudinal relaxation, corresponds to a 90˚ FA.

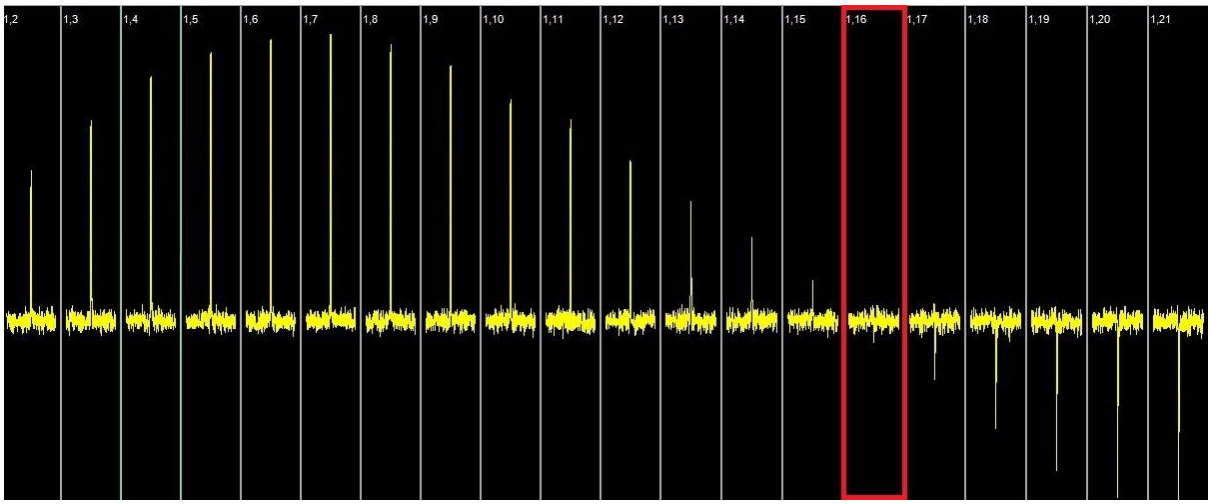

Figure 2.2 Radiofrequency pulse calibration of Rapid coil one.
Each spectrum here depicted is acquired at a different and incrementing flip angle (FA – shown on x-axis). Variations of FA are responsible for the differences in detected signal intensity. Spectrum 1.16 corresponds to the minimum, and, thus to a FA of 180˚ whereas 1.7 represents the maximum (90˚ FA).

2.4.1.2 Rapid coil one: spectroscopic and image signal to noise measurement

The SNR of Rapid coil one was first assessed in phantoms and then in *in vivo* experiments.

Spectral SNR, as measured on Sphere B using sequence 5, was calculated to be approximately 19.3 (Figure 2.3). In this case, the SNR was deemed to be abnormally low (approximately a third of expected) for a phantom containing high concentrations of phosphorus.

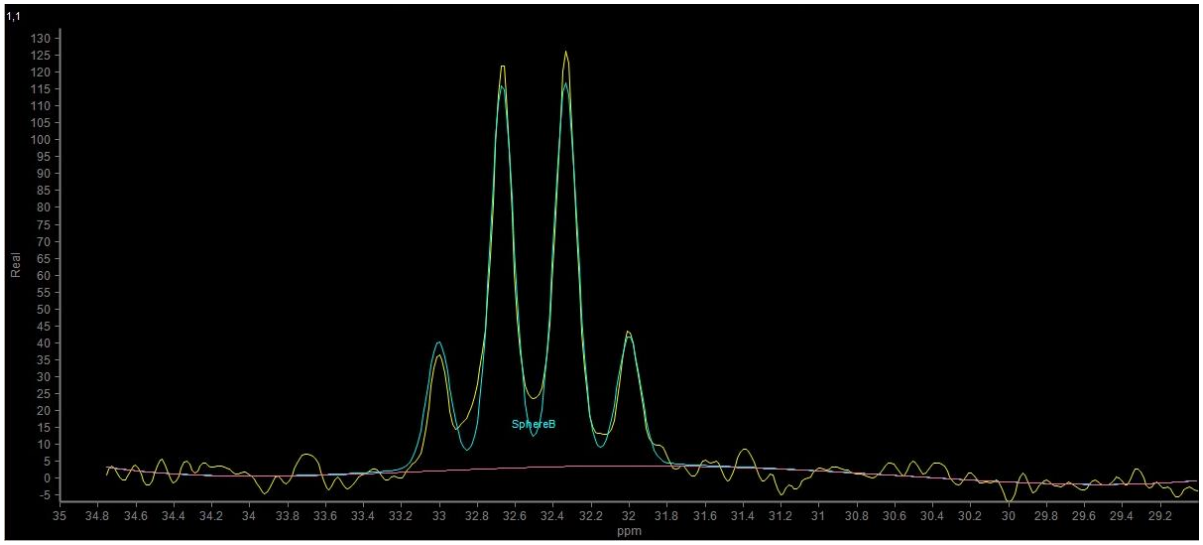

Figure 2.3 Spectrum acquired from Sphere B containing methylphosphonic acid.
The compound, which produces quadruplet (i.e. four peaks) due to scalar coupling, is centred at 32.5 ppm. The yellow line represents the actual spectrum, the blue line is the best fit according to SpectroView, and the red line depicts the estimate of the baseline. The x-axis illustrates the chemical shift in ppm, and the y-axis the signal amplitude in arbitrary units.

Image SNR (i.e, based on standard anatomical MRI and, hence, on proton signal) was estimated using a 85% H_3PO_4 phantom using sequence 17, and the experiment was repeated ten times. The resulting mean and SD of both phantom and loading containers are reported in Table 2.5. As in the experiment above, results were deemed suboptimal in terms of measured SNR.

Table 2.5 Mean signal to noise ratio (SNR) and standard deviations of H_3PO_4 phantom and loading containers.
The imaging sequence was repeated ten times.

	Mean SNR	***Standard deviation of SNR***
Methylphosphonic acid	32.1	7.2
Loading containers	15.4	5.1

Results of *in vivo* acquisitions using Rapid coil one are depicted in Figure 2.4 to Figure 2.6. A spectrum could only be resolved using a PA sequence (sequence 6, Figure 2.4), whereas no signal could be detected in any of the SV (Figure 2.5) or 2D CSI (Figure 2.6) acquisitions. In an attempt to increase SNR, three SV acquisitions were tested: two employing different numbers of signals averages (NSA), 64 in sequence 7 and 128 in sequence 8, and a further acquisition with increased voxel dimensions (sequence 9). 2D CSI sequences with both short and long TEs (sequences 13 and 14) were also tested. On the basis of these experiments, Rapid coil one was deemed not appropriate for reliable ^{31}P-MRS measurements *in vivo*: a fault with the pre-amplifier was subsequently identified and the coil was substituted with Rapid coil two, which was used in all subsequent experiments.

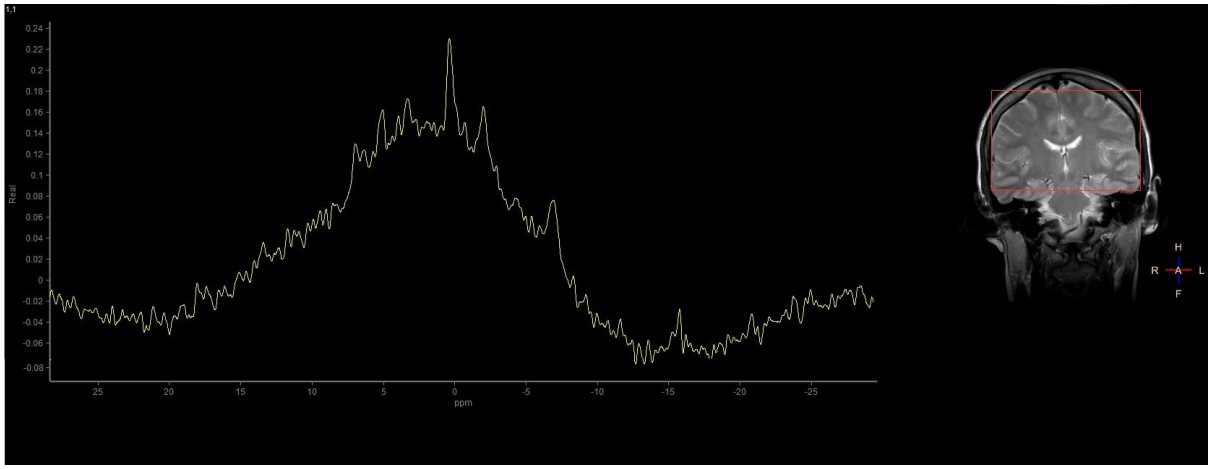

Figure 2.4 A poorly resolved spectrum acquired with Rapid coil one using a pulse acquire sequence.
The shimming box is bordered in red in the anatomical image.

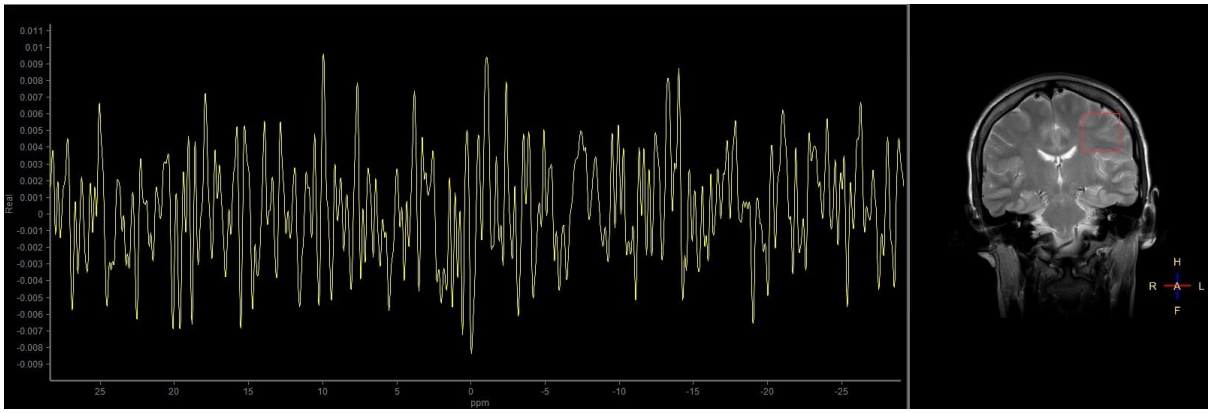

Figure 2.5 A single voxel acquisition from the area framed in red.
Only white noise could be detected in all single voxel acquisitions with Rapid coil one.

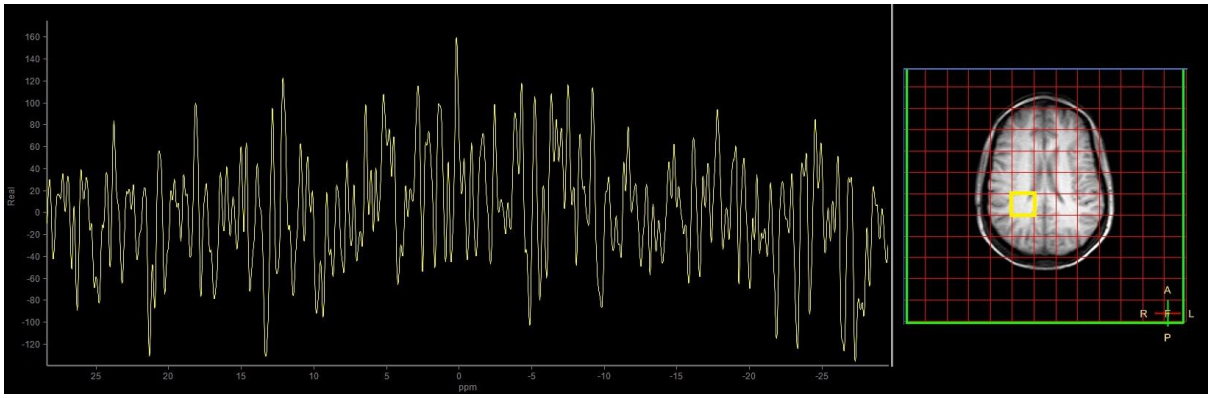

Figure 2.6 A 2D chemical shift imaging acquisition illustrating that no phosphorus signal could be detected using Rapid coil one.
The red grid corresponds to areas on which the sequence was applied. The illustrated white noise was derived from the voxel depicted in yellow. White noise resulted from all tested 2D-chemical shift imaging sequences tested using Rapid coil one

2.4.1.3 Radio frequency pulse calibration of Rapid coil two

An RF pulse calibration analogous to that conducted for Rapid coil one is illustrated in Figure 2.7. The maximal value was recorded for spectrum 1.7 and the minimum was well defined at spectrum 1.16.

Additional experiments were conducted to assess T_1 saturation effects and their impact on the calibration curves by conducting a series of acquisitions altering only TR values (sequences two to four).

Decreasing the TR to five seconds (Figure 2.8), caused the peak of the calibration curve to shift to the left (at spectrum 1.6) although the minimum remained at spectrum 1.16. This left shift was more pronounced for a TR of one second (Figure 2.9) with the maximum at 1.3, whereas the minimum could not be associated with an individual spectrum since no signal was recorded between 1.15 and 1.17.

Prolonging the TR to 20 seconds did not cause a right shift of the curve, but produced the expected sinusoidal pattern, as shown in Figure 2.10 where the RF pulse corresponding to 90˚ FA is shown in the green rectangle whereas the signal minimum (corresponding to 180˚ FA) is shown in red.

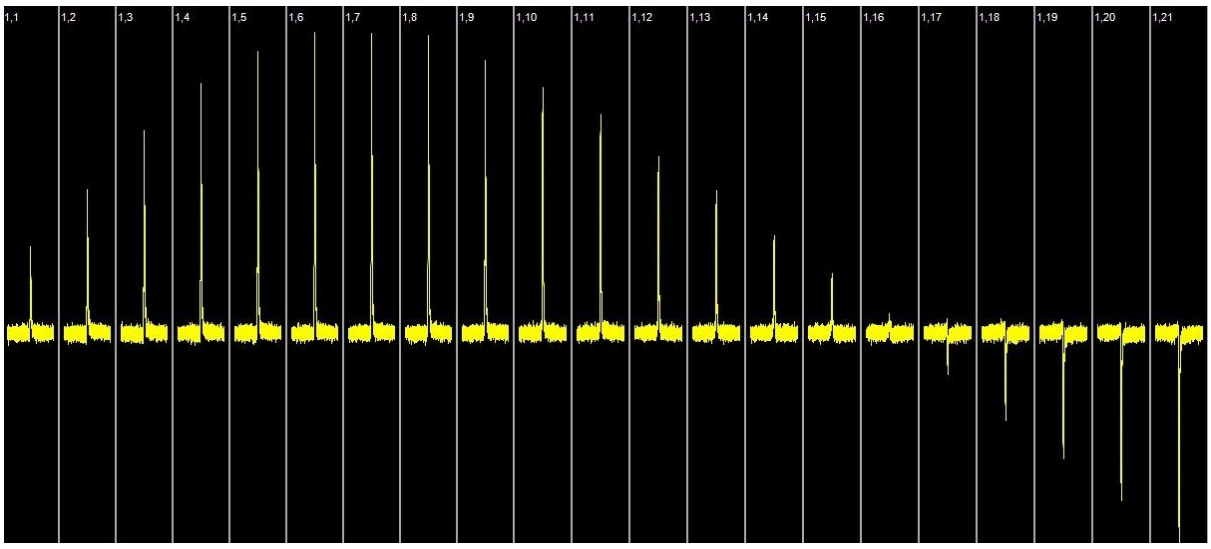

Figure 2.7 Radio frequency pulse calibration of Rapid coil two conducted at a repetition time of ten seconds using sequence one.

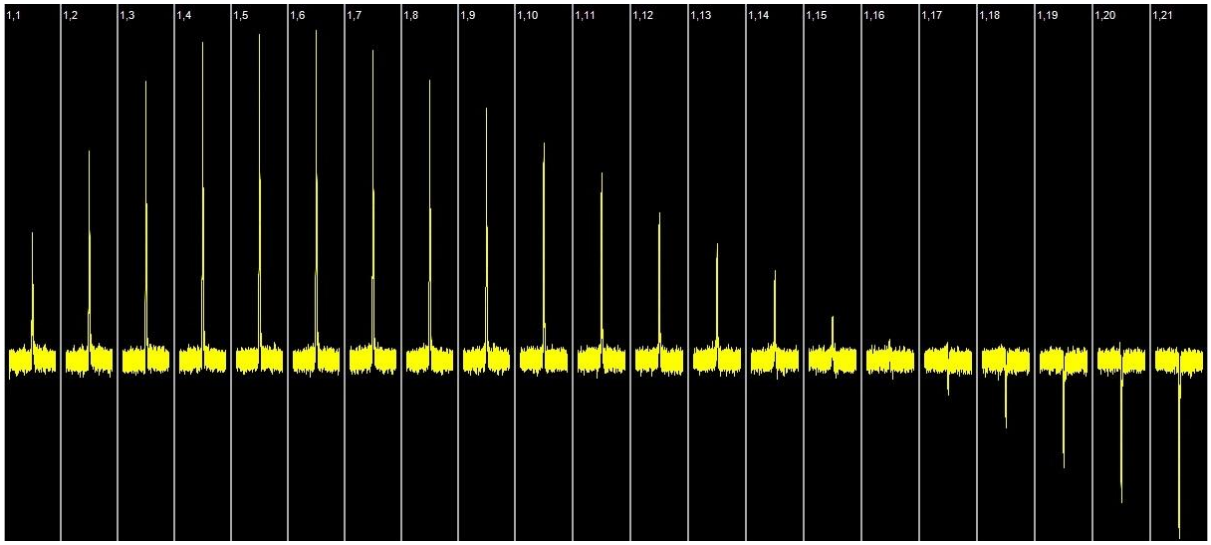

Figure 2.8 Radiofrequency calibration of Rapid coil two conducted at a repetition time of five seconds using sequence two.

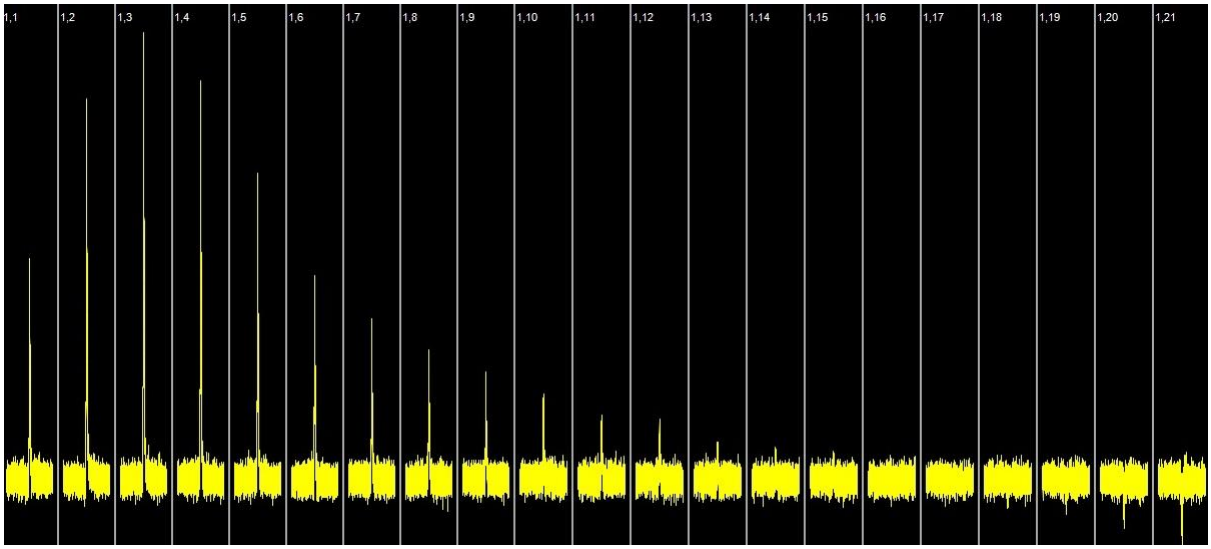

Figure 2.9 Radiofrequency calibration of Rapid coil two conducted at a repetition time of one second using sequence three.

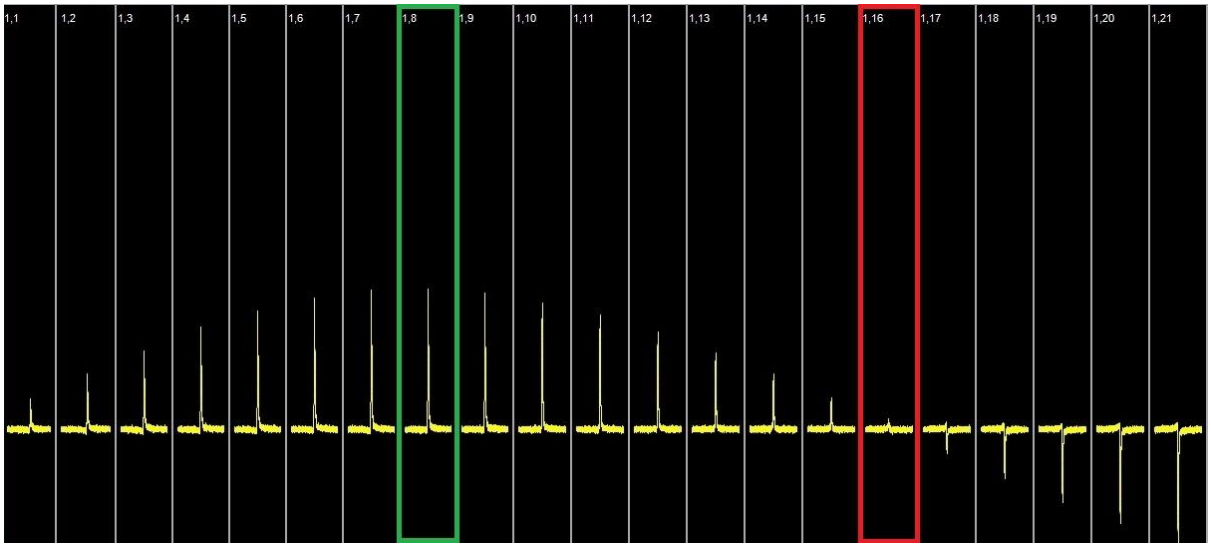

Figure 2.10 Radiofrequency calibration of Rapid coil two conducted at a repetition time of 20 seconds using sequence four. *The green box shows the spectrum generated by a 90˚ flip angle, whereas the red box indicates the minimum corresponding to a flip angle of 180˚.*

2.4.1.4 Rapid coil two: signal to noise ratio measurements

As for the previous coil, SNR for Rapid coil two was assessed first in phantoms and then *in vivo*.

SNR of methylphosphonic acid (Sphere B, sequence five) was calculated to be 71.0, approximately 3.5 times the SNR produced by Rapid coil one using the same phantom and sequence. The resulting spectrum is shown in Figure 2.11 which can be compared with Figure 2.3.

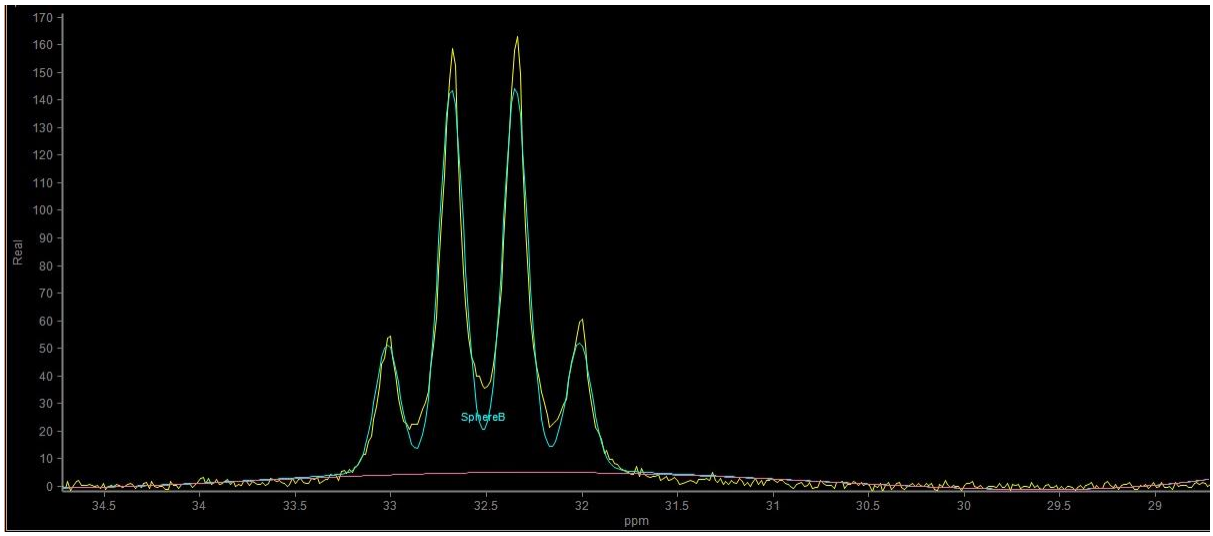

Figure 2.11 Spectrum acquired from Sphere B using Rapid coil two.
Visually it appears similar to spectrum in Figure 2.3 except that baseline noise is much less pronounced. The yellow line represents the actual spectrum, the blue line is the best fit according to SpectroView, and the red line depicts the estimate of the baseline. The x-axis illustrates the chemical shift in ppm, and the y-axis the signal amplitude in arbitrary units.

Rapid coil two was tested *in vivo* using various sequences. Results are detailed here and in the next section; all sequences produced well-resolved spectra. In Figure 2.12, a spectrum acquired with sequence 6 is illustrated; this is the same sequence displayed in Figure 2.4 as acquired with Rapid coil one. For a quantitative comparison, Table 2.6 lists peak SNR of each phosphorus metabolite from the two coils' PA acquisitions. The peak at 0 ppm represents PCr; peaks at -2.5, -8, and -16.5 ppm resolve the γ, α, and βATP phosphates, respectively. The γATP peak includes a resonance from βADP, whereas the αATP also comprises resonances from αADP, NAD^+, and NADH. At approximately 5 ppm, Pi is resolved, whereas, PDE and PME are located at 2.5 and 6 ppm, respectively. Linewidths appear broad. This is a characteristic of PA sequences because magnetic inhomogeneities, shortening transverse relaxation, are more prominent when the entire cranial region is sampled concurrently. Additionally, no decoupling (which also improves some of the linewidths) was conducted as this would have increased the specific absorption rate, an issue discussed further in later sections.

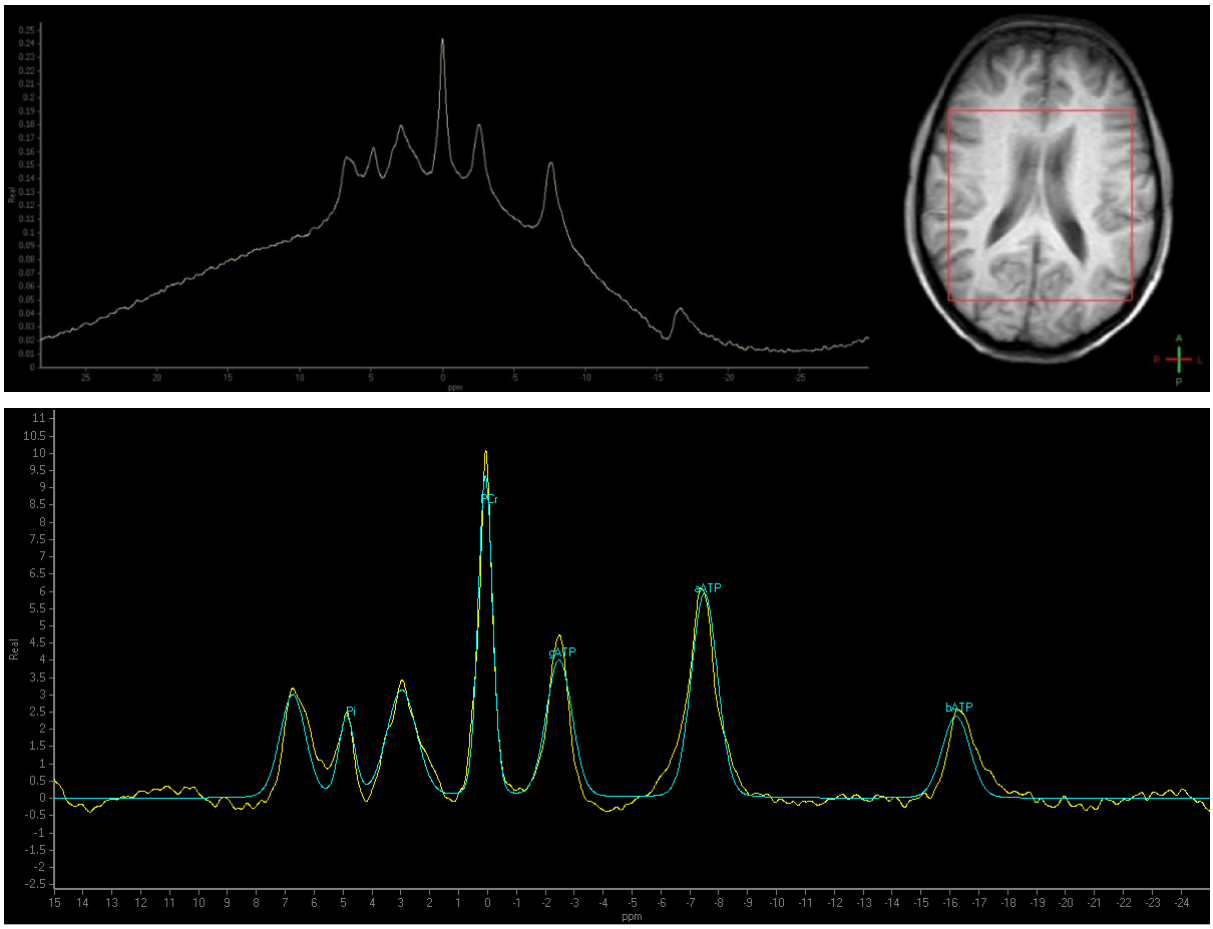

Figure 2.12 Spectrum acquired in vivo with Rapid coil two using a pulse acquire sequence.
The red box in the anatomical axial image represents the shimming box. In the lower spectrum, following baseline subtraction, resolved peaks are (from left to right): phosphomonoesters (PME), inorganic phosphate (Pi), phosphodiesters (PDE), phosphocreatine (PCr), γ adenosine triphosphate (ATP), αATP, and βATP. The spectrum is illustrated in yellow and the best-fit line is in blue.

Table 2.6 Peaks' signal to noise ratio (SNR) for the spectrum shown in Figure 2.4 (acquired with Rapid coil one) and the spectrum shown in Figure 2.12 (acquired with Rapid coil two).
The same pulse acquire sequence was used in both experiments. Not applicable (NA) indicates that SNR was too low for the peaks to be fitted appropriately. Metabolites are listed in the order of frequency the peaks resonate in a typical ^{31}P-MRS spectrum, from left to right.

	SNR Rapid coil one	***SNR Rapid coil two***
Phosphomonoesters	2.6	19.8
Inorganic phosphate	3.0	16.2
Phosphodiesters	2.4	20.8
Phosphocreatine	6.9	52.2
γ adenosine triphosphate	NA	13.2
α adenosine triphosphate	2.2	17.2
β adenosine triphosphate	NA	6.6

As spectroscopic SNR of Rapid coil two was deemed sufficient, it was not necessary to assess image SNR.

2.4.1.5 Optimisation of acquisition parameters and spectroscopic localisation

To determine the optimal acquisition parameters and localisation technique to be employed in the final protocol, the following sequences were tested and compared on a healthy volunteer: PA (described above and illustrated in Figure 2.12), SV with both long and short TR (sequences 10 and 11), 1D CSI (sequence 12), and 2D CSI with 2 NSA (sequences 15). A 2D CSI with 4 NSA (sequences 16) was also tested on a second volunteer. Representative spectra are shown in Figure 2.13 to Figure 2.16. Table 2.7, Table 2.8 and Figure 2.17 compare SNR and linewidth of tested sequences.

Linewidths for PA were larger compared to all other tested sequences for reasons explained above. In addition, linewidths of PDEs acquired with CSI sequences were smaller compared to those in SV. This was because heteronuclear decoupling (particularly effective for PMEs and PDEs) was only feasible with CSI acquisitions; decoupling improves line shape, as explained in 8.5.2.

Generally, SNR of SV sequences was markedly reduced compared to CSI. Hence, although βATP and PME peaks were visually discernible in all spectra, they could not be fitted accurately by the SpectroView software in SV localisations. In addition, shortening TR caused signal to be further reduced and the integral of Pi could not be calculated. Notably, signal of γ and αATP peaks was only moderately decreased by TR shortening, whereas signal intensity for PCr was diminished to a quarter of the value measured with the longer TR acquisition, representing a consequence of T_1 relaxation effects. Among the CSI sequences, 2D CSI 2 NSA (TR=4 sec) produced the highest spectral SNR, and this sequence was chosen for the final brain protocol. Whilst it was expected that the 2D CSI 2 NSA would have produced the highest SNR, this was not the case. possibly because the acquisition was

substantially longer (32 minutes) and hence likelihood of motion (which reduces SNR) greater. In addition, this sequence was tested on a different research participant, so differences in SNR might have been influenced by inter-individual variance in anatomy. This result illustrates some of the trade-offs that must be considered in optimising MRS sequences; in any case, a half an hour acquisition was deemed too lengthy for MND patients to tolerate in combination with other planned scans.

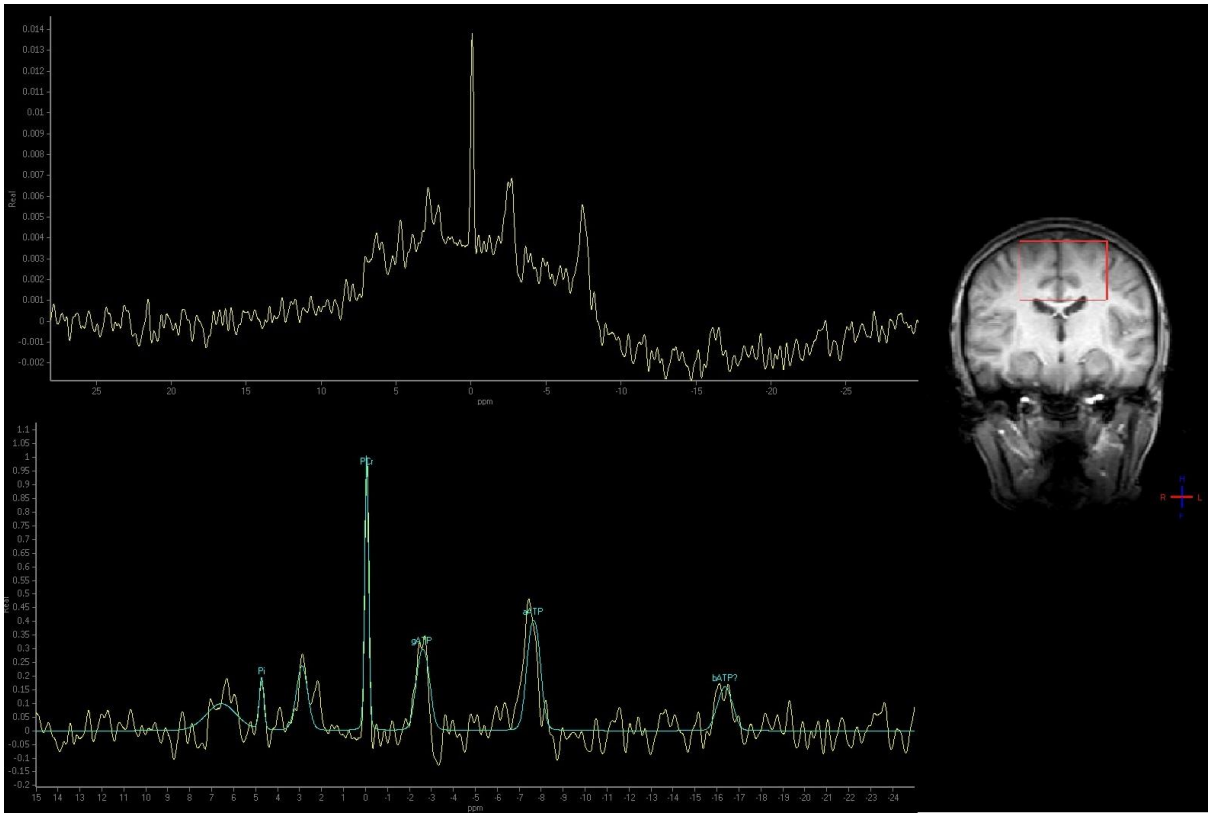

Figure 2.13 Spectrum acquired from the voxel delineated in red using a single voxel technique with long repetition time (four seconds).
The spectrum acquired from the red voxel in the coronal anatomical image is illustrated in yellow. The blue line in the lower graph is the best-fit line. Although phosphomonoester and β adenosine triphosphate appear visually fitted, the software could not calculate an accurate value for their signal intensities.

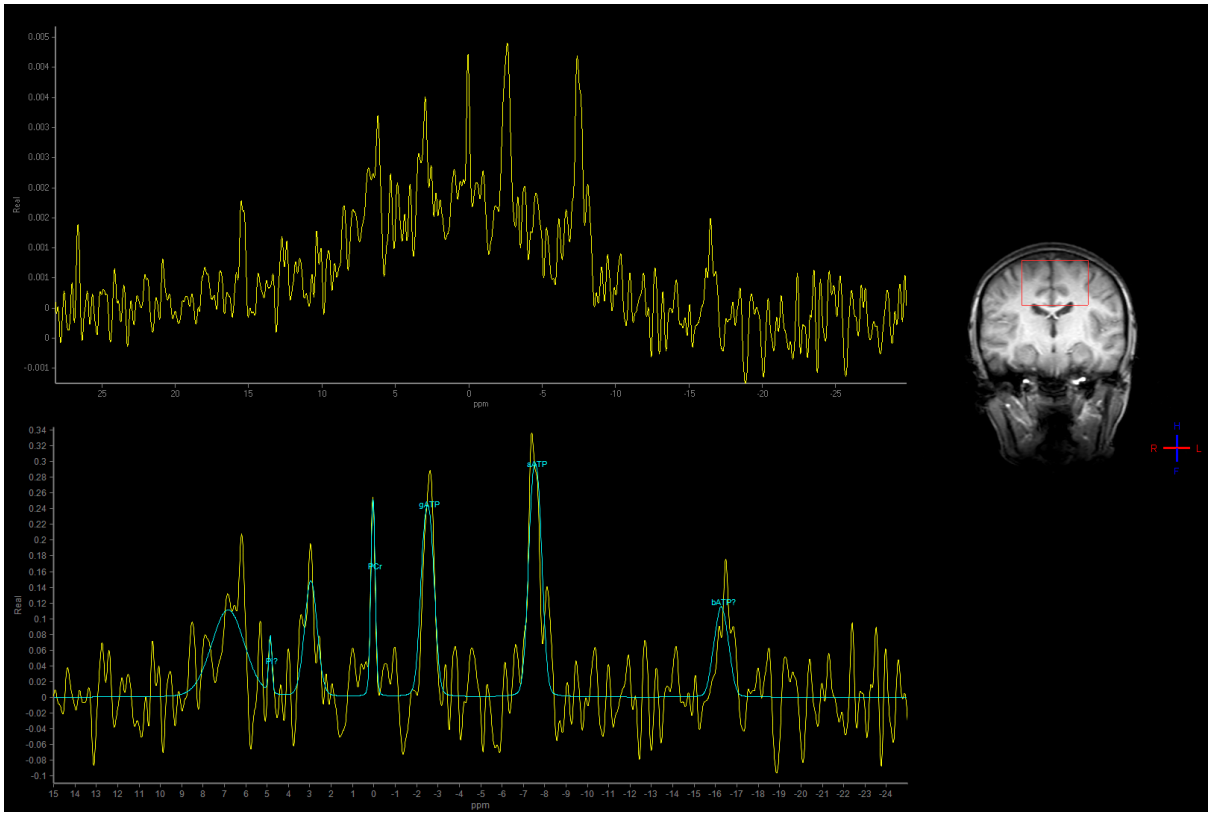

Figure 2.14 Spectrum acquired from voxel delineated in red using a single voxel technique short repetition time (721 ms). *The acquisition voxel is shown in red in the coronal anatomical image. The spectrum acquired is illustrated in yellow in the upper graph and, following baseline subtraction, in the lower graph. The blue line in the lower graph is the best-fit line. Although phosphomonoester (PME), inorganic phosphate (Pi), and β adenosine triphosphate (βATP) appear visually fitted, the software could not calculate an accurate value for their signal intensities. Proportions of peak intensities were different compared to the spectrum in Figure 2.13 due to T_1 weighting and noise is visually more prominent.*

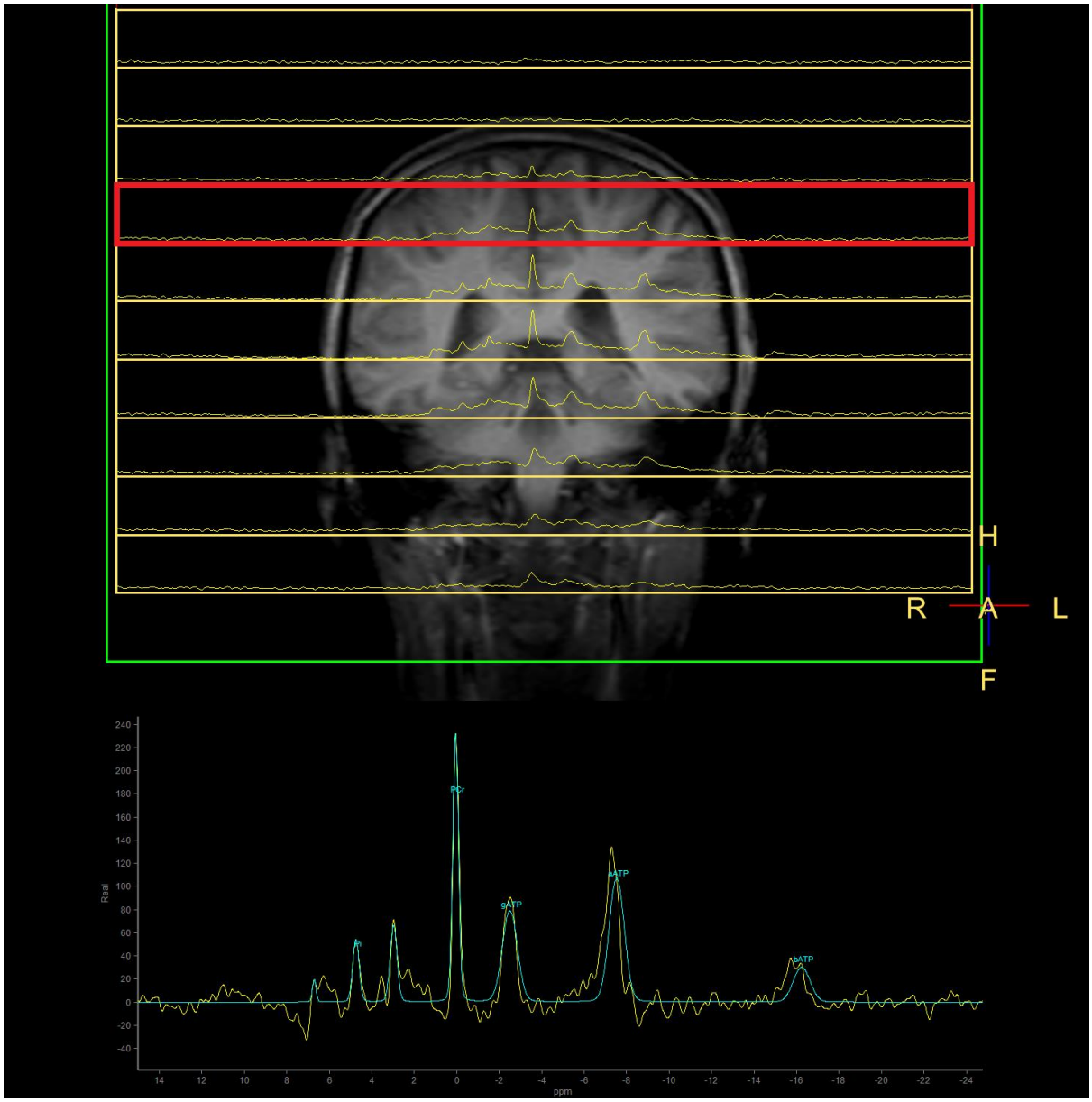

Figure 2.15 Spectra resulting from 1D chemical shift imaging technique.
The fitted spectrum was acquired from the voxel in red in the upper image. Signal was detected in the axial plane from regions including motor cortex. Spectra are illustrated in yellow. In the lower graph, baseline subtraction was performed and the best-fit line is depicted in blue. All peaks were well resolved and noise less prominent than in single voxel spectra.

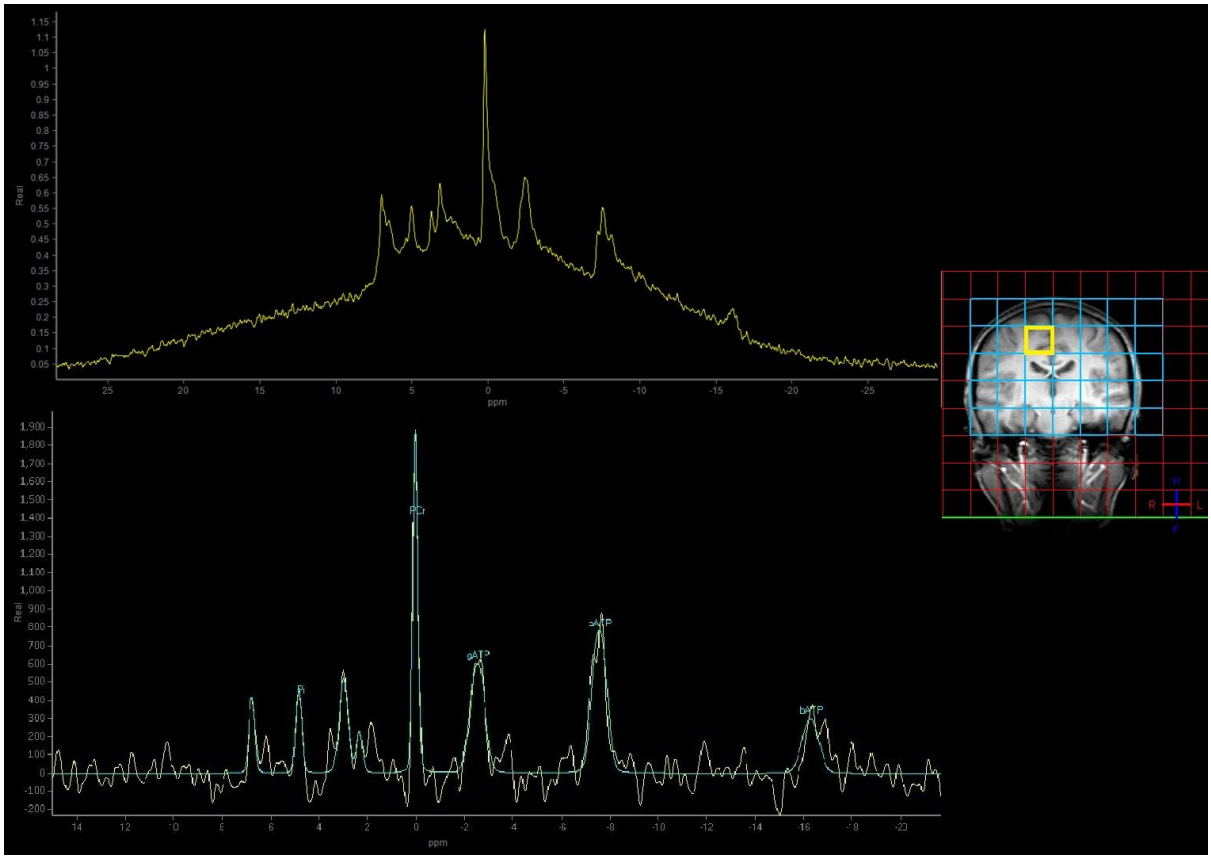

Figure 2.16 Spectrum acquired from right motor cortex (voxel in yellow in anatomical image) with 2D chemical shift imaging and two signal averages.
The fitted spectrum was acquired from the voxel in red in the anatomical coronal image. Signal was detected in the axial plane from regions including motor cortex. Spectra are illustrated in yellow. In the lower graph, baseline subtraction was performed and the best-fit line is depicted in blue. All peaks were well resolved and noise less prominent than in single voxel spectra. Although different in terms of calculated signal to noise ratios, doubling the number of signal averages did not appreciably change the appearance of the spectrum and these data are not shown.

Table 2.7 Comparison of metabolite signal to noise ratios resulting from tested sequences.
Sequences used were: pulse acquire (PA), single voxel (SV), and chemical shift imaging (CSI). Not applicable (NA) indicate inability of software to fit peaks. Metabolites are listed in the order the peaks resonate in a typical ^{31}P-MRS spectrum, from left to right: phosphomonoesters (PME), inorganic phosphate (Pi), phosphodiesters (PDE), phosphocreatine (PCr), γ adenosine triphosphate (ATP), αATP, and βATP. NSA=number of signal averages, TR=repetition time.

	PME	***Pi***	***PDE***	***PCr***	***γATP***	***αATP***	***βATP***
PA	19.8	16.2	20.8	52.2	13.2	17.2	6.6
SV long TR	NA	2.3	2.9	12.2	2.4	3.3	NA
SV short TR	NA	NA	2.0	3.4	2.3	2.8	NA
1D CSI	2.3	4.7	6.0	20.8	4.5	5.4	2.3
2D CSI 2 NSA	38.1	32.3	69.2	134.5	31.6	41.3	24.5
2D CSI 4 NSA	13.4	21.3	25.3	66.1	19.5	20.0	11.8

Table 2.8 Comparison of metabolite linewidths (expressed in parts per million or ppm) resulting from tested sequences. *Sequences used were: pulse acquire (PA), single voxel (SV), and chemical shift imaging (CSI). Not applicable (NA) indicate inability of software to fit peaks. Metabolites are listed in the order the peaks resonate in a typical ^{31}P-MRS spectrum, from left to right: phosphomonoesters (PME), inorganic phosphate (Pi), phosphodiesters (PDE), phosphocreatine (PCr), γ adenosine triphosphate (ATP), αATP, and βATP. NSA=number of signal averages, TR=repetition time.*

	PME	***Pi***	***PDE***	***PCr***	***γATP***	***αATP***	***βATP***
PA	1.27	0.97	1.44	0.63	1.03	1.03	1.03
SV long TR	NA	0.24	0.61	0.21	0.51	0.51	NA
SV short TR	NA	NA	0.70	0.25	0.49	0.49	NA
1D CSI	0.31	0.47	0.53	0.29	0.63	0.63	0.63
2D CSI 2 NSA	0.72	0.38	0.38	0.30	0.72	0.72	0.72
2D CSI 4 NSA	0.46	0.33	0.33	0.26	0.46	0.46	0.46

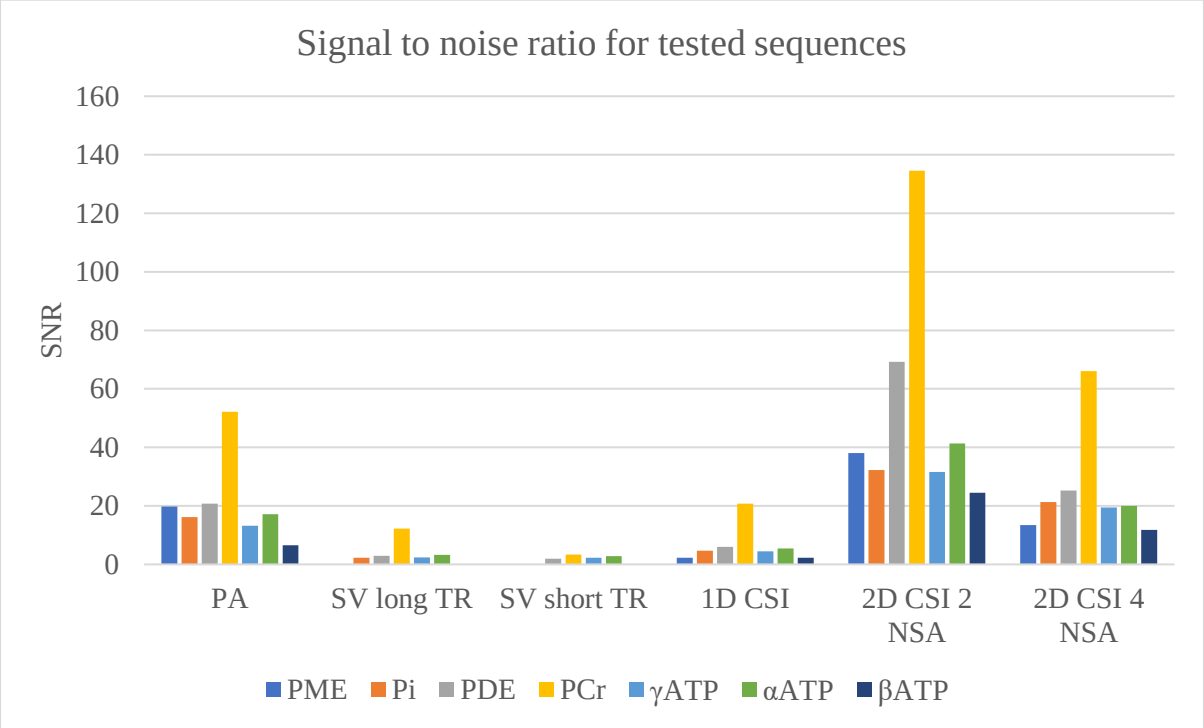

Figure 2.17 Bar chart depicting signal to noise values (SNR) for resolved metabolites across tested acquisition sequences. *Sequences used were: pulse acquire (PA), single voxel (SV), and chemical shift imaging (CSI). All experiments were conducted on the same volunteer with the exception of the 2D CSI NSA=4. The following metabolites are reported: phosphomonoesters (PME), inorganic phosphate (Pi), phosphodiesters (PDE), phosphocreatine (PCr), γ adenosine triphosphate (ATP), αATP, and βATP. TR: Repetition time.*

2.4.1.6 Accuracy of brain spectroscopic measurements

Phantoms of known incrementing concentration of Pi were scanned to assess whether signal response to test objects was linear, in order to estimate sequence accuracy. The optimal sequence selected from previous experiments (2D CSI 2 NSA) was assessed.

When all Pi phantoms were scanned concomitantly, only the 50 mM, 100 mM, and 200 mM phantoms' peaks were resolved (Figure 2.18). Lack of signal from low concentration phantoms was interpreted as likely due to higher concentration phantoms forcing the dynamic range of the hardware to be wider than optimum and causing low signals not to be detected, a process similar in principle to photographic over-exposure.

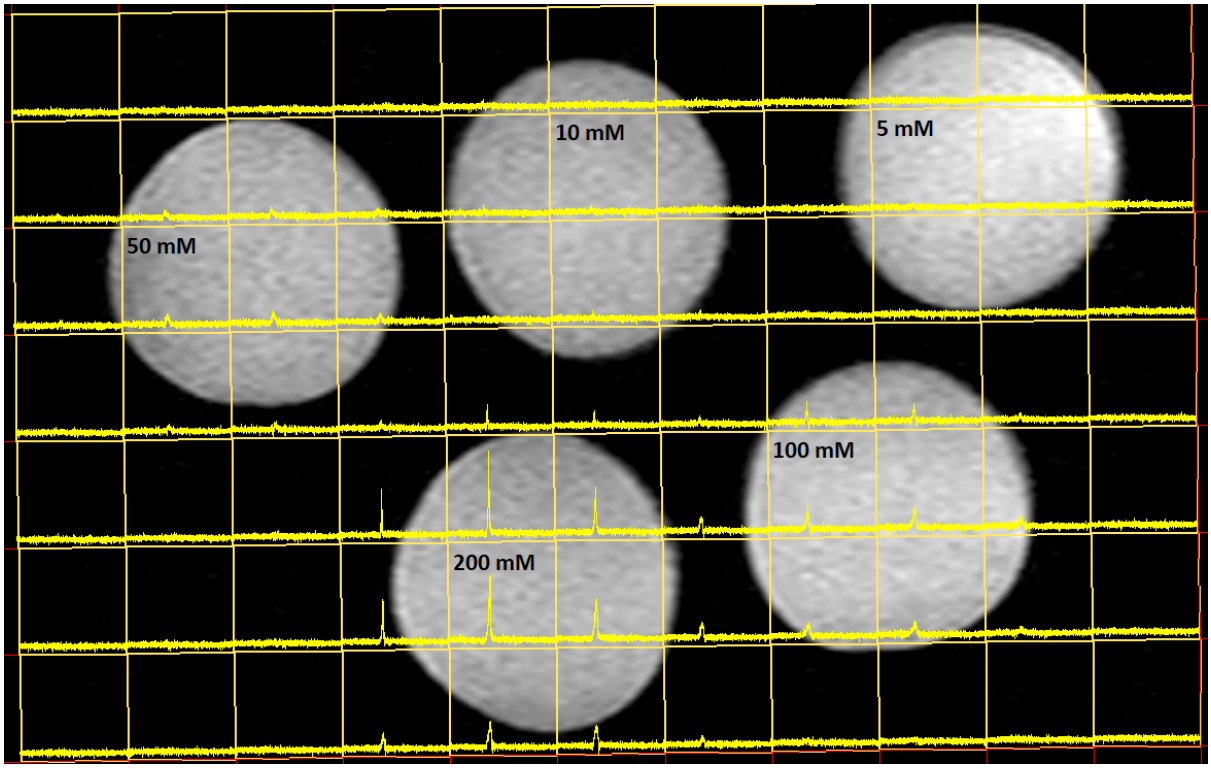

Figure 2.18 Image overlaid spectra acquired from five phantoms containing different concentrations of inorganic phosphate using 2D chemical shift imaging sequence.
No peaks were detected from the five mM and ten mM phantoms.

To address this problem, a different experimental design was adopted. Phantoms were scanned individually rather than together, starting from five mM and preventing recalibration between acquisitions as detailed in the Methods (section 2.3.3). This allowed acquisition of signals from all phantoms including resonances at five and ten mM concentrations. The experiment showed an almost perfect linear relationship (R^2=0.99) between measured signal intensity and phantoms concentrations; signal intensity as a function of phantom concentration is plotted in Figure 2.19. This result confirmed the accuracy of the technique.

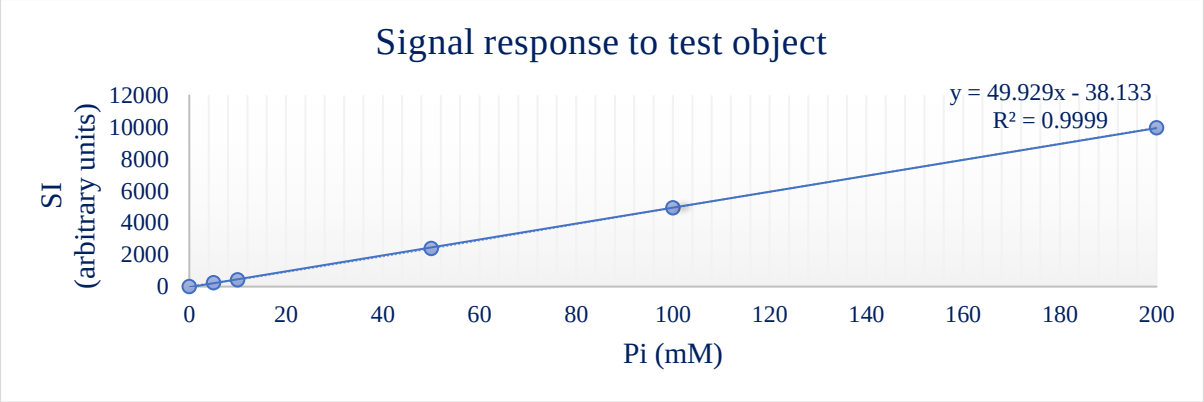

Figure 2.19 Signal intensity (SI) of inorganic phosphate (Pi) resonances as a function of Pi concentration.
A phantom containing water was scanned last as a negative control (zero value). There is a linear relationship between signal intensity and metabolite concentrations.

2.4.1.7 An external reference for metabolite quantification

As discussed in this chapter's introduction and expanded in 8.6, an external reference phantom can be used to help address some of the technical challenges inherent in achieving genuine metabolite quantification and was investigated in the next series of experiments. Phantoms containing Pi were scanned cranial to two subjects' heads to explore feasibility as an external reference for absolute metabolite quantification. Based on the previous observation that high phantom concentrations widen the dynamic range, hampering detection of lower signals, only ten and 50 mM phantoms were tested *in vivo*.

Figure 2.20 shows results for the two volunteers scanned: one with a 50 mM Pi phantom (image on the left) and the other with a ten mM Pi phantom (image on the right), placed above their head. The 2D CSI 2NSA sequence was used to acquire spectra from both the brain and the phantom. Resolution of brain spectra in the experiment with the 50 mM phantom was worse and SNR was consistently decreased compared to the ten mM acquisition. In addition, signal from 50 mM phantom was partially detectable in voxels outside the container. In experiments using the ten mM phantom, brain spectra were well resolved and signal was exclusively measurable from voxels within the phantom. Based on the results of these experiments, the ten mM phantom was included in the final protocol.

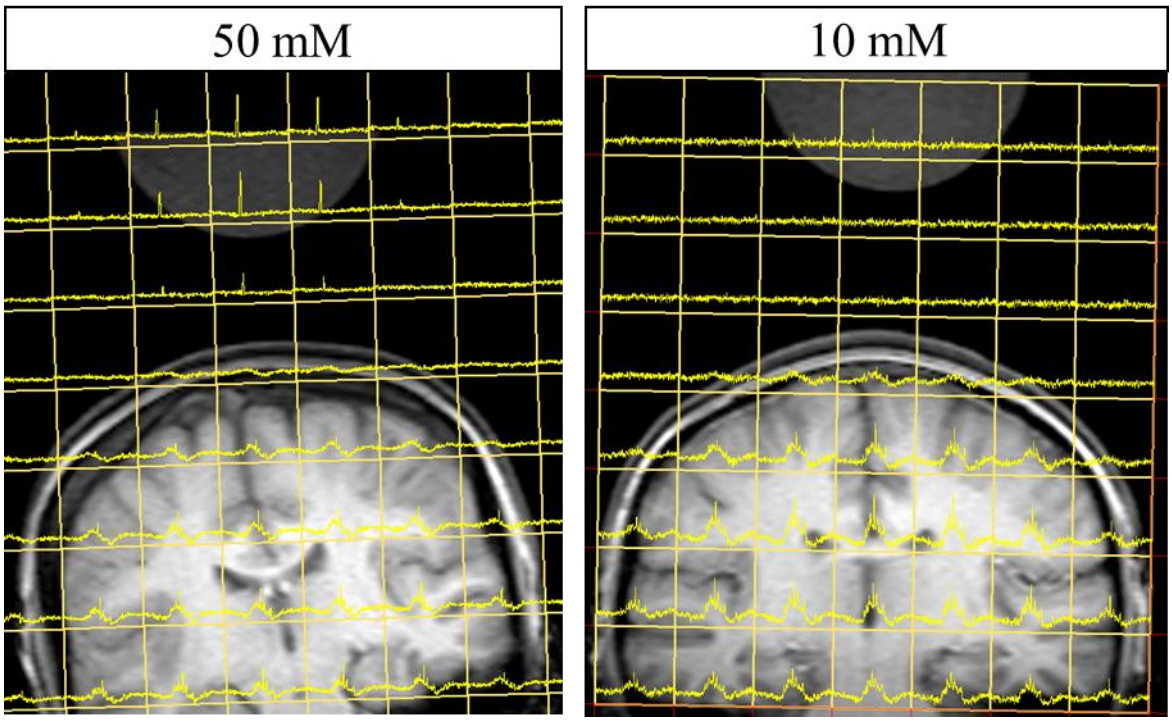

Figure 2.20 Phosphorus spectra overlaid onto a structural T_1-weighted MRI image.
The image on the left shows prominent peaks measured from a 50 mM inorganic phosphate (Pi) phantom located above the head, but detectable also in voxels outside the container. Phosphorus signal detected from the brain was relatively decreased compared to image on the right in which a 10 mM Pi phantom was used instead, and signal observed exclusively localised within the container.

2.4.1.8 T_1-weighted volumetric acquisitions

Inclusion of a T_1-weighted volumetric sequence was necessary for image co-registration and to assess putative effects of partial volume effects on results, for example possible differential CSF content of voxels between patients and controls. Images resulting from the various T_1-weighted volumetric acquisitions tested are shown in Figure 2.21, and calculated contrast to noise ratios for each volumetric image are reported in Figure 2.22 (showing results averaged between right and left sides) and Figure 2.23 (comparing the right and left sides). Contrast to noise ratio measured on the left side was consistently higher than the right. Sequence 18 was chosen for the final protocol based on highest and most uniform contrast to noise ratio among the tested acquisitions and because voxels were isotropic, which is advantageous for image reconstruction, improving efficiency without losing spatial resolution (Edelman, Dunkle et al. 2009).

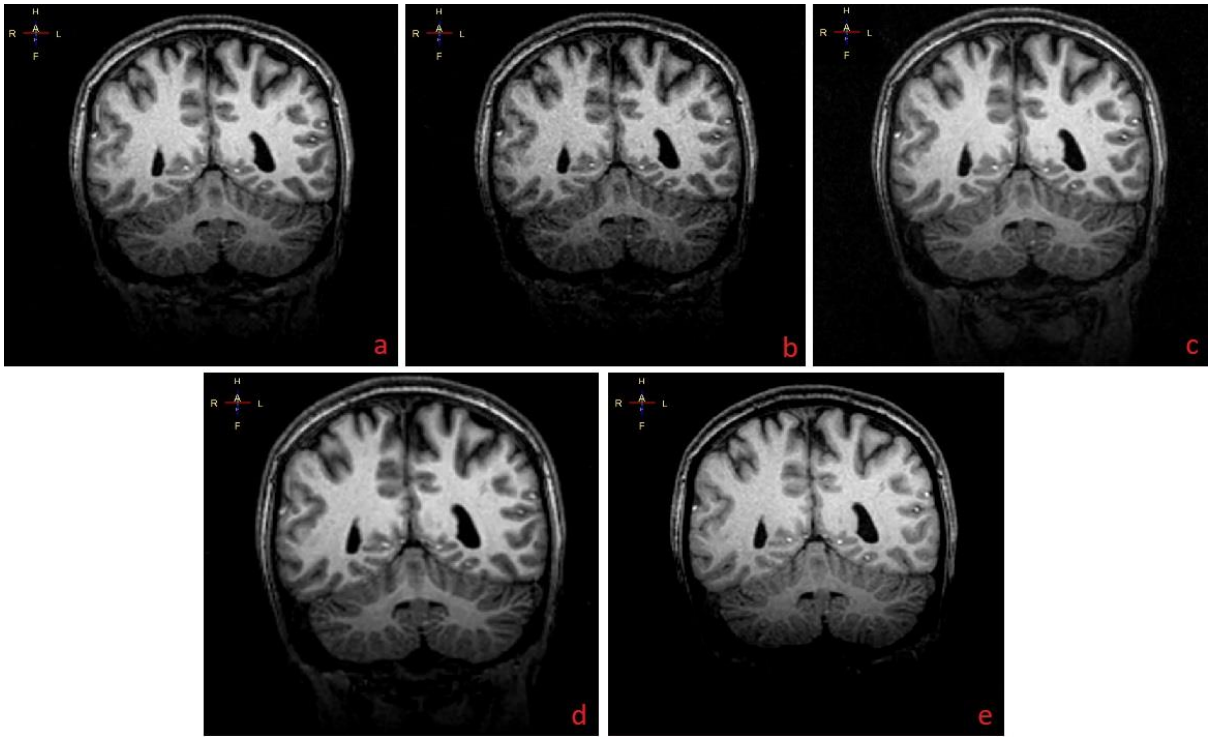

Figure 2.21 Tested T_1-weighted volumetric images.
Image a was acquired with sequence 18 (oversampling=2, FOV=240 mm, TI=1000 ms), image b with sequence 19 (default sampling frequency, FOV=240, TI=1000 ms), image c with sequence 20 (FOV=320, TI=1000 ms, matrix reconstruction=320 mm^3), image d with sequence 21 (FOV=320, TI=1000 ms, matrix reconstruction=256 mm^3), and image e with sequence 22 (oversampling=2, FOV=240 mm, TI=1400). All images are shown at the level of the same coronal slice encompassing cerebellum, occipital horn of lateral ventricles, inferior and middle occipital gyrus, inferior and superior parietal gyrus, precuneus, and cingulate gyrus.

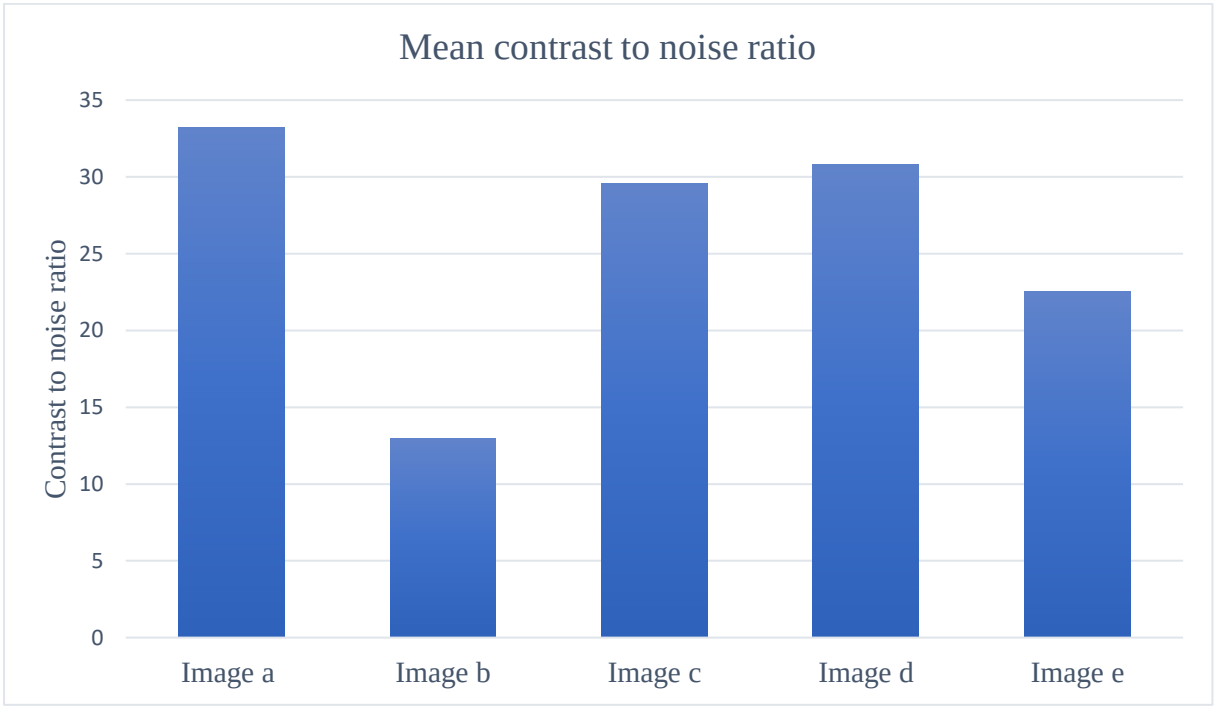

Figure 2.22 Mean (averaged between right and left side) contrast to noise ratio for T_1-weighted volumetric acquisitions depicted in Figure 2.21.
Image a demonstrated the highest contrast to noise ratio.

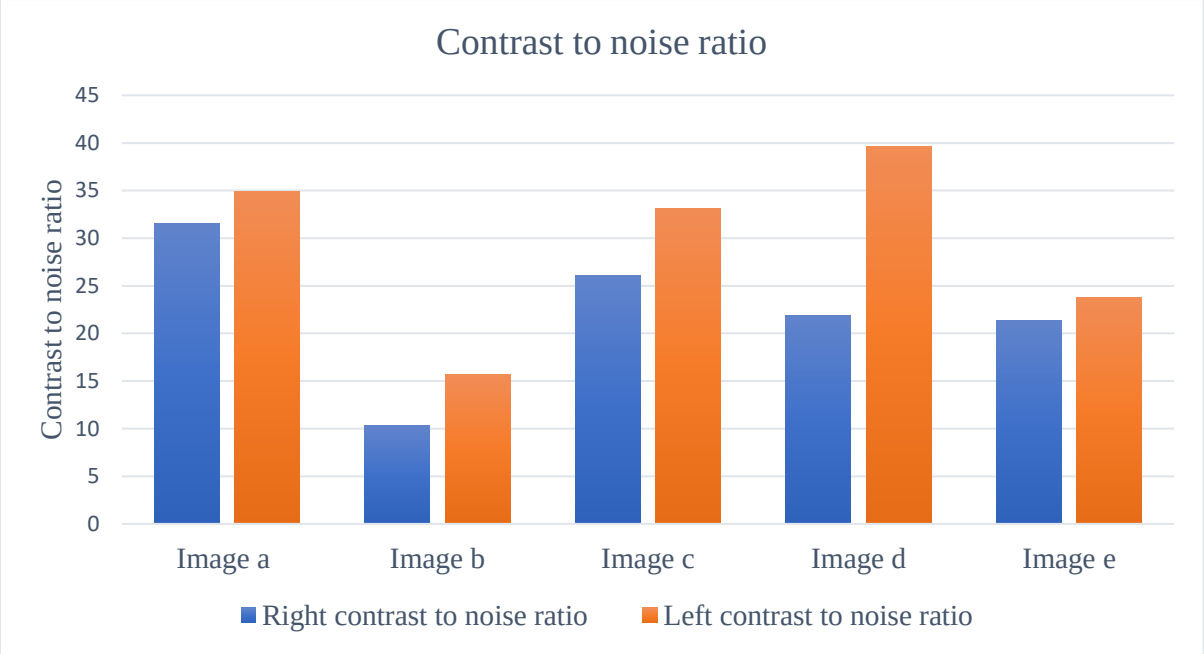

Figure 2.23 Contrast to noise ratio for T_1-weighted volumetric acquisitions depicted in Figure 2.21.
Comparison between right and left side is shown. Contrast to noise ratio measured on the left side was consistently higher than the right.

2.4.2 Experiments conducted to optimise muscle protocol

2.4.2.1 Muscle acquisitions at rest

A muscle spectrum was acquired from a healthy volunteer using a PA sequence (sequence 24), as illustrated below in Figure 2.24. SNR and linewidth of metabolites are reported in Table 2.9. The PA spectrum was remarkably superior in terms of resolution and SNR compared to brain acquisitions illustrated in previous sections. In contrast to brain, precise anatomical localisation was not considered critical for the planned muscle experiments and so further experiments were not performed. This PA sequence was included in the final protocol to assess muscle metabolism at rest in MND.

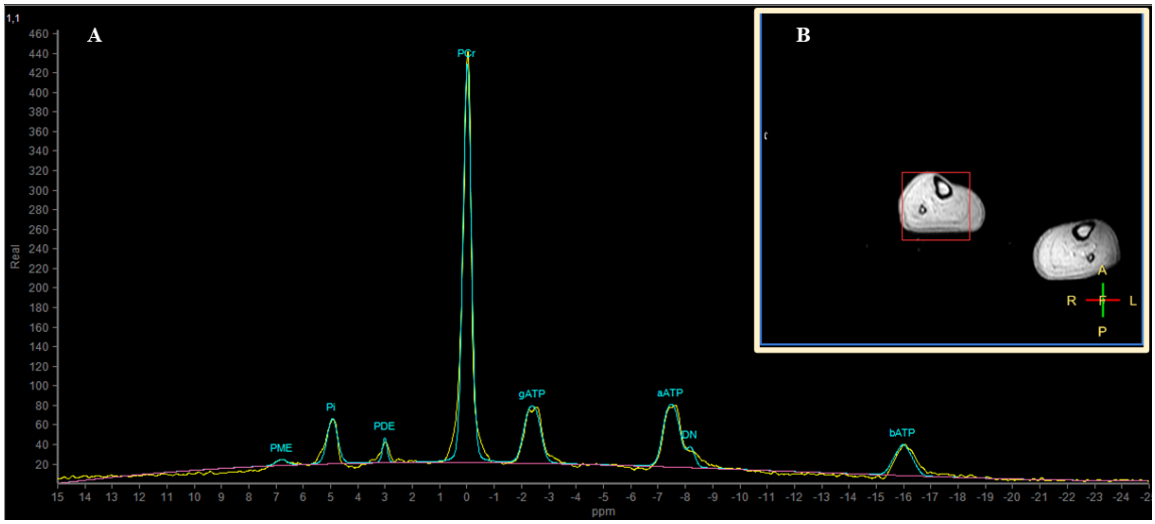

Figure 2.24 Spectrum acquired in vivo from ankle dorsiflexors using a pulse acquire sequence (A).
The red box in B represents the shimming box. The spectrum is illustrated in yellow, best-fit line in blue, and baseline estimate (already subtracted from results) in purple. Resolved peaks (from left to right): phosphomonoesters (PME), inorganic phosphate (Pi), phosphodiesters (PDE), phosphocreatine (PCr), γ adenosine triphosphate (ATP), αATP, and βATP.

Table 2.9 Peak signal to noise ratios (SNR) for spectrum shown in Figure 2.24 acquired from skeletal muscle with the coil located over the proximal anterior compartment of the lower leg.
A pulse acquire sequence was used. Metabolites are listed in the order the peaks resonate in a typical ^{31}P-MRS spectrum, from left to right. Linewidth is expressed in parts per million (ppm). NAD(P)$^+$+NAD(P)H represent reduced and oxidised nicotinamide adenine dinucleotide, respectively.

	Muscle SNR	***Muscle linewidth (ppm)***
Phosphomonoesters	4.4	0.48
Inorganic phosphate	33.2	0.44
Phosphodiesters	18.2	0.20
Phosphocreatine	292.6	0.36
γ adenosine triphosphate	30.2	0.46
α adenosine triphosphate	33.0	0.46
NAD(P)$^+$+NAD(P)H	13.9	0.36
β adenosine triphosphate	18.2	0.46

An initial dynamic acquisition with sequence 25 was conducted at rest, which resulted in 16 spectra (6 NSA), each representing a 30 second time-bin, shown in Figure 2.25. Pi, PDE, PCr, ATPs, as well as NAD(P)$^+$ + NAD(P)H (denoted DN for dinucleotides in SpectroView and in the image below) all exhibited excellent resolution and SNR. PME peaks could not be fitted by SpectroView, but this was expected since concentrations of PMEs are extremely low in healthy individuals in muscle.

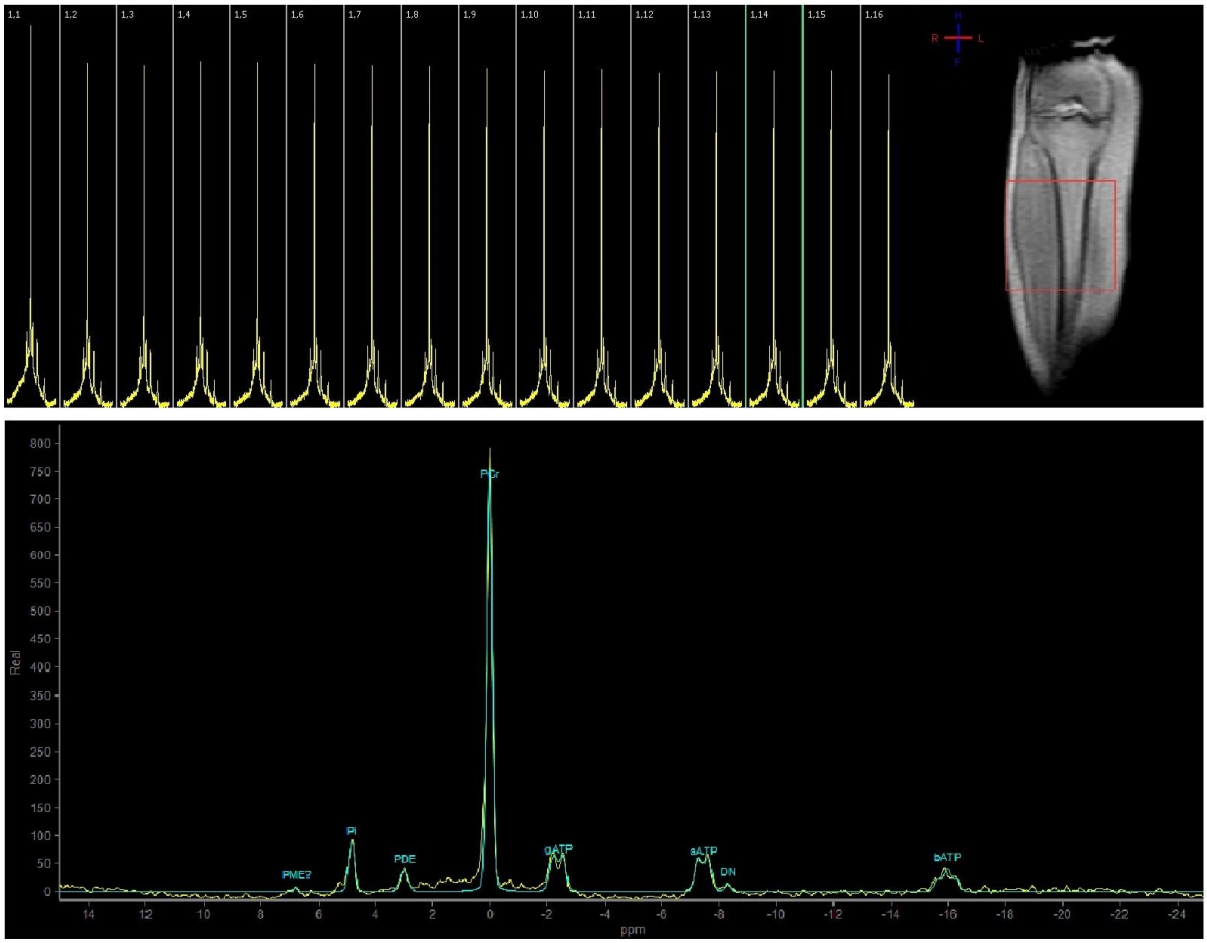

Figure 2.25 Phosphorus spectra acquired from the anterior compartment of the leg.
The dynamic series is illustrated in the upper graph. In the anatomical image, the red square indicates the shimming box. In C, the yellow line represents the spectrum following baseline subtraction, in blue is the best-fit line. Each spectrum was acquired over a 30-second period and the sequence depicted lasted eight minutes in total. No contraction was performed hence signal intensity did not vary over time. The phosphorus spectrum in muscle is analogous to brain spectra with the exception that phosphomonoester peak is very low and was not fitted.

Table 2.10 lists means, SDs, and CVs for metabolite ratios for spectra acquired during the sequence depicted in Figure 2.25. The CVs reported were derived from measurements on the 16 spectra shown above and are an indicator of measurement stability over time rather than reproducibility of the technique. Notably, CVs for brain were included in the next chapter where reproducibility data are reported.

Table 2.10 Means, standard deviations, and coefficients of variation (expressed as percentages) for metabolite area for spectra acquired during the sequence depicted in Figure 2.25.

	Mean (± standard deviation)	***Coefficients of variability (%)***
Phosphomonoesters	NA	NA
Inorganic phosphate	11.16 (±1.96)	17.54
Phosphodiesters	3.76 (±2.01)	53.45
Phosphocreatine	143.62 (±5.20)	3.62
γ adenosine triphosphate	38.20 (±3.17)	8.30
α adenosine triphosphate	26.67 (±1.69)	6.33
NAD^++NADH	6.16 (±0.82)	13.29
β adenosine triphosphate	15.03 (±0.92)	6.16

2.4.2.2 Exercise muscle acquisitions

Figure 2.26 shows spectra resulting from a dynamic scan acquisition (sequence 25) during which the subject performed isometric exercise, contracting muscles of the anterior compartment of the leg against a static load calculated to represent half their MVIC for one minute. The load was determined by QMA fixed myometry and implemented within the scanner by means of an MR-compatible pulley system. Following a two-minute rest period, muscle contraction caused PCr to drop and Pi to increase (spectra 1.5 and 1.6). When contraction ceased, PCr and Pi recovered to their initial values. Example spectra at rest and at the end of muscle contraction are also illustrated.

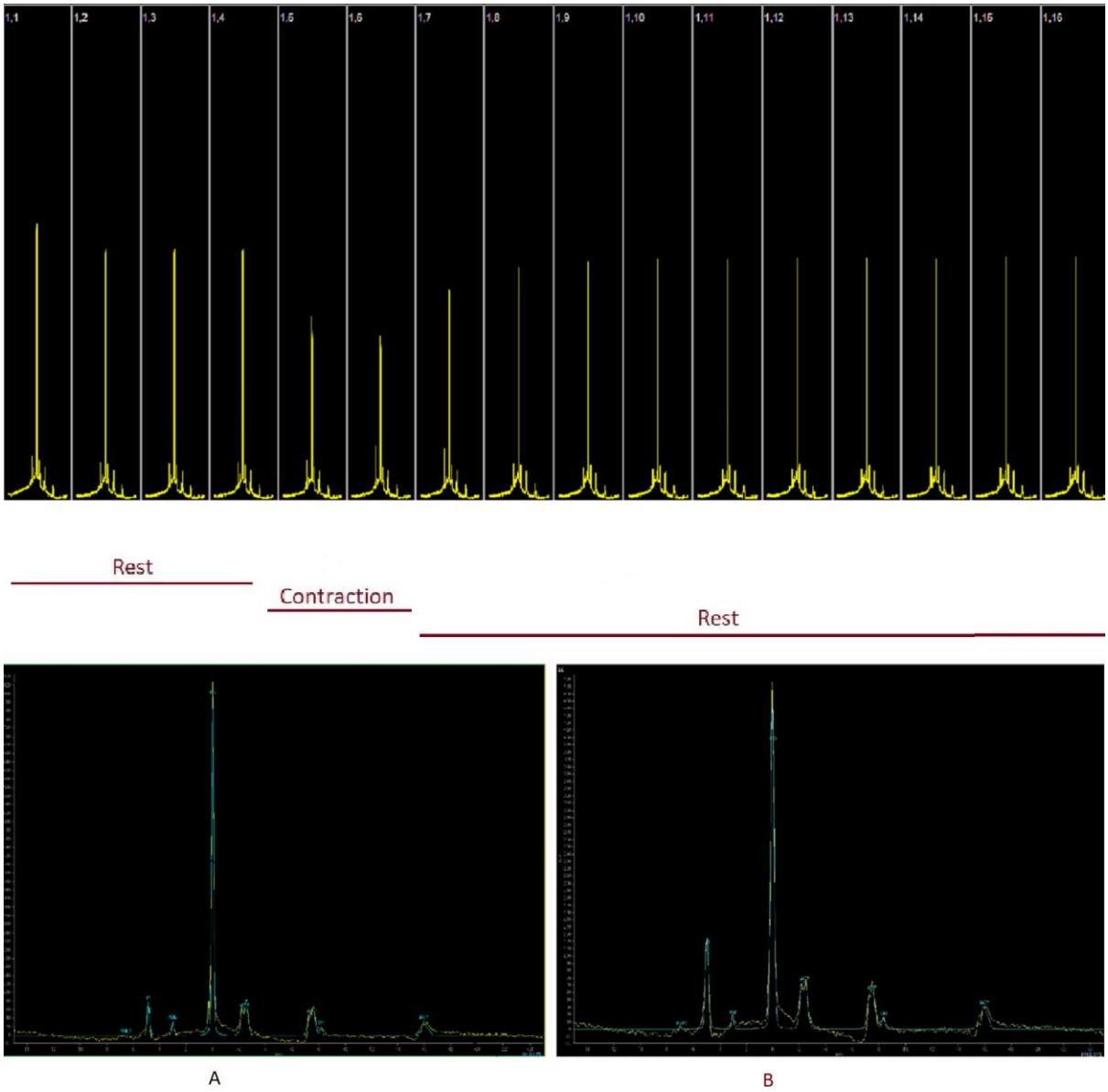

Figure 2.26 Dynamic muscle spectroscopy at half maximal voluntary isometric contraction with 30-second time bins (sequence 25).
The dynamic series is illustrated in the top panel. The subject was at rest for initial two minutes (four bins), ankle dorsiflexed for one minute (two bins), and rested for the subsequent five minutes (ten bins). The drop in phosphocreatine (PCr) on contraction, followed by an increase towards baseline on recovery is evident. In the bottom two panels, full spectra are illustrated. During muscle contraction PCr decreased whilst inorganic phosphate (Pi) increased (panel B, spectrum 1.6) compared to a spectrum acquired at rest (panel A, spectrum 1.3).

Figure 2.27 shows results of a third scan in which the number of averages was reduced to three and the number of acquired spectra was doubled to 32 (sequence 26). These sequence modifications were performed to assess the effect of improving temporal resolution to 15-second bins without increasing scan time. A consequence of diminishing the number of averages is a loss of spectral resolution. Nonetheless, the spectra acquired with sequence 26 were deemed sufficiently well resolved and no issues with peak fitting software were evident. Another difference in the acquisition below was that research participant was asked to sustain contraction for two minutes as opposed to one, in order to

assess kinetics of parameter changes, and specifically whether metabolites kept changing after one-minute contraction.

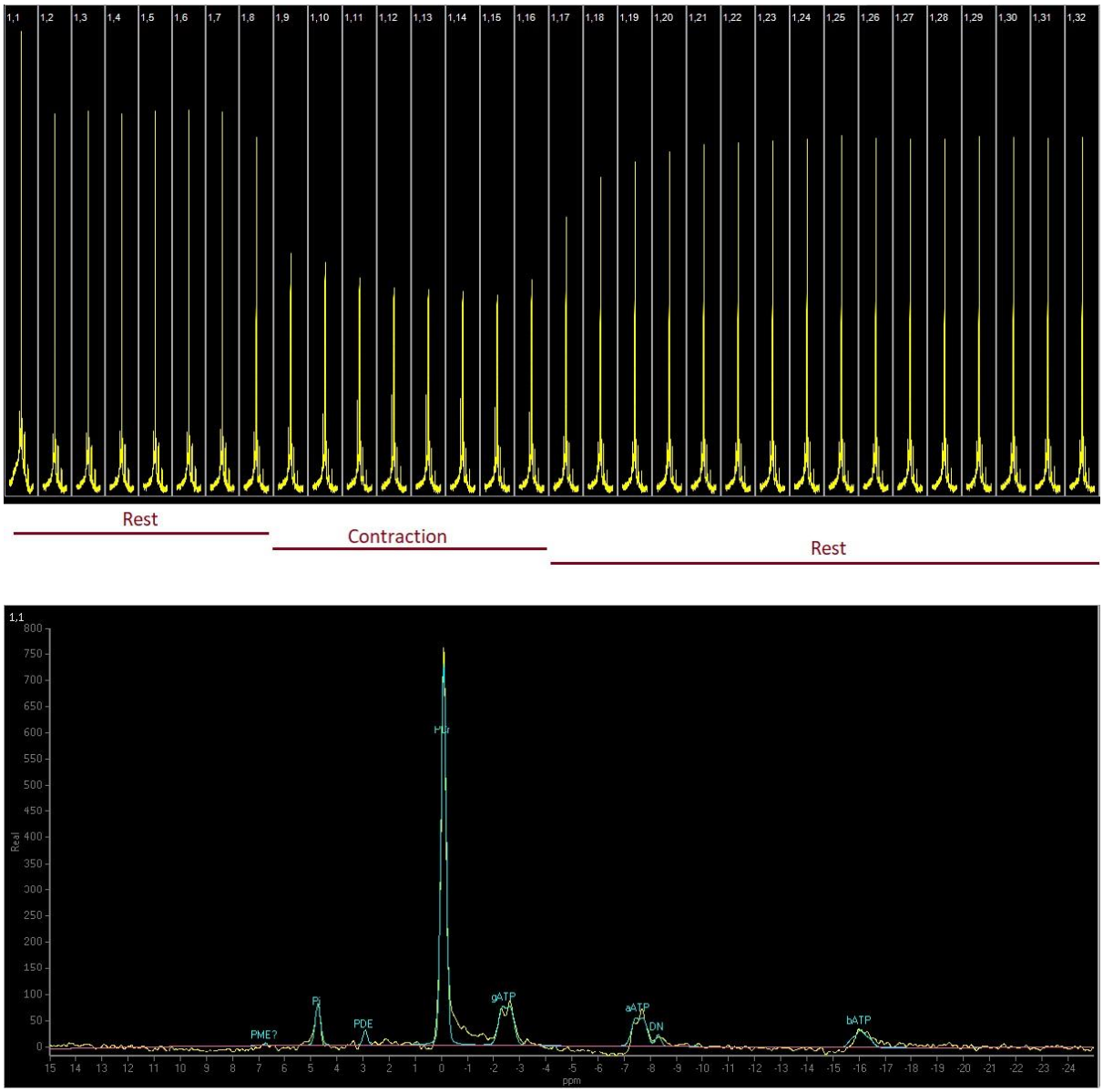

Figure 2.27 Dynamic muscle series with increased time resolution (15 seconds) at half maximal voluntary contraction. *Effects of improving time resolution by increasing the number of acquired spectra per unit time: each spectrum depicted was acquired over a 15-second time period. Spectral resolution was considered sufficient for analysis with SpectroView.*

In the previously reported experiment, the subject exerted a force corresponding to half the MVIC. In order to assess the effect of participant effort, the dynamic protocol was repeated with the subject performing contraction at a quarter of MVIC; results are depicted in Figure 2.28. Visually, the PCr drop is reduced compared to Figure 2.27. This difference is quantified in Figure 2.29.

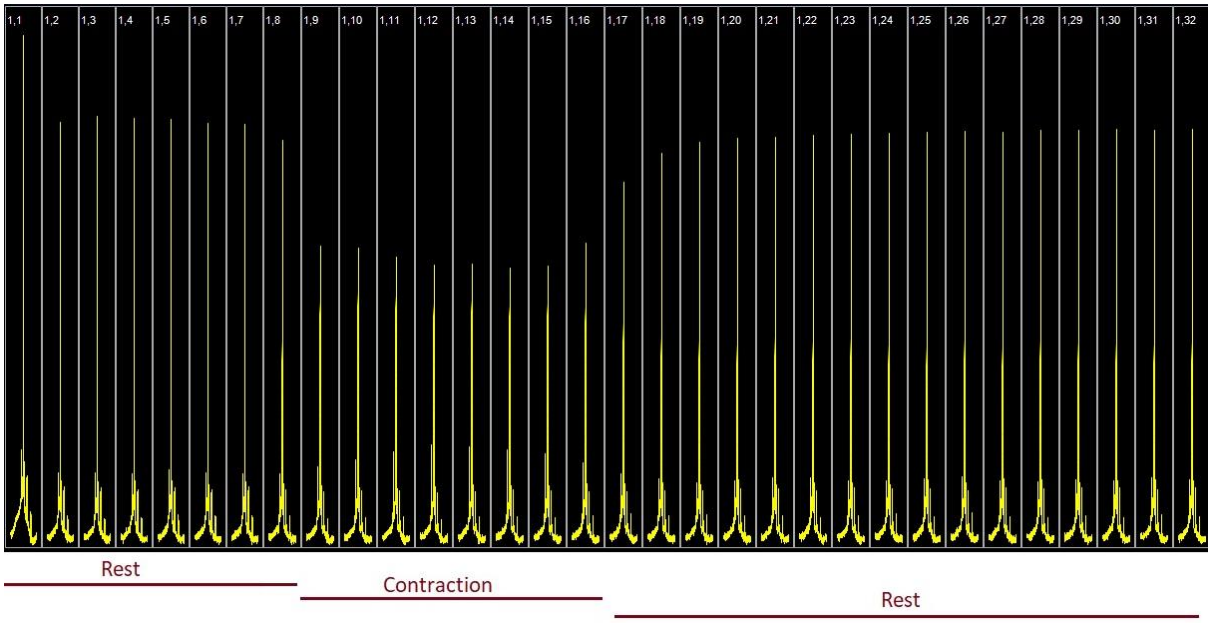

Figure 2.28 Dynamic muscle time series at quarter of maximal voluntary isometric contraction (MVIC).
Experimental parameters were as in Figure 2.27 with the exception that subject's exerted force was a quarter of measured MVIC. This resulted in a smaller drop in PCr compared to half MVIC dynamic sequences.

In Figure 2.29, quantification of PCr/Pi changes detected over time when subject exerted half MVIC (blue line) and a quarter MVIC (red line) are compared. The ratio doubled when a quarter of MVIC was exerted, whereas it almost tripled at half MVIC, showing that magnitude of metabolite variation was proportional to the force of contraction. The experiment also showed that changes in metabolites plateaued within the first minute of contraction, indicating that one-minute exercise was sufficient duration in the final protocol.

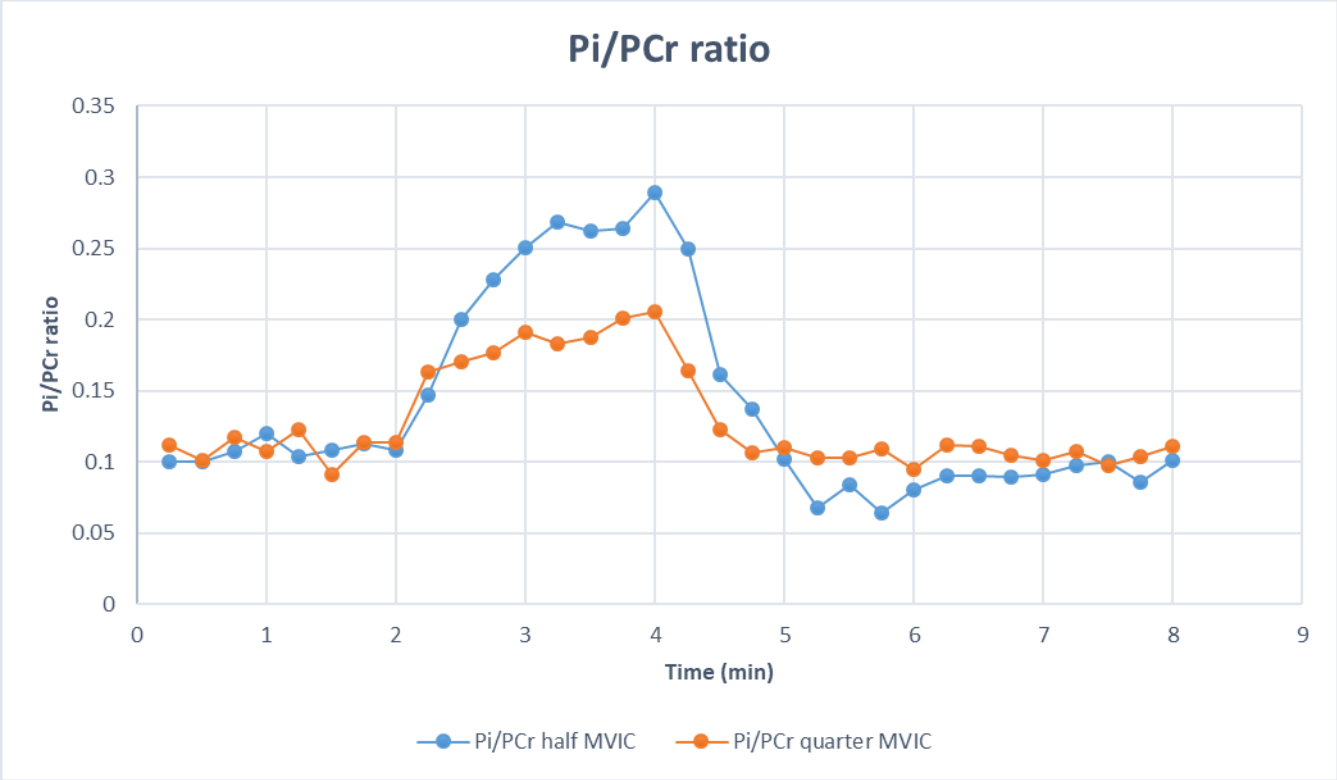

Figure 2.29 Variations of inorganic phosphate to phosphocreatine ratio (Pi/PCr) over time when contractions at half and quarter maximal voluntary isometric contraction (MVIC) were performed.
During an initial resting period, the ratio was approximately 0.1. As contraction was exerted (minute two) PCr levels reduced as phosphates were provided to adenosine diphosphate (ADP) to synthesise adenosine triphosphate (ATP) and Pi increased as the result of ATP hydrolysis. At minute four, muscle contraction ceased and the measured parameters gradually returned to baseline values.

The signal resulting from other metabolites did not vary during muscle contraction with the exception of γATP and NADH+NAD^+ (DN peak). The amplitude of these latter peaks fluctuated slightly during both half and quarter MVIC protocols, but change was not clearly proportional to contractile force. Figure 2.30 depicts changes of γATP/DN ratios during exercise protocols. This phenomenon has not been previously reported in the literature and the significance of these variations is yet to be determined.

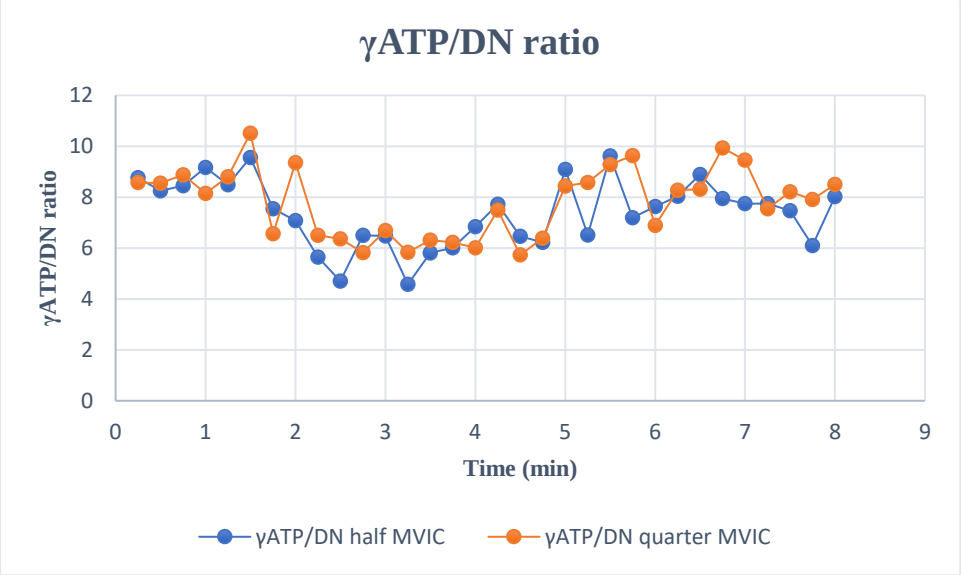

Figure 2.30 Adenosine triphosphate to di-nucleotides ratio (γATP/DN) variation over time upon muscle contraction. *Muscle contraction was exerted at half and quarter of participant's maximal voluntary isometric contraction force (MVIC). Exercise started at minute two and ceased at minute four.*

2.5 DISCUSSION

The goal of the experiments conducted in this chapter was to achieve maximal SNR, appropriate spatial localisation to regions of interest in brain, and optimise acquisitions in resting and dynamic muscle data.

2.5.1 Rapid coil one

Initial experiments aimed at acquired brain spectra using Rapid coil one did not produce expected results. Spectra could not be resolved by any sequence, with the exception of the PA acquisition that produced a spectrum characterised by a very low SNR. Loading containers and phantom image SNR were also deemed to be abnormally low. The lack of detectable signal of appropriate intensity was subsequently identified to be caused by a defect in the pre-amplifier and Rapid coil one was substituted with Rapid coil two.

2.5.2 Rapid coil two: calibration

Initial experiments employing Rapid coil two were conducted to illustrate effects of T_1 relaxation on the RF calibration curve. The theoretical framework necessary to understand the paragraphs below is detailed in 8.4). More specifically, a TR that does not allow full longitudinal relaxation (i.e. $TR < 5T_1$)[14] causes signal intensity to be affected by T_1 saturation effects. The magnitude of the transverse magnetisation vector is proportional to $M_0 sin\beta$ and so is the signal intensity. In RF calibration, FA (β)

[14] Longitudinal relaxation is considered complete once a time of $\geq 5T_1$ has elapsed.

is altered while M_0 is maintained constant by employing a sufficiently long TR. Conversely, if longitudinal relaxation is not complete (i.e. a short TR is used) M_0 decreases by a factor proportional to $1\text{-}e^{-TR/T1}$ causing signal intensity variations not to be solely dependent on β. The practical consequence is that decreasing TR to $<5T_1$ caused the calibration curve to be skewed to the left whereas, when increased, the curve remained symmetrical.

These experiments also illustrated that, in RF calibration, zero values can always (as long as they are well defined) be used to assign an appropriate value to the 180˚ FA since they are independent of TR length (because $M_0\sin(180^\circ)=0$). On the other hand, if maxima are used, then a $TR \geq 5T_1$ must be employed to avoid underestimation of RF length (or power) as maxima tend towards shorter FA as TR diminishes. Another cause of a skewed calibration curve is non-linearity of the RF amplifier output, which was not the case in these experiments as the calibration curve became symmetrical when increasing TR.

2.5.3 Optimisation of acquisition parameters and spatial localisation

Both SV and multi-voxel localisation techniques were tested to choose an optimal localisation sequence for the final study protocol.

2.5.3.1 Single voxel acquisitions at varying repetition times: T_1 saturation effects in in vivo spectra.

Short (721 ms) and long (4 s) TR SV acquisitions were compared. *In vivo*, in the short TR spectra, there was incomplete longitudinal relaxation manifested as a relatively greater reduction of signal intensity of longer-T_1 metabolites (such as PCr and Pi) compared to short-T_1 metabolites (such as ATP). This effect was apparent considering that, in the short TR acquisition, signal intensity of ATP peaks was almost unchanged compared to the long TR, whereas PCr decreased to about a quarter of the long TR spectrum. Notably, in the short TR sequences, signal intensity of Pi was reduced to such an extent that its resonance could not be discriminated from noise by the peak-fitting software.

There is considerable heterogeneity of sequences employed in MRS research, and both long and short TR acquisitions have been applied in published ^{31}P-MRS studies (Hattingen, Magerkurth et al. 2009, Weiduschat, Mao et al. 2015). Long TR acquisitions have the advantage that measured signal intensity is relatively independent of T_1 saturation effects, but at the expense of relatively longer scan times. At shorter TR acquisitions, it can be impossible to discriminate whether measured differences are due to genuine variation in metabolite concentrations or T_1 saturation effects. Theoretically, it is possible to correct for these effects, either by measuring T_1 directly in participants or by using values reported in the literature (Ren, Sherry et al. 2015). However, literature values are typically measured in healthy volunteers, and may not be applicable to patients in whom pathological cellular changes are also likely

to alter nuclear relaxation properties. On the other hand, direct measurement of T_1 relaxation constants again significantly adds to scan times. To avoid the need to correct for undesirable T_1 saturation effects, a long TR acquisition was chosen for the final protocol as a pragmatic solution.

2.5.3.2 Chemical Shift Imaging: varying dimensions, number of signal averages, and discussion on chemical shift artefact

There was a substantial improvement in SNR when using CSI sequences compared to SV ones, likely because Nuclear Overhauser Effect (NOE)[15], could be used in the multi-voxel scans but not in the SV acquisitions. This was due to concerns over excessive power deposition to tissues (the specific absorption rate) which would have exceeded safety limits in SV acquisitions.

Among the CSI sequences tested (1D CSI, 2D CSI with 2 NSA, and 2D CSI with 4 NSA), spectra acquired with 2D CSI 2 NSA were undoubtedly superior in terms of SNR. This was an expected finding when comparing 2D to 1D CSI: in the latter, localisation is achieved following summation of two signals whereas, in 2D CSI, summation of four FIDs is necessary (see section 8.8 – addition of signals has a denoising effect).

Comparison of 2D CSI 2 NSA and 2D CSI 4 NSA produced unexpected results. When all other conditions are unchanged, doubling NSA should, theoretically, improve SNR, but this was found to be consistently lower in all 2D CSI 4 NSA spectra. Notably, the two sequences were not acquired in the same subject (because of limited length of individual scanning sessions and unavailability of the initial research participant for a follow-up scan session); SNR may vary between individuals in *in vivo* acquisitions. Nonetheless the extent of decrease was substantial and unanticipated. It is therefore possible that subject movement may have contributed. Motion artefacts can be easily detectable in standard MRI, but they are not directly visible in MRS and manifest only as a decrease in SNR (Kreis 2004). Unfortunately, we were unable to test this hypothesis because no structural imaging or localisers after the MRS acquisition were obtained, hence direct estimation of participant motion during MRS acquisition was not possible. Hence, it was decided against the use of 2D CSI 4 NSA because it was deemed to be an overly lengthy sequence (over 30 minutes) and, besides increasing the risk of participants' motion, it was unlikely to be well tolerated by MND patients, who have specific symptoms (e.g. sialorrhoea, orthopnoea) that can make prolonged sequences problematic.

[15] An effect related to dipolar coupling in which saturation of a population of nuclei enhances (or diminishes) the signal of another population of nuclei. It is used in analytical chemistry to elucidate structure of molecules and, in this case, to improve SNR of spectra. Of note, it requires irradiating nuclei to saturate them causing an increase in the specific absorption rate and was, hence, not possible in some sequences.

Ultimately, the 2D CSI 2 NSA sequence was chosen for the final protocol because it enabled concomitant acquisition of spectra from all cerebral motor regions of interests in an acceptable scanning time (15 min) and produced good SNR spectra.

In this work, it was not possible to experimentally correct for chemical shift displacement artefact although we did consider its potential impact. Chemical shift displacement artefact occurs when compounds that resonate at different frequencies do not localise to the same location in space, but have an offset relatively to each other. The formula for calculating this displacement is: $\Delta x = \Delta\omega * V_x / \max \omega = \Delta\omega / \gamma * G_x$. Where Δx is the displacement in a direction "x" subjected to gradient encoding, $\Delta\omega$ is the chemical shift between two metabolites of interest (in Hz), V_x is the voxel size in the x dimension, max ω is the spectral bandwidth of the RF pulse, γ is the gyromagnetic ratio, and G_x is the gradient in the x direction. The formula above can be understood and derived from equations described in the appendix. In this thesis, the localisation sequence that was ultimately used caused a displacement artefact only in the anterior-posterior dimension. This could have been corrected by acquiring spectroscopic slices immediately anterior and posterior to the one utilised and interpolate results. Another possibility could have been to repeat the 2D-CSI acquisition inverting the gradient along the z axis, and again interpolate spectroscopic results. Both these options would have increased scan time substantially, which was deemed unfeasible for the patient population studied. The extent of the displacement was, nonetheless, calculated and was considered to be negligible. This is illustrated in the figure below. In addition, this artefact does not cause a systematic error affecting putative group level changes.

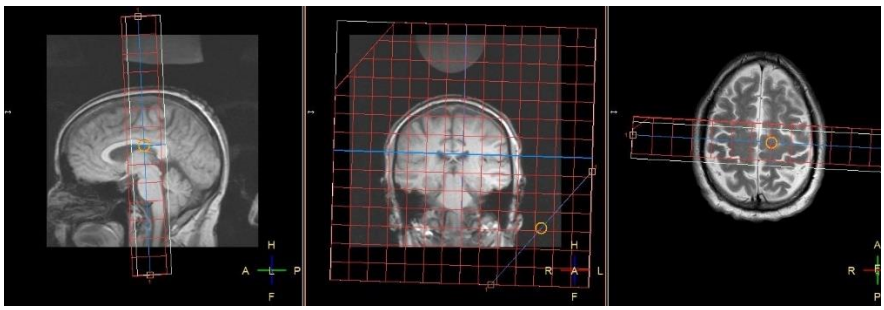

Figure 2.31 Axial, coronal, and sagittal anatomical images of a healthy volunteer with superimposed spectroscopic slice (red) and calculated putative chemical shift artefact for PME (in white) which is found at the far right end of the spectrum (i.e. most prone to this artefact). Notably, the artefact does not occur on the coronal plane as this is phase encoded, whereas it only takes place in the anterior-posterior direction.

2.5.4 Experimental accuracy and phantom for external reference

Linear dependency of signal intensity of metabolite concentration was excellent, offering some reassurance on accuracy of the technique. Experiments also illustrated the importance of using a phantom of concentration comparable to metabolites *in vivo* to avoid expanding the dynamic range of

the hardware resulting in failure of detection of lower concentrations. On this basis, the ten mM phantom was included as external reference in the final protocol.

2.5.5 T_1-weighted volumetric acquisitions

A T_1-weighted volumetric image was added to the protocol with a view to spectral co-registration and white matter, grey matter, and CSF segmentation, to assess partial volume effects. To maximise T_1 contrast, an inversion recovery sequence characterised by a relatively long inversion time (TI=1000 ms) was chosen and different sampling frequencies, field of view (FOV), and reconstruction matrices were tested.

Oversampling was employed to achieve a denoising effect. This was the reason for the substantially improved contrast to noise ratio in Figure 2.21 a, c, d, and e (which were acquired with an oversampling factor of 2) compared to image b (the only volumetric image acquired with standard oversampling). Of the various parameters tested, increasing sampling rate had the most prominent effect on SNR.

Although signal was markedly increased by increasing FOV (Figure 2.21 d), there was a visually evident loss of spatial resolution associated with relatively larger voxel size. Interestingly, contrast to noise ratio was variable across brain regions (Figure 2.23) and was higher in regions of interests on the left compared to the right.

To improve the spatial resolution of Figure 2.21 d, the reconstructed matrix size was increased (Figure 2.21 c). This caused signal to slightly decrease and, with it, the contrast to noise ratio dropped to values slightly lower than those measured in Figure 2.21 d.

Prolongation of TI from 1000 ms to 1400 ms to acquire Figure 2.21 e slightly reduced contrast to noise ratio, possibly because, for a given TE and TR, there is a TI length that produces optimal T_1 contrast, which decreases if TI is changed.

The image that produced the best contrast to noise ratio (Figure 2.21 a) was selected for the final protocol. This choice was also based on the fact that voxels in Figure 2.21 a were near isotropic, a desirable feature when reconstructing and segmenting high-resolution images (Edelman, Dunkle et al. 2009).

2.5.6 Optimisation of muscle ^{31}P-MRS

The PA sequence in muscle was included in the final protocol to provide information on resting status of muscle metabolites. The quality of spectra from muscle PA was far superior to brain PA sequences. This is likely because: 1) a surface coil placed in close proximity to the region of interest was employed; 2) muscle contains significantly larger concentrations of ATP and PCr compared to brain; ATP

concentration is approximately 3 mM in brain and 8 mM in muscle, whilst PCr has a concentration of 3 mM in neural tissue and 11 mM in myocytes (Thulborn and Atkinson 2014); 3) decoupling and NOE, which improve line shape and SNR, respectively, were included in the PA sequence in muscle, but not in brain. This is because they would have increased the specific absorption rate to unsafe levels in brain; 4) the muscle sequence comprised 32 NSA whereas the brain PA sequence comprised 4 NSA.

For the purpose of protocol set up of dynamic exercise studies, it was first essential to ensure that force exerted within bore of the magnet was directly proportional to each individual's MVIC, for two main reasons. Firstly, experiments performed at submaximal contraction provide information on mitochondrial oxidative capacity (as explained in chapter one, section three), whereas experiments at stronger contraction are more informative on changes associated with muscle fatigability. Secondly, considering that the cardinal feature of MND is muscle weakness, ensuring that all participants performed the exercise at a proportion of their own MVIC addressed a potential systematic bias. To gauge force of contraction, MVIC was first measured in healthy controls in a dedicated room using a hand-held dynamometer. Following the observation that, on a number of occasions, the volunteers' force of contraction exceeded that of the researcher, it was decided to employ the QMA fixed myometry system, which is independent of operator force, unlike hand-held dynamometry.

A dynamic exercise protocol was developed which enabled assessment of variation in phosphorus metabolites during muscular contraction. The anterior compartment of the leg was selected as tibialis anterior has been shown to be affected consistently in MND patients (Pierry, Alix et al. 2017). Particular care was taken to optimise temporal resolution (four spectra per minute) while still maintaining a manageable scan time for participants and good quality spectra. A one-minute contraction (instead of two minutes) was chosen as results showed that, after one minute, no further significant changes in PCr and Pi occurred. In addition, time of recovery acquisition was decreased to three minutes (for a total dynamic sequence acquisition time of six minutes), as metabolites returned to baseline and remained stable within this time frame. Dynamic protocols showed that contraction-induced PCr and Pi changes were proportional to force exerted by ankle dorsiflexors and, hence, that the pulley system was capable of appropriately gauging contractile force. For the final protocol, a third of MVIC was to balance the relative benefits of the half and quarter MVIC experiments and considering previous literature that suggested a decreased PCr decrement in patients at 25% MVIC which may have affected appropriate fitting of recovery constants (Grehl, Fischer et al. 2007). Thirty percent MVIC is still low enough not to induce substantial pH changes but, given these data, was judged to slightly increase the likelihood of detecting PCr changes in patients, compared to 25% MVIC. PCr and Pi dynamics can be particularly informative since they are indirect indicators of muscular oxidative capacity and they were assessed in the patient group as detailed in following chapters.

As detailed in chapter one, previous studies which have applied ^{31}P-MRS to muscle in MND have not demonstrated clear disease-related changes, but none have assessed the muscle metabolic phenotype concurrently with the brain and carefully gauging contraction force. Additionally, we aim to determine whether DN concentration is altered in patients' muscles; the peak has been only recently discovered representative of NADH and NAD^+ (Lu, Zhu et al. 2016) and no study conducted to date in MND has measured the concentrations of these two metabolites. Results are reported in chapter four. Another observation from dynamic data was that γATP/DN changed during muscle contraction, a new finding not previously reported in the literature. This finding could be due to increasing energy demand leading to increased flux through the ETC requiring more reducing equivalents (NADH) to maintain stable ATP concentrations, although this hypothesis needs corroboration in future studies.

2.6 CONCLUSIONS

In summary, an optimised ^{31}P-MRS protocol to assess brain and muscle phosphorus metabolites in MND patients was established. The final protocol included a long-TR 2D CSI sequence with 2 NSA lasting 16 minutes, a T_1-weighted volumetric image (voxel size=1.00/1.08/1.00 mm, oversampling=2, FOV=240 mm, TI=1000 ms), a T_2-weighted acquisition used to position the spectroscopic grid, one PA muscle sequence at rest, and two muscle dynamic sequences each lasting six minutes with bin duration of 15 seconds, during which subjects exerted one third submaximal and maximal contractile forces. A ten mM phantom was chosen as an external reference for metabolite quantification of spectra acquired from primary motor cortex and motor tracts. In the next chapter, methodological considerations in relation to spectroscopic pre- and post-processing will be discussed, and an optimised processing protocol developed.

CHAPTER 3:
31-PHOSPHORUS MAGNETIC RESONANCE SPECTROSCOPY: DATA PROCESSING AND PRECISION

This chapter concludes reporting on spectroscopic protocol development and includes data on precision of the technique.

The initial sections of the introduction are dedicated to ^{31}P-MRS data processing. The main spectroscopic analysis steps are described and divided into pre-processing (phasing, frequency shifting, and denoising) and post-processing (peak-fitting, resonance integration, baseline estimation, quantification of parameters, correction for relaxation effects, and co-registration of spectroscopic data to anatomical images). Each processing stage is defined and described, and experimental data are included, whenever necessary, to elucidate concepts and to support the rationale for specific analysis choices applied in the final protocol used for clinical experiments. A brief section at the end of the introduction presents concepts related to precision.

Experiments related to characterisation of precision are detailed in methods, results, and discussion sections of this chapter. Specifically, whilst developing the analysis protocol, the impact of using different fitting algorithms (from different software packages), phasing, (a user-dependent step) and apodisation (recommended in some guidelines, but not in others) was assessed in terms of effects on reproducibility of brain results. Results of these analyses were used to choose the most reproducible post-processing protocol.

When not otherwise cited, the following sources were used for theoretical treatment of processing steps (de Graaf 2007, Keeler 2010) as well as jMRUI technical documentation (available at http://www.jmrui.eu/) and SpectroView user documentation available on the Philips' scanner software.

3.1 INTRODUCTION

Spectroscopic analysis is conventionally divided into pre-processing and post-processing stages. Broadly speaking, pre-processing refers to those analysis steps that are conducted in the time domain to maximise spectral quality prior to integration of peaks and calculation of signal intensity. These steps include phasing, alignment of signal to desired reference frequency, and denoising steps. Some authorities also consider baseline correction to be a pre-processing step (de Graaf 2007), but this is debated, and distinction between pre-processing and post-processing is somewhat arbitrary. In this

thesis, baseline correction was included amongst post-processing steps since it is conducted concomitantly to integration of resonance areas in both software packages utilised in this experimental work: jMRUI and SpectroView. At the post-processing stage, the various resonances are fitted and integrated and additional parameters, such as pH and free Mg^{++} concentration, can also be calculated. Fitting can be rendered more robust by specifying starting values and prior knowledge and by ensuring optimal baseline estimation. These steps decrease uncertainty and improve reliability of measurements. Goodness of fit and maximal accuracy of individual measurements can be characterised by the Cramér-Rao lower bound (CRLB, defined in 3.1.2.3), which was calculated and reported in this chapter. Additional steps following calculation of results include correction for relaxation effects and co-localisation of spectroscopic signal to anatomical region of interest, which is necessary to determine whether the relative proportion of white matter, grey matter, and CSF differs between patients and controls in analysed voxels. This is particularly important in case-control studies assessing diseases such as MND which may cause brain atrophy (Mezzapesa, Ceccarelli et al. 2007).

3.1.1 Spectroscopic pre-processing

3.1.1.1 Opening localised spectroscopic data: a note of caution

Prior to starting analysis, it is important to ensure that 2D spectroscopic data maintain the correct spatial orientation (in the case of coronal acquisitions, right to left and head to foot) when opened in the chosen analysis software (e.g. jMRUI). Spectroscopic data can be saved in different formats, for instance, the Philips MR system used in this thesis allows DICOM (standard or enhanced) and SPAR-SDAT (Philips proprietary) formats; both enhanced DICOM and SPAR-SDAT can be read by jMRUI software. To determine whether the correct spatial orientation was retained in jMRUI, an additional scan was conducted using two phosphorus phantoms (Philips' Sphere B, containing 524 cc of 30 g/l methylphosphonic acid placed in the top left area of FOV and a 450-mL glass container made in-house filled with 50 mM Pi and autoclaved for sterility placed in the bottom right corner) as illustrated in the figure below. SpectroView was taken as illustrating the correct orientation as this is the Philips' proprietary software for spectroscopic analysis.

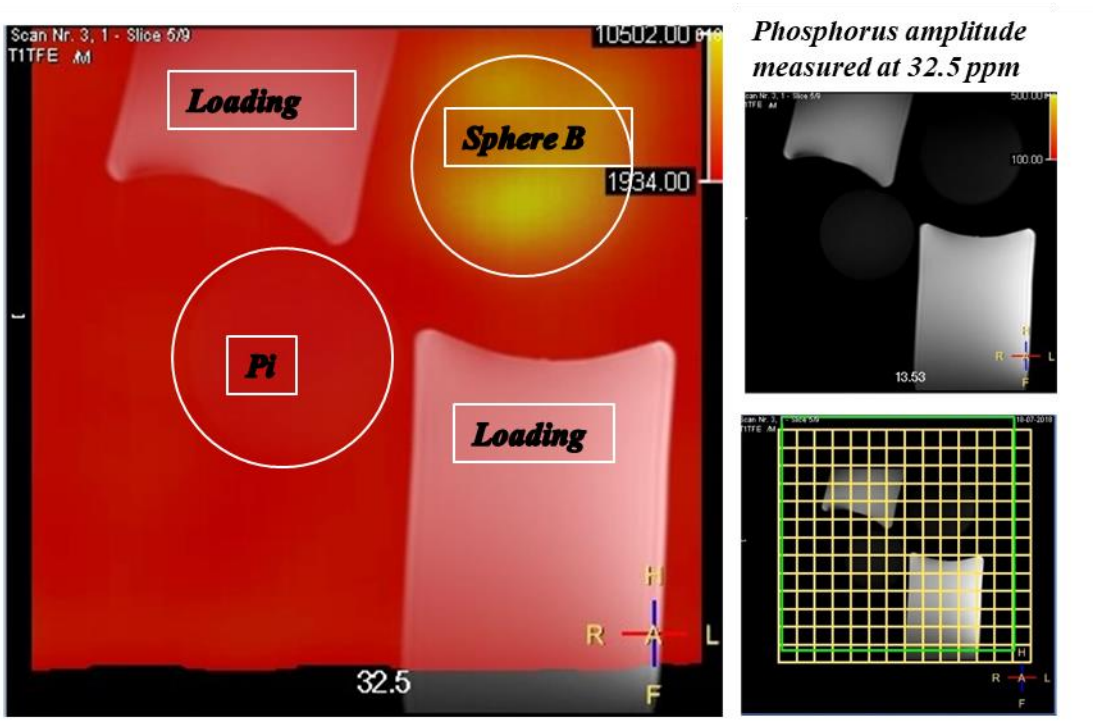

Figure 3.1 2D Chemical shift imaging (CSI) acquisition of two phantoms containing phosphorus.
The sequence used is the 2D CSI selected from experiments in chapter two (sequence 15). Sphere B refers to Philips' Sphere B, containing 524 cc of 30 g/l methylphosphonic acid, whereas the area denoted Pi contained a 450-mL glass container made in-house filled with 50 mM inorganic phosphate. The two areas labelled "loading" refer to the loading containers (two two-litre plastic bottles containing five g/l NaCl each, made in-house). The image on the left includes a heatmap (in red and yellow) overlaid onto a localiser in coronal orientation. The heatmap depicts signal intensity of peak detected at 32.5 ppm i.e. at the resonance frequency of methylphosphonic acid. This is the reason that the area of Sphere B is visualised in yellow whereas inorganic phosphate is not visible. Proton signal intensity of the two phosphorus phantoms on the MR image is lower compared to loading containers, hence, they are not well delineated on the localiser. The localiser and spectroscopic grid are also included (images on top and bottom right, respectively) to aid comparison with spectroscopic data opened in jMRUI in the figure below.

Spectroscopic data in enhanced DICOM and SPAR-SDAT formats were then opened in jMRUI as illustrated in the figure below. Enhanced DICOM returned the correct spatial orientation matching SpectroView, whereas this was not the case for SPAR-SDAT data, which returned a mirror image inverted along the head-to-foot direction. This was due to differences in indexing of spectra. To minimise risk of inadvertently introducing orientation errors, enhanced DICOM were used for all remaining analyses.

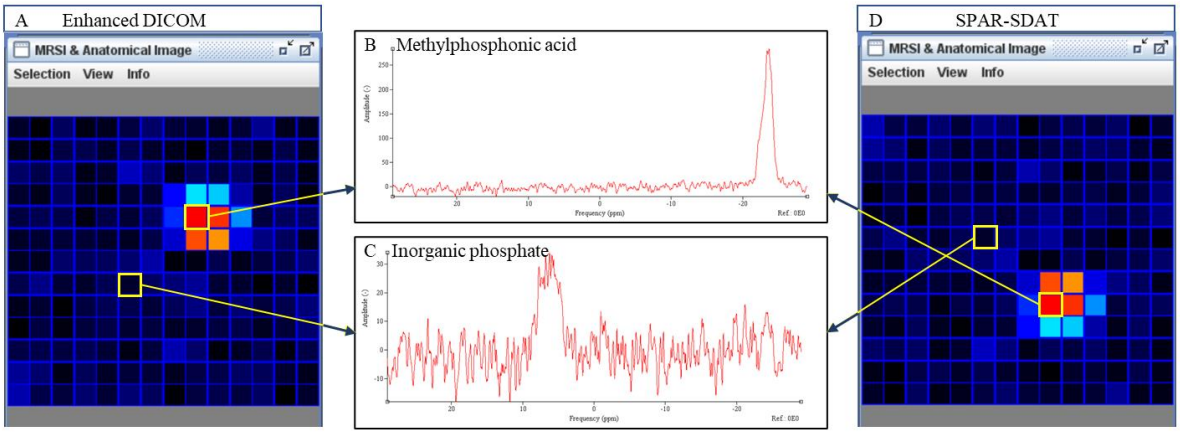

Figure 3.2 Spatial orientation of 2D chemical shift imaging data opened in jMRUI.
The acquisition protocol including positioning is detailed in Figure 3.1. A and D illustrate spectroscopic grids resulting from opening data in enhanced DICOM and SPAR-SDAT formats, respectively. Heatmaps represent total signal intensity and are most prominent in the areas of Sphere B. B and C illustrate spectra resulting from methylphosphonic acid (B) and inorganic phosphate (C). Methylphosphonic acid is displayed on the right of the spectrum even though it resonates at 32.5 ppm. This is only a consequence of a wrap-around artefact. Inorganic phosphate was present at much lower concentrations than methylphosphonic acid, hence the substantially reduced SNR. Line shape of all peaks was poor due difficulties with shimming encountered on the day. Spatial localisation of enhanced DICOM was correct and matched SpectroView, whereas SPAR-SDAT data were inverted along the foot-to-head dimension. All spectra were visually checked and compared to ensure that enhanced DICOM opening order corresponded to SpectroView, which was the case.

3.1.1.2 Phasing

The Fourier transformation of an exponentially decaying cosinusoidal function results in a peak having exclusively positive y values. The shape of such a peak is referred to as "absorptive". Conversely, the Fourier transform of a cosinusoidal function shifted in the x-axis and beginning at its minimum results in a negative peak. If the function is shifted and neither its maximum nor minimum correspond to the first point on the x-axis, the resulting Fourier transform is a biphasic wave having a "dispersive" line shape, characterised by both positive and negative components, as illustrated in the top spectrum in Figure 3.3. A correctly phased phosphorus spectrum (see bottom-left in the figure below) contains peaks of exclusively absorptive line shapes. Dispersive peaks are due to phase errors which can result from imperfections of transmitter, receiver, or sequence timing (for instance, suboptimal timing of recording of the FID), RF pulses, or other hardware factors (such as analogue to digital converter – ADC – and incorrect sampling intervals), or consequent to subject motion and off-resonance effects. These latter errors occur when the RF pulse frequency used for excitation of a specific metabolite is not fully on resonance with the metabolite's Larmor frequency. Consequently, the path followed by the metabolite's net magnetisation vector during excitation is more complex causing it to maintain a z component even when FA is 90° (hence signal intensity is diminished) and acquire a phase difference. There are two types of phase errors: zeroth- and first-order. Zeroth-order errors affect all frequencies and peaks in the same way (i.e. they are not frequency-dependent) and might be due to hardware imperfections or subject motion. First-order errors may result from off-resonance effects and depend on frequency; hence, they are more prominent for peaks such as βATP, that lie at the extreme ends of the horizontal axis of the

resulting spectrum. It is possible to correct such errors and convert dispersive line shapes into absorptive ones through zeroth- and first-order phasing. This is a trial-and-error process in which the phase angle is adjusted, FID shifted to ensure that maxima correspond to first x-axis point, and line shape improved. Phasing may be automated, especially when working with large datasets, but, whenever possible, manual input is preferred as this can reduce evident errors, as illustrated in the figure below in which manual and automated phasing using jMRUI are compared (own data). The brain spectrum shown was acquired from a healthy volunteer using the 2D CSI protocol selected from experiments detailed in previous chapter (sequence 15).

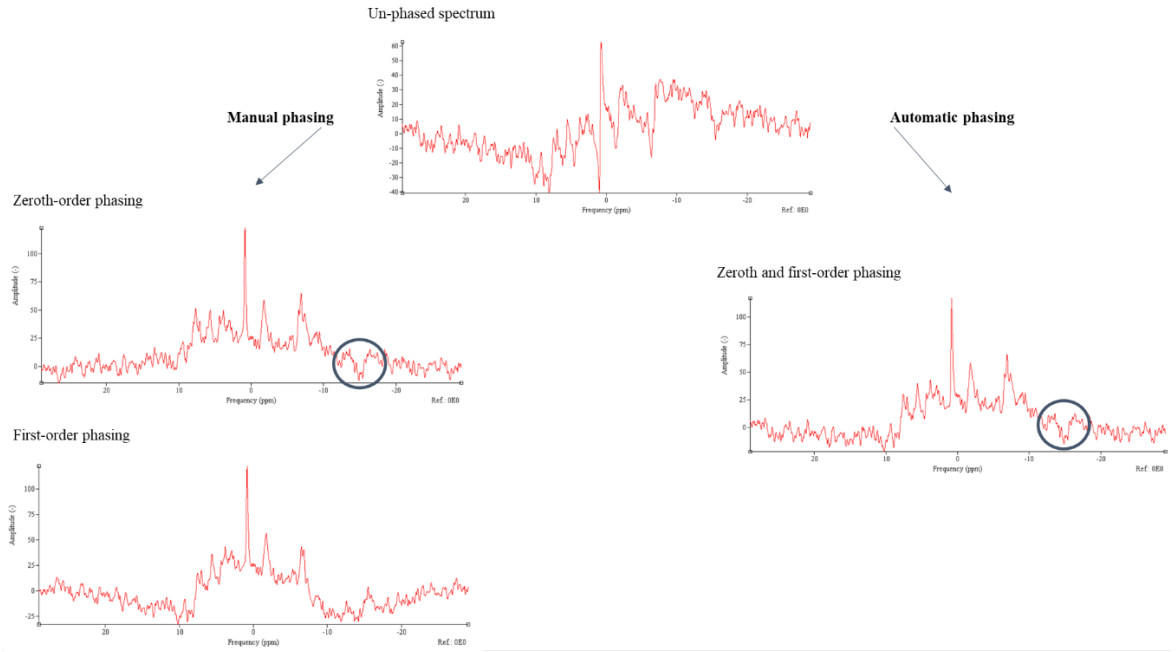

Figure 3.3 Manual and automatic phasing of a brain spectrum acquired from white matter in a healthy volunteer (own data, acquisition using sequence 15 as detailed in chapter two).
Phasing was conducted using jMRUI. The spectrum on the top is unphased and line shapes are dispersive with both positive and negative components. Such a spectrum would be very challenging to fit automatically as these line shapes are difficult to model. The two graphs on the left illustrate manual phasing: zeroth-order (middle-left graph) improves line shape of most peaks but the βATP peak (blue circle) is subjected to off-resonance effects and a first-order frequency-dependent phasing error, hence it remains negative. This error can be resolved by first-order phasing (lower-left graph), yielding an appropriately phased spectrum. The graph on the right illustrates the same spectrum phased using the automated function in jMRUI; this automated step did not resolve the phase error of the βATP peak (blue circle) and hence, was not used in subsequent analyses.

Although modern fitting algorithms such as the *advanced method for accurate, robust, and efficient spectral fitting* (AMARES, typically employed in ^{31}P-MRS analyses and included with jMRUI, http://www.jmrui.eu) (Vanhamme, van den Boogaart et al. 1997, Naressi, Couturier et al. 2001, Stefan, Cesare et al. 2009) are relatively robust to phase variations, incorporating them in their models, phasing is still important as large phase errors, such as those in the image above, can lead to improper peak integration and consequent inaccurate concentration estimates. This is because a dispersive line shape is more difficult to model than an absorptive one, leading to decreased precision of fit and affecting the integration step.

Manual phasing was chosen for the remainder of the experiments (based on results such as those shown in Figure 3.3), but it was recognised that this added an additional user-dependent step to analysis of brain data, with potential to introduce subjectivity. Of note, phasing of muscle spectra was always unambiguous. Since phasing is the main user-dependent step of spectroscopic analysis, the impact of this step on measurement reliability and agreement was assessed in subsequent experiments on brain data (detailed in methods, results, and discussion) to select the optimal spectroscopic analysis software and methodology.

3.1.1.3 Frequency shift

Following phasing, the spectrum is shifted on the x-axis to assign a value of 0 ppm to the PCr peak maximum, which is the reference compound in ^{31}P-MRS. Small variations in chemical shift along the x-axis can result from B_0 drifts (described in appendix). An example of frequency shift is provided in the figure below (own data acquired from the deep white matter of a healthy volunteer using sequence 15, as described in the previous chapter).

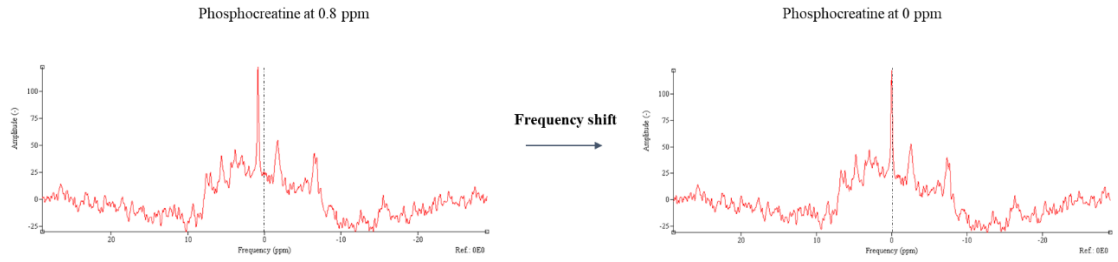

Figure 3.4 Illustration of frequency shift of a spectrum to assign a zero ppm chemical shift to phosphocreatine, the reference compound in ^{31}P-MRS.
Spectrum was acquired from white matter in a healthy volunteer using the 2D chemical shift imaging sequence selected following protocol optimisation experiments described in previous chapter.

Frequency shift is also a manual step, although it is much less likely to result in inter-operator variability than manual phasing. This is because fitting algorithms such as AMARES (and to a lesser extent SpectroView) can account well for such minute changes in chemical shift by imposing soft constraints to peak frequencies prior to fitting. When a soft constraint on frequency is imposed, the algorithm searches for the peak maximum by iterating within the chosen frequency interval. In the analyses conducted in this thesis, frequency shift was always unambiguous, and user-dependent bias at this stage was excluded as a potential source of variability.

3.1.1.4 Denoising

At the pre-processing stage, it is also possible to denoise the signal. Denoising methods are based on the observation that, as the MRS signal decays over time, most of the information of interest is contained at the beginning of the FID, whereas latter points comprise primarily noise.

The most common denoising method is apodisation. This involves multiplying the FID by a smoothing function also decaying over time, which results in additional weighting being assigned to points at the beginning of the FID, whilst reducing the relative weight of those at the end. In jMRUI, it is possible to choose between a Lorentzian (a decaying exponential) and a Gaussian function (which is a half-normal curve in the time domain) to perform this process. Apodisation by a decaying function has a denoising effect, but it also broadens the linewidth as it causes the MRS signal to decay faster (the Fourier transform of a quickly decaying signal returns a broad peak and *vice versa*). Hence these modifications are sometimes defined as "line broadening" and the degree of apodisation is expressed in Hz (i.e. by how many hertz the resulting peak is broadened following apodisation). It is also possible to improve (i.e. reduce) linewidth by multiplying the FID by a function which increases over time. This is the default in SpectroView in which all signals are multiplied both by a decaying exponential, to reduce SNR, and an ascending function to improve linewidth.

Use of apodisation exclusively for illustrative purposes (but without altering the signal prior to fitting) is a standard procedure in the field and was performed throughout the experiments in this thesis. However, apodisation that alters the signal prior to fitting is controversial. This technique is used in analytical chemistry and recommended in recently published muscle spectroscopic guidelines (Meyerspeer, Boesch et al. 2020), but strongly discouraged by many authors and in the guidelines published for brain analysis (Wilson, Andronesi et al. 2019). Opponents argue that, by enhancing the initial points of the FID, apodisation may also affect the information contained in the measurement, possibly introducing bias to results. In addition, the AMARES algorithm was especially designed for low SNR signals, such as those resulting from ^{31}P-MRS acquisitions, so there might be no need for additional denoising. Additional experiments (described in subsequent sections of this chapter) were conducted to assess reproducibility and potential bias following apodisation of spectroscopic brain data. Of note, muscle data are much less noisy than brain data, hence, apodisation was not required in muscle, even for illustrative purposes.

An alternative means of denoising is to truncate the latter points of the FID (containing primarily noise) and replace them with points having intensity values equivalent to zeros, in a process known as truncation and zero-filling. This method is generally not recommended as it generates a discontinuous function which, following Fourier transformation, results in peaks having smaller waves on each side (known as "sync waves") that may affect quantification. This phenomenon is referred to as a truncation artefact.

3.1.2 Spectroscopic post-processing

3.1.2.1 AMARES and peak fitting

In ^{31}P-MRS, one of the most frequently used fitting algorithms is AMARES, which was developed for noisy signals and overlapping resonances and is, hence, particularly apt for phosphorus spectroscopy. SpectroView also employs a non-linear least square algorithm which enables modelling of individual resonances. Fitting by these non-linear least square algorithms occurs in the time domain and benefits from imposition of prior knowledge and additional modelling of phase and frequency variations. For instance, in the experiments conducted in this thesis, linewidths were fixed to each other for each ATP multiplet, with coupling constants taken to be 18 Hz for brain and 15.6 Hz for muscle and amplitudes fixed to a 1:1 ratio for each ATP doublet and to a 1:2:1 for each ATP triplet. In addition, linewidths were constrained between 5.0 and 20.0 Hz for PCr and between 5.0 and 30 Hz for all other resonances. Values were chosen on the basis of published literature (de Graaf 2007, Hattingen, Magerkurth et al. 2009), AMARES documentation (http://www.jmrui.eu), and following a process of trial and error to select parameters yielding optimal fit. In AMARES, it is also possible to impose prior knowledge to each peak's line shape, either Gaussian or Lorentzian: Lorentzian peaks represent purely exponentially decaying signals, whereas Gaussians are more apt for lines broadened by magnetic inhomogeneities. In this thesis, both were tested and no substantial difference in fitting results between the two was observed. Lorentzian line shapes were employed for all further analyses in this thesis.

In addition, in SpectroView, there is also the option of using a Voigt curve, which incorporates both Lorentzian and Gaussian characters, although its use is controversial as it has been shown to add an additional factor to the results that might introduce bias into the data (Stagg 2014).

Example of fitted spectra are shown in Figure 3.5 B.

3.1.2.2 Baseline estimation

The broad baseline visible especially in brain spectra is due to phosphorus containing macromolecules (Hattingen, Magerkurth et al. 2009). This can be regarded as a broad peak, represented by a rapidly decaying signal in the time domain. Therefore, it is possible to estimate the baseline from the initial points of the FID. AMARES accounts for this by weighting the initial FID points by a quarter sine wave, a procedure resulting in flattening of the baseline[16]. There is no set number of initial datapoints to be taken for this procedure. To optimise the analysis protocol, the first 5, 10, 20, 50, 100, and 200

[16] Of note, SpectroView employs a different method for baseline estimation, fitting a polynomial line and the user can specify the number of polynomial terms.

points of the FID were each tested, in turn, to assess effects on baseline estimation in two brain spectra acquired from deep white matter in a healthy control. Visual assessment of goodness of fit was then conducted. When the initial 5 or 10 points were chosen, the baseline was underestimated and resonances' signal intensity overestimated, as illustrated in Figure 3.5, column A. Conversely, when baseline was estimated from the initial 50, 100, or 200 points, the baseline appeared overestimated whilst resonances' signal intensity was underestimated, as illustrated in Figure 3.5, column C. Based on these experiments, the first 20 points of the FID were chosen (Figure 3.5 B) for the optimised spectroscopic analysis protocol; of note, this is also the AMARES pre-set value. This approach was chosen to limit user interaction (i.e. arbitrarily altering baseline estimates on a case-by-case basis), although does not account for potential individual variations in baseline. An alternative approach would have been to adjust baseline estimates for each individual spectrum, but this was considered an inherently arbitrary process prone to bias and likely to add substantial operator variability; in addition, analysis time would have been substantially increased.

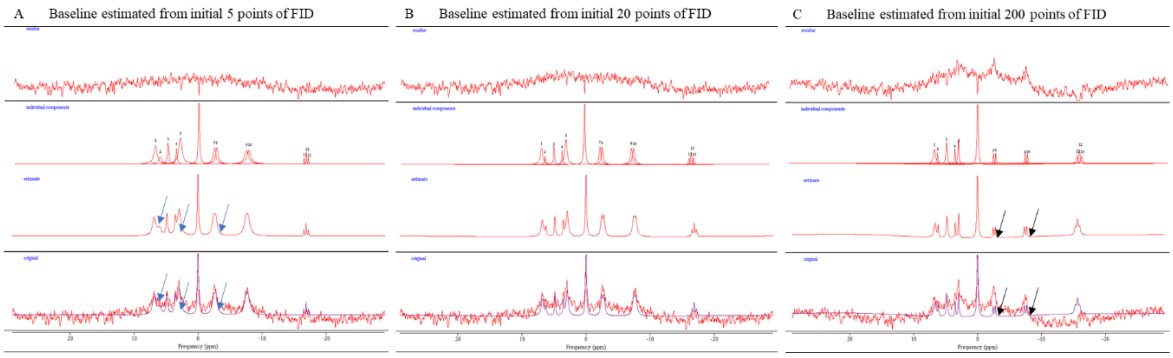

Figure 3.5 Peak fitting results following baseline estimation from initial five points (A-spectra on the left), 20 points (B-spectra in the middle), and 200 points (C-spectra on the right) of free induction decay (FID).
The first row illustrates estimated baselines, the second row the individual resonance components, the third row the sum of all estimates and the fourth row illustrates the spectrum overlaid onto the estimate. In A, baseline was underestimated leading to overestimation of metabolites' areas (arrows in blue). In C, baseline was overestimated and resonances underestimated (black arrows). Results for baseline estimates employing 10, 50, and 100 points are not shown as they were visually undistinguishable form results in A (when using 10 datapoints) and in C (when using 50 and 100 datapoints).

3.1.2.3 Resulting parameters: amplitudes, CRLB, pH, and Mg^{++}

The procedures described above return the area under the curve, the SD of the fit, linewidth, and chemical shift for each spectral peak.

The peaks' area under the curve is the main parameter employed in spectroscopic studies (as this is proportional to metabolite concentration), although considerable heterogeneity exists in terms of quantification methods and parameters reported in ^{31}P-MRS literature. Issues related to quantification are detailed in section 8.6: calculated signal intensities must be normalised to account for technical factors (expressed as *K* in equation 8.30) affecting the amplitudes of resonances. In addition, it is also possible to calculate metabolite concentrations using an appropriate reference compound of known

concentration, as detailed in section 2.5.4. In this thesis, quantification of metabolites was initially planned to take place employing the external reference method using a phantom[17] scanned at the same time as each research participant. For this purpose, experiments detailed in chapter two were conducted to optimise concentration within phantom (section 2.4.1.7). Over the course of experiments conducted in this chapter, it emerged that signal from the reference phantom placed cranially to the participants' head could not always be resolved. To investigate this, a scan was conducted to assess the sensitivity profile of the phosphorus coil. A phantom containing a three-litre bottle filled with the synthetic polymer polyalphaolefin (Spectrasyn four, Philips Healthcare, Best, The Netherlands) was scanned employing a turbo spin echo sequence (TR=3 s, TE=80 ms, FA=90°, 33 slices, matrix=0.53x0.53x4.00 mm^3). Total signal intensity per voxel was calculated and displayed as a function of distance from the top of the coil. Results are shown in the figure below.

[17] Ideally two phantoms of different concentrations would have been more apt to create a calibration line, but no space for a second phantom was present in the coil.

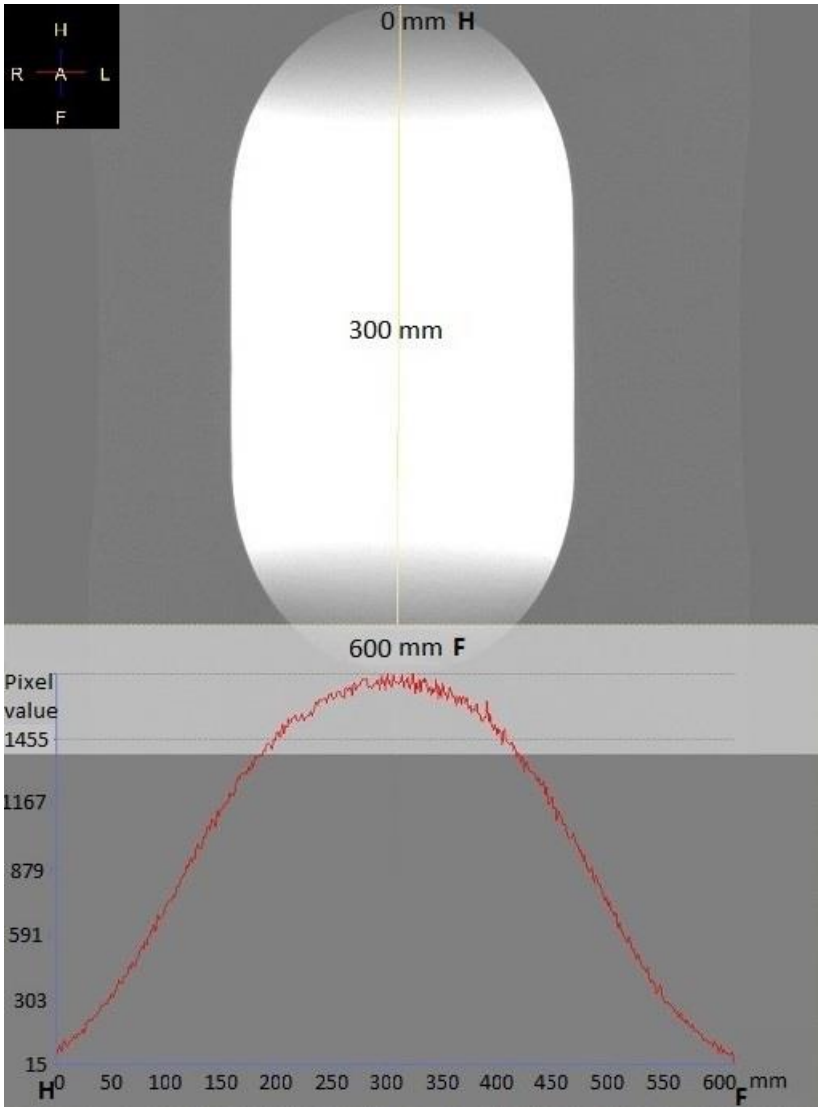

Figure 3.6 Top panel depicts the Spectrasyn four phantom imaged with turbo spin echo sequence detailed in text above. *The yellow line marks the area from where voxel values were measured (H: head, i.e. cranial direction, F: foot i.e. caudal direction). The graph shows voxel values on the y-axis and position along the yellow line on the x-axis. Maximal signal intensities were recorded in areas corresponding to centre of coil (250-350 mm). Signal intensity steeply diminished with distance from centre especially after 200 mm of coil and was reduced to almost zero at the coil's edges. There was no concern that this effect would be relevant for acquisition from human brain as it was calculated that, by centring at glabella (corresponding to the centre of the brain on sagittal plane) and taking standard brain anthropometric measures (nasion to prosthion), it was estimated that the maximal distance between centre of coil and most distal part of medulla would fall within 7 cm from isocentre i.e. the entire volume of the brain would fall within the high sensitivity area of the coil.*

This experiment illustrated that signal intensity was not homogeneous throughout the entire sensitivity volume of the coil, but steeply declined at the edges. It is important to note that the above experiment illustrates the sensitivity profile of proton-based, rather than ^{31}P-MRS, measurements, and the latter are likely to be more homogeneous; adiabatic pulses were used in all phosphorus spectroscopic CSI sequences and the characteristic feature of such pulses is generation of homogeneous B_1 fields. Nonetheless, some inhomogeneities might remain, especially at the edge of the FOV, which is where the reference phantom had to be placed. To directly assess the B_1 effect, it would have been necessary to acquire a B_1 map prior to each participant's spectroscopic acquisition, but this was not possible as it

would have rendered acquisition time exceedingly lengthy. Another alternative would have been to use an external reference phantom scanned at a separate time and, subsequently, correct for technical factors including receiver gain and differences in coil loading. This was not possible as the scanner was no longer available for such experiments to the author. Of note, B_1 effects are not relevant when using ratios acquired from the same spectrum; such effects can be included as part of the "K factor" and, hence, cancel each other out in the ratio. Spectroscopic parameters are frequently reported as ratios, and this procedure eliminates technical factors such as coil loading (see further theoretical detail in 8.7). The advantage is that differences between patients and controls are likely to result from underlying biological processes rather than acquisition-related factors. A disadvantage is that this approach does not provide an absolute concentration value which could be of use when comparing spectroscopic data with alternative modalities, such as, for instance, tissue biopsies. In proton spectroscopy, total creatine is often placed at the denominator as this has been shown to be relatively constant in diseases, including in MND (as detailed in introduction, section two). Nonetheless, it is not possible to assume *a priori* that any of the metabolites resolved by ^{31}P-MRS are unchanged by pathology, so the choice of reference compound is challenging. One option is to assign the sum of all metabolites (i.e. the total phosphorus signal) as the denominator, after having ensured that this is not significantly different between patients and controls. Data can then be expressed either as a proportion or as a percentage of total signal intensity. This latter approach was chosen for the remaining experiments in this thesis as it was considered to minimise potential biases and assumptions (Klunk, Xu et al. 1994, de Graaf 2007).

The AMARES algorithm also returns CRLBs, which is the minimum achievable variance of a given estimator. This is a theoretical bound, and the real estimator might have higher variance, but it can never have lower variance than the CRLB. Small values of CRLB are desirable. Numerous different CRLB thresholds have been used in the literature, although, generally, a CRLB below 20% is considered adequate in proton spectroscopy (Sidek, Ramli et al. 2016), whereas higher values are accepted in heteronuclear spectroscopy (for example, values above 30% were rejected in published ^{31}P-MRS literature (van de Bank, Maas et al. 2018)). The reason for this higher threshold is that the main determinant of CRLB of amplitudes is noise, which is relatively more prominent in heteronuclear spectroscopy (Cavassila, Deval et al. 2000).

At this stage of the analysis, it is also possible to calculate free Mg^{++} concentration and pH from the chemical shift of βATP and Pi, respectively (Iotti, Frassineti et al. 1996, Iotti and Malucelli 2008, Ren, Sherry et al. 2015). The chemical shift of resonances varies with the chemical environment surrounding the metabolites. This property can be exploited to calculate concentration of Mg^{++} from the chemical shift difference between PCr and βATP using empirical formulas (at physiological pH, ATP is a negatively charged molecule which often is found bound to Mg^{++} *in vivo*). Calculation of pH relies on the assumption that the Pi resonance is composed of two almost completely superimposed peaks representing protonated and de-protonated moieties. As pH varies, the ratio of protonated to

deprotonated peaks changes, causing minute alterations in the position of the Pi peak maximum on the x-axis, which reflects pH variation. Such changes can be incorporated in the Henderson-Hasselbalch equation and used to calculate pH. Of note, such equations require coefficients derived from empirical titrations which also vary from tissue to tissue. Hence, slightly different equations can be used for brain and muscle (Iotti, Frassineti et al. 2000, Iotti and Malucelli 2008, Rata, Giles et al. 2014, Cichocka, Kozub et al. 2015). In jMRUI, the following is used: (Iotti, Frassineti et al. 2000).

3.1.2.4 Correction for relaxation effects

As detailed in 8.6, signal intensity is dependent on concentration of metabolites, but also on their specific T_1 and T_2 relaxation properties. Since the shape of the relaxation function is established, if the relaxation constants of metabolites of interest are known, it is possible to correct for such relaxation effects. In the ^{31}P-MRS acquisition protocol employed in this thesis, T_2 saturation effects were considered negligible; TE was relatively short and the localisation sequence did not involve refocussing pulses, which increas T_2 weighting (lack of T_2 weighting is one of the advantages of Image selected in vivo spectroscopy – ISIS – localisation (Ordidge, Connelly et al. 1986)). T_1 saturation effects are potentially more relevant and, although they were minimised by using long TR (see experiments in previous chapter), calculated amplitudes were also corrected using known phosphorus T_1 values from published literature: for brain (Peeters, van Uden et al. 2019) was used, whereas for muscle (Meyerspeer, Kršśák et al. 2003, Bogner, Chmelik et al. 2009) were employed. The formula linking T_1 relaxation to TR and amplitudes (which can be arranged to correct for T_1 saturation effects) is:

Equation 4.1

$$M_{z(TR)} = M_0\left(1 - e^{-\frac{TR}{T1}}\right)/(1 - cos\alpha e^{-\frac{TR}{T1}})$$

M_z is the measured amplitude, M_0 is the amplitude corrected for T_1 relaxation effects, TR is the repetition time, T_1 is the longitudinal magnetisation relaxation time constant for the given metabolite, and α is the nutation angle (90^o in the acquisition protocol here employed).

In chapter two, it was discussed that spectroscopic metabolite relaxation constants may be affected by disease. Therefore, a limitation of correction for T_1 relaxation effects using this methodology is that it cannot account for putative individual alterations of T_1, which may be of interest due to pathology and therefore differ between patient and control groups. Empirical measurement of longitudinal relaxation parameters in individual patients is possible, but time consuming and was not feasible within achievable timeframes for participants in this study. This represents a potential limitation of the methodology which nonetheless was selected as a pragmatic approach to address the T_1 relaxation issue, in combination with the choice of a long TR.

3.1.2.5 Image segmentation

T_1-weighted images were initially segmented into white matter, grey matter, and CSF using the fuzzy-c algorithm described by (Chuang, Tzeng et al. 2006) in MATLAB (R2017b, The MathWorks, Inc., Natick, Massachusetts, United States; script curtesy of Dr Maria-Eleni Dounavi). Representative segmentation masks are shown in the figure below.

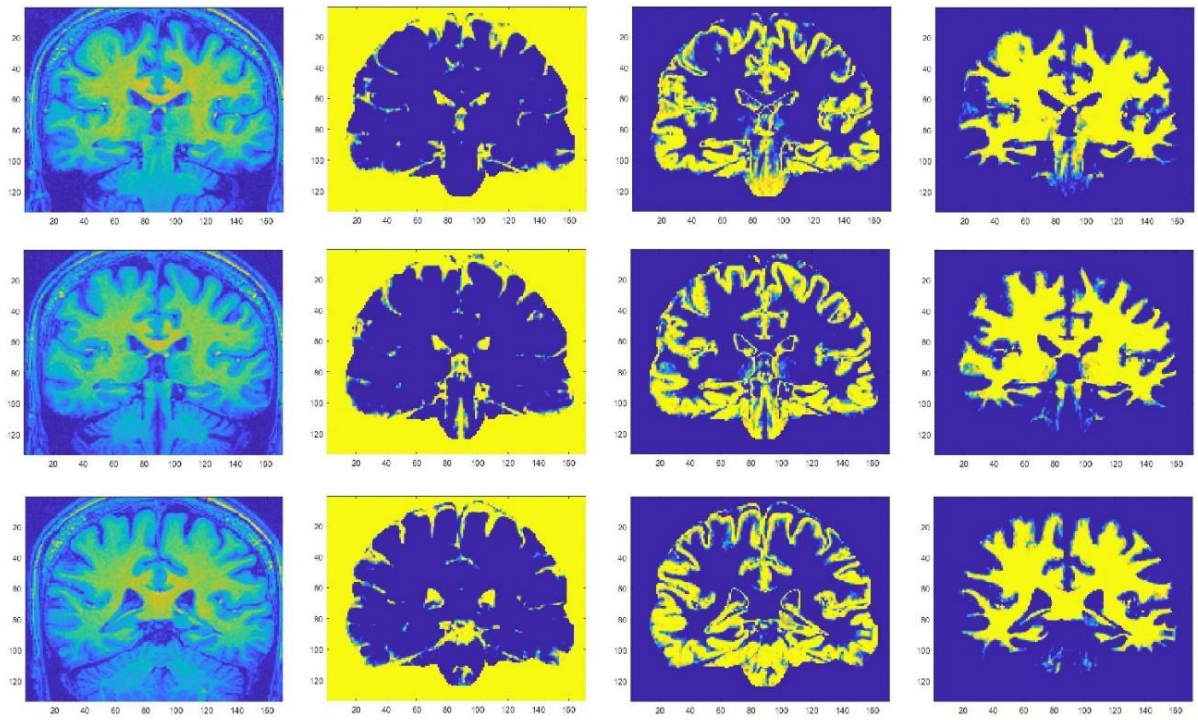

Figure 3.7 Coronal slice and relevant segmentation masks (fuzzy-c algorithm).
Cerebrospinal fluid masks, grey matter masks, and white matter masks are shown in second column from left, second column from right, and in right column, respectively. The algorithm used for segmentation is described by (Chuang, Tzeng et al. 2006) and courtesy of Dr Maria-Eleni Dounavi.

Although cortical regions were segmented satisfactorily, errors were evident in brainstem segmentation using this algorithm. Hence segmentation was repeated using Statistical Parametric Mapping software (SPM12, https://www.fil.ion.ucl.ac.uk/spm/software/spm12/) as illustrated below.

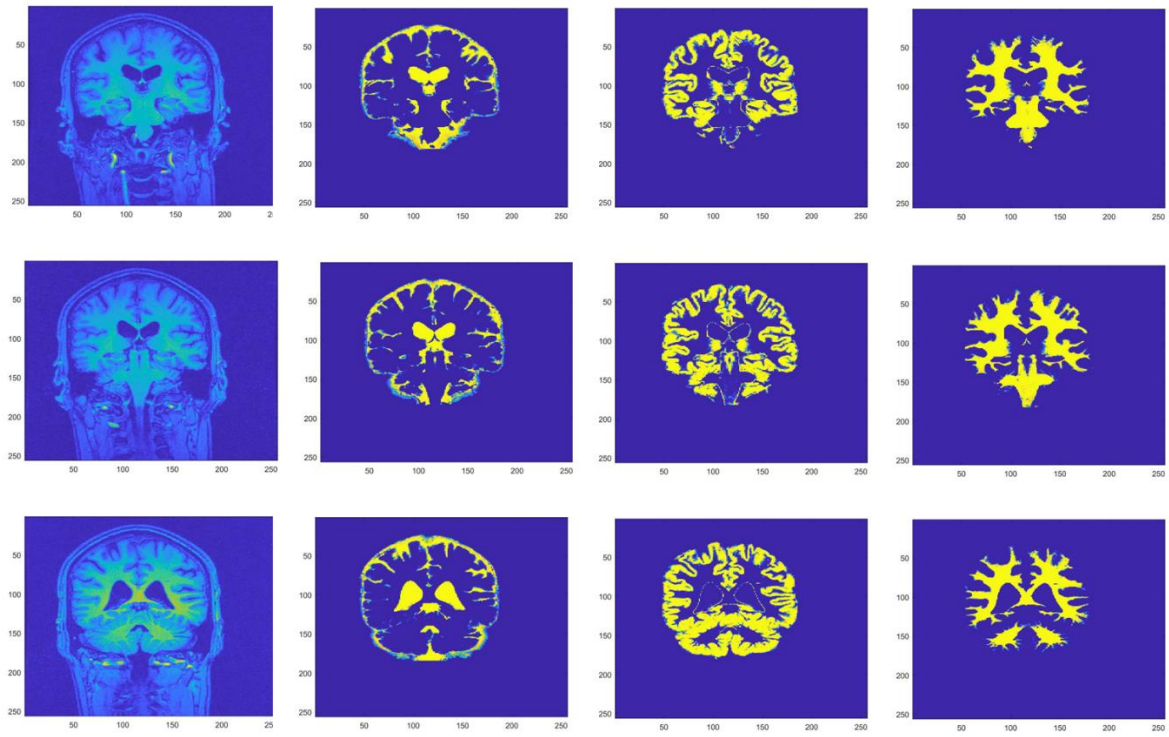

Figure 3.8 Coronal slice and relevant segmentation masks (Statistical Parametric Mapping).
Cerebrospinal fluid masks, grey matter masks, and white matter masks are shown in second column from left, second column from right, and in right column, respectively. Segmentation was conducted with Statistical Parametric Mapping 12.

Although the segmentation quality of cortical areas appeared equivalent between the two tested methods, the SPM algorithm was chosen, as it was clearly more robust in the brainstem region. Usage of this software within the research community is widespread and standardised, and this methodology was chosen for subsequent experiments.

3.1.2.6 Selection of relevant voxels

Coregistration scripts were then developed by the author in-house using MATLAB (R2019b, The MathWorks, Inc., Natick, Massachusetts, United States) on the basis of (Quadrelli, Mountford et al. 2016), which was readapted and simplified for a multivoxel grid. In brief, care was taken to ensure that FOV coordinates of spectroscopic grid and T_1-weighted volumetric acquisition coincided in all dimensions. This removed the need for complex affine transformations as both spectroscopy and imaging measurements were acquired from the same region of interest and had the same 3D coordinates. Of note, the anterior-posterior thickness of the T_1-weighted image was 60 mm with a slice thickness of 1 mm, whereas the 2D CSI slice had a thickness of 40 mm (for detailed parameters see chapter two). This was necessary as a wrap-around artefact could have appeared in the first and last slices of the T_1-weighted image, hence the ten most anterior and ten most posterior slices were removed prior to co-

registration (resulting in a thickness of 40 mm equivalent to the thickness of the spectroscopic slab). The images below illustrate co-registration performed in MATLAB against the spectroscopic grid in SpectroView (which was taken as the reference, as this is the Philips proprietary software) for the brainstem voxel. All other voxels were also visually checked and corresponded to the SpectroView grid.

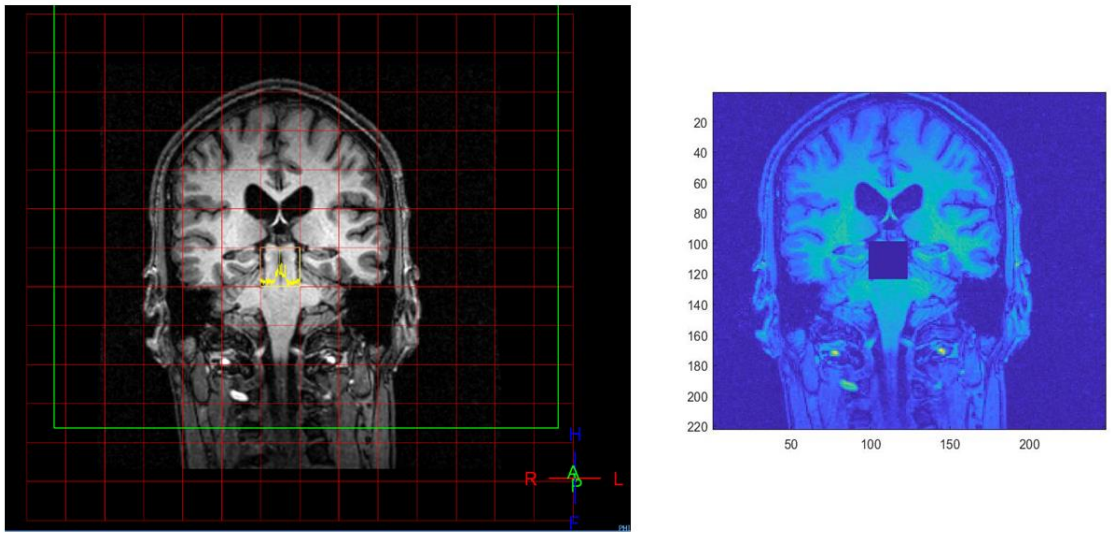

Figure 3.9 Coregistration of spectroscopic voxel onto anatomical T_1-weighted volumetric image in MATLAB.
An example of coregistration of voxel located at the level of the midbrain represented with superimposed yellow spectrum on the left and dark voxel on the right.

Segmentation and coregistration of the spectroscopic voxel was used in chapter four to adjust for any potential partial volume effects in results.

3.1.3 Accuracy and precision

Generally speaking, quantitative techniques can be characterised by two fundamental properties: accuracy and precision. Accuracy refers to how close a given measurement is to its underlying "true value", whereas precision is related to characterisation of measurements' variability. A visual illustration of these concepts is provided in Figure 3.10 A. In spectroscopy, linearity of signal to concentration is necessary to ensure accuracy; this was the case in this protocol, as illustrated in chapter two (section 2.5.4).

A

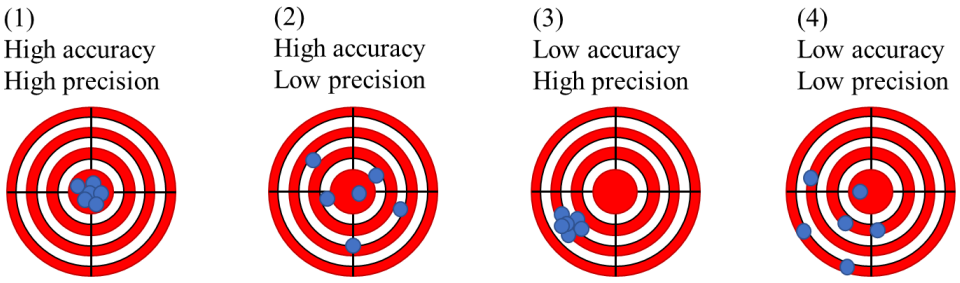

B

	Precision	
	Repeatability	*Reproducibility*
Variability	Coefficient of variability	Coefficient of variability
Reliability	Repeatability coefficient	Intraclass correlation coefficient
Agreement	Bland-Altman's limits of agreement	Bland-Altman's limits of agreement

Figure 3.10 A visual exemplification of accuracy and precision (A) and a table illustrating which measures of precisions can be used in repeatability and reproducibility studies to assess agreement and reliability (B).
In A, the first illustration (1) shows a set of measurements (represented by blue dots) that cluster tightly around the "true value" (here represented as the centre of the target) indicating that the technique is both highly accurate and precise. If measured values cluster around the target, but are more disperse, the technique is still very accurate, but lacks precision (2). An inaccurate, but precise technique returns values that cluster tightly around the "wrong value" (3). An inaccurate and imprecise technique is characterised by highly variable measurements clustering around a mean that does not correspond to ground truth (4). In B: to measure reliability it is advised to calculate the reliability coefficient in repeatability studies and the intraclass correlation coefficient (ICC) in reproducibility studies. Bland-Altman plots are apt to characterise agreement between measures in both repeatability and reproducibility studies. The figure was drawn by the author.

There are numerous metrics that can be used to characterise the precision of a measurement (summarised in Figure 3.10 B) A relatively intuitive parameter is the CV which is the SD of a given set of measurements divided by the mean. CVs can also be calculated from the difference of repeated measures and can be used to characterise variability of test-retest experiments in repeatability and reproducibility assessments prior to starting clinical studies.

In a repeatability study, two (or more) measures are acquired under exactly the same conditions to assess inherent measurement errors. In reproducibility studies, repeated measures are taken after a factor potentially contributing to variability is arbitrarily changed, to assess impact of that specific factor on measurement precision. For instance, two measurements may be acquired after a specific time interval has elapsed (to determine instrument stability over time, assuming constant biological values) or after they have been analysed by two different researchers (to assess inter-operator variability) (Bartlett and Frost 2008).

Within the context of repeatability and reproducibility studies, additional parameters have been developed to characterise reliability and agreement of repeated measures.

Reliability is a concept that is particularly important in case-control studies when the main aim is to differentiate between two (or more) cohorts of research participants. In such cases, to be able to discriminate between two distributions with high statistical power, the technique needs to have a lower measurement error than the inherent variability present between the subjects within the groups of interest, i.e. technique needs to be reliable. Reliability is, hence, dependent on the variability of the technique employed, but also on the heterogeneity of the sample populations investigated. In repeatability studies, where the assumption is that measurement error is negligible, it is sufficient to report the within-subject SD (or the repeatability coefficient which is equivalent to within-subject SD times $1.96\sqrt{2}$) (Bartlett and Frost 2008). In reproducibility studies, the main reliability measure is the intraclass correlation coefficient (ICC), which incorporates both within-subject and between-subject variances: the assumption is that between-subject variance corresponds to the "true" variance of the distributions of interest, whereas the within-subject variance represents the variability of the technique. The ICC is defined as between-subjects variance / (between-subject variance + within-subject variance), as calculated by repeated measure ANOVA. Over the years, the ICC formula has been constantly refined and there are now multiple ICCs in use in published literature which differ primarily in the way they incorporate additional error terms. The choice of correct ICC depends on the specific research question and guidelines are available (Koo and Li 2016). ICC values generally fall between 0 and 1 (although some formulas may also return negative values, indicating very poor reliability). For a given population, values close to 0 denote that most variability is caused by experimental factors, whereas values that approximate 1 imply that variations between measurements are to be ascribed to "true variance" amongst subjects in the cohort of interest (i.e. excellent reliability).

On the other hand, agreement refers to how similar individual measurements acquired from the same subject are when repeated. In general, reliability is useful parameter when considering group-level cross-sectional comparisons, whereas agreement is relevant to longitudinal studies (in which it is important to detect variations in individual research participants that correspond to biological changes over time). Agreement parameters may be visualised through Bland-Altman plots (an example from the data from this study is provided in the figure below) (Bland and Altman 1986). In a Bland-Altman plot, the mean derived from two measurements conducted on the same individual is plotted on the x-axis and the difference between those two values on the y-axis. The spread of the values on the y-axis indicates the magnitude of measurements' agreement (larger spread indicating lower agreement and *vice versa*); this can be quantified through the Bland-Altman upper and lower limits of agreements, i.e. the values within which 95% of the differences between measurements is expected to fall. In addition, it is possible to determine whether one set of measurements has systematic biases at higher or lower measurement values, as illustrated in the figure below.

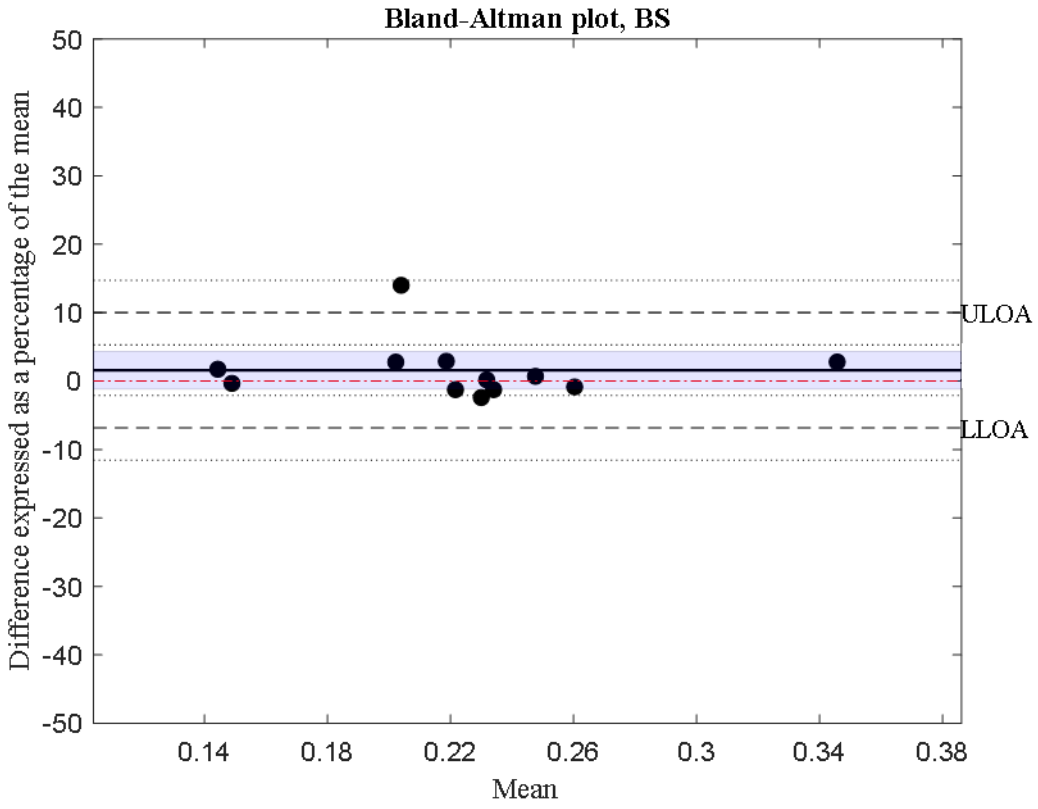

Figure 3.11 An example of a Bland-Altman plot (own data).
Own data acquired from a voxel in the pons in 12 healthy controls using sequence 15, as detailed in the methodology session of this chapter. The measured parameter is phosphocreatine (expressed as a proportion of total signal intensity), calculated twice for each participant employing slightly different manual phasing methods in jMRUI. Each datapoint represents one individual participant's result which is derived from two repeated measurements. The mean of the two values is plotted on the x-axis and the difference between the two values on the y-axis. In this example, values on the y-axis are expressed as a percentage difference from the mean of the two values, to simplify interpretation. The upper and lower limits of agreements (ULOA and LLOA, respectively) are illustrated with dashed lines, falling between 10% and -7% in this case, which indicates that the difference between two measurements conducted on the same individual is within 10% of the "true" value in 95% of cases. Dotted lines illustrate the ULOA and LLOA confidence intervals (which are necessary as they are also estimates). Additional information that can be derived from this graph is whether one analysis methodology produces systematically biased results compared to the other, which can be visually determined from the graph as follows: if the average value between the ULOA and the LLOA (here illustrated with a continuous black line) and its confidence interval (here illustrated with an area in blue) encompass the 0% value on the y-axis (red dotted line), then there is no systematic bias between the two techniques. On the other hand, if this value falls outside the confidence interval, then one of the two analyses systematically produces overestimates (or underestimates). Lastly, it is possible to draw a linear regression line across all points to determine whether there is a systematic bias at higher (or lower) measured values. In this case, all points cluster uniformly around the mean and the 0% value also falls within the confidence interval of the mean, indicating no systematic bias of any kind (Giavarina 2015).

In summary, on the basis of experiments above, the following analysis protocols were chosen: manual phasing and frequency shifting were followed by fitting, employing a non-linear least square algorithm (in SpectroView and jMRUI), using appropriate prior knowledge to return resonance amplitudes which were then corrected for T_1 relaxation effects. In jMRUI, CRLBs, pH, and Mg^{++} concentrations were also calculated (this was not feasible in SpectroView). Experiments were then conducted to: (1) select the optimal analysis software to employ (jMRUI or SpectroView); (2) assess the necessity for apodisation; and (3) assess whether CRLB of metabolite estimates were sufficiently low.

3.2 AIMS AND OBJECTIVES

Experiments detailed in the remainder of this chapter were aimed at selecting an optimised processing protocol and characterising the precision of resulting ^{31}P-MRS metabolite estimates for the final clinical study. To compare jMRUI and SpectroView and to determine robustness of software in terms of reliability, agreement, and CRLB, the same set of data was analysed five times: twice employing different phasing methods in jMRUI, a third time including apodisation in jMRUI, and twice more with rephased datasets in SpectroView.

Specifically, the objectives were the following:

1) Compare mean and CV values resulting from each tested analysis protocol.
2) Assess quality of measurements in terms of CRLB and the number of spectra that could be fitted.
3) Assess and compare reliability parameters in jMRUI and SpectroView.
4) Assess and compare agreement parameters in jMRUI and SpectroView.

3.3 METHODS

3.3.1 Participants

Twelve healthy volunteers were scanned after obtaining written informed consent (STH 15418 Yorkshire and Humber REC 09/H1310/79, approved by the local ethical committee according to the Declaration of Helsinki). Exclusion criteria were: pregnancy, a previous history of neurological disease, pacemaker or any other non-MR compatible magnetic/electronic implant, claustrophobia, and cognitive problems sufficient to impair informed consent.

3.3.2 Study design

Data were analysed five times: three times employing the software jMRUI and twice using the Philips proprietary software SpectroView. jMRUI data were analysed twice with the author manually rephasing the same dataset (denoted phasing “A” and phasing “B”) to assess intra-operator variability. For the third analysis, apodisation was performed on the “B” dataset, to generate dataset “C” to assess the effect of denoising and to allow comparison with SpectroView datasets. Analysis with SpectroView was conducted twice with the author again phasing data twice (phasing “D” and phasing “E”). Of note, it is not possible to analyse spectroscopic data in SpectroView without prior apodisation (the software returns an error); this is the reason only analysis of denoised data was conducted on the Philips software. Hence, to allow direct comparison between jMRUI and SpectroView, dataset C was necessary.

The figure below is an illustration of the experimental design including calculated parameters, as further detailed in paragraphs below.

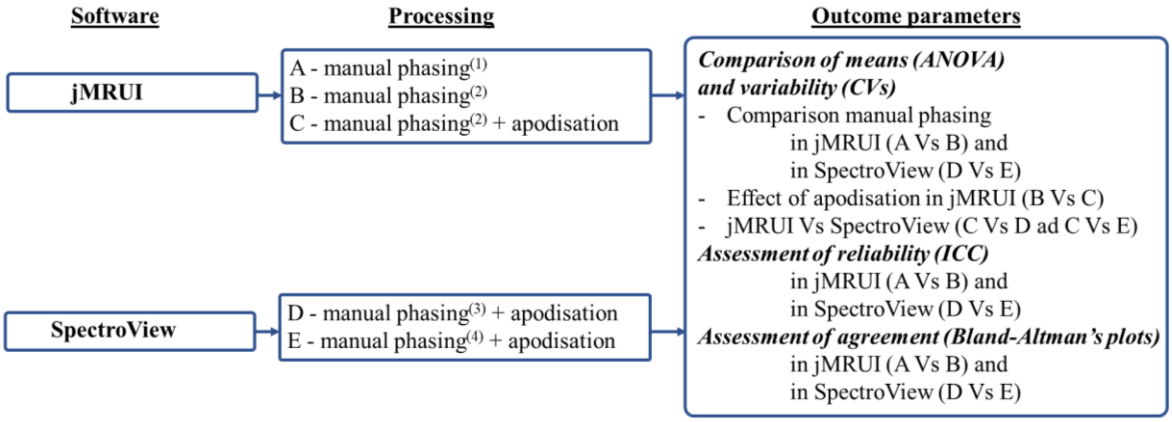

Figure 3.12 A schematic representation of the design of reproducibility experiments described in chapter three.
Spectroscopic data acquired from 12 healthy research participants were processed five times: three times using jMRUI and twice with SpectroView. In jMRUI, the set of brain spectra was analysed twice employing two different manual phasing methods (A and B) and a third time adding apodisation (C) to method B. In SpectroView, two different manual phasing methods (D and E) were tested, both following apodisation (which could not be excluded from the protocol). Comparisons of interest between analyses are listed in the righthand panel. ANOVA: Analysis of variance, CVs: coefficient of variability, ICC: intra-class correlation coefficient; Vs: versus.

3.3.3 Hardware and sequences

Acquisitions were carried out on the 3 Tesla Philips Ingenia wide bore MR system (Philips Healthcare, Best, The Netherlands) with heteronuclear capability, employing the dual-tuned ($^{31}P/^{1}H$) transmit-receive quadrature birdcage head coil (Rapid Biomed GmbH, Würzburg-Rimpar, Germany), denoted "Rapid coil two" in the previous chapter. A T_2-weighted sequence (TR=3000 msec, TE=80 msec, FA=90°, voxel size=0.55x0.67x4.00 mm^3, FOV=230, reconstructed matrix=432) was used to localise the phosphorus spectroscopic slab to motor regions as illustrated and described in the previous chapter (sequence 23). Phosphorus spectra were localised using a 2D CSI sequence and ISIS. Positioning of the voxel grid was always conducted by the same assessor and always crosschecked by a second researcher. On axial imaging, the marginal ramus of the cingulate sulcus was identified as a consistent landmark and the sulcus anterior to it as the central sulcus. This enabled identification of primary motor cortex within the precentral gyrus immediately anterior to the central sulcus. The voxel was placed on a coronally orientated image with its centre over the midline, the first row of voxels was located with the upper border placed over the pial surface ensuring location on primary motor cortex. This resulted in voxel *k* being consistently placed over third ventricle, *p* over midbrain, and *t* over pons. Voxels *o* and *q* were placed over the hippocampi (Figure 3.13). Spectra were acquired at 51.7 Hz centre-frequency, spectral bandwidth 3000 Hz, and 2048 sample points. Second order pencil beam shim with WALTZ-4 heteronuclear decoupling and NOE were carried out and the following sequence parameters were used

for ^{31}P-MRS acquisitions: TR=4000 ms, TE=0.26 ms, 2 signal averages, with a native voxel size of 25x25x40 mm^3 for a total scan length of 16.24 minutes (sequence 15 in chapter two).

3.3.4 Processing

3.3.4.1 Software

Spectroscopic data were processed with jMRUI 6.0 (available at http://www.jmrui.eu/license-and-download/download-beta-release/) (Vanhamme, van den Boogaart et al. 1997, Naressi, Couturier et al. 2001, Stefan, Cesare et al. 2009) and SpectroView (Philips Healthcare, Best, The Netherlands).

T_1 relaxation correction and statistical analyses (including relevant graphs) were conducted in MATLAB (R2019b, The MathWorks, Inc., Natick, Massachusetts, United States) using scripts created by the author with the exception of ANOVA comparisons which were conducted in Graphpad Prism (version 8.3.0 for Windows, GraphPad Software, San Diego, California USA, www.graphpad.com) and the function to plot categorical scatter plots (Dinesh Natesan, 2016 https://github.com/AbstractGeek/CategoricalScatterplot).

3.3.4.2 Pre-processing

In jMRUI, the real part of each spectrum was manually phased to a purely absorptive line shape using both zeroth and first-order terms. Manual phasing was repeated twice by the author, to generate two datasets. Spectra of the B dataset were saved and also apodised to 2 Hz (Lorentzian function) to generate dataset C.

In SpectroView, phasing of all spectra was conducted manually twice by the author. Phasing of these datasets took place following multiplication by the following functions: an exponential (factor -3), to filter noise, and a Gaussian (factor 12), to improve linewidth.

In all cases, spectra were shifted on the abscissa to assign a value of 0 ppm to PCr.

Datasets were not analysed simultaneously: dataset B and E were analysed only after phasing of A and D were completed, after an approximately two-week interval.

3.3.4.3 Post-processing

Peak fitting in jMRUI was conducted as detailed in the introduction of this chapter.

In SpectroView, PME, Pi, PDE, PCr, and the α, β, and γ phosphates of ATP were fitted using a Voigt curve with a Gaussian character of 90%. Linewidths of the resonances of each ATP phosphate were

fixed to each other. Baseline was estimated using a polynomial curve with 11 terms. An example of a spectrum fitted with SpectroView is illustrated in chapter two (Figure 2.16).

All amplitudes were corrected for T_1 relaxation effects as detailed in the introduction of this chapter.

3.3.4.4 Resulting parameters

Analysis from jMRUI returned thirteen resonances per spectrum: phosphocholine (PC), phosphoethanolamine (PE), Pi, glycerophosphocholine (GPC), glycerophosphoethanolamine (GPE), PCr, γATP doublet, αATP doublet, and βATP triplet. In addition to summing the relevant ATP multiplets to each other (i.e. to generate γ, α, and βATP estimates), PC and PE were summed to yield a PME estimate, whilst GPE and GPC were summed resulting in a PDE estimate. Mg^{++}, pH, and CRLBs were also computed in jMRUI as detailed in the introduction.

In SpectroView, only PME, Pi, PDE, PCr, and the α, β, and γ phosphates of ATP could be fitted, and the software did not allow computation of Mg^{++} or pH, nor calculation of CRLBs.

For each spectrum, resonances were reported as a ratio of the sum of all peaks i.e. expressed as relative proportion of total phosphorus signal.

3.3.4.5 Statistical analysis

3.3.4.5.1 Comparison of mean values through analysis of variance

For dataset analysed with five alternative methods, mean values, SDs, and CVs were calculated for all amplitudes as well as for pH and Mg^{++} in all spectroscopic voxels. For each voxel encompassing motor tracts (i.e. the voxels of interest in the MND study, highlighted in blue in Figure 3.13), mean values derived from the five different analysis protocols were compared using 2-way ANOVA followed by Tukey's multiple comparisons test.

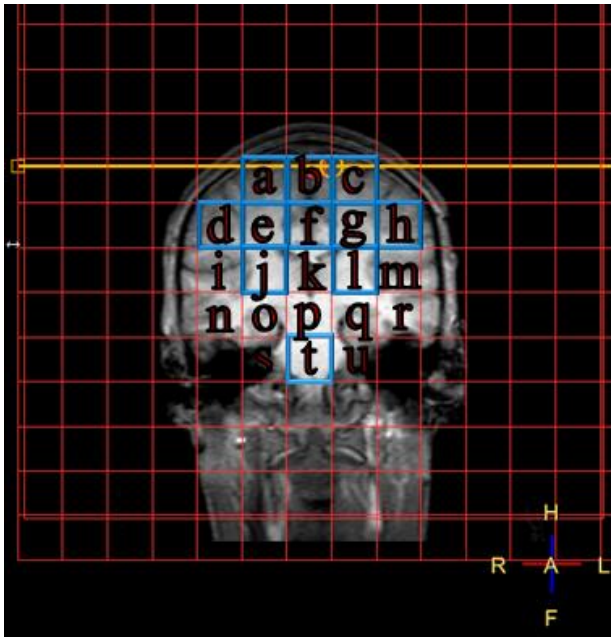

Figure 3.13 Voxels in blue (encompassing motor regions of brain) represent areas analysed.
Letters refer to voxel indices used in results sections. Landmarks used for reproducible positioning are detailed in methods. Positioning of voxel grid was conducted by the same assessor and always crosschecked by a second researcher.

The ANOVA analysis allowed (and corrected) for comparisons of all possible pairings of analysis protocols, but, in the results, only comparisons of interest specified a priori were reported: protocol A Vs B (to assess the effect of phasing in jMRUI), B Vs C (to assess the effect of apodisation in jMRUI), C Vs D and C Vs E (jMRUI compared to SpectroView), and D Vs E (to assess the effect of phasing in SpectroView). Box and whisker plots (indicating median, interquartile range, minimum, and maximum) and ANOVA tables were reported.

3.3.4.5.2 Quality control

For each dataset analysed with five alternative methods, amplitudes, pH, and Mg^{++} values that could not be fitted or calculated were reported together with CRLBs of spectra, CRLBs of pH, and CRLBs of Mg^{++}.

3.3.4.5.3 Reliability and agreement

For the first acquisition, reliability (ICC) and agreement (Bland-Altman plots) parameters were also calculated for all voxels of interest and for all measured parameters to compare analysis protocols. Specifically, these parameters were calculated from alternative phasing methods in both jMRUI and SpectroView to assess software robustness to phasing. Phasing was the main operator-dependent step;

hence, these analyses were conducted to assess intra-operator reproducibility and robustness of software and fitting algorithms.

For the purpose of this thesis, ICC for test-retest reliability for a single rater was calculated employing the following formula: (between-subjects variance - error) / [between-subjects variance + (k-1)error + (k/number of subjects) * (within-subjects variance – between-subjects variance] according to (Koo and Li 2016).

Bland-Altman plots were calculated as detailed in the introduction.

3.4 RESULTS

3.4.1 Cohort characteristics

Twelve research participants were scanned: five women (mean age=24.8 years, SD=±3.1 years) and seven men (mean age=31.3 years, SD=±6.1 years).

3.4.2 Descriptive statistics

3.4.2.1 Amplitudes

Means and SDs for each measured metabolite from each tested voxel are listed in the table below. The five tested analysis methods (A to E) are detailed in the methods. Voxels are labelled *a* to *u*, corresponding to anatomical localisations visualised in Figure 3.13.

Table 3.1 Means and standard deviations (SD) for voxels a to u as depicted in Figure 3.13.

Metabolites are expressed as proportion of total phosphorus signal. PME: Phosphomonoesters, Pi: Inorganic phosphate, PDE: Phosphodiesters, PCr: Phosphocreatine, ATP: Adenosine triphosphate.

	a		***b***		***c***		***d***		***e***		***f***		***g***		***h***		***i***		***j***	
A	*mean*	*(±SD)*	*mean*	*(±SD)*	*mean*	*(±SD)*	*mean*	*(±SD)*	*mean*	*(±SD)*	*mean*	*(±SD)*	*mean*	*(±SD)*	*mean*	*(±SD)*	*mean*	*(±SD)*	*mean*	*(±SD)*
PME	0.172	0.053	0.149	0.030	0.136	0.039	0.159	0.046	0.153	0.043	0.134	0.026	0.135	0.031	0.150	0.042	0.143	0.036	0.126	0.030
Pi	0.067	0.031	0.075	0.029	0.080	0.025	0.071	0.035	0.071	0.019	0.082	0.021	0.087	0.023	0.081	0.029	0.074	0.018	0.079	0.027
PDE	0.183	0.067	0.178	0.051	0.181	0.035	0.157	0.039	0.170	0.039	0.168	0.052	0.181	0.048	0.185	0.045	0.151	0.043	0.192	0.037
PCr	0.193	0.024	0.212	0.028	0.207	0.016	0.226	0.049	0.202	0.025	0.214	0.030	0.203	0.023	0.215	0.036	0.236	0.052	0.207	0.025
γATP	0.186	0.051	0.181	0.032	0.177	0.026	0.186	0.026	0.187	0.035	0.177	0.023	0.169	0.023	0.154	0.031	0.165	0.025	0.166	0.021
αATP	0.143	0.042	0.135	0.045	0.158	0.056	0.135	0.035	0.138	0.031	0.141	0.027	0.156	0.032	0.158	0.037	0.156	0.037	0.145	0.019
βATP	0.056	0.036	0.069	0.033	0.060	0.036	0.072	0.030	0.079	0.031	0.083	0.046	0.070	0.028	0.057	0.028	0.076	0.037	0.085	0.032

	a		***b***		***c***		***d***		***e***		***f***		***g***		***h***		***i***		***j***	
B	*mean*	*(±SD)*	*mean*	*(±SD)*	*mean*	*(±SD)*	*mean*	*(±SD)*	*mean*	*(±SD)*	*mean*	*(±SD)*	*mean*	*(±SD)*	*mean*	*(±SD)*	*mean*	*(±SD)*	*mean*	*(±SD)*
PME	0.174	0.054	0.154	0.030	0.136	0.041	0.156	0.053	0.151	0.046	0.133	0.026	0.138	0.030	0.146	0.031	0.146	0.035	0.124	0.029
Pi	0.066	0.031	0.073	0.034	0.080	0.025	0.061	0.027	0.070	0.018	0.077	0.022	0.082	0.021	0.080	0.027	0.070	0.017	0.076	0.027
PDE	0.174	0.066	0.175	0.054	0.176	0.034	0.141	0.042	0.165	0.042	0.158	0.044	0.165	0.046	0.177	0.042	0.149	0.045	0.181	0.035
PCr	0.195	0.026	0.209	0.024	0.212	0.017	0.233	0.048	0.203	0.031	0.219	0.030	0.207	0.018	0.222	0.040	0.242	0.049	0.210	0.025
γATP	0.189	0.054	0.179	0.024	0.184	0.031	0.194	0.035	0.185	0.030	0.182	0.031	0.172	0.020	0.159	0.029	0.169	0.034	0.167	0.021
αATP	0.144	0.044	0.137	0.056	0.165	0.053	0.137	0.036	0.137	0.034	0.142	0.025	0.156	0.031	0.166	0.041	0.161	0.045	0.152	0.013
βATP	0.058	0.037	0.072	0.038	0.053	0.033	0.092	0.032	0.098	0.060	0.089	0.052	0.079	0.031	0.054	0.024	0.077	0.033	0.091	0.042

	a		***b***		***c***		***d***		***e***		***f***		***g***		***h***		***i***		***j***	
C	*mean*	*(±SD)*	*mean*	*(±SD)*	*mean*	*(±SD)*	*mean*	*(±SD)*	*mean*	*(±SD)*	*mean*	*(±SD)*	*mean*	*(±SD)*	*mean*	*(±SD)*	*mean*	*(±SD)*	*mean*	*(±SD)*
PME	0.179	0.056	0.153	0.028	0.137	0.039	0.161	0.043	0.152	0.042	0.137	0.026	0.136	0.030	0.147	0.032	0.151	0.034	0.130	0.031
Pi	0.069	0.031	0.073	0.031	0.079	0.027	0.069	0.032	0.070	0.016	0.085	0.026	0.085	0.022	0.081	0.025	0.070	0.017	0.078	0.028
PDE	0.191	0.062	0.182	0.057	0.180	0.045	0.160	0.047	0.177	0.054	0.170	0.053	0.182	0.037	0.183	0.047	0.154	0.048	0.186	0.038
PCr	0.176	0.030	0.189	0.022	0.196	0.018	0.210	0.051	0.185	0.027	0.188	0.030	0.191	0.014	0.206	0.032	0.235	0.049	0.198	0.025
γATP	0.175	0.050	0.174	0.026	0.175	0.027	0.176	0.023	0.177	0.023	0.170	0.025	0.166	0.020	0.151	0.024	0.165	0.032	0.161	0.020
αATP	0.144	0.046	0.151	0.056	0.169	0.045	0.151	0.043	0.137	0.037	0.144	0.031	0.160	0.028	0.159	0.038	0.159	0.041	0.152	0.015
βATP	0.067	0.030	0.078	0.034	0.072	0.036	0.088	0.029	0.102	0.050	0.107	0.055	0.079	0.031	0.073	0.021	0.088	0.023	0.094	0.034

	a		***b***		***c***		***d***		***e***		***f***		***g***		***h***		***i***		***j***	
D	*mean*	*(±SD)*	*mean*	*(±SD)*	*mean*	*(±SD)*	*mean*	*(±SD)*	*mean*	*(±SD)*	*mean*	*(±SD)*	*mean*	*(±SD)*	*mean*	*(±SD)*	*mean*	*(±SD)*	*mean*	*(±SD)*
PME	0.144	0.077	0.104	0.050	0.086	0.035	0.105	0.043	0.098	0.041	0.077	0.035	0.076	0.029	0.106	0.040	0.098	0.032	0.075	0.034
Pi	0.068	0.032	0.069	0.018	0.075	0.030	0.065	0.031	0.063	0.017	0.072	0.027	0.075	0.025	0.070	0.024	0.057	0.022	0.078	0.043
PDE	0.213	0.117	0.289	0.108	0.305	0.090	0.222	0.114	0.229	0.107	0.283	0.176	0.295	0.152	0.267	0.152	0.178	0.101	0.243	0.073
PCr	0.215	0.041	0.208	0.039	0.211	0.034	0.239	0.048	0.217	0.039	0.201	0.050	0.200	0.040	0.233	0.064	0.254	0.054	0.216	0.036
γATP	0.164	0.052	0.145	0.037	0.150	0.037	0.159	0.056	0.159	0.031	0.149	0.041	0.148	0.040	0.143	0.031	0.149	0.040	0.140	0.024
αATP	0.148	0.075	0.134	0.058	0.124	0.031	0.135	0.055	0.150	0.045	0.145	0.056	0.138	0.041	0.142	0.054	0.158	0.046	0.153	0.031
βATP	0.057	0.037	0.062	0.039	0.058	0.043	0.074	0.041	0.083	0.041	0.080	0.040	0.067	0.047	0.061	0.038	0.106	0.042	0.096	0.038

	a		***b***		***c***		***d***		***e***		***f***		***g***		***h***		***i***		***j***	
E	*mean*	*(±SD)*	*mean*	*(±SD)*	*mean*	*(±SD)*	*mean*	*(±SD)*	*mean*	*(±SD)*	*mean*	*(±SD)*	*mean*	*(±SD)*	*mean*	*(±SD)*	*mean*	*(±SD)*	*mean*	*(±SD)*
PME	0.130	0.046	0.107	0.044	0.092	0.035	0.106	0.037	0.092	0.034	0.075	0.031	0.083	0.026	0.108	0.034	0.108	0.029	0.070	0.028
Pi	0.068	0.033	0.061	0.023	0.069	0.026	0.061	0.027	0.081	0.067	0.070	0.028	0.076	0.018	0.067	0.019	0.057	0.017	0.072	0.026
PDE	0.239	0.125	0.306	0.154	0.293	0.098	0.206	0.115	0.228	0.124	0.284	0.181	0.270	0.093	0.237	0.126	0.208	0.096	0.245	0.083
PCr	0.209	0.048	0.190	0.048	0.202	0.031	0.225	0.037	0.203	0.039	0.198	0.050	0.199	0.023	0.224	0.048	0.228	0.031	0.213	0.035
γATP	0.160	0.052	0.145	0.042	0.155	0.031	0.158	0.048	0.152	0.033	0.149	0.040	0.150	0.030	0.150	0.029	0.137	0.038	0.139	0.020
αATP	0.158	0.075	0.136	0.060	0.142	0.044	0.154	0.057	0.154	0.051	0.152	0.057	0.151	0.032	0.159	0.053	0.154	0.048	0.159	0.029
βATP	0.078	0.044	0.077	0.037	0.057	0.029	0.090	0.038	0.091	0.049	0.071	0.037	0.071	0.028	0.076	0.034	0.108	0.028	0.103	0.035

	k		***l***		***m***		***n***		***o***		***p***		***q***		***r***		***s***		***t***		***u***	
A	*mean*	*(±SD)*	*mean*	*(±SD)*	*mean*	*(±SD)*	*mean*	*(±SD)*	*mean*	*(±SD)*	*mean*	*(±SD)*	*mean*	*(±SD)*	*mean*	*(±SD)*	*mean*	*(±SD)*	*mean*	*(±SD)*	*mean*	*(±SD)*
PME	0.123	0.034	0.131	0.031	0.147	0.036	0.147	0.040	0.156	0.036	0.171	0.038	0.175	0.047	0.180	0.070	0.205	0.082	0.202	0.064	0.247	0.114
Pi	0.075	0.025	0.078	0.019	0.082	0.028	0.064	0.032	0.074	0.025	0.073	0.015	0.063	0.027	0.066	0.030	0.072	0.035	0.081	0.034	0.066	0.038
PDE	0.177	0.032	0.179	0.041	0.165	0.039	0.165	0.050	0.197	0.039	0.183	0.027	0.166	0.046	0.168	0.049	0.177	0.059	0.166	0.038	0.135	0.053
PCr	0.219	0.027	0.211	0.027	0.213	0.025	0.217	0.045	0.210	0.031	0.225	0.046	0.212	0.046	0.196	0.052	0.223	0.054	0.226	0.052	0.236	0.042
γATP	0.169	0.023	0.170	0.024	0.153	0.020	0.141	0.050	0.151	0.029	0.154	0.030	0.155	0.045	0.154	0.032	0.160	0.070	0.158	0.044	0.133	0.026
αATP	0.156	0.022	0.155	0.030	0.157	0.031	0.172	0.047	0.137	0.041	0.145	0.034	0.158	0.036	0.171	0.059	0.131	0.070	0.141	0.056	0.152	0.076
βATP	0.080	0.045	0.077	0.039	0.084	0.025	0.093	0.054	0.076	0.034	0.049	0.017	0.076	0.037	0.103	0.055	0.052	0.051	0.035	0.022	0.062	0.035

	k		***l***		***m***		***n***		***o***		***p***		***q***		***r***		***s***		***t***		***u***	
B	*mean*	*(±SD)*	*mean*	*(±SD)*	*mean*	*(±SD)*	*mean*	*(±SD)*	*mean*	*(±SD)*	*mean*	*(±SD)*	*mean*	*(±SD)*	*mean*	*(±SD)*	*mean*	*(±SD)*	*mean*	*(±SD)*	*mean*	*(±SD)*
PME	0.123	0.030	0.129	0.029	0.145	0.033	0.152	0.032	0.156	0.031	0.176	0.037	0.172	0.043	0.176	0.063	0.194	0.079	0.199	0.069	0.204	0.074
Pi	0.072	0.022	0.075	0.017	0.079	0.030	0.058	0.031	0.068	0.027	0.069	0.015	0.058	0.021	0.065	0.031	0.060	0.032	0.078	0.033	0.053	0.028
PDE	0.167	0.029	0.162	0.037	0.156	0.031	0.159	0.057	0.179	0.048	0.176	0.024	0.160	0.048	0.149	0.052	0.152	0.071	0.164	0.046	0.150	0.061
PCr	0.220	0.028	0.215	0.029	0.224	0.030	0.225	0.054	0.213	0.031	0.225	0.039	0.215	0.049	0.212	0.060	0.217	0.058	0.222	0.052	0.240	0.059
γATP	0.169	0.022	0.173	0.025	0.160	0.013	0.145	0.046	0.155	0.030	0.157	0.030	0.161	0.046	0.162	0.031	0.157	0.052	0.159	0.039	0.129	0.040
αATP	0.157	0.024	0.157	0.030	0.164	0.031	0.179	0.047	0.140	0.044	0.147	0.032	0.166	0.040	0.176	0.059	0.132	0.048	0.138	0.051	0.149	0.076
βATP	0.092	0.050	0.090	0.042	0.079	0.044	0.109	0.074	0.090	0.047	0.050	0.018	0.075	0.046	0.081	0.054	0.096	0.107	0.052	0.054	0.128	0.165

	k		***l***		***m***		***n***		***o***		***p***		***q***		***r***		***s***		***t***		***u***	
C	*mean*	*(±SD)*	*mean*	*(±SD)*	*mean*	*(±SD)*	*mean*	*(±SD)*	*mean*	*(±SD)*	*mean*	*(±SD)*	*mean*	*(±SD)*	*mean*	*(±SD)*	*mean*	*(±SD)*	*mean*	*(±SD)*	*mean*	*(±SD)*
PME	0.127	0.022	0.130	0.029	0.151	0.024	0.156	0.039	0.159	0.032	0.174	0.036	0.168	0.042	0.166	0.050	0.199	0.080	0.199	0.066	0.231	0.065
Pi	0.074	0.023	0.075	0.016	0.081	0.024	0.066	0.032	0.080	0.018	0.075	0.020	0.060	0.024	0.067	0.033	0.074	0.031	0.080	0.032	0.064	0.034
PDE	0.178	0.037	0.173	0.035	0.160	0.032	0.160	0.057	0.193	0.039	0.184	0.019	0.172	0.045	0.145	0.058	0.155	0.069	0.160	0.043	0.150	0.052
PCr	0.201	0.024	0.199	0.026	0.218	0.033	0.220	0.054	0.202	0.034	0.213	0.035	0.212	0.049	0.208	0.058	0.208	0.055	0.216	0.045	0.232	0.038
γATP	0.164	0.021	0.167	0.022	0.154	0.013	0.147	0.041	0.143	0.023	0.152	0.025	0.153	0.042	0.142	0.047	0.154	0.045	0.155	0.038	0.121	0.029
αATP	0.154	0.023	0.157	0.030	0.165	0.029	0.171	0.056	0.146	0.046	0.144	0.036	0.162	0.038	0.181	0.044	0.126	0.036	0.141	0.049	0.157	0.067
βATP	0.100	0.045	0.099	0.032	0.095	0.028	0.106	0.059	0.084	0.041	0.059	0.017	0.080	0.043	0.108	0.061	0.101	0.105	0.048	0.041	0.067	0.029

	k		***l***		***m***		***n***		***o***		***p***		***q***		***r***		***s***		***t***		***u***	
D	*mean*	*(±SD)*	*mean*	*(±SD)*	*mean*	*(±SD)*	*mean*	*(±SD)*	*mean*	*(±SD)*	*mean*	*(±SD)*	*mean*	*(±SD)*	*mean*	*(±SD)*	*mean*	*(±SD)*	*mean*	*(±SD)*	*mean*	*(±SD)*
PME	0.071	0.043	0.074	0.023	0.113	0.044	0.120	0.036	0.088	0.038	0.096	0.043	0.101	0.057	0.132	0.076	0.122	0.069	0.136	0.043	0.150	0.079
Pi	0.067	0.012	0.061	0.020	0.076	0.052	0.063	0.041	0.081	0.066	0.070	0.021	0.059	0.029	0.074	0.073	0.059	0.032	0.086	0.056	0.065	0.037
PDE	0.243	0.106	0.283	0.119	0.266	0.158	0.226	0.178	0.304	0.122	0.270	0.091	0.288	0.123	0.281	0.210	0.192	0.102	0.214	0.100	0.258	0.219
PCr	0.216	0.039	0.208	0.044	0.220	0.057	0.216	0.077	0.200	0.052	0.220	0.043	0.206	0.049	0.182	0.055	0.246	0.047	0.224	0.045	0.205	0.061
γATP	0.150	0.026	0.141	0.025	0.123	0.036	0.119	0.038	0.122	0.030	0.136	0.032	0.124	0.042	0.114	0.054	0.154	0.057	0.145	0.054	0.115	0.038
αATP	0.163	0.046	0.148	0.049	0.132	0.036	0.140	0.061	0.123	0.040	0.137	0.052	0.139	0.049	0.158	0.091	0.159	0.067	0.148	0.079	0.140	0.082
βATP	0.090	0.039	0.085	0.027	0.070	0.031	0.116	0.063	0.082	0.038	0.070	0.027	0.083	0.040	0.093	0.054	0.075	0.035	0.052	0.028	0.068	0.055

	k		***l***		***m***		***n***		***o***		***p***		***q***		***r***		***s***		***t***		***u***	
E	*mean*	*(±SD)*	*mean*	*(±SD)*	*mean*	*(±SD)*	*mean*	*(±SD)*	*mean*	*(±SD)*	*mean*	*(±SD)*	*mean*	*(±SD)*	*mean*	*(±SD)*	*mean*	*(±SD)*	*mean*	*(±SD)*	*mean*	*(±SD)*
PME	0.060	0.025	0.074	0.026	0.114	0.037	0.119	0.031	0.096	0.040	0.093	0.046	0.107	0.063	0.147	0.079	0.140	0.062	0.150	0.049	0.146	0.073
Pi	0.067	0.014	0.058	0.017	0.062	0.027	0.066	0.044	0.079	0.059	0.069	0.024	0.058	0.032	0.086	0.089	0.059	0.028	0.093	0.071	0.065	0.035
PDE	0.230	0.092	0.282	0.099	0.257	0.147	0.237	0.155	0.300	0.137	0.262	0.093	0.277	0.108	0.209	0.173	0.180	0.103	0.189	0.096	0.257	0.179
PCr	0.218	0.033	0.204	0.044	0.219	0.051	0.212	0.081	0.196	0.048	0.222	0.040	0.205	0.046	0.193	0.059	0.239	0.039	0.235	0.063	0.224	0.060
γATP	0.155	0.025	0.140	0.022	0.126	0.034	0.115	0.031	0.120	0.031	0.138	0.033	0.127	0.044	0.120	0.054	0.164	0.067	0.143	0.056	0.122	0.044
αATP	0.176	0.043	0.155	0.043	0.140	0.034	0.137	0.046	0.128	0.042	0.144	0.052	0.144	0.045	0.157	0.063	0.160	0.056	0.145	0.076	0.143	0.081
βATP	0.095	0.032	0.086	0.021	0.082	0.034	0.114	0.054	0.083	0.032	0.072	0.024	0.082	0.041	0.106	0.061	0.075	0.040	0.058	0.020	0.063	0.048

3.4.2.1.1 Phosphomonoesters

For PME measurements, no statistically significant differences emerged between the following analysis methods: A compared to B (comparison of phasing in jMRUI), B compared to C (apodisation in jMRUI), and D compared to E (phasing in SpectroView). Statistically significant differences emerged between mean values resulting from jMRUI (analysis C) and SpectroView (analysis D and E) in all voxels. Scatter plots and ANOVA tables are reported below.

Analyses with jMRUI resulted in lower CVs compared to SpectroView for all assessed voxels. For jMRUI data, CVs were below 30% with the exception of a right-sided cortical region and within the pons, where they were just over 30% (Figure 3.15).

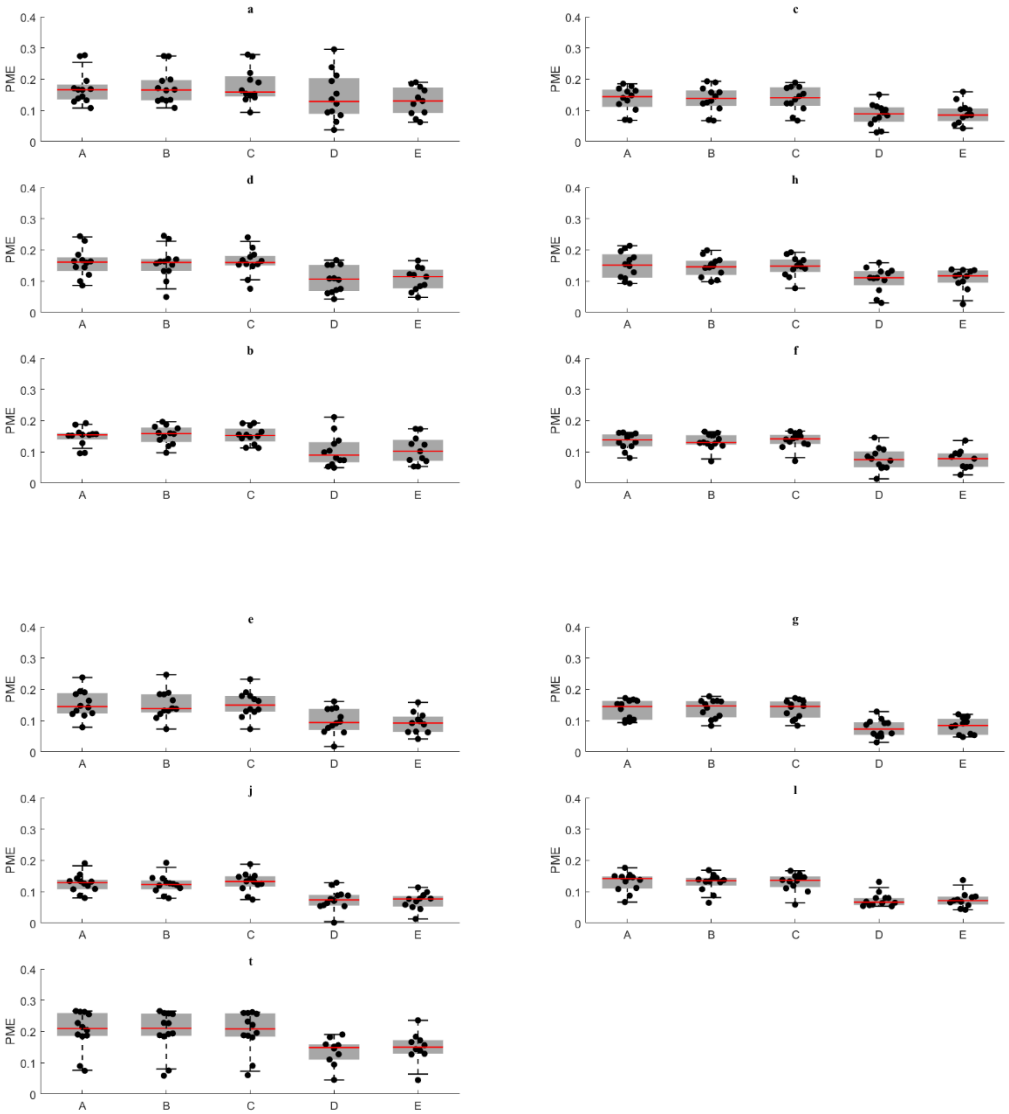

Figure 3.14 Box and whisker plots illustrating phosphomonoester (PME) values in each participant in each voxel calculated using methods A to E (detailed in methods section of this chapter).
Only voxels located within motor regions are included in this figure. Voxel location is indicated above each graph, index is illustrated in Figure 3.13.

Table 3.2 ANOVA tables illustrating multiple comparisons for phosphomonoesters (PME).

Comparisons took place between method A and B (phasing in jMRUI), B and C (no apodisation Vs apodisation in jMRUI), C compared to D and C compared to E (analysis in jMRUI compared to analysis in SpectroView), and D compared to E (effect of different phasing in SpectroView) for phosphomonoesters (PME). Relevant voxel indices are reported above each table as illustrated in Figure 3.13. CI: Confidence interval, diff: Difference, ns: Not significant, Vs: Versus

a

Tukey's multiple comparisons test	Mean Diff.	95.00% CI of diff.	Summary	Adjusted P Value
A vs. B	-0.00115	-0.04005 to 0.03775	ns	>0.9999
B vs. C	-0.005498	-0.04439 to 0.03340	ns	0.9942
C vs. D	0.03826	-0.0006319 to 0.07716	ns	0.0558
C vs. E	0.05317	0.01428 to 0.09207	**	0.0031
D vs. E	0.01491	-0.02399 to 0.05380	ns	0.8082

b

Tukey's multiple comparisons test	Mean Diff.	95.00% CI of diff.	Summary	Adjusted P Value
A vs. B	-0.006516	-0.03242 to 0.01938	ns	0.951
B vs. C	0.001593	-0.02431 to 0.02749	ns	0.9998
C vs. D	0.05031	0.02441 to 0.07621	****	<0.0001
C vs. E	0.04721	0.02132 to 0.07311	****	<0.0001
D vs. E	-0.003093	-0.02899 to 0.02281	ns	0.997

c

Tukey's multiple comparisons test	Mean Diff.	95.00% CI of diff.	Summary	Adjusted P Value
A vs. B	0.00001317	-0.02180 to 0.02182	ns	>0.9999
B vs. C	0.00006454	-0.02175 to 0.02188	ns	>0.9999
C vs. D	0.05103	0.02922 to 0.07284	****	<0.0001
C vs. E	0.05008	0.02827 to 0.07189	****	<0.0001
D vs. E	-0.0009508	-0.02276 to 0.02086	ns	>0.9999

d

Tukey's multiple comparisons test	Mean Diff.	95.00% CI of diff.	Summary	Adjusted P Value
A vs. B	0.004379	-0.02967 to 0.03843	ns	0.996
B vs. C	-0.005805	-0.03985 to 0.02824	ns	0.9881
C vs. D	0.0524	0.01835 to 0.08644	***	0.0007
C vs. E	0.0555	0.02145 to 0.08955	***	0.0003
D vs. E	0.003106	-0.03094 to 0.03715	ns	0.9989

e

Tukey's multiple comparisons test	Mean Diff.	95.00% CI of diff.	Summary	Adjusted P Value
A vs. B	0.001752	-0.02534 to 0.02885	ns	0.9997
B vs. C	-0.001735	-0.02883 to 0.02536	ns	0.9997
C vs. D	0.05484	0.02774 to 0.08194	****	<0.0001
C vs. E	0.05736	0.03026 to 0.08446	****	<0.0001
D vs. E	0.002517	-0.02458 to 0.02961	ns	0.9989

f

Tukey's multiple comparisons test	Mean Diff.	95.00% CI of diff.	Summary	Adjusted P Value
A vs. B	0.001727	-0.02394 to 0.02739	ns	0.9997
B vs. C	-0.004175	-0.02984 to 0.02149	ns	0.9901
C vs. D	0.06361	0.03794 to 0.08928	****	<0.0001
C vs. E	0.05912	0.03346 to 0.08479	****	<0.0001
D vs. E	-0.004486	-0.03015 to 0.02118	ns	0.987

g

Tukey's multiple comparisons test	Mean Diff.	95.00% CI of diff.	Summary	Adjusted P Value
A vs. B	0.002749	-0.009405 to 0.01490	ns	0.9664
B vs. C	0.001928	-0.01023 to 0.01408	ns	0.991
C vs. D	0.05364	0.04149 to 0.06580	****	<0.0001
C vs. E	0.05114	0.03899 to 0.06330	****	<0.0001
D vs. E	-0.002498	-0.01465 to 0.009656	ns	0.9763

h

Tukey's multiple comparisons test	Mean Diff.	95.00% CI of diff.	Summary	Adjusted P Value
A vs. B	0.0052	-0.01764 to 0.02804	ns	0.9656
B vs. C	0.0007758	-0.02206 to 0.02361	ns	>0.9999
C vs. D	0.03741	0.01457 to 0.06024	***	0.0003
C vs. E	0.04113	0.01829 to 0.06396	****	<0.0001
D vs. E	0.003721	-0.01912 to 0.02656	ns	0.99

j

Tukey's multiple comparisons test	Mean Diff.	95.00% CI of diff.	Summary	Adjusted P Value
A vs. B	0.004086	-0.01948 to 0.02766	ns	0.9874
B vs. C	-0.007231	-0.03080 to 0.01634	ns	0.9039
C vs. D	0.05855	0.03498 to 0.08212	****	<0.0001
C vs. E	0.05878	0.03521 to 0.08235	****	<0.0001
D vs. E	0.0002319	-0.02334 to 0.02380	ns	>0.9999

l

Tukey's multiple comparisons test	Mean Diff.	95.00% CI of diff.	Summary	Adjusted P Value
A vs. B	0.001439	-0.01754 to 0.02042	ns	0.9995
B vs. C	-0.001852	-0.02083 to 0.01713	ns	0.9986
C vs. D	0.0507	0.03172 to 0.06968	****	<0.0001
C vs. E	0.05246	0.03348 to 0.07144	****	<0.0001
D vs. E	0.00176	-0.01722 to 0.02074	ns	0.9989

t

Tukey's multiple comparisons test	Mean Diff.	95.00% CI of diff.	Summary	Adjusted P Value
A vs. B	0.001681	-0.02875 to 0.03211	ns	0.9998
B vs. C	-0.001925	-0.03235 to 0.02850	ns	0.9997
C vs. D	0.06484	0.03442 to 0.09527	****	<0.0001
C vs. E	0.0656	0.03518 to 0.09603	****	<0.0001
D vs. E	0.0007589	-0.02967 to 0.03119	ns	>0.9999

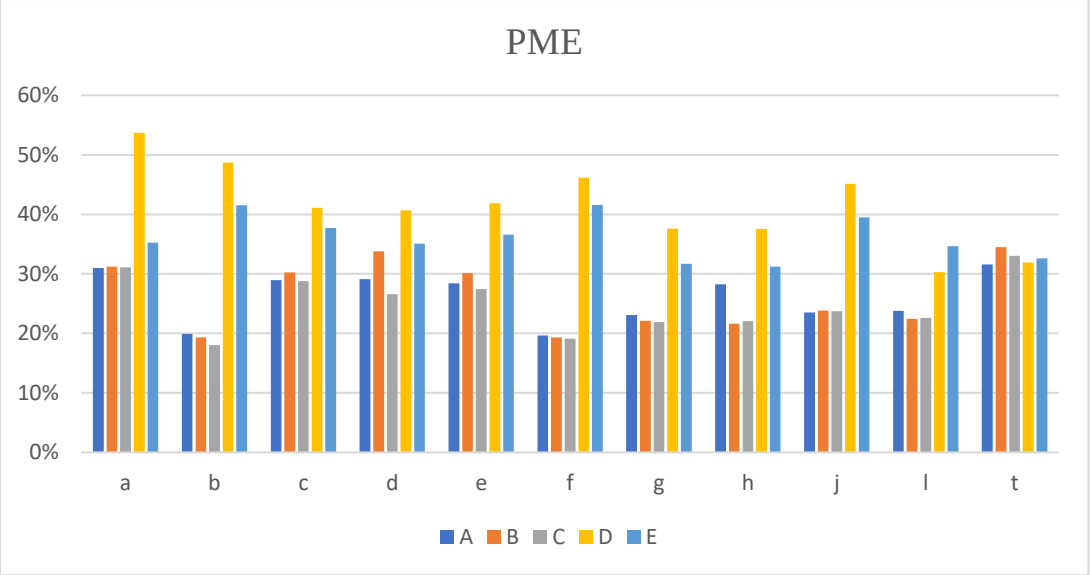

Figure 3.15 Coefficients of variability for phosphomonoesters (PME)calculated from voxels encompassing motor regions as depicted in Figure 3.13.
PMEs are expressed as proportion of total phosphorus signal.

3.4.2.1.2 Inorganic phosphate

Mean Pi values were not affected by any analysis methodology (Figure 3.16 and Table 3.3), except for voxel *l* where analysis in jMRUI returned significantly higher mean values than analysis in SpectroView. Data variability was high both in jMRUI and SpectroView especially in cortical regions (voxels *a*, *b*, *c*, *d*, *h*) and in the brainstem (voxel *t*) with CVs exceeding 30% (Figure 3.17).

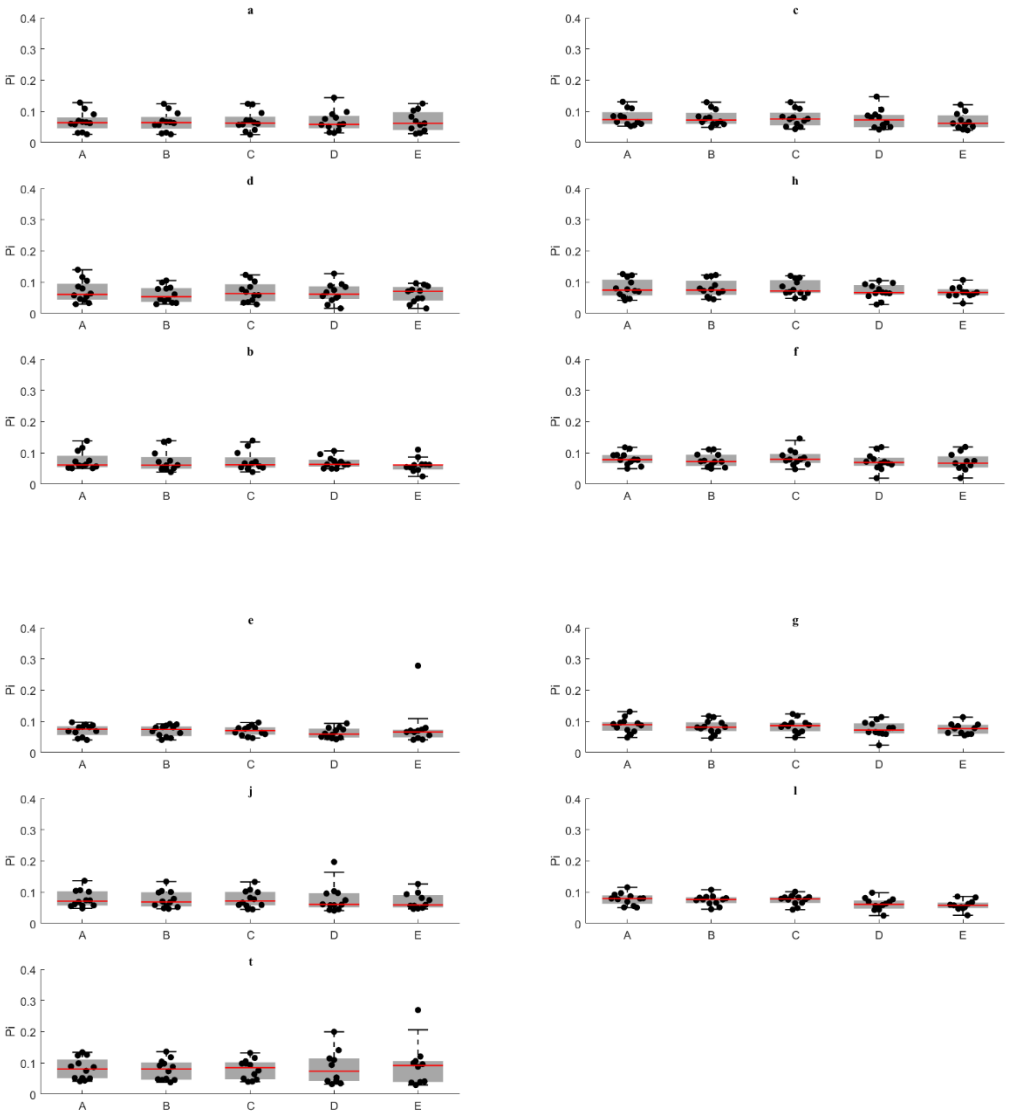

Figure 3.16 Box and whisker plots illustrating inorganic phosphate (Pi) values in each participant in each voxel calculated using methods A to E (detailed in method section of this chapter).
Only voxels located in motor regions are included in this figure. Voxel location is indicated above each graph. Index is illustrated in Figure 3.13.

Table 3.3 ANOVA tables illustrating multiple comparisons between method A and B (phasing in jMRUI), B and C (no apodisation Vs apodisation in jMRUI), C compared to D and C compared to E (analysis in jMRUI compared to analysis in SpectroView), and D compared to E (effect of different phasing in SpectroView) for inorganic phosphate (Pi).
Relevant voxel indices are reported above each table as illustrated in Figure 3.13. CI: Confidence interval, diff: Difference, ns=not significant, Vs=versus.

a

Tukey's multiple comparisons test	Mean Diff.	95.00% CI of diff.	Summary	Adjusted P Value
A vs. B	0.0002513	-0.01487 to 0.01538	ns	>0.9999
B vs. C	-0.002836	-0.01796 to 0.01229	ns	0.9831
C vs. D	0.0007374	-0.01439 to 0.01586	ns	>0.9999
C vs. E	0.001774	-0.01335 to 0.01690	ns	0.9972
D vs. E	0.001037	-0.01409 to 0.01616	ns	0.9997

c

Tukey's multiple comparisons test	Mean Diff.	95.00% CI of diff.	Summary	Adjusted P Value
A vs. B	0.0008574	-0.01332 to 0.01504	ns	0.9998
B vs. C	0.001101	-0.01308 to 0.01528	ns	0.9994
C vs. D	-0.0003919	-0.01457 to 0.01379	ns	>0.9999
C vs. E	0.00526	-0.008920 to 0.01944	ns	0.8258
D vs. E	0.005652	-0.008528 to 0.01983	ns	0.7853

d

Tukey's multiple comparisons test	Mean Diff.	95.00% CI of diff.	Summary	Adjusted P Value
A vs. B	0.01266	-0.01015 to 0.03547	ns	0.5149
B vs. C	-0.008648	-0.03146 to 0.01416	ns	0.8142
C vs. D	0.002248	-0.02056 to 0.02506	ns	0.9986
C vs. E	0.007099	-0.01571 to 0.02991	ns	0.8993
D vs. E	0.004851	-0.01796 to 0.02766	ns	0.9731

h

Tukey's multiple comparisons test	Mean Diff.	95.00% CI of diff.	Summary	Adjusted P Value
A vs. B	-0.0003724	-0.01762 to 0.01687	ns	>0.9999
B vs. C	-0.0006763	-0.01792 to 0.01657	ns	>0.9999
C vs. D	0.009534	-0.007711 to 0.02678	ns	0.5191
C vs. E	0.01008	-0.007159 to 0.02733	ns	0.4632
D vs. E	0.0005512	-0.01669 to 0.01780	ns	>0.9999

b

Tukey's multiple comparisons test	Mean Diff.	95.00% CI of diff.	Summary	Adjusted P Value
A vs. B	0.001174	-0.01282 to 0.01517	ns	0.9992
B vs. C	0.0007905	-0.01321 to 0.01479	ns	0.9998
C vs. D	0.003321	-0.01068 to 0.01732	ns	0.9601
C vs. E	0.00955	-0.004447 to 0.02355	ns	0.3093
D vs. E	0.006229	-0.007768 to 0.02023	ns	0.71

f

Tukey's multiple comparisons test	Mean Diff.	95.00% CI of diff.	Summary	Adjusted P Value
A vs. B	0.006062	-0.01080 to 0.02292	ns	0.8414
B vs. C	-0.008511	-0.02537 to 0.008348	ns	0.6051
C vs. D	0.0117	-0.005156 to 0.02856	ns	0.2928
C vs. E	0.01347	-0.003385 to 0.03033	ns	0.1718
D vs. E	0.00177	-0.01509 to 0.01863	ns	0.9982

e

Tukey's multiple comparisons test	Mean Diff.	95.00% CI of diff.	Summary	Adjusted P Value
A vs. B	0.001713	-0.03407 to 0.03750	ns	>0.9999
B vs. C	-0.0007621	-0.03655 to 0.03502	ns	>0.9999
C vs. D	0.006479	-0.02930 to 0.04226	ns	0.9851
C vs. E	-0.01024	-0.04603 to 0.02554	ns	0.9237
D vs. E	-0.01672	-0.05251 to 0.01906	ns	0.6716

g

Tukey's multiple comparisons test	Mean Diff.	95.00% CI of diff.	Summary	Adjusted P Value
A vs. B	0.005186	-0.007892 to 0.01826	ns	0.7884
B vs. C	-0.002795	-0.01587 to 0.01028	ns	0.9726
C vs. D	0.008436	-0.004642 to 0.02151	ns	0.3645
C vs. E	0.006012	-0.007066 to 0.01909	ns	0.6849
D vs. E	-0.002424	-0.01550 to 0.01065	ns	0.9838

j

Tukey's multiple comparisons test	Mean Diff.	95.00% CI of diff.	Summary	Adjusted P Value
A vs. B	0.002032	-0.02799 to 0.03205	ns	0.9997
B vs. C	-0.001982	-0.03200 to 0.02804	ns	0.9997
C vs. D	-0.0002169	-0.03024 to 0.02980	ns	>0.9999
C vs. E	0.008932	-0.02109 to 0.03895	ns	0.9132
D vs. E	0.009149	-0.02087 to 0.03917	ns	0.906

l

Tukey's multiple comparisons test	Mean Diff.	95.00% CI of diff.	Summary	Adjusted P Value
A vs. B	0.003069	-0.008477 to 0.01461	ns	0.9407
B vs. C	0.0003872	-0.01116 to 0.01193	ns	>0.9999
C vs. D	0.01484	0.003292 to 0.02638	**	0.006
C vs. E	0.01595	0.004407 to 0.02750	**	0.0027
D vs. E	0.001114	-0.01043 to 0.01266	ns	0.9987

t

Tukey's multiple comparisons test	Mean Diff.	95.00% CI of diff.	Summary	Adjusted P Value
A vs. B	0.001883	-0.03941 to 0.04318	ns	>0.9999
B vs. C	-0.004092	-0.04539 to 0.03720	ns	0.9984
C vs. D	-0.01683	-0.05813 to 0.02446	ns	0.7636
C vs. E	-0.01864	-0.05993 to 0.02266	ns	0.6906
D vs. E	-0.001804	-0.04310 to 0.03949	ns	>0.9999

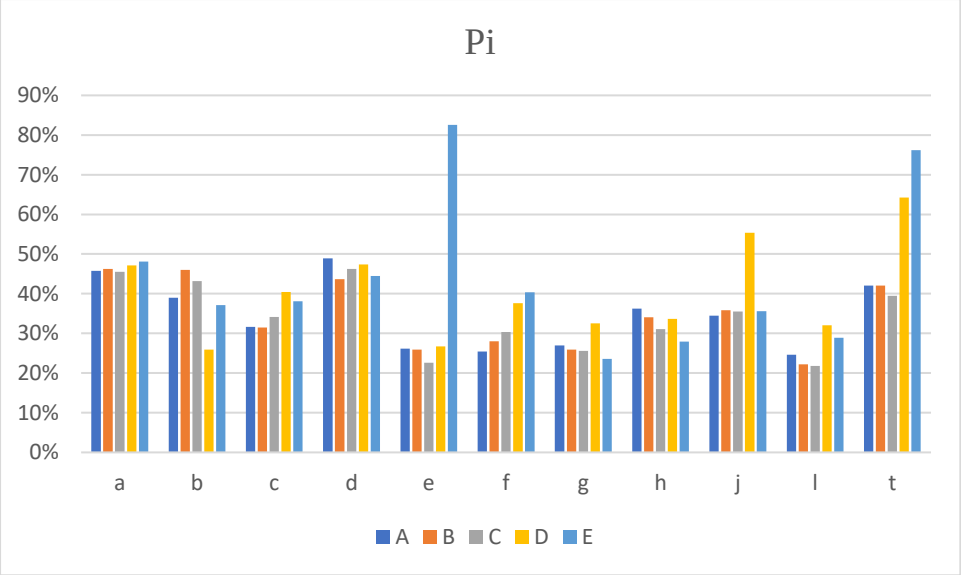

Figure 3.17 Coefficients of variability for inorganic phosphate (Pi) calculated from voxels encompassing motor regions as depicted in Figure 3.13.
Pi is expressed as proportion of total phosphorus signal.

3.4.2.1.3 Phosphodiesters

Mean PDE results analysed with SpectroView were elevated in all assessed voxels compared to JMRUI although did not reach statistical significance in *a*, *d*, *e*, and *t*. No significant differences were found between different phasing methods and apodisation in jMRUI did not affect results significantly. A substantial difference in variability between analysis in jMRUI and SpectroView was observed; CVs in jMRUI were approximately equivalent or lower than 30%, whereas they were considerably elevated in all SpectroView analyses. Scatter plots and ANOVA tables are reported below.

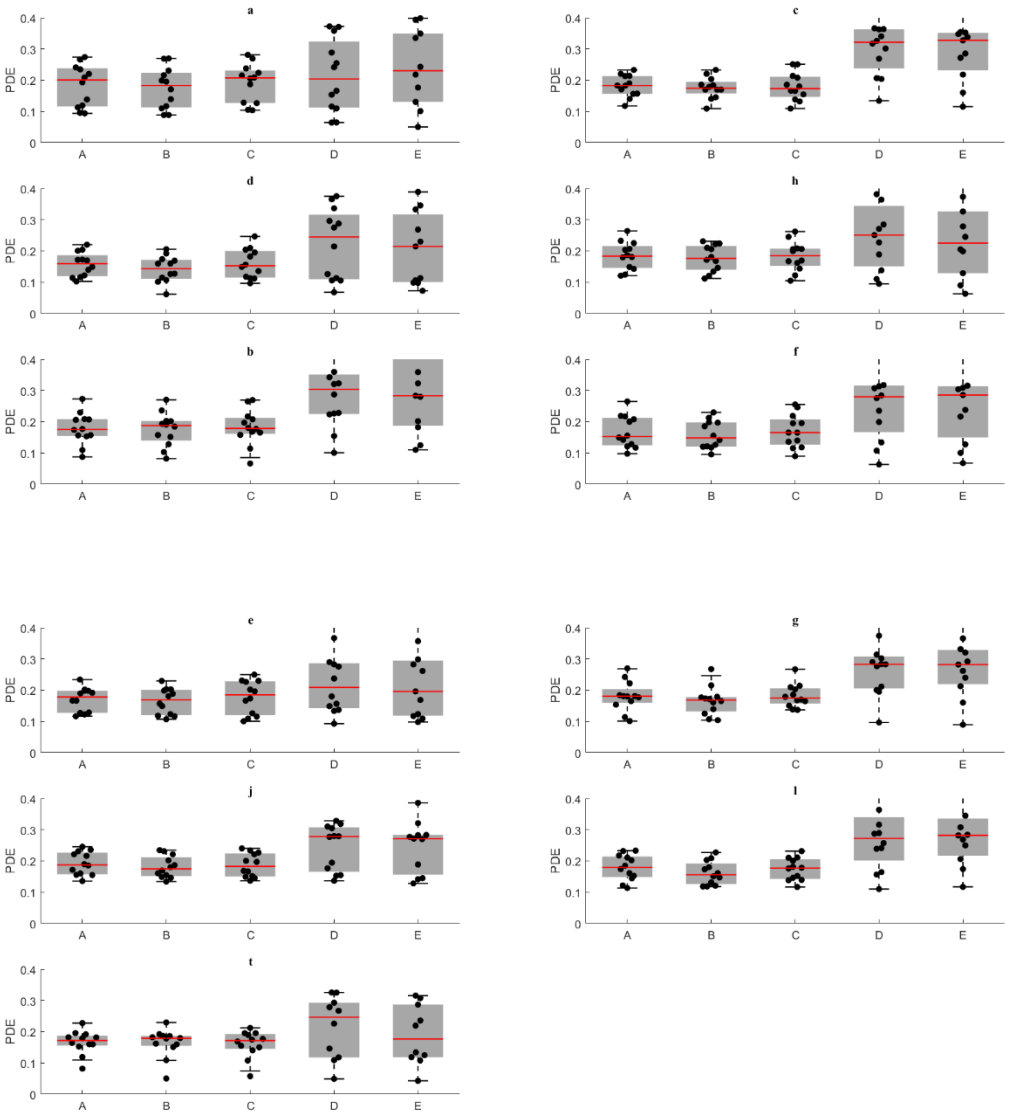

Figure 3.18 Box and whisker plots illustrating phosphodiesters (PDE) values for each participant for each voxel calculated using methods A to E (detailed in methods section of this chapter).
Only voxels located in motor regions are included in this figure. Voxel location is indicated above each graph. Index is illustrated in Figure 3.13. Of note, the y-axis was scaled 0 to 0.4 as in all other figures in this sub-chapter to allow for a more intuitive graphical comparison. As some values acquired from SpectroView exceeded 0.4, these results are also reported in the appendix with the axis scaled to include all datapoints.

Table 3.4 ANOVA tables illustrating multiple comparisons between method A and B (phasing in jMRUI), B and C (no apodisation Vs apodisation in jMRUI), C compared to D and C compared to E (analysis in jMRUI compared to analysis in SpectroView), and D compared to E (effect of different phasing in SpectroView) for phosphodiesters (PDE).
Relevant voxel indices are reported above each table as illustrated in Figure 3.13. CI: Confidence interval, diff: Difference, ns: Not significant, Vs: Versus.

a

Tukey's multiple comparisons test	Mean Diff.	95.00% CI of diff.	Significant?	Summary	Adjusted P Value
A vs. B	0.008047	-0.04835 to 0.06445	No	ns	0.9938
B vs. C	-0.02125	-0.07764 to 0.03515	No	ns	0.8148
C vs. D	-0.02561	-0.08201 to 0.03078	No	ns	0.6906
C vs. E	-0.04451	-0.1009 to 0.01189	No	ns	0.1797
D vs. E	-0.01889	-0.07529 to 0.03751	No	ns	0.8703

c

Tukey's multiple comparisons test	Mean Diff.	95.00% CI of diff.	Significant?	Summary	Adjusted P Value
A vs. B	0.005378	-0.05927 to 0.07003	No	ns	0.9993
B vs. C	-0.004191	-0.06884 to 0.06046	No	ns	0.9997
C vs. D	-0.1133	-0.1779 to -0.04862	Yes	***	0.0001
C vs. E	-0.1075	-0.1721 to -0.04284	Yes	***	0.0002
D vs. E	0.005778	-0.05887 to 0.07043	No	ns	0.999

d

Tukey's multiple comparisons test	Mean Diff.	95.00% CI of diff.	Significant?	Summary	Adjusted P Value
A vs. B	0.01201	-0.06737 to 0.09138	No	ns	0.9925
B vs. C	-0.01677	-0.09614 to 0.06260	No	ns	0.9737
C vs. D	-0.07097	-0.1503 to 0.008406	No	ns	0.099
C vs. E	-0.04078	-0.1202 to 0.03859	No	ns	0.589
D vs. E	0.03019	-0.04919 to 0.1096	No	ns	0.8125

h

Tukey's multiple comparisons test	Mean Diff.	95.00% CI of diff.	Significant?	Summary	Adjusted P Value
A vs. B	0.007329	-0.08349 to 0.09815	No	ns	0.9993
B vs. C	-0.008225	-0.09904 to 0.08259	No	ns	0.9989
C vs. D	-0.09184	-0.1827 to -0.001028	Yes	*	0.0463
C vs. E	-0.04451	-0.1353 to 0.04631	No	ns	0.6272
D vs. E	0.04733	-0.04348 to 0.1381	No	ns	0.5715

b

Tukey's multiple comparisons test	Mean Diff.	95.00% CI of diff.	Significant?	Summary	Adjusted P Value
A vs. B	0.001801	-0.07435 to 0.07795	No	ns	>0.9999
B vs. C	-0.007523	-0.08367 to 0.06863	No	ns	0.9986
C vs. D	-0.0998	-0.1760 to -0.02365	Yes	**	0.0049
C vs. E	-0.1219	-0.1981 to -0.04578	Yes	***	0.0004
D vs. E	-0.02212	-0.09827 to 0.05403	No	ns	0.9198

f

Tukey's multiple comparisons test	Mean Diff.	95.00% CI of diff.	Significant?	Summary	Adjusted P Value
A vs. B	0.01027	-0.1042 to 0.1247	No	ns	0.999
B vs. C	-0.01205	-0.1265 to 0.1024	No	ns	0.9981
C vs. D	-0.1184	-0.2329 to -0.004005	Yes	*	0.0393
C vs. E	-0.1189	-0.2334 to -0.004493	Yes	*	0.0382
D vs. E	-0.0004879	-0.1149 to 0.1140	No	ns	>0.9999

e

Tukey's multiple comparisons test	Mean Diff.	95.00% CI of diff.	Significant?	Summary	Adjusted P Value
A vs. B	0.005126	-0.05742 to 0.06767	No	ns	0.9993
B vs. C	-0.01291	-0.07546 to 0.04964	No	ns	0.9759
C vs. D	-0.05016	-0.1127 to 0.01239	No	ns	0.1692
C vs. E	-0.04942	-0.1120 to 0.01312	No	ns	0.1804
D vs. E	0.0007341	-0.06181 to 0.06328	No	ns	>0.9999

g

Tukey's multiple comparisons test	Mean Diff.	95.00% CI of diff.	Significant?	Summary	Adjusted P Value
A vs. B	0.0143	-0.06500 to 0.09361	No	ns	0.9854
B vs. C	-0.01705	-0.09636 to 0.06225	No	ns	0.972
C vs. D	-0.1076	-0.1870 to -0.02834	Yes	**	0.0034
C vs. E	-0.08398	-0.1633 to -0.004671	Yes	*	0.0333
D vs. E	0.02367	-0.05564 to 0.1030	No	ns	0.9123

j

Tukey's multiple comparisons test	Mean Diff.	95.00% CI of diff.	Significant?	Summary	Adjusted P Value
A vs. B	0.006663	-0.03079 to 0.04412	No	ns	0.9861
B vs. C	-0.005438	-0.04290 to 0.03202	No	ns	0.9936
C vs. D	-0.04864	-0.08610 to -0.01118	Yes	**	0.0054
C vs. E	-0.05695	-0.09441 to -0.01949	Yes	***	0.0008
D vs. E	-0.00831	-0.04577 to 0.02915	No	ns	0.9687

l

Tukey's multiple comparisons test	Mean Diff.	95.00% CI of diff.	Significant?	Summary	Adjusted P Value
A vs. B	0.01875	-0.05629 to 0.09378	No	ns	0.9522
B vs. C	-0.01254	-0.08758 to 0.06250	No	ns	0.989
C vs. D	-0.1093	-0.1843 to -0.03426	Yes	**	0.0015
C vs. E	-0.1089	-0.1839 to -0.03385	Yes	**	0.0015
D vs. E	0.0004037	-0.07463 to 0.07544	No	ns	>0.9999

t

Tukey's multiple comparisons test	Mean Diff.	95.00% CI of diff.	Significant?	Summary	Adjusted P Value
A vs. B	-0.001299	-0.06758 to 0.06498	No	ns	>0.9999
B vs. C	0.003949	-0.06233 to 0.07023	No	ns	0.9998
C vs. D	-0.02939	-0.09567 to 0.03689	No	ns	0.7043
C vs. E	-0.02532	-0.09160 to 0.04096	No	ns	0.8033
D vs. E	0.004072	-0.06221 to 0.07035	No	ns	0.9998

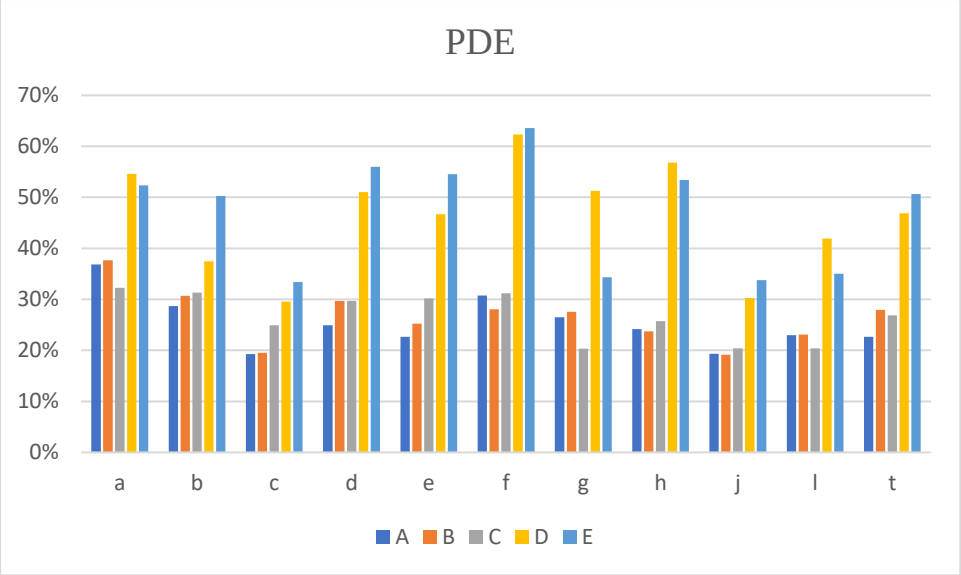

Figure 3.19 Coefficients of variability for phosphodiesters (PDE) calculated from voxels encompassing motor regions as depicted in Figure 3.13.
PDE is expressed as proportion of total phosphorus signal.

3.4.2.1.4 Phosphocreatine

For PCr (Figure 3.20, Table 3.5), analysis with SpectroView resulted in statistically increased mean values in voxel *a* and in *e* compared to analysis in jMRUI, although in the latter voxel this was true only for the comparison between protocol C and D. Type of analysis protocol had no effect on results in all other voxels. PCr values were characterised by low variability, with CVs well below 30% in all assessed voxels and using all analysis methodologies (Figure 3.21).

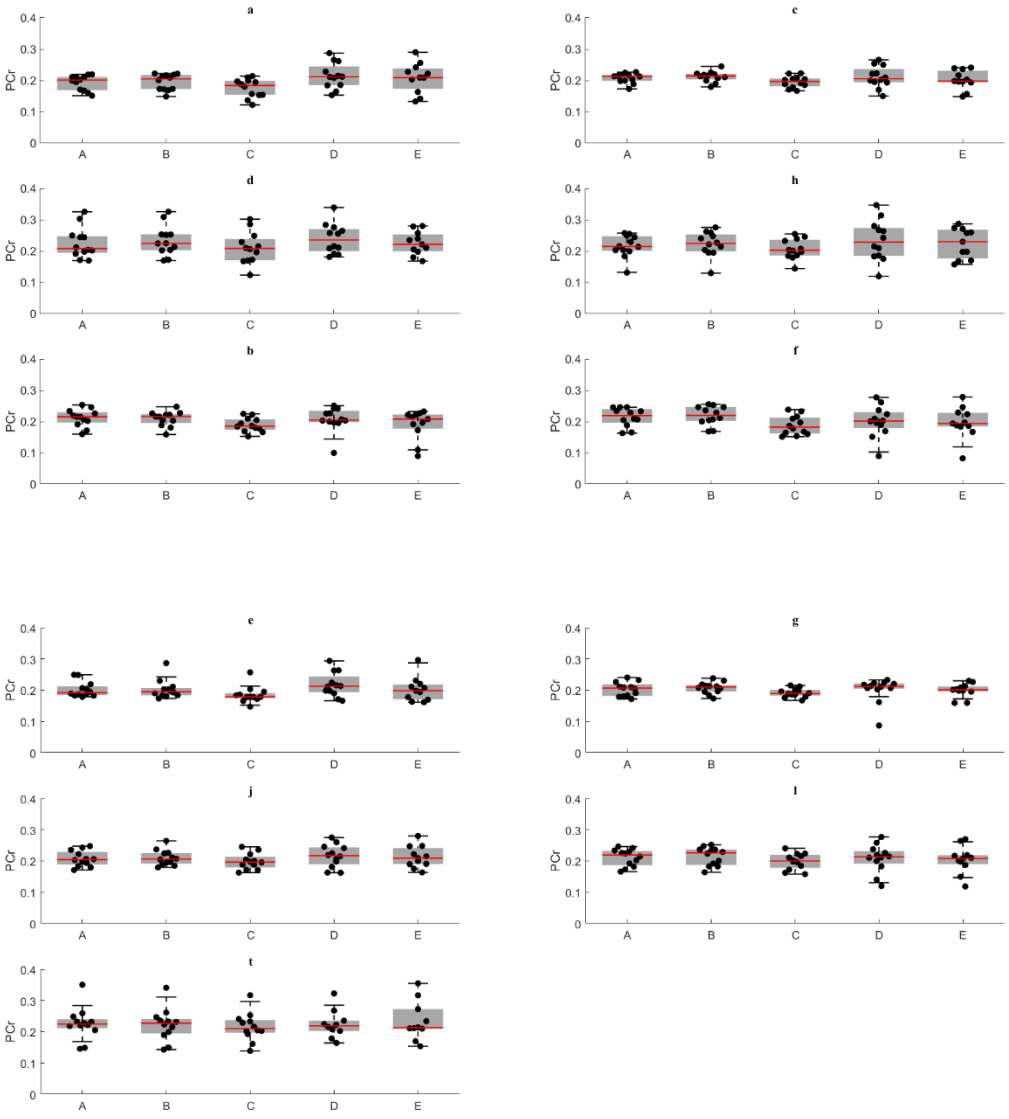

Figure 3.20 Box and whisker plots illustrating phosphocreatine (PCr) values for each participant for each voxel calculated using methods A to E (detailed in method section of this chapter).
Only voxels located on motor regions are included in this figure. Voxel location is indicated above each graph. Index is illustrated in Figure 3.13.

Table 3.5 ANOVA tables illustrating multiple comparisons between method A and B (phasing in jMRUI), B and C (no apodisation Vs apodisation in jMRUI), C compared to D and C compared to E (analysis in jMRUI compared to analysis in SpectroView), and D compared to E (effect of different phasing in SpectroView) for phosphocreatine (PCr).

Relevant voxel indices are reported above each table as illustrated in Figure 3.13. CI: Confidence interval, diff: Difference, ns: Not significant, Vs: Versus.

a

Tukey's multiple comparisons test	Mean Diff.	95.00% CI of diff.	Significant?	Summary	Adjusted P Value
A vs. B	-0.0008961	-0.02622 to 0.02443	No	ns	>0.9999
B vs. C	0.01879	-0.006535 to 0.04412	No	ns	0.2321
C vs. D	-0.0439	-0.06923 to -0.01857	Yes	***	0.0001
C vs. E	-0.03525	-0.06058 to -0.009923	Yes	**	0.0025
D vs. E	0.008647	-0.01668 to 0.03397	No	ns	0.8648

b

Tukey's multiple comparisons test	Mean Diff.	95.00% CI of diff.	Significant?	Summary	Adjusted P Value
A vs. B	0.001929	-0.02723 to 0.03108	No	ns	0.9997
B vs. C	0.02159	-0.007563 to 0.05075	No	ns	0.2338
C vs. D	-0.02195	-0.05111 to 0.007203	No	ns	0.2196
C vs. E	-0.003536	-0.03269 to 0.02562	No	ns	0.9968
D vs. E	0.01841	-0.01074 to 0.04757	No	ns	0.3855

c

Tukey's multiple comparisons test	Mean Diff.	95.00% CI of diff.	Significant?	Summary	Adjusted P Value
A vs. B	-0.005057	-0.03049 to 0.02038	No	ns	0.979
B vs. C	0.0183	-0.007134 to 0.04374	No	ns	0.2595
C vs. D	-0.0153	-0.04074 to 0.01013	No	ns	0.4348
C vs. E	-0.007447	-0.03288 to 0.01799	No	ns	0.9177
D vs. E	0.007854	-0.01758 to 0.03329	No	ns	0.9019

d

Tukey's multiple comparisons test	Mean Diff.	95.00% CI of diff.	Significant?	Summary	Adjusted P Value
A vs. B	-0.007395	-0.03650 to 0.02171	No	ns	0.9493
B vs. C	0.02299	-0.006108 to 0.05210	No	ns	0.1805
C vs. D	-0.02664	-0.05575 to 0.002458	No	ns	0.0867
C vs. E	-0.02116	-0.05026 to 0.007946	No	ns	0.2502
D vs. E	0.005489	-0.02361 to 0.03459	No	ns	0.9827

e

Tukey's multiple comparisons test	Mean Diff.	95.00% CI of diff.	Significant?	Summary	Adjusted P Value
A vs. B	-0.0004838	-0.02647 to 0.02550	No	ns	>0.9999
B vs. C	0.01888	-0.007099 to 0.04486	No	ns	0.2505
C vs. D	-0.03381	-0.05979 to -0.007830	Yes	**	0.0053
C vs. E	-0.0174	-0.04338 to 0.008584	No	ns	0.3275
D vs. E	0.01641	-0.009568 to 0.04240	No	ns	0.3854

f

Tukey's multiple comparisons test	Mean Diff.	95.00% CI of diff.	Significant?	Summary	Adjusted P Value
A vs. B	-0.004535	-0.03921 to 0.03014	No	ns	0.9957
B vs. C	0.03205	-0.002621 to 0.06672	No	ns	0.082
C vs. D	-0.01366	-0.04833 to 0.02101	No	ns	0.7922
C vs. E	-0.0065	-0.04117 to 0.02817	No	ns	0.9831
D vs. E	0.007162	-0.02751 to 0.04183	No	ns	0.9758

g

Tukey's multiple comparisons test	Mean Diff.	95.00% CI of diff.	Significant?	Summary	Adjusted P Value
A vs. B	-0.006344	-0.03113 to 0.01845	No	ns	0.948
B vs. C	0.01635	-0.008439 to 0.04114	No	ns	0.3423
C vs. D	-0.007879	-0.03267 to 0.01691	No	ns	0.8923
C vs. E	-0.008505	-0.03330 to 0.01629	No	ns	0.8627
D vs. E	-0.0006261	-0.02542 to 0.02416	No	ns	>0.9999

h

Tukey's multiple comparisons test	Mean Diff.	95.00% CI of diff.	Significant?	Summary	Adjusted P Value
A vs. B	-0.007134	-0.04314 to 0.02887	No	ns	0.9792
B vs. C	0.01671	-0.01929 to 0.05271	No	ns	0.6771
C vs. D	-0.02116	-0.05716 to 0.01484	No	ns	0.4582
C vs. E	-0.02247	-0.05847 to 0.01353	No	ns	0.3977
D vs. E	-0.001308	-0.03731 to 0.03469	No	ns	>0.9999

j

Tukey's multiple comparisons test	Mean Diff.	95.00% CI of diff.	Significant?	Summary	Adjusted P Value
A vs. B	-0.001787	-0.02849 to 0.02492	No	ns	0.9997
B vs. C	0.01076	-0.01594 to 0.03747	No	ns	0.7784
C vs. D	-0.01884	-0.04554 to 0.007865	No	ns	0.2776
C vs. E	-0.01099	-0.03770 to 0.01571	No	ns	0.7648
D vs. E	0.007845	-0.01886 to 0.03455	No	ns	0.9168

l

Tukey's multiple comparisons test	Mean Diff.	95.00% CI of diff.	Significant?	Summary	Adjusted P Value
A vs. B	-0.004697	-0.02917 to 0.01977	No	ns	0.9815
B vs. C	0.01748	-0.006985 to 0.04195	No	ns	0.2659
C vs. D	-0.005678	-0.03015 to 0.01879	No	ns	0.9632
C vs. E	-0.001591	-0.02606 to 0.02288	No	ns	0.9997
D vs. E	0.004087	-0.02038 to 0.02856	No	ns	0.989

t

Tukey's multiple comparisons test	Mean Diff.	95.00% CI of diff.	Significant?	Summary	Adjusted P Value
A vs. B	0.0004904	-0.03240 to 0.03338	No	ns	>0.9999
B vs. C	0.008575	-0.02431 to 0.04147	No	ns	0.9419
C vs. D	-0.01094	-0.04383 to 0.02195	No	ns	0.8703
C vs. E	-0.00585	-0.03874 to 0.02704	No	ns	0.9853
D vs. E	0.00509	-0.02780 to 0.03798	No	ns	0.9913

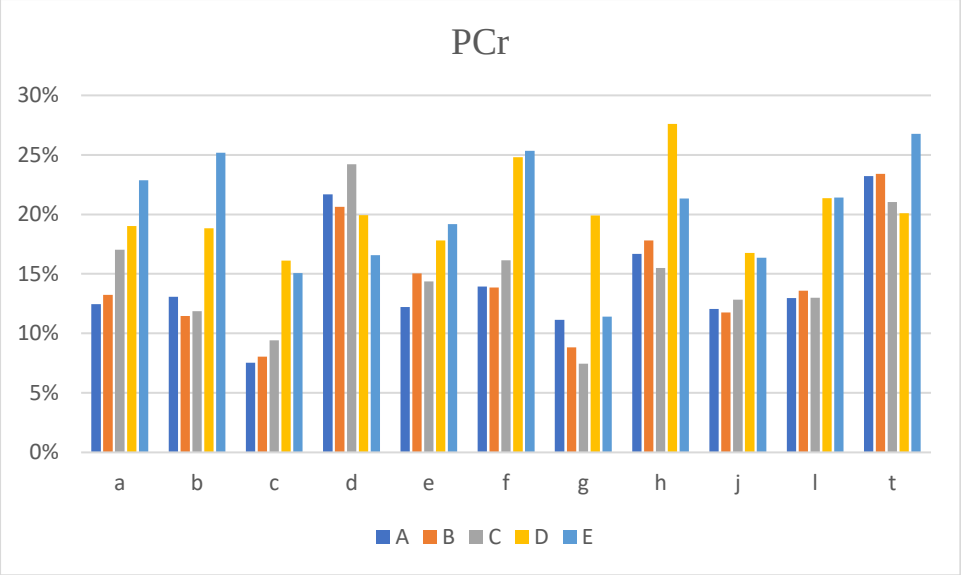

Figure 3.21 Coefficients of variability for phosphocreatine (PCr) calculated from voxels encompassing motor regions as depicted in Figure 3.13.
PCr is expressed as proportion of total phosphorus signal.

3.4.2.1.5 γ Adenosine triphosphate

For γATP, no statistically significant differences emerged from comparisons between alternative phasing methods and between non-apodised and apodised jMRUI protocols. In voxels *b*, *c*, *f*, and *l*, analysis with SpectroView resulted in statistically decreased mean values compared to jMRUI. Data for motor regions are illustrated in Figure 3.22 and summarised in Table 3.6. Variability with SpectroView was higher compared to analyses with jMRUI. CVs with jMRUI were consistently below 30% whereas higher values were recorded for SpectroView in right cortical regions (voxels *a* and *d*) and in the pons (voxel *t*).

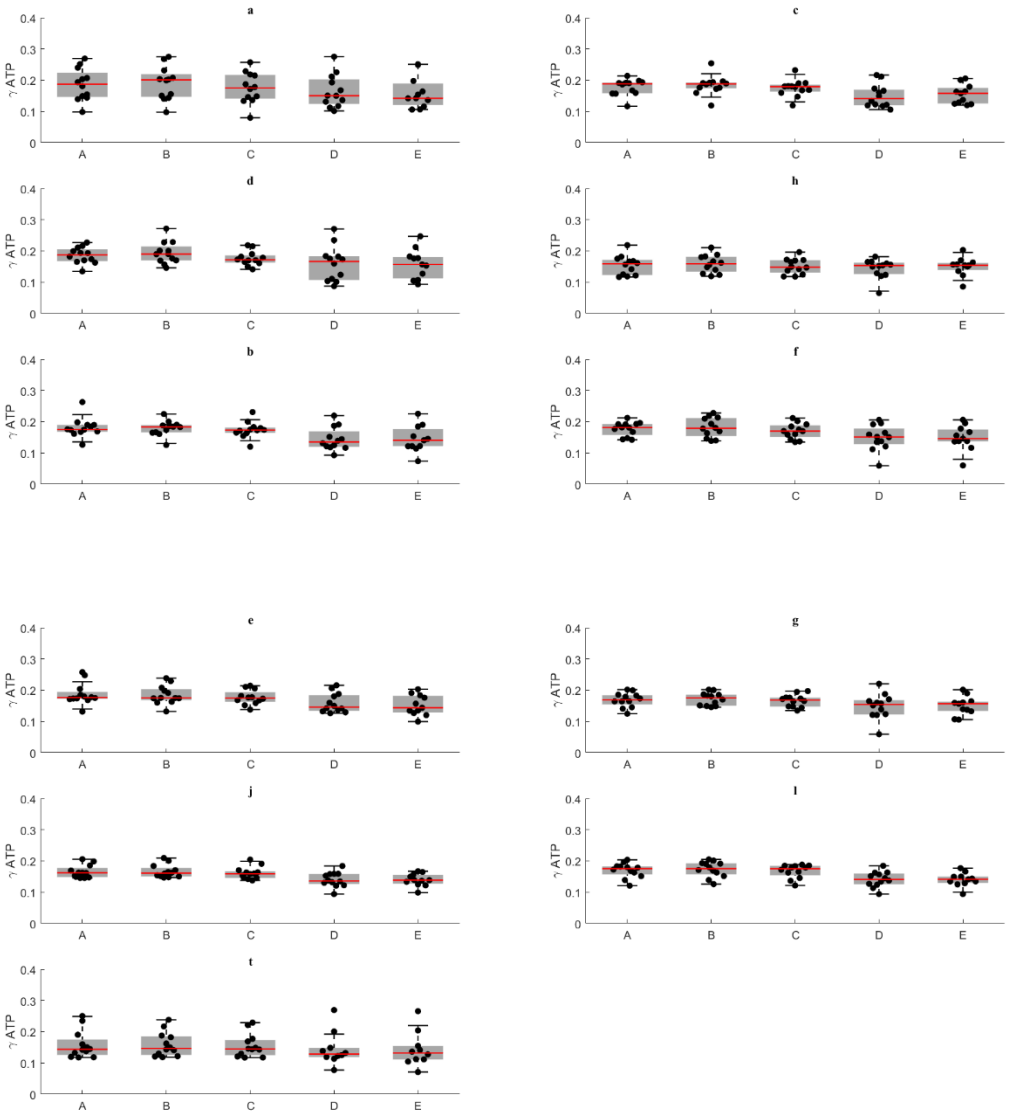

Figure 3.22 Box and whisker plots illustrating γ phosphate of adenosine triphosphate (γATP) values for each participant for each voxel calculated using methods A to E (detailed in method section of this chapter).
Only voxels located on motor regions are included in this figure. Voxel location is indicated above each graph. Index is illustrated in Figure 3.13.

Table 3.6 ANOVA tables illustrating multiple comparisons between method A and B (phasing in jMRUI), B and C (no apodisation Vs apodisation in jMRUI), C compared to D and C compared to E (analysis in jMRUI compared to analysis in SpectroView), and D compared to E (effect of different phasing in SpectroView) for γ phosphate of adenosine triphosphate (γATP).

Relevant voxel indices are reported above each table as illustrated in Figure 3.13. CI: Confidence interval, diff: Difference, ns: Not significant, Vs: Versus.

a

Tukey's multiple comparisons test	Mean Diff.	95.00% CI of diff.	Significant?	Summary	Adjusted P Value
A vs. B	-0.003081	-0.03529 to 0.02913	No	ns	0.9987
B vs. C	0.01434	-0.01787 to 0.04656	No	ns	0.7095
C vs. D	0.006539	-0.02567 to 0.03875	No	ns	0.9773
C vs. E	0.01351	-0.01870 to 0.04572	No	ns	0.7526
D vs. E	0.006969	-0.02524 to 0.03918	No	ns	0.9714

c

Tukey's multiple comparisons test	Mean Diff.	95.00% CI of diff.	Significant?	Summary	Adjusted P Value
A vs. B	-0.007463	-0.02668 to 0.01176	No	ns	0.8009
B vs. C	0.009989	-0.009233 to 0.02921	No	ns	0.5784
C vs. D	0.0235	0.004282 to 0.04273	Yes	**	0.0098
C vs. E	0.0212	0.001974 to 0.04042	Yes	*	0.0243
D vs. E	-0.002308	-0.02153 to 0.01691	No	ns	0.9969

d

Tukey's multiple comparisons test	Mean Diff.	95.00% CI of diff.	Significant?	Summary	Adjusted P Value
A vs. B	-0.008365	-0.04312 to 0.02639	No	ns	0.9581
B vs. C	0.01802	-0.01674 to 0.05278	No	ns	0.5806
C vs. D	0.01986	-0.01489 to 0.05462	No	ns	0.4862
C vs. E	0.0184	-0.01635 to 0.05316	No	ns	0.5607
D vs. E	-0.00146	-0.03622 to 0.03330	No	ns	>0.9999

h

Tukey's multiple comparisons test	Mean Diff.	95.00% CI of diff.	Significant?	Summary	Adjusted P Value
A vs. B	-0.004356	-0.02809 to 0.01938	No	ns	0.9844
B vs. C	0.00773	-0.01601 to 0.03147	No	ns	0.8835
C vs. D	0.005937	-0.01780 to 0.02967	No	ns	0.952
C vs. E	-0.001284	-0.02502 to 0.02245	No	ns	0.9999
D vs. E	-0.007221	-0.03096 to 0.01652	No	ns	0.9066

b

Tukey's multiple comparisons test	Mean Diff.	95.00% CI of diff.	Significant?	Summary	Adjusted P Value
A vs. B	0.001246	-0.01900 to 0.02149	No	ns	0.9998
B vs. C	0.005363	-0.01488 to 0.02561	No	ns	0.9414
C vs. D	0.02545	0.005203 to 0.04569	Yes	**	0.0075
C vs. E	0.03005	0.009805 to 0.05029	Yes	**	0.0012
D vs. E	0.004602	-0.01564 to 0.02485	No	ns	0.9658

f

Tukey's multiple comparisons test	Mean Diff.	95.00% CI of diff.	Significant?	Summary	Adjusted P Value
A vs. B	-0.004716	-0.02371 to 0.01428	No	ns	0.9532
B vs. C	0.01247	-0.006527 to 0.03146	No	ns	0.3472
C vs. D	0.02044	0.001450 to 0.03944	Yes	*	0.0294
C vs. E	0.02362	0.004628 to 0.04261	Yes	**	0.0084
D vs. E	0.003178	-0.01582 to 0.02217	No	ns	0.9889

e

Tukey's multiple comparisons test	Mean Diff.	95.00% CI of diff.	Significant?	Summary	Adjusted P Value
A vs. B	0.002619	-0.02507 to 0.03031	No	ns	0.9988
B vs. C	0.008149	-0.01954 to 0.03584	No	ns	0.9163
C vs. D	0.01636	-0.01133 to 0.04405	No	ns	0.4531
C vs. E	0.0259	-0.001790 to 0.05360	No	ns	0.0765
D vs. E	0.009544	-0.01815 to 0.03724	No	ns	0.8608

g

Tukey's multiple comparisons test	Mean Diff.	95.00% CI of diff.	Significant?	Summary	Adjusted P Value
A vs. B	-0.004458	-0.02463 to 0.01572	No	ns	0.9691
B vs. C	0.005995	-0.01418 to 0.02617	No	ns	0.9136
C vs. D	0.01731	-0.002867 to 0.03749	No	ns	0.123
C vs. E	0.01728	-0.002898 to 0.03745	No	ns	0.1241
D vs. E	-0.00003093	-0.02021 to 0.02015	No	ns	>0.9999

j

Tukey's multiple comparisons test	Mean Diff.	95.00% CI of diff.	Significant?	Summary	Adjusted P Value
A vs. B	0.000005871	-0.02356 to 0.02358	No	ns	>0.9999
B vs. C	0.004815	-0.01876 to 0.02838	No	ns	0.9768
C vs. D	0.01919	-0.004380 to 0.04276	No	ns	0.1581
C vs. E	0.02122	-0.002348 to 0.04479	No	ns	0.0952
D vs. E	0.002033	-0.02154 to 0.02560	No	ns	0.9992

l

Tukey's multiple comparisons test	Mean Diff.	95.00% CI of diff.	Significant?	Summary	Adjusted P Value
A vs. B	-0.003853	-0.02530 to 0.01760	No	ns	0.9856
B vs. C	0.006856	-0.01459 to 0.02831	No	ns	0.8902
C vs. D	0.02736	0.005911 to 0.04881	Yes	**	0.0065
C vs. E	0.02924	0.007793 to 0.05069	Yes	**	0.0032
D vs. E	0.001882	-0.01957 to 0.02333	No	ns	0.9991

t

Tukey's multiple comparisons test	Mean Diff.	95.00% CI of diff.	Significant?	Summary	Adjusted P Value
A vs. B	-0.005579	-0.02942 to 0.01827	No	ns	0.9602
B vs. C	0.006335	-0.01751 to 0.03018	No	ns	0.938
C vs. D	0.006951	-0.01689 to 0.03079	No	ns	0.9153
C vs. E	0.005851	-0.01799 to 0.02969	No	ns	0.9529
D vs. E	-0.0011	-0.02494 to 0.02274	No	ns	>0.9999

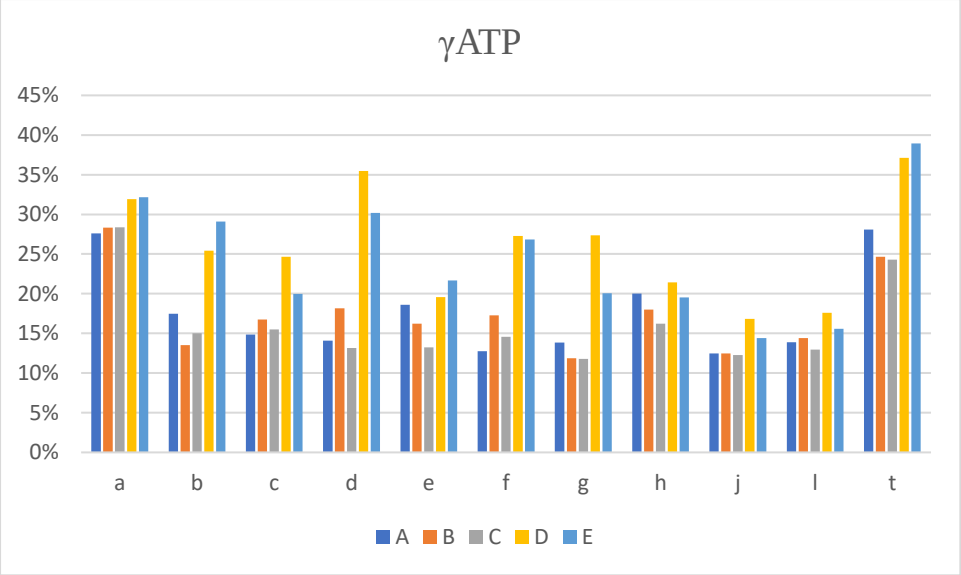

Figure 3.23 Coefficients of variability for γ phosphate of adenosine triphosphate (γATP) calculated from voxels encompassing motor regions as depicted in Figure 3.13.
γATP is expressed as proportion of total phosphorus signal.

3.4.2.1.6 α Adenosine triphosphate

αATP mean values were not affected by any of the analysis methods (Figure 3.24 and Table 3.7), except for voxel *c* where a statistically significant difference between analysis C (jMRUI) and D (SpectroView) was found. Variability for αATP measurements was higher compared to γATP with CVs ranging from 8% to 54%. As for other measurements, variability was greater in cortical and basal regions.

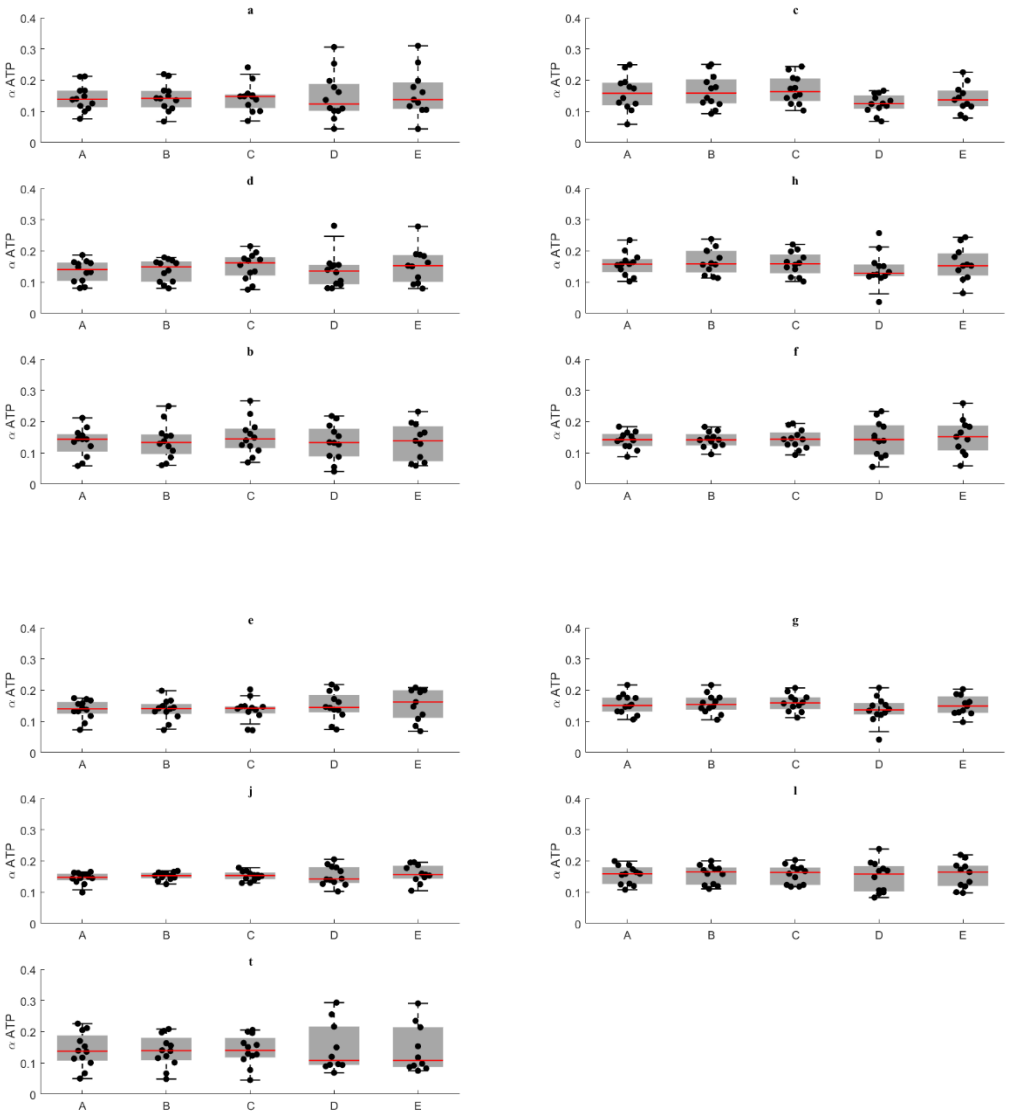

Figure 3.24 Box and whisker plots illustrating α phosphate of adenosine triphosphate (αATP) values for each participant for each voxel calculated using methods A to E (detailed in method section of this chapter).
Only voxels located on motor regions are included in this figure. Voxel location is indicated above each graph. Index is illustrated in Figure 3.13.

Table 3.7 ANOVA tables illustrating multiple comparisons between method A and B (phasing in jMRUI), B and C (no apodisation Vs apodisation in jMRUI), C compared to D and C compared to E (analysis in jMRUI compared to analysis in SpectroView), and D compared to E (effect of different phasing in SpectroView) for α phosphate of adenosine triphosphate (αATP).

Relevant voxel indices are reported above each table as illustrated in Figure 3.13. CI: Confidence interval, diff: Difference, ns: Not significant, Vs: Versus.

a

Tukey's multiple comparisons test	Mean Diff.	95.00% CI of diff.	Significant?	Summary	Adjusted P Value
A vs. B	-0.0009908	-0.02994 to 0.02795	No	ns	>0.9999
B vs. C	0.0006183	-0.02833 to 0.02956	No	ns	>0.9999
C vs. D	-0.005727	-0.03467 to 0.02322	No	ns	0.9793
C vs. E	-0.01472	-0.04367 to 0.01422	No	ns	0.5981
D vs. E	-0.008997	-0.03794 to 0.01995	No	ns	0.8997

c

Tukey's multiple comparisons test	Mean Diff.	95.00% CI of diff.	Significant?	Summary	Adjusted P Value
A vs. B	-0.006453	-0.04066 to 0.02776	No	ns	0.9827
B vs. C	-0.006238	-0.04045 to 0.02797	No	ns	0.9847
C vs. D	0.03736	0.003149 to 0.07157	Yes	*	0.0263
C vs. E	0.02176	-0.01244 to 0.05597	No	ns	0.3783
D vs. E	-0.01559	-0.04980 to 0.01862	No	ns	0.6916

d

Tukey's multiple comparisons test	Mean Diff.	95.00% CI of diff.	Significant?	Summary	Adjusted P Value
A vs. B	-0.002532	-0.03594 to 0.03087	No	ns	0.9995
B vs. C	-0.01346	-0.04687 to 0.01994	No	ns	0.7786
C vs. D	0.02088	-0.01253 to 0.05428	No	ns	0.3962
C vs. E	0.0003901	-0.03302 to 0.03380	No	ns	>0.9999
D vs. E	-0.02049	-0.05389 to 0.01292	No	ns	0.4153

h

Tukey's multiple comparisons test	Mean Diff.	95.00% CI of diff.	Significant?	Summary	Adjusted P Value
A vs. B	-0.008865	-0.05249 to 0.03476	No	ns	0.9772
B vs. C	0.007518	-0.03611 to 0.05115	No	ns	0.9877
C vs. D	0.02442	-0.01921 to 0.06804	No	ns	0.5071
C vs. E	0.001359	-0.04227 to 0.04499	No	ns	>0.9999
D vs. E	-0.02306	-0.06668 to 0.02057	No	ns	0.5626

b

Tukey's multiple comparisons test	Mean Diff.	95.00% CI of diff.	Significant?	Summary	Adjusted P Value
A vs. B	-0.0031	-0.03385 to 0.02765	No	ns	0.9984
B vs. C	-0.01504	-0.04579 to 0.01571	No	ns	0.6329
C vs. D	0.01529	-0.01546 to 0.04603	No	ns	0.6189
C vs. E	0.01724	-0.01350 to 0.04799	No	ns	0.505
D vs. E	0.001959	-0.02879 to 0.03271	No	ns	0.9997

f

Tukey's multiple comparisons test	Mean Diff.	95.00% CI of diff.	Significant?	Summary	Adjusted P Value
A vs. B	-0.001264	-0.03323 to 0.03070	No	ns	>0.9999
B vs. C	-0.001037	-0.03300 to 0.03093	No	ns	>0.9999
C vs. D	-0.0007425	-0.03271 to 0.03122	No	ns	>0.9999
C vs. E	-0.008797	-0.04076 to 0.02317	No	ns	0.9332
D vs. E	-0.008055	-0.04002 to 0.02391	No	ns	0.9507

e

Tukey's multiple comparisons test	Mean Diff.	95.00% CI of diff.	Significant?	Summary	Adjusted P Value
A vs. B	0.00113	-0.01865 to 0.02091	No	ns	0.9998
B vs. C	0.0006509	-0.01913 to 0.02043	No	ns	>0.9999
C vs. D	-0.01348	-0.03326 to 0.006299	No	ns	0.3104
C vs. E	-0.01747	-0.03724 to 0.002312	No	ns	0.1058
D vs. E	-0.003987	-0.02377 to 0.01579	No	ns	0.9779

g

Tukey's multiple comparisons test	Mean Diff.	95.00% CI of diff.	Significant?	Summary	Adjusted P Value
A vs. B	-0.002422	-0.02828 to 0.02344	No	ns	0.9988
B vs. C	-0.003858	-0.02972 to 0.02200	No	ns	0.9929
C vs. D	0.02198	-0.003883 to 0.04784	No	ns	0.129
C vs. E	0.008955	-0.01690 to 0.03482	No	ns	0.8587
D vs. E	-0.01302	-0.03888 to 0.01284	No	ns	0.6074

j

Tukey's multiple comparisons test	Mean Diff.	95.00% CI of diff.	Significant?	Summary	Adjusted P Value
A vs. B	-0.006103	-0.02722 to 0.01501	No	ns	0.9212
B vs. C	0.001981	-0.01913 to 0.02310	No	ns	0.9988
C vs. D	-0.0055	-0.02661 to 0.01561	No	ns	0.9447
C vs. E	-0.008897	-0.03001 to 0.01222	No	ns	0.7494
D vs. E	-0.003397	-0.02451 to 0.01772	No	ns	0.9905

l

Tukey's multiple comparisons test	Mean Diff.	95.00% CI of diff.	Significant?	Summary	Adjusted P Value
A vs. B	-0.002225	-0.02492 to 0.02047	No	ns	0.9986
B vs. C	0.0003732	-0.02232 to 0.02307	No	ns	>0.9999
C vs. D	0.01203	-0.01067 to 0.03473	No	ns	0.5599
C vs. E	0.004676	-0.01802 to 0.02737	No	ns	0.976
D vs. E	-0.007353	-0.03005 to 0.01534	No	ns	0.8854

t

Tukey's multiple comparisons test	Mean Diff.	95.00% CI of diff.	Significant?	Summary	Adjusted P Value
A vs. B	0.0002216	-0.05481 to 0.05526	No	ns	>0.9999
B vs. C	-0.001873	-0.05691 to 0.05316	No	ns	>0.9999
C vs. D	-0.007078	-0.06211 to 0.04796	No	ns	0.9957
C vs. E	-0.007164	-0.06220 to 0.04787	No	ns	0.9955
D vs. E	-0.00008626	-0.05512 to 0.05495	No	ns	>0.9999

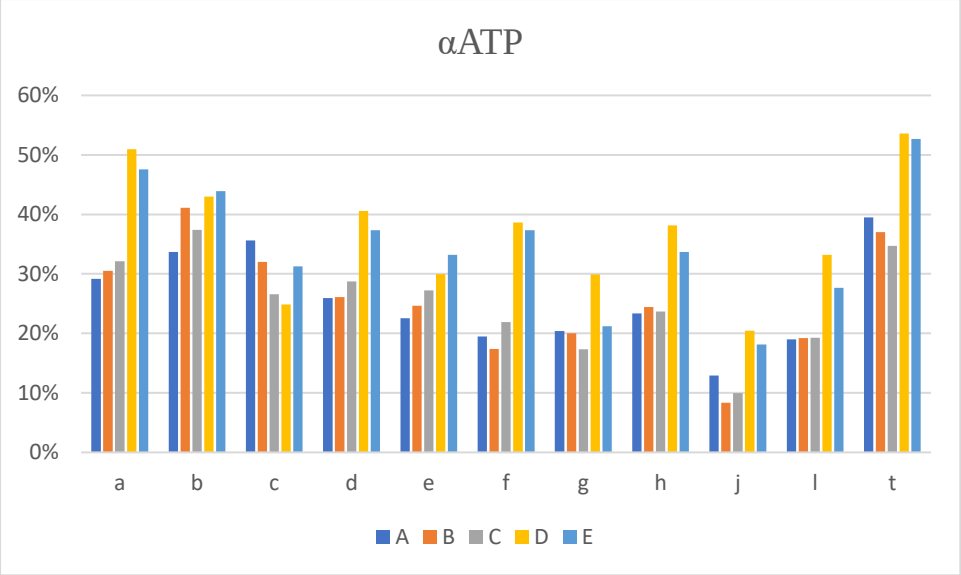

Figure 3.25 Coefficients of variability for α phosphate of adenosine triphosphate (αATP) calculated from voxels encompassing motor regions as depicted in Figure 3.13.
αATP is expressed as proportion of total phosphorus signal.

3.4.2.1.7 β Adenosine triphosphate

βATP mean values were equivalent in all tested protocols as no statistically significant differences were found in any of the assessed voxels. This is illustrated in Figure 3.26 and Table 3.8. CVs for βATP were elevated throughout the assessed voxels (the majority being over 30%). In addition, there did not appear to be any consistent difference in CVs with jMRUI analysis compared to SpectroView.

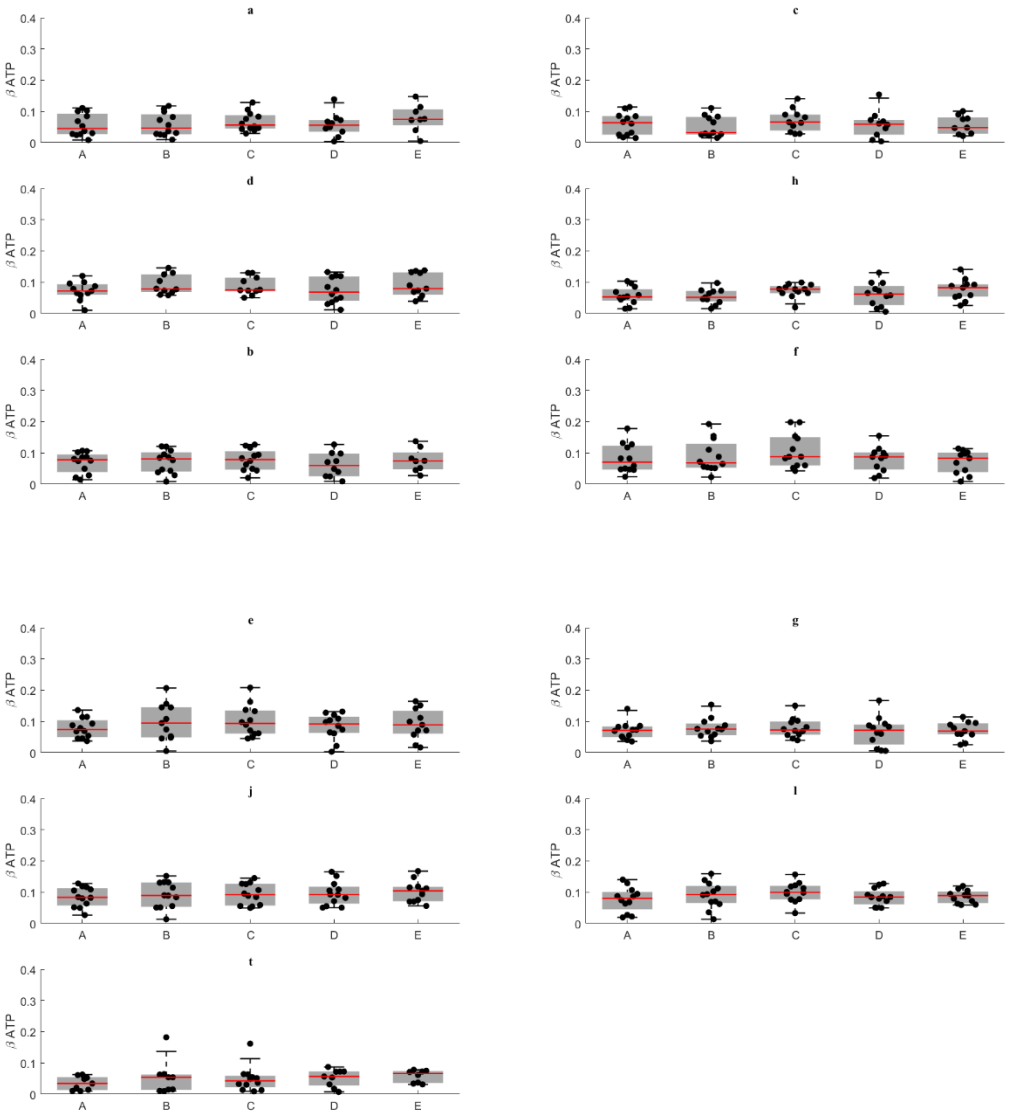

Figure 3.26 βATP Box and whisker plots illustrating β phosphate of adenosine triphosphate (βATP) values for each participant for each voxel calculated using methods A to E (detailed in method section of this chapter).
Only voxels located on motor regions are included in this figure. Voxel location is indicated above each graph. Index is illustrated in Figure 3.13.

Table 3.8 ANOVA tables illustrating multiple comparisons between method A and B (phasing in jMRUI), B and C (no apodisation Vs apodisation in jMRUI), C compared to D and C compared to E (analysis in jMRUI compared to analysis in SpectroView), and D compared to E (effect of different phasing in SpectroView) for β phosphate of adenosine triphosphate (βATP).

Relevant voxel indices are reported above each table as illustrated in Figure 3.13. CI: Confidence interval, diff: Difference, ns: Not significant, Vs: Versus.

a

Tukey's multiple comparisons test	Mean Diff.	95.00% CI of diff.	Summary	Adjusted P Value
A vs. B	-0.003257	-0.03272 to 0.02621	ns	0.9974
B vs. C	-0.00927	-0.03874 to 0.02020	ns	0.8837
C vs. D	0.005821	-0.02365 to 0.03529	ns	0.9765
C vs. E	-0.01873	-0.04820 to 0.01073	ns	0.358
D vs. E	-0.02456	-0.05402 to 0.004913	ns	0.1351

c

Tukey's multiple comparisons test	Mean Diff.	95.00% CI of diff.	Summary	Adjusted P Value
A vs. B	0.009713	-0.03574 to 0.05517	ns	0.9688
B vs. C	-0.02242	-0.06788 to 0.02303	ns	0.6009
C vs. D	0.02332	-0.02213 to 0.06877	ns	0.5654
C vs. E	0.005023	-0.04043 to 0.05048	ns	0.9974
D vs. E	-0.0183	-0.06375 to 0.02716	ns	0.7592

d

Tukey's multiple comparisons test	Mean Diff.	95.00% CI of diff.	Summary	Adjusted P Value
A vs. B	-0.0121	-0.04051 to 0.01632	ns	0.7284
B vs. C	0.005024	-0.02339 to 0.03344	ns	0.9851
C vs. D	0.01503	-0.01338 to 0.04345	ns	0.5454
C vs. E	-0.003775	-0.03219 to 0.02464	ns	0.995
D vs. E	-0.01881	-0.04722 to 0.009606	ns	0.3263

h

Tukey's multiple comparisons test	Mean Diff.	95.00% CI of diff.	Summary	Adjusted P Value
A vs. B	0.003929	-0.02531 to 0.03316	ns	0.9951
B vs. C	-0.021	-0.05023 to 0.008234	ns	0.2584
C vs. D	0.01673	-0.01250 to 0.04597	ns	0.4807
C vs. E	0.003697	-0.02554 to 0.03293	ns	0.9961
D vs. E	-0.01304	-0.04227 to 0.01620	ns	0.7048

b

Tukey's multiple comparisons test	Mean Diff.	95.00% CI of diff.	Summary	Adjusted P Value
A vs. B	-0.002516	-0.02926 to 0.02423	ns	0.9986
B vs. C	-0.009407	-0.03615 to 0.01734	ns	0.8361
C vs. D	0.01235	-0.01439 to 0.03910	ns	0.6572
C vs. E	-0.00848	-0.03522 to 0.01826	ns	0.8808
D vs. E	-0.02083	-0.04758 to 0.005909	ns	0.1811

f

Tukey's multiple comparisons test	Mean Diff.	95.00% CI of diff.	Summary	Adjusted P Value
A vs. B	-0.007629	-0.06328 to 0.04802	ns	0.9947
B vs. C	-0.02078	-0.07643 to 0.03486	ns	0.8194
C vs. D	0.03558	-0.02007 to 0.09123	ns	0.3697
C vs. E	0.03748	-0.01817 to 0.09313	ns	0.3187
D vs. E	0.001896	-0.05375 to 0.05754	ns	>0.9999

e

Tukey's multiple comparisons test	Mean Diff.	95.00% CI of diff.	Summary	Adjusted P Value
A vs. B	-0.01985	-0.06049 to 0.02080	ns	0.6305
B vs. C	-0.004599	-0.04525 to 0.03605	ns	0.9975
C vs. D	0.02562	-0.01503 to 0.06626	ns	0.3841
C vs. E	0.01767	-0.02298 to 0.05831	ns	0.7238
D vs. E	-0.007951	-0.04860 to 0.03269	ns	0.9797

g

Tukey's multiple comparisons test	Mean Diff.	95.00% CI of diff.	Summary	Adjusted P Value
A vs. B	-0.009016	-0.03234 to 0.01431	ns	0.8035
B vs. C	-0.0005688	-0.02390 to 0.02276	ns	>0.9999
C vs. D	0.01416	-0.009164 to 0.03749	ns	0.4255
C vs. E	0.009094	-0.01423 to 0.03242	ns	0.7985
D vs. E	-0.005068	-0.02840 to 0.01826	ns	0.9709

j

Tukey's multiple comparisons test	Mean Diff.	95.00% CI of diff.	Summary	Adjusted P Value
A vs. B	-0.004897	-0.01809 to 0.008294	ns	0.8255
B vs. C	-0.002908	-0.01610 to 0.01028	ns	0.9694
C vs. D	-0.00454	-0.01773 to 0.008651	ns	0.8614
C vs. E	-0.01209	-0.02528 to 0.001100	ns	0.0861
D vs. E	-0.007551	-0.02074 to 0.005640	ns	0.4846

l

Tukey's multiple comparisons test	Mean Diff.	95.00% CI of diff.	Summary	Adjusted P Value
A vs. B	-0.01248	-0.04550 to 0.02054	ns	0.816
B vs. C	-0.01071	-0.04373 to 0.02231	ns	0.885
C vs. D	0.01004	-0.02298 to 0.04307	ns	0.9066
C vs. E	0.00815	-0.02487 to 0.04117	ns	0.9542
D vs. E	-0.001895	-0.03492 to 0.03113	ns	0.9998

t

Tukey's multiple comparisons test	Mean Diff.	95.00% CI of diff.	Summary	Adjusted P Value
A vs. B	0.002891	-0.01897 to 0.02475	ns	0.9937
B vs. C	-0.003137	-0.02500 to 0.01872	ns	0.9915
C vs. D	-0.0162	-0.03806 to 0.005655	ns	0.2047
C vs. E	-0.0205	-0.04235 to 0.001363	ns	0.0716
D vs. E	-0.004293	-0.02615 to 0.01757	ns	0.9728

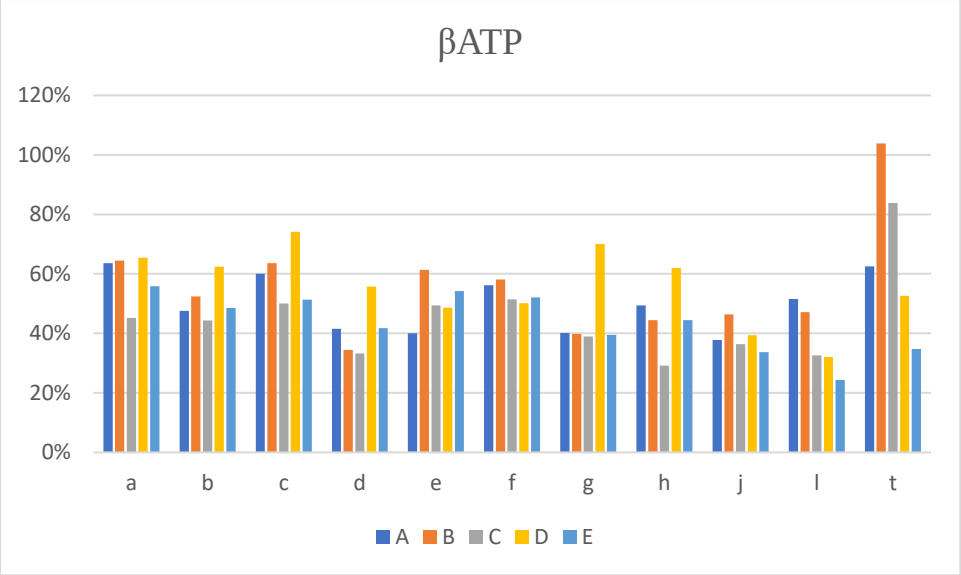

Figure 3.27 Coefficients of variability for β phosphate of adenosine triphosphate (βATP) calculated from voxels encompassing motor regions as depicted in Figure 3.13.
βATP is expressed as proportion of total phosphorus signal.

3.4.2.2 pH and Mg^{++}

The table below illustrates descriptive statistics for pH and Mg^{++} concentration (this latter expressed in mM) analysed using protocol A, B, and C. Of note, these parameters could not be calculated with SpectroView, hence protocols D and E were not testable.

There were no statistically significant differences between values derived from different analysis protocols with the exception of a weakly significant difference in pH between analysis B and C (testing the effects of apodisation) in *f* (p=0.048).

CVs of pH were below 1.5% whereas variability of Mg^{++} measurements was substantial with CVs around 40% in most voxels; phasing B returned values which were generally more variable compared to phasing A.

Table 3.9 Mean and standard deviations (SD), for voxels a to u as depicted in Figure 3.13 for pH and free magnesium concentration (Mg^{++}), this latter is expressed in millimolar (mM).

	a		***b***		***c***		***d***		***e***		***f***		***g***		***h***		***i***		***j***	
A	*mean*	*(±SD)*	*mean*	*(±SD)*	*mean*	*(±SD)*	*mean*	*(±SD)*	*mean*	*(±SD)*	*mean*	*(±SD)*	*mean*	*(±SD)*	*mean*	*(±SD)*	*mean*	*(±SD)*	*mean*	*(±SD)*
pH	7.042	0.025	7.071	0.068	7.069	0.100	7.057	0.089	7.010	0.036	7.021	0.026	7.035	0.036	7.033	0.034	7.069	0.058	7.028	0.048
Mg^{++}	0.137	0.048	0.150	0.045	0.110	0.053	0.118	0.044	0.104	0.043	0.107	0.035	0.100	0.041	0.121	0.058	0.116	0.041	0.108	0.029

	a		***b***		***c***		***d***		***e***		***f***		***g***		***h***		***i***		***j***	
B	*mean*	*(±SD)*	*mean*	*(±SD)*	*mean*	*(±SD)*	*mean*	*(±SD)*	*mean*	*(±SD)*	*mean*	*(±SD)*	*mean*	*(±SD)*	*mean*	*(±SD)*	*mean*	*(±SD)*	*mean*	*(±SD)*
pH	7.043	0.024	7.077	0.068	7.067	0.103	7.050	0.056	7.012	0.032	7.020	0.026	7.039	0.041	7.035	0.035	7.078	0.051	7.029	0.049
Mg^{++}	0.127	0.041	0.152	0.076	0.122	0.050	0.139	0.134	0.217	0.337	0.105	0.034	0.097	0.041	0.141	0.067	0.147	0.131	0.104	0.022

	a		***b***		***c***		***d***		***e***		***f***		***g***		***h***		***i***		***j***	
C	*mean*	*(±SD)*	*mean*	*(±SD)*	*mean*	*(±SD)*	*mean*	*(±SD)*	*mean*	*(±SD)*	*mean*	*(±SD)*	*mean*	*(±SD)*	*mean*	*(±SD)*	*mean*	*(±SD)*	*mean*	*(±SD)*
pH	7.050	0.027	7.079	0.066	7.074	0.095	7.060	0.087	7.016	0.040	7.031	0.035	7.042	0.041	7.033	0.031	7.080	0.049	7.029	0.049
Mg^{++}	0.126	0.045	0.139	0.054	0.112	0.041	0.140	0.099	0.108	0.039	0.103	0.033	0.099	0.040	0.127	0.067	0.118	0.037	0.103	0.022

	k		***l***		***m***		***n***		***o***		***p***		***q***		***r***		***s***		***t***		***u***	
A	*mean*	*(±SD)*	*mean*	*(±SD)*	*mean*	*(±SD)*	*mean*	*(±SD)*	*mean*	*(±SD)*	*mean*	*(±SD)*	*mean*	*(±SD)*	*mean*	*(±SD)*	*mean*	*(±SD)*	*mean*	*(±SD)*	*mean*	*(±SD)*
pH	7.044	0.081	7.037	0.021	7.034	0.039	7.119	0.114	7.087	0.075	7.079	0.049	7.067	0.034	7.117	0.101	7.087	0.094	7.112	0.087	7.165	0.169
Mg^{++}	0.108	0.027	0.099	0.037	0.117	0.050	0.114	0.042	0.098	0.020	0.104	0.043	0.095	0.033	0.103	0.058	0.149	0.071	0.133	0.068	0.179	0.296

	k		***l***		***m***		***n***		***o***		***p***		***q***		***r***		***s***		***t***		***u***	
B	*mean*	*(±SD)*	*mean*	*(±SD)*	*mean*	*(±SD)*	*mean*	*(±SD)*	*mean*	*(±SD)*	*mean*	*(±SD)*	*mean*	*(±SD)*	*mean*	*(±SD)*	*mean*	*(±SD)*	*mean*	*(±SD)*	*mean*	*(±SD)*
pH	7.046	0.081	7.037	0.024	7.034	0.047	7.133	0.105	7.085	0.064	7.082	0.050	7.068	0.036	7.094	0.080	7.061	0.112	7.113	0.088	7.101	0.100
Mg^{++}	0.102	0.027	0.102	0.036	0.142	0.041	0.137	0.062	0.094	0.023	0.097	0.036	0.107	0.048	0.118	0.075	0.300	0.566	0.134	0.080	0.161	0.079

	k		***l***		***m***		***n***		***o***		***p***		***q***		***r***		***s***		***t***		***u***	
C	*mean*	*(±SD)*	*mean*	*(±SD)*	*mean*	*(±SD)*	*mean*	*(±SD)*	*mean*	*(±SD)*	*mean*	*(±SD)*	*mean*	*(±SD)*	*mean*	*(±SD)*	*mean*	*(±SD)*	*mean*	*(±SD)*	*mean*	*(±SD)*
pH	7.046	0.078	7.041	0.026	7.043	0.040	7.139	0.112	7.096	0.077	7.088	0.048	7.070	0.039	7.093	0.076	7.075	0.101	7.113	0.079	7.128	0.148
Mg^{++}	0.099	0.026	0.090	0.031	0.149	0.049	0.136	0.055	0.096	0.023	0.086	0.035	0.104	0.071	0.111	0.050	0.112	0.068	0.100	0.060	0.160	0.096

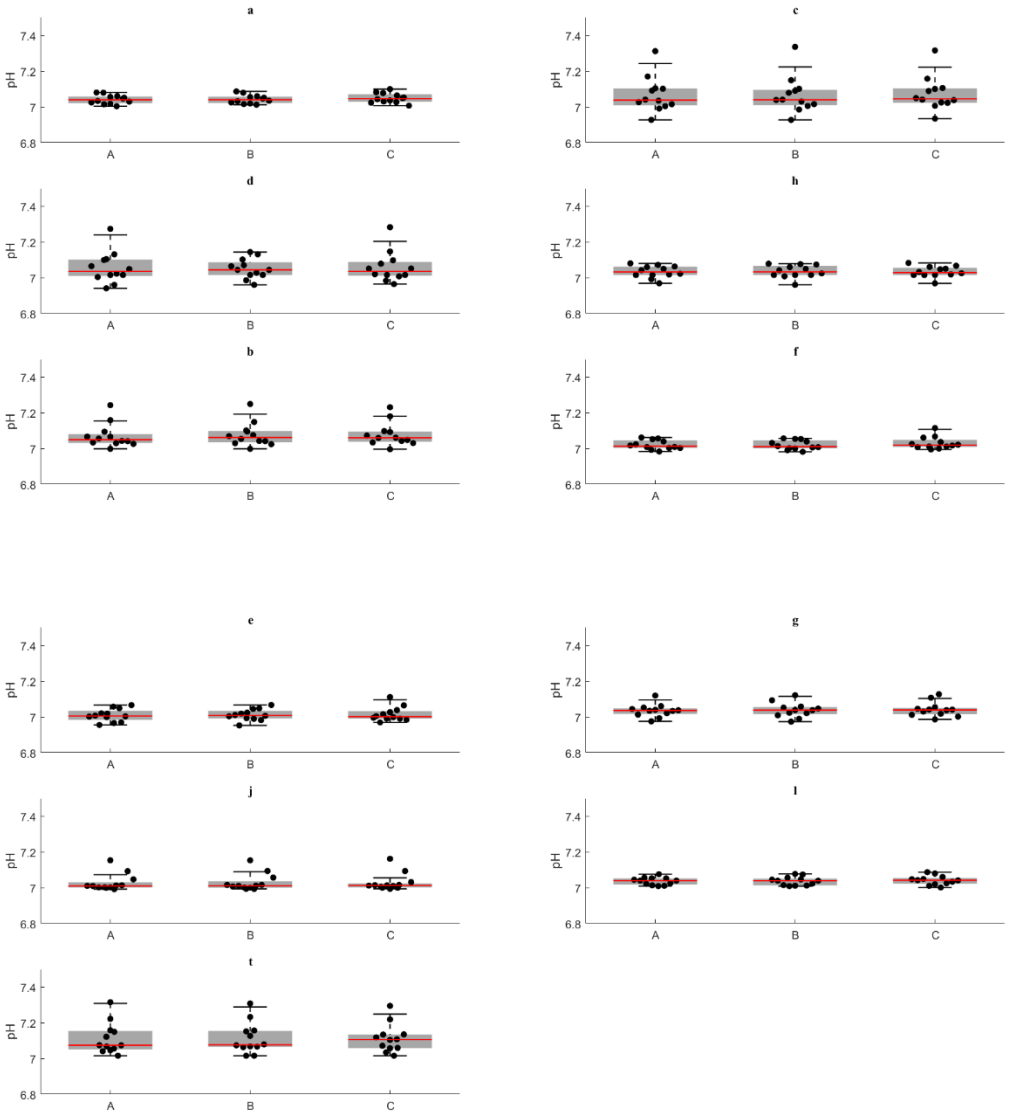

Figure 3.28 Box and whisker plots illustrating pH values for each participant for each voxel calculated using methods A to C (detailed in methods section of this chapter).
Only voxels located on motor regions are included in this figure. Voxel location is indicated above each graph. Index is illustrated in Figure 3.13.

Table 3.10 pH ANOVA tables illustrating multiple comparisons between method A and B (phasing in jMRUI) and B and C (no apodisation Vs apodisation in jMRUI) for pH.

Relevant voxel indices are reported above each table as illustrated in Figure 3.13. CI: Confidence interval, diff: Difference, ns: Not significant, Vs: Versus.

a

Tukey's multiple comparisons test	Mean Diff.	95.00% CI of diff.	Summary	Adjusted P Value
A vs. B	-0.001712	-0.01205 to 0.008624	ns	0.9094
A vs. C	-0.007838	-0.01817 to 0.002498	ns	0.161
B vs. C	-0.006126	-0.01646 to 0.004211	ns	0.3154

c

Tukey's multiple comparisons test	Mean Diff.	95.00% CI of diff.	Summary	Adjusted P Value
A vs. B	0.001689	-0.008023 to 0.01140	ns	0.9006
A vs. C	-0.005483	-0.01520 to 0.004229	ns	0.3491
B vs. C	-0.007172	-0.01688 to 0.002540	ns	0.1755

d

Tukey's multiple comparisons test	Mean Diff.	95.00% CI of diff.	Summary	Adjusted P Value
A vs. B	0.006337	-0.02016 to 0.03283	ns	0.8211
A vs. C	-0.002965	-0.02946 to 0.02353	ns	0.9574
B vs. C	-0.009302	-0.03580 to 0.01719	ns	0.6571

h

Tukey's multiple comparisons test	Mean Diff.	95.00% CI of diff.	Summary	Adjusted P Value
A vs. B	-0.001492	-0.008193 to 0.005208	ns	0.8427
A vs. C	0.0001632	-0.006537 to 0.006864	ns	0.9979
B vs. C	0.001655	-0.005045 to 0.008356	ns	0.8105

b

Tukey's multiple comparisons test	Mean Diff.	95.00% CI of diff.	Summary	Adjusted P Value
A vs. B	-0.006011	-0.01621 to 0.004183	ns	0.3189
A vs. C	-0.007446	-0.01764 to 0.002748	ns	0.1818
B vs. C	-0.001435	-0.01163 to 0.008759	ns	0.9336

f

Tukey's multiple comparisons test	Mean Diff.	95.00% CI of diff.	Summary	Adjusted P Value
A vs. B	0.001135	-0.009795 to 0.01206	ns	0.9633
A vs. C	-0.009865	-0.02079 to 0.001064	ns	0.0819
B vs. C	-0.011	-0.02193 to -7.036e-005	*	0.0483

e

Tukey's multiple comparisons test	Mean Diff.	95.00% CI of diff.	Summary	Adjusted P Value
A vs. B	-0.002111	-0.01446 to 0.01023	ns	0.9037
A vs. C	-0.006219	-0.01856 to 0.006126	ns	0.4289
B vs. C	-0.004108	-0.01645 to 0.008237	ns	0.6852

g

Tukey's multiple comparisons test	Mean Diff.	95.00% CI of diff.	Summary	Adjusted P Value
A vs. B	-0.003333	-0.01386 to 0.007196	ns	0.7098
A vs. C	-0.006598	-0.01713 to 0.003931	ns	0.2775
B vs. C	-0.003265	-0.01379 to 0.007264	ns	0.7195

j

Tukey's multiple comparisons test	Mean Diff.	95.00% CI of diff.	Summary	Adjusted P Value
A vs. B	-0.001336	-0.006781 to 0.004109	ns	0.8128
A vs. C	-0.001189	-0.006634 to 0.004257	ns	0.8484
B vs. C	0.0001473	-0.005298 to 0.005593	ns	0.9975

l

Tukey's multiple comparisons test	Mean Diff.	95.00% CI of diff.	Summary	Adjusted P Value
A vs. B	-0.0003943	-0.007296 to 0.006507	ns	0.9887
A vs. C	-0.00436	-0.01126 to 0.002542	ns	0.2722
B vs. C	-0.003965	-0.01087 to 0.002936	ns	0.3369

t

Tukey's multiple comparisons test	Mean Diff.	95.00% CI of diff.	Summary	Adjusted P Value
A vs. B	-0.001524	-0.01346 to 0.01042	ns	0.945
A vs. C	-0.0009708	-0.01291 to 0.01097	ns	0.9773
B vs. C	0.0005531	-0.01139 to 0.01249	ns	0.9926

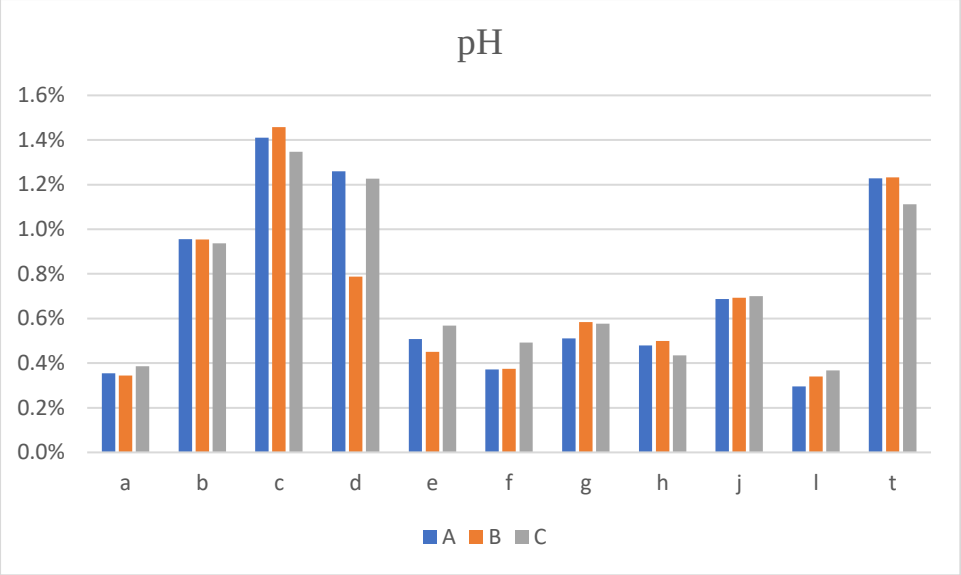

Figure 3.29 Coefficients of variability for pH calculated from voxels encompassing motor regions as depicted in Figure 3.13.

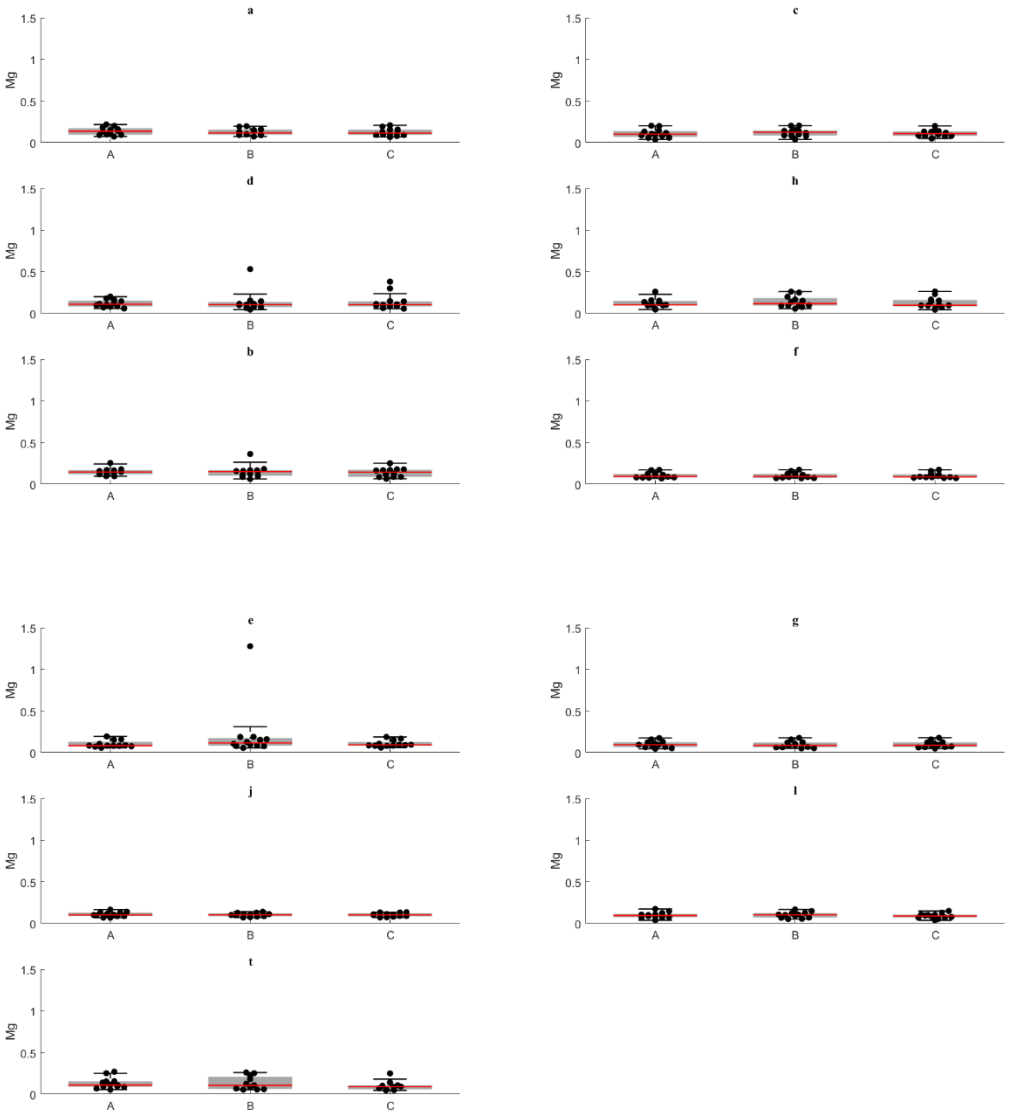

Figure 3.30 Box and whisker plots illustrating magnesium concentration (Mg) in millimolar (mM) calculated using methods A to C (detailed in method section of this chapter).
Only voxels located on motor regions are included in this figure. Voxel location is indicated above each graph. Index is illustrated in Figure 3.13.

Table 3.11 ANOVA tables illustrating multiple comparisons between method A and B (phasing in jMRUI) and B and C (no apodisation Vs apodisation in jMRUI) for free magnesium concentration.

Relevant voxel indices are reported above each table as illustrated in Figure 3.13. CI: Confidence interval, diff: Difference, ns: Not significant, Vs: Versus.

a

Tukey's multiple comparisons test	Mean Diff.	95.00% CI of diff.	Summary	Adjusted P Value
A vs. B	0.009748	-0.008516 to 0.02801	ns	0.3885
A vs. C	0.01086	-0.007407 to 0.02912	ns	0.3133
B vs. C	0.001109	-0.01715 to 0.01937	ns	0.9873

c

Tukey's multiple comparisons test	Mean Diff.	95.00% CI of diff.	Summary	Adjusted P Value
A vs. B	-0.01212	-0.04202 to 0.01779	ns	0.5737
A vs. C	-0.001816	-0.03172 to 0.02809	ns	0.9873
B vs. C	0.0103	-0.01961 to 0.04021	ns	0.6673

d

Tukey's multiple comparisons test	Mean Diff.	95.00% CI of diff.	Summary	Adjusted P Value
A vs. B	-0.02451	-0.1079 to 0.05891	ns	0.741
A vs. C	-0.01086	-0.09429 to 0.07257	ns	0.9421
B vs. C	0.01365	-0.06978 to 0.09708	ns	0.9103

h

Tukey's multiple comparisons test	Mean Diff.	95.00% CI of diff.	Summary	Adjusted P Value
A vs. B	-0.009471	-0.04558 to 0.02664	ns	0.787
A vs. C	0.003878	-0.03224 to 0.03999	ns	0.9602
B vs. C	0.01335	-0.02276 to 0.04946	ns	0.625

b

Tukey's multiple comparisons test	Mean Diff.	95.00% CI of diff.	Summary	Adjusted P Value
A vs. B	-0.001753	-0.02942 to 0.02591	ns	0.9859
A vs. C	0.01275	-0.01491 to 0.04042	ns	0.4862
B vs. C	0.01451	-0.01316 to 0.04217	ns	0.3973

f

Tukey's multiple comparisons test	Mean Diff.	95.00% CI of diff.	Summary	Adjusted P Value
A vs. B	0.001656	-0.009022 to 0.01234	ns	0.92
A vs. C	0.003963	-0.006716 to 0.01464	ns	0.6262
B vs. C	0.002306	-0.008373 to 0.01298	ns	0.8513

e

Tukey's multiple comparisons test	Mean Diff.	95.00% CI of diff.	Summary	Adjusted P Value
A vs. B	-0.1133	-0.3157 to 0.08918	ns	0.3554
A vs. C	-0.004078	-0.2065 to 0.1984	ns	0.9986
B vs. C	0.1092	-0.09325 to 0.3117	ns	0.381

g

Tukey's multiple comparisons test	Mean Diff.	95.00% CI of diff.	Summary	Adjusted P Value
A vs. B	0.003024	-0.003867 to 0.009914	ns	0.5227
A vs. C	0.0007827	-0.006108 to 0.007673	ns	0.9562
B vs. C	-0.002241	-0.009132 to 0.004650	ns	0.6967

j

Tukey's multiple comparisons test	Mean Diff.	95.00% CI of diff.	Summary	Adjusted P Value
A vs. B	0.004235	-0.007469 to 0.01594	ns	0.6405
A vs. C	0.005139	-0.006565 to 0.01684	ns	0.5224
B vs. C	0.0009039	-0.01080 to 0.01261	ns	0.9795

l

Tukey's multiple comparisons test	Mean Diff.	95.00% CI of diff.	Summary	Adjusted P Value
A vs. B	-0.002722	-0.01998 to 0.01453	ns	0.9174
A vs. C	0.008851	-0.008403 to 0.02610	ns	0.4162
B vs. C	0.01157	-0.005680 to 0.02883	ns	0.2332

t

Tukey's multiple comparisons test	Mean Diff.	95.00% CI of diff.	Summary	Adjusted P Value
A vs. B	-0.008358	-0.04998 to 0.03326	ns	0.8663
A vs. C	0.01681	-0.02481 to 0.05843	ns	0.5676
B vs. C	0.02517	-0.01645 to 0.06679	ns	0.2951

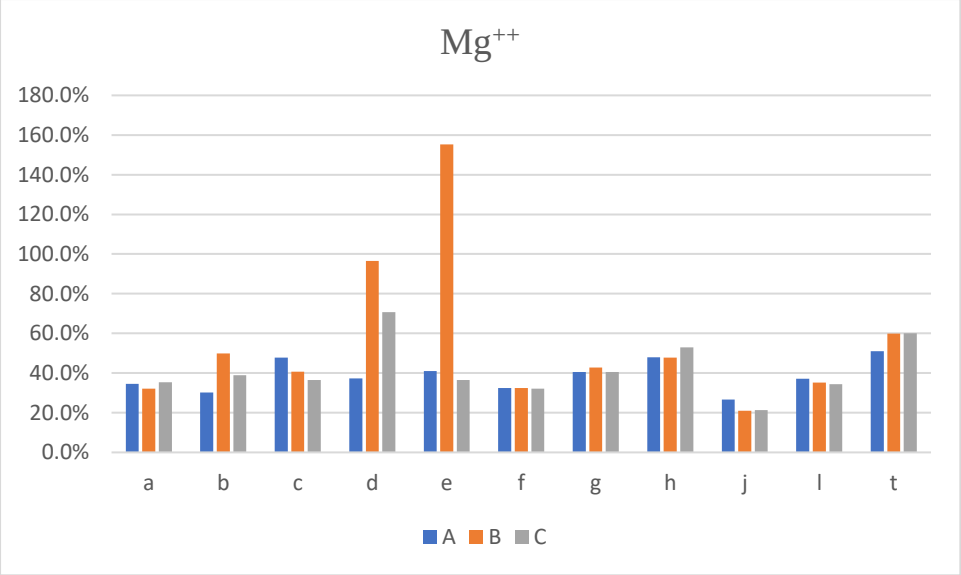

Figure 3.31 Coefficients of variability for free magnesium (Mg^{++}) calculated from voxels encompassing motor regions as depicted in Figure 3.13.

3.4.3 Quality control

Of all analysed data (264 spectra), 11 (4%) PME peaks could not be fitted with SpectroView. These data were located in voxels *r*, *s*, *t*, and *u*. Nine (3%) Pi peaks could not be fitted with SpectroView, all located in basal regions (*s*, *t*, and *u*). Fifteen (6%) PDE peaks could not be fitted with SpectroView and one (0.4%) with jMRUI. All (100%) PCr peaks could be fitted. Six (2%) γATP peaks could not be fitted with SpectroView (all located in basal voxels) and two (1%) in jMRUI (located in the left temporal lobe voxel). Nine (3%) αATP peaks could not be fitted in SpectroView, all located in basal voxels. Twenty-nine (11%) βATP peaks could not be fitted with SpectroView, whereas 54 (20%) βATP were not fitted with jMRUI; non-fitted peaks were found primarily in cortical regions and brainstem. pH values were calculated in all cases (100%) in jMRUI. Mg^{++} could not be calculated in 16 (6%) jMRUI spectra.

Mean CRLB of spectra (CRLB PCr), pH, and Mg^{++} are reported below for all analysed voxels and individual participant values are illustrated in scatter plots in Figure 3.32 to Figure 3.34. Across all voxels, individual CRLB of spectra (PCr) and pH were well below the 30% threshold for all spectra; whereas, 39 individual CRLB of Mg^{++} were above 30%, these spectra were not located in voxels encompassing motor regions.

Table 3.12 Mean Cramer-Rao lower bounds (CRLB-expressed in %) of spectra (CRLB PCr), of pH (CRLB pH), and of free magnesium concentration (CRLB Mg^{++}) for voxels a to u as depicted in Figure 3.13.

A	*a*	*b*	*c*	*d*	*e*	*f*	*g*	*h*	*i*	*j*	*k*	*l*	*m*	*n*	*o*	*p*	*q*	*r*	*s*	*t*	*u*
CRLB PCr	9.8%	7.8%	9.1%	8.8%	7.0%	6.4%	7.4%	8.7%	9.2%	7.5%	7.2%	7.2%	8.5%	16.7%	10.4%	8.3%	9.7%	16.4%	18.9%	11.5%	12.6%
CRLB pH	1.5%	1.6%	2.0%	1.5%	1.4%	1.2%	1.4%	1.5%	2.9%	1.6%	1.4%	1.5%	2.3%	3.0%	2.2%	1.8%	1.8%	2.7%	3.0%	3.2%	2.6%
CRLB Mg^{++}	7.2%	22.1%	12.0%	14.0%	12.9%	17.7%	11.4%	9.4%	11.0%	11.8%	11.3%	8.3%	16.9%	15.9%	13.6%	8.8%	9.9%	17.1%	17.6%	9.7%	8.4%

B	*a*	*b*	*c*	*d*	*e*	*f*	*g*	*h*	*i*	*j*	*k*	*l*	*m*	*n*	*o*	*p*	*q*	*r*	*s*	*t*	*u*
CRLB PCr	9.7%	7.9%	9.1%	9.4%	7.3%	6.6%	7.6%	8.9%	9.5%	7.6%	7.3%	6.9%	7.6%	19.8%	11.0%	8.4%	10.0%	16.2%	19.8%	11.9%	13.4%
CRLB pH	1.6%	1.6%	2.0%	2.5%	1.5%	1.1%	1.4%	1.3%	2.8%	1.6%	1.4%	1.5%	1.5%	3.1%	2.1%	1.8%	1.8%	3.4%	2.7%	3.3%	3.3%
CRLB Mg^{++}	7.7%	23.4%	7.4%	13.3%	17.5%	16.0%	12.6%	7.4%	12.6%	12.4%	13.1%	13.9%	19.2%	21.5%	15.7%	8.5%	9.5%	11.1%	56.9%	8.5%	86.8%

C	*a*	*b*	*c*	*d*	*e*	*f*	*g*	*h*	*i*	*j*	*k*	*l*	*m*	*n*	*o*	*p*	*q*	*r*	*s*	*t*	*u*
CRLB PCr	5.4%	4.7%	5.3%	5.5%	5.0%	4.3%	5.0%	5.4%	5.2%	4.4%	4.3%	4.1%	4.3%	9.9%	6.4%	4.9%	5.7%	9.8%	11.1%	6.7%	6.7%
CRLB pH	2.3%	2.0%	2.4%	2.9%	1.8%	1.6%	1.7%	2.0%	3.3%	2.0%	1.8%	1.8%	2.6%	4.6%	3.1%	2.4%	2.4%	4.6%	4.1%	4.1%	3.6%
CRLB Mg^{++}	14.3%	26.9%	15.3%	17.7%	30.6%	25.7%	16.3%	14.9%	17.8%	16.0%	18.7%	20.5%	23.6%	26.0%	19.9%	15.9%	16.0%	20.7%	31.3%	21.4%	15.5%

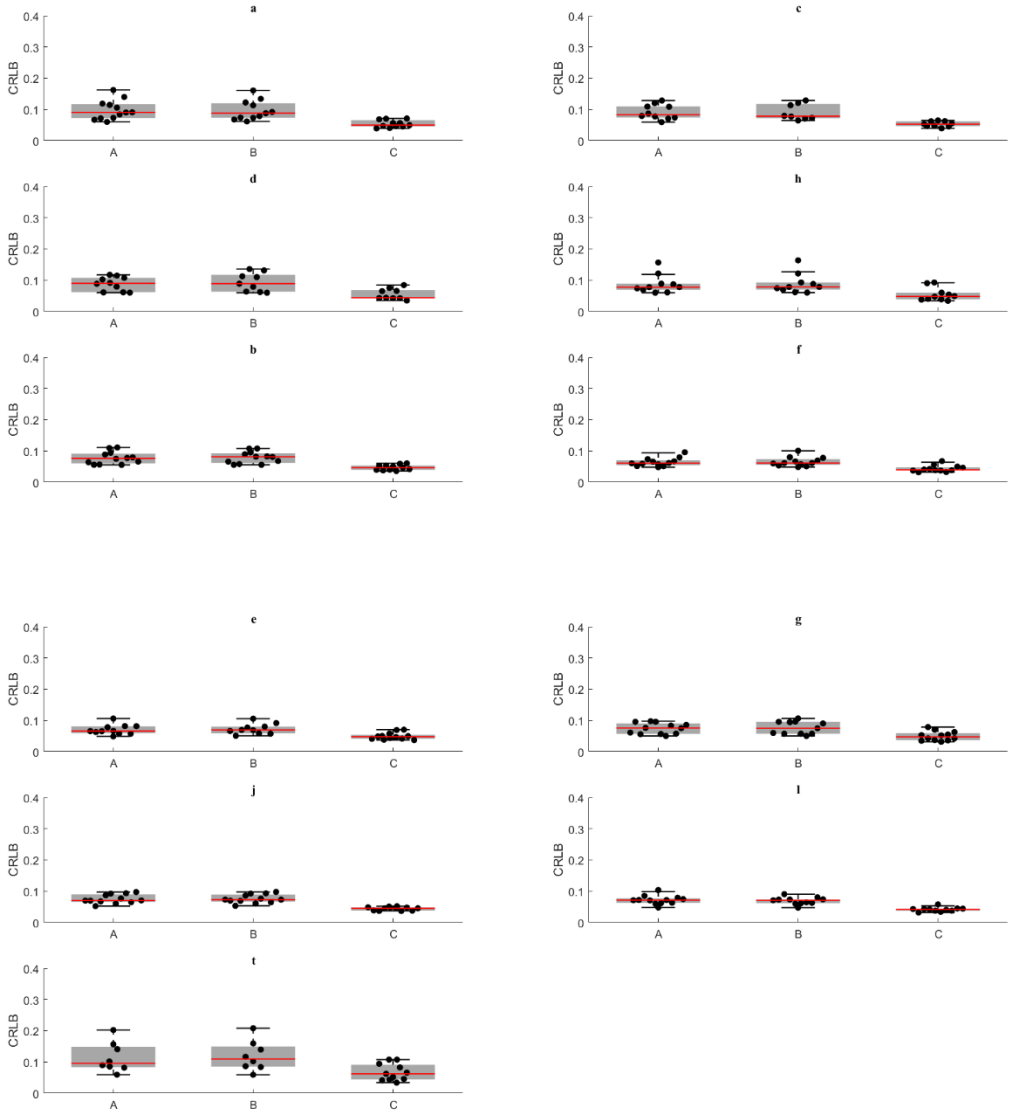

Figure 3.32 Cramer-Rao lower bounds (CRLB) of spectra (expressed as a proportion rather than a percentage) for each participant using method A to C (detailed in method section of this chapter) and for each voxel located in motor regions (as depicted in Figure 3.13).

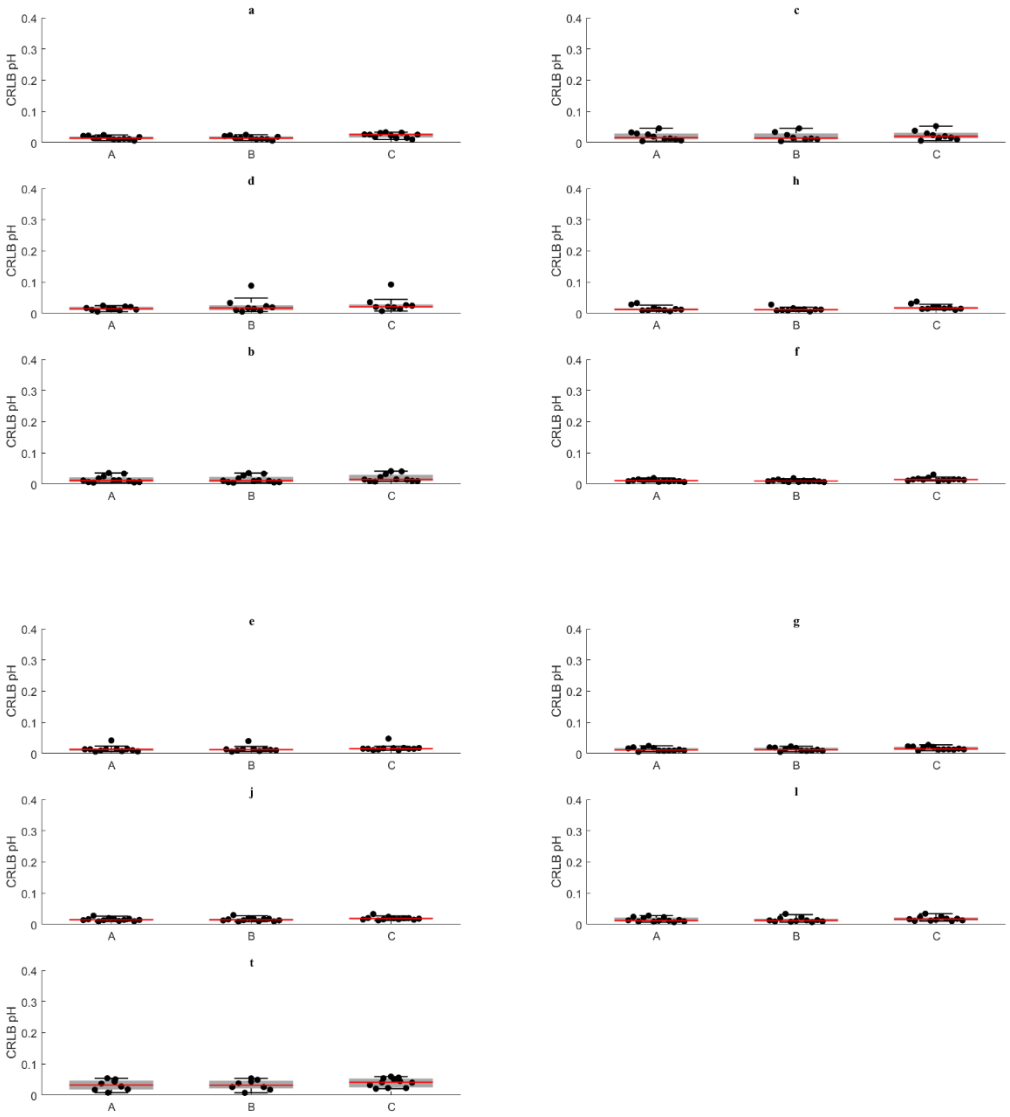

Figure 3.33 Cramer-Rao lower bounds (CRLB) of pH (expressed as a proportion rather than a percentage) for each participant using method A to C (detailed in method section of this chapter) and for each voxel located in motor regions (as depicted in Figure 3.13).

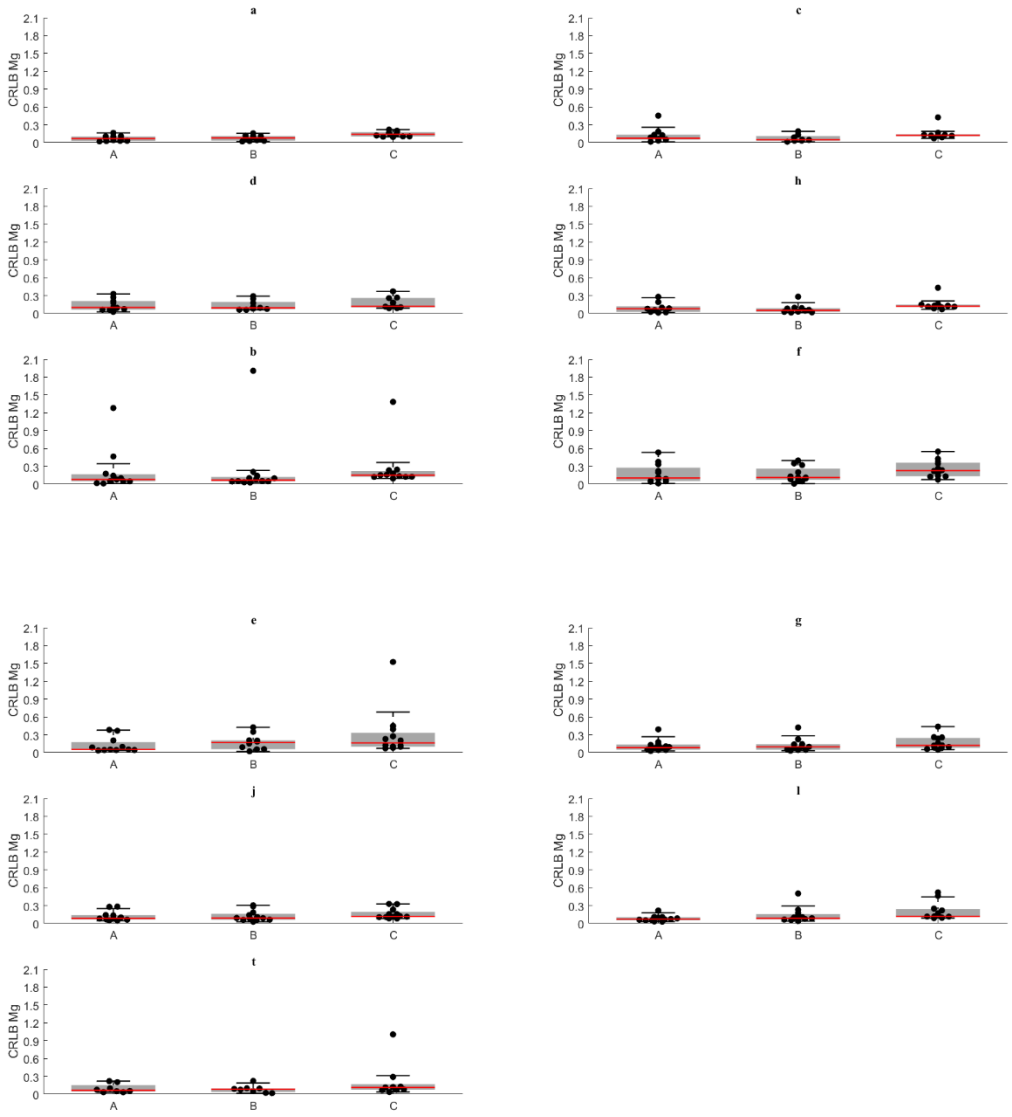

Figure 3.34 Cramer-Rao lower bounds (CRLB) of Mg^{++} (expressed as a proportion rather than a percentage) for each participant using method A to C (detailed in method section of this chapter) and for each voxel located in motor regions (as depicted in Figure 3.13).

3.4.4 Reliability: ICC

ICC results for voxels encompassing motor tracts are summarised in tables below. Specifically, reliability analysis for different phasing methods in jMRUI are summarised in Table 3.13 and for different phasing methods in SpectroView in Table 3.14. ICCs calculated for all brain voxels are reported in the appendix, as well as ICC comparing iMRUI and SpectroView analysis (protocol C and D).

In jMRUI, reliability of amplitudes was very good as ICC were above 60% for all amplitudes except for βATP which showed low reliability especially in voxels *f*, *h*, and *t*. ICCs for pH were excellent (all

above 90% except for voxel *d*, which was 84%). Reliability of Mg^{++} measurements was generally lower, as ICCs were lower than 60% in four voxels (*d*, *e*, *h*, and *t*).

ICCs calculated for analysis in SpectroView were generally lower compared to jMRUI with a greater proportion of ICCs below 80% (15 in jMRUI compared to 29 in SpectroView).

Table 3.13 Comparison of phasing methods in jMRUI. ICC calculated from protocol A and B, as detailed in this chapter's methods.
Motor voxels are illustrated in Figure 3.13. Colour legend is illustrated below table.

	a	***b***	***c***	***d***	***e***	***f***	***g***	***h***	***j***	***l***	***t***
PME	94.5%	86.5%	98.8%	91.6%	97.7%	81.4%	75.7%	82.9%	92.7%	96.4%	98.8%
Pi	99.8%	95.9%	99.2%	69.4%	94.0%	80.2%	94.6%	98.3%	98.8%	93.6%	98.0%
PDE	96.9%	92.5%	82.0%	81.9%	96.3%	92.4%	86.0%	94.7%	85.6%	64.8%	94.2%
PCr	93.3%	90.5%	85.7%	92.3%	88.9%	83.0%	81.2%	91.6%	95.0%	94.7%	98.4%
γATP	98.7%	88.1%	88.3%	79.7%	89.8%	81.7%	90.8%	94.5%	95.1%	94.0%	94.4%
αATP	99.4%	72.4%	97.3%	94.2%	96.0%	91.9%	97.8%	64.2%	68.1%	98.1%	98.7%
βATP	99.5%	60.7%	74.2%	71.3%	69.6%	-0.9%	92.8%	49.3%	92.8%	62.1%	-5.8%

	a	***b***	***c***	***d***	***e***	***f***	***g***	***h***	***j***	***l***	***t***
pH	99.0%	96.8%	99.3%	83.6%	96.4%	97.6%	92.6%	98.3%	99.6%	93.8%	99.3%
Mg^{++}	84.1%	80.3%	75.3%	-12.8%	-1.2%	85.0%	97.2%	53.6%	80.6%	90.6%	59.7%

Legend
≤ 0.0%
0.1% - 59.9%
60.0% - 69.9%
70.0% - 79.9%
≥80.0%

Table 3.14 Comparison of phasing methods in SpectroView. ICC calculated from protocol D and E, as detailed in this chapter's methods.
Motor voxels are illustrated in Figure 3.13. Colour legend is illustrated below table.

	a	***b***	***c***	***d***	***e***	***f***	***g***	***h***	***j***	***l***	***t***
PME	69.1%	91.1%	89.1%	90.5%	90.3%	91.2%	87.4%	95.0%	93.3%	88.9%	79.8%
Pi	87.6%	74.3%	93.4%	94.0%	2.4%	97.2%	66.7%	81.5%	80.8%	92.1%	92.4%
PDE	78.9%	59.3%	95.7%	63.8%	98.4%	99.4%	73.3%	65.8%	81.3%	94.1%	99.0%
PCr	77.6%	68.3%	94.1%	58.3%	66.8%	97.9%	75.1%	82.4%	87.6%	97.7%	98.5%
γATP	89.9%	94.0%	76.2%	89.0%	81.3%	98.8%	89.3%	68.1%	78.0%	93.5%	98.1%
αATP	96.0%	87.7%	68.5%	77.2%	92.7%	96.3%	81.3%	69.7%	72.9%	94.4%	99.0%
βATP	75.4%	76.8%	55.5%	70.3%	93.3%	75.9%	68.8%	63.8%	92.2%	81.4%	86.9%

Legend
≤ 0.0%
0.1% - 59.9%
60.0% - 69.9%
70.0% - 79.9%
≥80.0%

3.4.5 Agreement: Bland-Altman plots

Agreement parameters between repeated measurements following rephasing in both jMRUI (analysis A and B, graphs on the left-hand side) and SpectroView (analysis D and E, graphs on the right-hand side) are reported in the Bland-Altman plots below. On the y-axis, the difference is expressed as percentage of the mean. Agreement for measurement acquired with jMRUI was excellent (upper and lower limits of agreement - ULOA and LLOA - equivalent to approximately 25%) for Pi[18], PCr, and γATP, with slightly higher ranges (albeit still good agreement, with limits of agreement within 50%) for PME, PDE, and αATP. βATP had very poor agreement, with limits of agreement reaching 100% in some voxels (*b*, *c*, *e*, *f*, *l*, and *t*).

Agreement measures for SpectroView data were lower compared to jMRUI with limits of agreement over 50% in four voxels for PME, three voxels for Pi, and four voxels for PDE. As for jMRUI, βATP repeated measures also had poor agreement in SpectroView.

No systematic bias was detected.

[18] Except for voxel *d*, corresponding to a right-sided cortical region.

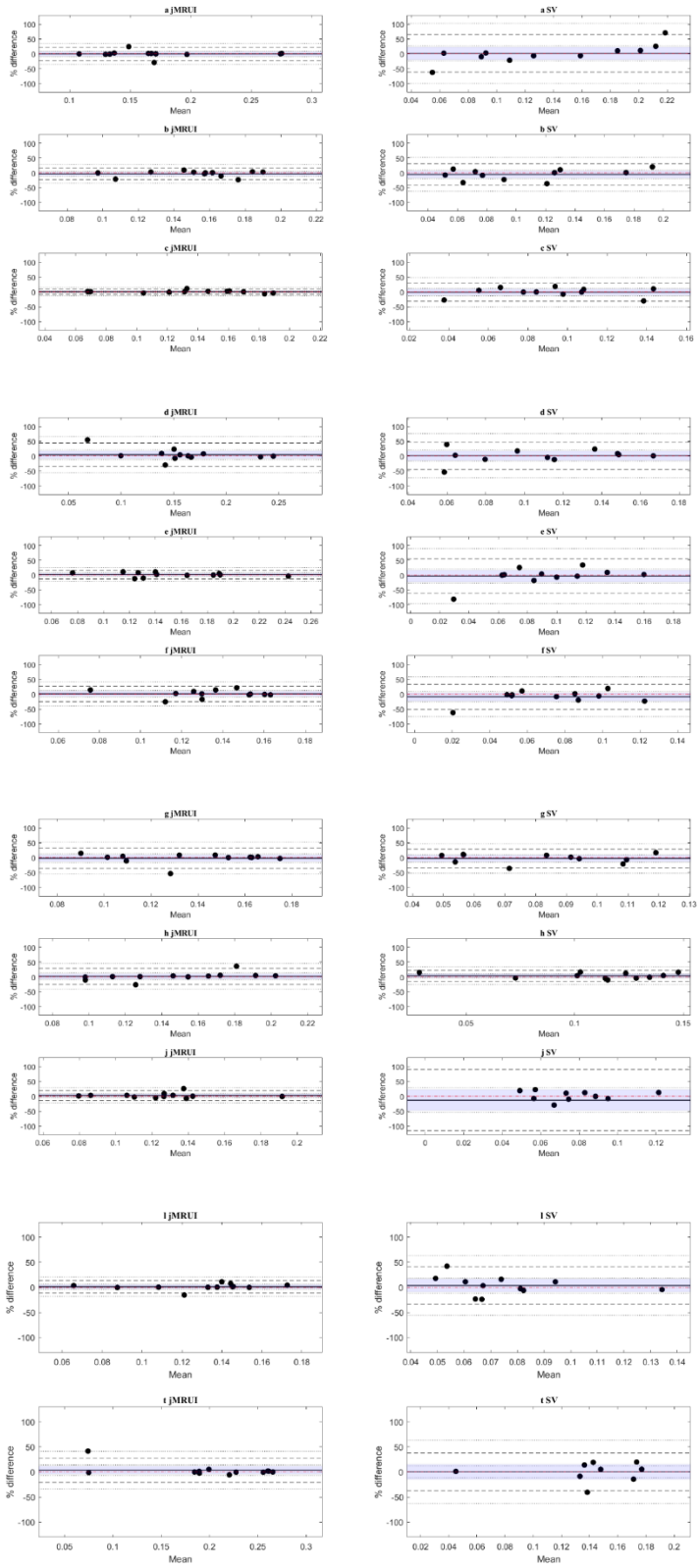

Figure 3.35 Bland-Altman plots illustrating agreement parameters for phosphomonoesters (PMEs) for repeated measurements (alternative phasing method) conducted in jMRUI (column on the left) and SpectroView (SV column on the right).

Voxels are indexed as illustrated in Figure 3.13. Details on the interpretation of Bland-Altman plots are found in this chapter's introduction

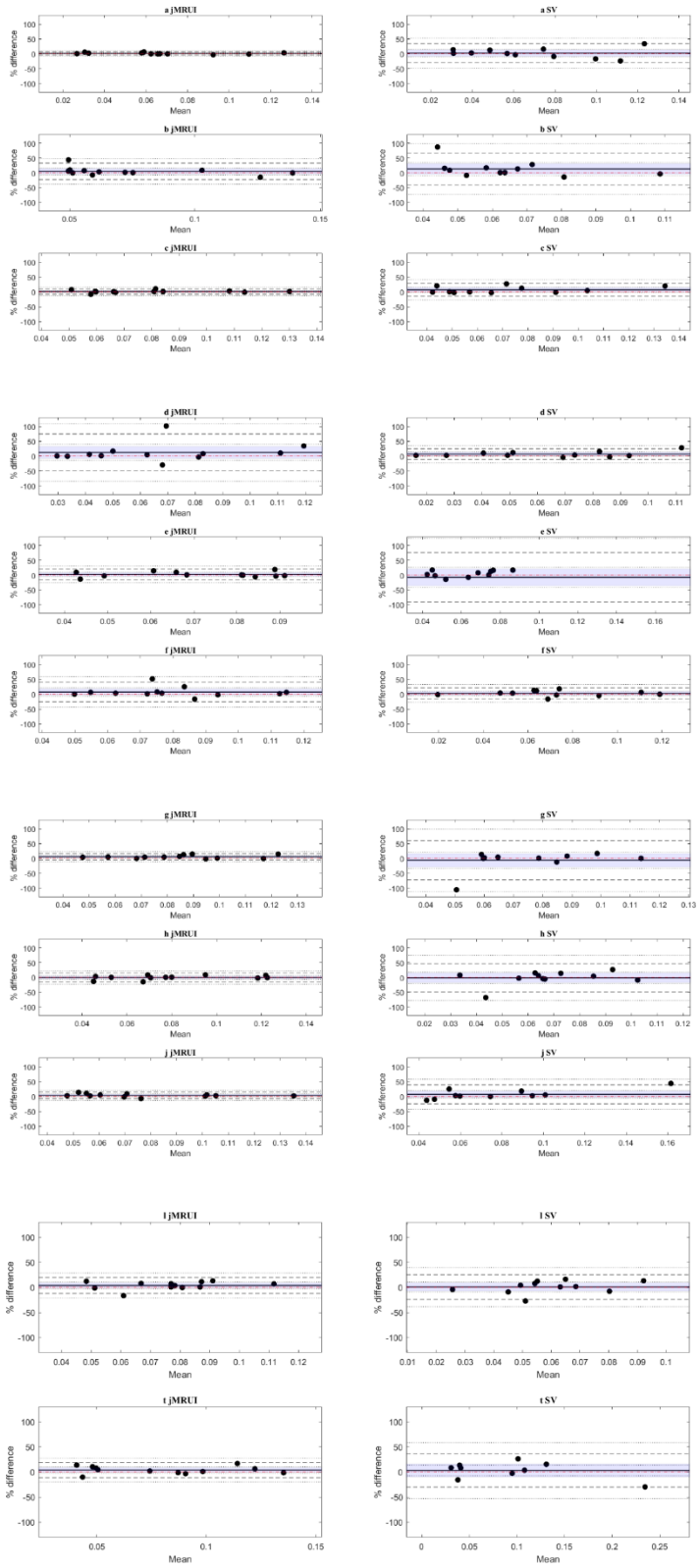

Figure 3.36 Bland-Altman plots illustrating agreement parameters form inorganic phosphate (Pi) for repeated measurements (with alternative phasing method) conducted in jMRUI (column on the left) and SpectroView (SV column on the right).

Voxels are indexed as illustrated in Figure 3.13. Details on the interpretation of Bland-Altman plots are found in this chapter's introduction

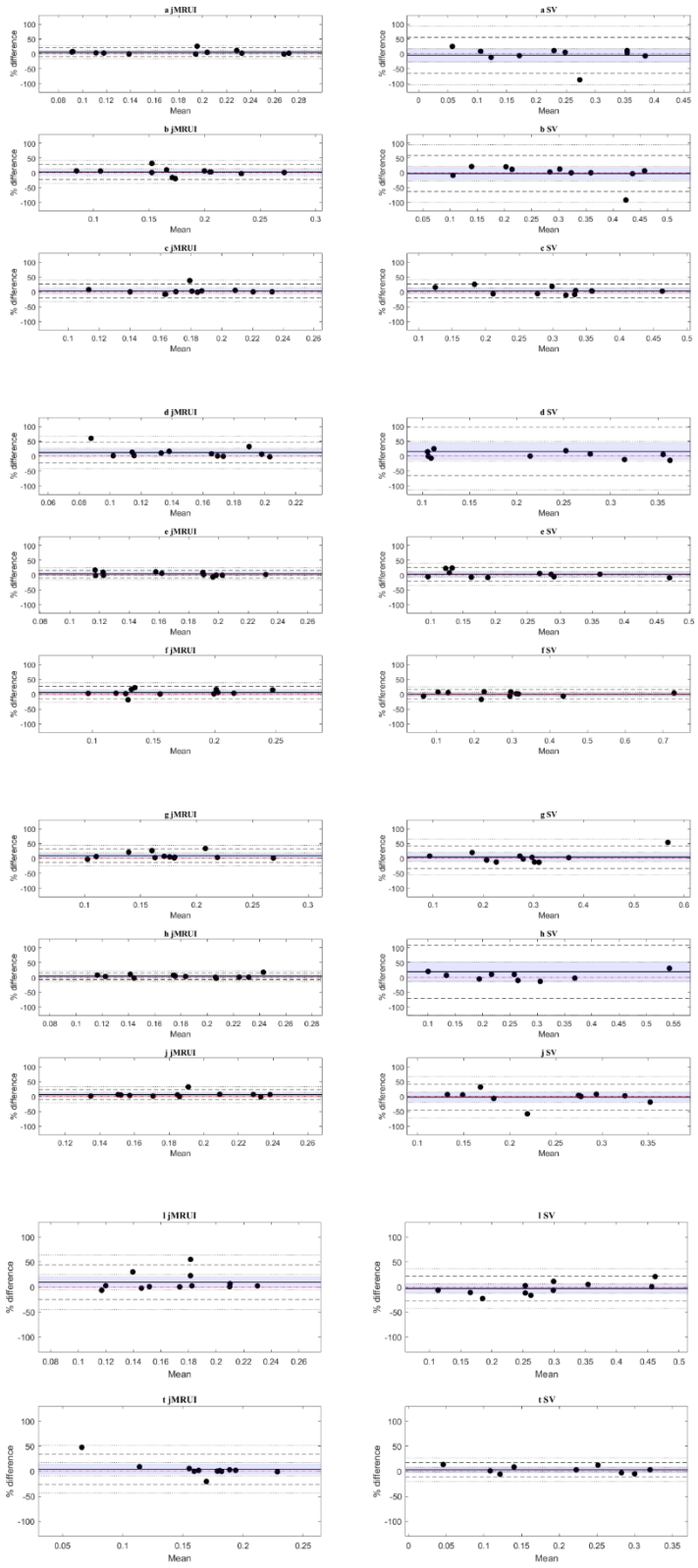

Figure 3.37 Bland-Altman plots illustrating agreement parameters form phosphodiesters (PDEs) for repeated measurements (with alternative phasing method) conducted in jMRUI (column on the left) and SpectroView (SV column on the right).

Voxels are indexed as illustrated in Figure 3.13. Details on the interpretation of Bland-Altman plots are found in this chapter's introduction

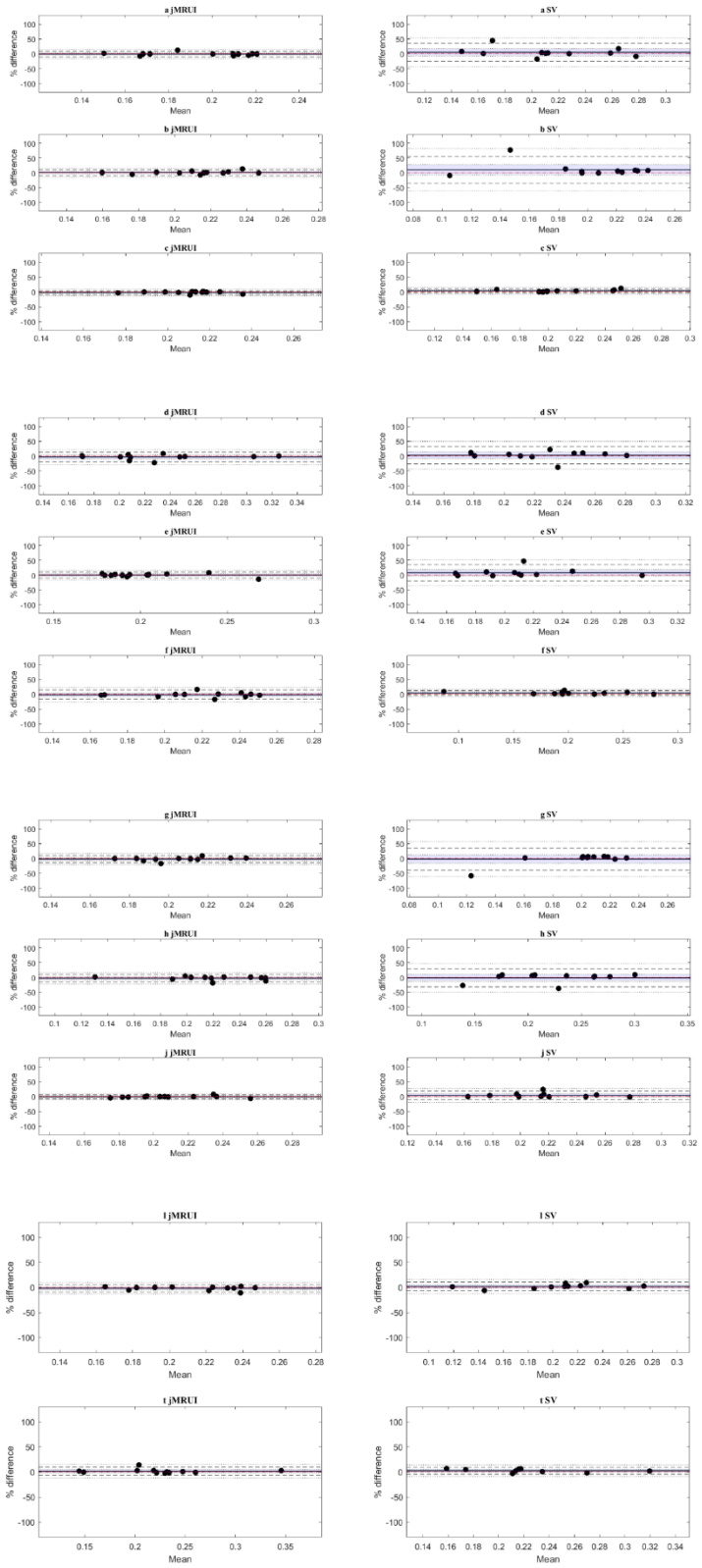

Figure 3.38 Bland-Altman plots illustrating agreement parameters form phosphocreatine (PCr) for repeated measurements (with alternative phasing method) conducted in jMRUI (column on the left) and SpectroView (SV column on the right). *Voxels are indexed as illustrated in Figure 3.13. Details on the interpretation of Bland-Altman plots are found in this chapter's introduction*

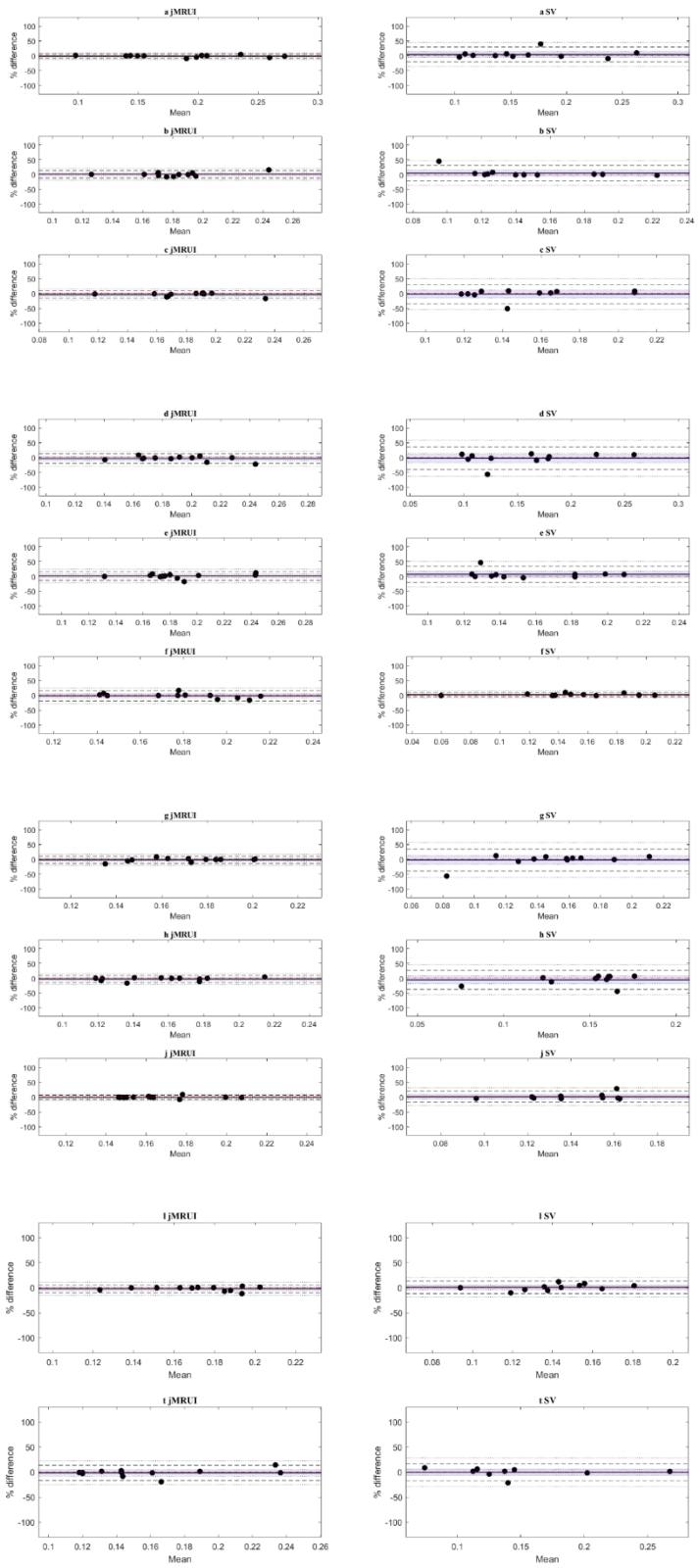

Figure 3.39 Bland-Altman plots illustrating agreement parameters form γ phosphate of adenosine diphosphate (γATP) for repeated measurements (with alternative phasing method) conducted in jMRUI (column on the left) and SpectroView (SV column on the right).
Voxels are indexed as illustrated in Figure 3.13. Details on the interpretation of Bland-Altman plots are found in this chapter's introduction.

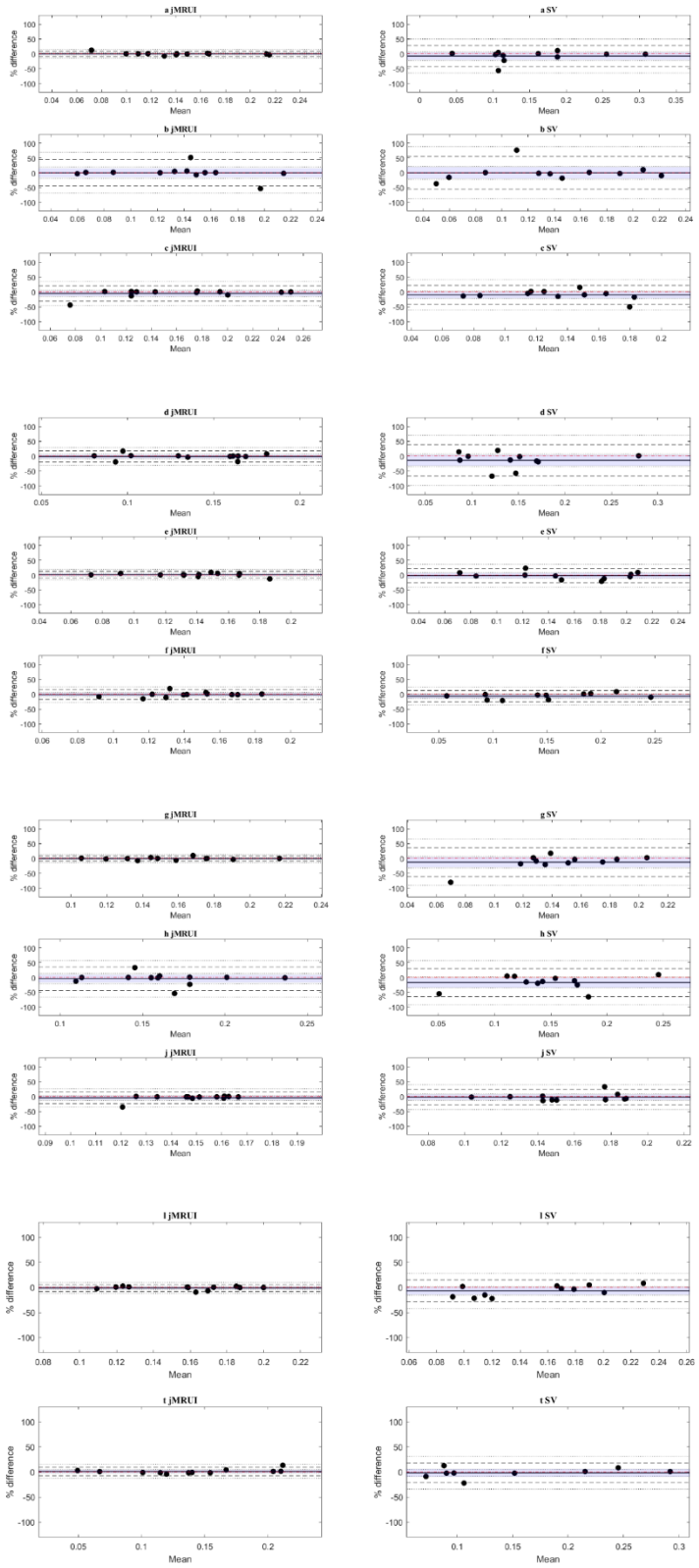

Figure 3.40 Bland-Altman plots illustrating agreement parameters form α phosphate of adenosine diphosphate (αATP) for repeated measurements (with alternative phasing method) conducted in jMRUI (column on the left) and SpectroView (SV column on the right).
Voxels are indexed as illustrated in Figure 3.13. Details on the interpretation of Bland-Altman plots are found in this chapter's introduction.

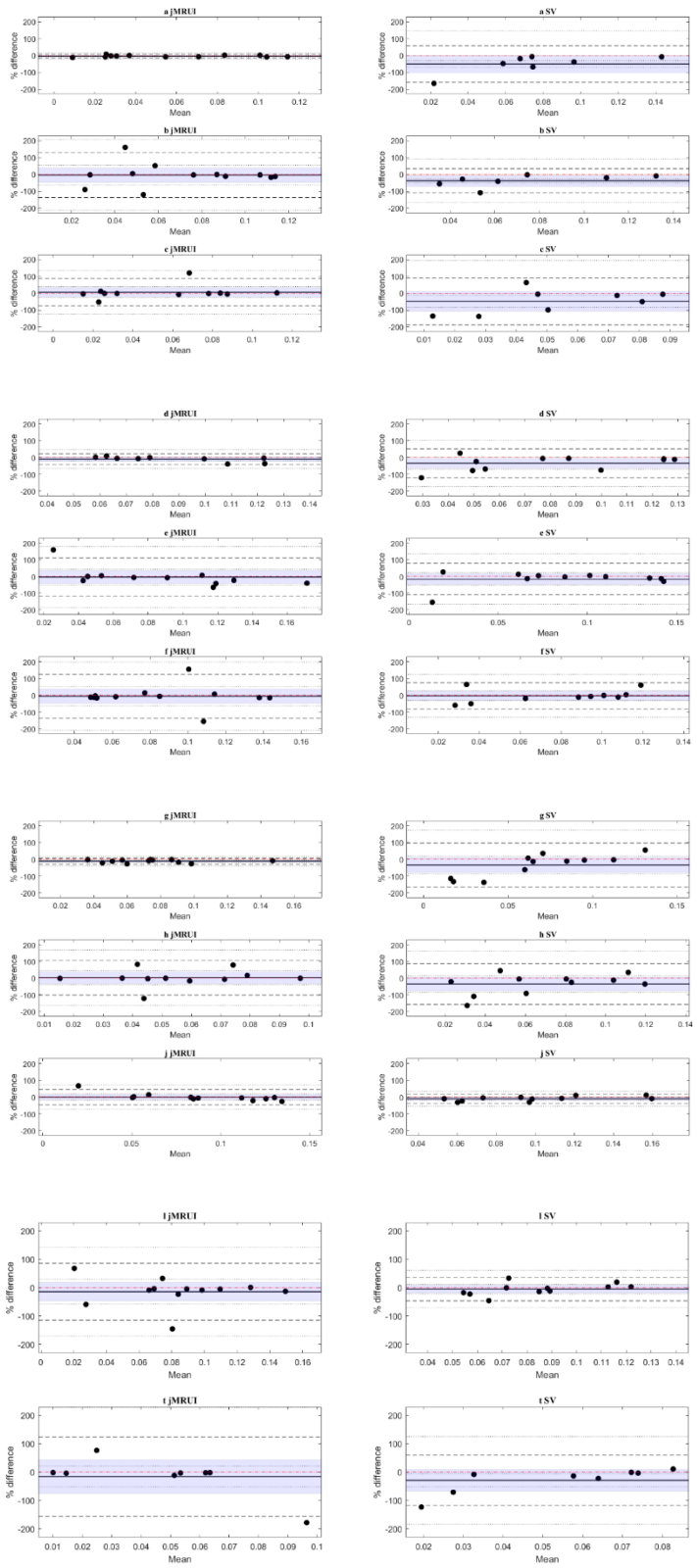

Figure 3.41 Bland-Altman plots illustrating agreement parameters form β phosphate of adenosine diphosphate (βATP) for repeated measurements (with alternative phasing method) conducted in jMRUI (column on the left) and SpectroView (SV column on the right).
Voxels are indexed as illustrated in Figure 3.13. Details on the interpretation of Bland-Altman plots are found in this chapter's introduction.

3.5 DISCUSSION

Substantial heterogeneity in analysis methodology and reported parameters is characteristic of the MR spectroscopic literature. To date, there are very few studies reporting effects of different methodologies on resulting metabolite estimates but the problem is recognised as, in recent years, there have been efforts to standardise methodology through publication of guidelines (Wilson, Andronesi et al. 2019, Meyerspeer, Boesch et al. 2020). In addition, most spectroscopic data processing protocols cannot be fully executed without a degree of user input, which may also contribute to variability of results. Of note, perhaps counter-intuitively, at present some user interaction is preferable to complete black-box methods as there are spectroscopic features and artefacts that can only be detected by careful visual inspection (Kreis 2004), as illustrated, for instance, in section 3.1.1.2 (manual phasing compared to automated phasing).

In the previous chapter, spectroscopic analysis was conducted using the Philips' manufacturer proprietary software SpectroView, which allows fast spectroscopic analysis and is particularly valuable when setting up acquisitions. As soon as measurements are completed, results can be viewed immediately on the scanner computer, permitting rapid assessment of SNR and consequent adjustment of sequence parameters (e.g. alteration of TR or voxel size, as in experiments reported in chapter two). However, SpectroView has some features that inhibit more in-depth spectral analysis. For instance, only analysis of apodised spectra is permitted which, as discussed above, is not always recommended. In addition, it is impossible to assign an individual phase to each spectrum so the same phasing must be applied to all spectra in a given acquisition[19]. Furthermore, the fitting algorithm does not account for subtle variations in chemical shift of individual peaks (unlike AMARES that allows imposition of soft constraints on peak frequencies). This may lead to overfitting of noise instead of signal of interest for peaks with a slightly different chemical shift to that defined in the SpectroView script. SpectroView does not return either the CRLB of parameters (and which cannot be calculated from output data), pH, or Mg^{++} concentration (these latter two parameters can be calculated from chemical shifts, but the manual procedure required is very time-consuming). Lastly, SpectroView is only available on Philips scanners, which is a major limitation to the goal of reproducible studies, as the data reported in this chapter show that processing methodology represents an additional source of variability which may render results across sites not directly comparable.

Following preliminary experiments aimed at optimising a post-processing protocol in both jMRUI and SpectroView, the study in twelve healthy participants was conducted to characterise reproducibility of the technique and compare results produced by the two available processing software. The most important questions were whether the main operator-dependent step (manual phasing) contributed

[19] It is theoretically possible to select an individual spectrum, phase it, run the pre- and post-processing scripts, save individual results, and repeat the whole procedure for each spectrum of interest. However, this is extremely time consuming and negates the main advantage (speed) of using SpectroView.

towards a significant bias in results or not, and how robust available software were to alternative manual phasing and apodisation.

Every effort was made to ensure that processing steps in jMRUI and in SpectroView were equivalent and, hence, comparable, although there were some differences in analysis steps which could not be eliminated. The main differences were: baseline estimation methods, PME and PDE line shape modelling, phase estimation, and presence of line-improving function in SpectroView, but not in jMRUI.

3.5.1 Comparison of analyses: mean values and coefficients of variability

Some statistically significant differences emerged between data analysed in jMRUI and in SpectroView, whereas neither phasing nor apodisation appeared to have a significant effect on results.

The main differences between jMRUI and SpectroView analyses were found in membrane phospholipids results. PMEs tended to be underestimated in SpectroView compared to jMRUI, whereas PDEs were overestimated. PMEs are found on the left side of the spectrum, at the inflection point of the large baseline. Hence it is possible that variability in PME results was due to differences in modelling of the baseline, which is estimated as a quarter sine wave in jMRUI and as a polynomial in SpectroView. In addition, following visual analysis, there appeared to be imprecise modelling of the line shapes of both phospholipid resonances in SpectroView (which assumed PMEs and PDEs to be composed by only one peak each) compared to jMRUI (in which they were modelled as two peaks and resulted from summation of PE and PC for PMEs and GPC and GPE for PDEs).

Some differences between results derived from jMRUI and SpectroView were also detected in other metabolites, although these were not consistently found across all voxels. Of note, correction for multiple comparisons was conducted for comparisons between different analysis methods, but not for all voxels of interest and for all metabolites. Therefore, it is likely that at least some of the resulting significant values (especially those found in isolation, e.g. pH differences in *f*, p=0.048) represented type 1 errors. Nonetheless, the overall goal of the analysis was to identify patterns of differences resulting from methodology, and the statistical leniency in this regard was intentional.

CVs of amplitudes in cortical regions were generally higher than in deeper brain structures. CVs in jMRUI were lower compared to those from analysis in SpectroView, with the exception of βATP which showed high variability across all voxels and methodologies. This was likely a result of difficulties modelling βATP line shape, low βATP SNR, and off-resonance effects.

Variability of pH was extremely low, reflecting both high precision of measurements and low biological variability of this highly homeostatic parameter. In contrast, Mg^{++} measures, although mostly in

biological range (Murphy 2000), were highly variable with CVs around 40%, and sometimes exceeding this value, especially in method B, indicating that phasing had an effect on the spread of Mg^{++} measurements. This was probably because Mg^{++} is calculated from βATP's chemical shift, which was also variable as a result of off-resonance effects, first order phasing errors, generally low SNR, and the fact that line shape is more complex to model and fit.

3.5.2 Quality control

In terms of fitting individual amplitudes, SpectroView performed worse than jMRUI for all metabolites with the exception of βATP in which a large number of peaks (54) could not be fitted by the AMARES algorithm. It is unclear why this was the case, although it is possible that apodisation and multiplication by a line-improving function in SpectroView might have aided fitting of particularly noisy βATP triplets. Another consequence of difficulties with βATP fitting was that Mg^{++} estimates could not be calculated on 16 occasions; in addition, on occasion outlier values (which were characterised by elevated CRLB) were not biologically plausible (i.e. Mg^{++} >1 mM) (Murphy 2000).

CRLB of spectra were all below 30% and below 20% for most spectra, indicating that the acquisition protocol performed well according to accepted norms. The goodness of fit of heteronuclear spectra is inherently less accurate than in proton spectroscopy, hence, 30% can be considered an acceptable threshold (van de Bank, Maas et al. 2018). The inverse dependency of CRLB of spectra on noise (Cavassila, Deval et al. 2000) also explains why this measure should not be employed for quality control in clinical studies; SNR can be decreased in disease following a pathophysiological reduction of metabolite (pathologically reduced signals result in lower SNR and elevates CRLBs). Hence, rejecting data on the basis of high CRLB can eliminate those spectra derived from more severely affected individuals and potentially lead to false negative results (Kreis 2016). Generally, it is considered useful to calculate CRLBs of spectra before starting a clinical study at the protocol development stage to determine whether developed sequences and analyses return spectra that can be fitted with sufficient accuracy and, if this is not the case, improve the protocol through an iterative process.

Since CRLB of pH and of Mg^{++} do not depend on noise (but on linewidth (Cavassila, Deval et al. 2000)), and since some CRLBs were higher than 30%, for the final protocol, it was decided a priori to exclude Mg^{++} and pH values with CRLB>30% due to likely imprecision.

3.5.3 Reliability and agreement

jMRUI returned results which were more reliable (higher ICC) and with better agreement (narrower limits of agreement) than SpectroView, indicating greater robustness to operator-dependent changes in manual phasing across all metabolites, with the exception of βATP.

In jMRUI, βATP had poor reliability in three voxels and generally lower ICCs compared to SpectroView. βATP is the peak most subject to first-order phasing errors (as detailed at the beginning of this chapter). Hence these findings may reflect variation in first-order phasing methodology in jMRUI compared to SpectroView. In addition, the ICC analysis was conducted on non-apodised data in jMRUI and on denoised data in SpectroView, indicating that low SNR may have contributed to confound results.

Generally, agreement of measurements was greater amongst values derived from jMRUI analysis compared to SpectroView. Of note, in Bland-Altman plots, there is no absolute measure of agreement: the ULOA and LLOA represent the best compound measures and, although no absolute threshold exists, comparison of width of limits of agreement can be used to compare techniques.

In summary, the AMARES algorithm in jMRUI resulted in greater reliability, higher agreement, and less variability than SpectroView, returning values generally characterised by sufficiently low CRLB, and was hence chosen for all subsequent analyses in this thesis.

This type of reproducibility study has not been conducted before. Implications in terms of future work and in the context of published literature are illustrated in chapter seven.

3.6 CONCLUSION

There have been attempts at standardising analysis protocols, but differences persist in published MR spectroscopic literature. In this thesis, we chose the methodology described above and justify the selected protocol based on an experimental approach. In the following chapters, we applied this optimised methodology to a clinical cohort of patients with MND and healthy controls to address hypotheses of bioenergetic dysfunction.

The experiments conducted in this chapter established a post-processing protocol (spectral analysis, image segmentation and coregistration) and characterised reproducibility parameters for analyses in jMRUI and SpectroView. Experiments focussed on intra-operator variability, software robustness to manual phasing, and on the effects of apodisation. Main differences in mean values between tested analyses protocols were found in phospholipid results likely as a result of differences in baseline modelling between software. Generally speaking, jMRUI returned less variable, more reliable measurements which were characterised by higher agreement than SpectroView.

Quality of fit was also assessed in terms of CRLB and number of spectra that could be fitted. Spectral quality was generally high, with the exception of Mg^{++} measurements some of which had high undesirable CRLB values, hence, for the final protocol, Mg^{++} results characterised by a CRLB > 30% were rejected as too inaccurate.

Based on these observations, the following protocol was chosen for subsequent analyses: jMRUI was chosen as software for analysis, apodisation took place only for visual purposes (as analysis did not demonstrate a requirement), manual phasing was conducted, followed by fitting with AMARES using appropriate prior knowledge, and correction for T_1 relaxation effects. Image coregistration and segmentation scripts were optimised and used in chapter four to correct for any putative partial volume effects. Normalisation of metabolites by total phosphorus signal was chosen instead of quantification based on an external reference phantom.

CHAPTER 4:
31-PHOSPHORUS MAGNETIC RESONANCE SPECTROSCOPY TO ASSESS BIOENERGETICS IN BRAIN AND MUSCLE IN MOTOR NEURON DISEASE: CROSS-SECTIONAL RESULTS

This chapter describes experiments performed to characterise the bioenergetic profile in brain and muscle in MND patients using the acquisition and processing protocols optimised in previous chapters.

The work has now been published in Brain (Sassani, Alix et al. 2020). Permission for reproduction in this thesis has been granted by the publisher, and the copyright licence is attached in the appendix.

Since this chapter is essentially equivalent to the published paper, it was removed from the version made available on the White Rose Research Online Repository. The reader can find the content published in Brain: "Matilde Sassani, James J Alix, Christopher J McDermott, Kathleen Baster, Nigel Hoggard, Jim M Wild, Heather J Mortiboys, Pamela J Shaw, Iain D Wilkinson, Thomas M Jenkins, Magnetic resonance spectroscopy reveals mitochondrial dysfunction in amyotrophic lateral sclerosis, Brain, Volume 143, Issue 12, December 2020, Pages 3603–3618, https://doi.org/10.1093/brain/awaa340". In addition, the full text is available from the White Rose Research Online Repository at Magnetic resonance spectroscopy reveals mitochondrial dysfunction in amyotrophic lateral sclerosis - White Rose Research Online.

CHAPTER 5:
31-PHOSPHORUS MAGNETIC RESONANCE SPECTROSCOPY TO ASSESS SKELETAL MUSCLE RESPONSE TO FATIGUE IN MOTOR NEURON DISEASE

This chapter completes the reporting of cross-sectional experiments conducted in the participant cohort introduced in chapter four. The experiments reported in this chapter aimed to quantify and characterise neuromuscular fatigue in MND patients using both ^{31}P-MRS and neurophysiology. Experiments are divided into those aimed at quantifying fatigue and those conducted to characterise and localise its origin (central or peripheral nervous system, muscular). The latter experiments are, in turn, subdivided into neurophysiological and spectroscopic protocols based on employed methodology. Lastly, parameters shown to change significantly following exercise were combined in multiple regression analyses to model fatigability in healthy controls and patients and to interrogate pathophysiology.

5.1 INTRODUCTION

The aim of the experiments reported in this chapter was to characterise fatigability, which is a common and debilitating symptom in MND. Fatigue is reported by over 80% of patients (compared to 20% of the general population), tends to progress with disease (Ramirez, Piemonte et al. 2008), and has a negative impact on quality of life (Lou, Reeves et al. 2003). Numerous medications and interventions have been trialled, but none, so far, has shown evidence of efficacy (Gibbons, Pagnini et al. 2018). Part of the challenge is that a formal definition of fatigue is elusive and localisation of pathophysiology is challenging.

MND patients report two types of fatigue: global and motor (Gibbons, Thornton et al. 2013). The former is described as “a general sensation of tiredness” and, although likely multifactorial, appears related to bulbar symptoms and respiratory dysfunction. The latter is associated with muscle contraction and movement and can be improved with rest. This motor fatigability, or neuromuscular fatigue, can be particularly debilitating in MND (Gibbons, Pagnini et al. 2018), and may be defined as the inability to maintain maximal voluntary force during prolonged contraction (Sanjak, Brinkmann et al. 2001).

Each anatomical constituent of the motor pathway (upper motor neuron, lower motor neuron, neuromuscular junction, and muscle) can be affected by motor fatigue. Mechanistically, pathophysiological variations in resting plasma membrane/sarcolemmal potential, alterations in excitation contraction coupling (i.e. the cellular processes occurring within myocytes in which electrical

alterations in membrane potential are transduced into mechanical contractile force), and/or a direct consequence of reduction in cellular number secondary to neurodegeneration and muscular atrophy (Sanjak, Brinkmann et al. 2001) are implicated. More complex changes in neural circuits involving excitatory and inhibitory interneurons, as well as alterations in volitional control may also be involved. Following quantification of motor fatigability, it is possible to apply neurophysiology and ^{31}P-MRS to localise sites affected by motor fatigue and probe pathophysiological mechanisms.

5.1.1 Quantification of motor fatigability

To quantify neuromuscular fatigability, various measurement indices have been used, each with advantages and disadvantages (Place and Millet 2020). In MND, the fatigue index has been developed (Sanjak, Brinkmann et al. 2001). This is calculated by measuring maximal voluntary isometric force of contraction over a period of time and using the formula below. By convention, fatigue index is expressed as a percentage.

Equation 5.1

$$Fatigue\ index\ (\%) = \left(1 - \frac{Area\ under\ the\ curve}{Maximal\ voluntary\ isometric\ contraction\ x\ time}\right) x\ 100$$

The figure below illustrates in blue the fatigue index as a resulting from equation 5.1. If the fatigue index equals zero, then maximal force of contraction is maintained throughout the experiment, whereas a high fatigue index indicates rapidly declining contraction force and high neuromuscular fatigue.

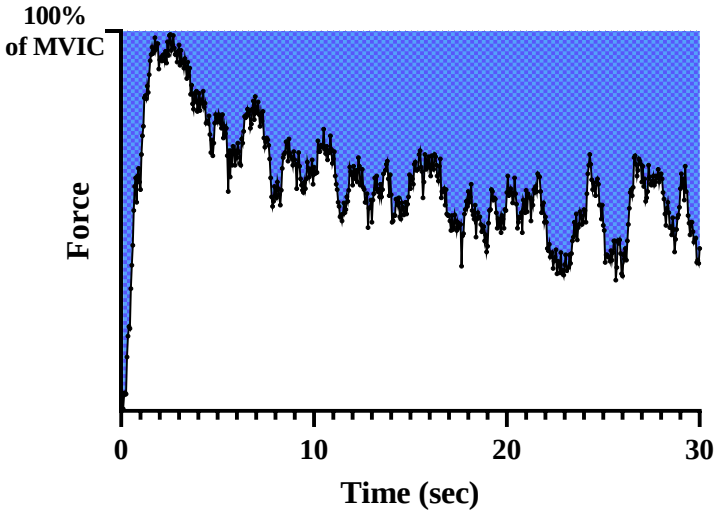

Figure 5.1 Fatigue index.
The area in blue is a graphical representation of the fatigue index (equation 5.1) (Sanjak, Brinkmann et al. 2001). Data illustrated were acquired from a research participant as described in methods of this chapter. MVIC: Maximal voluntary isometric contraction.

The result is normalised by maximal voluntary isometric contraction to allow comparison between research participants who may have differences in muscle power.

Fatigue index is calculated in this chapter. In addition, parameters resulting from fitting the force-time curve were calculated, namely, slope (from linear fit) and exponential decay constant (from exponential fit). A secondary aim of the experiments described was to assess whether modelling force linearly or exponentially represents a suitable alternative to fatigue index to quantify fatigability.

5.1.2 Neurophysiological assessment of post-contraction changes

Following quantification, the anatomical origin of neuromuscular fatigue can be investigated. For this purpose, fatigability is often divided into central and peripheral aspects. The former can be due to direct UMN alterations and/or changes in inhibitory modulatory circuits; volition may also play a role. The latter localises to alpha motor neurons, the neuromuscular junction, and muscle (i.e. it pertains to the peripheral nervous system). It is typically necessary to use a combination of techniques to localise fatigue, a particularly challenging process in MND, which affects all levels of the motor pathways. In this thesis, both neurophysiology and ^{31}P-MRS were applied. Specifically, to dissect central from peripheral elements of fatigue, f-wave amplitude, MUNIX, MUSIX, and f-wave persistence, were assessed prior and following one-minute maximal voluntary isometric contraction. ^{31}P-MRS was used to assess the muscular component of peripheral fatigability.

MUNIX is an index of the number of viable motor units in a given muscle group calculated using compound muscle action potential (CMAP) and surface interference pattern from electromyography (Nandedkar, Nandedkar et al. 2004). It is a useful measure of denervation, with values typically decreased in MND patients compared to healthy controls (Nandedkar, Barkhaus et al. 2010). Since motor unit loss is one of the hallmarks of MND, MUNIX has been widely used in MND research. It appears to be affected in the earliest stages of disease (Escorcio-Bezerra, Abrahao et al. 2016, Escorcio-Bezerra, Abrahao et al. 2018) and to decline concomitantly with disease progression (Neuwirth, Barkhaus et al. 2015). MUNIX can be acquired relatively quickly (an experiment lasts only a few minutes per muscle group) and the technique has shown high intra- and inter-rater reliability, including in multi-centre settings (Neuwirth, Barkhaus et al. 2015). In this study, MUNIX was measured prior and following contraction: the underlying hypothesis was that during prolonged and forceful muscle contraction, some of the motor units would fatigue and "drop out" resulting in lower MUNIX values post-exercise. It was hypothesised that this process would be more prominent in MND than in healthy controls, reflecting higher peripheral fatigability.

Pre- and post-exercise MUSIX is also reported in this chapter. MUSIX is a parameter derived from MUNIX and is an index of the average size of motor units (Nandedkar, Barkhaus et al. 2010). It is typically increased in MND as chronic reinnervation takes place resulting in sprouting at neuromuscular synapses (Nandedkar, Barkhaus et al. 2010, Gunes, Sirin et al. 2021) with consequent expansion of motor units. Analogously to MUNIX, changes can also be detected in subclinical MND (Nandedkar 2017) and the technique has high intra-rater and between-centre agreement (Alix, Neuwirth et al. 2019). In this thesis, it was hypothesised that strenuous muscle contraction would preferentially affect fast fatigable motor units innervating smaller muscle fibres, resulting in a relative increase in the average motor unit size post-exercise, reflecting sparing of larger, less fatigable fibres. It was hypothesised that this effect would be more pronounced in MND, resulting in a larger increase in MUSIX post-contraction compared to controls.

F-waves were also included in the neurophysiology protocol to assess spinal cord excitability. They represent a late response generated following supramaximal neurophysiological stimulation of motor neurons. They are thought to be the result of action potentials travelling antidromically (i.e. towards the spinal cord) and inducing, in turn, another motor stimulus which propagates orthodromically (i.e. away from the spinal cord towards muscles) along the same nerve. Hence, f-waves are useful to assess proximal segments of alpha motor neurons and their excitability, which is affected by central factors. Numerous parameters can be calculated. F-wave latency (i.e. the time between initial stimulus and f-wave response) is useful in the neurophysiological evaluation of radiculopathies, plexopathies, and neuropathies reflecting alterations in alpha motor neuron conduction velocity, which can be secondary both to axonal pathology and/or demyelination (Mesrati and Vecchierini 2004). F-wave persistence refers to the proportion of f-waves elicited per number of stimuli. In healthy individuals, it is typically 80 to 100%, whereas the proportion decreases if a LMN lesion is present (perhaps as action potential threshold increases). Lastly, increased f-wave amplitude has been suggested to reflect spinal cord excitability secondary to UMN lesions, and correlates with spasticity (Abbruzzese, Vische et al. 1985, Fierro, Raimondo et al. 1990, Bischoff, Schoenle et al. 1992, Lin and Floeter 2004). F-waves in MND show decreased persistence and increased amplitude, findings consistent with the characteristic mixed upper and lower motor neuron phenotype of this disease (Argyriou, Polychronopoulos et al. 2006). F-waves were assessed in this study to determine whether any post-contraction changes could be related to central fatigability, specifically excitability of the spinal cord, assessed using amplitude. In addition, f-waves at five- and ten-minutes post contraction were measured to determine whether recovery kinetics could be modelled and, if so, whether there were differences between patients and controls. It should be noted that the gold standard technique to assess UMN related central fatigue is considered TMS, but this was not available to researchers in this study.

5.1.3 Spectroscopic assessment of the muscular component of fatigue

^{31}P-MRS was applied in this chapter to assess the muscular contribution of peripheral fatigue. Resting parameters from the previous chapter were employed to determine whether resting bioenergetic status and/or intracellular cations play a role as predictors of fatigability. In addition, dynamic spectroscopy was conducted at MVIC and compared to dynamics at one third of MVIC (reported in the previous chapter) to characterise muscular responses to intense exercise in healthy controls and people living with MND.

5.2 AIMS AND HYPOTHESES

The aim of the experiments reported in this chapter was to characterise bioenergetic and neurophysiological changes occurring in muscle in MND during and after prolonged strenuous exercise to gain insights into the pathophysiology of fatigability.

Experiments were designed, firstly, to choose the optimal quantification method for fatigability; secondly, to assess differences between patients and controls in putative markers of central (f-wave amplitude), peripheral (MUNIX, MUSIX, f-wave persistence), and muscular (^{31}P-MRS) fatigue; and, finally, to select optimal measures to integrate into a multiple regression model to assess predictors of fatigability in MND and healthy controls.

The hypotheses were that:

1) Motor fatigability could be modelled and characterised by a constant (either slope or exponential decaying constant), independent of the duration of experiment.
2) Motor fatigability, from prolonged MVIC experiments, would be greater in MND patients compared to healthy controls.
3) MND patients would exhibit greater decline than controls in MUNIX post-contraction, indicating a larger proportion of motor units "dropping out" due to peripheral fatigue.
4) MND patients would exhibit a greater increase than controls in MUSIX post-contraction, indicating that remaining motor units are relatively larger as a result of smaller fast-fatigable fibres "dropping out", another indicator of peripheral fatigue.
5) Pre-contraction f-waves would show decreased persistence and increased amplitude in patients than controls, indicating damage to both LMNs and UMNs.
6) Post-contraction f-waves would show a decrease in persistence and increase in amplitude, compared to pre-contraction levels, indicating peripheral (persistence) and central (amplitude) fatigability. These changes would be greater in MND patients than controls.

7) Temporal changes in f-wave persistence and amplitude following contraction would be significant and allow modelling of f-wave recovery parameters using either a linear or exponential function.
8) Resting ^{31}P-MRS muscle parameters indicative of bioenergetic status and intracellular ionic composition would predict fatigability index, representing the muscular component of motor fatigue.
9) Differences in dynamic response to maximal muscle contraction would be present in patients compared to controls.
10) The results of the above experiments would allow selection of optimal central, peripheral, and muscular parameters to be entered into a multiple regression model as predictors of fatigability in controls and in patients.

5.3 METHODS

5.3.1 Research participants

Experiments were conducted concomitantly with those described in chapter four on the same cohort of research participants (Yorkshire and the Humber REC 13/YH/0273); the same inclusion and exclusion criteria were used.

5.3.2 Clinical and neurophysiological data

MVIC and standard neurophysiology acquisition were as previously reported in chapter four. The following protocol was conducted to characterise muscle fatigability and recovery. Neurophysiological measurements were acquired by Dr James Alix (consultant neurophysiologist), whilst the author conducted MVIC and spectroscopic measurements and timing (Place and Millet 2020) as well as all the analysis and interpretation of results.

Firstly, neurophysiological parameters (MUNIX, MUSIX, and f-waves) were acquired at rest (Nandedkar, Barkhaus et al. 2010, Neuwirth, Nandedkar et al. 2010), using the Dantec Keypoint electromyography machine (Natus Medical, Pleasanton, CA). Thirty stimuli were applied, to measure f-waves. F-wave number (persistence) and f-wave area corrected for CMAP (amplitude) were reported. These measurements provided a baseline for neurophysiological values pre-contraction.

Secondly, MVIC force of ankle dorsiflexors was recorded. Participants were asked to maintain maximal contraction for one minute; of note, this was different compared to the measurements described in chapter four where maximal voluntary contraction was assessed over a five-second period.

Lastly, to assess recovery kinetics, neurophysiological parameters were recorded following muscle contraction: specifically, MUNIX, MUSIX, and f-waves were recorded immediately after contraction ceased. In addition, f-waves measurements were repeated again at five and ten minutes post-contraction.

For each research participant, the same leg was tested, as for the experiments detailed in chapter four.

5.3.2.1 Analysis of one-minute maximal voluntary isometric contraction data

Fatigue index was calculated using the formula reported in the introduction (Sanjak, Brinkmann et al. 2001) for one minute-contraction data. Of note, the original definition of fatigue index refers to contraction performed over half a minute; hence the first 30 seconds of the measurement were also taken to calculate a separate 30-second fatigue index, to allow for numerical comparison with published literature.

Both linear and exponential fitting of the force-time curve were tested using GraphPad Prism (version 8.3.0 for Windows, GraphPad Software, San Diego, California USA, www.graphpad.com). In all cases, the first 20 datapoints (comprising the first second of measurement) were omitted from analysis, as they correspond to the "ramp time" (i.e. the time taken to initiate full contraction). For each research participant, one-minute force of contraction data were fitted first using a linear model; slope and R^2 (coefficient of determination) were reported. Next, a decaying exponential model was applied (i.e. $Y=(Y_0 - baseline)*exp(-K*time) + baseline$; where Y_0 is the initial Y value, baseline corresponds to the minimum Y value, and K corresponds to the reciprocal of the half-life of force of contraction. K and R^2 were reported for this model.

For all data, normality was first assessed using the D'Agostino-Pearson test. Between-group comparisons were conducted using two-tailed Mann-Whitney U tests as data were not normally distributed. Thirty- and 60-second fatigue indices were also compared using a paired t-test. Multiple regressions were conducted, entering status (patient/control), age, sex, and MVIC (measured as described in previous chapter) as independent variables to assess the effect of each of these factors, in turn, on fatigue index (as the dependent variable).

5.3.2.2 Analysis of neurophysiological parameters

For MUNIX and MUSIX, pre- and post-contraction data were first compared employing paired t-tests separately in the MND patient and healthy control groups. In addition, differences between pre- and post-contraction values were calculated at individual level ((post-contraction value - pre-contraction value) / pre-contraction value, expressed as a percentage). Differences between patient and control groups were compared using unpaired t-tests with Welch correction for normally distributed samples

or Mann-Whitney U tests for non-normally distributed data. Normality was tested using the D'Agostino Pearson test. Percentage change in MUNIX was correlated with percentage change in MUSIX both in controls and in patients to assess for a linear relationship, and R and p values were reported.

For f-wave persistence and f-wave amplitude, a mixed effects model with status (patient/control) and time as fixed effects was used to assess changes following contraction and during recovery, as well as differences in changes between patients and controls. In the mixed-effects model, correction for multiple comparisons was conducted using Šidák's test and between-group differences in mean with 95% CI were visualised at all timepoints to assess the stages of contraction at which significant between-group differences were present.

In addition, linear regression was used to assess whether f-wave persistence correlated with MUNIX, since both are considered measures of denervation. R and p values were reported.

GraphPad Prism (version 8.3.0 for Windows, GraphPad Software, San Diego, California USA, www.graphpad.com) was used to conduct the statistical tests described in this section.

5.3.3 Magnetic resonance imaging and spectroscopy

5.3.3.1 Hardware and sequences

The ^{31}P-MRS spectroscopic acquisition protocol was described in detail in chapter four. An additional spectroscopic measurement was included: the dynamic muscle protocol (sequence 26) was repeated at MVIC force.

5.3.3.2 Spectroscopic data processing and reported parameters

As in previous analyses, a random code was assigned to each research participant and analysis was conducted by the author, blinded to participant status.

Resting spectroscopic results from chapter four were correlated with fatigue index to test for linear relationships. The regression coefficient (R) and p values were reported and corrected using false discovery rate at Q=0.05 (Benjamini, Krieger et al. 2006).

Spectroscopic data acquired from dynamic experiments conducted at MVIC were analysed as detailed in chapter four (muscle analysis). The only difference was that recovery coefficients (from PCr and PCr/Pi) were not calculated for dynamics acquired at maximal contraction, as interpretation of these parameters is only possible when pH values remain constant throughout measurements (Meyerspeer, Boesch et al. 2020). This is not considered to be the case during strong contraction when anaerobic glycolysis predominates, generating lactate, and decreasing pH, as in these experiments.

Dynamic data originating from one third maximal (analysis detailed in previous chapter) and full maximal voluntary isometric contraction were compared using a mixed effect model with time and force of contraction (third or maximal) entered as main factors in GraphPad Prism (version 8.3.0 for Windows, GraphPad Software, San Diego, California USA, www.graphpad.com). For each metabolite, the mixed effect model was run twice: once for patient data and once for controls. Matching was specified for both time and force of contraction. Sphericity was not assumed, hence, Geisser-Greenhouse correction was applied. P values for the interaction, time, and force of contraction terms were reported. The effect of interest was the interaction term, indicating differences in the MVIC responses between one third and maximal force over time. In addition, to aid visualisation, Pi, PCr, and PCr/Pi curves were also plotted following normalisation by their baseline: for each dynamic curve, the mean of pre-exercise baseline (first two minutes) was taken as equivalent to one (expressed as 100%) and all remaining dynamic values were expressed as normalised by their baseline. Of note, all mixed effect analyses reported above were conducted on non-normalised data. As in the previous chapter, γATP percentage change post-contraction was also calculated, and results at one third and maximal effort were compared using a paired t-test. Analysis was conducted separately in patients and in controls.

5.3.4 Central, peripheral, and muscular predictors of fatigue index

The following parameters were each entered, in turn, as independent variables into a multiple regression with fatigue index always the dependent variable: percentage difference[20] in f-wave amplitude (as a surrogate of central excitability), percentage difference in MUNIX (peripheral denervation), and resting Mg^{++} concentration (reflecting exclusively muscular activation). Multiple linear regressions were run separately for patients and controls. In addition to p values, R^2 was reported to assess goodness of fit, and variance inflation factors (VIF) were also calculated to test for multicollinearity between predictors.

5.4 RESULTS

5.4.1 Participants

Twenty MND patients and ten healthy controls attended the research visit, this was the same cohort that participated in the study described in chapter four. Participants' characteristics are reported below.

[20] Difference MUNIX and difference f-amplitude were calculated as (post contraction value - pre contraction value)/pre-contraction value) expressed as a percentage.

Table 5.1 Participants' characteristics.
This table has now been published in Brain (Sassani, Alix et al. 2020). Permission for reproduction has been granted by the publisher, and the copyright licence is attached in the appendix.
Since this table is essentially equivalent to the published one, it was removed from the version made available on the White Rose Research Online Repository. The reader can find the content published in Brain: "Matilde Sassani, James J Alix, Christopher J McDermott, Kathleen Baster, Nigel Hoggard, Jim M Wild, Heather J Mortiboys, Pamela J Shaw, Iain D Wilkinson, Thomas M Jenkins, Magnetic resonance spectroscopy reveals mitochondrial dysfunction in amyotrophic lateral sclerosis, Brain, Volume 143, Issue 12, December 2020, Pages 3603–3618, https://doi.org/10.1093/brain/awaa340". In addition, the full text is available from the White Rose Research Online Repository at Magnetic resonance spectroscopy reveals mitochondrial dysfunction in amyotrophic lateral sclerosis - White Rose Research Online.

For the fatigability experiments here described, one research participant was unable to perform the extended exercise protocol due to complete paralysis of ankle dorsiflexors, although resting spectra were acquired. F-waves were not acquired in six participants due to unavailability of personnel, whereas, in another patient, no f-waves were elicitable. Due to an error in data exporting, the one-minute muscle fatigue series terminated at 38 seconds and 59 seconds in two participants, hence analyses for one-minute indices were run after removal of these two participants' data. Of note, the timing of the error meant that 30-second indices were unaffected. Lastly, maximal force of contraction in one participant exceeded the load that could be applied in dynamic spectroscopic experiments. For this participant, experiments at one third MVIC were conducted as per protocol, whereas no data from MVIC were included as submaximal exercise might have biased results.

5.4.2 One-minute force of contraction: descriptive statistics and between-group comparisons

In patients, mean 30-second fatigue index was 31.92 (SD±10.62), whereas in controls mean was 25.32 (SD±11.14). Mean 60-second fatigue index was 39.41 (SD±13.09) in patients and 33.96 (SD±9.94) in controls.

Mean slope following linear fit was -0.09 (SD±0.04) in controls and -0.05 (SD±0.06) in patients. Mean *K* following exponential fit was 0.06 (SD±0.05) in controls and 0.08 (SD±0.17) in patients. P values are not reported for these comparisons due to identified issues with model fit, described below.

Exponential fitting was superior to linear fitting in terms of R^2 values in 25/29 analysed participants (as explained in chapter four, one patient could not successfully complete this experiment due to complete paralysis). Nonetheless, despite R^2 values being available, five exponential fitting parameters were deemed ambiguous and unstable by the software. On this basis, fitted data were individually assessed visually by the researcher maintaining blinding to participants' status. Three types of pattern emerged: in a proportion of participants force declined in an exponential manner with linear fit being inappropriate (Figure 5.2 A); in some, force decline was linear, this could be fitted both linearly and exponentially (Figure 5.2 B); lastly, in a subset, although a decline in force was present in the initial stages of contraction, this did not follow a pattern that could be modelled (Figure 5.2 C).

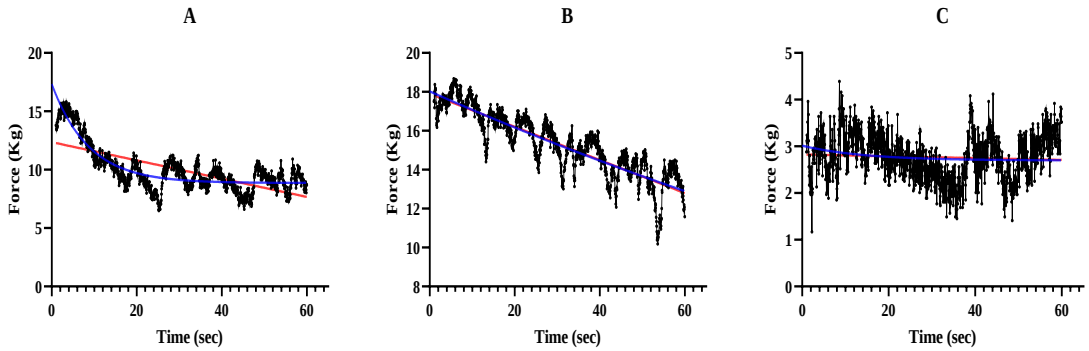

Figure 5.2 Three representative examples of fit of maximal voluntary contraction data (one-minute series) acquired from three research participants.
The black line illustrates measurement of force, blue line the decaying exponential fits, and red line linear fits, here included for comparison. In A, R^2 of exponential fit was 0.77, whereas R^2 for the linear model was 0.46 and the exponential model appeared visually more appropriate. In B linear (R^2=0.77) and exponential (R^2=0.77) fits largely overlapped. In C, although R^2 for linear fit was 0.00, whereas exponential R^2 was 0.02, the exponential fit was unstable and did not return additional parameters, whereas linear fit was feasible, but appeared inadequate to model the line shape of data.

Since it was not possible to model all force data using a univocal function representing gradient of change, fatigue index was used for all remaining analysis.

A significant increase in 60-second fatigue index compared to 30-second index was detected (mean difference 7.89, SD of difference±4.86, p<0.0001, paired t-test). This remained significant after accounting for patient/control status (p difference<0.0001, p status=0.579, multiple linear regression). For the final analysis, 30-second fatigue index was chosen as this allowed numerical comparison with literature and was not affected by the error in export of two research participants' data.

No significant difference in 30-second fatigue index was found between patients and controls (Figure 5.3), p=0.115, patients' median=27.82 (interquartile range=13.60), controls' median=21.40 (interquartile range=21.92), Mann-Whitney U test. Results remained non-significant following multiple regressions to adjust for, in turn, age (p status=0.237, p age=0.049), gender (p status=0.118, p gender=0.588), and baseline MVIC force (p status=0.340, p force=0.352), as calculated in chapter four.

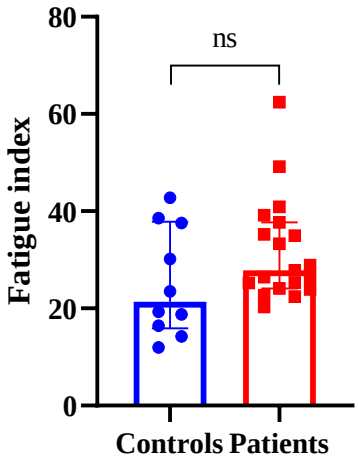

Figure 5.3 30-second fatigue index in patients (red) and controls (blue).
Median and interquartile range are shown. Mann-Whitney U test was conducted. Ns: Not significant.

5.4.3 Neurophysiological parameters

Following maximal contraction, MUNIX declined significantly in controls (mean of difference=-12.02, SD of difference=±11.25, p=0.008), but not in patients (mean of difference=-3.58, SD of difference=± 14.15, p=0.284), Figure 5.4.

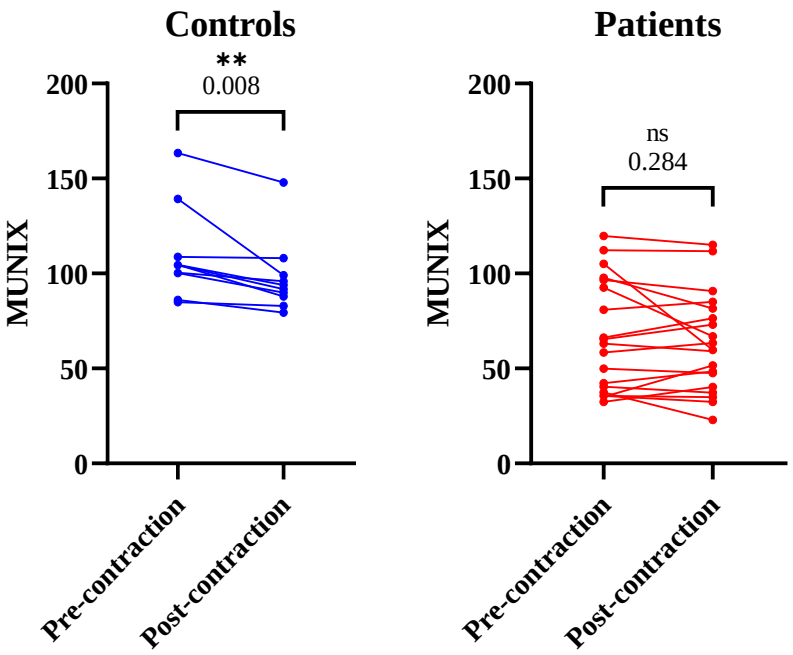

Figure 5.4 Motor unit number index values in controls (blue, left) and patients (red, right) prior and after one-minute maximal voluntary isometric contraction.

No significant differences were found between pre- and post-contraction MUSIX values (Figure 5.5) either in patients or controls (controls: mean of difference=1.22, SD of difference=±2.70, p=0.189; patients: mean of difference=-1.36, SD of difference=± 7.54, p=0.443).

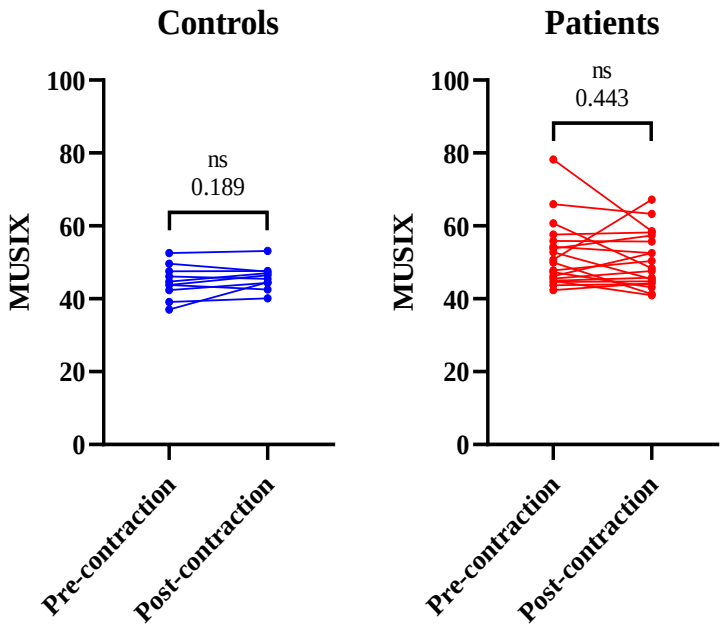

Figure 5.5 Motor unit size index values in controls (blue, left) and patients (red, right) prior and after one-minute maximal voluntary isometric contraction.

No significant differences were found between patients and controls when comparing percentage changes in MUNIX (controls' median= -9.85%, interquartile range=9.12%; patients' median= -4.00%, interquartile range=21.00%, p=0.092) and MUSIX (controls' median= 1.88%, interquartile range=7.22%; patients' median=0.00%, interquartile range=14.00%, p=0.261), Figure 5.6. However, Figure 5.6 illustrates that none of the controls exhibited an increase in MUNIX following exercise whereas, in seven out of 19 patients, MUNIX increased post-contraction. Analogously, MUSIX in controls either increased or fluctuated around zero, whereas in a subgroup of patients (seven out of 19) it decreased.

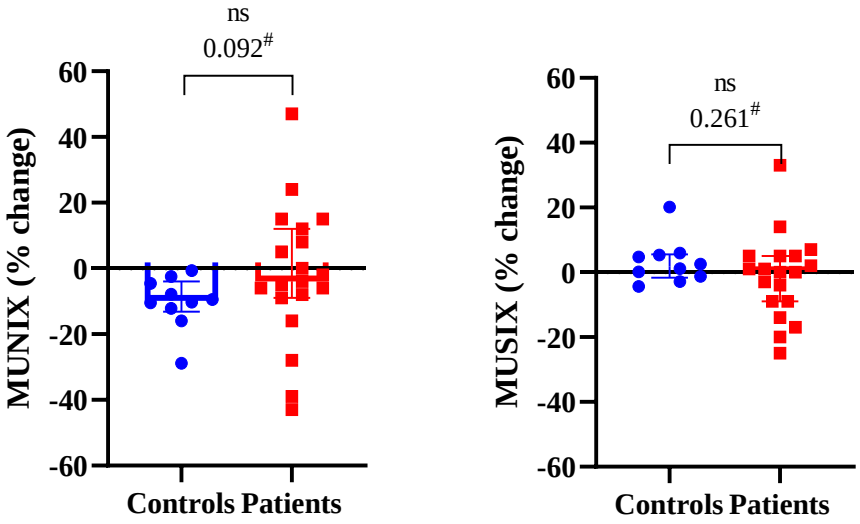

Figure 5.6 Motor unit number index (MUNIX - left) and motor unit size index (MUSIX - right) changes following prolonged maximal voluntary isometric contraction in controls (blue) and patients (red).
Changes are expressed as percentage of initial value: [(post-contraction value -precontraction value)/pre-contraction value] x 100. Median and interquartile range are shown. Mann-Whitney U test was used in both cases and is indicated in the graph with a hash symbol.

Significant correlations between contracting percentage changes in MUNIX and MUSIX were observed within both the control (R^2= 0.71, p= 0.002) and patient groups (R^2=0.50, p< 0.001), as illustrated in Figure 5.7 and Figure 5.8.

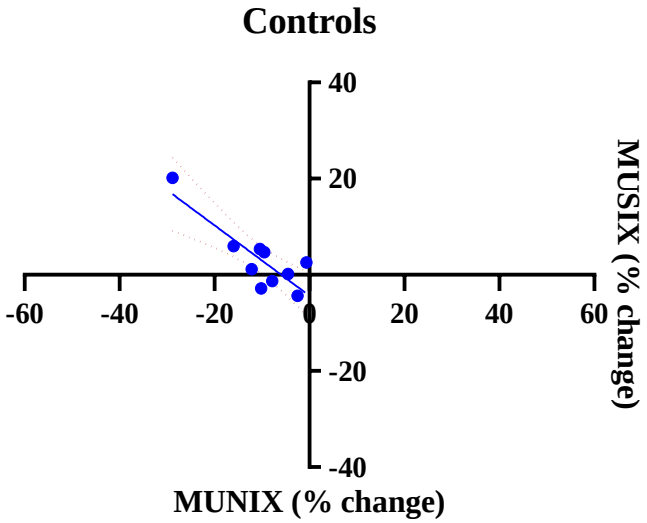

Figure 5.7 Correlation between motor unit number index (MUNIX) and motor unit size index (MUSIX) changes following prolonged maximal voluntary isometric contraction in controls.
Changes are expressed as percentage of initial value: [(post-contraction value -precontraction value)/pre-contraction value] x 100. Significant correlation was observed, p= 0.002.

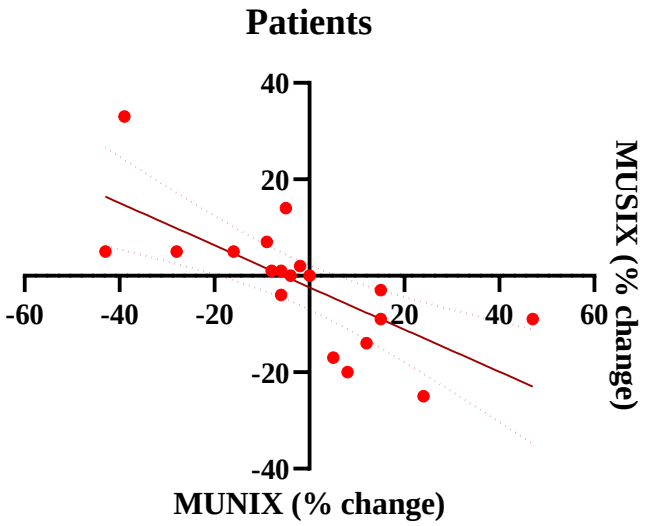

Figure 5.8 Correlation between motor unit number index (MUNIX) and motor unit size index (MUSIX) changes following prolonged maximal voluntary isometric contraction in patients.
Changes are expressed as percentage of initial value: [(post-contraction value -precontraction value)/pre-contraction value] x 100. Significant correlation was observed, p< 0.001.

Following the mixed effect analysis (Figure 5.9 and Figure 5.10), between- group differences in f-wave amplitude and f-wave persistence were detected in MND: patients showed higher amplitude (p=0.046) and lower persistence (p=0.011) than controls. Neither the time factor nor interaction term was significant (for f-wave amplitude p time=0.294, p interaction=0.564; for f-wave persistence p time=0.438, p interaction=0.801).

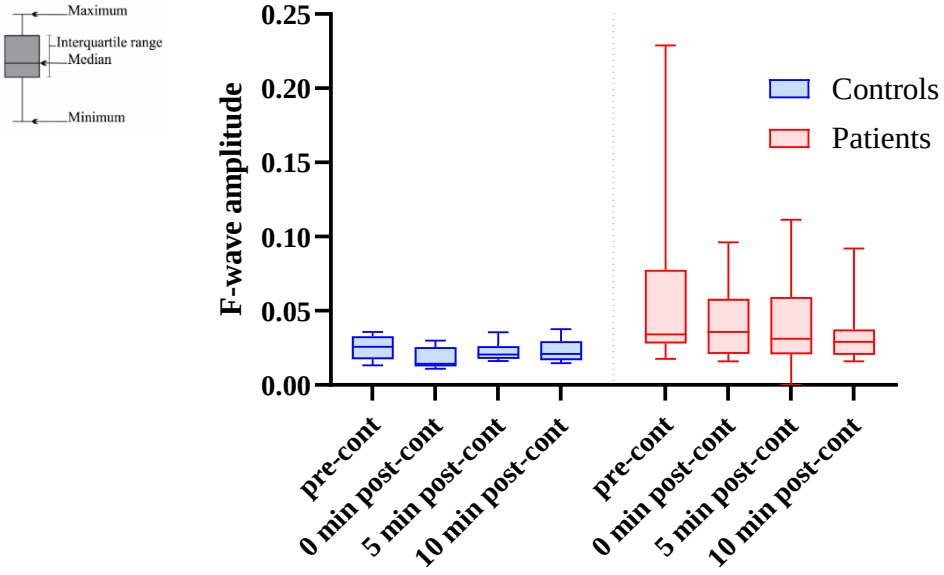

Figure 5.9 Box and whisker plots illustrating F-wave amplitude changes in controls (blue, left) and patients (red, right) pre-contraction, immediately following prolonged maximal voluntary isometric contraction, and after five- and ten-minutes.
Explanation for error bars is included in the figure above. Significant changes were detected between groups, but not across time.

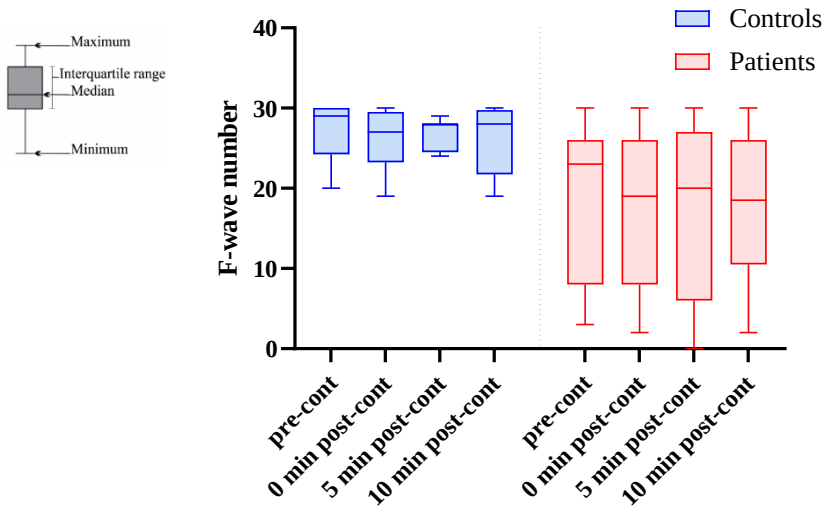

Figure 5.10 Box and whisker plots illustrating F-wave persistence changes in controls (blue, left) and patients (red, right) pre-contraction, immediately following prolonged maximal voluntary isometric contraction, and after five- and ten-minutes.
Explanation for error bars is included in the figure above. Thirty stimuli were conducted. Significant changes were detected between groups, but not across time.

On cross-sectional analysis of between-group differences at each time bin, differences in f-wave amplitude were recorded immediately post-contraction in patients (Figure 5.11), whereas differences in f-wave persistence were present throughout the experiment (Figure 5.12).

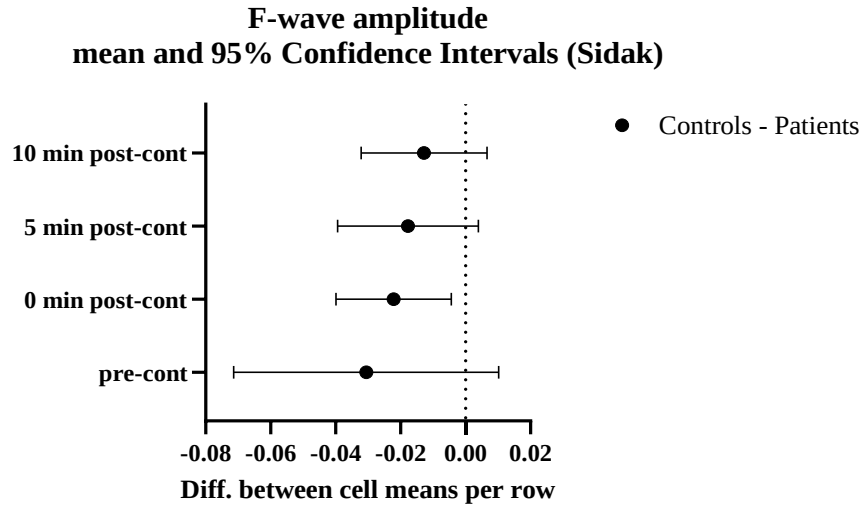

Figure 5.11 Graph illustrating mean and 95% confidence interval of differences (controls – patients) in F-wave amplitude during fatigability experiments.
Significant changes (i.e. confidence interval not crossing 0) were detected between groups, exclusively following muscle contraction. Row effect refers to time. Cont: Contraction; Diff: Difference

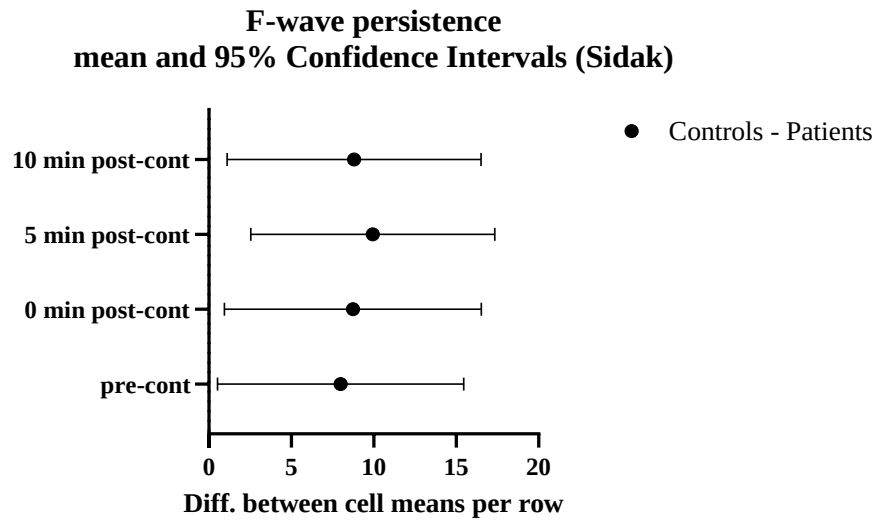

Figure 5.12 Graph illustrating mean and 95% confidence interval of differences (controls – patients) in F-wave persistence during fatigability experiments.
Significant changes (i.e. confidence interval not crossing 0) were detected throughout. Row effect refers to time. Cont: Contraction; Diff: Difference

Since the time factor was not shown to be significant in the mixed effect model, either in f-wave persistence or in f-amplitude, no attempts to fit recovery values were made. In addition, visual analysis of individual data showed that line shape of recovery could not have been univocally modelled either using a linear or an exponential function.

F-wave persistence correlated with MUNIX in patients (R^2=0.417, R=0.646, p=0.013), but not in controls (R^2=0.017, R=-0.129, p=0.762), Figure 5.13.

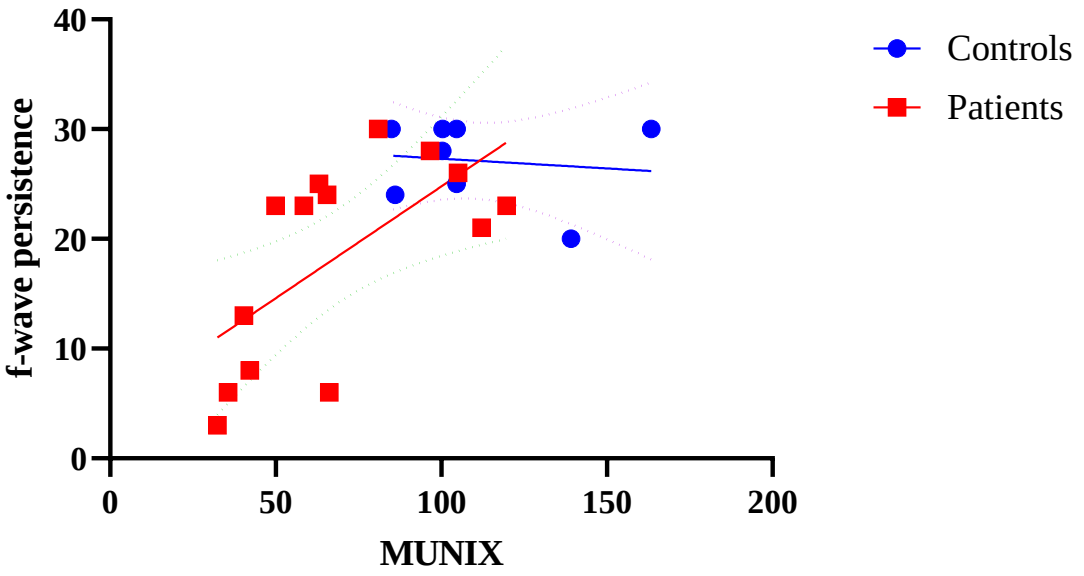

Figure 5.13 Relationship between motor unit number index (MUNIX) and f-wave persistence in controls (blue, left) and patients (red, right).
A significant linear relationship was present in patients, but not in controls. Notably, it is not possible to record values above 30 (i.e. 100% persistence) as only 30 f-wave stimuli were generated.

5.4.4 Spectroscopy

The tables below illustrate results (R and p values) for correlation analyses conducted between resting spectroscopy and fatigue index in controls and in patients. Significant associations were found in controls between fatigue index and both pH (R=-0.689, p=0.028) and intracellular free Mg^{++} concentration (R=0.869, p=0.001), the latter result surviving false discovery rate correction. No significant associations were detected in patients.

Table 5.2 Correlation coefficients and p values for correlation analyses of resting spectroscopy parameters and fatigue index in controls.

Significant associations were found between fatigue index and both pH and free magnesium concentration. Asterisk indicates that p value survived correction for multiple comparisons. ΔG_{ATP}: Gibbs free energy of ATP hydrolysis, ATP: adenosine triphosphate, NAD(P)H+NAD(P)$^+$ nicotinamide adenine dinucleotide.

Spectroscopic parameter	***R***	***p***
ΔG_{ATP} (kilojoule/mole)	0.077	*0.833*
γATP	0.176	*0.627*
Phosphocreatine	-0.064	*0.861*
Adenosine diphosphate (micromolar)	-0.323	*0.362*
Inorganic phosphate	0.221	*0.540*
pH	**-0.687**	***0.028***
Free magnesium (millimolar)	**0.869**	***0.001****
Phosphomonoesters	-0.177	*0.624*
Phosphodiesters	-0.169	*0.641*
NAD(P)H+NAD(P)$^+$	0.265	*0.459*

Table 5.3 Correlation coefficient and p values for correlation analyses of resting spectroscopy parameters and fatigue index in patients.

Spectroscopic metabolite values are expressed as a proportion of total phosphorus signal. No significant associations were found between fatigue index and any spectroscopy parameters. ΔG_{ATP}: Gibbs free energy of ATP hydrolysis, ATP: adenosine triphosphate, NAD(P)H+NAD(P)$^+$ nicotinamide adenine dinucleotide.

Spectroscopic parameter	***R***	***p***
ΔG_{ATP} (kilojoule/mole)	0.152	*0.534*
γATP	-0.014	*0.953*
Phosphocreatine	-0.109	*0.657*
Adenosine diphosphate (micromolar)	0.104	*0.671*
Inorganic phosphate	0.139	*0.570*
pH	0.372	*0.116*
Free magnesium (millimolar)	0.015	*0.952*
Phosphomonoesters	-0.125	*0.612*
Phosphodiesters	0.206	*0.397*
NAD(P)H+NAD(P)$^+$	0.371	*0.118*

Dynamic results are reported in Figure 5.14 to Figure 5.16. For Pi, the interaction term was significant in controls (p interaction=0.001, p force of contraction=0.082, p time<0.0001), but not in patients (p interaction=0.449, p force of contraction=0.980, and p time<0.0001). For PCr, the interaction term was significant in controls (p interaction 0.002, p force of contraction=0.083, p time<0.0001), but not in patients (p interaction= 0.701, p force of contraction=0.646, p time<0.0001). For PCr/Pi ratio, there was a non-significant trend towards significance in the interaction term in controls (p interaction=0.087, p force=0.698, and p time<0.0001), and not in patients (p interaction=0.338, p force=0.1484, p time<0.0001).

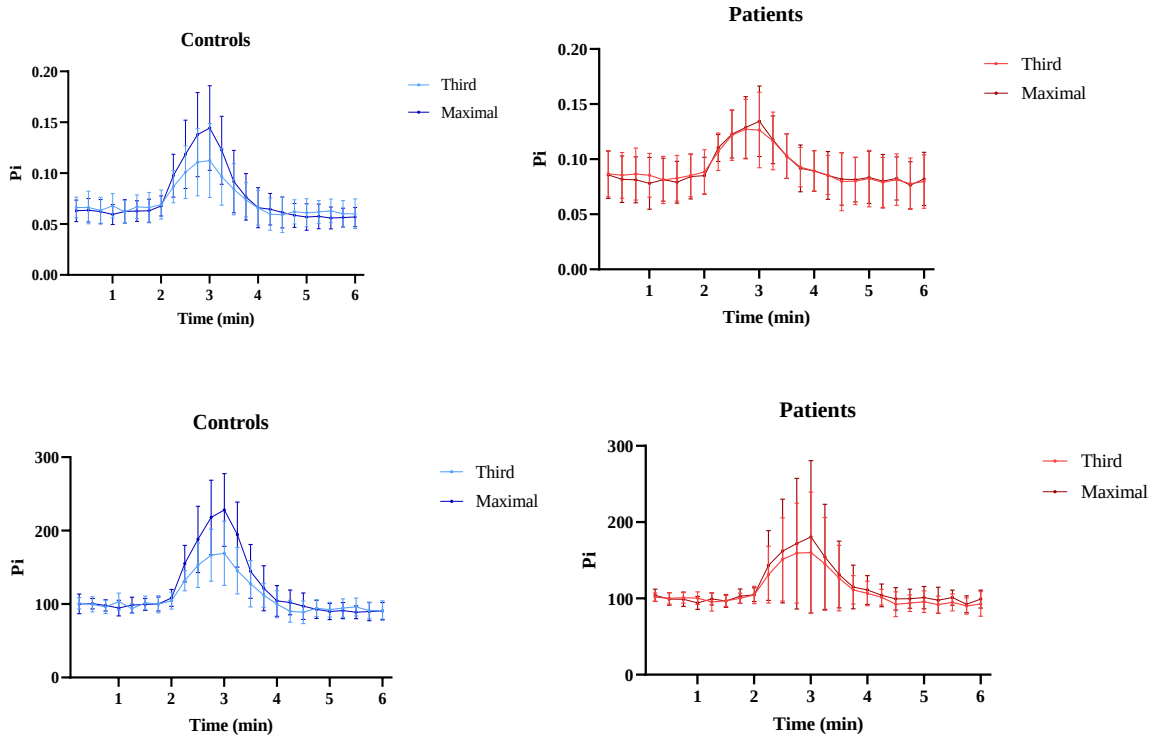

Figure 5.14 Inorganic phosphate (Pi) dynamic curves at third and maximal voluntary isometric force of contraction.
Mean and 95% confidence intervals are shown. Curves in blue (left) pertain to healthy controls, whereas those in red (right) to patients. In the second row, results normalised by baseline and expressed as a percentage of the baseline values are shown.

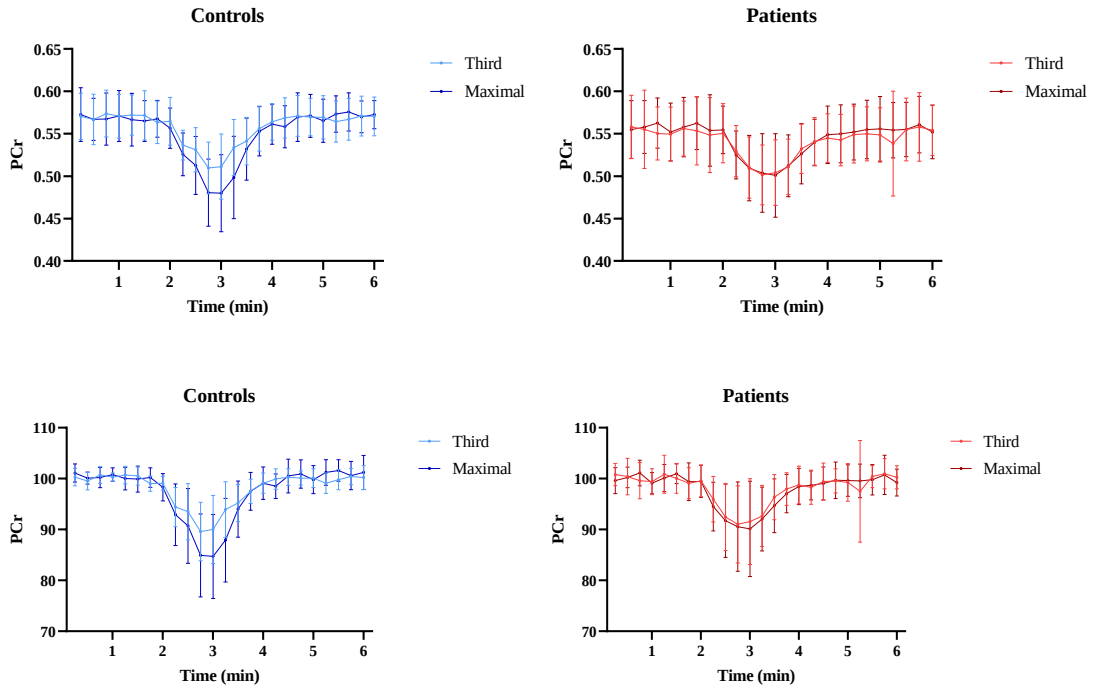

Figure 5.15 Phosphocreatine (PCr) dynamic curves at third and maximal voluntary isometric force of contraction.
Mean and 95% confidence intervals are shown. Curves in blue (left) pertain to healthy controls, whereas those in red (right) to patients. In the second row, results normalised by baseline and expressed as a percentage of baseline values are shown.

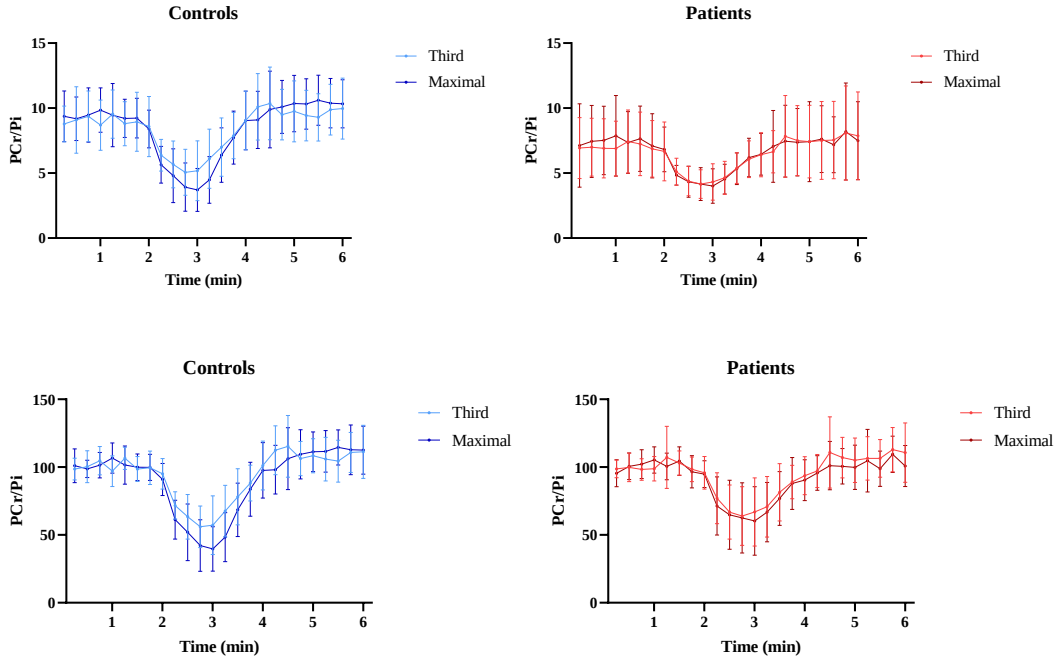

Figure 5.16 Phosphocreatine to inorganic phosphate (PCr/Pi) ratio dynamic curves at third and maximal voluntary isometric force of contraction.
Mean and 95% confidence intervals are shown. Curves in blue (left) pertain to healthy controls, whereas those in red (right) to patients. In the second row, results normalised by baseline and expressed as a percentage of baseline values are shown.

No significant differences were detected in γATP dynamics between third and MVIC either in controls or in patients. No significant differences were found between γATP percentage changes post-contraction, either in controls (p=0.547), or in patients (p=0.397), as illustrated in Figure 5.17.

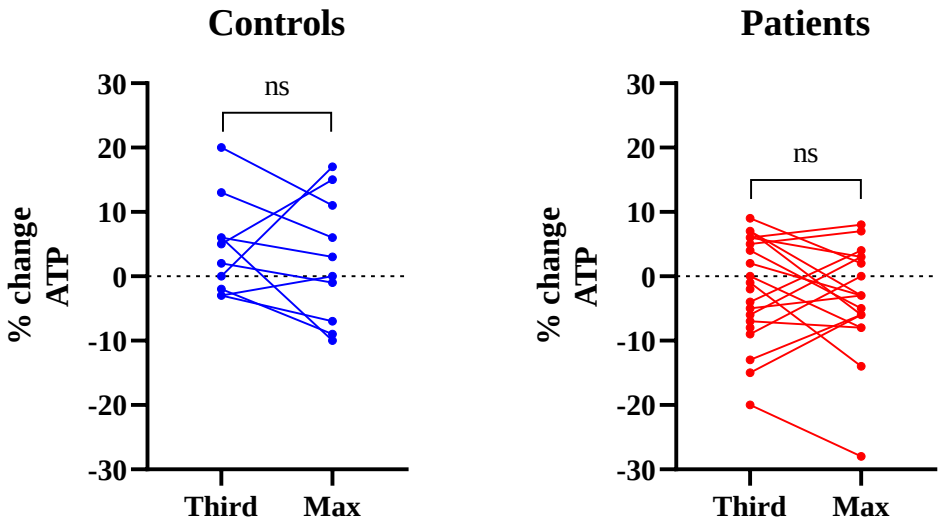

Figure 5.17 ATP percentage changes at end of contraction (i.e. at three minutes) in controls (blue, left) and patients (red, right).
No significant differences between third and maximal contraction percentage changes were found either in patients or in controls (paired t-test). ATP: Adenosine triphosphate,

5.4.5 Predictors of fatigue index

In multiple regression analyses to predict 30-second fatigue index in controls, free intracellular Mg^{++} concentration and post-contraction MUNIX difference emerged as significant variables (Table 5.4). R^2 for the model was 0.963. VIF values were: for Mg^{++}=1.35, for MUNIX post-contraction percentage change=1.14, and for f-wave amplitude post-contraction percentage change=1.43, indicating no multicollinearity.

Table 5.4 Multiple linear regression for controls.
The dependent variable was 30-second fatigue index. Difference in motor unit number index (MUNIX) and difference in f-amplitude were calculated as (post contraction value - pre contraction value)/pre-contraction value) expressed as a percentage. [Mg^{++}]: Free intracellular magnesium concentration.

Variable	*Estimate*	*Standard error*	*95% confidence interval*	*P value*
Intercept	-14.74	6.48	-32.74 to 3.26	*0.085*
[Mg^{2+}]	**84.53**	**10.59**	**55.13 to 113.90**	***0.001***
Difference MUNIX	**-0.52**	**0.14**	**-0.92 to -0.12**	***0.022***
Difference F-amplitude	0.05	0.07	-0.14 to 0.23	*0.532*

In multiple regression to estimate 30-second fatigue index in patients, free intracellular Mg^{++} concentration and post-contraction MUNIX difference were not significant variables (Table 5.5), but post-contraction f-wave amplitude was significant (p=0.019). R^2 for the model was 0.455. VIF values were: for Mg^{++}=1.01, for MUNIX post-contraction percentage change=1.33, and for f-wave amplitude post-contraction percentage change=1.34, indicating no multicollinearity.

Table 5.5 Multiple linear regression for patients.
The dependent variable was 30-second fatigue index. Difference in motor unit number index (MUNIX) and difference in f-amplitude were calculated as (post contraction value - pre contraction value)/pre-contraction value) expressed as a percentage. [Mg^{++}]: Free intracellular magnesium concentration.

Variable	*Estimate*	*Standard error*	*95% confidence interval*	*P value*
Intercept	**31.23**	**8.35**	**12.63 to 49.83**	**0.004**
[Mg^{2+}]	7.91	22.19	-41.55 to 57.36	0.729
Difference MUNIX	0.41	0.20	-0.04 to 0.86	0.068
Difference F-amplitude	**-0.13**	**0.05**	**-0.23 to -0.03**	**0.019**

5.5 DISCUSSION

In this chapter, neurophysiology was used in conjunction with ^{31}P-MRS to characterise motor fatigability in MND. No significant differences in fatigue index were found between patients and

controls; nonetheless, differential responses to fatigue were identified in patients in terms of MUNIX, f-waves, and dynamic spectroscopy.

5.5.1 Quantification of fatigability

Initial experiments aimed at quantifying and modelling neuromuscular fatigue illustrated that it was not possible to univocally model muscle force using a linear or exponential function. Hence, to avoid overfitting the data, fatigue index was used instead. In MND, the fatigue index refers to experiments conducted over 30 seconds (Sanjak, Brinkmann et al. 2001), but dynamic spectroscopic experiments in this thesis required a contraction of one minute, due to limitations in temporal resolution of ^{31}P-MRS (chapter two). In addition, neurophysiological protocols following one minute contraction, are commonly employed in literature (Vucic, Krishnan et al. 2007). Since one of the main aims of this chapter was to compare pre- and post-contraction neurophysiology with dynamic spectroscopy, force of contraction experiments were carried out for one minute to assess neurophysiological changes and their associations with ^{31}P-MRS data. Sixty-second fatigue indices were also calculated and values were significantly higher than 30-second indices. This is likely a result of force changing non-linearly in a proportion of participants (of note, this was independent of participant status: patients or controls), and is consistent with difficulties encountered in modelling the shape of data. To ensure consistent reporting with the published clinical literature, and to maximise use of available data, 30-second fatigue index was chosen for the remaining experiments.

In contrast to previous published studies (Sanjak, Brinkmann et al. 2001), no significant differences were found in fatigue index between patients and controls, and this did not appear to be attributable to differential effects of age, gender, or baseline maximal voluntary force of contraction. This latter finding is consistent with the observation that fatigability is a pathophysiological process that appears largely independent of muscle weakness (Sanjak, Brinkmann et al. 2001). Of note, in multiple regression, age appeared to influence fatigue in a model including participant status. Although this appears biologically plausible (Avlund 2010), interpretation needs to be cautious as the p value was 0.048 and so may represent a type I error. Fatigue index values were, on average, higher than those reported in (Sanjak, Brinkmann et al. 2001), both for patients and controls. The reason for this difference is unclear and may be methodological, for example in relation to measurement apparatus.

In summary, no significant differences between patients and controls in fatigue index were detected.

5.5.2 Neurophysiological response to fatigue

Some of the results from experiments conducted in this chapter were unexpected. It was hypothesised that a greater reduction in post-contraction MUNIX and greater increase in post-contraction MUSIX would be detected in patients compared to controls. On the contrary, there was an increase in MUNIX and decrease in MUSIX observed in a proportion of patients (although no statistically significant group-level differences between patients and control responses pre- and post-contraction were detected). Although interpretation needs to be cautious, these results are interesting as a quarter of patients (seven of 19 patients) responded to fatigue with both increased MUNIX and decreased MUSIX. This pattern post-contraction (increased MUNIX and decreased MUSIX) was not observed at all in controls. A hypothesis is that this discrepancy could reflect pathology. It is possible that such responses in MND could reflect relative sparing of type I motor units (comprising slow, less fatigable and oxidative muscle fibres) by the disease process. Previous studies have suggested that faster, more fatigable glycolytic motor units tend to be affected first in acute denervation (Pun, Santos et al. 2006, Hegedus, Putman et al. 2007). Furthermore, chronic reinnervation (leading to larger MUSIX) tends to be mediated by neurons supplying oxidative motor units (Frey, Schneider et al. 2000).

A significant decrease in persistence was detected in patients throughout fatigue measurements likely reflecting denervation. This is consistent with published literature and interpretation is strengthened by a linear relationship observed between patients' MUNIX and f-wave persistence. Of note, no linear relationship was found in controls, likely because f-wave persistence cannot exceed 100% (i.e. 30 in this experimental design), so results in controls may reflect a ceiling effect.

No differences in pre-contraction amplitude were detected between patients and controls but, in patients, amplitude increased substantially post-exercise, whereas it did not in controls. This may represent spinal cord hyperexcitability, unmasked by muscle contraction.

5.5.3 Skeletal muscle bioenergetic and ionic status as a predictor of fatigability

The resting spectroscopy parameters related to bioenergetics did not correlate with fatigue index. This was observed in both controls and patients. Numerous reports illustrate that neuromuscular fatigue is separate, in terms of pathophysiology, from MND-related degeneration, and general muscle weakness (Sanjak, Brinkmann et al. 2001). They are postulated to be two separate pathophysiological processes. This appears reflected in our data. Bioenergetic parameters (ΔG_{ATP} and Pi) were found to be associated with denervation, muscle weakness, and slower walking speed (chapter four), whereas free Mg^{++} concentration and pH were not. In this chapter it was shown that intracellular Mg^{++} and pH were significantly correlated with fatigue index in controls, but not in patients. This finding is consistent with previously published literature illustrating that fatigability on muscle level is affected by ionic

intracellular milieu (Westerblad, Allen et al. 2002). Interestingly, no correlation was found in patients, perhaps suggesting that other pathophysiological processes predominate in terms of fatigability in MND.

When comparing dynamic spectroscopic results acquired at one third and full maximal voluntary isometric contraction, the interaction term was significant for Pi and PCr curves in controls, but not in patients. In MND, the curves largely overlapped and no significant differences were detected either in the interaction terms, or in the between-group (i.e one third compared to maximal contraction) terms; the only significant factor was time. This finding is difficult to interpret, but may reflect decreased motor unit recruitment upon maximal contraction in a proportion of patients. An alternative explanation is that patients may be at near maximal oxidative capacity at a third MVIC contraction, hence at higher contraction forces, a relatively larger proportion of ATP is generated through glycolysis (as opposed of being of mitochondrial origin), hence not affecting the PCr pool.

5.5.4 Modelling fatigability in healthy and MND

Following the abovementioned experiments, parameters representing central, peripheral, and muscular fatigue were chosen and included in multiple regressions to assess contribution to fatigue index. F-wave amplitude was the only parameter thought to reflect central excitability. Percentage difference in MUNIX was selected as this may reflect smaller motor units dropping out due to fatigue, and hence represent an important peripheral phenomenon involved in fatigability. Correlations between f-wave persistence and MUSIX percentage difference meant that these latter two parameters were likely to be collinear. In addition, f-wave persistence has a ceiling effect in healthy controls, as previously discussed, so is not ideal for multiple linear regressions. Amongst spectroscopic parameters, pH and free intracellular magnesium concentration were the only metabolites shown to correlate with fatigue index in controls; free Mg^{++} was chosen because pH did not survive correction for multiple comparisons.

In healthy controls, resting intracellular free Mg^{++} concentration and MUNIX changes post-contraction were predictors of fatigability, indicating that peripheral factors were predominant, whereas this was not the case in patients. In MND, the main predictor of fatigability was post-contraction f-wave amplitude, an indicator of spinal cord excitability, suggesting that central factors may be more relevant to neuromuscular fatigue in MND.

5.5.5 Limitations and future directions

A major limitation of this study is the small sample size, increasing the risk of type II errors especially in results related to f-wave measurements (as there were additionally missing datapoints for this parameter).

Another limitation is lack of data inherent to subjective fatigue of patients (e.g. the Neurological Fatigue Index (Gibbons, Mills et al. 2011)). Inclusion of the Neurological Fatigue Index questionnaire would have required extra time of patients. Of note, experiments here described were conducted in conjunction to those in chapter four, with the entire research visit already lasting between two and a half and five hours. In addition, given the complex nature of global fatigue, results are difficult to interpret without additional data related to patients' premorbid and current psychological status, and this would have required additional questionnaires. Hence, the focus of this study was exclusively on motor fatigue.

Another limitation of this study is lack of other measures of central fatigability. The gold standard to assess excitability and central fatigability is TMS, but equipment was not available to researchers; hence assessment of central fatigue focussed on f-wave amplitude. TMS could be incorporated into future experimental protocols in combination with neurophysiological index (Vucic, Cheah et al. 2011) and potentially other central measures, such as modified MUNIX, to further elucidate motor fatigue (Uslu, Nüzket et al. 2018)

5.6 CONCLUSION

The aim of the experiments reported in this chapter was to characterise bioenergetic and neurophysiological changes occurring in muscle in MND during and after prolonged strenuous exercise to gain insights into pathophysiology of disease. No increase in fatigability measures was detected in people living with MND compared to healthy controls, but differential neurophysiological and spectroscopic responses to exercise were evident, indicating heterogeneous pathophysiological changes at central, peripheral, and muscular level. The main contributors to fatigue in healthy controls appear to relate to skeletal muscle resting ionic status and peripheral dropping out of motor units, whereas central factors appeared more prominent in MND.

CHAPTER 6:
31-PHOSPHORUS MAGNETIC RESONANCE SPECTROSCOPY TO ASSESS LONGITUDINAL BIOENERGETICS IN MUSCLE IN MOTOR NEURON DISEASE

This chapter concludes reporting of the experimental work applying ^{31}P-MRS to characterise MND. In the following experiments, ^{31}P-MRS was applied in conjunction with established clinical assessments and neurophysiology to assess longitudinal changes occurring in muscle in MND, and to establish whether the technique could be used as a biomarker of disease progression. To date, this is the first longitudinal study assessing bioenergetics in muscle *in vivo* in MND using ^{31}P-MRS.

6.1 AIMS AND HYPOTHESES

The aims of the experiments reported in this chapter were, firstly, to assess effects of disease progression on bioenergetic parameters over time, and, secondly, to determine whether ^{31}P-MRS results measured at baseline could predict participant attrition at follow-up visits. Attrition is a major issue in longitudinal MND imaging studies and is due primarily to patients being unable to attend follow-up visits due to rapidly progressing disability. These are the first steps necessary in establishing ^{31}P-MRS as a predictive biomarker.

The hypotheses were that:

1) The bioenergetic status of muscle would change in patients over time whereas it would remain stable in controls. It was hypothesised that longitudinal changes would be evident in the following parameters identified to be important in muscle in chapter four: ΔG_{ATP} absolute value, Pi, PME, and pH would increase and Mg^{++} would decline over the course of the disease.
2) It would be possible to use clinical, neurophysiological, and spectroscopic parameters to predict whether patients would be able to attend their follow-up visits or not.

6.2 METHODS

6.2.1 Research participants

Patient and control recruitment is detailed in chapter four and was conducted under the same ethical approval (Yorkshire and the Humber REC 13/YH/0273). The same group of patients recruited for study described in chapters four and five were invited to attend two additional research visits at four- and 12-month intervals. Healthy controls were invited to attend a single additional research visit after a four-month interval to ensure measurements' stability over time. The same inclusion and exclusion criteria used for the cross-sectional study were applied and all participants were aware that they could withdraw at any time from the research study.

6.2.2 Clinical and neurophysiological data

The same clinical and neurophysiological data acquired in chapter four were also collected at each subsequent follow-up visit.

6.2.3 Magnetic resonance imaging and spectroscopy

6.2.3.1 Hardware and sequences

All scans were conducted using the same hardware and muscle resting sequence (sequence 24 in chapter two) described in previous chapters. The resting muscle scanning protocol was identical to that described in chapter four, with the ipsilateral leg scanned at follow-up visits and positioning of the region of interest always cross-checked by the author to ensure consistency between visits.

6.2.3.2 Spectroscopic data processing and reported parameters

As in chapter four, data anonymisation was ensured by assigning a random number to all research participants, and analysis was performed by the author who was blinded to participant status and timepoint.

Spectroscopic signal processing methodology was identical to chapter four, except that no data were available for controls at visit three, hence it was not possible to calculate ADP and ΔG_{ATP} for patients using contemporaneously acquired healthy control values at this time-point. Since healthy control values were shown to be stable over time (as illustrated in this chapter's results), control data at visit two were substituted for this calculation for patients at both visits two and three.

6.2.4 Statistical analyses

As in previous chapters, continuous variables in patients and controls were compared using either unpaired t-tests with Welch correction or Mann-Whitney U tests depending on normality of data distribution, assessed using the D'Agostino-Pearson test, with significance set at $p<0.05$. Categorical data were compared using chi-squared tests. Correction for multiple comparisons was conducted using the two-stage linear step-up procedure (Benjamini, Krieger et al. 2006) with q set at 5%. These tests were conducted in GraphPad Prism (version 8.3.0 for Windows, GraphPad Software, San Diego, California USA, www.graphpad.com).

Longitudinal analysis was conducted using a multilevel mixed effect linear regression in STATA (StataCorp. 2019. Stata Statistical Software: Release 16. College Station, TX: StataCorp LLC) applying the *xtmixed* function. The longitudinal modelling approach in Stata accounts for participant drop-out and this is one of the reasons this approach was chosen. The predictive model includes all available data at each time-point. For any analysis returning significant results, the model was re-run with age and gender as additional predictors to assess for any influence of these potential confounders. P values, margins and adjusted 95% CIs were reported.

To assess whether baseline parameters could be used as predictors of patient attrition, ordered logistic regression models were specified in STATA (StataCorp. 2019. Stata Statistical Software: Release 16. College Station, TX: StataCorp LLC) using the *ologit* function with number of visits attended assigned as the dependent variable. The following independent variables were each entered in turn: weight, ALSFRS-R, slow vital capacity, UMN score, MVIC, 10-metre walk test, MUNIX, MUSIX, ΔG_{ATP} γATP, PCr, ADP, Pi, pH, Mg^{++}, PME, PDE, NAD(P)H+$NAD(P)^{+}$. P values were reported, and, for any significant results, values at baseline were plotted as a function of number of visits attended using GraphPad Prism (version 8.3.0 for Windows, GraphPad Software, San Diego, California USA, www.graphpad.com). Of note, these graphs were reported to visualise data and aid identification of direction of change, but statistical significance was assessed from the ordered logistic regression models.

6.3 RESULTS

6.3.1 Participants

Seven patients withdrew from the study prior to visit two: one did not provide a reason, and six were unable because of disease progression (two for general frailty/weakness and four because of neuromuscular respiratory failure). A further six patients were unable to attend the third visit: one had

died, two because of frailty, and three were unable to lie in scanner due to neuromuscular respiratory failure. All healthy controls attended both visits.

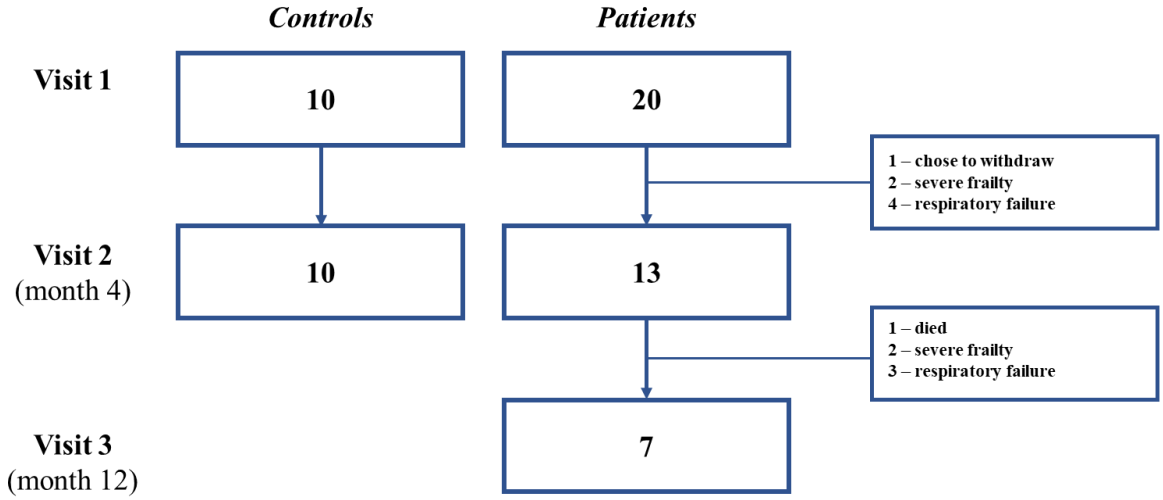

Figure 6.1 Flow chart illustrating number of participants that attended research visits.
All healthy controls were scanned at visit one and two. Seven patients withdrew prior to visit two and six patients prior to visit three.

Missing data at visit one were reported in chapter four.

In two patients attending the second visit, neurophysiological tests, 10-metre walk, and measurements of force could not be acquired: in one case because of complete muscle paralysis and, in the other, because the patient declined. Another patient was unable to perform the 10-metre walk test because they were now wheelchair-bound. In a further patient at visit two, neurophysiological data could not be acquired due to unavailability of personnel. At visit two, spectroscopy was conducted in all participants and all spectra could be fitted.

At visit three, one patient could not perform the 10-metre walk because they were wheelchair-bound. Neurophysiological data could not be collected from one of the remaining seven patients who attended visit three due to unavailability of personnel. Spectroscopy was conducted in all patients and all spectra could be fitted also at visit three.

6.3.2. Descriptive statistics and between-group comparisons

6.3.2.1. Clinical and neurophysiological parameters

Descriptive statistics and between-group comparisons of clinical, neurophysiological, and spectroscopic parameters at visit one were described in chapter four (results section).

The table below illustrates descriptive statistics for clinical and neurophysiological parameters at visit two. No statistically significant differences were found between patients and controls in age, gender, or weight. There was a trend towards lower force of contraction of tibialis anterior which did not reach statistical significance (p=0.099). Speed of walking and MUNIX were significantly reduced in patients (p=0.026 and p=0.005, respectively), whereas MUSIX was elevated (p=0.003). P values retained significance after correction for multiple comparisons.

Table 6.1 Clinical and neurophysiological parameters in patients and healthy controls at visit two.
A hash symbol indicates that groups were compared using Mann-Whitney U test as data were not normally distributed, hence, median and interquartile range (IQR) are reported instead of mean and standard deviation. Asterisks indicate values that remained significant following correction for multiple comparisons. Results were corrected for multiple comparisons using the Benjamini, Krieger, and Yekutieli method (q=0.05). 10m-WT: Ten-metre walk test, ALSFRS-R: Revised amyotrophic lateral sclerosis functional rating scale, F: Female, M: male, MUNIX: Motor unit number index, MUSIX: Motor unit number size index, MVIC: Maximal voluntary isometric contraction, NA: Not applicable, SD: Standard deviation, SVC: Slow vital capacity, UMN: Upper motor neuron.

	Controls ***mean (±SD)***	***Patients*** ***mean (±SD)***	***p***
n	10	13	
Age (years)	57.70 (±10.81)	62.31 (±13.45)	*0.387*
Gender	5 F : 5 M	4 F : 9 M	*0.373*
Weight (Kg)	73.00 (±13.79)	73.00 (±14.79)	*>0.999*
ALSFRS-R	NA	37.08 (±4.11)	*NA*
SVC (% predicted)	NA	78.54 (±19.06)	*NA*
UMN score	NA	10.62 (±2.93)	*NA*
MVIC (Kg)	median=13.67 (IQR=1.39)	median=7.29 (IQR=8.40)	*0.099#*
10m-WT (sec)	**4.56 (±0.74)**	**10.18 (±6.68)**	***0.026****
MUNIX	**111.5 (±19.75)**	**72.04 (±32.74)**	***0.005****
MUSIX (µV)	**45.01 (±4.46)**	**52.93 (±5.84)**	***0.003****

Table 6.2 illustrates descriptive statistics for patients at visit one, two, and three.

Table 6.2 Clinical and neurophysiological parameters in patients at visit one, two , and three.
10m-WT: Ten-metre walk test, ALSFRS-R: Revised amyotrophic lateral sclerosis functional rating scale, MUNIX: Motor unit number index, MUSIX: Motor unit number size index, MVIC: Maximal voluntary isometric contraction, SD: Standard deviation, SVC: Slow vital capacity, UMN: Upper motor neuron.

	Visit one mean (±SD)	***Visit two mean (±SD)***	***Visit three mean (±SD)***
n	20	13	7
Age (years)	62.45 (±12.36)	62.31 (±13.45)	56.14 (±14.02)
Gender	7 F : 13 M	4 F : 9 M	1 F : 6 M
Weight (Kg)	74.50 (±12.31)	73.00 (±14.79)	75.56 (±15.14)
ALSFRS-R	36.95 (±5.22)	37.08 (±4.11)	35.14 (±5.46)
SVC (% predicted)	85.60 (±22.85)	78.54 (±19.06)	84.00 (±15.72)
UMN score	10.22 (±2.92)	10.62 (±2.93)	10.71 (±4.75)
MVIC (Kg)	8.25 (±5.68)	8.38 (±5.59)	10.34 (±8.09)
10m-WT (sec)	8.73 (±3.73)	10.18 (±6.68)	6.24 (±1.73)
MUNIX	66.67 (±29.54)	72.04 (±32.74)	79.73 (±33.27)
MUSIX (μV)	51.96 (±8.98)	52.93 (±5.84)	48.98 (±9.67)

6.3.2.2 Resting spectroscopic parameters

Table 6.3 illustrates between-group comparisons of spectroscopic parameters acquired at rest at visit two. A significant increase in pH, Pi, and PMEs was detected in patients (p=0.048, p=0.025, and p=0.021, respectively), although none of significant p values survived correction for multiple comparisons. A non-significant trend toward lower values was found for γATP values (p=0.051). Table 6.4 details descriptive statistics for resting spectroscopic parameters in patients at visit three.

Table 6.3 Resting spectroscopic parameters in patients and healthy controls at visit two.
A hash symbol indicates that groups were compared using Mann-Whitney U test as data were not normally distributed, hence, median and interquartile range (IQR) are reported instead of mean and standard deviation. Significant p values did not survive correction for multiple comparisons. γATP: γ phosphate of adenosine triphosphate, SD: Standard deviation, NAD(P)H+NAD(P)$^+$: Nicotinamide adenine dinucleotides.

Spectroscopic parameter	***Controls mean (±SD)***	***Patients mean (±SD)***	***p***
ΔG_{ATP} (kilojoule/mole)	median=-62.68 (IQR=0.79)	median=-67.70 (IQR=3.55)	0.738$^{\#}$
γATP	0.13 (±0.02)	0.11 (±0.01)	*0.051*
Phosphocreatine	0.56 (±0.02)	0.55 (±0.05)	*0.609*
Adenosine diphosphate (μM)	median=24.12 (IQR=8.52)	median=25.63 (IQR=30.98)	*0.784$^{\#}$*
Inorganic phosphate	**0.07 (±0.01)**	**0.08 (±0.02)**	***0.025***
pH	**6.93 (±0.03)**	**6.96 (±0.03)**	***0.048***
Free magnesium (mM)	0.40 (±0.06)	0.32 (±0.15)	*0.117*
Phosphomonoesters	**median=0.02 (IQR=0.00)**	**median=0.03 (IQR=0.01)**	***0.021$^{\#}$***
Phosphodiesters	0.06 (±0.02)	0.06 (±0.02)	*0.870*
NAD(P)H+NAD(P)$^+$	0.02 (±0.01)	0.02 (±0.01)	*0.930*

Table 6.4 Resting spectroscopic parameters in patients at visit three.
γATP: γ phosphate of adenosine triphosphate, SD: Standard deviation, NAD(P)H+NAD(P)$^+$: Nicotinamide adenine dinucleotides.

Spectroscopic parameter	***Patients mean (±SD)***
ΔG$_{ATP}$ (kilojoule/mole)	-63.23 (±2.38)
γATP	0.11 (±0.01)
Phosphocreatine	0.57 (±0.05)
Adenosine diphosphate (μM)	33.08 (±47.76)
Inorganic phosphate	0.07 (±0.02)
pH	6.96 (±0.11)
Free magnesium (mM)	0.39 (±0.14)
Phosphomonoesters	0.04 (±0.02)
Phosphodiesters	0.06 (±0.03)
NAD(P)H+NAD(P)$^+$	0.02 (±0.02)

6.3.3 Longitudinal clinical, neurophysiological, and spectroscopic analysis

6.3.3.1 Clinical and neurophysiological parameters

Weight of controls remained stable over time (Figure 6.2, p=0.320, 95% CIs=from -0.58 to 1.78). Weight in patients declined over time, not significantly at visit two (p= 0.633, 95% CIs=from -2.16 to 1.32), reaching statistical significance at visit three (p=0.012, 95% CIs=from -5.08 to -0.62), and surviving correction for age (p=0.025, 95% CIs=from -4.83 to -0.33) and gender (p=0.012, 95% CIs=from -5.10 to -0.64), as illustrated below.

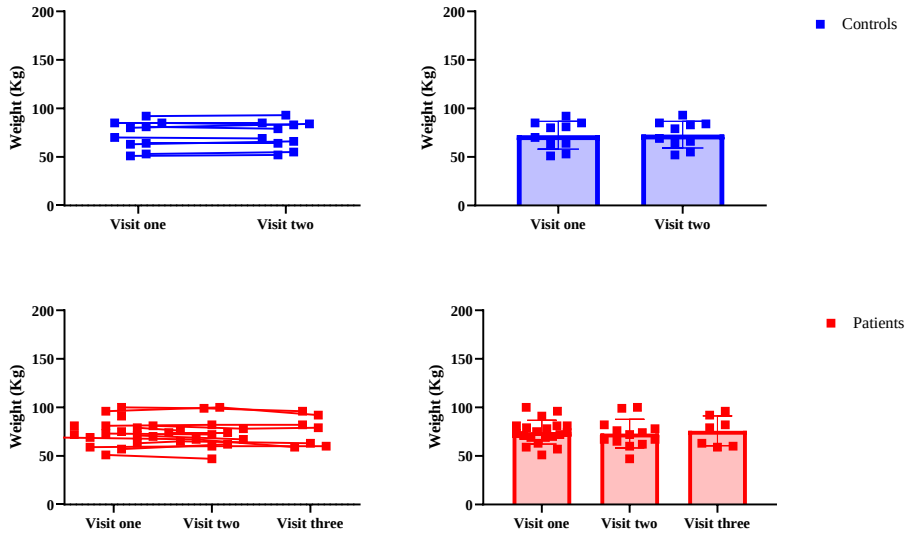

Figure 6.2 The graphs above illustrate individual datapoints for controls (blue) at visit one and two, and for patients (red) at visit one, two, and three. The parameter illustrated is weight, expressed in Kg. For clarity, line graphs connecting repeated values are reported on the left, whereas scatter plots with mean and standard deviations are reported on the right.
Weight of controls remained stable over time (blue). In patients, significant changes were detected at 12 months (i.e. between visit one and visit three and between visit two and visit three), whereas no significant differences were detected between visit one and visit two.

ALSFRS-R declined over time, as illustrated in Figure 6.3; no significant differences were found between visit one and two (p=0.369, 95% CIs=from -2.44 to 0.91), whereas a significant decline was detected after a year (p<0.001, 95% CIs=from -6.04 to -1.75) which survived correction for age (p<0.001, 95% CIs=from -6.04 to -1.75) and gender (p<0.001, 95% CIs=from -6.10 to -1.70).

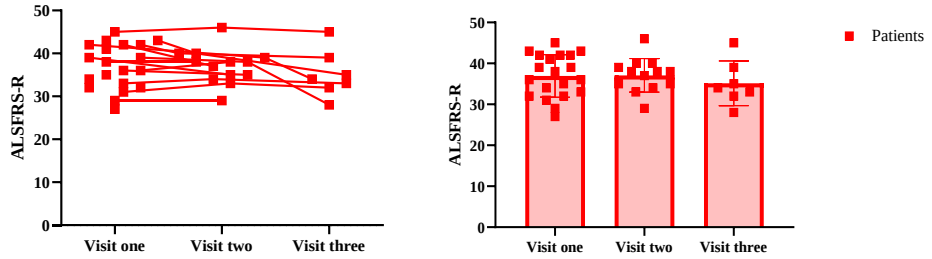

Figure 6.3 The graphs above illustrate individual datapoints for patients (red) at visit one, two, and three. The parameter illustrated is the revised amyotrophic lateral sclerosis functional rating scale (ALSFRS-R). For clarity, line graphs connecting repeated values are reported on the left, whereas scatter plots with mean and standard deviations are reported on the right.
Significant changes were detected at 12 months (i.e. between visit one and visit three and between visit two and visit three), whereas no significant differences were detected between visit one and visit two.

Figure 6.4 illustrates that slow vital capacity declined significantly in patients at visit two (p=0.005, 95% CIs=from -19.21 to -3.33) and three (p=0.030, 95% CIs=from -21.43 to -1.09), surviving correction for both age (visit one to visit two: p=0.005, 95% CIs=from -19.22 to -3.33; visit one to visit three: p=0.030, 95% CIs=from -21.43 to -1.08) and gender (visit one to visit two: p=0.007, 95% CIs=from -19.00 to -3.00; visit one to visit three: p=0.044, 95% CIs=from -20.78 to -0.29). The main decrease took place in the first four months, whereas values stabilised between visit two and visit three (p=0.998, 95% CIs=from -10.31 to 10.34).

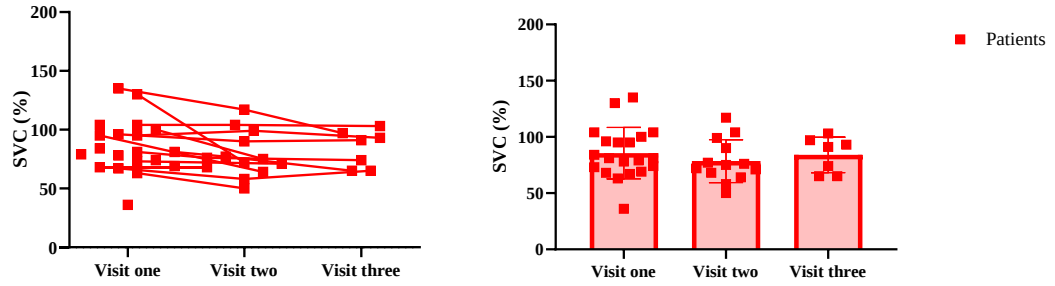

Figure 6.4 The graphs above illustrate individual datapoints for patients (red) at visit one, two, and three. The parameter illustrated is slow vital capacity (SVC) expressed as percentage of predicted. For clarity, line graphs connecting repeated values are reported on the left, whereas scatter plots with mean and standard deviations are reported on the right.
Significant decline was detected taking place in first four months.

UMN score remained stable over the study period (visit one to visit two: p=0.734, 95% CIs=from -1.87 to 2.66; visit one to visit three: p= 0.728, 95% CIs=from -2.28 to 3.27), although variability increased over time, as illustrated in Figure 6.5.

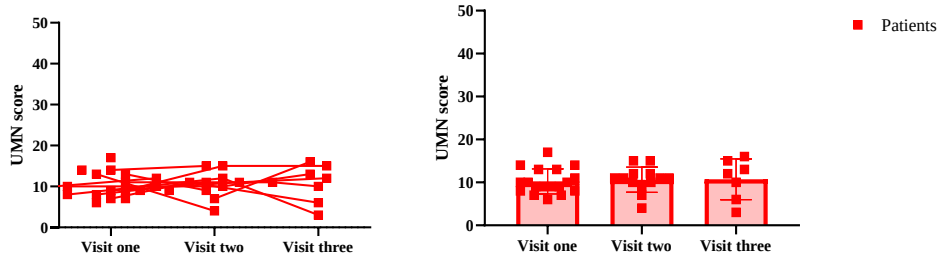

Figure 6.5 The graphs above illustrate individual datapoints for patients (red) at visit one, two, and three. The parameter illustrated is upper motor neuron (UMN) score. For clarity, line graphs connecting repeated values are reported on the left, whereas scatter plots with mean and standard deviations are reported on the right.
No significant changes were detected over time.

No significant longitudinal changes were detected in maximal voluntary contraction force either in controls (p=0.792, 95% CIs=from -1.66 to 2.18), or in patients (visit one to visit two: p=0.246, 95% CIs=from -3.71 to 0.95; visit one to visit three: p= 0.490, 95% CIs=from -3.77 to 1.81), as illustrated in Figure 6.6.

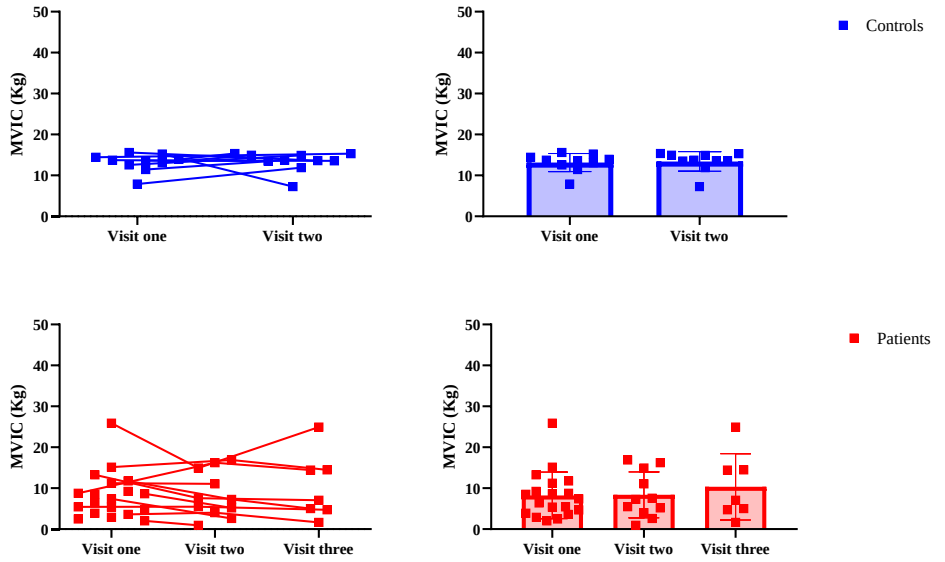

Figure 6.6 The graphs above illustrate individual datapoints for controls (blue) at visit one and two, and for patients (red) at visit one, two, and three. The parameter illustrated is maximal voluntary isometric contraction (MVIC) force, expressed in Kg. For clarity, line graphs connecting repeated values are reported on the left, whereas scatter plots with mean and standard deviations are reported on the right.
No significant changes were detected over time either in patients or in controls.

Speed of walking did not vary significantly over time in controls (p=0.781, 95% CIs=from -0.39 to 0.52). In patients, there was a trend towards slower walking speed at four months (p=0.076, 95% CIs=from -0.24 to 4.78), but measurements at one year were comparable to those at visit one (p=0.904, 95% CIs=from -2.89 to 3.27). Longitudinal speed of walking data are illustrated in Figure 6.7.

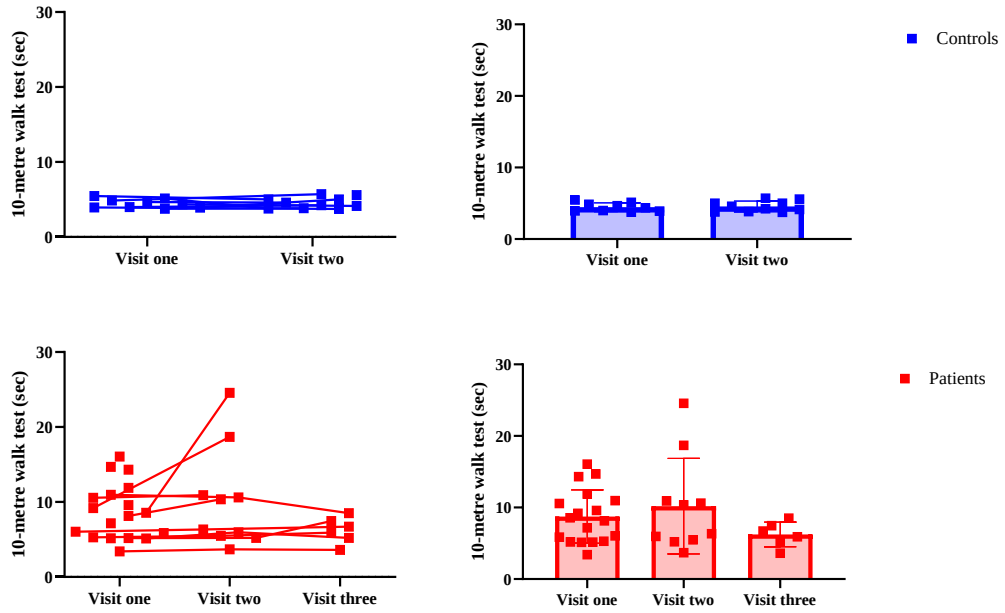

Figure 6.7 The graphs above illustrate individual datapoints for controls (blue) at visit one and two, and for patients (red) at visit one, two, and three. The parameter illustrated is ten-metre walk test (10m-WT) data, expressed in seconds. For clarity, line graphs connecting repeated values are reported on the left, whereas scatter plots with mean and standard deviations are reported on the right.
No significant changes were detected over time.

For MUNIX, no significant longitudinal changes were recorded in controls (p=0.620, 95% CIs=from -5.34 to 8.95). No changes were detected in MUNIX in patients either at visit two (p=0.680, 95% CIs=from -7.34 to 4.79) or at visit three (p=0.235, 95% CIs=from -11.94 to 2.92). Longitudinal MUNIX results are depicted in Figure 6.8.

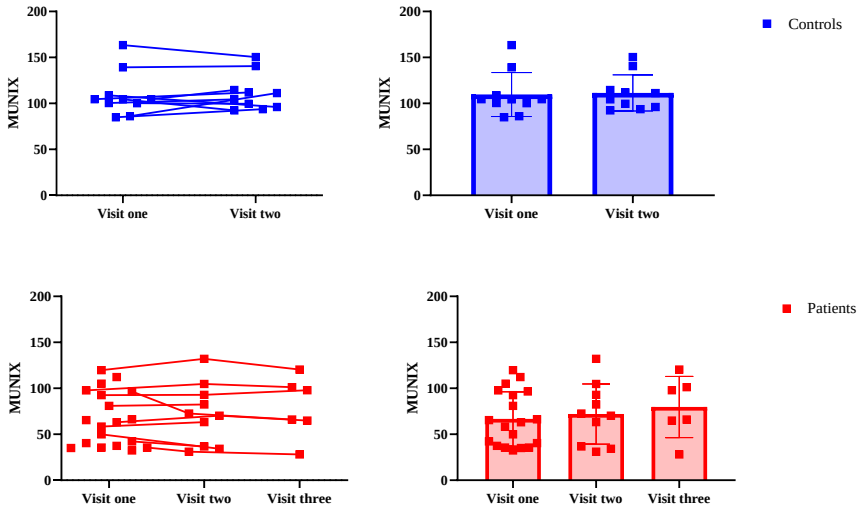

Figure 6.8 The graphs above illustrate individual datapoints for controls (blue) at visit one and two, and for patients (red) at visit one, two, and three. The parameter illustrated is the motor unit number index (MUNIX). For clarity, line graphs connecting repeated values are reported on the left, whereas scatter plots with mean and standard deviations are reported on the right.
No significant changes were detected over time.

For MUSIX, no longitudinal changes were detected in controls (p= 0.776, 95% CIs=from -1.96 to 2.63). Figure 6.9 shows that MUSIX did not vary significantly either at visit two (p=0.616, 95% CIs=from -3.72 to 6.28) or at visit three (p=0.648, 95% CIs=from -7.56 to 4.70) in patients.

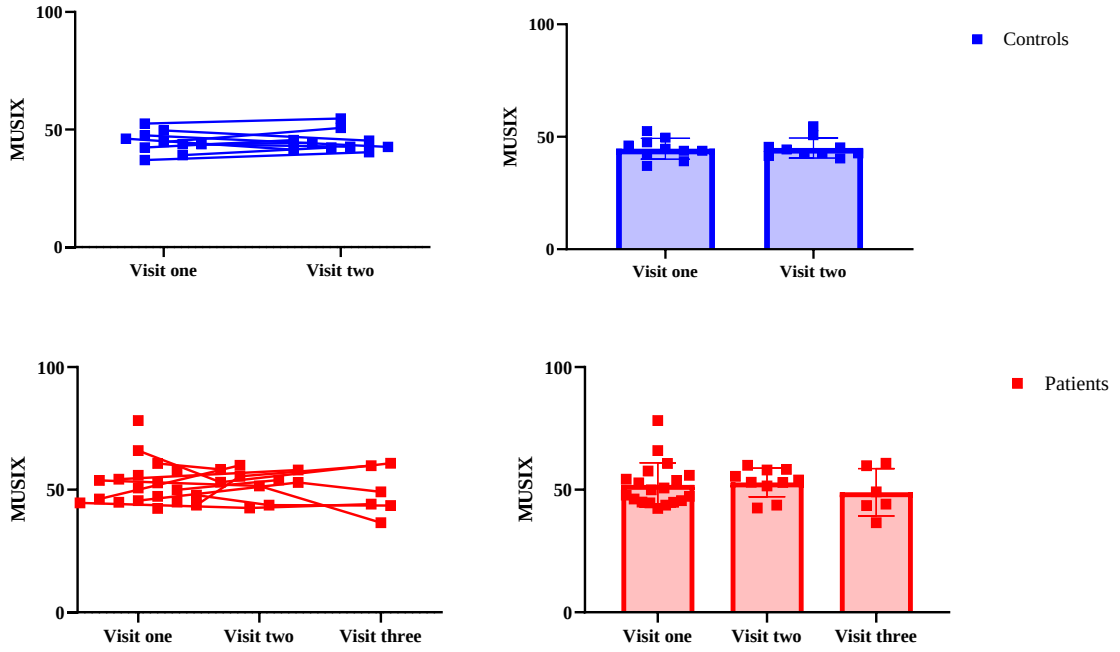

Figure 6.9 The graphs above illustrate individual datapoints for controls (blue) at visit one and two, and for patients (red) at visit one, two, and three. The parameter illustrated is the motor unit size index (MUSIX), expressed in μV. For clarity, line graphs connecting repeated values are reported on the left, whereas scatter plots with mean and standard deviations are reported on the right.
No significant changes were detected over time.

6.3.3.2 *Spectroscopic parameters*

ΔG_{ATP} of ATP hydrolysis remained stable in controls, although there was a non-significant trend toward lower absolute values after four months (p=0.059, 95% CIs=from -0.02 to 1.30; Figure 6.10). In patients, absolute values remained stable both at four months (p=0.168, 95% CIs=from -12.78 to 2.23) and after one year (p=0.879, 95% CIs=from -10.01 to 8.57; Figure 6.10).

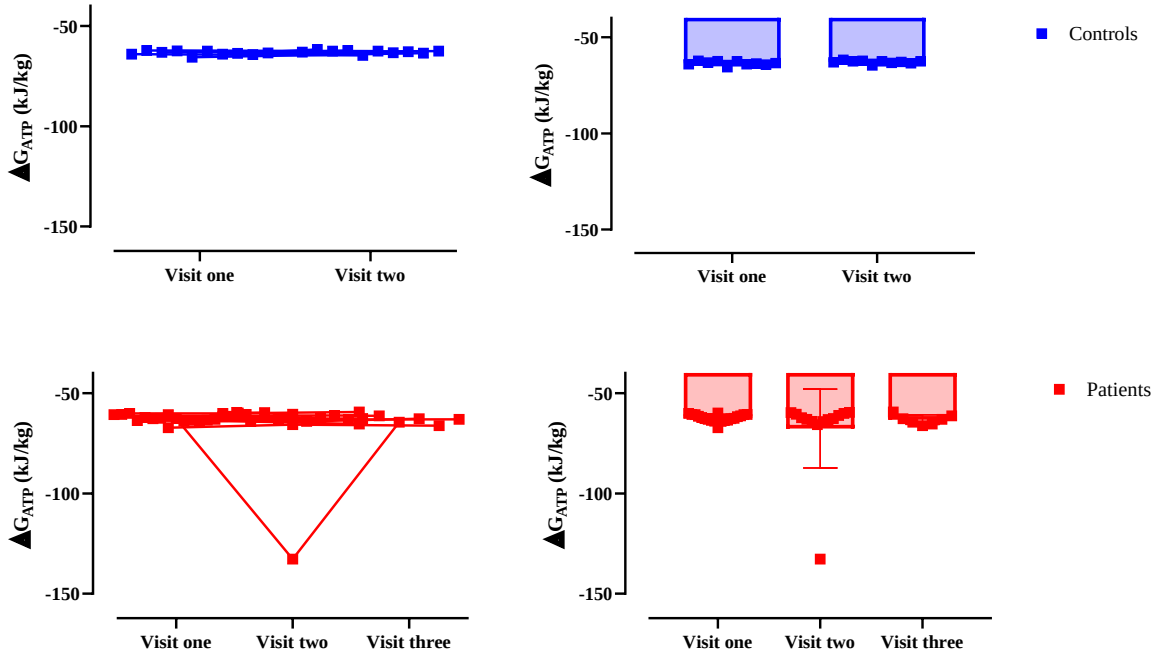

Figure 6.10 The graphs above illustrate individual datapoints for controls (blue) at visit one and two, and for patients (red) at visit one, two, and three. The parameter illustrated is Gibbs free energy (delta G) of ATP hydrolysis. For clarity, line graphs connecting repeated values are reported on the left, whereas scatter plots with mean and standard deviations are reported on the right.
No significant changes were detected over time.

ATP values remained stable in controls (p=0.468, 95% CIs=from -0.01 to 0.01), and declined in patients at visit two (p=0.153, 95% CIs=from -0.02 to 0.00), reaching statistical significance at visit three (p=0.036, 95% CIs=from -0.03 to -0.00), as illustrated in Figure 6.11. Significant results at visit three survived correction for age (p=0.024, 95% CIs=from -0.03 to -0.00) and gender (p=0.040, 95% CIs=from -0.03 to -0.00).

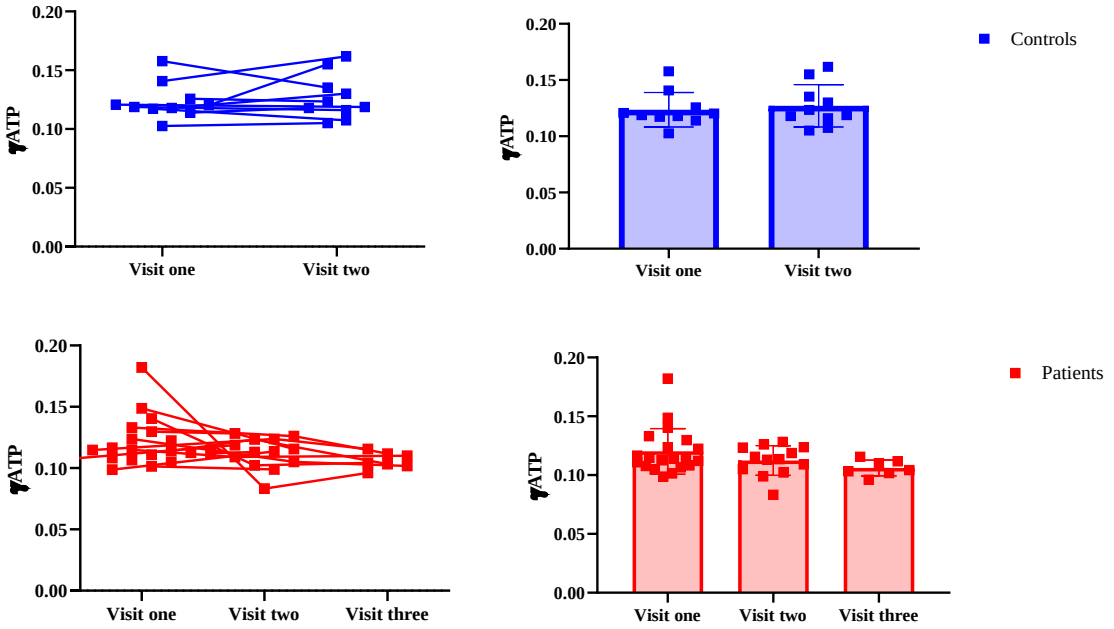

Figure 6.11 The graphs above illustrate individual datapoints for controls (blue) at visit one and two, and for patients (red) at visit one, two, and three. The parameter illustrated is ATP. For clarity, line graphs connecting repeated values are reported on the left, whereas scatter plots with mean and standard deviations are reported on the right.
No significant changes were detected over time in controls, whereas ATP declined significantly in patients at visit three.

Phosphocreatine remained stable over time both in controls (p=0.566, 95% CIs=from -0.02 to 0.01) and patients (at visit two: p=0.643, 95% CIs=from -0.01 to 0.02; at visit three: p=0.110, 95% CIs=from -0.00 to 0.04), as illustrated below.

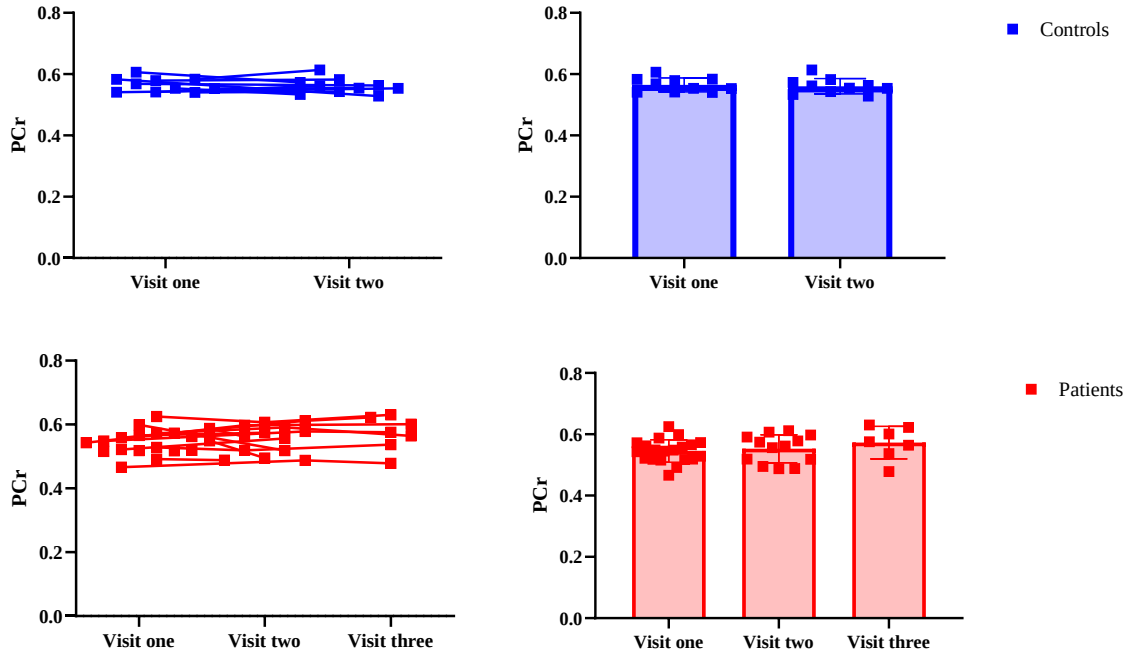

Figure 6.12 The graphs above illustrate individual datapoints for controls (blue) at visit one and two, and for patients (red) at visit one, two, and three. The parameter illustrated is phosphocreatine (PCr). For clarity, line graphs connecting repeated values are reported on the left, whereas scatter plots with mean and standard deviations are reported on the right.
No significant changes were detected over time.

ADP remained stable over time both in controls (p=0.103, 95% CIs=from -1.44 to 15.75) and patients (visit two: p= 0.455, 95% CIs=from -21.27 to 9.52; visit three: p=0.906, 95% CIs=from -20.82 to 18.45), as illustrated below.

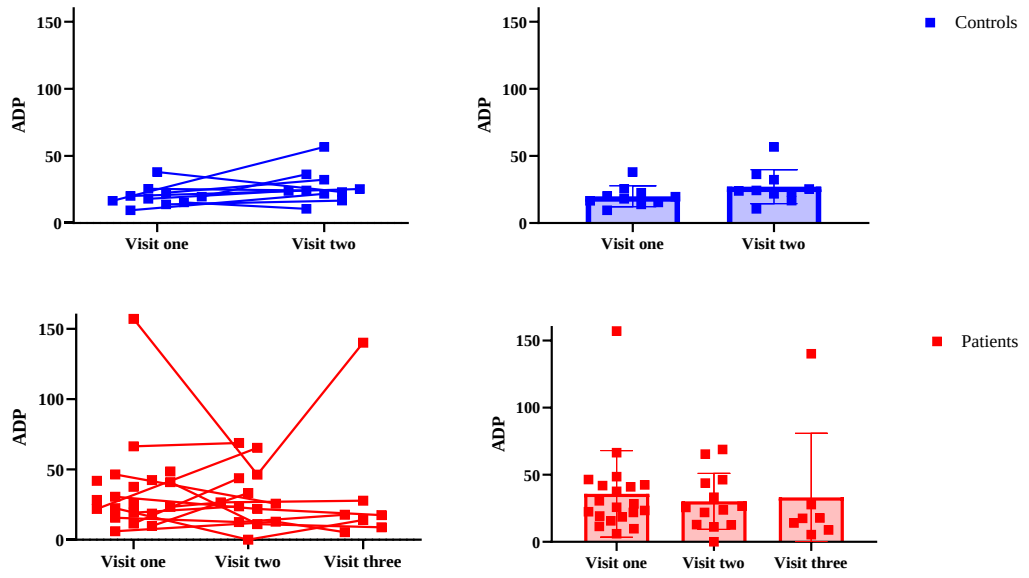

Figure 6.13 The graphs above illustrate individual datapoints for controls (blue) at visit one and two, and for patients (red) at visit one, two, and three. The parameter illustrated is ADP (expressed in micromolar uM). For clarity, line graphs connecting repeated values are reported on the left, whereas scatter plots with mean and standard deviations are reported on the right.
No significant changes were detected over time.

Inorganic phosphate remained stable over time both in controls (p=0.700, 95% CIs=from -0.01 to 0.01) and in patients (at visit two: p=0.374, 95% CIs=from -0.00 to 0.01; at visit three: p=0.676, 95% CIs=from -0.01 to 0.01), as illustrated below.

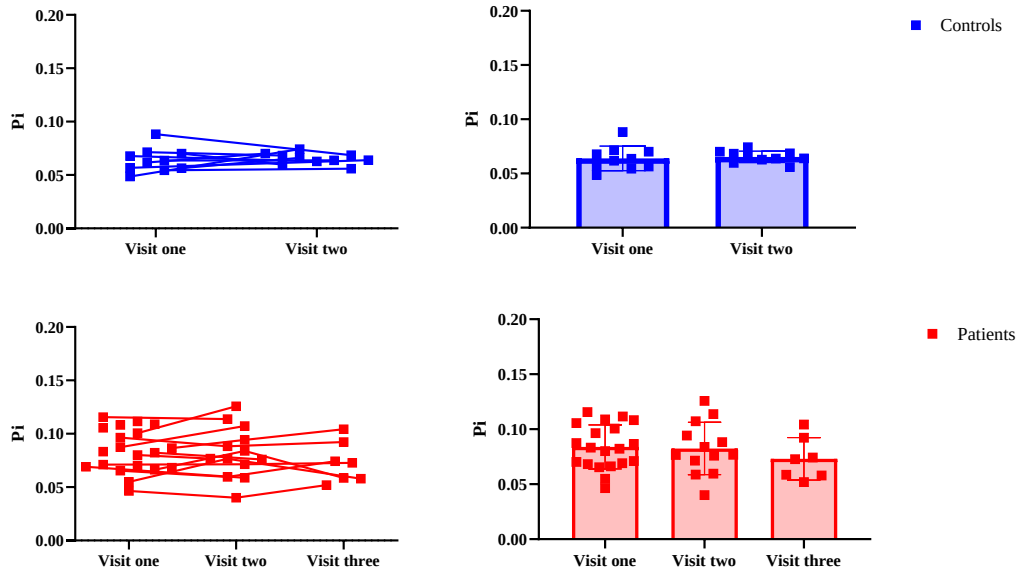

Figure 6.14 The graphs above illustrate individual datapoints for controls (blue) at visit one and two, and for patients (red) at visit one, two, and three. The parameter illustrated is inorganic phosphate (Pi). For clarity, line graphs connecting repeated values are reported on the left, whereas scatter plots with mean and standard deviations are reported on the right.
No significant changes were detected over time.

pH and Mg^{++} values remained stable both in controls and in patients, as illustrated below. For pH, in controls, p=0.912 (95% CI=-0.01 to 0.01); whereas for patients at visit two, p=0.897 (95% CIs=from -0.03 to 0.02) and at visit three p=0.744 (95% CIs=from -0.03 to 0.04). For Mg^{++} measurements, in controls, p= 0.367 (95% CI= -0.11 to 0.04); in patients, at visit two p=0.536 (95% CIs=from -0.11 to 0.06) and at visit three p=0.424 (95% CIs=from -0.06 to 0.15).

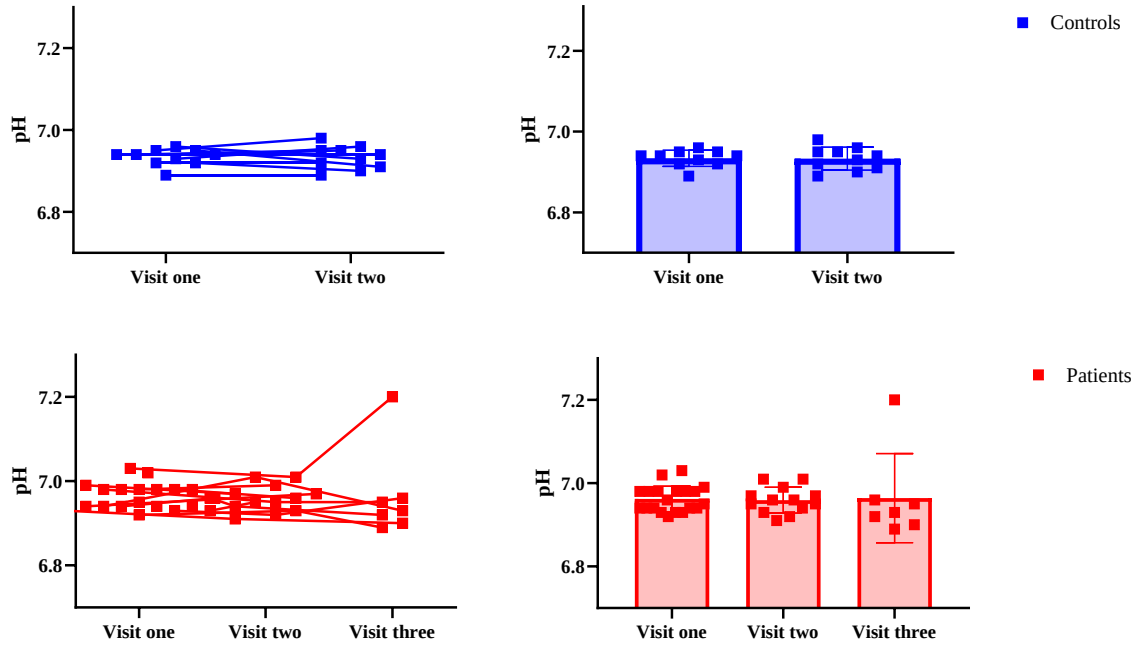

Figure 6.15 The graphs above illustrate individual datapoints for controls (blue) at visit one and two, and for patients (red) at visit one, two, and three. The parameter illustrated is pH. For clarity, line graphs connecting repeated values are reported on the left, whereas scatter plots with mean and standard deviations are reported on the right.
No significant changes were detected over time.

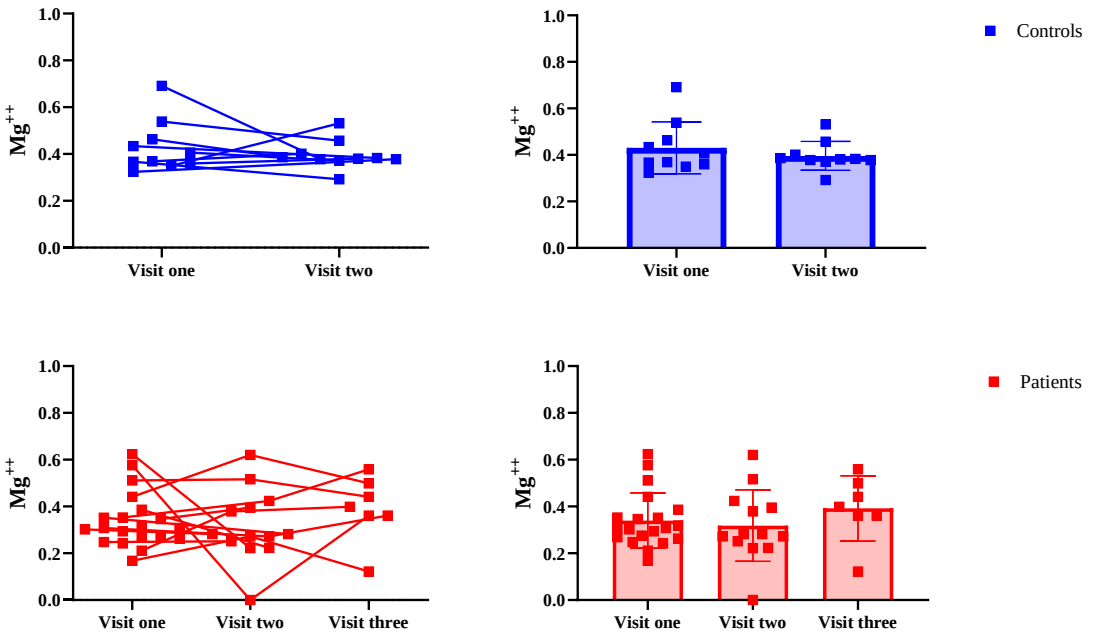

Figure 6.16 The graphs above illustrate individual datapoints for controls (blue) at visit one and two, and for patients (red) at visit one, two, and three. The parameter illustrated is free intracellular magnesium (Mg^{++}) expressed in millimolar. For clarity, line graphs connecting repeated values are reported on the left, whereas scatter plots with mean and standard deviations are reported on the right.
No significant changes were detected over time.

Phosphomonoesters were stable in controls (p=0.556, 95% CI= from -0.00 to 0.00). There was no change in patients at visit two (p=0.248, 95% CIs=from -0.00 to 0.01) and a non-significant trend towards higher values at visit three (p=0.094, 95% CIs=from -0.00 to 0.02; Figure 6.17).

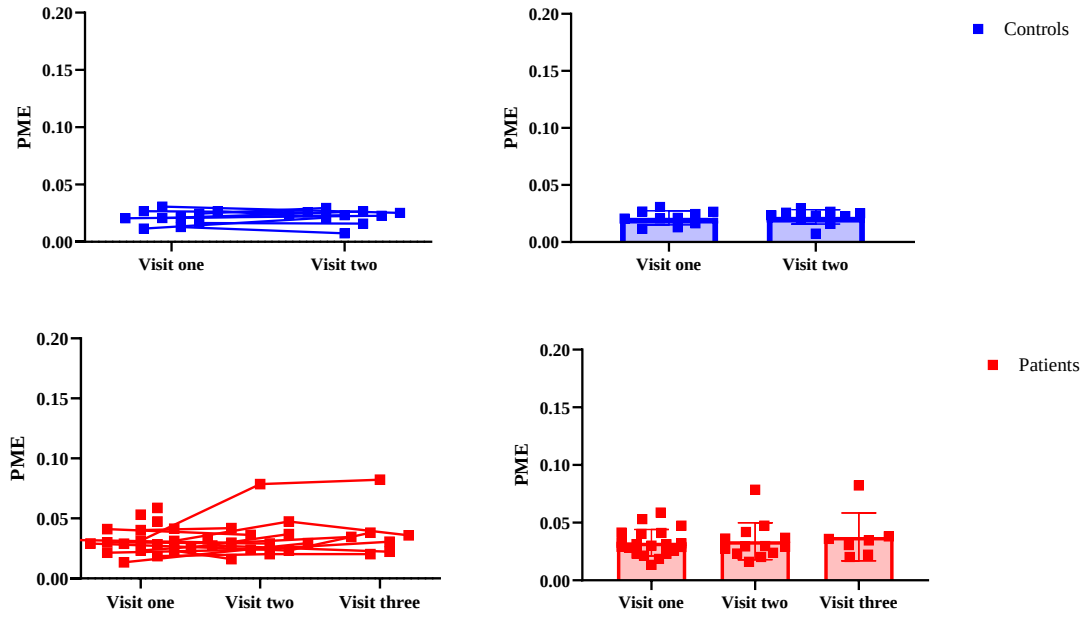

Figure 6.17 The graphs above illustrate individual datapoints for controls (blue) at visit one and two, and for patients (red) at visit one, two, and three. The parameter illustrated are phosphomonoesters (PME). For clarity, line graphs connecting repeated values are reported on the left, whereas scatter plots with mean and standard deviations are reported on the right. *No significant changes were detected over time.*

No longitudinal changes were detected in PDE and NAD(P^+ and NAD(P)H measurements either in controls or in patients, as illustrated in Figure 6.18 and Figure 6.19. In controls, for phosphodiesters p=0.439 (95% CI=from -0.02 to 0.01), whereas for NAD(P^+ and NAD(P)H p=0.940 (95% CI=from -0.00 to 0.00). In patients, PDE remained stable both at visit two (p=0.989, 95% CI=from-0.01 to 0.01) and visit three (p=0.390, 95% CI from=-0.02 to 0.01). For NAD(P^+ and NAD(P)H, in patients p=0.222 (95% CI from -0.00 to 0.01) at visit two and p=0.714 (95% CI=from -0.01 to 0.01) at visit three.

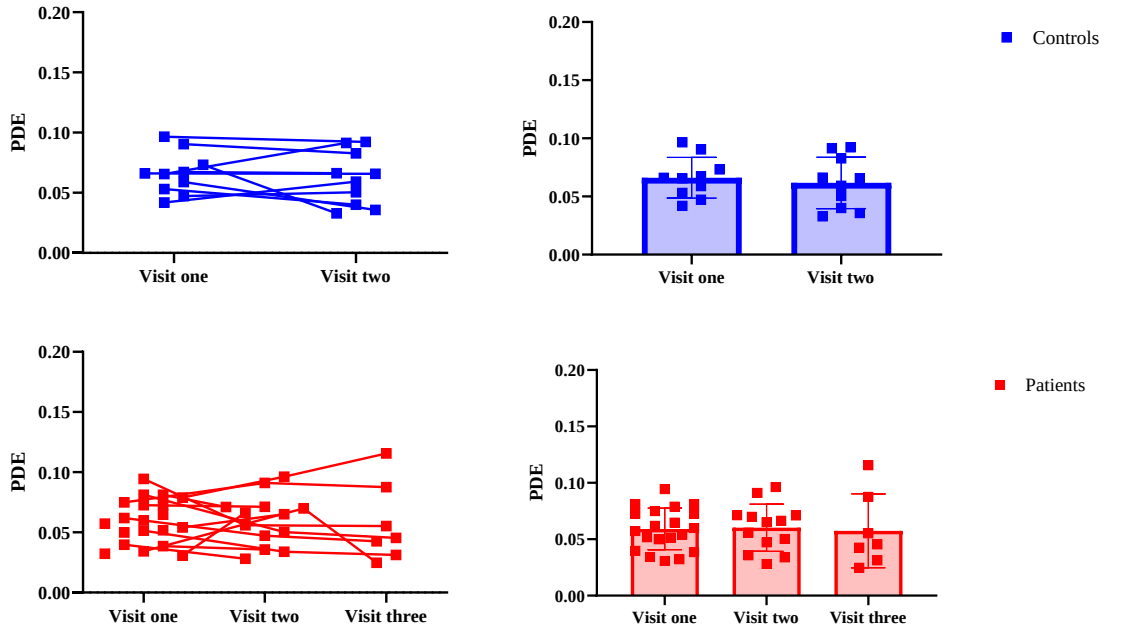

Figure 6.18 The graphs above illustrate individual datapoints for controls (blue) at visit one and two, and for patients (red) at visit one, two, and three. The parameter illustrated are phosphodiesters (PDE). For clarity, line graphs connecting repeated values are reported on the left, whereas scatter plots with mean and standard deviations are reported on the right.
No significant changes were detected over time.

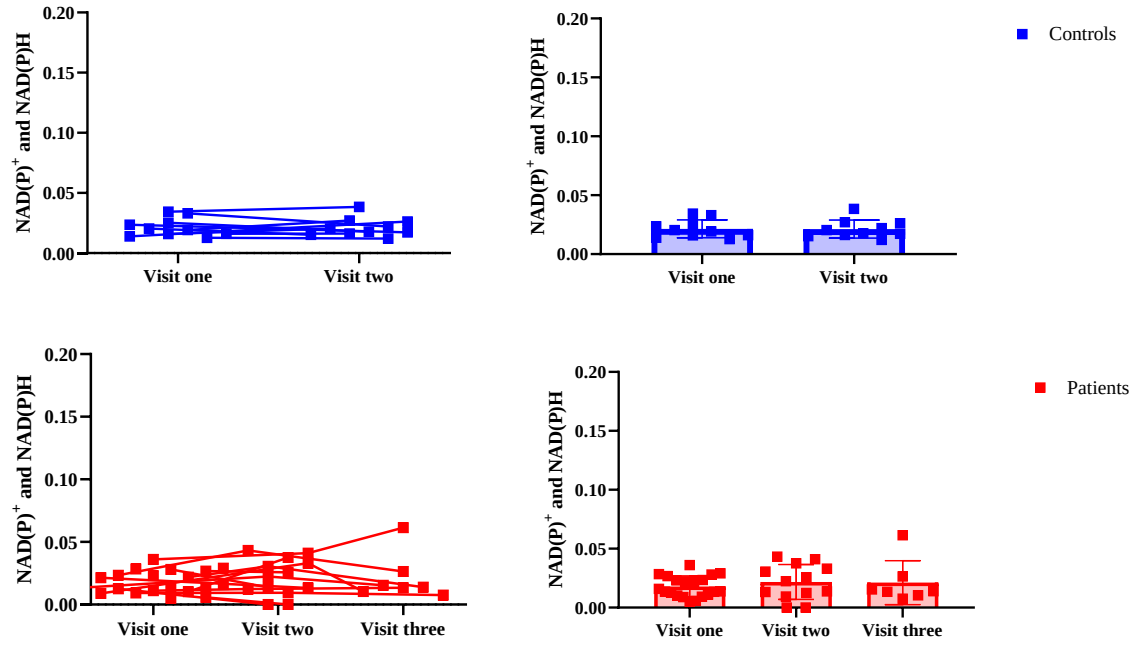

Figure 6.19 The graphs above illustrate individual datapoints for controls (blue) at visit one and two, and for patients (red) at visit one, two, and three. The parameter illustrated is nicotinamides dinucleotide (NAD(P$^+$ and NAD(P)H). For clarity, line graphs connecting repeated values are reported on the left, whereas scatter plots with mean and standard deviations are reported on the right.
No significant changes were detected over time.

6.3.4 Baseline predictors of attrition at follow-up visits

Results of ordered logistic regression are illustrated in table below. MVIC, 10-metre walk test, MUNIX, γATP, Pi, and PME were significant predictors of patient attrition.

Table 6.5 P values resulting from ordered logistic regression with number of visits attended as dependent variable and parameters listed in the left column each entered in turn as independent variables.
Maximal voluntary isometric contraction (MVIC), 10-metre walk test (10m-WT), motor unit number index (MUNIX), γ adenosine triphosphate (γATP), inorganic phosphate, and phosphomonoesters were significantly predictive. ALSFRS-R: Revised amyotrophic lateral sclerosis functional rating scale, MUSIX: Motor unit number size index, NAD(P)H+NAD(P)$^+$: Nicotinamide adenine dinucleotides, SVC: Slow vital capacity, UMN: Upper motor neuron.

Spectroscopic parameter	***p***
Weight (Kg)	0.771
ALSFRS-R	0.083
SVC (% predicted)	0.105
UMN score	0.396
MVIC (Kg)	**0.010**
10m-WT (sec)	**0.049**
MUNIX	**0.019**
MUSIX (μV)	0.644
ΔG$_{ATP}$ (kilojoule/mole)	0.116
γATP	**0.038**
Phosphocreatine	0.512
Adenosine diphosphate (μM)	0.637
Inorganic phosphate	**0.013**
pH	0.420
Free magnesium (mM)	0.163
Phosphomonoesters	**0.009**
Phosphodiesters	0.193
NAD(P)H+NAD(P)$^+$	0.891

In Figure 6.20, baseline predictors of number of follow-up visits are plotted. On the y-axis, baseline MVIC, 10-metre walk test, MUNIX, γATP, Pi, and PME values in patients are plotted against number of follow-up visits on the x-axis. The graphs below in conjunction with results of ordered logistic regression above illustrate that patients with stronger force of contraction, faster speed of walking, higher MUNIX and γATP, and lower Pi and PME at baseline were more likely to attend follow-up visits.

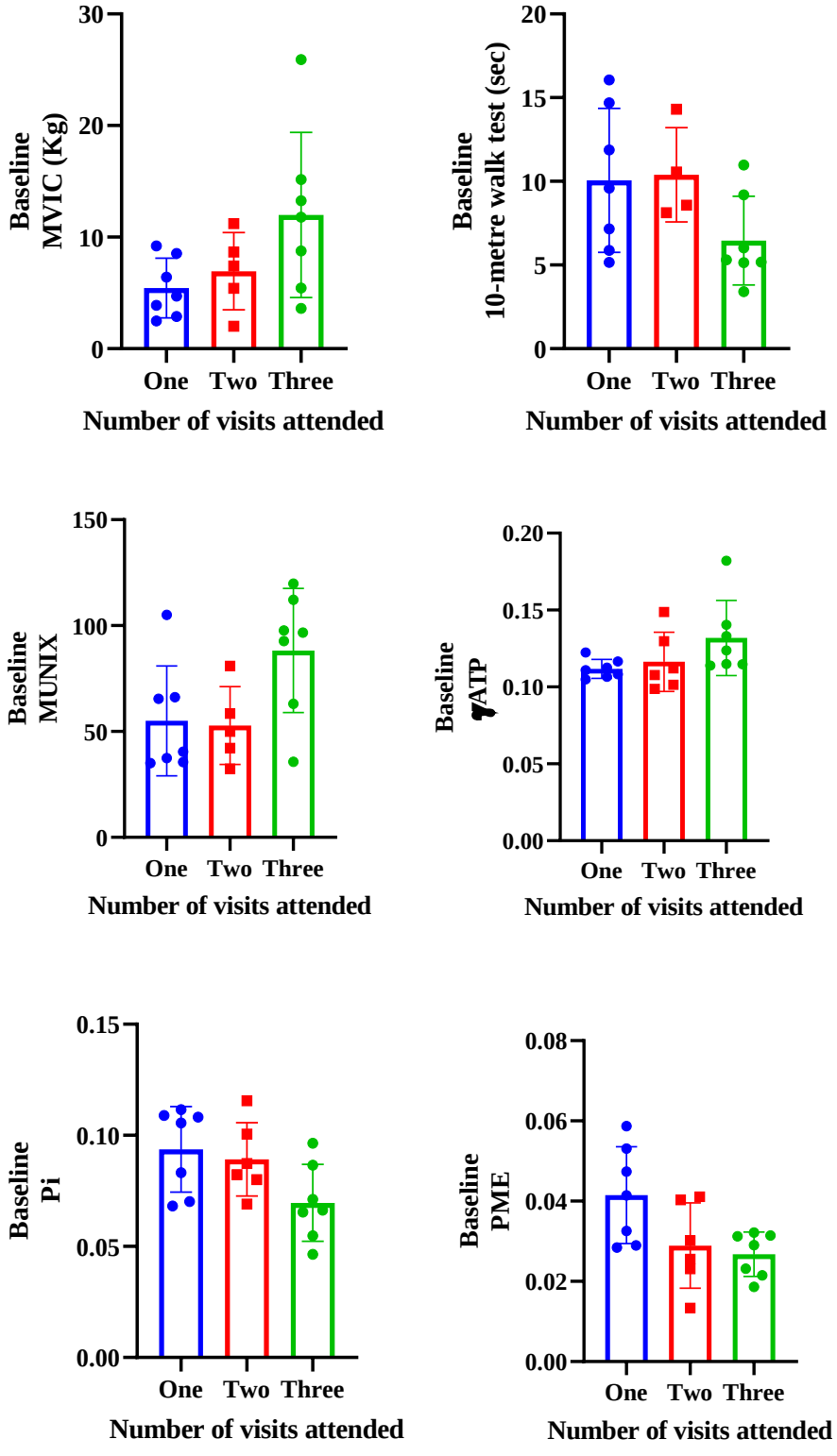

Figure 6.20 Baseline maximal voluntary isometric contraction (MVIC), 10-metre walk test, motor unit number index (MUNIX), γ adenosine triphosphate (γ ATP), inorganic phosphate (Pi), and phosphomonoesters (PME) in MND patients are illustrated on the y axis. On the x axis, the number of research visits attended is plotted (i.e. in blue those who attended only one research visit, red those who attended two research visits, and in green those who attended three research visits). This graphical depiction in conjunction with the statistics above illustrates that lower baseline force of contraction, MUNIX, or γATP values, slower speed of walking, higher Pi, or higher PME each predicted loss to follow up.
Mean and standard deviation are shown.

6.4 DISCUSSION

This is the first study to apply ^{31}P-MRS longitudinally to characterise the bioenergetic status of people living with MND. The experiments here described complement those reported in chapter four and provide further insights into spectroscopic muscle changes over time in MND. The follow-up times of 4 and 12 months were chosen based on considerations of feasibility in the MND patient population, balancing the need to avoid cohort attrition, but allow disease effects to become apparent. They were chosen based on previous experience of our group in clinical studies of this population (Jenkins, Alix et al. 2018, Jenkins, Alix et al. 2020).

6.4.1 Clinical and neurophysiological parameters

Between-group differences in patients and controls at visit two were consistent with those reported in chapter four, although some results were less statistically robust, likely as a consequence of patient attrition decreasing statistical power.

Weight, ALSFRS-R, and slow vital capacity decreased significantly in patients. These parameters are regularly measured in clinical practice and are among the most useful clinical biomarkers of disease progression (Verber, Shepheard et al. 2019). Weight loss is an established adverse prognostic factor in MND (Moglia, Calvo et al. 2019, Janse van Mantgem, van Eijk et al. 2020, Lee, Kazamel et al. 2021, Wei, Ou et al. 2021), which appears to be independent of dysphagia and likely reflects multifactorial pathology including hypermetabolism (Desport, Preux et al. 2001, Steyn, Ioannides et al. 2018, Nakayama, Shimizu et al. 2019), loss of appetite stemming from anxiety and depression (Wang, Ye et al. 2021) and respiratory dysfunction (Holm, Maier et al. 2013). ALSFRS-R (included in the appendix) is a validated questionnaire with high consistency and validity (Cedarbaum, Stambler et al. 1999) that exhibits high inter- and intra-rater reliability, even when self-administered (Bakker, Schröder et al. 2020). Lastly, slow vital capacity at diagnosis and slow vital capacity rate of decline are strong predictors of survival in MND (Andrews, Meng et al. 2018, Calvo, Vasta et al. 2020). UMN score did not vary significantly in patients at visit two and visit three. UMN signs are masked by LMN pathology. Hence, this metric is not particularly sensitive to corticospinal dysfunction and it is generally not used in clinical trials.

No significant between-group differences were detected in MVIC at visit two, although a non-significant trend was detected ($p=0.099$). In addition, MVIC did not decline in patients over time. Progressive muscle weakness is a defining feature of MND, hence these non-significant results are interpreted as likely a consequence of lack of statistical power and selection bias due to attrition. The latter hypothesis was corroborated by results reported in 6.3.4, illustrating that patients who were weaker at baseline were less likely to return for follow-up visits.

Slower walking speed, decreased MUNIX and increased MUSIX were detected in patients compared to controls, which are well established characteristics of MND (Inam, Vucic et al. 2010, Nandedkar, Barkhaus et al. 2010, Nandedkar 2017). No significant longitudinal changes were detected in 10-metre walk test, MUNIX, and MUSIX either in patients or in controls. Analogous to MVIC, the lack of longitudinal changes for 10-metre walk test and MUNIX are likely a result of patient attrition with loss of the most disabled patients from the cohort, and this factor also contributing to lack of statistical power. Results in 6.3.4 again support this hypothesis; patients with lower MUNIX and slower walking speed were less likely to attend four- and 12-month research visits. In contrast, MUSIX was not predictive of patient follow-up visits. Hence, it is possible that lack of longitudinal changes instead reflects the fact that MUSIX is a marker of compensatory reinnervation, a process that may fail as disease progresses.

6.4.2 Spectroscopic parameters

Spectroscopic results were also consistent with findings reported in chapter four. Interestingly, patients with higher γATP at baseline (as well as lower Pi and PME) were more likely to return at visit two and visit three. No longitudinal differences in Pi and PME were found, although, in the latter case, there was a non-significant trend towards an increase at 12-month.

There was substantial patient attrition at follow-up visits, an inevitable issue in MND imaging studies related to the progressive nature of disease which causes weakness and respiratory failure impairing patients from lying flat. The attrition rate was consistent with previously published studies (Jenkins, Alix et al. 2018) and was non-random, indicating that results of follow-up visits were biased towards stronger patients with relatively lower burden of denervation, lower Pi and PME, and higher γATP values.

Despite patients with lower γATP being less able to return for follow-ups, γATP was shown to decrease significantly over time. This is a biologically plausible effect and may reflect a different stage of bioenergetic failure where ATP can no longer be maintained by compensatory mechanisms identified in previous chapters.

6.5 CONCLUSION

To date, this is the first study to assess muscle in MND applying ^{31}P-MRS longitudinally. Measures were stable in healthy controls. The most important result was a significant decrease in γATP in MND patients over time which may represent a later stage of bioenergetic failure. Taken together with the results of previous chapters, this suggests a phase of compensation followed by a phase of

decompensation, which is important for therapeutic purposes as interventions may be more likely to succeed in the compensated phase.

CHAPTER 7:
31-PHOSPHORUS MAGNETIC RESONANCE SPECTROSCOPY IN MOTOR NEURON DISEASE: CONCLUSIONS AND FUTURE DIRECTIONS

The chapter summarises the salient findings of the experiments conducted in this thesis. The aim is to provide an overarching picture of the work that went into this PhD and of its broader impact. Results and concepts from previous chapters are connected whilst highlighting areas that remain to be investigated and novel questions arising from this experimental work. Salient results emerging from this work have provided the rationale for emerging research studies which are currently taking place at the University of Sheffield, discussed in this section.

Studies conducted in ^{1}H-MRS and detailed in chapter one illustrated that this technique can be used to elucidate pathophysiology and has potential as an imaging biomarker in MND, although there remain challenges related to reproducibility of results and applicability to non-specialised centres and in clinical practice (Kalra 2019). One of the central arguments of this thesis is that ^{31}P-MRS could be used analogously to investigate disease mechanisms and as a biomarker for bioenergetic dysfunction.

The first step was to establish a protocol that could be applied to the MR system available at the University of Sheffield. In chapter two, experiments conducted to optimise the acquisition protocol are reported. First, experiments that identified malfunctioning of the preamplifier of the ^{31}P-MRS coil are reported, which were the reason for initial low signal to noise. The Rapid coil was, hence, replaced and further experiments were required to ensure appropriate quality control. Although, the available coils were suitable to answer the main research questions of this thesis, in the future, it may be possible to modify the hardware to conduct both heteronuclear and homonuclear spectroscopy using simultaneous and interleaved acquisitions (Vanderthommen, Duteil et al. 2003, Meyerspeer, Magill et al. 2016). This would enable to explore the ^{1}H-MRS and ^{31}P-MRS signature (as well as putative biochemical associations) using a single acquisition, shortening research visits time. In MND this approach would facilitate incorporation of multiparametric MR techniques (i.e. ^{1}H-MRS and ^{31}P-MRS in this case) into a single predictive model which could be refined to assess speed of disease progression or response to treatment. Such models are urgently needed in MND, but there are numerous challenges to their development, including a relative dearth of longitudinal imaging studies, which are often characterised by large attrition due to the profoundly disabling nature of the disease. Interleaved acquisitions would enable incorporation of different modalities whilst reducing research visits time and potentially improving retention rate of participants.

Chapter two also details experiments conducted to select optimal acquisitions to answer the research questions. The sequence selected in brain (2D-CSI with 2 NSA) allowed acquisition of high SNR signals from multiple voxels located over primary motor regions and in an acceptable timeframe (just over 15 minutes). The muscle sequence produced high quality spectra with dynamic acquisitions designed to have appropriate time and spectral resolution to assess recovery parameters. Since no prior direct evidence for dysmetabolism in MND patients *in vivo* had yet been published, it was important to assess cerebral areas known to be consistently affected by the disease (i.e. primary motor cortex and descending corticospinal and corticobulbar tracts) as well as peripheral muscle. Future work focussing only on cerebral acquisitions could include more lengthy and complex sequences, such as 3D-CSI (Bakermans, Bazil et al. 2017), to sample larger anatomical areas. This would enable mapping of cerebral bioenergetic status in MND and answer questions related to presence of mitochondrial dysmetabolism in cortical and subcortical areas responsible for cognitive and executive processing which, as detailed in chapter one, are also affected in a proportion of patients. In such future putative studies, inclusion of cognitive tests would also be beneficial to assess clinical correlates.

To establish a biomarker that can be applied consistently across sites and in clinical practice, it is important to ensure repeatability and reproducibility. In chapter three, a reproducibility study was conducted to assess the effects of phasing and other processing steps on measurement variability. The same operator analysed data collected at a single timepoint, using a sequence optimised on the 3 tesla scanner. Better reliability and agreement were shown for data analysed in jMRUI, compared to SpectroView analyses. Hence, an important conclusion of this chapter was that choice of hardware, software and fitting algorithms substantially contributes to variability of measurements, an important issue for future multi-centre studies. Lack of standardisation has been recognised as one of the main factors limiting the diffusion of MRS techniques and efforts towards standardisation are being made (Wilson, Andronesi et al. 2019, Meyerspeer, Boesch et al. 2020). Numerous reproducibility studies have been conducted in ^{1}H-MRS to test both SV (Hoshino, Yoshikawa et al. 1999, Jang, Lee et al. 2005, Terpstra, Cheong et al. 2016, Al-iedani, Arm et al. 2018, Gonen, Moffat et al. 2020) and multivoxel (Maton, Londono et al. 2001, Zhang, Taub et al. 2020) sequences. These studies have illustrated that ^{1}H-MRS reproducibility across research centres is achievable (Träber, Block et al. 2006, Deelchand, Adanyeguh et al. 2015) in healthy controls. Two recently published studies applied ^{1}H-MRS to large cohorts of ALS patients across four and five sites. Findings illustrate the potential of ^{1}H-MRS as a biomarker of disease progression: (Srivastava, Hanstock et al. 2019) showed a correlation between NAA/Cho in motor cortex and rate of progression, whereas (Ta, Ishaque et al. 2021) showed that fast progressors had a larger longitudinal reduction of NAA in cortical motor areas. These studies represent also an important step towards reproducible implementation of ^{1}H-MRS in MND across multiple centres (Srivastava, Hanstock et al. 2019, Ta, Ishaque et al. 2021). There are fewer assessments of reproducibility in ^{31}P-MRS muscle (Layec, Bringard et al. 2009) and, to date, none in brain ^{31}P-MRS.

The next step is to conduct ^{31}P-MRS reproducibility experiments across different sites and scanners to test agreement and reliability in larger cohorts of healthy controls and patients, to optimise the technique for application to future clinical trials. Single voxel and CSI could be tested across sites, as well as comparing different scanner strengths (3 and 7 tesla) and manufacturers (Philips, General Electrics, and Siemens).

Chapter four addresses the main research question of this thesis: to determine whether bioenergetic dysfunction is present and detectable *in vivo* through application of ^{31}P-MRS to the brain and muscle of people living with MND. For the first time, abnormalities in brain phosphorus metabolites were demonstrated, which correlated with clinical and neurophysiological measures. A multifaceted picture emerged, in which a spectroscopic signature characteristic for primary mitochondrial dysfunction (i.e. low PCr) was present in the pons, whereas elevated Pi and PME were characteristic of muscle, possibly illustrating impaired mitochondrial responses to increased energy demand in peripheral tissue. The next step is replication in a larger cohort, but the results of this study demonstrate the wide-ranging potential of the technique to probe bioenergetic dynamics in neurodegenerative disease, including as a potential marker of target engagement for future trials of therapeutics targeting mitochondrial pathways. The results also lead to a number of further research questions; firstly, whether evidence for bioenergetic dysmetabolism is present in other cortical areas. Strategies to answer this question have been discussed in above sections of this chapter. Another important question is whether results are specific to MND or reflect non-specific consequences of diseased cells. This could be answered by further studies that include disease controls with exclusively UMN pathology (for example, multiple sclerosis), exclusively LMN denervation (for example, peripheral neuropathy), and exclusively primary muscle pathology. It was not possible to include disease controls in the work conducted in this thesis, but a study in primary progressive multiple sclerosis utilising the protocols here developed is underway at our institution (STH18781); data analysis is ongoing. Other questions related to features of MND pathophysiology could also be answered, for example in relation to hypermetabolism. The causes of this clinically relevant phenomenon which is associated with worse prognosis (Steyn, Ioannides et al. 2018) are still unclear, but mitochondrial uncoupling appears biologically plausible (Dupuis, Gonzalez de Aguilar et al. 2009, Ferri and Coccurello 2017). ^{31}P-MRS studies in conjunction with indirect calorimetry, the gold standard to assess basal metabolic rate (Gupta, Ramachandran et al. 2017), could investigate this issue in more detail. In this context it would be important to quantify and separate NADH and NAD^+ using ^{31}P-MRS. The NAD^+/NADH ratio is a measure of both the oxido-reductive status of a system as well as of mitochondrial coupling (Nicholls 2013). Nonetheless separation of those peaks remains a technical challenge which some groups have begun to address (Lu, Zhu et al. 2016); further developments in this field and establishment of reliable spectroscopic methodology would be crucial to answer such questions which are highly relevant to understanding MND. Lastly, it was not possible to assess for any effect of riluzole on phosphorus metabolites in this initial study, as only four patients were not on

riluzole due to intolerance, limiting statistical power. The mode of action of riluzole is elusive. Since it is the only drug to date proven to increase survival in MND, a better understanding of its pharmacology in patients is crucial. Studies using proton spectroscopy to assess effects on neuronal markers such as NAA have been conducted successfully and are described in greater detail in chapter one (Kalra, Cashman et al. 1998, Kalra, Tai et al. 2006). A large research project aimed at investigating the mode of action of riluzole using multiple imaging modalities, including the ^{31}P-MRS protocol reported in this thesis to assess mitochondrial effects, is currently in development (STH21550).

Chapter five reports a study in which ^{31}P-MRS was employed in conjunction with other techniques (neurophysiology and fixed dynamometry) to characterise a clinically relevant pathophysiological feature of MND: motor fatigability. These experiments showed that there is a differential response to muscle fatigue in patients compared to healthy controls: results suggest that fatigability is primarily related to central hyperexcitability in MND (assessed using f-wave amplitude), whereas the main determinants in healthy individuals are intracellular ionic concentration (primarily Mg^{++}) and fatigability at the neuromuscular junction (assessed using MUNIX), which are peripheral features. This approach in which features of motor fatigue are dissected could be used to measure target engagement in clinical trials for interventions to ameliorate this debilitating symptom, as none currently exist (Gibbons, Pagnini et al. 2018). In addition, the model proposed in this chapter should be corroborated using TMS, which is the gold standard technique for detection of UMN excitability. The study design described in chapter five could also be applied to other diseases in which motor fatigue is predominant. This protocol is being applied in the primary progressive multiple sclerosis study described above (STH18781) and in another study to assess the effects of preconditioning on fatigability in stroke patients (STH19508).

In addition to providing evidence of direct bioenergetic alterations, the results of experiments in chapter six (and chapter four) illustrate the potential for ^{31}P-MRS as an imaging biomarker to predict the course of disease. Correlations with ALSFRS-R, slow vital capacity (both well-established clinical biomarkers, predictive of disease progression and prognosis), and MVIC support clinical relevance, and associations with MUNIX support biological relevance. Although clinical correlations are not sufficient in isolation, they are, nonetheless, necessary in establishing a valid imaging biomarker. In addition, baseline spectroscopic parameters were shown to predict whether patients were able to attend repeated longitudinal visits. This type of non-random attrition can be considered a surrogate marker of progressive disability and speed of disease progression since 12 of the 13 patients that were lost to follow-up had to withdraw because of respiratory failure, severe frailty, and, in one case, death. Larger longitudinal studies are now necessary to investigate ^{31}P-MRS as a disease progression and prognostic biomarker in MND. Importantly, results from chapter six demonstrated that ^{31}P-MRS measures in healthy controls remain stable and, interestingly, it appears that during later stages of MND, ATP levels may start to fall, reflecting a decompensated phase of disease. It appears likely that therapeutics seeking

to address bioenergetic failure would have to be given before this occurred. This important point requires elucidation in future studies in larger cohorts. ^{31}P-MRS could also be employed as a biomarker of treatment response, to assess whether medications postulated to improve mitochondrial function show target engagement in areas affected by disease. Two studies of this kind are currently being conducted at the University of Sheffield using the optimised protocol developed in this thesis. Both studies aim to assess target engagement of bile acids suggested to be neuroprotective by improving bioenergetic profile of neurons. The first study is a double-blind, placebo-controlled trial testing ursodeoxycholic acid in Parkinson's disease (Payne, Sassani et al. 2020). The second study is an imaging sub-study adjunct to the phase III, multi-centre, randomised, double-blind, placebo-controlled study to evaluate efficacy of tauroursodeoxycholic acid in MND (NCT03800524; STH21256).

These studies emerging from the work of this thesis demonstrate the potential of ^{31}P-MRS as an important tool to develop to assess bioenergetics *in vivo* in neurological diseases in the future.

APPENDIX

The physics underpinning magnetic resonance spectroscopy

In the following text, the principles underlying generation and detection of the MRS signal, as well as an overview of necessary instrumentation, and localisation sequences will be detailed. This appendix is intended for readers who wish to understand the mathematical and physical reasons behind technical and analytical choices made during protocol development. The following sources were employed: (de Graaf 2007, de Graaf 2007, de Graaf 2007, de Graaf 2007, de Graaf 2007, Keeler 2010).

There are two central approaches to magnetic resonance (MR) physics which are not entirely reconcilable: the quantum mechanics description and the classic physics model. Quantum mechanics provides a comprehensive, but abstruse, theoretical framework of the physics underpinning MR phenomena. This approach will be briefly presented in section 8.1 to introduce the concept of nuclear energy levels and the Larmor frequency, which are particularly useful to understand phenomena such as coupling, described later on in the text. The classical model more intuitively exemplifies how MR signal is generated and detected, and moreover is necessary to understand the technical vocabulary used in MRI and MRS. Descriptions in 8.2 and 8.3 are primarily based on this model although parallels with the descriptions in 8.1 will be made. Section 8.4 will briefly present the concepts of relaxation and 8.5 will detail how different metabolites can be distinguished using MRS. Finally, section 8.6 will address theoretical issues encountered with metabolite quantification.

8.1 Quantum mechanical description: energy levels and the Larmor frequency

In MRS, nuclei are subjected to a strong external magnetic field (generated by the MR scanner) and RF pulses are applied to cause them to resonate. This process creates a signal that contains information on both the concentration of resonating compounds (which is proportional to the signal intensity, represented on the ordinate, y-axis, of the MR spectrum) as well as their frequency of precession (visualised on the abscissa, x-axis). Determining the frequency of these particles is equivalent to detecting their energy, because energy (E) and frequency (ν) are directly proportional, the proportionality factor being h, the Planck constant:

Equation 8.1

$$E = h\nu$$

To understand the rudiments of MRS, a basic description of nuclear energy statuses and their interactions with strong magnetic fields is, therefore, necessary.

In quantum mechanics, it is impossible to state *a priori* (i.e. before measuring) the actual energy level of a particle, which is said to be in a superposition state describable by a wavefunction. Nevertheless, it is possible to predict that, if a measurement is performed, this will definitely yield one of the allowed energy levels for that particle. Calculation of these observable energy levels for a nucleus positioned in a strong magnetic field is possible by means of the following equation:

Equation 8.2

$$\hat{\mathrm{H}} = -\gamma B_0 \hat{\mathrm{I}}_z$$

$\hat{H}$ is "the Hamiltonian" (the energy operator[21]), γ is the gyromagnetic ratio (which is an intrinsic property of a given nucleus, see Table 8.1), B_0 is the external magnetic field to which the sample is subjected, and $\hat{I}_z$ is the nuclear spin angular momentum operator, more specifically, its z-component, i.e. the component parallel to the main axis of the external magnetic field.

This equation can be applied to every nucleus located within B_0 and its solutions are determined by the eigenvalues and eigenfunctions[22] of $\hat{I}_z$; which, in turn, depend on the *nuclear spin angular momentum quantum number* (I) which, for dipolar nuclei[23] such as hydrogen and phosphorus-31, equals $\frac{1}{2}$. Values for various isotopes that can be used in MRS experiments are reported in Table 8.1.

[21] Operators in quantum mechanics denote measurable parameters; in case of the Hamiltonian, these observables are a particle's energy levels.

[22] Certain operators (such as $\hat{H}$ and $\hat{I}_z$) "operate" onto a wavefunction to extract another function equivalent to the initial one multiplied by a constant. These special types of wavefunctions are denoted eigenfunctions and the constant is, by definition, their eigenvalue.

[23] Dipolar nuclei are particularly suitable for MRS experiments because their charge is evenly spread over the nuclear surface and they generate stronger signal compared to quadripolar nuclei (i.e. nuclei having $I > \frac{1}{2}$).

Table 8.1 Spins (I), gyromagnetic ratios (γ), natural abundance, and sensitivity of isotopes that are regularly used in magnetic resonance spectroscopy (MRS) experiments.
Gyromagnetic ratio is expressed in 10^6 rad s^{-1} T^{-1}, natural abundance is expressed as percentage of element, sensitivity is proportional to natural abundance and to ($|\gamma^3|$ x I(I+1)) as per (de Graaf 2007). This table was readapted from (de Graaf 2007) - page 9.

Isotope	***Nuclear spin***	***Gyromagnetic ratio***	***Abundance in nature***	***MRS sensitivity***
Hydrogen-1	1/2	267.52	99.99	1
Deuterium-2	1	41.07	0.02	1.45×10^{-6}
Helium-3	1/2	-203.80	1.4×10^{-4}	5.75×10^{-7}
Carbon-13	1/2	67.28	1.11	1.76×10^{-4}
Nitrogen-14	1	19.34	99.63	1.00×10^{-3}
Nitrogen-15	1/2	-27.12	0.37	3.86×10^{-6}
Oxygen-17	5/2	-36.28	0.04	1.08×10^{-5}
Fluorine-19	1/2	251.81	100.00	8.34×10^{-1}
Sodium-23	3/2	70.80	100.00	9.27×10^{-2}
Phosphorus-31	1/2	108.41	100.00	6.65×10^{-2}
Potassium-39	3/2	12.50	93.10	4.75×10^{-4}
Xenon-129	1/2	-74.52	26.44	5.71×10^{-3}

Nuclear spin (listed in Table 8.1) is the intrinsic angular momentum of nuclei and has some properties that cannot be accounted for by the classical description: for instance, it is a quantised quantity (amplitude equals $\frac{h}{2\pi}\sqrt{I(I+1)}$) and can take only specific discrete orientations. Specifically, $\hat{I}_z$ is equal to $\left(\frac{h}{2\pi}\right)m$ where *h* is the Planck constant and, for hydrogen and phosphorus-31, *m* is $\pm\frac{1}{2}$). Only isotopes characterised by a non-zero spin (i.e. atoms which do not have an even mass number and an even atomic number) can generate an MRS signal.

It follows that, for dipolar nuclei, the result of equation 8.2 is:

Equation 8.3

$$E_m = -\frac{\gamma B_0 h m}{2\pi}$$

E_m describes the energy levels (in joules) allowed for a dipolar nucleus, *m* is $\pm\frac{1}{2}$, *h* is the Planck constant (in joule seconds), γ is the gyromagnetic ratio (in radian per second^{-1} tesla $^{-1}$), and B_0 is the external magnetic field (in tesla).

Equation 8.3 shows that only two energy states are allowed for nuclei that have spin of magnitude of 1/2 in a given B_0 (Figure 8.1): an α "spin up" state of energy $E_\alpha = -\frac{1}{2}\frac{\gamma B_0 h}{2\pi}$ where $m = +\frac{1}{2}$; and a β "spin down" state of energy $E_\beta = +\frac{1}{2}\frac{\gamma B_0 h}{2\pi}$ where $m = -\frac{1}{2}$. For nuclei characterised by a positive γ, E_β is the highest energy level. The transition from one level to another requires a quantum of energy equivalent to the energy difference $\Delta E = E_\beta - E_\alpha$ as shown in equation 8.4.

Equation 8.4

$$\Delta E = E_\beta - E_\alpha = \frac{\gamma B_0 h}{2\pi}$$

There are strict quantum rules governing transitions across energy levels; the transitions described in the equation above are generally allowed.

From equation 8.1, $E = h\nu$, it is possible to calculate the frequency ν (in hertz) characteristic for this energy difference:

Equation 8.5

$$\Delta E = \frac{\gamma B_0 h}{2\pi} = h\nu$$

Rearranging this last equation and solving for ν:

Equation 8.6

$$\nu = \frac{\Delta E}{h} = \frac{\gamma B_0}{2\pi}$$

MRS measurements provide information on the frequency and therefore energy absorbed or emitted during the transition between the α and the β states. This frequency is defined as the Larmor frequency and it can be expressed in hertz (ν_0) or radian per second (ω_0):

Equation 8.7

$$\nu_0 = -\frac{\gamma B_0}{2\pi}$$

Equation 8.8

$$\omega_0 = -\gamma B_0$$

At 3 tesla, as in the experiments reported in this thesis, ν_0 equals 127.9 MHz for hydrogen and 51.7 MHz for phosphorus-31; these values are in the radio frequency range of the electromagnetic spectrum. The negative sign is related to the phase of the FID as described in the following sections.

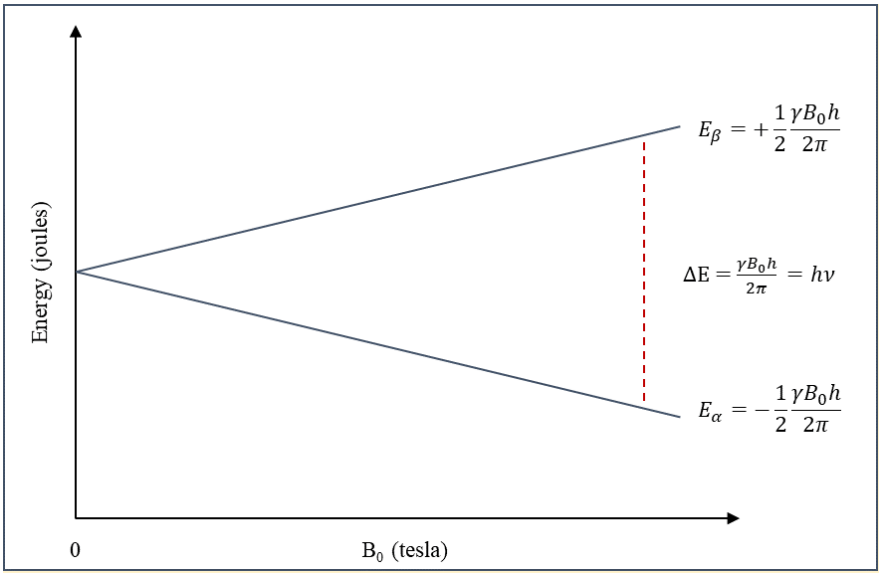

Figure 8.1 The relationship between energy difference (ΔE, illustrated by the red dotted line) and strength of magnetic field B_0 (x axis).
As the strength of B_0 increases so does the difference between the Eα (lower) and Eβ (higher) energy state. γ is the gyromagnetic ratio and h is the Plank constant. The figure was drawn by the author.

In MRS, resonance is induced by delivering electromagnetic radiation at the Larmor frequency to the sample by employing RF pulses in which an electromagnetic field oscillates perpendicular to the B_0 main axis. RF pulses increase the probability of spins flipping from the lower to the higher energy level.

Consequently, during RF irradiation, a greater proportion of the sampled nuclear population is found in the β higher energy state. Once the RF pulse subsides, the system relaxes, meaning that a proportion of the β spins return to the α state releasing electromagnetic radiation of frequency ω_0. It is this emission that is detected by the MRS receiver coils and provides the basis of the MRS signal.

8.2. Classical description: angular momentum and magnetic moments

Each particle that rotates at constant speed is characterised by angular momentum (L), a vectorial quantity perpendicular to the plane of motion which equals the product of the object's mass, its velocity, and its radius. Nuclei are charged particles, hence, as they rotate, a local magnetic field is generated, characterised by the *nuclear spin magnetic moment* (or magnetic dipole vector), μ. The equation below illustrates that L and μ are directly proportional.

Equation 8.9

$$\vec{\mu} = \frac{ev}{2\pi r}\pi r^2 = \gamma\vec{L}$$

e is the charge, v is the velocity, r is the radius, γ is the gyromagnetic ratio, and L is the angular momentum. Equation 8.9 illustrates that, as for all dipole moments, μ is the product of a current ($\frac{ev}{2\pi r}$) and the circle area (πr^2). The right-hand equality is obtained by substituting for L ($L=mvr$) and classic gyromagnetic ratio ($\gamma = \frac{e}{2m}$), which determine the magnitude of μ. Although descriptions in this section are based on the classical model, as mentioned in section 8.1, angular momentum for nuclei is quantised and, hence, so is the *nuclear spin magnetic moment*.

Isotopes such as hydrogen or phosphorus-31, that are characterised by a *nuclear spin magnetic moment*, can collectively exhibit nuclear magnetism. Nonetheless, in nature, these nuclei are typically found in a random orientation in space as they tumble due to Brownian motion (Figure 8.2) and are not collectively magnetised.

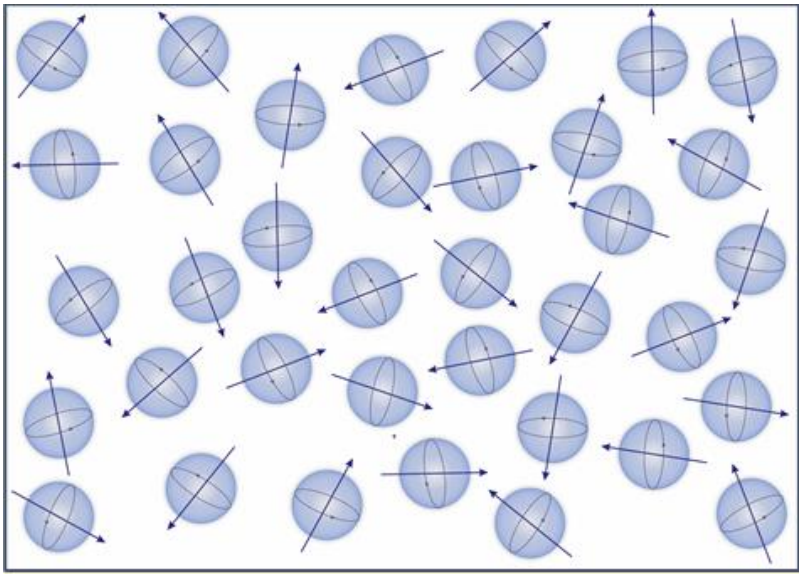

Figure 8.2 Nuclei tumbling due to Brownian motion.
Arrows represent nuclear magnetic moments which are found in random orientation; hence, their vectorial sum is zero and the sample is not magnetised. The figure was drawn by the author.

It is possible to alter the orientation of *magnetic moments*, μ, by subjecting nuclei to a strong external magnetic field (B_0) which effectively applies a rotational force, or torque (T):

Equation 8.10

$$\vec{T} = \vec{\mu} \times \overrightarrow{B_0}$$

Consequently, a proportion of the *magnetic moments* becomes arranged parallel to B_0 (an arrangement that corresponds to the α state previously described), whilst a smaller proportion is found in antiparallel orientation (corresponding to the β energy level). As discussed above, the α state is favoured, hence, overall, there is a slight excess of *magnetic moments* aligned parallel to the axis of B_0, the longitudinal or *z*-axis, by convention. This is the axis in which patients lie in the scanner. This excess, which can be calculated from the Boltzmann distribution, is about 1 spin in α state over 100000 nuclei, i.e. 0.001%. Although very small (it can be calculated that, at 9.4 tesla, this is in the order of 31 spins in a million), this difference is sufficient to magnetise the sample and provides the basis for generation of MRI and MRS signals.

Moreover, B_0 causes the spinning nuclei to acquire a rotational precessional motion $\frac{d\mu}{dt} = \gamma \mu B_0$. More specifically, these *magnetic moments* precess clockwise about the *z*-axis at the Larmor frequency (see equations 2.7 and 2.8). The precessional angle, θ, (which can be calculated as $cos\theta = \frac{m}{\sqrt{l(l+1)}}$, a formula derived from the quantum mechanical description) is equal to 54.74° for dipolar nuclei. The direction of precession around the *z*-axis follows the right-hand rule: this means that, by definition, an

anticlockwise motion about the z-axis is given a positive value. *Magnetic moments* of nuclei characterised by a positive γ precess clockwise about the z-axis because their Larmor frequency is negative, see equations 8.7 and 8.8. This process is depicted in Figure 8.3. In the x-y plane (i.e. the transverse plane which is, by definition, orthogonal to the z-axis), no orientation is favoured. Consequently, *magnetic moments* precess in a non-coherent phase and there is no net vectorial component in the transverse plane; hence equation 2.11 includes only the z component of μ. Specifically, the vectorial sum of a number *n* of *magnetic moments*, μ, in the α and β states, yields a *net longitudinal magnetisation vector*, M_0, parallel to the *z*-axis:

Equation 8.11

$$M_0 = \sum_{i=1}^{n} \mu_i = n_\alpha \mu_z + n_\beta \mu_z = \gamma \frac{h}{4\pi}(n_\alpha - n_\beta)$$

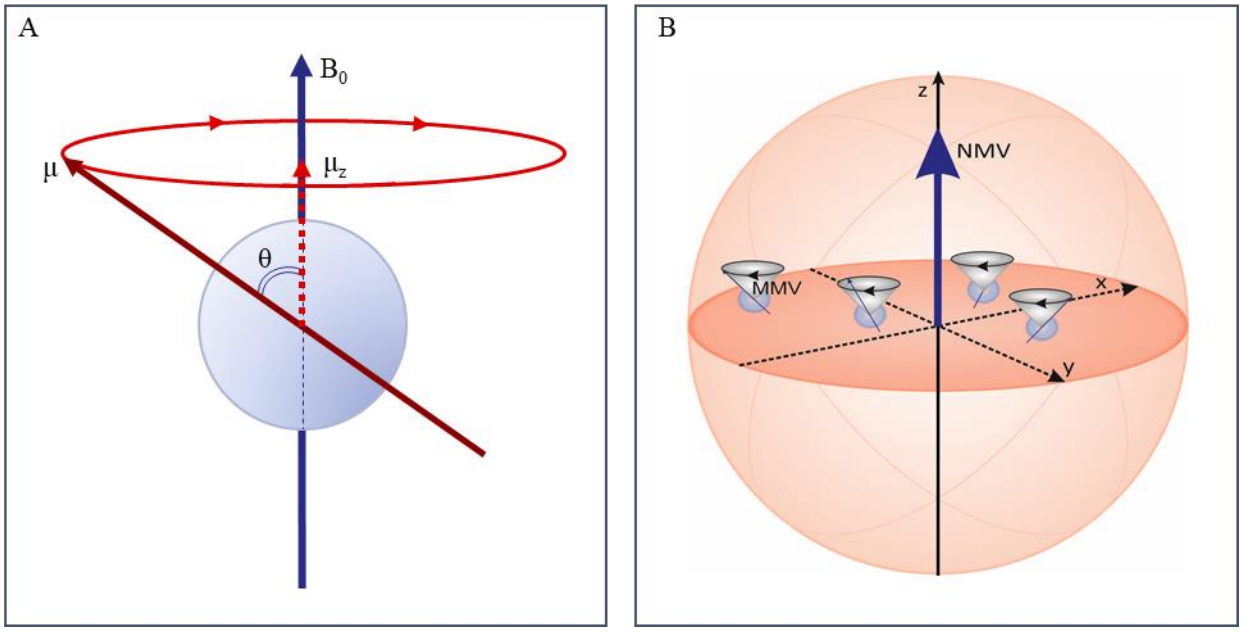

Figure 8.3 Effect of strong magnetic field on nuclear magnetic moments.
(A) A nucleus precessing about the main axis of a strong magnetic field (B_0). μ is the nuclear magnetic moment, μ_z is the component of the magnetic moment along the main axis of the magnetic field, and θ the precessional angle. (B) When subjected to a strong magnetic field, a portion of the nuclear magnetic moments (MMVs) is arranged parallel to B_0 (the z-axis) and precesses at the Larmor frequency in a non-coherent phase. Their vectorial sum yields a net magnetisation vector (NMV - here depicted in dark blue) which is a static vector, parallel to the z-axis, and devoid of longitudinal components on the x-y plane (the plane orthogonal to the z-axis). The figure was drawn by the author.

Even though the magnitude of the longitudinal *net magnetisation vector* is not directly measured, its amplitude, M_0, determines the intensity of the MRS signal. As described in equation 8.12, M_0 is dependent on the strength of the external magnetic field B_0, the square of γ (as the gyromagnetic ratio contributes to both the energy status and the magnetic moment), and the number *N* of nuclear spins in the sample. ħ is the reduced Planck constant (h/2π), and k_B is the Boltzmann constant.

Equation 8.12

$$M_0 = \frac{N\hbar^2\gamma^2 B_0}{4k_B T}$$

Equation 8.12 illustrates that, under otherwise equivalent conditions, ^{1}H-MRS generates a relatively more intense signal compared to ^{31}P-MRS both because hydrogen is much more abundant in biological tissues than phosphorus (M_0 linearly changes with *N*) and because the gyromagnetic ratio of hydrogen is approximately two and a half times greater than that of phosphorus (see Table 8.1). A major drawback of ^{31}P-MRS is its relative lower sensitivity and, consequently, lower signal to noise ratio (SNR) compared to ^{1}H-MRS. The relative sensitivity is estimated to be lower in ^{31}P-MRS by a factor of approximately 100 (de Graaf 2007). The linear dependency of M_0 on *N* also makes MRS a potentially quantitative modality as signal is directly proportional to concentration of particles. However, there are practical challenges, discussed in section 8.6, related to a number of technical factors, that render quantification difficult in the experimental setting. Lastly, equation 8.12 illustrates that, at higher magnetic field strengths, there is a gain in signal intensity.

8.3 From resonance to spectra

Once the longitudinal static *net magnetisation vector* reaches its maximum value (i.e. the populations of spins in the α and β states have attained a dynamic equilibrium), MRS signal can be generated. This is achieved by induction of resonance via RF pulses which applies a dynamic magnetic field B_1. The RF pulse causes the nuclei to synchronise their precession and acquire a coherent phase. The RF pulse is an electromagnetic wave and, therefore, has an associated magnetic field, oscillating at a given frequency, in this case, the Larmor frequency. Nuclei will, therefore, start to precess around the new magnetic field, which has an orientation perpendicular to B_0. Consequently, the *x* and *y* vectorial components of the *magnetic moment vectors* are summed to result in a *net transverse magnetisation vector* of increasing magnitude in the *x-y* plane, precessing clockwise at the Larmor frequency.
This dynamic vector can be considered a moving magnet that, by Faraday's law of induction, generates an electrical current which can be detected by an MR receiver coil placed in the transverse plane. Ultimately, the signal detected (i.e. the measured current) is proportional to the magnitude of the x and y components of the precessing *net transverse magnetisation vector* as shown in Figure 8.4 and according to equations 8.13 and 8.14.

Mathematically, the above process is described by the Bloch equations (Bloch 1946), briefly exemplified below, although a complete discussion is beyond the scope of this thesis.

When an RF pulse is applied, the *net magnetisation vector, M*, is subjected to both the B_0 and B_1 fields, the latter generated by the RF pulse describable as $B_1(t) = 2B_{1max}cos\omega t$ where B_1 is the amplitude of the RF pulse, ω is the carrier frequency of the RF which encompasses the Larmor frequency, and *t* is time:

Equation 8.13

$$\frac{d\vec{M}(t)}{d(t)} = \vec{M}(t) \times \gamma\vec{B}(t)$$

M is the *net magnetisation vector*, γ is the gyromagnetic ratio and *B* is any magnetic field to which the sample is subjected. This equation is a generalisation of the Larmor equation and a consequence of *M* being the sum of individual *magnetic moment vectors* (equation 8.11).

When $\frac{dM(t)}{d(t)} = 0$, no signal is detected. Following the RF pulse, the trajectory of the *net magnetisation vector* can be described either from the laboratory frame of reference or in the rotating frame of reference. The laboratory frame of reference is from the point of view of a hypothetical external observer "visualising" the vector forming a three dimensional spiral resulting from superposition of precession around B_0 and precession around the new field, B_1 (known as "nutation"), and increasing in the transverse plane. In the rotating frame of reference, the hypothetical observer is inside the system, rotating at the same speed and frequency as the *net magnetisation vector*, and, hence, "seeing" a two dimensional line going from a point on the z axis to a point on the x-y plane. Use of the rotating frame of reference is a convenient way to mathematically simplify the description of motion of the *net magnetisation vector,* as the time dependency of the B_1 field can be removed from the equations and the Larmor frequency appears to be zero.

Accordingly, in the laboratory frame of reference the *x* (equation 8.14), *y* (equation 8.15), and *z* (equation 8.16) components of the magnetisation vector, *M*, vary as:

Equation 8.14

$$\frac{dM_x(t)}{dt} = \gamma[M_y(t)B_0 - M_z(t)B_{1y}]$$

Equation 8.15

$$\frac{dM_y(t)}{dt} = \gamma[M_z(t)B_{1x} - M_x(t)B_0]$$

Equation 2.16

$$\frac{dM_z(t)}{dt} = \gamma[M_x(t)B_{1y} - M_y(t)B_{1x}]$$

Whereas, the components of on the x (M'_x), y (M'_y), and z (M'_z) axes in the rotating frame of reference can be described as follows:

Equation 8.17

$$M'_x = M_x cos\omega t + M_y sin\omega t$$

Equation 8.18

$$M'_y = M_y cos\omega t - M_x sin\omega t$$

Equation 8.19

$$M'_z = M_z$$

The *net magnetisation vector* motion can be described as:

Equation 8.20

$$M_x = M_0 sin\beta cos\omega t$$

Equation 8.21

$$M_y = -M_0 sin\beta sin\omega t$$

Equation 8.22

$$M_z = M_0 cos\beta$$

M_x and M_y are the transverse components of the *net magnetisation vector*, M_z is the component along the z axis, β is the FA (i.e. the angle between the *net magnetisation vector* and the z-axis), ω is the resonance frequency which should approximate the Larmor frequency). The term $M_o sin\beta$ represents the projection onto the transverse plane of the *net magnetisation vector*; if M_0 is constant then the signal intensity is maximal at a 90˚ FA (where sinβ is 1) and is zero when β is 180˚. The term $sin\omega_0 t$ relates to the precessional motion in the x-y plane.

Once the RF pulse ceases, the *net magnetisation vector* returns to its initial orientation (i.e. parallel to the *z*-axis), and a signal, the FID, is generated and detected by the MR receiver. A "pure" FID is an exponentially decaying[24] cosinusoid (Figure 8.4) containing information on the Larmor frequency of the resonating nuclei as well as on the amplitudes of the signal, both of which can be extracted by frequency analysis through Fourier transformation, shown in equation 8.23 and exemplified in Figure 8.4.

[24] The reasons for the decay are explained in section 8.4.2.

Equation 8.23

$$F(\omega) = \int_{-\infty}^{+\infty} f(t) e^{-i\omega t} dt$$

F(ω) is the amplitude of the signal in the frequency domain, *f(t)* is the signal in the time domain, *ω* is frequency, and *t* is time. Fourier transformation of the FID (i.e. signal acquired in the time domain) yields a spectrum (i.e. data displayed in the frequency domain) as explained in Figure 8.4. When a quadrature coil is used, both the x and y components of the FID are detected from (at least) two channels (I – *in phase* and Q – *quadrature*) and transformed yielding "real" (*r*) and "imaginary" (*im*) spectra, respectively, that can then be reconstructed into a complex magnitude signal (magnitude signal = *r* + i *im*, where i is the imaginary unit). Phase information can also be extracted. The nomenclature of the channels is arbitrary and does not denote that one signal is actually less real or more concerned with complex numbers than the other. Unlike in structural MRI, when the magnitude signal is employed in most applications (for instance in common anatomical images), in spectroscopy, the real component is analysed. This is because, although the magnitude spectrum has better SNR (by a factor 1.41 i.e. $\sqrt{2}$), the line shapes tend to be broader and, hence, it is more difficult to fit. In addition, for low SNR signals (such as signal acquired in MRS), the baseline noise of the real component is Gaussian whereas magnitude signal has a skewed distribution. Gaussian noise assumption aids baseline estimation.

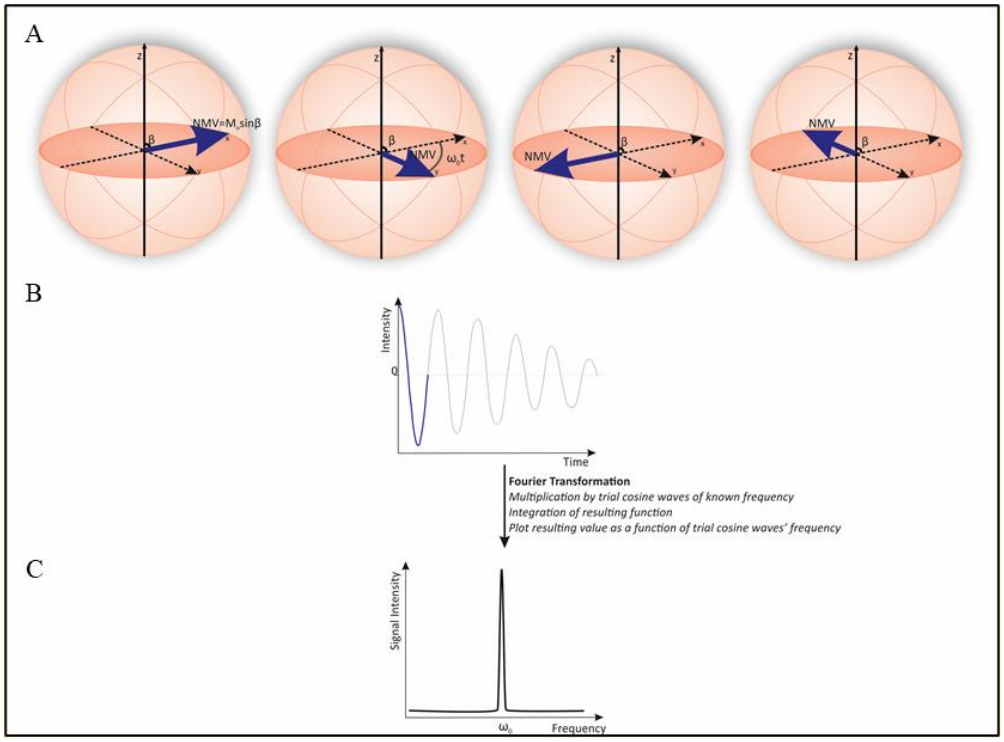

Figure 8.4 Generation of magnetic resonance spectroscopy signal.
(A) The net magnetisation vector (arrow in blue) precesses clockwise in the transverse plane at the Larmor frequency (ω_0) and, by Faraday's law of induction, generates an electrical current, the free induction decay (FID) signal (B - central graph). The frequency of precession of the net magnetisation vector can be extrapolated from detected current by Fourier transformation which converts the data from the time domain into the frequency domain (C - lower graph). The signal decays over time because the system relaxes. Relaxation and analysis of signal changes over time are detailed in section 8.4. The figure was drawn by the author.

8.4 Relaxation

As previously described, relaxation involves spins "flipping back" to their lower energy state with consequent release of energy. This process is dependent on the physical environment of the nuclei and therefore can provide unique information on its composition. In the classical model, it is possible to visualise this process by analysing the changes over time of the longitudinal (along the *z*-axis) and transverse (along *x*-*y* plane) components of the *net magnetisation vector*.

8.4.1 Longitudinal relaxation

Longitudinal relaxation is the process by which the *net magnetisation vector* reacquires its maximal longitudinal component and becomes realigned with the main magnetic field axis. This is characterised by a proportion of spins in the β state returning to the α energy level. The energy released in this process is transferred to the surroundings (the lattice), contributing to a negligible increase in thermal energy to the environment. This mechanism is often denoted spin-lattice relaxation. The lattice particles themselves generate local fluctuations in the magnetic field surrounding resonating nuclei which

influence energy transfer between spins and the lattice. In the vectorial model, longitudinal relaxation can be visualised as a progressive increase, over time, of the *z*-component of the *net magnetisation vector* (Figure 8.5) governed by equation 8.24, which is the solution of the Bloch equations for M_z when including T_1.

Equation 8.24

$$M_z = M_0\left(1 - e^{-\frac{t}{T1}}\right)$$

M_z is the actual longitudinal magnetisation of the *net magnetisation vector*, M_0 is the longitudinal magnetisation of the fully relaxed *net magnetisation vector*, and T_1 is the longitudinal magnetisation relaxation time constant.

The shape of the function described by equation 8.24 is determined by the time constant, T_1, which represents the time necessary for the longitudinal magnetisation to recover to 63% (i.e. $1 - (\frac{1}{e})$) of its maximal value (Figure 8.5). T_1 can be estimated using a number of sequences of which inversion recovery is the most common, and spoiled gradient echo and partial saturation recovery sequences are also used (Bojorquez, Bricq et al. 2017).

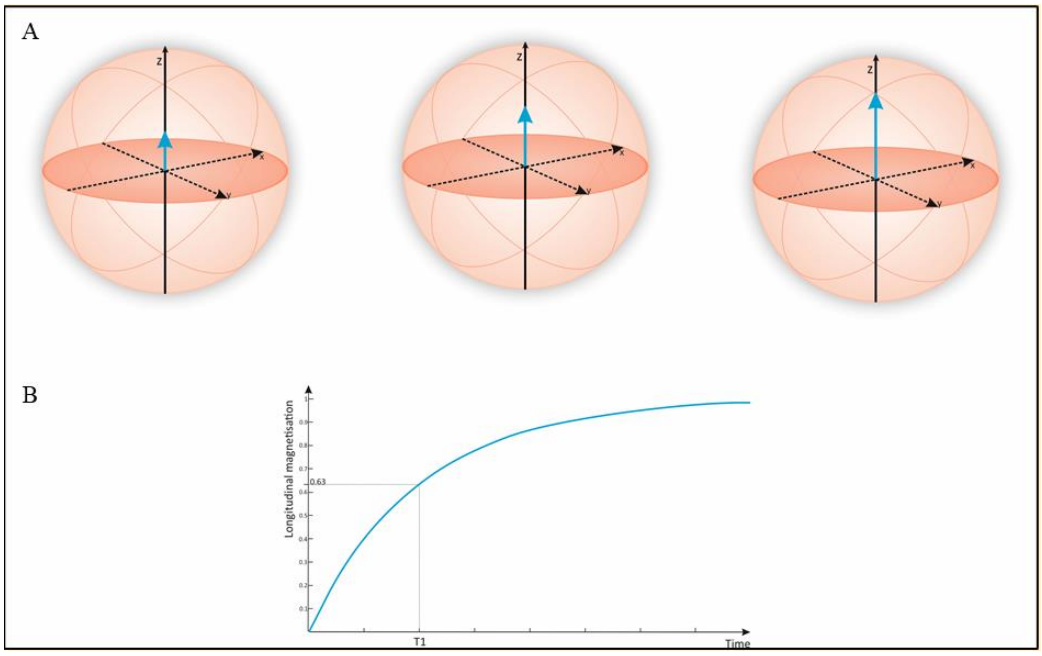

Figure 8.5 Longitudinal relaxation.
(A) The z component of the net magnetisation vector increases over time as the system relaxes. (B) The lower graph depicts the function described in equation 8.24. *The figure was drawn by the author.*

T_1 depends on the type of nucleus, molecule, and, hence, tissue. For hydrogen, *in vivo*, at 3 tesla, T_1 constants are between 0.3 and 4 seconds; in MRS, each resonant nucleus is characterised by a specific

T_1 relaxation constant. Broadly speaking, rapid recovery is characteristic of fat, whereas fluids, such as CSF, have prolonged relaxation. Notably, there are discrepancies in reported T_1 values due both to inherent biological variability and lack of standardisation of measurement protocols (Bojorquez, Bricq et al. 2017). To ensure adequate SNR, experiments are repeated multiple times and spectra averaged. The main parameters that determine signal weighting and contrast in MRI are the time between subsequent excitation pulses (TR) and the time between excitation and signal sampling (TE). The value of T_1 dictates the choice of time to repetition (TR) chosen for the pulse sequence which, in turn, influences the overall scanning time. A short TR maximises T_1 relaxation effects whereas a long TR tends to minimise them. TR shortening can be advantageous if the aim is to increase contrast based on longitudinal relaxation properties, such as in T_1-weighted images, but, often in spectroscopy, T_1 effects are undesirable and long TRs are preferred. Additionally, since the magnitude of the z component of the *net magnetisation vector* (M_z) before repeating the RF determines the amplitude of the signal, long TR sequences have higher SNR than with short TRs, provided that all other parameters are unchanged. Nonetheless, considering that it takes a period of five T_1 to reach 99% maximal longitudinal magnetisation, scan times can become extremely lengthy and a trade-off between competing considerations is often necessary. Scan time can be a limiting factor, especially in ^{31}P-MRS, as T_1 values for phosphorus are much longer than for hydrogen, or when using high field scanners, because T_1 becomes even more prolonged as the external magnetic field B_0 is increased.

8.4.2 Transverse Relaxation

Transverse or spin-spin relaxation is the process by which the transverse (i.e. x and y) components of the *net magnetisation vector* decay exponentially over time. As previously described, an RF pulse synchronises the precession of individual *magnetic moments* which causes their phase to become coherent. Once the pulse subsides, the precession of the *magnetic moments* is dephased. Two major factors contribute to this dephasing:

1) Between nuclei spin-spin energy exchange causes dephasing in the x-y plane in an overall homogeneous B_0. This is a time-dependent process and is responsible for the exponential decay of the transverse component of the *net magnetisation vector*, which is characterised by the time constant T_2, governed by equation 8.25 and 8.26, and depicted in Figure 8.6. Equation 8.25 takes into consideration T_1 saturation effects (which cause the net magnetisation to be smaller than M_0), whereas equation 8.26 applies to cases in which full longitudinal relaxation (i.e. TR >> 5 T_1) is achieved. T_2 is the time constant defining the time required to diminish initial transverse magnetisation to 37% (i.e. $\frac{1}{e}$) of its initial value. To calculate the value of T_2, a spin-echo sequence is necessary, in which the T_2' component (described below), is eliminated by rephasing sampling at multiple TEs. T_2 values generate tissue contrast in T_2-

weighted images and generally decrease at stronger magnetic fields. At 3 tesla, approximate T_2 values in brain range from 65 ms in white matter to 110 ms in grey matter (Bojorquez, Bricq et al. 2017), whereas fluids (such as CSF, which appears bright on T_2-weighted images) can have values over one second long (Spijkerman, Petersen et al. 2018). Notably, T_2 relaxation happens over a much shorter time scale compared to T_1 relaxation.

Equation 8.25

$$M_{xy(TR)} = M_0\,(1 - e^{-\frac{TR}{T1}})e^{-\frac{t}{T2}}$$

Equation 8.26

$$M_{xy} = M_0\,e^{-\frac{t}{T2}}$$

2) A time-independent dephasing characterised by a time constant T_2' which is caused by intrinsic inhomogeneities of B_0, spatial gradients, as well as inherent tissue magnetic susceptibility. This latter effect is more pronounced at air-tissue interphases or in the presence of metals, an additional potential source of contrast or, when unwanted, artefacts. The process by which B_0 is rendered homogeneous across a volume of interest is called shimming and is fundamental to acquire a spectrum of appropriate quality, although, in practice, it is not possible to achieve perfect B_0 homogeneity. In MRI, the T_2' component contributes to image contrast especially in T_2*- and susceptibility-weighted images which are based on gradient-echo sequences using small FAs with long TE and TR. T_2' values are particularly susceptible to the presence of calcification and iron. *In vivo*, iron is found primarily in blood as the main component of haem. This property renders these techniques particularly apt to image haemorrhages, to identify injury- or age-related depositions of iron and calcium (e.g. in macrophages, an example to applications to MND research is provided in the previous chapter) and in certain advanced imaging modalities such as perfusion and functional MRI (Chavhan, Babyn et al. 2009).

Those two transverse relaxation mechanisms cause a loss of coherence of individual *magnetic moments* progressively which reduces the result of the *net magnetisation vector* in the x-y plane; hence the overall measured signal decreases with a time constant T_2* (T_2 star) which is a combination of T_2 and T_2'. The relative contributions of T_2 and T_2' depend on the acquisition sequence: spin echo is designed to remove the effects of T_2' thus providing T_2-weighted signal. Conversely, gradient-echo sequences are always T_2*-weighted. Equation 8.27 shows the relationship between time constants characterising transverse relaxation. T_2* values are also important in MRS as, beside affecting amplitude of the signal (each peak is characterised by a transverse relaxation constant) and providing contrast (section 8.6), they are one of the factors that determine linewidth of spectral resonances. Specifically, following Fourier transformation, a rapidly decaying exponential cosinusoid (associated with short T_2 and T_2') results in

a broad linewidth, whereas a slowly decaying signal is transformed into a narrow peak (there is more discussion of this point in chapter three).

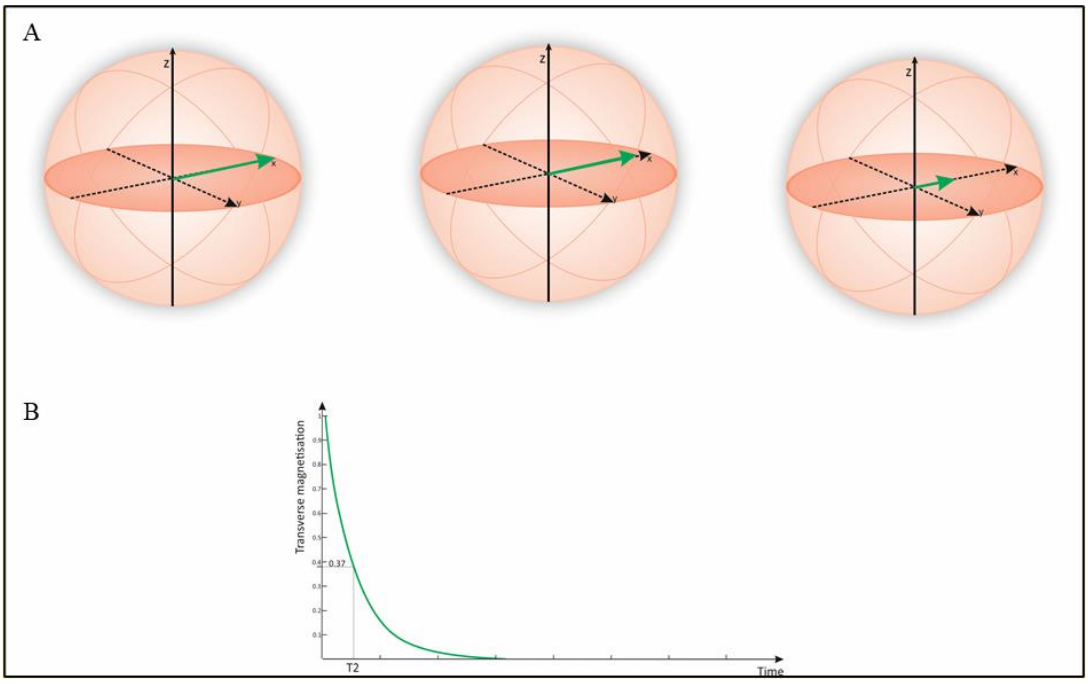

Figure 8.6 Transverse relaxation
(A) The x-y component of the net magnetisation vector decays over time as the system relaxes. (B) The lower graph depicts the function described in equation 4.2. The figure was drawn by the author.

Equation 8.27

$$\frac{1}{T_2^*} = \frac{1}{T_2} - \frac{1}{T_2'}$$

8.5 Differentiation of various compounds

The previous sections outlined the basis of signal generation by nuclear magnetic resonance. So far, for simplicity, all nuclei were assumed to belong to one molecular moiety and to be equivalent. Nevertheless, MRS is a powerful technique because it allows differentiation between various molecules. This is possible as the specific chemical environment that surrounds observed nuclei alters their frequency of precession. These changes in the resonance frequency, although minute, can be detected by spectrometers and result in multiple spectral peaks each representing a group of nuclei in their specific chemical milieu, i.e. a specific molecule. The two phenomena responsible for this alteration of *v* are chemical shift and scalar (or J) coupling.

8.5.1 Chemical shift

The basis of chemical shift is that the electron cloud surrounding a nucleus partially shields it from the effects of B_0. Electrons also have a *magnetic moment* which interacts with B_0 altering the magnetic field nuclei are subjected to by a factor σ, so that the effective magnetic field, B, is equal to $B=B_0(1-\sigma)$. This, in turn, alters the nuclear effective resonance frequency:

Equation 8.28

$$\nu_{effective} = -\frac{\gamma B_0}{2\pi}(1-\sigma)$$

σ is defined as the shielding constant and is dimensionless. As shown above, the extent of this frequency alteration is B_0 dependent; therefore, to compare spectra acquired at different magnetic fields, it is convenient to choose a reference compound and represent all other peaks in terms of relative shift from it expressed as parts per million (ppm, a concept analogous to percentage). The following equation shows how the Larmor frequency ν_0 (in hertz) is converted into chemical shift δ on the ppm scale. The reference compound for *in vivo* ^{31}P-MRS is PCr which is typically assigned a chemical shift of 0 ppm, whereas, for ^{1}H-MRS, the methyl group of NAA is conventionally assigned a 2.01 ppm value.

Equation 8.29

$$\delta = \frac{\nu_{measured} - \nu_{reference}}{\nu_{reference}} 10^6$$

These slight changes in the resonance frequency are embedded in the FID and so can be extrapolated by Fourier transformation. Thus, instead of obtaining one spectral line representing all phosphorus atoms (Figure 8.4), the resulting spectrum is characterised by multiple peaks each associated to a different population of atoms in their characteristic chemical environment (Figure 8.7).

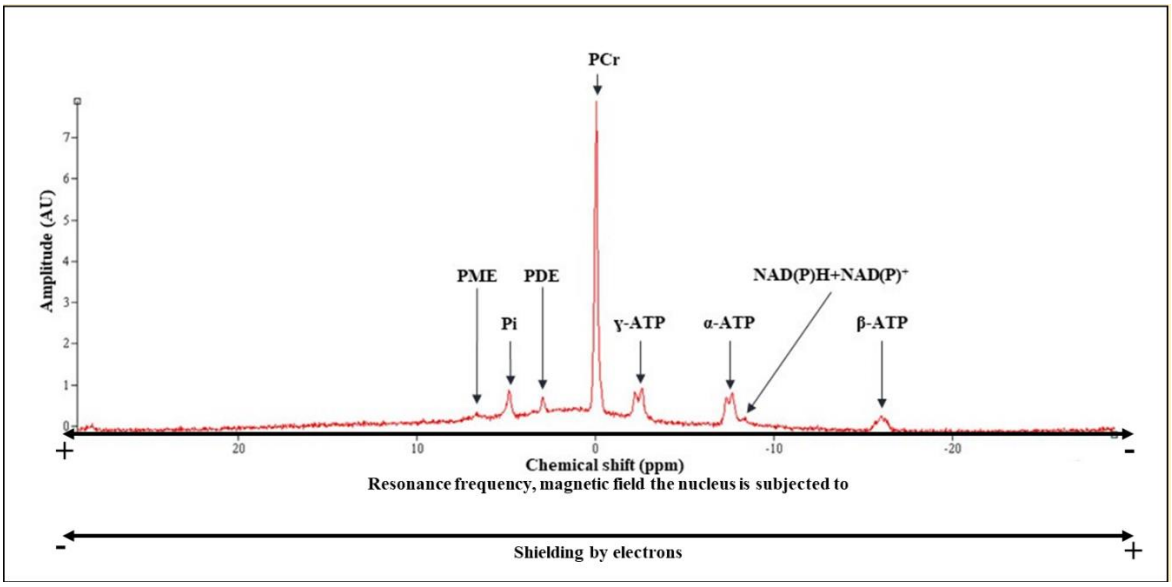

Figure 8.7 A phosphorus spectrum acquired from muscle of a healthy control at 3 tesla.
The spectrum is characterised by the following main peaks: phosphocreatine (PCr) at 0 ppm; γ, α, and β adenosine triphosphate (ATP) phosphates at -2.5, -8, and -15.5 ppm, respectively; respectively; nicotinamide adenine dinucleotide (NAD(P)H and NAD(P)$^+$) at 8.5 ppm; inorganic phosphate (Pi) at approximately 5 ppm; phosphodiesters (PDE) at approximately 2.5 ppm; and phosphomonoesters (PME) at approximately 6 ppm. The γ and α ATP peaks are composed of a doublet whereas the β ATP is a triplet because of scalar coupling. By convention, the x-axis is inverted with negative ppm values on the right of the graph. The concept of the figure (i.e. two x-axes) was readapted from (de Graaf 2007), but own data are shown and the figure was drawn by the author of the thesis.

8.5.2 Scalar coupling

Coupling processes are analogous to chemical shift, as *nuclear magnetic moments* are affected by nearby *magnetic moments*: in dipolar coupling, *magnetic moments* are those of neighbouring nuclei, whereas in scalar (or J) coupling, they are of electrons participating in covalent bonds. Dipolar coupling plays a major role in transverse relaxation (see section 8.4.2), whereas scalar coupling results in multiple spectral peaks for a given moiety. In scalar coupling, Figure 8.8, spins of electrons shared in a covalent bond must, according to Pauli's exclusion principle, be oriented antiparallel to each other. An antiparallel arrangement is favoured between nuclei and electrons too, but this is not possible when both nuclei are found in the same energy levels ($\alpha\alpha$ or $\beta\beta$). This leads to an increase in such energy states by a factor proportional to the coupling constant, *J*; consequently, multiple energy transitions become possible and, hence, more than one resonance is detected. This phenomenon can occur also across three bonds, although such magnetic interactions become negligible after the fourth. These multiple resonances (doublets or triplets) represent one nuclear population: in the example in Figure 8.8, one peak is related to the antiparallel state of nucleus-electron interactions and the other to the parallel state. Quantification of a given moiety can be achieved by integrating the area under all multiplets. The extent of the frequency splitting between the two spectral lines is determined by the coupling constant, *J*, which is independent of the strength of B_0 and invariably expressed in hertz.

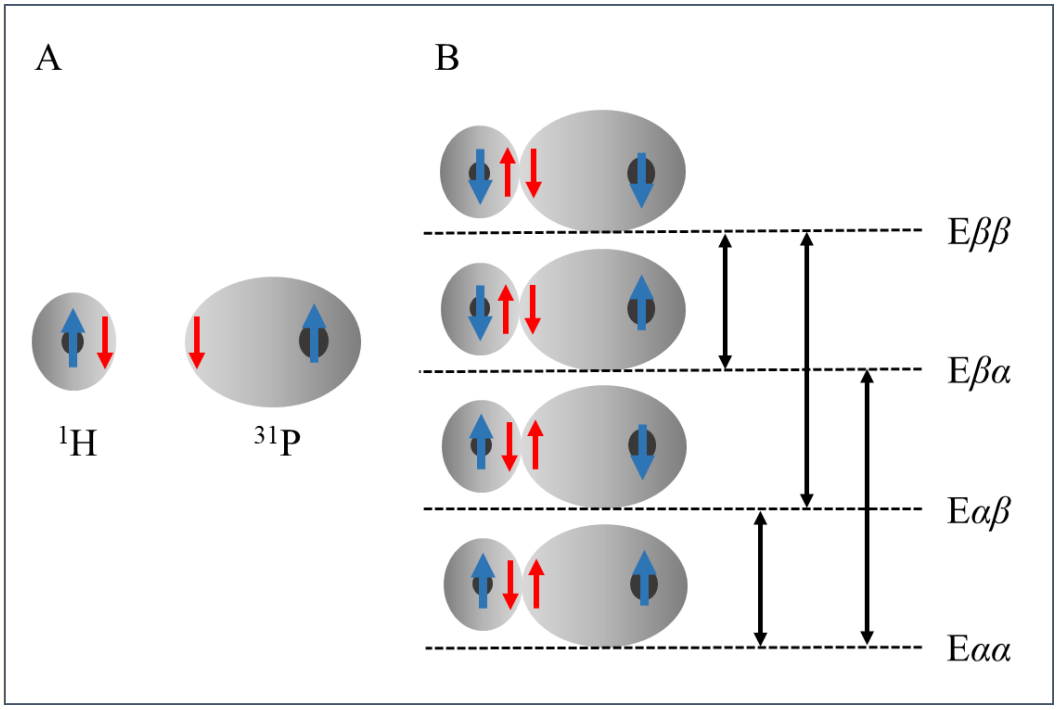

Figure 8.8 Scalar coupling.
(A) Antiparallel orientation of nuclear (blue) and electronic (red) spins is generally favoured. (B) According to Pauli's exclusion principle, in a covalent bond, electrons' spin must be antiparallel to each other. This results in alterations of nuclear energy levels and, consequently, more energy transitions become allowable. Concept from (de Graaf 2007) - page 27-28. The figure is drawn by the author.

Scalar coupling is widely exploited in analytical and structural chemistry to gain information on the nature of molecules and their bonds. In ^{31}P-MRS *in vivo*, homonuclear ^{31}P-^{31}P coupling is manifest in the ATP multiples[25] (Figure 8.7) which have a coupling constant of approximately 18 Hz. However, ^{1}H-^{31}P heteronuclear coupling, which is typically characterised by much smaller coupling constant (≤5 Hz), can decrease SNR and broaden the spectral linewidth which results in adjacent peaks merging, decreasing spectral resolution; it is, therefore, customary to uncouple phosphorous from hydrogen nuclei to obtain a clearer spectrum by selectively irradiating protons during acquisition of the FID.

8.6 Information encoded in signal

MRS is a powerful tool with the potential to quantitate concentration of constituent metabolites from localised anatomical regions. Detail on the methods by which spatial information is encoded and decoded from acquired signals is provided in the next section. Once signal from a specific region of interest is acquired, it is then possible to fit its components to characterise the local metabolic profile. Technical aspects on peak fitting are the topic of chapter three. Broadly speaking, the localised signal

[25] The ATP molecule is composed of three phosphates (α, β, and γ) which resonate at different frequencies, hence ATP is represented by three different peaks in the phosphorus spectrum. In turn, as a consequence of scalar coupling, the α and γ phosphate are each composed of two peaks whereas the β phosphate is a triplet.

intensity (which can be intuitively regarded as the integral of a specific peak, expressed in arbitrary units) is proportional to the number of nuclei resonating at that specific frequency and thus to the concentration of the associated molecule. Nonetheless, as shown in equation 8.30, peak intensity is also affected by transverse and longitudinal relaxation as well as other factors which include coil sensitivity, receiver gain, and external magnetic field strength.

Equation 8.30

$$Peak\ intensity = [A]\ \cdot N_A \cdot e^{-\frac{TE}{T2}} \cdot \left(1 - e^{-\frac{TR}{T1}}\right) \cdot K$$

[A] is the concentration of a compound *A* corresponding to the peak being fitted and N_A is the number of nuclei per molecule resonating at the peak's specific frequency. TE and TR are derived from the applied pulse sequence. T_1 and T_2 are the relaxation constants which are specific to each resonating compound (i.e. to each peak). The factor *K* includes technical variables such as the receiver gain, coil sensitivity, localisation techniques, and scanner's magnetic strength.

More specifically, it is extremely difficult to measure *K,* as MRI scanners are not designed for this purpose, and the parameter inevitably changes at each scanning session. To circumvent this issue, it is customary to compare two peaks belonging to the same spectrum, using one as a reference to the other. The *K* factors cancel out and a metabolite ratio is obtained. In ^{1}H-MRS, tCr and Cho are typically used as the denominator in these ratios, as concentrations are assumed to remain relatively constant in biological tissues. Some researchers employ total water content as a reference, a parameter that can be calculated from a spectrum acquired without water suppression. In ^{31}P-MRS, the choice of reference compound is much more controversial and optimal parameters and ratios to be reported have not yet been agreed; this aspect will be expanded further in this thesis. Alternatively, metabolite concentration can be estimated by employing an external reference which can be scanned either with the subject, or separately. The first option may be unfeasible due to limited space available in the sensitivity profile of the coil, whereas the latter requires corrections for coil loading and receiver gain which may be time consuming as they vary for each individual scanned.

The above equation shows that relaxation constants and scanning parameters (TR, TE) also affect quantitative measures. It is possible to correct for T_1 and T_2 relaxation effects, although values used are typically based on measurements from healthy controls. However, relaxation parameters can be changed by pathology: for instance (Hanstock, Cwik et al. 2002) measured T_2 in MND and healthy controls and showed that both T_2 of NAA and of T_2 of tCr are lower in patients' brainstem. This complicates between-group comparisons in the clinical setting. A possible solution to minimise the effects of T_1 relaxation is to employ a long TR sequence, whereas short TE acquisitions can minimise

effects of T_2. Failure to account for these effects could bias metabolite concentration estimates and resulting errors can be propagated when using ratios.

8.7 Magnetic resonance hardware

The main components of an MR system are described below. When not otherwise cited, the following sources were employed: (de Graaf 2007, de Graaf 2007, de Graaf 2007, de Graaf 2007, de Graaf 2007, Keeler 2010).

8.7.1 The MR magnet

This sophisticated apparatus generates an indefinitely preserved static magnetic field B_0 by exploiting the superconductive properties of alloys such as Niobium–titanium (NbTi) and Niobium–tin (Nb_3Sn). In superconductors, current flow is not accompanied by any electrical resistance and, hence, heat loss, as long as their temperature is maintained below a critical threshold. This is usually achieved by refrigeration using liquid nitrogen and liquid helium. Once the magnet is conducting, no electrical power is directly needed to generate the magnetic field, although there are substantial costs associated with maintenance of nitrogen and helium in their liquid state. The magnet is also designed to maintain optimal magnetic field homogeneity, which is achieved through superconductive and passive shimming. The former is a process completed at scanner installation and is analogous to the shimming performed prior to every acquisition *in vivo*: shim coils cancel out inhomogeneities by generating a magnetic field characterised by harmonics in the opposite direction to unwanted B_0 magnetic inhomogeneities. The latter type of shimming is achieved by introducing ferromagnetic materials in specific areas of the magnet which also directly counteract the unwanted magnetic fields. During high power or prolonged acquisitions, shimming metals may slightly warm up, which can have an impact on thermal stability and is important as even small variations in temperature may cause the magnetic field to drift. In spectroscopy, B_0 drifts result in the whole spectrum being shifted along the x (frequency) axis. The relationship between frequency and temperature can be appreciated by substituting γB_0 with Larmor frequency in equation 8.12. Frequency drift may introduce a bias in quantification of spectral edited metabolites such as GABA or GSH and broaden the linewidth of spectra resulting from repeated signal averaging (Harris, Glaubitz et al. 2014). This effect can be corrected at the post-processing stage by realigning the reference peak (e.g. NAA or PCr) to its reference ppm value (i.e. frequency shift, illustrated in more detail in chapter three), but neither of these biases were evident in the experiments conducted in this thesis.

8.7.2 The MR gradients

These are the coils that generate magnetic field gradients along the *x*, *y*, and *z* axes primarily used for spatial encoding. The spatial location at which the magnetic field gradients cancel out is called isocentre. With incrementing distance from isocentre, the fields increase in magnitude in one direction of each Cartesian axis and decrease in the other. The main properties of gradients are: (1) amplitude which contributes towards determining maximal spatial and temporal resolution; (2) homogeneity which indicates to what extent changes in gradients amplitude vary linearly in space; (3) rise time which is the minimum time necessary to reach 90% of maximal amplitude from ten percent; and (4) slew rate which is the maximum rate of change per unit of time, typically used to define the gradients' specifications. A description of gradient design is beyond the scope of this thesis.

8.7.3 The RF coils

This hardware is specifically designed for different heteronuclear acquisitions and must be tuned to phosphorus frequencies in order to acquire ^{31}P-MRS spectra. On clinical MRI scanners, all the electronics are optimised for ^{1}H (with a narrow bandwidth which does not include frequencies required for heteronuclei). Hence, other nuclei require special broadband transmitters, which are not standard equipment and are typically quite expensive.

Generally, by oscillating at resonance frequencies, a transmitter coil creates an RF pulse which generates a B_1 field orthogonal to B_0, necessary to tilt the *net magnetisation vector* onto the transverse plane. Once the RF pulse is turned off, the MR signal can then be detected by a receiver coil. Transmitter and receiver may either be located in different hardware or be part of the same device. Both comprise an inductor (i.e. the actual coil), a capacitor, and a resistor (i.e. the wires of the circuit).

Numerous different coil designs exist. The most basic is the linearly polarised (LP) coil which transmits and detects only along a single axis. This design is inefficient on a transmission level and phase information, available only when signal from two orthogonal directions is recorded, cannot be acquired and is, hence, lost. The most frequently used design is a quadrature coil (also known as circularly polarised or CP), characterised by coils orthogonal to each other, requires half the power of an LP coil and detects both the x and y components of the MR signal, as explained in more detail in section 2.3. CPs also have the advantage of generating a rather homogeneous B_1 magnetic field. B_1 homogeneity is an important parameter that can also be improved by using adiabatic RF pulses (i.e. RF is applied gradually, maintaining a constant pulse magnitude, but slowly varying frequency). In this thesis, the coil used for brain acquisitions was a transmit-receiver birdcage (a common type of quadrature arrangement) head-coil whereas, for muscle spectroscopy, the scanner's body (quadrature) coil was employed for transmission and a dedicated heteronuclear flat LP coil applied for signal detection.

In the transmitter, the RF generating circuit is powered by a voltage generator and amplified. This allows the system to resonate at appropriate frequencies with receivers set to detect and amplify signal in the same frequency range. Since transmitted and received frequencies are in the same range, but transmitted voltage is greater than received voltage, it is important to ensure that receivers and transmitters are not coupled so that the transmitted RF pulse does not burn out the receiver. This can be achieved by means of a "trap", which is a circuit that detunes and stops current at resonance frequency from flowing from transmitter to receiver.

As soon as signal is detected, it is amplified by low noise preamplifiers, digitalised by an ADC, and demodulated, i.e. filtered to remove the high frequency "carrier" wave, while maintaining relevant information contained in the signal. Amplifiers are key components as the signal is very small (in the mV to μV range). To digitise the signal (i.e. to transform the detected voltage to digital binary datapoints), FID must be sampled at regular intervals by the ADC. The sampling frequency should not be lower than the Nyquist rate to avoid artifacts. This means that, to digitise the FID appropriately, at least two points per cycle should be sampled. Increasing the sampling frequency (i.e. oversampling) is usually used in MRI to prevent aliasing and wrap-around artefacts. Additionally, oversampling results in a larger FOV and has a de-noising effect. The effect of oversampling on MRI volumetric images is demonstrated in later sections of this chapter in the sections reporting T_1-weighted preliminary work. The last step in the receiver chain is demodulation in which information pertaining to the various channels (see section 8.3) is extracted.

All coil electronics must be optimised to participant-specific resonance frequency and impedance in a process called tuning and matching which maximises the coil-specific SNR. Placement of any object (including humans) in an RF coil alters the coil loading, as magnetic and electrical interactions occur between the object and the coil. As a result, the homogeneity of the magnetic fields is affected and, following principles mentioned in the previous chapter, the nuclear effective resonance frequency is slightly altered. For this reason, it is necessary to tune the coil to the appropriate resonance frequency range. Analogously, the coil electronic loading (or impedance) also varies depending on the size and shape of objects scanned and needs to be optimised so that the impedance within the coil matches that of the electronics connecting the transmitter and amplifiers (50 Ω) to ensure maximal transfer of energy to the scanned object. This process is called matching. Usually, tuning and matching occurs automatically prior to every scan, although the flat coil employed for muscle required manual tuning and matching which was always performed by the author of this thesis for reproducibility.

A fundamental prerequisite of all MRS experiments to obtain optimal SNR and accurate localisation accuracy is to employ RF pulses that produce the desired FA. Therefore, RF pulse calibration is the initial, fundamental step when installing a new coil. Calibration is conducted by acquiring spectra at progressively increasing FA; this is possible by incrementing the RF duration or, in the case of adiabatic

pulses, maintaining the RF duration constant and incrementally increasing the transmitter power. Since signal intensity of the detected spectrum is proportional to the magnitude of the transverse magnetisation vector (which is proportional to $M_0 \sin\beta$ where M_0 is the z component of the net magnetisation vector and β is the FA, see equation 8.20), it is possible to determine the RF pulse duration that produces a 90˚ FA by detecting the spectrum with maximal signal. Analogously, no spectrum is recorded at β = 180˚(sin180˚=0). Figure 8. shows a typical calibration curve acquired from a hypothetical experiment. As expected by the linear dependence of signal intensity on sinβ, spectral signal varies in a symmetrical sinusoidal pattern so that the maximum falls exactly halfway between two zero values.

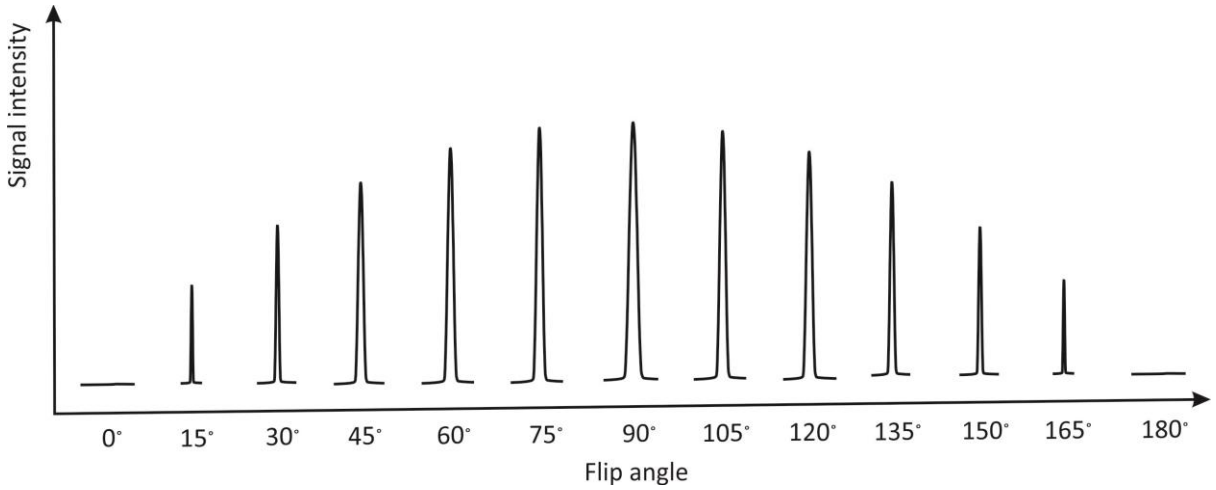

Figure 8.9 Radio frequency pulse calibration curve.
The maximum corresponds to a 90º flip angle whereas the minimum to 0º and 180º. The figure was drawn by the author.

8.7.4 The MR computer system.

This coordinates all the above-mentioned components as well as allowing sequence programming, acquisition planning, image reconstruction, and some data processing. This latter aspect is the topic of chapter three. Of note, the MR system used in this thesis (Philips Healthcare, Best, The Netherlands) included the spectral fitting software SpectroView which was used to analyse spectra acquired for protocol set-up experiments discussed in chapter two. The main advantage of this software is the speed of spectral analysis when setting up protocols, but it also confers some disadvantages, discussed in more detail in previous chapters (e.g. lower reliability than other software packages, no calculation of pH and Mg^{++} concentration).

8.8 Localisation and dynamic series in phosphorus magnetic resonance spectroscopy

An invaluable feature of both MRS and MRI is spatial localisation of pathology. To localise spectra, it is possible to use a SV sequence, in which only one spectrum is obtained from a selected three-

dimensional volume. Alternatively, there are techniques, such as CSI (used in heteronuclear spectroscopy) or magnetic resonance spectroscopic imaging (MRSI, used in ^{1}H-MRS), in which spectra are obtained from multiple voxels during the same acquisition. CSI and MRSI allow sampling and comparisons of larger tissue volumes, rather than a single region of interest. In ^{1}H-MRS, signal from extracranial lipids and water, which are otherwise the main "source" of ^{1}H) needs to be removed. ^{31}P-MRS does not present a problem in this regard, although PCr signal from neck skeletal muscles can still cause issues when using a PA sequence. This is one of the reasons that different localisation techniques are sometimes used for the two modalities. There are numerous technical reasons why SV localisation is preferred in ^{1}H-MRS, the most important of which is the necessity of water and fat suppression: water and fat would otherwise mask signal associated with macromolecules of interest. Suppression is particularly challenging in MRSI, especially in regions close to the skull where partially unsuppressed signal may "bleed" into brain regions. This is because RF pulses suppressing signals are effective over parallelepiped-like volumes which do not model the shape of the skull well. In phosphorus spectroscopy, both SV and CSI can be used and both were tested in the preliminary work reported in chapter two.

Spectroscopic localisation methods differ from classical MRI techniques, in which spatial encoding is typically carried out by means of slice selection with frequency and phase encoding. In MRS, frequency domain data needs to be displayed on the x-axis and, hence, cannot be manipulated for spatial localisation. Numerous different spectroscopic sequences have been invented: in ^{1}H-MRS, the most common are point resolved spectroscopy (PRESS) and stimulated echo acquisition mode (STEAM), whereas in ^{31}P-MRS the most frequently used by far is ISIS. ISIS was originally established as a SV technique, but was subsequently developed as a multivoxel method as well (Ordidge, Connelly et al. 1986, Ordidge, Bowley et al. 1988). Spatial information is encoded by 180˚ pre-pulses which invert and select a set of planes then sampled by a 90˚ RF pulse. This scheme is then repeated (twice in 1D ISIS, four times in 2D ISIS, and eight times in 3D ISIS) on different sets of planes and, following specific addition and subtraction schemes, it is then possible to localise the spectrum to a plane (1D ISIS), a series of voxels within a single plane (2D ISIS), or voxels within a three-dimensional volume (3D ISIS). An example illustrating 2D ISIS is shown in Figure10; the figure has been drawn by the author and adapted from (de Graaf 2007), page 300.

ISIS has become the technique of choice to localise ^{31}P-MRS because it is particularly apt to measure metabolites that have a short T_2, such as ATP. This is because sampling can take place immediately after the 90˚ RF pulse and refocusing pulses are not required. This implies that, since no echoes are generated, the method is almost devoid of T_2 weighting (Ordidge, Connelly et al. 1986).

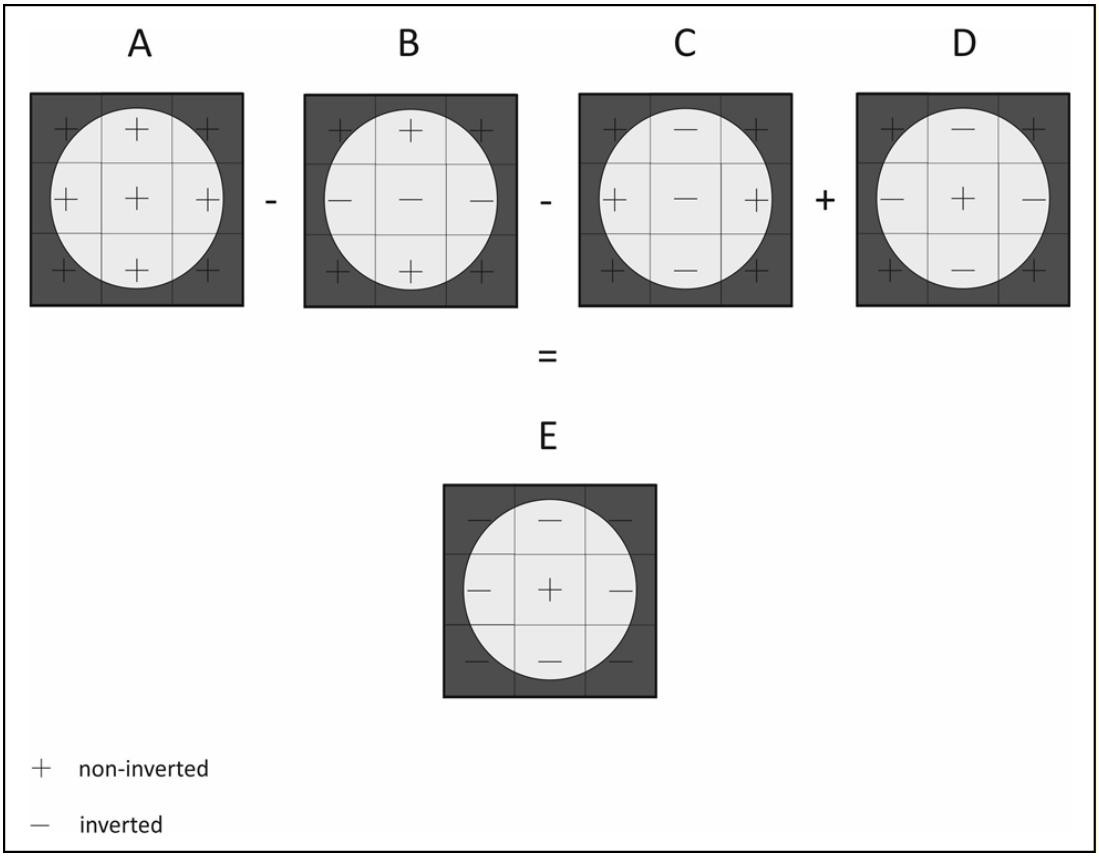

Figure 8.10 A visual example of how a 2D ISIS voxel is localised.
(A) An initial 90˚ radiofrequency (RF) pulse generates signal from the entire field of view. In two subsequent acquisitions, inversion RF pulses (i.e. at 180˚ angle) allow selection of horizontal (B) and vertical (C) volumes. A fourth acquisition where two inversion pulses are concomitantly switched on, generates signal as in (D). Following combination of data acquired (A-B-C+D), signal from the selected central voxel is recorded, whilst signals from surrounding volumes cancel out (E). The figure was drawn by the author after being readapted from (de Graaf 2007), page 300.

There are some circumstances when precise localisation of MRS spectra is not needed, and, in these cases, a simple PA sequence is sufficient. This sequence detects signal from the entire sensitivity profile of the coil, as it comprises only an RF pulse followed by sampling of FID. RF and sampling are repeated a number of times and FID averaged (reported as number of signals averaged or NSA in the acquisition) to improve SNR. PA is a quick way to obtain spectra as no additional time for spatial localisation steps is needed, which can be useful in some ^{31}P-MRS exercise experiments, for example in skeletal muscle, when the focus is on global changes within a tissue compartment rather than more precisely localised pathology. This was the case in this thesis as one of the research questions entailed investigating putative skeletal muscle metabolic alterations associated with denervation in MND.

In a typical dynamic protocol, spectra are acquired over time: following baseline measurements, the research participant is asked to contract the muscle of interest, which causes PCr to decline (as it transphosphorylates ADP to maintain ATP levels constant) and Pi (the end-product of ATP hydrolysis) to increase. Following relaxation of muscle, these metabolites return to baseline levels. It is generally postulated that, if pH changes are negligible (within 0.1 units, according to recently published

guidelines (Meyerspeer, Boesch et al. 2020)), PCr recovery can be considered an indirect indicator of mitochondrial oxidative capacity. In such experimental designs, to prevent pH from decreasing, contraction should take place at submaximal forces, typically a fourth or a third of MVIC. For this reason, it is important to have a system that allows force of contraction to be gauged within the MRI scanner. In this thesis, an in-house MR compatible pulley system was devised and tested for this purpose.

Copyright of Brain paper: licence to reproduce content in thesis/dissertation

OXFORD UNIVERSITY PRESS LICENSE
TERMS AND CONDITIONS

Apr 29, 2021

This Agreement between Dr. Matilde Sassani ("You") and Oxford University Press ("Oxford University Press") consists of your license details and the terms and conditions provided by Oxford University Press and Copyright Clearance Center.

License Number	5058370448258
License date	Apr 29, 2021
Licensed content publisher	Oxford University Press
Licensed content publication	Brain
Licensed content title	Magnetic resonance spectroscopy reveals mitochondrial dysfunction in amyotrophic lateral sclerosis
Licensed content author	Sassani, Matilde; Alix, James J
Licensed content date	Jan 13, 2021
Type of Use	Thesis/Dissertation
Institution name	
Title of your	INVESTIGATING ENERGY METABOLISM IN MOTOR NEURON

work	DISEASE USING PHOSPHORUS MAGNETIC RESONANCE SPECTROSCOPY
Publisher of your work	The University of Sheffield
Expected publication date	May 2021
Permissions cost	0.00 GBP
Value added tax	0.00 GBP
Total	0.00 GBP
Title	INVESTIGATING ENERGY METABOLISM IN MOTOR NEURON DISEASE USING PHOSPHORUS MAGNETIC RESONANCE SPECTROSCOPY
Institution name	The University of Sheffield
Expected presentation date	May 2021
Order reference number	doi.org/10.1093/brain/awaa340
Portions	Pages 3603–3618
Requestor Location	Dr. Matilde Sassani 2 Moorgate Avenue F 12 Sheffield, S10 1EQ United Kingdom Attn: Dr. Matilde Sassani

Publisher Tax ID GB125506730

Total 0.00 GBP

Terms and Conditions

STANDARD TERMS AND CONDITIONS FOR REPRODUCTION OF MATERIAL FROM AN OXFORD UNIVERSITY PRESS JOURNAL

1. Use of the material is restricted to the type of use specified in your order details.

2. This permission covers the use of the material in the English language in the following territory: world. If you have requested additional permission to translate this material, the terms and conditions of this reuse will be set out in clause 12.

3. This permission is limited to the particular use authorized in (1) above and does not allow you to sanction its use elsewhere in any other format other than specified above, nor does it apply to quotations, images, artistic works etc that have been reproduced from other sources which may be part of the material to be used.

4. No alteration, omission or addition is made to the material without our written consent. Permission must be re-cleared with Oxford University Press if/when you decide to reprint.

5. The following credit line appears wherever the material is used: author, title, journal, year, volume, issue number, pagination, by permission of Oxford University Press or the sponsoring society if the journal is a society journal. Where a journal is being published on behalf of a learned society, the details of that society must be included in the credit line.

6. For the reproduction of a full article from an Oxford University Press journal for whatever purpose, the corresponding author of the material concerned should be informed of the proposed use. Contact details for the corresponding authors of all Oxford University Press journal contact can be found alongside either the abstract or full text of the article concerned, accessible from www.oxfordjournals.org Should there be a problem clearing these rights, please contact journals.permissions@oup.com

7. If the credit line or acknowledgement in our publication indicates that any of the figures, images or photos was reproduced, drawn or modified from an earlier source it will be necessary for you to clear this permission with the original publisher as well. If this permission has not been obtained, please note that this material cannot be included in your publication/photocopies.

8. While you may exercise the rights licensed immediately upon issuance of the license at the end of the licensing process for the transaction, provided that you have disclosed complete and accurate details of your proposed use, no license is finally effective unless and until full payment is received from you (either by Oxford University Press or by Copyright Clearance Center (CCC)) as provided in CCC's Billing and Payment terms and conditions. If full payment is not received on a timely basis, then any license preliminarily granted shall be deemed automatically revoked and shall be void as if never granted. Further, in the event that you breach any of these terms and conditions or any of CCC's Billing and Payment

terms and conditions, the license is automatically revoked and shall be void as if never granted. Use of materials as described in a revoked license, as well as any use of the materials beyond the scope of an unrevoked license, may constitute copyright infringement and Oxford University Press reserves the right to take any and all action to protect its copyright in the materials.

9. This license is personal to you and may not be sublicensed, assigned or transferred by you to any other person without Oxford University Press's written permission.

10. Oxford University Press reserves all rights not specifically granted in the combination of (i) the license details provided by you and accepted in the course of this licensing transaction, (ii) these terms and conditions and (iii) CCC's Billing and Payment terms and conditions.

11. You hereby indemnify and agree to hold harmless Oxford University Press and CCC, and their respective officers, directors, employs and agents, from and against any and all claims arising out of your use of the licensed material other than as specifically authorized pursuant to this license.

12. Other Terms and Conditions:

v1.4

Questions? customercare@copyright.com or +1-855-239-3415 (toll free in the US) or +1-978-646-2777.

Figure 8.9 Copyright of Brain paper: licence to reproduce article's text in this thesis.

OXFORD UNIVERSITY PRESS LICENSE
TERMS AND CONDITIONS

Apr 29, 2021

This Agreement between Dr. Matilde Sassani ("You") and Oxford University Press ("Oxford University Press") consists of your license details and the terms and conditions provided by Oxford University Press and Copyright Clearance Center.

License Number	5058381474260
License date	Apr 29, 2021
Licensed content publisher	Oxford University Press
Licensed content publication	Brain
Licensed content title	Magnetic resonance spectroscopy reveals mitochondrial dysfunction in amyotrophic lateral sclerosis
Licensed content author	Sassani, Matilde; Alix, James J
Licensed content date	Jan 13, 2021
Type of Use	Thesis/Dissertation
Institution name	
Title of your	INVESTIGATING ENERGY METABOLISM IN MOTOR NEURON

work	DISEASE USING PHOSPHORUS MAGNETIC RESONANCE SPECTROSCOPY
Publisher of your work	The University of Sheffield
Expected publication date	May 2021
Permissions cost	0.00 GBP
Value added tax	0.00 GBP
Total	0.00 GBP
Title	INVESTIGATING ENERGY METABOLISM IN MOTOR NEURON DISEASE USING PHOSPHORUS MAGNETIC RESONANCE SPECTROSCOPY
Institution name	The University of Sheffield
Expected presentation date	May 2021
Order reference number	doi.org/10.1093/brain/awaa340
Requestor Location	Dr. Matilde Sassani 2 Moorgate Avenue F 12 Sheffield, S10 1EQ United Kingdom Attn: Dr. Matilde Sassani
Publisher Tax ID	GB125506730

Total 0.00 GBP

Terms and Conditions

STANDARD TERMS AND CONDITIONS FOR REPRODUCTION OF MATERIAL FROM AN OXFORD UNIVERSITY PRESS JOURNAL

1. Use of the material is restricted to the type of use specified in your order details.

2. This permission covers the use of the material in the English language in the following territory: world. If you have requested additional permission to translate this material, the terms and conditions of this reuse will be set out in clause 12.

3. This permission is limited to the particular use authorized in (1) above and does not allow you to sanction its use elsewhere in any other format other than specified above, nor does it apply to quotations, images, artistic works etc that have been reproduced from other sources which may be part of the material to be used.

4. No alteration, omission or addition is made to the material without our written consent. Permission must be re-cleared with Oxford University Press if/when you decide to reprint.

5. The following credit line appears wherever the material is used: author, title, journal, year, volume, issue number, pagination, by permission of Oxford University Press or the sponsoring society if the journal is a society journal. Where a journal is being published on behalf of a learned society, the details of that society must be included in the credit line.

6. For the reproduction of a full article from an Oxford University Press journal for whatever purpose, the corresponding author of the material concerned should be informed of the proposed use. Contact details for the corresponding authors of all Oxford University Press journal contact can be found alongside either the abstract or full text of the article concerned, accessible from www.oxfordjournals.org Should there be a problem clearing these rights, please contact journals.permissions@oup.com

7. If the credit line or acknowledgement in our publication indicates that any of the figures, images or photos was reproduced, drawn or modified from an earlier source it will be necessary for you to clear this permission with the original publisher as well. If this permission has not been obtained, please note that this material cannot be included in your publication/photocopies.

8. While you may exercise the rights licensed immediately upon issuance of the license at the end of the licensing process for the transaction, provided that you have disclosed complete and accurate details of your proposed use, no license is finally effective unless and until full payment is received from you (either by Oxford University Press or by Copyright Clearance Center (CCC)) as provided in CCC's Billing and Payment terms and conditions. If full payment is not received on a timely basis, then any license preliminarily granted shall be deemed automatically revoked and shall be void as if never granted. Further, in the event that you breach any of these terms and conditions or any of CCC's Billing and Payment terms and conditions, the license is automatically revoked and shall be void as if never granted. Use of materials as described in a revoked license, as well as any use of the

materials beyond the scope of an unrevoked license, may constitute copyright infringement and Oxford University Press reserves the right to take any and all action to protect its copyright in the materials.

9. This license is personal to you and may not be sublicensed, assigned or transferred by you to any other person without Oxford University Press's written permission.

10. Oxford University Press reserves all rights not specifically granted in the combination of (i) the license details provided by you and accepted in the course of this licensing transaction, (ii) these terms and conditions and (iii) CCC's Billing and Payment terms and conditions.

11. You hereby indemnify and agree to hold harmless Oxford University Press and CCC, and their respective officers, directors, employs and agents, from and against any and all claims arising out of your use of the licensed material other than as specifically authorized pursuant to this license.

12. Other Terms and Conditions:

v1.4

Questions? customercare@copyright.com or +1-855-239-3415 (toll free in the US) or +1-978-646-2777.

Figure 8.10 Copyright of Brain paper: licence to reproduce article's abstract in this thesis.

OXFORD UNIVERSITY PRESS LICENSE
TERMS AND CONDITIONS

Apr 29, 2021

This Agreement between Dr. Matilde Sassani ("You") and Oxford University Press ("Oxford University Press") consists of your license details and the terms and conditions provided by Oxford University Press and Copyright Clearance Center.

License Number	5058371024759
License date	Apr 29, 2021
Licensed content publisher	Oxford University Press
Licensed content publication	Brain
Licensed content title	Magnetic resonance spectroscopy reveals mitochondrial dysfunction in amyotrophic lateral sclerosis
Licensed content author	Sassani, Matilde; Alix, James J
Licensed content date	Jan 13, 2021
Type of Use	Thesis/Dissertation
Institution name	
Title of your	INVESTIGATING ENERGY METABOLISM IN MOTOR NEURON

work	DISEASE USING PHOSPHORUS MAGNETIC RESONANCE SPECTROSCOPY
Publisher of your work	The University of Sheffield
Expected publication date	May 2021
Permissions cost	0.00 GBP
Value added tax	0.00 GBP
Total	0.00 GBP
Title	INVESTIGATING ENERGY METABOLISM IN MOTOR NEURON DISEASE USING PHOSPHORUS MAGNETIC RESONANCE SPECTROSCOPY
Institution name	The University of Sheffield
Expected presentation date	May 2021
Order reference number	doi.org/10.1093/brain/awaa340
Portions	Figure 1, Figure 2, Figure 3, Table1, Table 2, Table 3, figure in supplementary materials.
Requestor Location	Dr. Matilde Sassani 2 Moorgate Avenue F 12 Sheffield, S10 1EQ United Kingdom Attn: Dr. Matilde Sassani

Publisher Tax ID GB125506730

Total 0.00 GBP

Terms and Conditions

STANDARD TERMS AND CONDITIONS FOR REPRODUCTION OF MATERIAL FROM AN OXFORD UNIVERSITY PRESS JOURNAL

1. Use of the material is restricted to the type of use specified in your order details.

2. This permission covers the use of the material in the English language in the following territory: world. If you have requested additional permission to translate this material, the terms and conditions of this reuse will be set out in clause 12.

3. This permission is limited to the particular use authorized in (1) above and does not allow you to sanction its use elsewhere in any other format other than specified above, nor does it apply to quotations, images, artistic works etc that have been reproduced from other sources which may be part of the material to be used.

4. No alteration, omission or addition is made to the material without our written consent. Permission must be re-cleared with Oxford University Press if/when you decide to reprint.

5. The following credit line appears wherever the material is used: author, title, journal, year, volume, issue number, pagination, by permission of Oxford University Press or the sponsoring society if the journal is a society journal. Where a journal is being published on behalf of a learned society, the details of that society must be included in the credit line.

6. For the reproduction of a full article from an Oxford University Press journal for whatever purpose, the corresponding author of the material concerned should be informed of the proposed use. Contact details for the corresponding authors of all Oxford University Press journal contact can be found alongside either the abstract or full text of the article concerned, accessible from www.oxfordjournals.org Should there be a problem clearing these rights, please contact journals.permissions@oup.com

7. If the credit line or acknowledgement in our publication indicates that any of the figures, images or photos was reproduced, drawn or modified from an earlier source it will be necessary for you to clear this permission with the original publisher as well. If this permission has not been obtained, please note that this material cannot be included in your publication/photocopies.

8. While you may exercise the rights licensed immediately upon issuance of the license at the end of the licensing process for the transaction, provided that you have disclosed complete and accurate details of your proposed use, no license is finally effective unless and until full payment is received from you (either by Oxford University Press or by Copyright Clearance Center (CCC)) as provided in CCC's Billing and Payment terms and conditions. If full payment is not received on a timely basis, then any license preliminarily granted shall be

deemed automatically revoked and shall be void as if never granted. Further, in the event that you breach any of these terms and conditions or any of CCC's Billing and Payment terms and conditions, the license is automatically revoked and shall be void as if never granted. Use of materials as described in a revoked license, as well as any use of the materials beyond the scope of an unrevoked license, may constitute copyright infringement and Oxford University Press reserves the right to take any and all action to protect its copyright in the materials.

9. This license is personal to you and may not be sublicensed, assigned or transferred by you to any other person without Oxford University Press's written permission.

10. Oxford University Press reserves all rights not specifically granted in the combination of (i) the license details provided by you and accepted in the course of this licensing transaction, (ii) these terms and conditions and (iii) CCC's Billing and Payment terms and conditions.

11. You hereby indemnify and agree to hold harmless Oxford University Press and CCC, and their respective officers, directors, employs and agents, from and against any and all claims arising out of your use of the licensed material other than as specifically authorized pursuant to this license.

12. Other Terms and Conditions:

v1.4

Questions? customercare@copyright.com or +1-855-239-3415 (toll free in the US) or +1-978-646-2777.

Figure 8.11 Copyright of Brain paper: licence to reproduce article's figures and tables in this thesis.

ALSFRS-R

ALS Functional Rating Scale Revised (ALS-FRS-R)

Date:.....**Name patient:**.....**Date of Birth:**.....

Patient's number.....**Right-/left-handed**

Item 1: SPEECH

- 4 ☐ Normal speech process
- 3 ☐ Detectable speech disturbance
- 2 ☐ Intelligible with repeating
- 1 ☐ Speech combined with non-vocal communication
- 0 ☐ Loss of useful speech

Item 2: SALIVATION

- 4 ☐ Normal
- 3 ☐ Slight but definite excess of saliva in mouth; may have nighttime drooling
- 2 ☐ Moderately excessive saliva; may have minimal drooling (during the day)
- 1 ☐ Marked excess of saliva with some drooling
- 0 ☐ Marked drooling; requires constant tissue or handkerchief

Item 3: SWALLOWING

- 4 ☐ Normal eating habits
- 3 ☐ Early eating problems – occasional choking
- 2 ☐ Dietary consistency changes
- 1 ☐ Needs supplement tube feeding
- 0 ☐ NPO (exclusively parenteral or enteral feeding)

Item 4: HANDWRITING

- 4 ☐ Normal
- 3 ☐ Slow or sloppy: all words are legible
- 2 ☐ Not all words are legible
- 1 ☐ Able to grip pen, but unable to write
- 0 ☐ Unable to grip pen

Item 5a: CUTTING FOOD AND HANDLING UTENSILS

Patients <u>without</u> gastrostomy → Use 5b if >50% is through g-tube

- 4 ☐ Normal
- 3 ☐ Somewhat slow and clumsy, but no help needed
- 2 ☐ Can cut most foods (>50%), although slow and clumsy; some help needed
- 1 ☐ Food must be cut by someone, but can still feed slowly
- 0 ☐ Needs to be fed

Item 5b: CUTTING FOOD AND HANDLING UTENSILS

Patients <u>with</u> gastrostomy → 5b option is used if the patient has a gastrostomy and only if it is the primary method (more than 50%) of eating .

- 4 ☐ Normal
- 3 ☐ Clumsy, but able to perform all manipulations independently
- 2 ☐ Some help needed with closures and fasteners
- 1 ☐ Provides minimal assistance to caregiver
- 0 ☐ Unable to perform any aspect of task

ALS Functional Rating Scale Revised (ALS-FRS-R). Version: May 2015

Item 6: DRESSING AND HYGIENE

- 4 ☐ Normal function
- 3 ☐ Independent and complete self-care with effort or decreased efficiency
- 2 ☐ Intermittent assistance or substitute methods
- 1 ☐ Needs attendant for self-care
- 0 ☐ Total dependence

Item 7: TURNING IN BED AND ADJUSTING BED CLOTHES

- 4 ☐ Normal function
- 3 ☐ Somewhat slow and clumsy, but no help needed
- 2 ☐ Can turn alone, or adjust sheets, but with great difficulty
- 1 ☐ Can initiate, but not turn or adjust sheets alone
- 0 ☐ Helpless

Item 8: WALKING

- 4 ☐ Normal
- 3 ☐ Early ambulation difficulties
- 2 ☐ Walks with assistance
- 1 ☐ Non-ambulatory functional movement
- 0 ☐ No purposeful leg movement

Item 9: CLIMBING STAIRS

- 4 ☐ Normal
- 3 ☐ Slow
- 2 ☐ Mild unsteadiness or fatigue
- 1 ☐ Needs assistance
- 0 ☐ Cannot do

Item 10: DYSPNEA

- 4 ☐ None
- 3 ☐ Occurs when walking
- 2 ☐ Occurs with one or more of the following: eating, bathing, dressing (ADL)
- 1 ☐ Occurs at rest: difficulty breathing when either sitting or lying
- 0 ☐ Significant difficulty: considering using mechanical respiratory support

Item 11: ORTHOPNEA

- 4 ☐ None
- 3 ☐ Some difficulty sleeping at night due to shortness of breath, does not routinely use more than two pillows
- 2 ☐ Needs extra pillows in order to sleep (more than two)
- 1 ☐ Can only sleep sitting up
- 0 ☐ Unable to sleep without mechanical assistance

Item 12: RESPIRATORY INSUFFICIENCY

- 4 ☐ None
- 3 ☐ Intermittent use of BiPAP
- 2 ☐ Continuous use of BiPAP during the night
- 1 ☐ Continuous use of BiPAP during day & night
- 0 ☐ Invasive mechanical ventilation by intubation or tracheostomy

Interviewer's name.....

ALS Functional Rating Scale Revised (ALS-FRS-R). Version: May 2015

Figure 8.12 ALSFRS-R questionnaire used in experiments conducted in this thesis (Cedarbaum, Stambler et al. 1999). *Participants' names and personal details were not recorded on the form, a unique identifier was assigned instead.*

Processing protocols comparisons for PDE

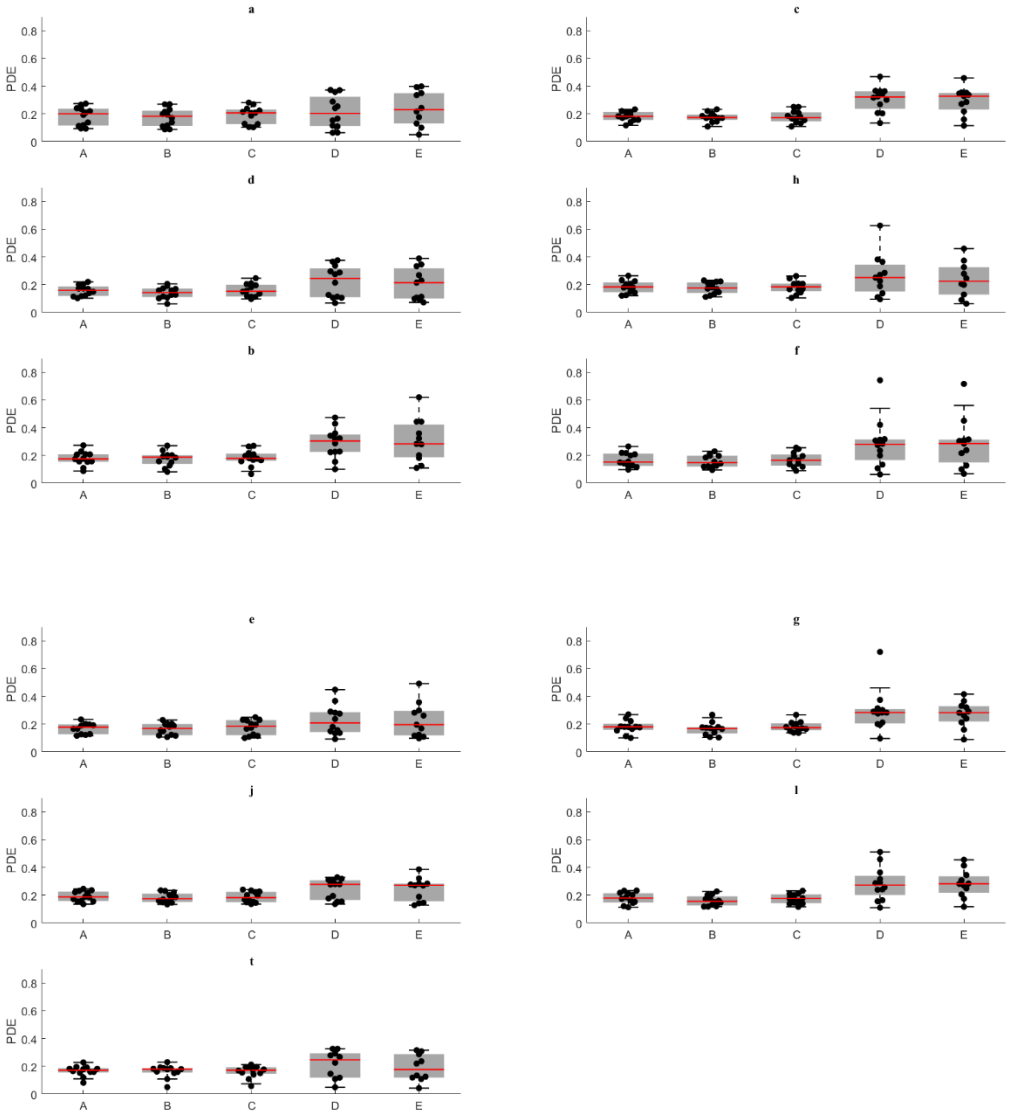

Figure 8.13 Box and whisker plots illustrating phosphodiesters (PDE) values calculated using methods A to E (detailed in method section of chapter three), y-axis scaled to illustrate all datapoints.

ICC, all voxels

Table 8.2 ICC calculated from protocol A and B (i.e. reliability of jMRUI to phasing), as detailed in chapter three, methods.
Voxels are illustrated in Figure 3.13. Legend is illustrated below table.

	a	*b*	*c*	*d*	*e*	*f*	*g*	*h*	*i*	*j*	*k*	*l*	*m*	*n*	*o*	*p*	*q*	*r*	*s*	*t*	*u*
pH	99.0%	96.8%	99.3%	83.6%	96.4%	97.6%	92.6%	98.3%	85.5%	99.6%	99.8%	93.8%	95.7%	89.5%	95.2%	98.6%	96.8%	62.6%	72.5%	99.3%	53.7%
Mg^{++}	84.1%	80.3%	75.3%	-12.8%	-1.2%	85.0%	97.2%	53.6%	-7.7%	80.6%	86.7%	90.6%	48.3%	19.3%	79.0%	58.2%	20.1%	56.2%	-12.1%	59.7%	-11.7%
PME	94.5%	86.5%	98.8%	91.6%	97.7%	81.4%	75.7%	82.9%	91.6%	92.7%	94.1%	96.4%	91.2%	81.6%	95.4%	96.0%	95.4%	95.3%	97.9%	98.8%	54.1%
Pi	99.8%	95.9%	99.2%	69.4%	94.0%	80.2%	94.6%	98.3%	88.6%	98.8%	97.8%	93.6%	93.4%	73.4%	80.4%	93.8%	93.6%	97.0%	70.4%	98.0%	76.5%
PDE	96.9%	92.5%	82.0%	81.9%	96.3%	92.4%	86.0%	94.7%	93.9%	85.6%	89.0%	64.8%	85.7%	97.1%	53.8%	89.2%	91.7%	60.9%	95.5%	94.2%	10.7%
PCr	93.3%	90.5%	85.7%	92.3%	88.9%	83.0%	81.2%	91.6%	93.7%	95.0%	97.4%	94.7%	82.8%	90.9%	91.3%	97.5%	95.8%	90.9%	76.1%	98.4%	62.7%
γATP	98.7%	88.1%	88.3%	79.7%	89.8%	81.7%	90.8%	94.5%	84.5%	95.1%	97.5%	94.0%	75.8%	95.3%	94.4%	96.4%	97.5%	88.7%	78.0%	94.4%	57.1%
αATP	99.4%	72.4%	97.3%	94.2%	96.0%	91.9%	97.8%	64.2%	88.5%	68.1%	97.7%	98.1%	91.8%	95.1%	98.4%	96.7%	92.4%	98.6%	76.1%	98.7%	84.9%
βATP	99.5%	60.7%	74.2%	71.3%	69.6%	-0.9%	92.8%	49.3%	50.1%	92.8%	88.8%	62.1%	78.3%	92.5%	74.4%	44.3%	96.6%	79.7%	22.6%	-5.8%	-21.4%

Legend
≤ 0.0%
0.1% - 59.9%
60.0% - 69.9%
70.0% - 79.9%
≥80.0%

Table 8.3 ICC calculated from protocol B and C (i.e. comparing analysis in jMRUI with SpectroView), as detailed in chapter three, methods.
Voxels are illustrated in Figure 3.13. Legend is illustrated below table.

	a	*b*	*c*	*d*	*e*	*f*	*g*	*h*	*i*	*j*	*k*	*l*	*m*	*n*	*o*	*p*	*q*	*r*	*s*	*t*	*u*
PME	94.4%	95.1%	95.9%	91.5%	97.5%	89.3%	96.2%	91.9%	94.8%	85.9%	75.9%	93.9%	83.3%	87.1%	90.5%	97.3%	98.0%	93.0%	98.7%	99.6%	75.9%
Pi	98.0%	98.5%	96.0%	73.1%	95.0%	71.9%	97.2%	96.6%	97.2%	98.2%	95.2%	98.4%	93.1%	67.1%	49.8%	67.9%	96.4%	84.7%	67.6%	90.6%	76.7%
PDE	89.8%	89.8%	79.8%	75.9%	85.6%	89.6%	82.1%	93.0%	93.2%	96.6%	82.7%	79.3%	94.0%	98.2%	74.2%	61.7%	90.1%	92.1%	96.2%	97.7%	92.8%
PCr	77.4%	63.0%	40.4%	84.6%	74.0%	49.6%	45.7%	82.9%	95.3%	84.2%	64.4%	70.4%	93.5%	96.8%	79.4%	91.1%	98.3%	96.7%	95.0%	96.3%	60.6%
γATP	93.6%	92.5%	90.0%	69.4%	86.7%	83.9%	93.3%	92.2%	96.2%	94.2%	91.4%	80.9%	83.3%	96.5%	76.8%	92.5%	96.8%	90.1%	88.7%	97.6%	51.6%
αATP	97.9%	86.9%	93.3%	65.9%	90.9%	93.6%	96.7%	94.9%	97.5%	74.3%	91.4%	96.4%	96.4%	72.0%	92.1%	96.4%	97.1%	81.7%	66.9%	97.9%	87.8%
βATP	89.9%	92.8%	66.0%	96.5%	95.2%	53.9%	96.6%	43.2%	94.2%	93.5%	93.9%	65.8%	98.5%	96.4%	96.2%	50.6%	92.2%	76.6%	96.6%	94.9%	72.3%

Legend
≤ 0.0%
0.1% - 59.9%
60.0% - 69.9%
70.0% - 79.9%
≥80.0%

Table 8.4 ICC calculated from protocol D and E (i.e. reliability of SpectroView to phasing), as detailed in chapter three, methods.
Voxels are illustrated in Figure 3.13. Legend is illustrated below table.

	a	*b*	*c*	*d*	*e*	*f*	*g*	*h*	*i*	*j*	*k*	*l*	*m*	*n*	*o*	*p*	*q*	*r*	*s*	*t*	*u*
PME	69.1%	91.1%	89.1%	90.5%	90.3%	91.2%	87.4%	95.0%	52.6%	93.3%	92.9%	88.9%	87.0%	77.6%	53.2%	93.6%	96.7%	86.6%	93.5%	79.8%	91.2%
Pi	87.6%	74.3%	93.4%	94.0%	2.4%	97.2%	66.7%	81.5%	84.2%	80.8%	71.7%	92.1%	61.8%	98.1%	97.8%	95.8%	98.8%	97.0%	93.4%	92.4%	88.1%
PDE	78.9%	59.3%	95.7%	63.8%	98.4%	99.4%	73.3%	65.8%	31.4%	81.3%	95.9%	94.1%	97.8%	96.7%	99.1%	98.2%	94.8%	41.2%	99.7%	99.0%	90.2%
PCr	77.6%	68.3%	94.1%	58.3%	66.8%	97.9%	75.1%	82.4%	51.0%	87.6%	97.2%	97.7%	94.6%	96.7%	94.4%	98.9%	97.3%	61.0%	94.1%	98.5%	80.9%
γATP	89.9%	94.0%	76.2%	89.0%	81.3%	98.8%	89.3%	68.1%	71.9%	78.0%	95.7%	93.5%	95.6%	90.7%	95.7%	99.2%	97.1%	81.7%	98.6%	98.1%	77.2%
αATP	96.0%	87.7%	68.5%	77.2%	92.7%	96.3%	81.3%	69.7%	51.5%	72.9%	92.0%	94.4%	89.8%	91.0%	94.2%	97.9%	92.8%	71.5%	97.9%	99.0%	92.0%
βATP	75.4%	76.8%	55.5%	70.3%	93.3%	75.9%	68.8%	63.8%	13.6%	92.2%	92.7%	81.4%	84.0%	94.0%	93.2%	91.6%	95.3%	71.6%	93.2%	86.9%	92.3%

Legend
≤ 0.0%
0.1% - 59.9%
60.0% - 69.9%
70.0% - 79.9%
≥80.0%

Upper Motor Neuron Score

Original Range: 0-33

Without thoracic segment included: 0-32

Spasticity Scoring:

Ashworth 1 = 0

Ashworth 2-3 = 1

Ashworth 4-5 = 2

Ashworth Spasticity Scale

1 = normal, no increase in tone

2 = slight increase in tone, giving a “catch” when affected part is moved

3 = more marked increase in tone, but affected part easily moved

4 = considerable increase in tone; passive movement difficult

5 = affected part rigid, immobile

Reflex Scoring:

Normal or absent = 0

Pathologically brisk = 1

Retained reflex in a weak or wasted limb = 1

Thoracic = 0 for present, 1 for absent

Pseudobulbar Affect Scoring:

CNS-LS 7-12 = 0

CNS-LS 13-35 = 1

(see below)

UMN Score - score sheet

Bulbar

Jaw Jerk (0-1)	
Facial Reflex (0-1)	
Palmomental Sign (0-1)	
Pseudobulbar Affect (0-1, see below)	(CNS-LS)

Right Cervical

Spasticity (0-2)	(Ashworth)
Triceps Reflex (0-1)	
Biceps Reflex (0-1)	
Finger Flexors (0-1)	
Clonus (0-1)	
Hoffman's Sign (0-1)	

Left Cervical

Spasticity (0-2)	(Ashworth)
Triceps Reflex (0-1)	
Biceps Reflex (0-1)	
Finger Flexors (0-1)	
Clonus (0-1)	
Hoffman's Sign (0-1)	

Thoracic

Abdominal Reflex (0-1)	

Right Lumbosacral

Spasticity (0-2)	(Ashworth)
Patellar Reflex (0-1)	
Crossed Adduction (0-1)	
Ankle Reflex (0-1)	
Clonus (0-1)	
Babinski Sign (0-1)	

Left Lumbosacral

Spasticity (0-2)	(Ashworth)
Patellar Reflex (0-1)	
Crossed Adduction (0-1)	
Ankle Reflex (0-1)	
Clonus (0-1)	
Babinski Sign (0-1)	

Pseudobulbar affect scoring

Using the scale below, circle the number that describes the degree to which each item applies to you *DURING THE PAST WEEK*. Circle only one number for each item:

Applies Never	Applies Rarely	Applies Occasionally	Applies Frequently	Applies Most of the Time

1	2	3	4	5

1. There are times when I feel fine one minute, and then I'll become tearful the next over something small or for no reason at all.

1 2 3 4 5

2. Others have told me that I seem to become amused very easily or that I seem to become amused about things that really aren't funny.

1 2 3 4 5

3. I find myself crying very easily.

1 2 3 4 5

4. I find that even when I try to control my laughter I am often unable to do so.

1 2 3 4 5

5. There are times when I won't be thinking of anything happy or funny at all, but then I'll suddenly be overcome by funny or happy thoughts.

1 2 3 4 5

6. I find that even when I try to control my crying I am often unable to do so.

1 2 3 4 5

7. I find that I am easily overcome by laughter.

1 2 3 4 5

REFERENCES

Abbruzzese, G., M. Vische, S. Ratto, M. Abbruzzese and E. Favale (1985). "Assessment of motor neuron excitability in parkinsonian rigidity by the F wave." J Neurol **232**(4): 246-249.

Abe K, A. M., Tsuji S, Itoyama Y, Sobue G, Togo M, Hamada C, Tanaka M, Akimoto M, Nakamura K, Takahashi F, Kondo K, Yoshino H, Abe K, Aoki M, Tsuji S, Itoyama Y, Sobue G, Togo M, Hamada C, Sasaki H, Yabe I, Doi S, Warita H, Imai T, Ito H, Fukuchi M, Osumi E, Wada M, Nakano I, Morita M, Ogata K, Maruki Y, Ito K, Kano O, Yamazaki M, Takahashi Y, Ishiura H, Ogino M, Koike R, Ishida C, Uchiyama T, Mizoguchi K, Obi T, Watanabe H, Atsuta N, Aiba I, Taniguchi A, Sawada H, Hazama T, Fujimura H, Kusaka H, Kunieda T, Kikuchi H, Matsuo H, Ueyama H, Uekawa K, Tanaka M, Akimoto M, Ueda M, Murakami A, Sumii R, Kudou T, Nakamura K, Morimoto K, Yoneoka T, Hirai M, Sasaki K, Terai H, Natori T, Matsui H, Kotani K, Yoshida K, Iwasaki T, Takahashi F, Kondo K, Yoshino H. (2017). "Safety and efficacy of edaravone in well defined patients with amyotrophic lateral sclerosis: a randomised, double-blind, placebo-controlled trial." Lancet Neurol **16**(7): 505-512.

Abrahams, S., L. H. Goldstein, J. J. Kew, D. J. Brooks, C. M. Lloyd, C. D. Frith and P. N. Leigh (1996). "Frontal lobe dysfunction in amyotrophic lateral sclerosis. A PET study." Brain **119 (Pt 6)**: 2105-2120.

Abrahams, S., L. H. Goldstein, A. Simmons, M. Brammer, S. C. R. Williams, V. Giampietro and P. N. Leigh (2004). "Word retrieval in amyotrophic lateral sclerosis: a functional magnetic resonance imaging study." Brain **127**(7): 1507-1517.

Abrahams, S., L. H. Goldstein, J. Suckling, V. Ng, A. Simmons, X. Chitnis, L. Atkins, S. C. Williams and P. N. Leigh (2005). "Frontotemporal white matter changes in amyotrophic lateral sclerosis." J Neurol **252**(3): 321-331.

Abrahams, S., P. N. Leigh, A. Harvey, G. N. Vythelingum, D. Grisé and L. H. Goldstein (2000). "Verbal fluency and executive dysfunction in amyotrophic lateral sclerosis (ALS)." Neuropsychologia **38**(6): 734-747.

Abrahams, S., J. Newton, E. Niven, J. Foley and T. H. Bak (2014). "Screening for cognition and behaviour changes in ALS." Amyotroph Lateral Scler Frontotemporal Degener **15**(1-2): 9-14.

Adachi, Y., N. Sato, Y. Saito, Y. Kimura, Y. Nakata, K. Ito, K. Kamiya, H. Matsuda, T. Tsukamoto and M. Ogawa (2015). "Usefulness of SWI for the Detection of Iron in the Motor Cortex in Amyotrophic Lateral Sclerosis." Journal of Neuroimaging **25**(3): 443-451.

Agosta, F., E. Pagani, M. A. Rocca, D. Caputo, M. Perini, F. Salvi, A. Prelle and M. Filippi (2007). "Voxel-based morphometry study of brain volumetry and diffusivity in amyotrophic lateral sclerosis patients with mild disability." Human Brain Mapping **28**(12): 1430-1438.

Ahmed, R. M., K. Phan, E. Highton-Williamson, C. Strikwerda-Brown, J. Caga, E. Ramsey, M. Zoing, E. Devenney, W. S. Kim, J. R. Hodges, O. Piguet, G. M. Halliday and M. C. Kiernan (2019). "Eating peptides: biomarkers of neurodegeneration in amyotrophic lateral sclerosis and frontotemporal dementia." Ann Clin Transl Neurol **6**(3): 486-495.

Al-Chalabi, A., A. Calvo, A. Chio, S. Colville, C. M. Ellis, O. Hardiman, M. Heverin, R. S. Howard, M. H. B. Huisman, N. Keren, P. N. Leigh, L. Mazzini, G. Mora, R. W. Orrell, J. Rooney, K. M. Scott, W. J. Scotton, M. Seelen, C. E. Shaw, K. S. Sidle, R. Swingler, M. Tsuda, J. H. Veldink, A. E. Visser,

L. H. van den Berg and N. Pearce (2014). "Analysis of amyotrophic lateral sclerosis as a multistep process: a population-based modelling study." Lancet Neurol **13**(11): 1108-1113.

Al-Chalabi, A. and O. Hardiman (2013). "The epidemiology of ALS: a conspiracy of genes, environment and time." Nat Rev Neurol **9**(11): 617-628.

Al-iedani, O., J. Arm, K. Ribbons, R. Lea, J. Lechner-Scott and S. Ramadan (2018). "Diurnal stability and long-term repeatability of neurometabolites using single voxel 1H magnetic resonance spectroscopy." European Journal of Radiology **108**: 107-113.

Alix, J. J. P., C. Neuwirth, L. Gelder, C. Burkhardt, J. Castro, M. de Carvalho, M. Gawel, S. Goedee, J. Grosskreutz, T. Lenglet, C. Moglia, T. Omer, M. Schrooten, S. Nandedkar, E. Stalberg, P. E. Barkhaus, J. Furtula, J. P. van Dijk, R. Baldinger, J. Costa, M. Otto, A. Sandberg and M. Weber (2019). "Assessment of the reliability of the motor unit size index (MUSIX) in single subject “round-robin” and multi-centre settings." Clinical Neurophysiology **130**(5): 666-674.

Almeida, V., M. de Carvalho, M. Scotto, S. Pinto, A. Pinto, B. Ohana and M. Swash (2013). "Primary lateral sclerosis: predicting functional outcome." Amyotroph Lateral Scler Frontotemporal Degener **14**(2): 141-145.

Amick, J., A. Roczniak-Ferguson and S. M. Ferguson (2016). "C9orf72 binds SMCR8, localizes to lysosomes, and regulates mTORC1 signaling." Mol Biol Cell **27**(20): 3040-3051.

Andres, R. H., A. D. Ducray, U. Schlattner, T. Wallimann and H. R. Widmer (2008). "Functions and effects of creatine in the central nervous system." Brain Research Bulletin **76**(4): 329-343.

Andrews, J. A., L. Meng, S. F. Kulke, S. A. Rudnicki, A. A. Wolff, M. E. Bozik, F. I. Malik and J. M. Shefner (2018). "Association Between Decline in Slow Vital Capacity and Respiratory Insufficiency, Use of Assisted Ventilation, Tracheostomy, or Death in Patients With Amyotrophic Lateral Sclerosis." JAMA neurology **75**(1): 58-64.

Argyriou, A. A., P. Polychronopoulos, P. Talelli and E. Chroni (2006). "F wave study in amyotrophic lateral sclerosis: assessment of balance between upper and lower motor neuron involvement." Clin Neurophysiol **117**(6): 1260-1265.

Ariyannur, P. S., J. R. Moffett, P. Manickam, N. Pattabiraman, P. Arun, A. Nitta, T. Nabeshima, C. N. Madhavarao and A. M. Namboodiri (2010). "Methamphetamine-induced neuronal protein NAT8L is the NAA biosynthetic enzyme: implications for specialized acetyl coenzyme A metabolism in the CNS." Brain Res **1335**: 1-13.

Atassi, N., E. M. Ratai, D. J. Greenblatt, D. Pulley, Y. Zhao, J. Bombardier, S. Wallace, J. Eckenrode, M. Cudkowicz and A. Dibernardo (2010). "A phase I, pharmacokinetic, dosage escalation study of creatine monohydrate in subjects with amyotrophic lateral sclerosis." Amyotroph Lateral Scler **11**(6): 508-513.

Atassi, N., M. Xu, C. Triantafyllou, B. Keil, R. Lawson, P. Cernasov, E. Ratti, C. J. Long, S. Paganoni, A. Murphy, N. Salibi, R. Seethamraju, B. Rosen and E. M. Ratai (2017). "Ultra high-field (7tesla) magnetic resonance spectroscopy in Amyotrophic Lateral Sclerosis." PLoS One **12**(5): e0177680.

Avlund, K. (2010). "Fatigue in older adults: an early indicator of the aging process?" Aging Clinical and Experimental Research **22**(2): 100-115.

Ayala, Y. M., S. Pantano, A. D'Ambrogio, E. Buratti, A. Brindisi, C. Marchetti, M. Romano and F. E. Baralle (2005). "Human, Drosophila, and C.elegans TDP43: nucleic acid binding properties and splicing regulatory function." J Mol Biol **348**(3): 575-588.

Ayers, J. I. and N. R. Cashman (2018). "Prion-like mechanisms in amyotrophic lateral sclerosis." Handb Clin Neurol **153**: 337-354.

Bak, T. H. (2010). "Motor neuron disease and frontotemporal dementia: One, two, or three diseases?" Annals of Indian Academy of Neurology **13**(Suppl 2): S81-S88.

Baker, J. S., M. C. McCormick and R. A. Robergs (2010). "Interaction among Skeletal Muscle Metabolic Energy Systems during Intense Exercise." Journal of Nutrition and Metabolism **2010**: 905612.

Baker, M. R. (2014). "ALS—dying forward, backward or outward?" Nature Reviews Neurology **10**(11): 660-660.

Bakermans, A. J., J. N. Bazil, A. J. Nederveen, G. J. Strijkers, S. M. Boekholdt, D. A. Beard and J. A. L. Jeneson (2017). "Human Cardiac 31P-MR Spectroscopy at 3 Tesla Cannot Detect Failing Myocardial Energy Homeostasis during Exercise." Frontiers in Physiology **8**: 939.

Bakker, L. A., C. D. Schröder, H. H. G. Tan, S. M. A. G. Vugts, R. P. A. van Eijk, M. A. van Es, J. M. A. Visser-Meily and L. H. van den Berg (2020). "Development and assessment of the inter-rater and intra-rater reproducibility of a self-administration version of the ALSFRS-R." Journal of Neurology, Neurosurgery & Psychiatry **91**(1): 75.

Baldwin, K. R., V. K. Godena, V. L. Hewitt and A. J. Whitworth (2016). "Axonal transport defects are a common phenotype in Drosophila models of ALS." Hum Mol Genet **25**(12): 2378-2392.

Balendra, R. and A. M. Isaacs (2018). "C9orf72-mediated ALS and FTD: multiple pathways to disease." Nature reviews. Neurology **14**(9): 544-558.

Barber, S. C. and P. J. Shaw (2010). "Oxidative stress in ALS: key role in motor neuron injury and therapeutic target." Free Radic Biol Med **48**(5): 629-641.

Barbiroli, B., R. Medori, H. J. Tritschler, T. Klopstock, P. Seibel, H. Reichmann, S. Iotti, R. Lodi and P. Zaniol (1995). "Lipoic (thioctic) acid increases brain energy availability and skeletal muscle performance as shown by in vivo 31P-MRS in a patient with mitochondrial cytopathy." J Neurol **242**(7): 472-477.

Barbiroli, B., P. Montagna, P. Cortelli, S. Iotti, R. Lodi, P. Barboni, L. Monari, E. Lugaresi, C. Frassineti and P. Zaniol (1995). "Defective brain and muscle energy metabolism shown by in vivo ³¹P magnetic resonance spectroscopy in nonaffected carriers of 11778 mtDNA mutation." Neurology **45**(7): 1364.

Barbiroli, B., P. Montagna, P. Martinelli, R. Lodi, S. Iotti, P. Cortelli, R. Funicello and P. Zaniol (1993). "Defective Brain Energy Metabolism Shown by in vivo 31P MR Spectroscopy in 28 Patients with Mitochondrial Cytopathies." Journal of Cerebral Blood Flow & Metabolism **13**(3): 469-474.

Barmada, S. J., G. Skibinski, E. Korb, E. J. Rao, J. Y. Wu and S. Finkbeiner (2010). "Cytoplasmic mislocalization of TDP-43 is toxic to neurons and enhanced by a mutation associated with familial amyotrophic lateral sclerosis." J Neurosci **30**(2): 639-649.

Bartlett, J. W. and C. Frost (2008). "Reliability, repeatability and reproducibility: analysis of measurement errors in continuous variables." Ultrasound Obstet Gynecol **31**(4): 466-475.

Bartolome, F., H.-C. Wu, V. S. Burchell, E. Preza, S. Wray, C. J. Mahoney, N. C. Fox, A. Calvo, A. Canosa, C. Moglia, J. Mandrioli, A. Chiò, R. W. Orrell, H. Houlden, J. Hardy, A. Y. Abramov and H. Plun-Favreau (2013). "Pathogenic VCP mutations induce mitochondrial uncoupling and reduced ATP levels." Neuron **78**(1): 57-64.

Benjamini, Y., A. M. Krieger and D. Yekutieli (2006). "Adaptive linear step-up procedures that control the false discovery rate." Biometrika **93**(3): 491-507.

Benny, R. and K. Shetty (2012). "The split hand sign." Annals of Indian Academy of Neurology **15**(3): 175-176.

Bensimon, G., L. Lacomblez and V. Meininger (1994). "A controlled trial of riluzole in amyotrophic lateral sclerosis. ALS/Riluzole Study Group." N Engl J Med **330**(9): 585-591.

Bhakoo, K. K. and D. Pearce (2000). "In vitro expression of N-acetyl aspartate by oligodendrocytes: implications for proton magnetic resonance spectroscopy signal in vivo." J Neurochem **74**(1): 254-262.

Bischoff, C., P. W. Schoenle and B. Conrad (1992). "Increased F-wave duration in patients with spasticity." Electromyogr Clin Neurophysiol **32**(9): 449-453.

Bland, J. M. and D. G. Altman (1986). "Statistical methods for assessing agreement between two methods of clinical measurement." Lancet **1**(8476): 307-310.

Bloch, F. (1946). "Nuclear Induction." Physical Review **70**(7-8): 460-474.

Bogner, W., M. Chmelik, A. I. Schmid, E. Moser, S. Trattnig and S. Gruber (2009). "Assessment of (31)P relaxation times in the human calf muscle: a comparison between 3 T and 7 T in vivo." Magnetic resonance in medicine **62**(3): 574-582.

Bojorquez, J. Z., S. Bricq, C. Acquitter, F. Brunotte, P. M. Walker and A. Lalande (2017). "What are normal relaxation times of tissues at 3 T?" Magnetic Resonance Imaging **35**: 69-80.

Borthwick, G. M., M. A. Johnson, P. G. Ince, P. J. Shaw and D. M. Turnbull (1999). "Mitochondrial enzyme activity in amyotrophic lateral sclerosis: implications for the role of mitochondria in neuronal cell death." Ann Neurol **46**(5): 787-790.

Boss, A., L. Heskamp, V. Breukels, L. J. Bains, M. J. van Uden and A. Heerschap (2018). "Oxidative capacity varies along the length of healthy human tibialis anterior." J Physiol **596**(8): 1467-1483.

Bourke, S. C., M. Tomlinson, T. L. Williams, R. E. Bullock, P. J. Shaw and G. J. Gibson (2006). "Effects of non-invasive ventilation on survival and quality of life in patients with amyotrophic lateral sclerosis: a randomised controlled trial." Lancet Neurol **5**(2): 140-147.

Bouteloup, C., J. C. Desport, P. Clavelou, N. Guy, H. Derumeaux-Burel, A. Ferrier and P. Couratier (2009). "Hypermetabolism in ALS patients: an early and persistent phenomenon." J Neurol **256**(8): 1236-1242.

Bowen, B. C., P. M. Pattany, W. G. Bradley, J. B. Murdoch, F. Rotta, A. A. Younis, R. C. Duncan and R. M. Quencer (2000). "MR imaging and localized proton spectroscopy of the precentral gyrus in amyotrophic lateral sclerosis." AJNR Am J Neuroradiol **21**(4): 647-658.

Bowling, A. C., J. B. Schulz, R. H. Brown, Jr. and M. F. Beal (1993). "Superoxide dismutase activity, oxidative damage, and mitochondrial energy metabolism in familial and sporadic amyotrophic lateral sclerosis." J Neurochem **61**(6): 2322-2325.

Braak, H., J. Brettschneider, A. C. Ludolph, V. M. Lee, J. Q. Trojanowski and K. Del Tredici (2013). Amyotrophic lateral sclerosis--a model of corticofugal axonal spread. Nat Rev Neurol. **9:** 708-714.

Bradley, W. G., B. C. Bowen, P. M. Pattany and F. Rotta (1999). "1H-magnetic resonance spectroscopy in amyotrophic lateral sclerosis." J Neurol Sci **169**(1-2): 84-86.

Brettschneider, J., K. Del Tredici, J. B. Toledo, J. L. Robinson, D. J. Irwin, M. Grossman, E. Suh, V. M. Van Deerlin, E. M. Wood, Y. Baek, L. Kwong, E. B. Lee, L. Elman, L. McCluskey, L. Fang, S. Feldengut, A. C. Ludolph, V. M. Lee, H. Braak and J. Q. Trojanowski (2013). "Stages of pTDP-43 pathology in amyotrophic lateral sclerosis." Ann Neurol **74**(1): 20-38.

Briese, M., L. Saal-Bauernschubert, P. Lüningschrör, M. Moradi, B. Dombert, V. Surrey, S. Appenzeller, C. Deng, S. Jablonka and M. Sendtner (2020). "Loss of Tdp-43 disrupts the axonal transcriptome of motoneurons accompanied by impaired axonal translation and mitochondria function." Acta Neuropathologica Communications **8**(1): 116.

Brooks, B. R., R. G. Miller, M. Swash and T. L. Munsat (2000). "El Escorial revisited: revised criteria for the diagnosis of amyotrophic lateral sclerosis." Amyotroph Lateral Scler Other Motor Neuron Disord **1**(5): 293-299.

Browne, S. E., A. C. Bowling, M. J. Baik, M. Gurney, R. H. Brown, Jr. and M. F. Beal (1998). "Metabolic dysfunction in familial, but not sporadic, amyotrophic lateral sclerosis." J Neurochem **71**(1): 281-287.

Bunton-Stasyshyn, R. K., R. A. Saccon, P. Fratta and E. M. Fisher (2015). "SOD1 Function and Its Implications for Amyotrophic Lateral Sclerosis Pathology: New and Renascent Themes." Neuroscientist **21**(5): 519-529.

Burant, C. F., S. K. Lemmon, M. K. Treutelaar and M. G. Buse (1984). "Insulin resistance of denervated rat muscle: a model for impaired receptor-function coupling." American Journal of Physiology-Endocrinology and Metabolism **247**(5): E657-E666.

Burstein, S. R., F. Valsecchi, H. Kawamata, M. Bourens, R. Zeng, A. Zuberi, T. A. Milner, S. M. Cloonan, C. Lutz, A. Barrientos and G. Manfredi (2018). "In vitro and in vivo studies of the ALS-FTLD

protein CHCHD10 reveal novel mitochondrial topology and protein interactions." Hum Mol Genet **27**(1): 160-177.

Calvo, A., R. Vasta, C. Moglia, E. Matteoni, A. Canosa, A. Mattei, C. La Mancusa, L. Focaraccio, L. Mazzini, A. Chiò, F. D'Ovidio and U. Manera (2020). "Prognostic role of slow vital capacity in amyotrophic lateral sclerosis." Journal of Neurology **267**(6): 1615-1621.

Capozzella, A., C. Sacco, A. Chighine, B. Loreti, B. Scala, T. Casale, F. Sinibaldi, G. Tomei, R. Giubilati, F. Tomei and M. V. Rosati (2014). "Work related etiology of amyotrophic lateral sclerosis (ALS): a meta-analysis." Ann Ig **26**(5): 456-472.

Cappellari, A., A. Ciammola and V. Silani (2008). "The pseudopolyneuritic form of amyotrophic lateral sclerosis (Patrikios' disease)." Electromyogr Clin Neurophysiol **48**(2): 75-81.

Carew, J. D., G. Nair, P. M. Andersen, J. Wuu, S. Gronka, X. Hu and M. Benatar (2011). "Presymptomatic spinal cord neurometabolic findings in SOD1-positive people at risk for familial ALS." Neurology **77**(14): 1370-1375.

Carew, J. D., G. Nair, N. Pineda-Alonso, S. Usher, X. Hu and M. Benatar (2011). "Magnetic resonance spectroscopy of the cervical cord in amyotrophic lateral sclerosis." Amyotroph Lateral Scler **12**(3): 185-191.

Caselli, R. J., B. E. Smith and D. Osborne (1995). "Primary lateral sclerosis: a neuropsychological study." Neurology **45**(11): 2005-2009.

Cavassila, S., S. Deval, C. Huegen, D. van Ormondt and D. Graveron-Demilly (2000). "Cramér-Rao Bound Expressions for Parametric Estimation of Overlapping Peaks: Influence of Prior Knowledge." Journal of Magnetic Resonance **143**(2): 311-320.

Cedarbaum, J. M., N. Stambler, E. Malta, C. Fuller, D. Hilt, B. Thurmond and A. Nakanishi (1999). "The ALSFRS-R: a revised ALS functional rating scale that incorporates assessments of respiratory function. BDNF ALS Study Group (Phase III)." J Neurol Sci **169**(1-2): 13-21.

Cervo, A., S. Cocozza, F. Saccà, S. M. Giorgio, V. B. Morra, E. Tedeschi, A. Marsili, G. Vacca, V. Palma, A. Brunetti and M. Quarantelli (2015). "The combined use of conventional MRI and MR spectroscopic imaging increases the diagnostic accuracy in amyotrophic lateral sclerosis." Eur J Radiol **84**(1): 151-157.

Chakraborty, G., P. Mekala, D. Yahya, G. Wu and R. W. Ledeen (2001). "Intraneuronal N-acetylaspartate supplies acetyl groups for myelin lipid synthesis: evidence for myelin-associated aspartoacylase." J Neurochem **78**(4): 736-745.

Chan, S., D. C. Shungu, A. Douglas-Akinwande, D. J. Lange and L. P. Rowland (1999). "Motor neuron diseases: comparison of single-voxel proton MR spectroscopy of the motor cortex with MR imaging of the brain." Radiology **212**(3): 763-769.

Charil, A., M. Corbo, M. Filippi, C. Kesavadas, F. Agosta, E. Munerati, A. Gambini, G. Comi, G. Scotti and A. Falini (2009). "Structural and metabolic changes in the brain of patients with upper motor neuron disorders: a multiparametric MRI study." Amyotrophic Lateral Sclerosis **10**(5-6): 269-279.

Chavhan, G. B., P. S. Babyn, B. Thomas, M. M. Shroff and E. M. Haacke (2009). "Principles, techniques, and applications of T2*-based MR imaging and its special applications." Radiographics : a review publication of the Radiological Society of North America, Inc **29**(5): 1433-1449.

Chenji, S., D. Mah, W. Johnston, R. Camicioli, N. Fisher and S. Kalra (2018). "Utility of the Addenbrooke's Cognitive Examination in Amyotrophic Lateral Sclerosis." Canadian Journal of Neurological Sciences / Journal Canadien des Sciences Neurologiques **45**(5): 527-532.

Cheong, I., M. Marjanska, D. K. Deelchand, L. E. Eberly, D. Walk and G. Oz (2017). "Ultra-High Field Proton MR Spectroscopy in Early-Stage Amyotrophic Lateral Sclerosis." Neurochem Res **42**(6): 1833-1844.

Chevin, M. and G. Sébire (2021). "Necroptosis in ALS: a hot topic in-progress." Cell Death Discovery **7**(1): 79.

Chew, J., C. Cook, T. F. Gendron, K. Jansen-West, G. del Rosso, L. M. Daughrity, M. Castanedes-Casey, A. Kurti, J. N. Stankowski, M. D. Disney, J. D. Rothstein, D. W. Dickson, J. D. Fryer, Y.-J. Zhang and L. Petrucelli (2019). "Aberrant deposition of stress granule-resident proteins linked to C9orf72-associated TDP-43 proteinopathy." Molecular Neurodegeneration **14**(1): 9.

Chiò, A., A. Calvo, L. Mazzini, R. Cantello, G. Mora, C. Moglia, L. Corrado, S. Alfonso, E. Majounie, A. Renton, F. Pisano, I. Ossola, M. Brunetti, B. J. Traynor and G. Restagno (2012). "Extensive genetics of ALS." Neurology **79**(19): 1983.

Chiò, A., L. Mazzini, S. Alfonso, L. Corrado, A. Canosa, C. Moglia, U. Manera, E. Bersano, M. Brunetti, M. Barberis, J. H. Veldink, L. H. van den Berg, N. Pearce, W. Sproviero, R. McLaughlin, A. Vajda, O. Hardiman, J. Rooney, G. Mora, A. Calvo and A. Al-Chalabi (2018). "The multistep hypothesis of ALS revisited." Neurology **91**(7): e635.

Choi, S. Y., R. Lopez-Gonzalez, G. Krishnan, H. L. Phillips, A. N. Li, W. W. Seeley, W. D. Yao, S. Almeida and F. B. Gao (2019). "C9ORF72-ALS/FTD-associated poly(GR) binds Atp5a1 and compromises mitochondrial function in vivo." Nat Neurosci **22**(6): 851-862.

Christensen, J. D., M. J. Kaufman, J. M. Levin, J. H. Mendelson, B. L. Holman, B. M. Cohen and P. F. Renshaw (1996). "Abnormal cerebral metabolism in polydrug abusers during early withdrawal: A 31P MR spectroscopy study." Magnetic Resonance in Medicine **35**(5): 658-663.

Chuang, K. S., H. L. Tzeng, S. Chen, J. Wu and T. J. Chen (2006). "Fuzzy c-means clustering with spatial information for image segmentation." Comput Med Imaging Graph **30**(1): 9-15.

Ciccarelli, O., T. E. Behrens, H. Johansen-Berg, K. Talbot, R. W. Orrell, R. S. Howard, R. G. Nunes, D. H. Miller, P. M. Matthews, A. J. Thompson and S. M. Smith (2009). "Investigation of white matter pathology in ALS and PLS using tract-based spatial statistics." Human Brain Mapping **30**(2): 615-624.

Ciccarelli, O., A. T. Toosy, N. De Stefano, C. A. Wheeler-Kingshott, D. H. Miller and A. J. Thompson (2010). "Assessing neuronal metabolism in vivo by modeling imaging measures." J Neurosci **30**(45): 15030-15033.

Cichocka, M., J. Kozub and A. Urbanik (2015). "PH Measurements of the Brain Using Phosphorus Magnetic Resonance Spectroscopy ((31)PMRS) in Healthy Men - Comparison of Two Analysis Methods." Pol J Radiol **80**: 509-514.

Conlon, E. G., L. Lu, A. Sharma, T. Yamazaki, T. Tang, N. A. Shneider and J. L. Manley (2016). "The C9ORF72 GGGGCC expansion forms RNA G-quadruplex inclusions and sequesters hnRNP H to disrupt splicing in ALS brains." Elife **5**.

Cosottini, M., I. Pesaresi, S. Piazza, S. Diciotti, G. Belmonte, M. Battaglini, A. Ginestroni, G. Siciliano, N. De Stefano and M. Mascalchi (2011). "Magnetization transfer imaging demonstrates a distributed pattern of microstructural changes of the cerebral cortex in amyotrophic lateral sclerosis." AJNR American Journal of Neuroradiology **32**(4): 704-708.

Costa, J., M. Swash and M. de Carvalho (2012). "Awaji criteria for the diagnosis of amyotrophic lateral sclerosis:a systematic review." Arch Neurol **69**(11): 1410-1416.

Crespi, C., A. Dodich, S. F. Cappa, N. Canessa, S. Iannaccone, M. Corbo, C. Lunetta, A. Falini and C. Cerami (2018). "Multimodal MRI quantification of the common neurostructural bases within the FTD-ALS continuum." Neurobiology of Aging **62**: 95-104.

Crugnola, V., C. Lamperti, V. Lucchini, D. Ronchi, L. Peverelli, A. Prelle, M. Sciacco, A. Bordoni, E. Fassone, F. Fortunato, S. Corti, V. Silani, N. Bresolin, S. Di Mauro, G. P. Comi and M. Moggio (2010). "Mitochondrial respiratory chain dysfunction in muscle from patients with amyotrophic lateral sclerosis." Arch Neurol **67**(7): 849-854.

Cwik, V. A., C. C. Hanstock, P. S. Allen and W. R. Martin (1998). "Estimation of brainstem neuronal loss in amyotrophic lateral sclerosis with in vivo proton magnetic resonance spectroscopy." Neurology **50**(1): 72-77.

Damiano, M., A. A. Starkov, S. Petri, K. Kipiani, M. Kiaei, M. Mattiazzi, M. Flint Beal and G. Manfredi (2006). "Neural mitochondrial Ca2+ capacity impairment precedes the onset of motor symptoms in G93A Cu/Zn-superoxide dismutase mutant mice." Journal of neurochemistry **96**(5): 1349-1361.

Daoud, H., P. N. Valdmanis, E. Kabashi, P. Dion, N. Dupré, W. Camu, V. Meininger and G. A. Rouleau (2009). "Contribution of TARDBP mutations to sporadic amyotrophic lateral sclerosis." Journal of Medical Genetics **46**(2): 112.

de Albuquerque, M., L. M. Branco, T. J. Rezende, H. M. de Andrade, A. Nucci and M. C. Franca, Jr. (2017). "Longitudinal evaluation of cerebral and spinal cord damage in Amyotrophic Lateral Sclerosis." Neuroimage Clin **14**: 269-276.

de Carvalho, M., R. Dengler, A. Eisen, J. D. England, R. Kaji, J. Kimura, K. Mills, H. Mitsumoto, H. Nodera, J. Shefner and M. Swash (2008). "Electrodiagnostic criteria for diagnosis of ALS." Clin Neurophysiol **119**(3): 497-503.

de Carvalho, M., R. Dengler, A. Eisen, J. D. England, R. Kaji, J. Kimura, K. Mills, H. Mitsumoto, H. Nodera, J. Shefner and M. Swash (2011). "The Awaji criteria for diagnosis of ALS." Muscle Nerve **44**(3): 456-457; author reply 457.

De Giorgio, F., C. Maduro, E. M. C. Fisher and A. Acevedo-Arozena (2019). "Transgenic and physiological mouse models give insights into different aspects of amyotrophic lateral sclerosis." Disease Models & Mechanisms **12**(1).

de Graaf, R. A. (2007). Basic Principles. In Vivo NMR Spectroscopy, John Wiley & Sons, Ltd**:** 1-42.

de Graaf, R. A. (2007). In Vivo NMR Spectroscopy – Dynamic Aspects. In Vivo NMR Spectroscopy, John Wiley & Sons, Ltd**:** 111-190.

de Graaf, R. A. (2007). In Vivo NMR Spectroscopy – Static Aspects. In Vivo NMR Spectroscopy, John Wiley & Sons, Ltd**:** 43-110.

de Graaf, R. A. (2007). Single Volume Localization and Water Suppression. In Vivo NMR Spectroscopy, John Wiley & Sons, Ltd**:** 297-348.

de Graaf, R. A. (2007). Spectral Quantification. In Vivo NMR Spectroscopy, John Wiley & Sons, Ltd**:** 445-477.

De Marco, M., A. Merico, G. Berta, N. Segato, V. Citton, A. Baglione and A. Venneri (2015). "Morphometric correlates of dysarthric deficit in amyotrophic lateral sclerosis." Amyotroph Lateral Scler Frontotemporal Degener **16**(7-8): 464-472.

De Vos, K. J. and M. Hafezparast (2017). "Neurobiology of axonal transport defects in motor neuron diseases: Opportunities for translational research?" Neurobiology of disease **105**: 283-299.

De Vos, K. J., G. M. Morotz, R. Stoica, E. L. Tudor, K. F. Lau, S. Ackerley, A. Warley, C. E. Shaw and C. C. Miller (2012). "VAPB interacts with the mitochondrial protein PTPIP51 to regulate calcium homeostasis." Hum Mol Genet **21**(6): 1299-1311.

Deelchand, D. K., I. M. Adanyeguh, U. E. Emir, T.-M. Nguyen, R. Valabregue, P.-G. Henry, F. Mochel and G. Öz (2015). "Two-site reproducibility of cerebellar and brainstem neurochemical profiles with short-echo, single-voxel MRS at 3T." Magnetic Resonance in Medicine **73**(5): 1718-1725.

DeJesus-Hernandez, M., I. R. Mackenzie, B. F. Boeve, A. L. Boxer, M. Baker, N. J. Rutherford, A. M. Nicholson, N. A. Finch, H. Flynn, J. Adamson, N. Kouri, A. Wojtas, P. Sengdy, G. Y. Hsiung, A. Karydas, W. W. Seeley, K. A. Josephs, G. Coppola, D. H. Geschwind, Z. K. Wszolek, H. Feldman, D. S. Knopman, R. C. Petersen, B. L. Miller, D. W. Dickson, K. B. Boylan, N. R. Graff-Radford and R. Rademakers (2011). "Expanded GGGGCC hexanucleotide repeat in noncoding region of C9ORF72 causes chromosome 9p-linked FTD and ALS." Neuron **72**(2): 245-256.

del Aguila, M. A., W. T. Longstreth, Jr., V. McGuire, T. D. Koepsell and G. van Belle (2003). "Prognosis in amyotrophic lateral sclerosis: a population-based study." Neurology **60**(5): 813-819.

Deng, J., P. Wang, X. Chen, H. Cheng, J. Liu, K. Fushimi, L. Zhu and J. Y. Wu (2018). "FUS interacts with ATP synthase beta subunit and induces mitochondrial unfolded protein response in cellular and animal models." Proc Natl Acad Sci U S A **115**(41): E9678-e9686.

Desport, J. C., P. M. Preux, L. Magy, Y. Boirie, J. M. Vallat, B. Beaufrere and P. Couratier (2001). "Factors correlated with hypermetabolism in patients with amyotrophic lateral sclerosis." Am J Clin Nutr **74**(3): 328-334.

Desport, J. C., F. Torny, M. Lacoste, P. M. Preux and P. Couratier (2005). "Hypermetabolism in ALS: correlations with clinical and paraclinical parameters." Neurodegener Dis **2**(3-4): 202-207.

Dietrich, O., J. G. Raya, S. B. Reeder, M. F. Reiser and S. O. Schoenberg (2007). "Measurement of signal-to-noise ratios in MR images: influence of multichannel coils, parallel imaging, and reconstruction filters." J Magn Reson Imaging **26**(2): 375-385.

Dinh, T., J. Doupis, T. E. Lyons, S. Kuchibhotla, W. Julliard, C. Gnardellis, B. I. Rosenblum, X. Wang, J. M. Giurini, R. L. Greenman and A. Veves (2009). "Foot muscle energy reserves in diabetic patients without and with clinical peripheral neuropathy." Diabetes care **32**(8): 1521-1524.

Dobrowolny, G., E. Lepore, M. Martini, L. Barberi, A. Nunn, B. M. Scicchitano and A. Musarò (2018). "Metabolic Changes Associated With Muscle Expression of SOD1(G93A)." Frontiers in physiology **9**: 831-831.

Drory, V. E., M. Birnbaum, L. Peleg, B. Goldman and A. D. Korczyn (2003). "Hexosaminidase A deficiency is an uncommon cause of a syndrome mimicking amyotrophic lateral sclerosis." Muscle & Nerve **28**(1): 109-112.

Dubois, B., A. Slachevsky, I. Litvan and B. Pillon (2000). "The FAB: a Frontal Assessment Battery at bedside." Neurology **55**(11): 1621-1626.

Dupuis, L., F. di Scala, F. Rene, M. de Tapia, H. Oudart, P. F. Pradat, V. Meininger and J. P. Loeffler (2003). "Up-regulation of mitochondrial uncoupling protein 3 reveals an early muscular metabolic defect in amyotrophic lateral sclerosis." FASEB J **17**(14): 2091-2093.

Dupuis, L., J. L. Gonzalez de Aguilar, A. Echaniz-Laguna, J. Eschbach, F. Rene, H. Oudart, B. Halter, C. Huze, L. Schaeffer, F. Bouillaud and J. P. Loeffler (2009). "Muscle mitochondrial uncoupling dismantles neuromuscular junction and triggers distal degeneration of motor neurons." PLoS One **4**(4): e5390.

Dupuis, L., P. F. Pradat, A. C. Ludolph and J. P. Loeffler (2011). "Energy metabolism in amyotrophic lateral sclerosis." Lancet Neurol **10**(1): 75-82.

Echaniz-Laguna, A., J. Zoll, E. Ponsot, B. N'Guessan, C. Tranchant, J. P. Loeffler and E. Lampert (2006). "Muscular mitochondrial function in amyotrophic lateral sclerosis is progressively altered as the disease develops: a temporal study in man." Exp Neurol **198**(1): 25-30.

Edelman, R. R., E. Dunkle, I. Koktzoglou, A. Griffin, E. J. Russell, W. Ankenbrandt, A. Ragin and A. Carrillo (2009). "Rapid whole-brain magnetic resonance imaging with isotropic resolution at 3 Tesla." Invest Radiol **44**(1): 54-59.

Efimova, A. D., R. K. Ovchinnikov, A. Y. Roman, A. V. Maltsev, V. V. Grigoriev, E. A. Kovrazhkina and V. I. Skvortsova (2017). "The FUS protein: Physiological functions and a role in amyotrophic lateral sclerosis." Molecular Biology **51**(3): 341-351.

Eisen, A. and S. Kuwabara (2012). "The split hand syndrome in amyotrophic lateral sclerosis." Journal of Neurology, Neurosurgery & Psychiatry **83**(4): 399.

Eleff, S. M., P. B. Barker, S. J. Blackband, J. C. Chatham, N. W. Lutz, D. R. Johns, R. N. Bryan and O. Hurko (1990). "Phosphorus magnetic resonance spectroscopy of patients with mitochondrial cytopathies demonstrates decreased levels of brain phosphocreatine." Annals of Neurology **27**(6): 626-630.

Ellis, C. M., A. Simmons, C. Andrews, J. M. Dawson, S. C. Williams and P. N. Leigh (1998). "A proton magnetic resonance spectroscopic study in ALS: correlation with clinical findings." Neurology **51**(4): 1104-1109.

Ellis, C. M., A. Simmons, D. K. Jones, J. Bland, J. M. Dawson, M. A. Horsfield, S. C. Williams and P. N. Leigh (1999). "Diffusion tensor MRI assesses corticospinal tract damage in ALS." Neurology **53**(5): 1051-1058.

Ellis, C. M., J. Suckling, E. Amaro, Jr., E. T. Bullmore, A. Simmons, S. C. Williams and P. N. Leigh (2001). "Volumetric analysis reveals corticospinal tract degeneration and extramotor involvement in ALS." Neurology **57**(9): 1571-1578.

Escorcio-Bezerra, M. L., A. Abrahao, I. de Castro, M. A. T. Chieia, L. A. de Azevedo, D. S. Pinheiro, N. I. de Oliveira Braga, A. S. B. de Oliveira and G. M. Manzano (2016). "MUNIX: Reproducibility and clinical correlations in Amyotrophic Lateral Sclerosis." Clinical Neurophysiology **127**(9): 2979-2984.

Escorcio-Bezerra, M. L., A. Abrahao, K. F. Nunes, N. I. De Oliveira Braga, A. S. B. Oliveira, L. Zinman and G. M. Manzano (2018). "Motor unit number index and neurophysiological index as candidate biomarkers of presymptomatic motor neuron loss in amyotrophic lateral sclerosis." Muscle Nerve **58**(2): 204-212.

Evans, M. C., Y. Couch, N. Sibson and M. R. Turner (2013). "Inflammation and neurovascular changes in amyotrophic lateral sclerosis." Mol Cell Neurosci **53**: 34-41.

Fagerberg, L., B. M. Hallström, P. Oksvold, C. Kampf, D. Djureinovic, J. Odeberg, M. Habuka, S. Tahmasebpoor, A. Danielsson, K. Edlund, A. Asplund, E. Sjöstedt, E. Lundberg, C. A. Szigyarto, M. Skogs, J. O. Takanen, H. Berling, H. Tegel, J. Mulder, P. Nilsson, J. M. Schwenk, C. Lindskog, F. Danielsson, A. Mardinoglu, A. Sivertsson, K. von Feilitzen, M. Forsberg, M. Zwahlen, I. Olsson, S. Navani, M. Huss, J. Nielsen, F. Ponten and M. Uhlén (2014). "Analysis of the human tissue-specific expression by genome-wide integration of transcriptomics and antibody-based proteomics." Mol Cell Proteomics **13**(2): 397-406.

Fahed, A. C., B. McDonough, C. M. Gouvion, K. L. Newell, L. S. Dure, M. Bebin, A. G. Bick, J. G. Seidman, D. H. Harter and C. E. Seidman (2014). "UBQLN2 mutation causing heterogeneous X-linked dominant neurodegeneration." Ann Neurol **75**(5): 793-798.

Ferraiuolo, L., A. Higginbottom, P. R. Heath, S. Barber, D. Greenald, J. Kirby and P. J. Shaw (2011). "Dysregulation of astrocyte-motoneuron cross-talk in mutant superoxide dismutase 1-related amyotrophic lateral sclerosis." Brain **134**(Pt 9): 2627-2641.

Ferreira, G. C. and P. L. Pedersen (1993). "Phosphate transport in mitochondria: past accomplishments, present problems, and future challenges." Journal of bioenergetics and biomembranes **25**(5): 483-492.

Ferri, A. and R. Coccurello (2017). "What is "Hyper" in the ALS Hypermetabolism?" Mediators of inflammation **2017**: 7821672-7821672.

Fierro, B., D. Raimondo and A. Modica (1990). "Analysis of F response in upper motoneurone lesions." Acta Neurol Scand **82**(5): 329-334.

Filippini, N., G. Douaud, C. E. Mackay, S. Knight, K. Talbot and M. R. Turner (2010). "Corpus callosum involvement is a consistent feature of amyotrophic lateral sclerosis." Neurology **75**(18): 1645-1652.

Foerster, B. R., B. C. Callaghan, M. Petrou, R. A. Edden, T. L. Chenevert and E. L. Feldman (2012). "Decreased motor cortex γ-aminobutyric acid in amyotrophic lateral sclerosis." Neurology **78**(20): 1596-1600.

Foerster, B. R., R. C. Carlos, B. A. Dwamena, B. C. Callaghan, M. Petrou, R. A. Edden, M. A. Mohamed, R. C. Welsh, P. B. Barker, E. L. Feldman and M. G. Pomper (2014). "Multimodal MRI as a diagnostic biomarker for amyotrophic lateral sclerosis." Ann Clin Transl Neurol **1**(2): 107-114.

Foerster, B. R., M. G. Pomper, B. C. Callaghan, M. Petrou, R. A. Edden, M. A. Mohamed, R. C. Welsh, R. C. Carlos, P. B. Barker and E. L. Feldman (2013). "An imbalance between excitatory and inhibitory neurotransmitters in amyotrophic lateral sclerosis revealed by use of 3-T proton magnetic resonance spectroscopy." JAMA Neurol **70**(8): 1009-1016.

Forsberg, K., P. M. Andersen, S. L. Marklund and T. Brännström (2011). "Glial nuclear aggregates of superoxide dismutase-1 are regularly present in patients with amyotrophic lateral sclerosis." Acta Neuropathol **121**(5): 623-634.

Fratta, P., S. Mizielinska, A. J. Nicoll, M. Zloh, E. M. C. Fisher, G. Parkinson and A. M. Isaacs (2012). "C9orf72 hexanucleotide repeat associated with amyotrophic lateral sclerosis and frontotemporal dementia forms RNA G-quadruplexes." Scientific Reports **2**(1): 1016.

Freibaum, B. D., Y. Lu, R. Lopez-Gonzalez, N. C. Kim, S. Almeida, K.-H. Lee, N. Badders, M. Valentine, B. L. Miller, P. C. Wong, L. Petrucelli, H. J. Kim, F.-B. Gao and J. P. Taylor (2015). "GGGGCC repeat expansion in C9orf72 compromises nucleocytoplasmic transport." Nature **525**(7567): 129-133.

Frey, D., C. Schneider, L. Xu, J. Borg, W. Spooren and P. Caroni (2000). "Early and selective loss of neuromuscular synapse subtypes with low sprouting competence in motoneuron diseases." J Neurosci **20**(7): 2534-2542.

Fujita, K., M. Yamauchi, K. Shibayama, M. Ando, M. Honda and Y. Nagata (1996). "Decreased cytochrome c oxidase activity but unchanged superoxide dismutase and glutathione peroxidase activities in the spinal cords of patients with amyotrophic lateral sclerosis." J Neurosci Res **45**(3): 276-281.

Fukai, T. and M. Ushio-Fukai (2011). "Superoxide dismutases: role in redox signaling, vascular function, and diseases." Antioxidants & redox signaling **15**(6): 1583-1606.

Funalot, B., J. C. Desport, F. Sturtz, W. Camu and P. Couratier (2009). "High metabolic level in patients with familial amyotrophic lateral sclerosis." Amyotroph Lateral Scler **10**(2): 113-117.

Furukawa, Y. and T. V. O'Halloran (2005). "Amyotrophic lateral sclerosis mutations have the greatest destabilizing effect on the apo- and reduced form of SOD1, leading to unfolding and oxidative aggregation." J Biol Chem **280**(17): 17266-17274.

Gallo, V., H. B. Bueno-De-Mesquita, R. Vermeulen, P. M. Andersen, A. Kyrozis, J. Linseisen, R. Kaaks, N. E. Allen, A. W. Roddam, H. C. Boshuizen, P. H. Peeters, D. Palli, A. Mattiello, S. Sieri, R. Tumino, J. M. Jiménez-Martín, M. J. Díaz, L. R. Suarez, A. Trichopoulou, A. Agudo, L. Arriola, A. Barricante-Gurrea, S. Bingham, K. T. Khaw, J. Manjer, B. Lindkvist, K. Overvad, F. W. Bach, A. Tjønneland, A. Olsen, M. M. Bergmann, H. Boeing, F. Clavel-Chapelon, E. Lund, G. Hallmans, L. Middleton, P. Vineis and E. Riboli (2009). "Smoking and risk for amyotrophic lateral sclerosis: analysis of the EPIC cohort." Ann Neurol **65**(4): 378-385.

Gao, J., L. Wang, T. Yan, G. Perry and X. Wang (2019). "TDP-43 proteinopathy and mitochondrial abnormalities in neurodegeneration." Mol Cell Neurosci **100**: 103396.

Garcia Santos, J. M., A. Inuggi, J. Gomez Espuch, C. Vazquez, F. Iniesta, M. Blanquer, J. Maria Moraleda and S. Martinez (2016). "Spinal cord infusion of stem cells in amyotrophic lateral sclerosis: Magnetic resonance spectroscopy shows metabolite improvement in the precentral gyrus." Cytotherapy **18**(6): 785-796.

Garg, N., S. B. Park, S. Vucic, C. Yiannikas, J. Spies, J. Howells, W. Huynh, J. M. Matamala, A. V. Krishnan, J. D. Pollard, D. R. Cornblath, M. M. Reilly and M. C. Kiernan (2017). "Differentiating lower motor neuron syndromes." Journal of Neurology, Neurosurgery & Psychiatry **88**(6): 474.

Gautier, G., A. Verschueren, A. Monnier, S. Attarian, E. Salort-Campana and J. Pouget (2010). "ALS with respiratory onset: clinical features and effects of non-invasive ventilation on the prognosis." Amyotroph Lateral Scler **11**(4): 379-382.

Geevasinga, N., C. T. Loy, P. Menon, M. de Carvalho, M. Swash, M. Schrooten, P. Van Damme, M. Gawel, M. Sonoo, M. Higashihara, Y. Noto, S. Kuwabara, M. C. Kiernan, P. Macaskill and S. Vucic (2016). "Awaji criteria improves the diagnostic sensitivity in amyotrophic lateral sclerosis: A systematic review using individual patient data." Clin Neurophysiol **127**(7): 2684-2691.

Genin, E. C., M. Plutino, S. Bannwarth, E. Villa, E. Cisneros-Barroso, M. Roy, B. Ortega-Vila, K. Fragaki, F. Lespinasse, E. Pinero-Martos, G. Auge, D. Moore, F. Burte, S. Lacas-Gervais, Y. Kageyama, K. Itoh, P. Yu-Wai-Man, H. Sesaki, J. E. Ricci, C. Vives-Bauza and V. Paquis-Flucklinger (2016). "CHCHD10 mutations promote loss of mitochondrial cristae junctions with impaired mitochondrial genome maintenance and inhibition of apoptosis." EMBO Mol Med **8**(1): 58-72.

Giavarina, D. (2015). "Understanding Bland Altman analysis." Biochemia medica **25**(2): 141-151.

Gibbons, C., F. Pagnini, T. Friede and C. A. Young (2018). "Treatment of fatigue in amyotrophic lateral sclerosis/motor neuron disease." The Cochrane database of systematic reviews **1**(1): CD011005-CD011005.

Gibbons, C. J., R. J. Mills, E. W. Thornton, J. Ealing, J. D. Mitchell, P. J. Shaw, K. Talbot, A. Tennant and C. A. Young (2011). "Development of a patient reported outcome measure for fatigue in motor neurone disease: the Neurological Fatigue Index (NFI-MND)." Health and Quality of Life Outcomes **9**(1): 101.

Gibbons, C. J., E. W. Thornton and C. A. Young (2013). "The patient experience of fatigue in motor neurone disease." Frontiers in psychology **4**: 788-788.

Gluud, C. and L. L. Gluud (2005). "Evidence based diagnostics." Bmj **330**(7493): 724-726.

Goldstein, L. H., I. C. Newsom-Davis, V. Bryant, M. Brammer, P. N. Leigh and A. Simmons (2011). "Altered patterns of cortical activation in ALS patients during attention and cognitive response inhibition tasks." Journal of Neurology **258**(12): 2186-2198.

Gonen, O. M., B. A. Moffat, P. Kwan, T. J. O'Brien, P. M. Desmond and E. Lui (2020). "Reproducibility of Glutamate, Glutathione, and GABA Measurements in vivo by Single-Voxel STEAM Magnetic Resonance Spectroscopy at 7-Tesla in Healthy Individuals." Frontiers in Neuroscience **14**: 968.

Gorges, M., P. Vercruysse, H. P. Muller, H. J. Huppertz, A. Rosenbohm, G. Nagel, P. Weydt, A. Petersen, A. C. Ludolph, J. Kassubek and L. Dupuis (2017). "Hypothalamic atrophy is related to body mass index and age at onset in amyotrophic lateral sclerosis." J Neurol Neurosurg Psychiatry **88**(12): 1033-1041.

Gosselt, I. K., T. C. W. Nijboer and M. A. Van Es (2020). "An overview of screening instruments for cognition and behavior in patients with ALS: selecting the appropriate tool for clinical practice." Amyotrophic Lateral Sclerosis and Frontotemporal Degeneration **21**(5-6): 324-336.

Govind, V., K. R. Sharma, A. A. Maudsley, K. L. Arheart, G. Saigal and S. Sheriff (2012). "Comprehensive evaluation of corticospinal tract metabolites in amyotrophic lateral sclerosis using whole-brain 1H MR spectroscopy." PLoS One **7**(4): e35607.

Govindaraju, V., K. Young and A. A. Maudsley (2000). "Proton NMR chemical shifts and coupling constants for brain metabolites." NMR Biomed **13**(3): 129-153.

Graham, J. M., N. Papadakis, J. Evans, E. Widjaja, C. A. Romanowski, M. N. Paley, L. I. Wallis, I. D. Wilkinson, P. J. Shaw and P. D. Griffiths (2004). "Diffusion tensor imaging for the assessment of upper motor neuron integrity in ALS." Neurology **63**(11): 2111-2119.

Gramegna, L. L., M. P. Giannoccaro, D. N. Manners, C. Testa, S. Zanigni, S. Evangelisti, C. Bianchini, F. Oppi, R. Poda, P. Avoni, R. Lodi, R. Liguori and C. Tonon (2018). "Mitochondrial dysfunction in myotonic dystrophy type 1." Neuromuscul Disord **28**(2): 144-149.

Gredal, O., S. Rosenbaum, S. Topp, M. Karlsborg, P. Strange and L. Werdelin (1997). "Quantification of brain metabolites in amyotrophic lateral sclerosis by localized proton magnetic resonance spectroscopy." Neurology **48**(4): 878-881.

Grehl, T., S. Fischer, K. Muller, J. P. Malin and J. Zange (2007). "A prospective study to evaluate the impact of 31P-MRS to determinate mitochondrial dysfunction in skeletal muscle of ALS patients." Amyotroph Lateral Scler **8**(1): 4-8.

Grolez, G., M. Kyheng, R. Lopes, C. Moreau, K. Timmerman, F. Auger, G. Kuchcinski, A. Duhamel, P. Jissendi-Tchofo, P. Besson, C. Laloux, M. Petrault, J. C. Devedjian, T. Pérez, P. F. Pradat, L. Defebvre, R. Bordet, V. Danel-Brunaud and D. Devos (2018). "MRI of the cervical spinal cord predicts respiratory dysfunction in ALS." Scientific Reports **8**: 1828.

Grosskreutz, J., J. Kaufmann, J. Fradrich, R. Dengler, H. J. Heinze and T. Peschel (2006). "Widespread sensorimotor and frontal cortical atrophy in Amyotrophic Lateral Sclerosis." BMC Neurol **6**: 17.

Gunes, T., N. G. Sirin, S. Sahin, E. Kose and B. Isak (2021). "Use of CMAP, MScan fit-MUNE, and MUNIX in understanding neurodegeneration pattern of ALS and detection of early motor neuron loss in daily practice." Neuroscience Letters **741**: 135488.

Gupta, R. D., R. Ramachandran, P. Venkatesan, S. Anoop, M. Joseph and N. Thomas (2017). "Indirect Calorimetry: From Bench to Bedside." Indian journal of endocrinology and metabolism **21**(4): 594-599.

Gurney Mark, E., H. Pu, Y. Chiu Arlene, C. Dal Canto Mauro, Y. Polchow Cynthia, D. Alexander Denise, J. Caliendo, A. Hentati, W. Kwon Young, H.-X. Deng, W. Chen, P. Zhai, L. Sufit Robert and T. Siddique (1994). "Motor Neuron Degeneration in Mice that Express a Human Cu,Zn Superoxide Dismutase Mutation." Science **264**(5166): 1772-1775.

Hall, C. E., Z. Yao, M. Choi, G. E. Tyzack, A. Serio, R. Luisier, J. Harley, E. Preza, C. Arber, S. J. Crisp, P. M. D. Watson, D. M. Kullmann, A. Y. Abramov, S. Wray, R. Burley, S. H. Y. Loh, L. M. Martins, M. M. Stevens, N. M. Luscombe, C. R. Sibley, A. Lakatos, J. Ule, S. Gandhi and R. Patani (2017). "Progressive Motor Neuron Pathology and the Role of Astrocytes in a Human Stem Cell Model of VCP-Related ALS." Cell Rep **19**(9): 1739-1749.

Hamakawa, H., J. U. N. Murashita, N. Yamada, T. Inubushi, N. Kato and T. Kato (2004). "Reduced intracellular pH in the basal ganglia and whole brain measured by 31P-MRS in bipolar disorder." Psychiatry and Clinical Neurosciences **58**(1): 82-88.

Han, J. and L. Ma (2010). "Study of the features of proton MR spectroscopy ((1)H-MRS) on amyotrophic lateral sclerosis." J Magn Reson Imaging **31**(2): 305-308.

Hanstock, C. C., V. A. Cwik and W. R. Martin (2002). "Reduction in metabolite transverse relaxation times in amyotrophic lateral sclerosis." J Neurol Sci **198**(1-2): 37-41.

Hardiman, O. and L. H. van den Berg (2017). "Edaravone: a new treatment for ALS on the horizon?" Lancet Neurol **16**(7): 490-491.

Harris, A. D., B. Glaubitz, J. Near, C. John Evans, N. A. J. Puts, T. Schmidt-Wilcke, M. Tegenthoff, P. B. Barker and R. A. E. Edden (2014). "Impact of frequency drift on gamma-aminobutyric acid-edited MR spectroscopy." Magnetic resonance in medicine **72**(4): 941-948.

Harwood, C. A., K. Westgate, S. Gunstone, S. Brage, N. J. Wareham, C. J. McDermott and P. J. Shaw (2016). "Long-term physical activity: an exogenous risk factor for sporadic amyotrophic lateral sclerosis?" Amyotrophic Lateral Sclerosis and Frontotemporal Degeneration **17**(5-6): 377-384.

Hattingen, E., J. Magerkurth, U. Pilatus, A. Mozer, C. Seifried, H. Steinmetz, F. Zanella and R. Hilker (2009). "Phosphorus and proton magnetic resonance spectroscopy demonstrates mitochondrial dysfunction in early and advanced Parkinson's disease." Brain **132**(Pt 12): 3285-3297.

Hecht, M. J., F. Fellner, C. Fellner, M. J. Hilz, D. Heuss and B. Neundorfer (2001). "MRI-FLAIR images of the head show corticospinal tract alterations in ALS patients more frequently than T2-, T1- and proton-density-weighted images." Journal of the Neurological Sciences **186**(1-2): 37-44.

Hegedus, J., C. T. Putman and T. Gordon (2007). "Time course of preferential motor unit loss in the SOD1 G93A mouse model of amyotrophic lateral sclerosis." Neurobiol Dis **28**(2): 154-164.

Hirayama, K., M. Tomonaga, K. Kitano, T. Yamada, S. Kojima and K. Arai (1987). "Focal cervical poliopathy causing juvenile muscular atrophy of distal upper extremity: a pathological study." Journal of Neurology, Neurosurgery & Psychiatry **50**(3): 285.

Hoang, T. Q., S. Bluml, D. J. Dubowitz, R. Moats, O. Kopyov, D. Jacques and B. D. Ross (1998). "Quantitative proton-decoupled 31P MRS and 1H MRS in the evaluation of Huntington's and Parkinson's diseases." Neurology **50**(4): 1033-1040.

Hobson, E. V. and C. J. McDermott (2016). "Supportive and symptomatic management of amyotrophic lateral sclerosis." Nat Rev Neurol **12**(9): 526-538.

Hodgins, F., S. Mulhern and S. Abrahams (2020). "The clinical impact of the Edinburgh Cognitive and Behavioural ALS Screen (ECAS) and neuropsychological intervention in routine ALS care." Amyotroph Lateral Scler Frontotemporal Degener **21**(1-2): 92-99.

Holm, T., A. Maier, P. Wicks, D. Lang, P. Linke, C. Münch, L. Steinfurth, R. Meyer and T. Meyer (2013). "Severe loss of appetite in amyotrophic lateral sclerosis patients: online self-assessment study." Interactive journal of medical research **2**(1): e8-e8.

Hooijmans, M. T., N. Doorenweerd, C. Baligand, J. J. G. M. Verschuuren, I. Ronen, E. H. Niks, A. G. Webb and H. E. Kan (2017). "Spatially localized phosphorous metabolism of skeletal muscle in Duchenne muscular dystrophy patients: 24–month follow-up." PLOS ONE **12**(8): e0182086.

Hooijmans, M. T., E. H. Niks, J. Burakiewicz, J. J. G. M. Verschuuren, A. G. Webb and H. E. Kan (2017). "Elevated phosphodiester and T(2) levels can be measured in the absence of fat infiltration in Duchenne muscular dystrophy patients." NMR in biomedicine **30**(1): 10.1002/nbm.3667.

Hoshino, Y., K. Yoshikawa, Y. Inoue, S. Asai, T. Nakamura, T. Ogino, M. Umeda and A. Iwamoto (1999). "Reproducibility of short echo time proton magnetic resonance spectroscopy using point-resolved spatially localized spectroscopy sequence in normal human brains." Radiation medicine **17**(2): 115-120.

Hu, M. T., C. M. Ellis, A. Al-Chalabi, P. N. Leigh and C. E. Shaw (1998). "Flail arm syndrome: a distinctive variant of amyotrophic lateral sclerosis." J Neurol Neurosurg Psychiatry **65**(6): 950-951.

Hu, M. T. M., S. D. Taylor-Robinson, K. R. Chaudhuri, J. D. Bell, C. Labbé, V. J. Cunningham, M. J. Koepp, A. Hammers, R. G. Morris, N. Turjanski and D. J. Brooks (2000). "Cortical dysfunction in non-demented Parkinson's disease patients: A combined 31P-MRS and 18FDG-PET study." Brain **123**(2): 340-352.

Huai, J. and Z. Zhang (2019). "Structural Properties and Interaction Partners of Familial ALS-Associated SOD1 Mutants." Frontiers in Neurology **10**: 527.

Ignjatovic, A., Z. Stevic, S. Lavrnic, M. Dakovic and G. Bacic (2013). "Brain iron MRI: a biomarker for amyotrophic lateral sclerosis." Journal of Magnetic Resonance Imaging **38**(6): 1472-1479.

Ikeda, K., K. Murata, Y. Kawase, K. Kawabe, O. Kano, Y. Yoshii, T. Takazawa, T. Hirayama and Y. Iwasaki (2013). "Relationship between cervical cord 1H-magnetic resonance spectroscopy and clinoco-electromyographic profile in amyotrophic lateral sclerosis." Muscle Nerve **47**(1): 61-67.

Inam, S., S. Vucic, N. E. Brodaty, M. C. Zoing and M. C. Kiernan (2010). "The 10-metre gait speed as a functional biomarker in amyotrophic lateral sclerosis." Amyotroph Lateral Scler **11**(6): 558-561.

Ince, P. G., J. Evans, M. Knopp, G. Forster, H. H. Hamdalla, S. B. Wharton and P. J. Shaw (2003). "Corticospinal tract degeneration in the progressive muscular atrophy variant of ALS." Neurology **60**(8): 1252-1258.

Iotti, S., C. Frassineti, L. Alderighi, A. Sabatini, A. Vacca and B. Barbiroli (1996). "In vivo assessment of free magnesium concentration in human brain by 31P MRS. A new calibration curve based on a mathematical algorithm." NMR Biomed **9**(1): 24-32.

Iotti, S., C. Frassineti, L. Alderighi, A. Sabatini, A. Vacca and B. Barbiroli (2000). "In vivo 31P-MRS assessment of cytosolic [Mg2+] in the human skeletal muscle in different metabolic conditions." Magnetic Resonance Imaging **18**(5): 607-614.

Iotti, S., C. Frassineti, L. Alderighi, A. Sabatini, A. Vacca and B. Barbiroli (2000). "In vivo (31)P-MRS assessment of cytosolic [Mg(2+)] in the human skeletal muscle in different metabolic conditions." Magnetic resonance imaging **18**(5): 607-614.

Iotti, S., C. Frassineti, A. Sabatini, A. Vacca and B. Barbiroli (2005). "Quantitative mathematical expressions for accurate in vivo assessment of cytosolic [ADP] and ΔG of ATP hydrolysis in the human brain and skeletal muscle." Biochimica et Biophysica Acta (BBA) - Bioenergetics **1708**(2): 164-177.

Iotti, S. and E. Malucelli (2008). "In vivo assessment of Mg2+ in human brain and skeletal muscle by 31P-MRS." Magnes Res **21**(3): 157-162.

Isaacs, J. D., A. F. Dean, C. E. Shaw, A. Al-Chalabi, K. R. Mills and P. N. Leigh (2007). "Amyotrophic lateral sclerosis with sensory neuropathy: part of a multisystem disorder?" Journal of neurology, neurosurgery, and psychiatry **78**(7): 750-753.

Ishigaki, S. and G. Sobue (2018). "Importance of Functional Loss of FUS in FTLD/ALS." Frontiers in molecular biosciences **5**: 44-44.

Jang, D.-P., J.-M. Lee, E. Lee, S. Park, J.-J. Kim, K. Namkoong, K.-J. Yoon, I.-Y. Kim and S. I. Kim (2005). "Interindividual reproducibility of glutamate quantification using 1.5-T proton magnetic resonance spectroscopy." Magnetic Resonance in Medicine **53**(3): 708-712.

Jani, M. P. and G. B. Gore (2016). "Swallowing characteristics in Amyotrophic Lateral Sclerosis." NeuroRehabilitation **39**: 273-276.

Janse van Mantgem, M. R., R. P. A. van Eijk, H. K. van der Burgh, H. H. G. Tan, H.-J. Westeneng, M. A. van Es, J. H. Veldink and L. H. van den Berg (2020). "Prognostic value of weight loss in patients with amyotrophic lateral sclerosis: a population-based study." Journal of Neurology, Neurosurgery & Psychiatry **91**(8): 867.

Jellinger, K. A. (2009). "Cerebrospinal Fluid in Clinical Practice." European Journal of Neurology **16**(5): e109-e109.

Jeneson, J. A., H. V. Westerhoff, T. R. Brown, C. J. Van Echteld and R. Berger (1995). "Quasi-linear relationship between Gibbs free energy of ATP hydrolysis and power output in human forearm muscle." American Journal of Physiology-Cell Physiology **268**(6): C1474-C1484.

Jenkins, T. M., J. J. P. Alix, C. David, E. Pearson, D. G. Rao, N. Hoggard, E. O'Brien, K. Baster, M. Bradburn, J. Bigley, C. J. McDermott, I. D. Wilkinson and P. J. Shaw (2018). "Imaging muscle as a potential biomarker of denervation in motor neuron disease." J Neurol Neurosurg Psychiatry **89**(3): 248-255.

Jenkins, T. M., J. J. P. Alix, J. Fingret, T. Esmail, N. Hoggard, K. Baster, C. J. McDermott, I. D. Wilkinson and P. J. Shaw (2020). "Longitudinal multi-modal muscle-based biomarker assessment in motor neuron disease." J Neurol **267**(1): 244-256.

Jones, A. P., W. J. Gunawardena, C. M. Coutinho, J. A. Gatt, I. C. Shaw and J. D. Mitchell (1995). "Preliminary results of proton magnetic resonance spectroscopy in motor neurone disease (amytrophic lateral sclerosis)." J Neurol Sci **129 Suppl**: 85-89.

Julian, T. H., N. Glascow, A. D. F. Barry, T. Moll, C. Harvey, Y. C. Klimentidis, M. Newell, S. Zhang, M. P. Snyder, J. Cooper-Knock and P. J. Shaw (2021). "Physical exercise is a risk factor for amyotrophic lateral sclerosis: Convergent evidence from Mendelian randomisation, transcriptomics and risk genotypes." EBioMedicine **68**.

Kabashi, E., L. Lin, M. L. Tradewell, P. A. Dion, V. Bercier, P. Bourgouin, D. Rochefort, S. Bel Hadj, H. D. Durham, C. Vande Velde, G. A. Rouleau and P. Drapeau (2010). "Gain and loss of function of ALS-related mutations of TARDBP (TDP-43) cause motor deficits in vivo." Hum Mol Genet **19**(4): 671-683.

Kalra, S. (2019). "Magnetic Resonance Spectroscopy in ALS." Frontiers in Neurology **10**: 482.

Kalra, S., N. R. Cashman, Z. Caramanos, A. Genge and D. L. Arnold (2003). "Gabapentin therapy for amyotrophic lateral sclerosis: lack of improvement in neuronal integrity shown by MR spectroscopy." AJNR Am J Neuroradiol **24**(3): 476-480.

Kalra, S., N. R. Cashman, A. Genge and D. L. Arnold (1998). "Recovery of N-acetylaspartate in corticomotor neurons of patients with ALS after riluzole therapy." Neuroreport **9**(8): 1757-1761.

Kalra, S., P. Tai, A. Genge and D. L. Arnold (2006). "Rapid improvement in cortical neuronal integrity in amyotrophic lateral sclerosis detected by proton magnetic resonance spectroscopic imaging." J Neurol **253**(8): 1060-1063.

Kassubek, J., A. Unrath, H. J. Huppertz, D. Lule, T. Ethofer, A. D. Sperfeld and A. C. Ludolph (2005). "Global brain atrophy and corticospinal tract alterations in ALS, as investigated by voxel-based morphometry of 3-D MRI." Amyotroph Lateral Scler Other Motor Neuron Disord **6**(4): 213-220.

Kato, T., T. Inubushi and N. Kato (2000). "Prediction of lithium response by 31P-MRS in bipolar disorder." International Journal of Neuropsychopharmacology **3**(1): 83-85.

Kato, T., T. Shioiri, J. Murashita, H. Hamakawa, Y. Takahashi, T. Inubushi and S. Takahashi (1995). "Lateralized abnormality of high energy phosphate metabolism in the frontal lobes of patients with bipolar disorder detected by phase-encoded 31P-MRS." Psychological Medicine **25**(3): 557-566.

Kato, Y., K. Matsumura, Y. Kinosada, Y. Narita, S. Kuzuhara and T. Nakagawa (1997). "Detection of pyramidal tract lesions in amyotrophic lateral sclerosis with magnetization-transfer measurements." AJNR American Journal of Neuroradiology **18**(8): 1541-1547.

Kaufmann, P., S. L. Pullman, D. C. Shungu, S. Chan, A. P. Hays, M. L. Del Bene, M. A. Dover, M. Vukic, L. P. Rowland and H. Mitsumoto (2004). "Objective tests for upper motor neuron involvement in amyotrophic lateral sclerosis (ALS)." Neurology **62**(10): 1753-1757.

Keeler, J. (2010). Understanding NMR Spectroscopy, Wiley.

Kemp, G. J., R. E. Ahmad, K. Nicolay and J. J. Prompers (2015). "Quantification of skeletal muscle mitochondrial function by 31P magnetic resonance spectroscopy techniques: a quantitative review." Acta Physiologica **213**(1): 107-144.

Kemp, G. J., M. Meyerspeer and E. Moser (2007). "Absolute quantification of phosphorus metabolite concentrations in human muscle in vivo by 31P MRS: a quantitative review." NMR in biomedicine **20**(6): 555-565.

Kent-Braun, J. A. and R. G. Miller (2000). "Central fatigue during isometric exercise in amyotrophic lateral sclerosis." Muscle Nerve **23**(6): 909-914.

Khiat, A., M. D'Amour, F. Souchon and Y. Boulanger (2010). "MRS study of the effects of minocycline on markers of neuronal and microglial integrity in ALS." Magn Reson Imaging **28**(10): 1456-1460.

Kim, W. K., X. Liu, J. Sandner, M. Pasmantier, J. Andrews, L. P. Rowland and H. Mitsumoto (2009). "Study of 962 patients indicates progressive muscular atrophy is a form of ALS." Neurology **73**(20): 1686-1692.

King, A. E., A. Woodhouse, M. T. Kirkcaldie and J. C. Vickers (2016). "Excitotoxicity in ALS: Overstimulation, or overreaction?" Exp Neurol **275 Pt 1**: 162-171.

Kirkinezos, I. G., S. R. Bacman, D. Hernandez, J. Oca-Cossio, L. J. Arias, M. A. Perez-Pinzon, W. G. Bradley and C. T. Moraes (2005). "Cytochrome c association with the inner mitochondrial membrane is impaired in the CNS of G93A-SOD1 mice." The Journal of neuroscience : the official journal of the Society for Neuroscience **25**(1): 164-172.

Klunk, W. E., C.-J. Xu, K. Panchalingam, R. J. McClure and J. W. Pettegrew (1994). "Analysis of magnetic resonance spectra by mole percent: Comparison to absolute units." Neurobiology of Aging **15**(1): 133-140.

Ko, Y. H., S. Hong and P. L. Pedersen (1999). "Chemical mechanism of ATP synthase. Magnesium plays a pivotal role in formation of the transition state where ATP is synthesized from ADP and inorganic phosphate." The Journal of biological chemistry **274**(41): 28853-28856.

Kollewe, K., T. F. Munte, A. Samii, R. Dengler, S. Petri and B. Mohammadi (2011). "Patterns of cortical activity differ in ALS patients with limb and/or bulbar involvement depending on motor tasks." Journal of Neurology **258**(5): 804-810.

Konrad, C., H. Henningsen, J. Bremer, B. Mock, M. Deppe, C. Buchinger, P. Turski, S. Knecht and B. Brooks (2002). "Pattern of cortical reorganization in amyotrophic lateral sclerosis: a functional magnetic resonance imaging study." Experimental Brain Research **143**(1): 51-56.

Konrad, C., A. Jansen, H. Henningsen, J. Sommer, P. A. Turski, B. R. Brooks and S. Knecht (2006). "Subcortical reorganization in amyotrophic lateral sclerosis." Experimental Brain Research **172**(3): 361-369.

Koo, T. K. and M. Y. Li (2016). "A Guideline of Selecting and Reporting Intraclass Correlation Coefficients for Reliability Research." Journal of chiropractic medicine **15**(2): 155-163.

Kovanda, A., M. Zalar, P. Šket, J. Plavec and B. Rogelj (2015). "Anti-sense DNA d(GGCCCC)n expansions in C9ORF72 form i-motifs and protonated hairpins." Scientific Reports **5**(1): 17944.

Kowaltowski, A. J. and A. E. Vercesi (1999). "Mitochondrial damage induced by conditions of oxidative stress." Free Radical Biology and Medicine **26**(3): 463-471.

Krasnianski, A., M. Deschauer, S. Neudecker, F. N. Gellerich, T. Muller, B. G. Schoser, M. Krasnianski and S. Zierz (2005). "Mitochondrial changes in skeletal muscle in amyotrophic lateral sclerosis and other neurogenic atrophies." Brain **128**(Pt 8): 1870-1876.

Kreis, R. (2004). "Issues of spectral quality in clinical 1H-magnetic resonance spectroscopy and a gallery of artifacts." NMR Biomed **17**(6): 361-381.

Kreis, R. (2016). "The trouble with quality filtering based on relative Cramér-Rao lower bounds." Magn Reson Med **75**(1): 15-18.

Kwiatkowski, T. J., Jr., D. A. Bosco, A. L. Leclerc, E. Tamrazian, C. R. Vanderburg, C. Russ, A. Davis, J. Gilchrist, E. J. Kasarskis, T. Munsat, P. Valdmanis, G. A. Rouleau, B. A. Hosler, P. Cortelli, P. J. de Jong, Y. Yoshinaga, J. L. Haines, M. A. Pericak-Vance, J. Yan, N. Ticozzi, T. Siddique, D. McKenna-Yasek, P. C. Sapp, H. R. Horvitz, J. E. Landers and R. H. Brown, Jr. (2009). "Mutations in the FUS/TLS gene on chromosome 16 cause familial amyotrophic lateral sclerosis." Science **323**(5918): 1205-1208.

Kwon, I., S. Xiang, M. Kato, L. Wu, P. Theodoropoulos, T. Wang, J. Kim, J. Yun, Y. Xie and S. L. McKnight (2014). "Poly-dipeptides encoded by the C9orf72 repeats bind nucleoli, impede RNA biogenesis, and kill cells." Science **345**(6201): 1139-1145.

Lacomblez, L., G. Bensimon, P. N. Leigh, P. Guillet and V. Meininger (1996). "Dose-ranging study of riluzole in amyotrophic lateral sclerosis. Amyotrophic Lateral Sclerosis/Riluzole Study Group II." Lancet **347**(9013): 1425-1431.

Lacorte, E., L. Ferrigno, E. Leoncini, M. Corbo, S. Boccia and N. Vanacore (2016). "Physical activity, and physical activity related to sports, leisure and occupational activity as risk factors for ALS: A systematic review." Neurosci Biobehav Rev **66**: 61-79.

Lattante, S., G. A. Rouleau and E. Kabashi (2013). "TARDBP and FUS mutations associated with amyotrophic lateral sclerosis: summary and update." Hum Mutat **34**(6): 812-826.

Layec, G., A. Bringard, Y. Le Fur, C. Vilmen, J.-P. Micallef, S. Perrey, P. J. Cozzone and D. Bendahan (2009). "Reproducibility assessment of metabolic variables characterizing muscle energetics in Vivo: A 31P-MRS study." Magnetic Resonance in Medicine **62**(4): 840-854.

Lee, I., M. Kazamel, T. McPherson, J. McAdam, M. Bamman, A. Amara, D. L. Smith, Jr. and P. H. King (2021). "Fat mass loss correlates with faster disease progression in amyotrophic lateral sclerosis patients: Exploring the utility of dual-energy x-ray absorptiometry in a prospective study." PLoS One **16**(5): e0251087.

Lehmer, C., M. H. Schludi, L. Ransom, J. Greiling, M. Junghanel, N. Exner, H. Riemenschneider, J. van der Zee, C. Van Broeckhoven, P. Weydt, M. T. Heneka and D. Edbauer (2018). "A novel CHCHD10 mutation implicates a Mia40-dependent mitochondrial import deficit in ALS." EMBO Mol Med **10**(6).

Leyton, C. E. and J. R. Hodges (2010). "Frontotemporal dementias: Recent advances and current controversies." Annals of Indian Academy of Neurology **13**(Suppl 2): S74-S80.

Liewluck, T. and D. S. Saperstein (2015). "Progressive Muscular Atrophy." Neurologic Clinics **33**(4): 761-773.

Lillo, P., E. Mioshi, M. C. Zoing, M. C. Kiernan and J. R. Hodges (2011). "How common are behavioural changes in amyotrophic lateral sclerosis?" Amyotrophic Lateral Sclerosis **12**(1): 45-51.

Lin, J. Z. and M. K. Floeter (2004). "Do F-wave measurements detect changes in motor neuron excitability?" Muscle Nerve **30**(3): 289-294.

Liu, C., R. Jiang, X. Yi, W. Zhu and B. Bu (2015). "Role of diffusion tensor imaging or magnetic resonance spectroscopy in the diagnosis and disability assessment of amyotrophic lateral sclerosis." J Neurol Sci **348**(1-2): 206-210.

Lodi, R., P. Montagna, S. Iotti, P. Zaniol, P. Barboni, P. Puddu and B. Barbiroli (1994). "Brain and muscle energy metabolism studied in vivo by 31P-magnetic resonance spectroscopy in NARP syndrome." J Neurol Neurosurg Psychiatry **57**(12): 1492-1496.

Logroscino, G., B. J. Traynor, O. Hardiman, A. Chio, D. Mitchell, R. J. Swingler, A. Millul, E. Benn and E. Beghi (2010). "Incidence of amyotrophic lateral sclerosis in Europe." J Neurol Neurosurg Psychiatry **81**(4): 385-390.

Lopez-Gonzalez, R., Y. Lu, T. F. Gendron, A. Karydas, H. Tran, D. Yang, L. Petrucelli, B. L. Miller, S. Almeida and F. B. Gao (2016). "Poly(GR) in C9ORF72-Related ALS/FTD Compromises Mitochondrial Function and Increases Oxidative Stress and DNA Damage in iPSC-Derived Motor Neurons." Neuron **92**(2): 383-391.

Lou, J. S., A. Reeves, T. Benice and G. Sexton (2003). "Fatigue and depression are associated with poor quality of life in ALS." Neurology **60**(1): 122-123.

Lu, M., X. H. Zhu and W. Chen (2016). "In vivo (31) P MRS assessment of intracellular NAD metabolites and NAD(+) /NADH redox state in human brain at 4 T." NMR Biomed **29**(7): 1010-1017.

Lu, Z. H., G. Chakraborty, R. W. Ledeen, D. Yahya and G. Wu (2004). "N-Acetylaspartate synthase is bimodally expressed in microsomes and mitochondria of brain." Brain Res Mol Brain Res **122**(1): 71-78.

Ludtmann, M. H. R., C. Arber, F. Bartolome, M. de Vicente, E. Preza, E. Carro, H. Houlden, S. Gandhi, S. Wray and A. Y. Abramov (2017). "Mutations in valosin-containing protein (VCP) decrease ADP/ATP translocation across the mitochondrial membrane and impair energy metabolism in human neurons." J Biol Chem **292**(21): 8907-8917.

Lule, D., V. Diekmann, S. Anders, J. Kassubek, A. Kubler, A. C. Ludolph and N. Birbaumer (2007). "Brain responses to emotional stimuli in patients with amyotrophic lateral sclerosis (ALS)." J Neurol **254**(4): 519-527.

Lule, D., V. Diekmann, H. P. Muller, J. Kassubek, A. C. Ludolph and N. Birbaumer (2010). "Neuroimaging of multimodal sensory stimulation in amyotrophic lateral sclerosis." J Neurol Neurosurg Psychiatry **81**(8): 899-906.

Luo, G., J. Yi, C. Ma, Y. Xiao, F. Yi, T. Yu and J. Zhou (2013). "Defective mitochondrial dynamics is an early event in skeletal muscle of an amyotrophic lateral sclerosis mouse model." PloS one **8**(12): e82112-e82112.

Mackenzie, I. R. and H. Feldman (2004). "Neurofilament inclusion body disease with early onset frontotemporal dementia and primary lateral sclerosis." Clin Neuropathol **23**(4): 183-193.

Madhavarao, C. N., J. R. Moffett, R. A. Moore, R. E. Viola, M. A. Namboodiri and D. M. Jacobowitz (2004). "Immunohistochemical localization of aspartoacylase in the rat central nervous system." J Comp Neurol **472**(3): 318-329.

Mahoney, D. J., J. J. Kaczor, J. Bourgeois, N. Yasuda and M. A. Tarnopolsky (2006). "Oxidative stress and antioxidant enzyme upregulation in SOD1-G93A mouse skeletal muscle." Muscle & Nerve **33**(6): 809-816.

Majumder, V., J. M. Gregory, M. A. Barria, A. Green and S. Pal (2018). "TDP-43 as a potential biomarker for amyotrophic lateral sclerosis: a systematic review and meta-analysis." BMC Neurology **18**(1): 90.

Mann, D. M. A., S. Rollinson, A. Robinson, J. Bennion Callister, J. C. Thompson, J. S. Snowden, T. Gendron, L. Petrucelli, M. Masuda-Suzukake, M. Hasegawa, Y. Davidson and S. Pickering-Brown (2013). "Dipeptide repeat proteins are present in the p62 positive inclusions in patients with frontotemporal lobar degeneration and motor neurone disease associated with expansions in C9ORF72." Acta neuropathologica communications **1**: 68-68.

Manno, C., A. Lipari, V. Bono, A. C. Taiello and V. La Bella (2013). "Sporadic Parkinson disease and Amyotrophic Lateral Sclerosis complex (Brait–Fahn–Schwartz Disease)." Journal of the Neurological Sciences **326**(1): 104-106.

Marin, B., J. C. Desport, P. Kajeu, P. Jesus, B. Nicolaud, M. Nicol, P. M. Preux and P. Couratier (2011). "Alteration of nutritional status at diagnosis is a prognostic factor for survival of amyotrophic lateral sclerosis patients." J Neurol Neurosurg Psychiatry **82**(6): 628-634.

Martin, L. J. (1999). "Neuronal death in amyotrophic lateral sclerosis is apoptosis: possible contribution of a programmed cell death mechanism." J Neuropathol Exp Neurol **58**(5): 459-471.

Mathis, S., C. Goizet, A. Soulages, J.-M. Vallat and G. L. Masson (2019). "Genetics of amyotrophic lateral sclerosis: A review." Journal of the Neurological Sciences **399**: 217-226.

Mathuranath, P. S., P. J. Nestor, G. E. Berrios, W. Rakowicz and J. R. Hodges (2000). "A brief cognitive test battery to differentiate Alzheimer's disease and frontotemporal dementia." Neurology **55**(11): 1613-1620.

Maton, B., A. Londono, S. Sawrie, R. Knowlton, J. DenHollander and R. Kuzniecky (2001). "Reproducibility of Proton Magnetic Resonance Spectroscopy Imaging Measurements of Normal Human Hippocampus at 1.5 T: Clinical Implications." Journal of Neuroimaging **11**(2): 194-201.

Mattiazzi, M., M. D'Aurelio, C. D. Gajewski, K. Martushova, M. Kiaei, M. F. Beal and G. Manfredi (2002). "Mutated human SOD1 causes dysfunction of oxidative phosphorylation in mitochondria of transgenic mice." The Journal of biological chemistry **277**(33): 29626-29633.

McDermott, C. J. and P. J. Shaw (2008). "Diagnosis and management of motor neurone disease." BMJ **336**(7645): 658-662.

McEachin, Z. T., J. Parameswaran, N. Raj, G. J. Bassell and J. Jiang (2020). "RNA-mediated toxicity in C9orf72 ALS and FTD." Neurobiology of Disease **145**: 105055.

Menon, P., N. Geevasinga, C. Yiannikas, J. Howells, M. C. Kiernan and S. Vucic (2015). "Sensitivity and specificity of threshold tracking transcranial magnetic stimulation for diagnosis of amyotrophic lateral sclerosis: a prospective study." Lancet Neurol **14**(5): 478-484.

Mesrati, F. and M. F. Vecchierini (2004). "F-waves: neurophysiology and clinical value." Neurophysiologie Clinique/Clinical Neurophysiology **34**(5): 217-243.

Meyerspeer, M., C. Boesch, D. Cameron, M. Dezortová, S. C. Forbes, A. Heerschap, J. A. L. Jeneson, H. E. Kan, J. Kent, G. Layec, J. J. Prompers, H. Reyngoudt, A. Sleigh, L. Valkovič, G. J. Kemp and P. M. R. S. o. S. M. Experts' Working Group on (2020). "(31) P magnetic resonance spectroscopy in skeletal muscle: Experts' consensus recommendations." NMR in biomedicine: e4246-e4246.

Meyerspeer, M., M. Krššák and E. Moser (2003). "Relaxation times of 31P-metabolites in human calf muscle at 3 T." Magnetic Resonance in Medicine **49**(4): 620-625.

Meyerspeer, M., A. W. Magill, A. Kuehne, R. Gruetter, E. Moser and A. I. Schmid (2016). "Simultaneous and interleaved acquisition of NMR signals from different nuclei with a clinical MRI scanner." Magnetic resonance in medicine **76**(5): 1636-1641.

Mezzapesa, D. M., A. Ceccarelli, F. Dicuonzo, A. Carella, M. F. De Caro, M. Lopez, V. Samarelli, P. Livrea and I. L. Simone (2007). "Whole-brain and regional brain atrophy in amyotrophic lateral sclerosis." AJNR Am J Neuroradiol **28**(2): 255-259.

Mezzapesa, D. M., E. D'Errico, R. Tortelli, E. Distaso, R. Cortese, M. Tursi, F. Federico, S. Zoccolella, G. Logroscino, F. Dicuonzo and I. L. Simone (2013). "Cortical thinning and clinical heterogeneity in amyotrophic lateral sclerosis." PLoS One **8**(11): e80748.

Mierisová, Š. and M. Ala-Korpela (2001). "MR spectroscopy quantitation: a review of frequency domain methods." NMR in Biomedicine **14**(4): 247-259.

Miller, R. G., J. D. Mitchell and D. H. Moore (2012). "Riluzole for amyotrophic lateral sclerosis (ALS)/motor neuron disease (MND)." Cochrane Database Syst Rev(3): Cd001447.

Miller, T., M. Cudkowicz, P. J. Shaw, P. M. Andersen, N. Atassi, R. C. Bucelli, A. Genge, J. Glass, S. Ladha, A. L. Ludolph, N. J. Maragakis, C. J. McDermott, A. Pestronk, J. Ravits, F. Salachas, R. Trudell, P. Van Damme, L. Zinman, C. F. Bennett, R. Lane, A. Sandrock, H. Runz, D. Graham, H. Houshyar, A. McCampbell, I. Nestorov, I. Chang, M. McNeill, L. Fanning, S. Fradette and T. A. Ferguson (2020). "Phase 1-2 Trial of Antisense Oligonucleotide Tofersen for SOD1 ALS." N Engl J Med **383**(2): 109-119.

Mimuro, M., Y. Kokubo and S. Kuzuhara (2007). "Similar topographical distribution of neurofibrillary tangles in amyotrophic lateral sclerosis and parkinsonism-dementia complex in people living in the Kii peninsula of Japan suggests a single tauopathy." Acta Neuropathol **113**(6): 653-658.

Mitchell, J. C., P. McGoldrick, C. Vance, T. Hortobagyi, J. Sreedharan, B. Rogelj, E. L. Tudor, B. N. Smith, C. Klasen, C. C. J. Miller, J. D. Cooper, L. Greensmith and C. E. Shaw (2013). "Overexpression of human wild-type FUS causes progressive motor neuron degeneration in an age- and dose-dependent fashion." Acta Neuropathologica **125**(2): 273-288.

Mitsumoto, H., A. M. Ulug, S. L. Pullman, C. L. Gooch, S. Chan, M. X. Tang, X. Mao, A. P. Hays, A. G. Floyd, V. Battista, J. Montes, S. Hayes, S. Dashnaw, P. Kaufmann, P. H. Gordon, J. Hirsch, B. Levin, L. P. Rowland and D. C. Shungu (2007). "Quantitative objective markers for upper and lower motor neuron dysfunction in ALS." Neurology **68**(17): 1402-1410.

Moglia, C., A. Calvo, M. Grassano, A. Canosa, U. Manera, F. Ovidio, A. Bombaci, E. Bersano, L. Mazzini, G. Mora and A. Chiò (2019). "Early weight loss in amyotrophic lateral sclerosis: outcome relevance and clinical correlates in a population-based cohort." Journal of Neurology, Neurosurgery & Psychiatry **90**(6): 666.

Moller, A., C. S. Bauer, R. N. Cohen, C. P. Webster and K. J. De Vos (2017). "Amyotrophic lateral sclerosis-associated mutant SOD1 inhibits anterograde axonal transport of mitochondria by reducing Miro1 levels." Hum Mol Genet **26**(23): 4668-4679.

Montuschi, A., B. Iazzolino, A. Calvo, C. Moglia, L. Lopiano, G. Restagno, M. Brunetti, I. Ossola, A. Lo Presti, S. Cammarosano, A. Canosa and A. Chio (2015). "Cognitive correlates in amyotrophic lateral sclerosis: a population-based study in Italy." J Neurol Neurosurg Psychiatry **86**(2): 168-173.

Mori, K., S.-M. Weng, T. Arzberger, S. May, K. Rentzsch, E. Kremmer, B. Schmid, A. Kretzschmar Hans, M. Cruts, C. Van Broeckhoven, C. Haass and D. Edbauer (2013). "The C9orf72 GGGGCC

Repeat Is Translated into Aggregating Dipeptide-Repeat Proteins in FTLD/ALS." Science **339**(6125): 1335-1338.

Morotz, G. M., K. J. De Vos, A. Vagnoni, S. Ackerley, C. E. Shaw and C. C. Miller (2012). "Amyotrophic lateral sclerosis-associated mutant VAPBP56S perturbs calcium homeostasis to disrupt axonal transport of mitochondria." Hum Mol Genet **21**(9): 1979-1988.

Murphy, E. (2000). "Mysteries of Magnesium Homeostasis." Circulation Research **86**(3): 245-248.

Mélé, N., G. Berzero, T. Maisonobe, F. Salachas, G. Nicolas, N. Weiss, G. Beaudonnet, F. Ducray, D. Psimaras and T. Lenglet (2018). "Motor neuron disease of paraneoplastic origin: a rare but treatable condition." J Neurol **265**(7): 1590-1599.

Nakaya, T. and M. Maragkakis (2018). "Amyotrophic Lateral Sclerosis associated FUS mutation shortens mitochondria and induces neurotoxicity." Sci Rep **8**(1): 15575.

Nakayama, Y., T. Shimizu, C. Matsuda, M. Haraguchi, K. Hayashi, K. Bokuda, M. Nagao, A. Kawata, K. Ishikawa-Takata and E. Isozaki (2019). "Body weight variation predicts disease progression after invasive ventilation in amyotrophic lateral sclerosis." Scientific Reports **9**(1): 12262.

Nalbandian, A., K. J. Llewellyn, A. Gomez, N. Walker, H. Su, A. Dunnigan, M. Chwa, J. Vesa, M. C. Kenney and V. E. Kimonis (2015). "In vitro studies in VCP-associated multisystem proteinopathy suggest altered mitochondrial bioenergetics." Mitochondrion **22**: 1-8.

Nandedkar, S. (2017). "S71 Motor unit number index (MUNIX)." Clinical Neurophysiology **128**(9): e201.

Nandedkar, S. D., P. E. Barkhaus and E. V. Stålberg (2010). "Motor unit number index (MUNIX): principle, method, and findings in healthy subjects and in patients with motor neuron disease." Muscle Nerve **42**(5): 798-807.

Nandedkar, S. D., D. S. Nandedkar, P. E. Barkhaus and E. V. Stalberg (2004). "Motor unit number index (MUNIX)." IEEE Trans Biomed Eng **51**(12): 2209-2211.

Naressi, A., C. Couturier, J. M. Devos, M. Janssen, C. Mangeat, R. d. Beer and D. Graveron-Demilly (2001). "Java-based graphical user interface for the MRUI quantitation package." Magnetic Resonance Materials in Physics, Biology and Medicine **12**(2): 141.

Nasreddine, Z. S., N. A. Phillips, V. Bédirian, S. Charbonneau, V. Whitehead, I. Collin, J. L. Cummings and H. Chertkow (2005). "The Montreal Cognitive Assessment, MoCA: A Brief Screening Tool For Mild Cognitive Impairment." Journal of the American Geriatrics Society **53**(4): 695-699.

Neumann, M., R. Rademakers, S. Roeber, M. Baker, H. A. Kretzschmar and I. R. Mackenzie (2009). "A new subtype of frontotemporal lobar degeneration with FUS pathology." Brain **132**(Pt 11): 2922-2931.

Neumann, M., D. M. Sampathu, L. K. Kwong, A. C. Truax, M. C. Micsenyi, T. T. Chou, J. Bruce, T. Schuck, M. Grossman, C. M. Clark, L. F. McCluskey, B. L. Miller, E. Masliah, I. R. Mackenzie, H. Feldman, W. Feiden, H. A. Kretzschmar, J. Q. Trojanowski and V. M. Lee (2006). "Ubiquitinated TDP-

43 in frontotemporal lobar degeneration and amyotrophic lateral sclerosis." Science **314**(5796): 130-133.

Neuwirth, C., P. E. Barkhaus, C. Burkhardt, J. Castro, D. Czell, M. de Carvalho, S. Nandedkar, E. Stålberg and M. Weber (2015). "Tracking motor neuron loss in a set of six muscles in amyotrophic lateral sclerosis using the Motor Unit Number Index (MUNIX): a 15-month longitudinal multicentre trial." J Neurol Neurosurg Psychiatry **86**(11): 1172-1179.

Neuwirth, C., S. Nandedkar, E. StåLberg and M. Weber (2010). "Motor unit number index (MUNIX): A novel neurophysiological technique to follow disease progression in amyotrophic lateral sclerosis." Muscle & Nerve **42**(3): 379-384.

Nicholls, D. G. (2013). Bioenergetics, Amsterdam : Academic Press, 2013.

Nihei, Y., K. Mori, G. Werner, T. Arzberger, Q. Zhou, B. Khosravi, J. Japtok, A. Hermann, A. Sommacal, M. Weber, F. Kamp, B. Nuscher, D. Edbauer and C. Haass (2020). "Poly-glycine-alanine exacerbates C9orf72 repeat expansion-mediated DNA damage via sequestration of phosphorylated ATM and loss of nuclear hnRNPA3." Acta Neuropathol **139**(1): 99-118.

Niven, E., J. Newton, J. Foley, S. Colville, R. Swingler, S. Chandran, T. H. Bak and S. Abrahams (2015). "Validation of the Edinburgh Cognitive and Behavioural Amyotrophic Lateral Sclerosis Screen (ECAS): A cognitive tool for motor disorders." Amyotrophic Lateral Sclerosis and Frontotemporal Degeneration **16**(3-4): 172-179.

Nordengen, K., C. Heuser, J. E. Rinholm, R. Matalon and V. Gundersen (2015). "Localisation of N-acetylaspartate in oligodendrocytes/myelin." Brain Struct Funct **220**(2): 899-917.

O'Rourke, J. G., L. Bogdanik, A. Yáñez, D. Lall, A. J. Wolf, A. K. M. G. Muhammad, R. Ho, S. Carmona, J. P. Vit, J. Zarrow, K. J. Kim, S. Bell, M. B. Harms, T. M. Miller, C. A. Dangler, D. M. Underhill, H. S. Goodridge, C. M. Lutz and R. H. Baloh (2016). "C9orf72 is required for proper macrophage and microglial function in mice." Science (New York, N.Y.) **351**(6279): 1324-1329.

Oba, H., T. Araki, K. Ohtomo, S. Monzawa, G. Uchiyama, K. Koizumi, Y. Nogata, K. Kachi, Z. Shiozawa and M. Kobayashi (1993). "Amyotrophic lateral sclerosis: T2 shortening in motor cortex at MR imaging." Radiology **189**(3): 843-846.

Onesto, E., C. Colombrita, V. Gumina, M. O. Borghi, S. Dusi, A. Doretti, G. Fagiolari, F. Invernizzi, M. Moggio, V. Tiranti, V. Silani and A. Ratti (2016). "Gene-specific mitochondria dysfunctions in human TARDBP and C9ORF72 fibroblasts." Acta Neuropathol Commun **4**(1): 47.

Ordidge, R. J., R. M. Bowley and G. McHale (1988). "A general approach to selection of multiple cubic volume elements using the ISIS technique." Magnetic Resonance in Medicine **8**(3): 323-331.

Ordidge, R. J., A. Connelly and J. A. B. Lohman (1986). "Image-selected in Vivo spectroscopy (ISIS). A new technique for spatially selective nmr spectroscopy." Journal of Magnetic Resonance (1969) **66**(2): 283-294.

Orozco, D. and D. Edbauer (2013). "FUS-mediated alternative splicing in the nervous system: consequences for ALS and FTLD." J Mol Med (Berl) **91**(12): 1343-1354.

Osborne, R. A., R. Sekhon, W. Johnston and S. Kalra (2014). "Screening for frontal lobe and general cognitive impairment in patients with amyotrophic lateral sclerosis." J Neurol Sci **336**(1-2): 191-196.

Ou, S. H., F. Wu, D. Harrich, L. F. García-Martínez and R. B. Gaynor (1995). "Cloning and characterization of a novel cellular protein, TDP-43, that binds to human immunodeficiency virus type 1 TAR DNA sequence motifs." J Virol **69**(6): 3584-3596.

Pache, T. and H. Reichmann (1990). "On the stability of key enzymes of energy metabolism in muscle biopsies." Enzyme **43**(4): 183-187.

Paganoni, S., E. A. Macklin, A. Lee, A. Murphy, J. Chang, A. Zipf, M. Cudkowicz and N. Atassi (2014). "Diagnostic timelines and delays in diagnosing amyotrophic lateral sclerosis (ALS)." Amyotroph Lateral Scler Frontotemporal Degener **15**(5-6): 453-456.

Palmieri, A., M. Naccarato, S. Abrahams, M. Bonato, C. D'Ascenzo, S. Balestreri, V. Cima, G. Querin, R. Dal Borgo, L. Barachino, C. Volpato, C. Semenza, E. Pegoraro, C. Angelini and G. Soraru (2010). "Right hemisphere dysfunction and emotional processing in ALS: an fMRI study." J Neurol **257**(12): 1970-1978.

Pancani, S., W. Tindale, P. J. Shaw, C. J. McDermott and C. Mazzà (2017). "An Objective Functional Characterisation of Head Movement Impairment in Individuals with Neck Muscle Weakness Due to Amyotrophic Lateral Sclerosis." PLoS One **12**(1): e0169019.

Paré, B., M. Lehmann, M. Beaudin, U. Nordström, S. Saikali, J.-P. Julien, J. D. Gilthorpe, S. L. Marklund, N. R. Cashman, P. M. Andersen, K. Forsberg, N. Dupré, P. Gould, T. Brännström and F. Gros-Louis (2018). "Misfolded SOD1 pathology in sporadic Amyotrophic Lateral Sclerosis." Scientific Reports **8**(1): 14223.

Patel, T. B. and J. B. Clark (1979). "Synthesis of N-acetyl-L-aspartate by rat brain mitochondria and its involvement in mitochondrial/cytosolic carbon transport." Biochem J **184**(3): 539-546.

Paulukonis, S. T., E. M. Roberts, J. P. Valle, N. N. Collins, P. B. English and W. E. Kaye (2015). "Survival and Cause of Death among a Cohort of Confirmed Amyotrophic Lateral Sclerosis Cases." PLoS One **10**(7): e0131965.

Payne, T., M. Sassani, E. Buckley, S. Moll, A. Anton, M. Appleby, S. Maru, R. Taylor, A. McNeill, N. Hoggard, C. Mazza, I. D. Wilkinson, T. Jenkins, T. Foltynie and O. Bandmann (2020). "Ursodeoxycholic acid as a novel disease-modifying treatment for Parkinson's disease: protocol for a two-centre, randomised, double-blind, placebo-controlled trial, The 'UP' study." BMJ Open **10**(8): e038911.

Peeters, T. H., M. J. van Uden, A. Rijpma, T. W. J. Scheenen and A. Heerschap (2019). "3D 31P MR spectroscopic imaging of the human brain at 3 T with a 31P receive array: An assessment of 1H decoupling, T1 relaxation times, 1H-31P nuclear Overhauser effects and NAD+." NMR in Biomedicine **n/a**(n/a): e4169.

Pelmenschikov, V. and P. E. M. Siegbahn (2005). "Copper−Zinc Superoxide Dismutase: Theoretical Insights into the Catalytic Mechanism." Inorganic Chemistry **44**(9): 3311-3320.

Peretti-Viton, P., J. P. Azulay, S. Trefouret, H. Brunel, C. Daniel, J. M. Viton, A. Flori, B. Salazard, J. Pouget, G. Serratrice and G. Salamon (1999). "MRI of the intracranial corticospinal tracts in amyotrophic and primary lateral sclerosis." Neuroradiology **41**(10): 744-749.

Perrin, S. (2014). "Preclinical research: Make mouse studies work." Nature **507**(7493): 423-425.

Petersen, K. F., S. Dufour and G. I. Shulman (2005). "Decreased insulin-stimulated ATP synthesis and phosphate transport in muscle of insulin-resistant offspring of type 2 diabetic parents." PLoS medicine **2**(9): e233-e233.

Petrov, D., C. Mansfield, A. Moussy and O. Hermine (2017). "ALS Clinical Trials Review: 20 Years of Failure. Are We Any Closer to Registering a New Treatment?" Front Aging Neurosci **9**: 68.

Phukan, J., N. P. Pender and O. Hardiman (2007). "Cognitive impairment in amyotrophic lateral sclerosis." Lancet Neurol **6**(11): 994-1003.

Piccione, E. A., D. M. Sletten, N. P. Staff and P. A. Low (2015). "Autonomic system and amyotrophic lateral sclerosis." Muscle & nerve **51**(5): 676-679.

Pierry, I. A., J. Alix, D. G. Rao, N. Hoggard, J. Bigley, C. J. McDermott, I. D. Wilkinson, P. J. Shaw and T. M. Jenkins (2017). "Longitudinal Diffusion-Weighted Whole-Body MRI Demonstrates Dynamic Changes in Muscle Integrity in Motor Neuron Disease." J Neuromuscul Dis.

Pinkhardt, E. H., R. Jürgens, W. Becker, M. Mölle, J. Born, A. C. Ludolph and H. Schreiber (2008). "Signs of impaired selective attention in patients with amyotrophic lateral sclerosis." J Neurol **255**(4): 532-538.

Pioro, E. P. (1997). "MR spectroscopy in amyotrophic lateral sclerosis/motor neuron disease." J Neurol Sci **152 Suppl 1**: S49-53.

Pioro, E. P., A. W. Majors, H. Mitsumoto, D. R. Nelson and T. C. Ng (1999). "1H-MRS evidence of neurodegeneration and excess glutamate + glutamine in ALS medulla." Neurology **53**(1): 71-79.

Place, N. and G. Y. Millet (2020). "Quantification of Neuromuscular Fatigue: What Do We Do Wrong and Why?" Sports Med **50**(3): 439-447.

Pohl, C., W. Block, F. Traber, S. Schmidt, H. Pels, C. Grothe, H. H. Schild and T. Klockgether (2001). "Proton magnetic resonance spectroscopy and transcranial magnetic stimulation for the detection of upper motor neuron degeneration in ALS patients." J Neurol Sci **190**(1-2): 21-27.

Prasad, A., V. Bharathi, V. Sivalingam, A. Girdhar and B. K. Patel (2019). "Molecular Mechanisms of TDP-43 Misfolding and Pathology in Amyotrophic Lateral Sclerosis." Frontiers in Molecular Neuroscience **12**: 25.

Pringle, C. E., A. J. Hudson, D. G. Munoz, J. A. Kiernan, W. F. Brown and G. C. Ebers (1992). "Primary lateral sclerosis. Clinical features, neuropathology and diagnostic criteria." Brain **115 (Pt 2)**: 495-520.

ProGas (2015). "Gastrostomy in patients with amyotrophic lateral sclerosis (ProGas): a prospective cohort study." Lancet Neurol **14**(7): 702-709.

Pugdahl, K., A. Fuglsang-Frederiksen, M. de Carvalho, B. Johnsen, P. R. W. Fawcett, A. Labarre-Vila, R. Liguori, W. A. Nix and I. S. Schofield (2007). "Generalised sensory system abnormalities in amyotrophic lateral sclerosis: a European multicentre study." Journal of neurology, neurosurgery, and psychiatry **78**(7): 746-749.

Pun, S., A. F. Santos, S. Saxena, L. Xu and P. Caroni (2006). "Selective vulnerability and pruning of phasic motoneuron axons in motoneuron disease alleviated by CNTF." Nat Neurosci **9**(3): 408-419.

Pyra, T., B. Hui, C. Hanstock, L. Concha, J. C. Wong, C. Beaulieu, W. Johnston and S. Kalra (2010). "Combined structural and neurochemical evaluation of the corticospinal tract in amyotrophic lateral sclerosis." Amyotroph Lateral Scler **11**(1-2): 157-165.

Quadrelli, S., C. Mountford and S. Ramadan (2016). "Hitchhiker's Guide to Voxel Segmentation for Partial Volume Correction of In Vivo Magnetic Resonance Spectroscopy." Magnetic Resonance Insights **9**: 1-8.

Quinn, C., L. Elman, L. McCluskey, K. Hoskins, C. Karam, J. H. Woo, H. Poptani, S. Wang, S. Chawla, S. E. Kasner and M. Grossman (2012). "Frontal lobe abnormalities on MRS correlate with poor letter fluency in ALS." Neurology **79**(6): 583-588.

Radakovic, R., L. Stephenson, S. Colville, R. Swingler, S. Chandran and S. Abrahams (2016). "Multidimensional apathy in ALS: validation of the Dimensional Apathy Scale." Journal of Neurology, Neurosurgery & Psychiatry **87**(6): 663.

Ramirez, C., M. E. Piemonte, D. Callegaro and H. C. Da Silva (2008). "Fatigue in amyotrophic lateral sclerosis: frequency and associated factors." Amyotroph Lateral Scler **9**(2): 75-80.

Rascovsky, K., J. R. Hodges, D. Knopman, M. F. Mendez, J. H. Kramer, J. Neuhaus, J. C. van Swieten, H. Seelaar, E. G. P. Dopper, C. U. Onyike, A. E. Hillis, K. A. Josephs, B. F. Boeve, A. Kertesz, W. W. Seeley, K. P. Rankin, J. K. Johnson, M.-L. Gorno-Tempini, H. Rosen, C. E. Prioleau-Latham, A. Lee, C. M. Kipps, P. Lillo, O. Piguet, J. D. Rohrer, M. N. Rossor, J. D. Warren, N. C. Fox, D. Galasko, D. P. Salmon, S. E. Black, M. Mesulam, S. Weintraub, B. C. Dickerson, J. Diehl-Schmid, F. Pasquier, V. Deramecourt, F. Lebert, Y. Pijnenburg, T. W. Chow, F. Manes, J. Grafman, S. F. Cappa, M. Freedman, M. Grossman and B. L. Miller (2011). "Sensitivity of revised diagnostic criteria for the behavioural variant of frontotemporal dementia." Brain **134**(9): 2456-2477.

Rata, M., S. L. Giles, N. M. deSouza, M. O. Leach and G. S. Payne (2014). "Comparison of three reference methods for the measurement of intracellular pH using 31P MRS in healthy volunteers and patients with lymphoma." NMR Biomed **27**(2): 158-162.

Ratai, E.-M., M. J. Alshikho, N. R. Zürcher, M. L. Loggia, C. L. Cebulla, P. Cernasov, B. Reynolds, J. Fish, R. Seth, S. Babu, S. Paganoni, J. M. Hooker and N. Atassi (2018). "Integrated imaging of [11C]-PBR28 PET, MR diffusion and magnetic resonance spectroscopy 1H-MRS in amyotrophic lateral sclerosis." NeuroImage: Clinical **20**: 357-364.

Reddi, P. P. (2017). "Transcription and Splicing Factor TDP-43: Role in Regulation of Gene Expression in Testis." Semin Reprod Med **35**(2): 167-172.

Redmond, O. M., J. P. Stack, N. G. O'Connor, D. N. Carney, P. A. Dervan, B. J. Hurson and J. T. Ennis (1992). "31P MRS as an early prognostic indicator of patient response to chemotherapy." Magnetic Resonance in Medicine **25**(1): 30-44.

Ren, J., A. D. Sherry and C. R. Malloy (2015). "(31)P-MRS of healthy human brain: ATP synthesis, metabolite concentrations, pH, and T1 relaxation times." NMR Biomed **28**(11): 1455-1462.

Renton, A. E., A. Chio and B. J. Traynor (2014). "State of play in amyotrophic lateral sclerosis genetics." Nat Neurosci **17**(1): 17-23.

Renton, A. E., E. Majounie, A. Waite, J. Simon-Sanchez, S. Rollinson, J. R. Gibbs, J. C. Schymick, H. Laaksovirta, J. C. van Swieten, L. Myllykangas, H. Kalimo, A. Paetau, Y. Abramzon, A. M. Remes, A. Kaganovich, S. W. Scholz, J. Duckworth, J. Ding, D. W. Harmer, D. G. Hernandez, J. O. Johnson, K. Mok, M. Ryten, D. Trabzuni, R. J. Guerreiro, R. W. Orrell, J. Neal, A. Murray, J. Pearson, I. E. Jansen, D. Sondervan, H. Seelaar, D. Blake, K. Young, N. Halliwell, J. B. Callister, G. Toulson, A. Richardson, A. Gerhard, J. Snowden, D. Mann, D. Neary, M. A. Nalls, T. Peuralinna, L. Jansson, V. M. Isoviita, A. L. Kaivorinne, M. Holtta-Vuori, E. Ikonen, R. Sulkava, M. Benatar, J. Wuu, A. Chio, G. Restagno, G. Borghero, M. Sabatelli, D. Heckerman, E. Rogaeva, L. Zinman, J. D. Rothstein, M. Sendtner, C. Drepper, E. E. Eichler, C. Alkan, Z. Abdullaev, S. D. Pack, A. Dutra, E. Pak, J. Hardy, A. Singleton, N. M. Williams, P. Heutink, S. Pickering-Brown, H. R. Morris, P. J. Tienari and B. J. Traynor (2011). "A hexanucleotide repeat expansion in C9ORF72 is the cause of chromosome 9p21-linked ALS-FTD." Neuron **72**(2): 257-268.

Rijpma, A., M. van der Graaf, O. Meulenbroek, M. G. M. Olde Rikkert and A. Heerschap (2018). "Altered brain high-energy phosphate metabolism in mild Alzheimer's disease: A 3-dimensional (31)P MR spectroscopic imaging study." NeuroImage. Clinical **18**: 254-261.

Rizzu, P., C. Blauwendraat, S. Heetveld, E. M. Lynes, M. Castillo-Lizardo, A. Dhingra, E. Pyz, M. Hobert, M. Synofzik, J. Simón-Sánchez, M. Francescatto and P. Heutink (2016). "C9orf72 is differentially expressed in the central nervous system and myeloid cells and consistently reduced in C9orf72, MAPT and GRN mutation carriers." Acta neuropathologica communications **4**(1): 37-37.

Rohrer, J. D. (2012). "Structural brain imaging in frontotemporal dementia." Biochimica et Biophysica Acta (BBA) - Molecular Basis of Disease **1822**(3): 325-332.

Rosen, D. R., T. Siddique, D. Patterson, D. A. Figlewicz, P. Sapp, A. Hentati, D. Donaldson, J. Goto, J. P. O'Regan, H. X. Deng and et al. (1993). "Mutations in Cu/Zn superoxide dismutase gene are associated with familial amyotrophic lateral sclerosis." Nature **362**(6415): 59-62.

Ruegsegger, C. and S. Saxena (2016). "Proteostasis impairment in ALS." Brain Res **1648**(Pt B): 571-579.

Rule, R. R., J. Suhy, N. Schuff, D. F. Gelinas, R. G. Miller and M. W. Weiner (2004). "Reduced NAA in motor and non-motor brain regions in amyotrophic lateral sclerosis: a cross-sectional and longitudinal study." Amyotroph Lateral Scler Other Motor Neuron Disord **5**(3): 141-149.

Ryan, T. E., M. L. Erickson, A. Verma, J. Chavez, M. H. Rivner and K. K. McCully (2014). "Skeletal muscle oxidative capacity in amyotrophic lateral sclerosis." Muscle Nerve **50**(5): 767-774.

Saberi, S., J. E. Stauffer, D. J. Schulte and J. Ravits (2015). "Neuropathology of Amyotrophic Lateral Sclerosis and Its Variants." Neurologic clinics **33**(4): 855-876.

Sacca, F., M. Quarantelli, C. Rinaldi, T. Tucci, R. Piro, G. Perrotta, B. Carotenuto, A. Marsili, V. Palma, G. De Michele, A. Brunetti, V. Brescia Morra, A. Filla and M. Salvatore (2012). "A randomized controlled clinical trial of growth hormone in amyotrophic lateral sclerosis: clinical, neuroimaging, and hormonal results." J Neurol **259**(1): 132-138.

Saccon, R. A., R. K. A. Bunton-Stasyshyn, E. M. C. Fisher and P. Fratta (2013). "Is SOD1 loss of function involved in amyotrophic lateral sclerosis?" Brain : a journal of neurology **136**(Pt 8): 2342-2358.

Sage, C. A., W. Van Hecke, R. Peeters, J. Sijbers, W. Robberecht, P. Parizel, G. Marchal, A. Leemans and S. Sunaert (2009). "Quantitative diffusion tensor imaging in amyotrophic lateral sclerosis: revisited." Human Brain Mapping **30**(11): 3657-3675.

Sako, W., T. Abe, Y. Izumi, M. Harada and R. Kaji (2016). "The ratio of N-acetyl aspartate to glutamate correlates with disease duration of amyotrophic lateral sclerosis." J Clin Neurosci **27**: 110-113.

Sangwan, S. and D. S. Eisenberg (2016). "Perspective on SOD1 mediated toxicity in Amyotrophic Lateral Sclerosis." Postepy Biochem **62**(3): 362-369.

Sanjak, M., J. Brinkmann, D. S. Belden, K. Roelke, A. Waclawik, H. E. Neville, S. P. Ringel, J. R. Murphy and B. R. Brooks (2001). "Quantitative assessment of motor fatigue in amyotrophic lateral sclerosis." J Neurol Sci **191**(1-2): 55-59.

Santangelo, G., M. Siciliano, L. Trojano, C. Femiano, M. R. Monsurrò, G. Tedeschi and F. Trojsi (2017). "Apathy in amyotrophic lateral sclerosis: insights from Dimensional Apathy Scale." Amyotrophic Lateral Sclerosis and Frontotemporal Degeneration **18**(5-6): 434-442.

Sarchielli, P., G. P. Pelliccioli, R. Tarducci, P. Chiarini, O. Presciutti, G. Gobbi and V. Gallai (2001). "Magnetic resonance imaging and 1H-magnetic resonance spectroscopy in amyotrophic lateral sclerosis." Neuroradiology **43**(3): 189-197.

Sassani, M., J. J. Alix, C. J. McDermott, K. Baster, N. Hoggard, J. M. Wild, H. J. Mortiboys, P. J. Shaw, I. D. Wilkinson and T. M. Jenkins (2020). "Magnetic resonance spectroscopy reveals mitochondrial dysfunction in amyotrophic lateral sclerosis." Brain **143**(12): 3603-3618.

Schoenfeld, M. A., C. Tempelmann, C. Gaul, G. R. Kuhnel, E. Duzel, J. M. Hopf, H. Feistner, S. Zierz, H. J. Heinze and S. Vielhaber (2005). "Functional motor compensation in amyotrophic lateral sclerosis." Journal of Neurology **252**(8): 944-952.

Schuff, N., W. D. Rooney, R. Miller, D. F. Gelinas, D. L. Amend, A. A. Maudsley and M. W. Weiner (2001). "Reanalysis of multislice (1)H MRSI in amyotrophic lateral sclerosis." Magn Reson Med **45**(3): 513-516.

Seals, R. M., M. A. Kioumourtzoglou, O. Gredal, J. Hansen and M. G. Weisskopf (2017). "Occupational formaldehyde and amyotrophic lateral sclerosis." Eur J Epidemiol.

Segers, K., H. Kadhim, C. Colson, R. Duttmann and G. Glibert (2012). "Adult polyglucosan body disease masquerading as "ALS with dementia of the Alzheimer type": an exceptional phenotype in a rare pathology." Alzheimer Dis Assoc Disord **26**(1): 96-99.

Sellier, C., M.-L. Campanari, C. Julie Corbier, A. Gaucherot, I. Kolb-Cheynel, M. Oulad-Abdelghani, F. Ruffenach, A. Page, S. Ciura, E. Kabashi and N. Charlet-Berguerand (2016). "Loss of C9ORF72 impairs autophagy and synergizes with polyQ Ataxin-2 to induce motor neuron dysfunction and cell death." The EMBO journal **35**(12): 1276-1297.

Shang, Y. and E. J. Huang (2016). "Mechanisms of FUS mutations in familial amyotrophic lateral sclerosis." Brain research **1647**: 65-78.

Sharma, K. R., J. A. Kent-Braun, S. Majumdar, Y. Huang, M. Mynhier, M. W. Weiner and R. G. Miller (1995). "Physiology of fatigue in amyotrophic lateral sclerosis." Neurology **45**(4): 733-740.

Sharma, K. R., G. Saigal, A. A. Maudsley and V. Govind (2011). "1H MRS of basal ganglia and thalamus in amyotrophic lateral sclerosis." NMR Biomed **24**(10): 1270-1276.

Shaw, P. J. (2005). "Molecular and cellular pathways of neurodegeneration in motor neurone disease." Journal of Neurology, Neurosurgery & Psychiatry **76**(8): 1046.

Shaw, P. J. and P. G. Ince (1997). "Glutamate, excitotoxicity and amyotrophic lateral sclerosis." J Neurol **244 Suppl 2**: S3-14.

Shefner, J. M., A. Al-Chalabi, M. R. Baker, L.-Y. Cui, M. de Carvalho, A. Eisen, J. Grosskreutz, O. Hardiman, R. Henderson, J. Manuel Matamala, H. Mitsumoto, W. Paulus, N. Simon, M. Swash, K. Talbot, M. R. Turner, Y. Ugawa, L. H. van den Berg, R. Verdugo, S. Vucic, R. Kaji, D. Burke and M. C. Kiernan (2020). "A proposal for new diagnostic criteria for ALS." Clinical Neurophysiology.

Shi, K. Y., E. Mori, Z. F. Nizami, Y. Lin, M. Kato, S. Xiang, L. C. Wu, M. Ding, Y. Yu, J. G. Gall and S. L. McKnight (2017). "Toxic PR_n poly-dipeptides encoded by the C9orf72 repeat expansion block nuclear import and export." Proceedings of the National Academy of Sciences **114**(7): E1111.

Shi, Y., S. Lin, K. A. Staats, Y. Li, W. H. Chang, S. T. Hung, E. Hendricks, G. R. Linares, Y. Wang, E. Y. Son, X. Wen, K. Kisler, B. Wilkinson, L. Menendez, T. Sugawara, P. Woolwine, M. Huang, M. J. Cowan, B. Ge, N. Koutsodendris, K. P. Sandor, J. Komberg, V. R. Vangoor, K. Senthilkumar, V. Hennes, C. Seah, A. R. Nelson, T. Y. Cheng, S. J. Lee, P. R. August, J. A. Chen, N. Wisniewski, V. Hanson-Smith, T. G. Belgard, A. Zhang, M. Coba, C. Grunseich, M. E. Ward, L. H. van den Berg, R. J. Pasterkamp, D. Trotti, B. V. Zlokovic and J. K. Ichida (2018). "Haploinsufficiency leads to neurodegeneration in C9ORF72 ALS/FTD human induced motor neurons." Nat Med **24**(3): 313-325.

Shimizu, S. and K. Kuriaki (1960). "Effect of denervation on the total metal content of skeletal muscle." American Journal of Physiology-Legacy Content **198**(5): 943-944.

Sidek, S., N. Ramli, K. Rahmat, N. M. Ramli, F. Abdulrahman and T. L. Kuo (2016). "In vivo proton magnetic resonance spectroscopy (1H-MRS) evaluation of the metabolite concentration of optic radiation in primary open angle glaucoma." European Radiology **26**(12): 4404-4412.

Simmons, M. L., C. G. Frondoza and J. T. Coyle (1991). "Immunocytochemical localization of N-acetyl-aspartate with monoclonal antibodies." Neuroscience **45**(1): 37-45.

Singer, M. A., J. M. Statland, G. I. Wolfe and R. J. Barohn (2007). "Primary lateral sclerosis." Muscle & Nerve **35**(3): 291-302.

Sivak, S., M. Bittsansky, E. Kurca, M. Turcanova-Koprusakova, M. Grofik, V. Nosal, H. Polacek and D. Dobrota (2010). "Proton magnetic resonance spectroscopy in patients with early stages of amyotrophic lateral sclerosis." Neuroradiology **52**(12): 1079-1085.

Smith, E. F., P. J. Shaw and K. J. De Vos (2017). "The Role of Mitochondria in Amyotrophic Lateral Sclerosis." Neurosci Lett.

Song, W., Y. Song, B. Kincaid, B. Bossy and E. Bossy-Wetzel (2013). "Mutant SOD1G93A triggers mitochondrial fragmentation in spinal cord motor neurons: Neuroprotection by SIRT3 and PGC-1α." Neurobiology of Disease **51**: 72-81.

Soraru, G., L. Vergani, L. Fedrizzi, C. D'Ascenzo, A. Polo, B. Bernazzi and C. Angelini (2007). "Activities of mitochondrial complexes correlate with nNOS amount in muscle from ALS patients." Neuropathol Appl Neurobiol **33**(2): 204-211.

Spijkerman, J. M., E. T. Petersen, J. Hendrikse, P. Luijten and J. J. M. Zwanenburg (2018). "T (2) mapping of cerebrospinal fluid: 3 T versus 7 T." Magma (New York, N.Y.) **31**(3): 415-424.

Sreedharan, J., I. P. Blair, V. B. Tripathi, X. Hu, C. Vance, B. Rogelj, S. Ackerley, J. C. Durnall, K. L. Williams, E. Buratti, F. Baralle, J. de Belleroche, J. D. Mitchell, P. N. Leigh, A. Al-Chalabi, C. C. Miller, G. Nicholson and C. E. Shaw (2008). "TDP-43 mutations in familial and sporadic amyotrophic lateral sclerosis." Science **319**(5870): 1668-1672.

Srivastava, O., C. Hanstock, S. Chenji, D. Mah, D. Eurich, D. Ta, P. Seres, C. Luk, L. Zinman, A. Abrahao, S. J. Graham, A. Genge, L. Korngut, R. Frayne and S. Kalra (2019). "Cerebral degeneration in amyotrophic lateral sclerosis: A prospective multicenter magnetic resonance spectroscopy study." Neurology. Clinical practice **9**(5): 400-407.

Srivastava, O., C. Hanstock, S. Chenji, D. Mah, D. Eurich, D. Ta, P. Seres, C. Luk, L. Zinman, A. Abrahao, S. J. Graham, A. Genge, L. Korngut, R. Frayne and S. Kalra (2019). "Cerebral degeneration in amyotrophic lateral sclerosis: A prospective multicenter magnetic resonance spectroscopy study." Neurol Clin Pract **9**(5): 400-407.

Stagg, C. (2014). Magnetic resonance spectroscopy : tools for neuroscience research and emerging clinical applications. Amsterdam, Amsterdam : Elsevier, 2014.

Stagg, C. J., S. Knight, K. Talbot, M. Jenkinson, A. A. Maudsley and M. R. Turner (2013). "Whole-brain magnetic resonance spectroscopic imaging measures are related to disability in ALS." Neurology **80**(7): 610-615.

Stanton, B. R., V. C. Williams, P. N. Leigh, S. C. Williams, C. R. Blain, J. M. Jarosz and A. Simmons (2007). "Altered cortical activation during a motor task in ALS. Evidence for involvement of central pathways." Journal of Neurology **254**(9): 1260-1267.

Stefan, D., F. D. Cesare, A. Andrasescu, E. Popa, A. Lazariev, E. Vescovo, O. Strbak, S. Williams, Z. Starcuk, M. Cabanas, D. van Ormondt and D. Graveron-Demilly (2009). "Quantitation of magnetic resonance spectroscopy signals: the jMRUI software package." Measurement Science and Technology **20**(10): 104035.

Steyn, F. J., Z. A. Ioannides, R. P. A. van Eijk, S. Heggie, K. A. Thorpe, A. Ceslis, S. Heshmat, A. K. Henders, N. R. Wray, L. H. van den Berg, R. D. Henderson, P. A. McCombe and S. T. Ngo (2018). "Hypermetabolism in ALS is associated with greater functional decline and shorter survival." Journal of Neurology, Neurosurgery & Psychiatry **89**(10): 1016.

Stoica, R., S. Paillusson, P. Gomez-Suaga, J. C. Mitchell, D. H. Lau, E. H. Gray, R. M. Sancho, G. Vizcay-Barrena, K. J. De Vos, C. E. Shaw, D. P. Hanger, W. Noble and C. C. Miller (2016). "ALS/FTD-associated FUS activates GSK-3beta to disrupt the VAPB-PTPIP51 interaction and ER-mitochondria associations." EMBO Rep **17**(9): 1326-1342.

Straub, I. R., A. Janer, W. Weraarpachai, L. Zinman, J. Robertson, E. Rogaeva and E. A. Shoubridge (2018). "Loss of CHCHD10-CHCHD2 complexes required for respiration underlies the pathogenicity of a CHCHD10 mutation in ALS." Hum Mol Genet **27**(1): 178-189.

Strauss, M., K. Koehler, M. Krumbholz, A. Huebner, S. Zierz and M. Deschauer (2008). "Triple A syndrome mimicking ALS." Amyotrophic Lateral Sclerosis **9**(5): 315-317.

Strong, M. J., S. Abrahams, L. H. Goldstein, S. Woolley, P. McLaughlin, J. Snowden, E. Mioshi, A. Roberts-South, M. Benatar, T. HortobaGyi, J. Rosenfeld, V. Silani, P. G. Ince and M. R. Turner (2017). "Amyotrophic lateral sclerosis - frontotemporal spectrum disorder (ALS-FTSD): Revised diagnostic criteria." Amyotroph Lateral Scler Frontotemporal Degener **18**(3-4): 153-174.

Strong, M. J., S. Abrahams, L. H. Goldstein, S. Woolley, P. McLaughlin, J. Snowden, E. Mioshi, A. Roberts-South, M. Benatar, T. HortobáGyi, J. Rosenfeld, V. Silani, P. G. Ince and M. R. Turner (2017). "Amyotrophic lateral sclerosis - frontotemporal spectrum disorder (ALS-FTSD): Revised diagnostic criteria." Amyotroph Lateral Scler Frontotemporal Degener **18**(3-4): 153-174.

Strong, M. J., G. M. Grace, J. B. Orange, H. A. Leeper, R. S. Menon and C. Aere (1999). "A prospective study of cognitive impairment in ALS." Neurology **53**(8): 1665-1670.

Sudharshan, N., C. Hanstock, B. Hui, T. Pyra, W. Johnston and S. Kalra (2011). "Degeneration of the mid-cingulate cortex in amyotrophic lateral sclerosis detected in vivo with MR spectroscopy." AJNR Am J Neuroradiol **32**(2): 403-407.

Swash, M. (2019). "Clinical trials in the ALS syndrome: it is time for change." Journal of Neurology, Neurosurgery & Psychiatry: jnnp-2019-321411.

Ta, D., A. Ishaque, O. Srivastava, C. Hanstock, P. Seres, D. T. Eurich, C. Luk, H. Briemberg, R. Frayne, A. L. Genge, S. J. Graham, L. Korngut, L. Zinman and S. Kalra (2021). "Progressive Neurochemical Abnormalities in Cognitive and Motor Subgroups of Amyotrophic Lateral Sclerosis." Neurology **97**(8): e803.

Tainer, J. A., E. D. Getzoff, J. S. Richardson and D. C. Richardson (1983). "Structure and mechanism of copper, zinc superoxide dismutase." Nature **306**(5940): 284-287.

Talbot, K. (2002). "Motor neurone disease." Postgrad Med J **78**(923): 513-519.

Tan, W., P. Pasinelli and D. Trotti (2014). "Role of mitochondria in mutant SOD1 linked amyotrophic lateral sclerosis." Biochimica et Biophysica Acta (BBA) - Molecular Basis of Disease **1842**(8): 1295-1301.

Tanabe, J. L., M. Vermathen, R. Miller, D. Gelinas, M. W. Weiner and W. D. Rooney (1998). "REDUCED MTR IN THE CORTICOSPINAL TRACT AND NORMAL T(2) IN AMYOTROPHIC LATERAL SCLEROSIS." Magnetic resonance imaging **16**(10): 1163-1169.

Tang, M., X. Chen, Q. Zhou, B. Liu, Y. Liu, S. Liu and Z. Chen (2015). "Quantitative assessment of amyotrophic lateral sclerosis with diffusion tensor imaging in 3.0T magnetic resonance." International Journal of Clinical and Experimental Medicine **8**(5): 8295-8303.

Tang, X., A. Toro, S. T.G, J. Gao, J. Chalk, B. E. Oskarsson and K. Zhang (2020). "Divergence, Convergence, and Therapeutic Implications: A Cell Biology Perspective of C9ORF72-ALS/FTD." Molecular Neurodegeneration **15**(1): 34.

Terada, T., T. Obi, M. Yoshizumi, T. Murai, H. Miyajima and K. Mizoguchi (2011). "Frontal lobe-mediated behavioral changes in amyotrophic lateral sclerosis: are they independent of physical disabilities?" J Neurol Sci **309**(1-2): 136-140.

Terpstra, M., I. Cheong, T. Lyu, D. K. Deelchand, U. E. Emir, P. Bednařík, L. E. Eberly and G. Öz (2016). "Test-retest reproducibility of neurochemical profiles with short-echo, single-voxel MR spectroscopy at 3T and 7T." Magnetic Resonance in Medicine **76**(4): 1083-1091.

Thivard, L., P. F. Pradat, S. Lehéricy, L. Lacomblez, D. Dormont, J. Chiras, H. Benali and V. Meininger (2007). "Diffusion tensor imaging and voxel based morphometry study in amyotrophic lateral sclerosis: relationships with motor disability." Journal of Neurology, Neurosurgery, and Psychiatry **78**(8): 889-892.

Thulborn, K. and I. Atkinson (2014). Quantitative Metabolic Magnetic Resonance Imaging of Sodium, Oxygen, Phosphorus and Potassium in the Human Brain.

Traxinger, K., C. Kelly, B. A. Johnson, R. H. Lyles and J. D. Glass (2013). "Prognosis and epidemiology of amyotrophic lateral sclerosis: Analysis of a clinic population, 1997-2011." Neurology. Clinical practice **3**(4): 313-320.

Traynor, B. J., M. Alexander, B. Corr, E. Frost and O. Hardiman (2003). "Effect of a multidisciplinary amyotrophic lateral sclerosis (ALS) clinic on ALS survival: a population based study, 1996-2000." J Neurol Neurosurg Psychiatry **74**(9): 1258-1261.

Traynor, B. J., M. B. Codd, B. Corr, C. Forde, E. Frost and O. Hardiman (1999). "Incidence and prevalence of ALS in Ireland, 1995-1997: a population-based study." Neurology **52**(3): 504-509.

Träber, F., W. Block, N. Freymann, O. Gür, T. Kucinski, T. Hammen, G. Ende, U. Pilatus, H. Hampel, H. H. Schild, R. Heun and F. Jessen (2006). "A multicenter reproducibility study of single-voxel 1H-MRS of the medial temporal lobe." European Radiology **16**(5): 1096-1103.

Tsitkanou, S., A. Lindsay and P. Della Gatta (2019). "The role of skeletal muscle in amyotrophic lateral sclerosis: a ‘dying-back’ or ‘dying-forward’ phenomenon?" The Journal of Physiology **597**(23): 5527-5528.

Turnbull, J. (2018). "Is edaravone harmful? (A placebo is not a control)." Amyotroph Lateral Scler Frontotemporal Degener **19**(7-8): 477-482.

Turner, M. R., R. J. Barohn, P. Corcia, J. K. Fink, M. B. Harms, M. C. Kiernan, J. Ravits, V. Silani, Z. Simmons, J. Statland, L. H. van den Berg and H. Mitsumoto (2020). "Primary lateral sclerosis: consensus diagnostic criteria." Journal of Neurology, Neurosurgery & Psychiatry **91**(4): 373.

Turner, M. R., A. Brockington, J. Scaber, H. Hollinger, R. Marsden, P. J. Shaw and K. Talbot (2010). "Pattern of spread and prognosis in lower limb-onset ALS." Amyotrophic lateral sclerosis : official publication of the World Federation of Neurology Research Group on Motor Neuron Diseases **11**(4): 369-373.

Turner, M. R., M. C. Kiernan, P. N. Leigh and K. Talbot (2009). "Biomarkers in amyotrophic lateral sclerosis." Lancet Neurol **8**(1): 94-109.

Turner, M. R., M. J. Parton, C. E. Shaw, P. N. Leigh and A. Al-Chalabi (2003). "Prolonged survival in motor neuron disease: a descriptive study of the King's database 1990-2002." J Neurol Neurosurg Psychiatry **74**(7): 995-997.

Turner, M. R., J. Scaber, J. A. Goodfellow, M. E. Lord, R. Marsden and K. Talbot (2010). "The diagnostic pathway and prognosis in bulbar-onset amyotrophic lateral sclerosis." J Neurol Sci **294**(1-2): 81-85.

Turner, M. R. and K. Talbot (2013). "Mimics and chameleons in motor neurone disease." Pract Neurol **13**(3): 153-164.

Turner, M. R., P. Wicks, C. A. Brownstein, M. P. Massagli, M. Toronjo, K. Talbot and A. Al-Chalabi (2011). "Concordance between site of onset and limb dominance in amyotrophic lateral sclerosis." J Neurol Neurosurg Psychiatry **82**(8): 853-854.

Uemura, M., T. Kosaka, T. Shimohata, M. Ishikawa, Y. Nishihira, Y. Toyoshima, K. Yanagawa, I. Kawachi, H. Takahashi and M. Nishizawa (2013). "Dropped head syndrome in amyotrophic lateral sclerosis." Amyotroph Lateral Scler Frontotemporal Degener **14**(3): 232-233.

Unrath, A., A. C. Ludolph and J. Kassubek (2007). "Brain metabolites in definite amyotrophic lateral sclerosis. A longitudinal proton magnetic resonance spectroscopy study." J Neurol **254**(8): 1099-1106.

Urenjak, J., S. R. Williams, D. G. Gadian and M. Noble (1992). "Specific expression of N-acetylaspartate in neurons, oligodendrocyte-type-2 astrocyte progenitors, and immature oligodendrocytes in vitro." J Neurochem **59**(1): 55-61.

Uslu, S., T. Nüzket and H. Uysal (2018). "Modified motor unit number index (MUNIX) algorithm for assessing excitability of alpha motor neuron in spasticity." Clinical Neurophysiology Practice **3**: 127-133.

Usman, U., C. Choi, R. Camicioli, P. Seres, M. Lynch, R. Sekhon, W. Johnston and S. Kalra (2011). "Mesial prefrontal cortex degeneration in amyotrophic lateral sclerosis: a high-field proton MR spectroscopy study." AJNR Am J Neuroradiol **32**(9): 1677-1680.

Valkovič, L., M. Chmelík and M. Krššák (2017). "In-vivo 31P-MRS of skeletal muscle and liver: A way for non-invasive assessment of their metabolism." Analytical Biochemistry **529**: 193-215.

van Blitterswijk, M., T. F. Gendron, M. C. Baker, M. DeJesus-Hernandez, N. A. Finch, P. H. Brown, L. M. Daughrity, M. E. Murray, M. G. Heckman, J. Jiang, C. Lagier-Tourenne, D. Edbauer, D. W. Cleveland, K. A. Josephs, J. E. Parisi, D. S. Knopman, R. C. Petersen, L. Petrucelli, B. F. Boeve, N. R. Graff-Radford, K. B. Boylan, D. W. Dickson and R. Rademakers (2015). "Novel clinical associations with specific C9ORF72 transcripts in patients with repeat expansions in C9ORF72." Acta Neuropathol **130**(6): 863-876.

van de Bank, B. L., M. C. Maas, L. J. Bains, A. Heerschap and T. W. J. Scheenen (2018). "Is visual activation associated with changes in cerebral high-energy phosphate levels?" Brain Structure and Function **223**(6): 2721-2731.

Van Den Bosch, L., P. Van Damme, E. Bogaert and W. Robberecht (2006). "The role of excitotoxicity in the pathogenesis of amyotrophic lateral sclerosis." Biochimica et Biophysica Acta (BBA) - Molecular Basis of Disease **1762**(11): 1068-1082.

Vance, C., B. Rogelj, T. Hortobagyi, K. J. De Vos, A. L. Nishimura, J. Sreedharan, X. Hu, B. Smith, D. Ruddy, P. Wright, J. Ganesalingam, K. L. Williams, V. Tripathi, S. Al-Saraj, A. Al-Chalabi, P. N. Leigh, I. P. Blair, G. Nicholson, J. de Belleroche, J. M. Gallo, C. C. Miller and C. E. Shaw (2009). "Mutations in FUS, an RNA processing protein, cause familial amyotrophic lateral sclerosis type 6." Science **323**(5918): 1208-1211.

Vance, J. E. (2015). "Phospholipid Synthesis and Transport in Mammalian Cells." Traffic **16**(1): 1-18.

Vanderthommen, M., S. Duteil, C. Wary, J. S. Raynaud, A. Leroy-Willig, J. M. Crielaard and P. G. Carlier (2003). "A comparison of voluntary and electrically induced contractions by interleaved 1H- and 31P-NMRS in humans." J Appl Physiol (1985) **94**(3): 1012-1024.

Vandoorne, T., K. De Bock and L. Van Den Bosch (2018). "Energy metabolism in ALS: an underappreciated opportunity?" Acta neuropathologica **135**(4): 489-509.

Vanhamme, L., A. van den Boogaart and S. Van Huffel (1997). "Improved method for accurate and efficient quantification of MRS data with use of prior knowledge." Journal of magnetic resonance (San Diego, Calif. : 1997) **129**(1): 35-43.

Veech, R. L., J. W. Lawson, N. W. Cornell and H. A. Krebs (1979). "Cytosolic phosphorylation potential." J Biol Chem **254**(14): 6538-6547.

Verber, N. S., S. R. Shepheard, M. Sassani, H. E. McDonough, S. A. Moore, J. J. P. Alix, I. D. Wilkinson, T. M. Jenkins and P. J. Shaw (2019). "Biomarkers in Motor Neuron Disease: A State of the Art Review." Frontiers in Neurology **10**: 291.

Verde, F., K. Del Tredici, H. Braak and A. Ludolph (2017). "The multisystem degeneration amyotrophic lateral sclerosis - neuropathological staging and clinical translation." Arch Ital Biol **155**(4): 118-130.

Verma, G., J. H. Woo, S. Chawla, S. Wang, S. Sheriff, L. B. Elman, L. F. McCluskey, M. Grossman, E. R. Melhem, A. A. Maudsley and H. Poptani (2013). "Whole-brain analysis of amyotrophic lateral sclerosis by using echo-planar spectroscopic imaging." Radiology **267**(3): 851-857.

Vielhaber, S., K. Winkler, E. Kirches, D. Kunz, M. Buchner, H. Feistner, C. E. Elger, A. C. Ludolph, M. W. Riepe and W. S. Kunz (1999). "Visualization of defective mitochondrial function in skeletal muscle fibers of patients with sporadic amyotrophic lateral sclerosis." J Neurol Sci **169**(1-2): 133-139.

Vucic, S. and M. C. Kiernan (2007). "Abnormalities in cortical and peripheral excitability in flail arm variant amyotrophic lateral sclerosis." Journal of Neurology, Neurosurgery & Psychiatry **78**(8): 849.

Vucic, S., A. V. Krishnan and M. C. Kiernan (2007). "Fatigue and activity dependent changes in axonal excitability in amyotrophic lateral sclerosis." Journal of Neurology, Neurosurgery & Psychiatry **78**(11): 1202.

Waite, A. J., D. Bäumer, S. East, J. Neal, H. R. Morris, O. Ansorge and D. J. Blake (2014). "Reduced C9orf72 protein levels in frontal cortex of amyotrophic lateral sclerosis and frontotemporal degeneration brain with the C9ORF72 hexanucleotide repeat expansion." Neurobiol Aging **35**(7): 1779.e1775-1779.e1713.

Walhout, R., E. Verstraete, M. P. van den Heuvel, J. H. Veldink and L. H. van den Berg (2018). "Patterns of symptom development in patients with motor neuron disease." Amyotrophic Lateral Sclerosis and Frontotemporal Degeneration **19**(1-2): 21-28.

Walhout, R., H. J. Westeneng, E. Verstraete, J. Hendrikse, J. H. Veldink, M. P. van den Heuvel and L. H. van den Berg (2015). "Cortical thickness in ALS: towards a marker for upper motor neuron involvement." J Neurol Neurosurg Psychiatry **86**(3): 288-294.

Walker, C., S. Herranz-Martin, E. Karyka, C. Liao, K. Lewis, W. Elsayed, V. Lukashchuk, S. C. Chiang, S. Ray, P. J. Mulcahy, M. Jurga, I. Tsagakis, T. Iannitti, J. Chandran, I. Coldicott, K. J. De Vos, M. K. Hassan, A. Higginbottom, P. J. Shaw, G. M. Hautbergue, M. Azzouz and S. F. El-Khamisy (2017). "C9orf72 expansion disrupts ATM-mediated chromosomal break repair." Nat Neurosci **20**(9): 1225-1235.

Walsh, M. J., J. Cooper-Knock, J. E. Dodd, M. J. Stopford, S. R. Mihaylov, J. Kirby, P. J. Shaw and G. M. Hautbergue (2015). "Invited review: decoding the pathophysiological mechanisms that underlie RNA dysregulation in neurodegenerative disorders: a review of the current state of the art." Neuropathol Appl Neurobiol **41**(2): 109-134.

Wang, H. Y., I. F. Wang, J. Bose and C. K. Shen (2004). "Structural diversity and functional implications of the eukaryotic TDP gene family." Genomics **83**(1): 130-139.

Wang, J., G. Xu and D. R. Borchelt (2006). "Mapping superoxide dismutase 1 domains of non-native interaction: roles of intra- and intermolecular disulfide bonding in aggregation." J Neurochem **96**(5): 1277-1288.

Wang, W., L. Wang, J. Lu, S. L. Siedlak, H. Fujioka, J. Liang, S. Jiang, X. Ma, Z. Jiang, E. L. da Rocha, M. Sheng, H. Choi, P. H. Lerou, H. Li and X. Wang (2016). "The inhibition of TDP-43 mitochondrial localization blocks its neuronal toxicity." Nat Med **22**(8): 869-878.

Wang, Y., X. Li, W. Chen, Z. Wang, Y. Xu, J. Luo, H. Lin and G. Sun (2017). "Detecting neuronal dysfunction of hand motor cortex in ALS: A MRSI study." Somatosens Mot Res **34**(1): 15-20.

Wang, Y., S. Ye, L. Chen, L. Tang and D. Fan (2021). "Loss of appetite in patients with amyotrophic lateral sclerosis is associated with weight loss and anxiety/depression." Scientific Reports **11**(1): 9119.

Webster, C. P., E. F. Smith, C. S. Bauer, A. Moller, G. M. Hautbergue, L. Ferraiuolo, M. A. Myszczynska, A. Higginbottom, M. J. Walsh, A. J. Whitworth, B. K. Kaspar, K. Meyer, P. J. Shaw, A. J. Grierson and K. J. De Vos (2016). "The C9orf72 protein interacts with Rab1a and the ULK1 complex to regulate initiation of autophagy." Embo j **35**(15): 1656-1676.

Wei, Q.-Q., R. Ou, B. Cao, Y. Chen, Y. Hou, L. Zhang, F. Wu and H. Shang (2021). "Early weight instability is associated with cognitive decline and poor survival in amyotrophic lateral sclerosis." Brain Research Bulletin **171**: 10-15.

Weiduschat, N., X. Mao, M. F. Beal, M. J. Nirenberg, D. C. Shungu and C. Henchcliffe (2015). "Usefulness of proton and phosphorus MR spectroscopic imaging for early diagnosis of Parkinson's disease." J Neuroimaging **25**(1): 105-110.

Weiduschat, N., X. Mao, J. Hupf, N. Armstrong, G. Kang, D. J. Lange, H. Mitsumoto and D. C. Shungu (2014). "Motor cortex glutathione deficit in ALS measured in vivo with the J-editing technique." Neurosci Lett **570**: 102-107.

Weisskopf, M. G., M. E. Cudkowicz and N. Johnson (2015). "Military Service and Amyotrophic Lateral Sclerosis in a Population-based Cohort." Epidemiology **26**(6): 831-838.

Westerblad, H., D. G. Allen and J. Lännergren (2002). "Muscle Fatigue: Lactic Acid or Inorganic Phosphate the Major Cause?" Physiology **17**(1): 17-21.

Wiame, E., D. Tyteca, N. Pierrot, F. Collard, M. Amyere, G. Noel, J. Desmedt, M. C. Nassogne, M. Vikkula, J. N. Octave, M. F. Vincent, P. J. Courtoy, E. Boltshauser and E. van Schaftingen (2009). "Molecular identification of aspartate N-acetyltransferase and its mutation in hypoacetylaspartia." Biochem J **425**(1): 127-136.

Wiedemann, F. R., G. Manfredi, C. Mawrin, M. F. Beal and E. A. Schon (2002). "Mitochondrial DNA and respiratory chain function in spinal cords of ALS patients." J Neurochem **80**(4): 616-625.

Wiedemann, F. R., K. Winkler, A. V. Kuznetsov, C. Bartels, S. Vielhaber, H. Feistner and W. S. Kunz (1998). "Impairment of mitochondrial function in skeletal muscle of patients with amyotrophic lateral sclerosis." J Neurol Sci **156**(1): 65-72.

Wijesekera, L. C., S. Mathers, P. Talman, C. Galtrey, M. H. Parkinson, J. Ganesalingam, E. Willey, M. A. Ampong, C. M. Ellis, C. E. Shaw, A. Al-Chalabi and P. N. Leigh (2009). "Natural history and clinical features of the flail arm and flail leg ALS variants." Neurology **72**(12): 1087-1094.

Wilson, M., O. Andronesi, P. B. Barker, R. Bartha, A. Bizzi, P. J. Bolan, K. M. Brindle, I.-Y. Choi, C. Cudalbu, U. Dydak, U. E. Emir, R. G. Gonzalez, S. Gruber, R. Gruetter, R. K. Gupta, A. Heerschap, A. Henning, H. P. Hetherington, P. S. Huppi, R. E. Hurd, K. Kantarci, R. A. Kauppinen, D. W. J. Klomp, R. Kreis, M. J. Kruiskamp, M. O. Leach, A. P. Lin, P. R. Luijten, M. Marjańska, A. A. Maudsley, D. J. Meyerhoff, C. E. Mountford, P. G. Mullins, J. B. Murdoch, S. J. Nelson, R. Noeske, G. Öz, J. W. Pan, A. C. Peet, H. Poptani, S. Posse, E.-M. Ratai, N. Salibi, T. W. J. Scheenen, I. C. P. Smith, B. J. Soher, I. Tkáč, D. B. Vigneron and F. A. Howe (2019). "Methodological consensus on clinical proton MRS of the brain: Review and recommendations." Magnetic Resonance in Medicine **82**(2): 527-550.

Witgert, M., A. R. Salamone, A. M. Strutt, A. Jawaid, P. J. Massman, M. Bradshaw, D. Mosnik, S. H. Appel and P. E. Schulz (2010). "Frontal-lobe mediated behavioral dysfunction in amyotrophic lateral sclerosis." Eur J Neurol **17**(1): 103-110.

Woolley, S. C., M. K. York, D. H. Moore, A. M. Strutt, J. Murphy, P. E. Schulz and J. S. Katz (2010). "Detecting frontotemporal dysfunction in ALS: utility of the ALS Cognitive Behavioral Screen (ALS-CBS)." Amyotroph Lateral Scler **11**(3): 303-311.

Wu, F., J. A. L. Jeneson and D. A. Beard (2007). "Oxidative ATP synthesis in skeletal muscle is controlled by substrate feedback." American Journal of Physiology-Cell Physiology **292**(1): C115-C124.

Yang, L., J. Gal, J. Chen and H. Zhu (2014). "Self-assembled FUS binds active chromatin and regulates gene transcription." Proceedings of the National Academy of Sciences **111**(50): 17809.

Yedavalli, V. S., A. Patil and P. Shah (2018). "Amyotrophic Lateral Sclerosis and its Mimics/Variants: A Comprehensive Review." Journal of clinical imaging science **8**: 53-53.

Zago, S., B. Poletti, M. Corbo, L. Adobbati and V. Silani (2008). "Dysgraphia in patients with primary lateral sclerosis: a speech-based rehearsal deficit?" Behav Neurol **19**(4): 169-175.

Zhang, H., L. Chen, J. Tian and D. Fan (2021). "Disease duration of progression is helpful in identifying isolated bulbar palsy of amyotrophic lateral sclerosis." BMC Neurology **21**(1): 405.

Zhang, K., C. J. Donnelly, A. R. Haeusler, J. C. Grima, J. B. Machamer, P. Steinwald, E. L. Daley, S. J. Miller, K. M. Cunningham, S. Vidensky, S. Gupta, M. A. Thomas, I. Hong, S. L. Chiu, R. L. Huganir, L. W. Ostrow, M. J. Matunis, J. Wang, R. Sattler, T. E. Lloyd and J. D. Rothstein (2015). "The C9orf72 repeat expansion disrupts nucleocytoplasmic transport." Nature **525**(7567): 56-61.

Zhang, Q., C. Mao, J. Jin, C. Niu, L. Bai, J. Dang and M. Zhang (2014). "Side of limb-onset predicts laterality of gray matter loss in amyotrophic lateral sclerosis." Biomed Res Int **2014**: 473250.

Zhang, Y., A. Burberry, J.-Y. Wang, J. Sandoe, S. Ghosh, N. D. Udeshi, T. Svinkina, D. A. Mordes, J. Mok, M. Charlton, Q.-Z. Li, S. A. Carr and K. Eggan (2018). "The C9orf72-interacting protein Smcr8 is a negative regulator of autoimmunity and lysosomal exocytosis." Genes & development **32**(13-14): 929-943.

Zhang, Y., E. Taub, C. Mueller, J. Younger, G. Uswatte, T. P. DeRamus and D. C. Knight (2020). "Reproducibility of whole-brain temperature mapping and metabolite quantification using proton magnetic resonance spectroscopy." NMR in Biomedicine **33**(7): e4313.

Zhang, Y. J., L. Guo, P. K. Gonzales, T. F. Gendron, Y. Wu, K. Jansen-West, A. D. O'Raw, S. R. Pickles, M. Prudencio, Y. Carlomagno, M. A. Gachechiladze, C. Ludwig, R. Tian, J. Chew, M. DeTure, W. L. Lin, J. Tong, L. M. Daughrity, M. Yue, Y. Song, J. W. Andersen, M. Castanedes-Casey, A. Kurti, A. Datta, G. Antognetti, A. McCampbell, R. Rademakers, B. Oskarsson, D. W. Dickson, M. Kampmann, M. E. Ward, J. D. Fryer, C. D. Link, J. Shorter and L. Petrucelli (2019). "Heterochromatin anomalies and double-stranded RNA accumulation underlie C9orf72 poly(PR) toxicity." Science **363**(6428).

Zhou, J., J. Yi, R. Fu, E. Liu, T. Siddique, E. Ríos and H.-X. Deng (2010). "Hyperactive Intracellular Calcium Signaling Associated with Localized Mitochondrial Defects in Skeletal Muscle of an Animal Model of Amyotrophic Lateral Sclerosis." Journal of Biological Chemistry **285**(1): 705-712.

Zhu, Q., J. Jiang, T. F. Gendron, M. McAlonis-Downes, L. Jiang, A. Taylor, S. Diaz Garcia, S. Ghosh Dastidar, M. J. Rodriguez, P. King, Y. Zhang, A. R. La Spada, H. Xu, L. Petrucelli, J. Ravits, S. Da Cruz, C. Lagier-Tourenne and D. W. Cleveland (2020). "Reduced C9ORF72 function exacerbates gain of toxicity from ALS/FTD-causing repeat expansion in C9orf72." Nat Neurosci **23**(5): 615-624.

Zoccolella, S., G. Palagano, A. Fraddosio, I. Russo, E. Ferrannini, L. Serlenga, F. Maggio, S. Lamberti and G. Iliceto (2002). "ALS-plus: 5 cases of concomitant amyotrophic lateral sclerosis and parkinsonism." Neurological Sciences **23**(2): s123-s124.

Zochodne, D. W., R. T. Thompson, A. A. Driedger, M. J. Strong, D. Gravelle and C. F. Bolton (1988). "Metabolic changes in human muscle denervation: topical 31P NMR spectroscopy studies." Magn Reson Med **7**(4): 373-383.